Geoarchaeological Investigations of Late Pleistocene Physical Environments and Impacts of Prehistoric Foragers on the Ecosystem in Northern Malawi and Austria

Dissertation

der Mathematisch-Naturwissenschaftlichen Fakultät

der Eberhard Karls Universität Tübingen

zur Erlangung des Grades eines

Doktors der Naturwissenschaften

(Dr. rer. nat.)

vorgelegt von

Flora Cecilia Schilt

aus Amstelveen, Niederlande

Tübingen

2022

Gedruckt mit Genehmigung der Mathematisch-Naturwissenschaftlichen Fakultät der Eberhard Karls Universität Tübingen.

Tag der mündlichen Qualifikation:	28.10.2022
Dekan:	Prof. Dr. Thilo Stehle
1. Berichterstatter/-in:	Jun.-Prof. Dr. Annett Junginger
2. Berichterstatter/-in:	Prof. Dr. Nicholas Conard
3. Berichterstatter/-in, falls zutreffend	Prof. Dr. Christopher Miller

Doctoral committee

1) Prof. Dr. Christopher Miller (supervisor)

2) Dr. Jessica Thompson (supervisor)

3) Prof. Dr. Nicholas Conard (supervisor)

4) Dr. Annett Junginger (external member)

Acknowledgements

I would like to express my very sincere appreciation to my main supervisor, Prof. Christopher Miller, for his valuable and constructive suggestions during the planning and development of this research. I would also like to thank my second supervisor, Prof. Nicholas Conard, for his supervision and personal support. I feel especially honored to have a third supervisor, Dr. Jessica Thompson, to whom I am very grateful for her endless care in the field and her invaluable insights during the writing of our publications. Dr. Susan Mentzer joined me in the field before the beginning of my PhD and was the real brain behind the initial development of the project. It is thanks to her that I got to work in Malawi. Thank you, Susan! I am also very grateful to Prof. David Wright, who showed me landscape archaeology and whom I joined on many fieldtrips through the Karonga and Mzimba region. It has always been a great pleasure for me to learn from a geoarchaeologist with so much experience in both commercial archaeology and academic research. For my work outside of Malawi, I owe many thanks to Dr. Alexander Verpoorte, who so kindly offered me the chance to study samples from Grub am Kranawetberg. I would like to thank Dr. Annett Junginger for so kindly accepting to review this thesis and take part of the oral committee at my defense. This PhD was only possible because of the funding provided by the German Research Foundation (DFG), for which I am very grateful.

I would also like to extend my thanks to Dr. Peter Kühn at the University of Tübingen, for his helpful insights in matters related to micromorphological analysis and providing me the chance to participate in the micromorphology course with George Stoops in Tübingen. Em. Prof. George Stoops was an incredible teacher and always responsive to my e-mails regarding strange microscopic features in tropical soils. I also much appreciated my correspondence with Dr. Rob Crossley, who shared his observations near Chaminade Church and sent me a copy of one of his more "obscure" publications on fossil termite mounds and carbonate nodule piles.

I would further like to acknowledge my friends and colleagues in Tübingen, Dr. Mareike Stahlschmidt, Dr. Haydar Martinez, Alessandra Zanoni, and many others, and in the Algarve, where I was given the chance to finish writing my final article at the

Interdisciplinary Center for Archaeology and the Evolution of Human Behavior (ICArEHB) in Faro: Dr. Vera Aldeias, Prof. Nuno Bicho, thanks for your support.

Thanks to Dipl.-Ing. Panos Kritikakis, for producing many of my thin sections, and Dr. Christoph Berthold, for letting me use the cathodoluminescence microscopy set-up in the Laboratory for Applied Mineralogy in Tübingen. Many thanks to Dr. Heinrich Taubald, Dr. Christoph Wissing, Prof. Hervé Bocherens, for carrying out isotope analyses on my water and carbonate samples, Dr. Carla Hadden and the Center of Applied Isotope Studies (CAIS) for radiocarbon dating, and Drs. Jian Zhao and Nicole Leonard at the Radiogenic Isotope Facility of Queensland University for assessing the suitability of our carbonate nodules for U-Th series dating. Dr. Michael Toffolo was very helpful in advising me on the dating of pedogenic carbonate nodules with radiocarbon. I enjoyed my time in the field with Prof. Stan Ambrose, and greatly benefited from his broad knowledge and canoeing skills.

I owe many thanks to my MEMSAP colleagues Sheila Nightingale, Jacob Davis, Drs. Andrew Zipkin, Marina Bravo Foster, Scott Robinson, and Victor de Moor. Many thanks to Davie Simengwa, Liton Adhikari, Gervasio Ngumbira, and a local crew including Henry Kalinga, Moses Nyondo, Kondwani Mwafulirwa, Daudi Mwangomba, Gladys Salanga, Violet Chirambo, Frank Kumwenda, Welani Ng'ambi, Petros Mwanganda, Nelson Sichali, Bodwin Kasimba, and many others. I further wish to thank Dr. Elizabeth Gomani Chindebvu, Oris Malijani, Joseph Tembo, Frederick Mapemba, Chrissy Chiumia and Malani Chinula at the Malawi Department of Museums and Monuments, and Menno Welling of African Heritage Research and Consultancy

Finally, I wish to thank my dear parents, Anneke Schilt-Plate and Dirk-Jan Schilt, for their encouragement, as well as my partner Dr. Alvise Barbieri for his loving support.

Table of Contents

List of publications:

A. Wright, D.K., Thompson, J.C., **Schilt, F.C.**, Cohen, A., Choi, J-H., Mercader, J., Nightingale, S., Miller, C.E., Mentzer, S.M., Walde, D., Welling, M., and Gomani Chindebvu, E. "Approaches to Middle Stone Age landscape archaeology in tropical Africa". Special issue Geoarchaeology of the Tropics, *Journal of Archaeological Science* 77:64-77. http://dx.doi.org/10.1016/j.jas.2016.01.014

B. **Schilt, F.C.**, Verpoorte, A., Antl, W. "Micromorphology of an Upper Paleolithic cultural layer at Grub-Kranawetberg, Austria". *Journal of Archaeological Science: Reports* 14:152-162. http://dx.doi.org/10.1016/j.jasrep.2017.05.041

C. Nightingale, S., **Schilt, F.C.**, Thompson, J.C., Wright, D.K., Forman, S., Mercader, J., Moss, P., Clarke, S. Itambu, M., Gomani Chindebvu, E., Welling, M. Late Middle Stone Age Behavior and Environments at Chaminade I (Karonga, Malawi). *Journal of Paleolithic Archaeology* 2-3:258-397. https://doi.org/10.1007/s41982-019-00035-3

D. Thompson, J.C.*, Wright, D.K.*, Ivory, S.J.*, Choi, J-H., Nightingale, S., Mackay, A., **Schilt, F.C.**, Otárola-Castillo, E., Mercader, J., Forman, S.L., Pietsch, T., Cohen, A.S., Arrowsmith, J.R., Welling, M., Davis, J., Schiery, B., Kaliba, P., Malijani, O., Blome, M.W., O'Driscoll, C., Mentzer, S.M., Miller, C., Heo, S., Choi, J., Tembo, J., Mapemba, F., Simengwa, D., and Gomani Chindebvu, E. "Early human impacts and ecosystem reorganization in southern-central Africa". *Science Advances* 7(19): eabf9776. *equal contribution https://doi.org/10.1126/sciadv.abf9776

E. **Schilt, F.C.**, Miller, C.M., Wright, D.K., Mentzer, S.M., Mercader, J., Moss, Choi, J.-H., Siljedal, G., Clarke, S., Mwambwiga, A., Thomas, K., Barbieri, A., Kaliba, P., Gomani Chindebvu, E., Thompson, J.C. "Hunter-gatherer environments at the Late Pleistocene sites of Bruce and Mwanganda´s Village, northern Malawi". *Quaternary Science Reviews* 292: 107638. https://www.sciencedirect.com/science/article/pii/S0277379122002694

Summary

It is becoming increasingly clear that not only did environmental changes play an important role in human evolution, but human behavior in turn has impacted ecosystems and landscape evolution since the late Pleistocene. In this thesis, I have investigated physical paleoenvironments and detected behavioral footprints left by Middle Stone Age (MSA) and middle Upper Paleolithic foragers that lived along the shores of Lake Malawi and in Lower Austria. Geoarchaeological analyses, combining field observations with micromorphology, cathodoluminescence microscopy, Micro X-ray Fluorescence, and Micro Fourier Transform Infrared Spectroscopy, were the backbone of this dissertation, providing context to multiscale ecological results from stable isotope analysis, phytoliths, palynology, and chronometric data from radiocarbon dating and optically stimulated luminescence. Such innovative approach enabled me to reconstruct site formation processes and assess the impacts of human behaviors on local and regional environments.

At Grub-Kranawetberg (Lower Austria), I was able to link the production of combustion-related waste materials by hunter-gatherer activities with soil formation processes, which may have had long-lasting effects on the Late Pleistocene local environment. In the Karonga area (Malawi), where I conducted most of my PhD research, I revealed several aspects of interaction between the local MSA foragers and their dynamic landscapes. My work has helped recognize that late MSA activity and tool production occurred in locally more open riparian environments within a regional vegetation dominated by miombo and evergreen gallery forest. Additionally, I showed that MSA hunter-gatherers exploited the confluence of river and wetland areas at the margins of Lake Malawi, which likely served as important corridors for the dispersal of biota. My work contributed to detecting impacts of burning by MSA hunter-gatherers on vegetation structures and sedimentation in the region, as early as 80 thousand years ago, by comparing data from the archaeological investigations and lake core records. These findings not only proved it possible to uncover ecosystem changes caused by human activity deep in time, but also emphasize the importance of fire in early forager lives in tropical environments. Investigating late Pleistocene open-air sites in Malawi and at Grub-Kranawetberg, I have used the environmental contexts and impacts of human activity to reveal aspects of past human behavior.

Zusammenfassung

Es hat sich gezeigt, dass bereits seit dem späten Pleistozän nicht nur die Umwelt den Mensch in seiner Evolution beeinflusst hat, sondern dass auch umgekehrt der Mensch Einfluss auf die Landschaftsentwicklung und Evolutionsökologie gehabt hat. In meiner Arbeit habe ich untersucht, welche Spuren Menschen in der Mittleren Steinzeit am Malawisee und der jüngeren Altsteinzeit in Niederösterreich diesbezüglich hinterlassen haben. Zu diesem Zweck habe ich mich geoarchäologischer Methoden bedient, der Mikromorphologie, Kathodolumineszenz, mikro- Fourier-Transform-Infrarotspektroskopie und der Röntgenfluoreszenz, die zudem auch den Kontext für andere Analysen gestellt haben, die auf unterschiedlichen Skalen die lokale Ökologie anhand von Isotopen-Untersuchungen, Palynologie, Phytolithen-Analysen sowie für chronometrische Datierungen anhand der Radiokarbonmethode und der Optisch-Stimulierten-Lumineszenz rekonstruiert haben. Dieser innovative Ansatz hat mir erlaubt die Genese der untersuchten Fundplätze zu rekonstruieren sowie auch wie das Verhalten der Menschen an diesen Fundplätze die lokale und regionale Umwelt beeinflusst hat.

In meiner Arbeit an der Fundstelle Grub-Kranawetberg (Niederösterreich) ist es mir gelungen die Ablagerung von Feuer-Abfallprodukte durch den Menschen mit der lokalen Bodenbildungen in Verbindung zu setzen sowie ihre potenzielle lange Auswirkung auf diese. Der Hauptteil meiner Doktorarbeit habe ich in dem Karonga Distrikt (Malawi) durchgeführt und auch hier ist es mir gelungen vielfache Interaktion zwischen lokalen Menschengruppen und ihrer dynamischen Umwelt während der Mittleren Steinzeit Afrikas zu rekonstruieren.

Die Untersuchungsergebnisse zeigen, dass die menschlichen Aktivitäten und die Anfertigung von Stein-Werkzeugen in offenen Bereichen in Flussnähe stattfanden, während die Region selbst aber generell dicht bewaldet war. Zusätzlich hat meine Arbeit gezeigt, dass Jäger-Sammler die Einmündungsbereiche von Flüssen in den Feuchtgebiete entlang des Ufers des Malawisees aufsuchten, wo eine große Artenvielfalt Menschen vermutlich angezogen hat. Weiterhin hat meine Arbeit mit dazu beigetragen frühe Auswirkungen der menschlichen Nutzung von Feuer auf die Zusammensetzung der

lokalen Vegetation und auf Sedimentationsprozesse zu entdecken, dieses konnten wir schon vor 80 tausend Jahre vor heute festhalten. Dies wurde ermöglicht durch den Vergleich der archäologischen Ergebnisse in Karonga mit Daten aus Bohrkernen aus dem Malawisee. Diese Erkenntnisse zeigen, dass es möglich ist, auch in tiefer Vergangenheit Änderungen im Ökosystem durch menschliche Aktivität aufzudecken. Außerdem wurde die Bedeutung von Feuernutzung in frühen Jäger-Sammlergruppen in den Tropen hiermit hervorgehoben. Mit meinen Untersuchungen an Freilandfundstellen in Malawi und Niederösterreich, habe ich örtliche Umweltbedingungen und unbeabsichtigte Auswirkungen von menschlicher Aktivität benutzt, um neue Aspekte über unsere Vorfahren ans Licht zu bringen.

"Some things are worth remembering, and some things are not. That´s all I meant."

"And you can say which is which?"

"No, I can´t. But piling rocks on top of rocks might not be the ticket. Maybe we should admire people the most for living in this jungle without leaving one mark on it."

From *The Lacuna* by Barbara Kingsolver.

Geoarchaeological Investigations of Late Pleistocene Environments and Impacts of Prehistoric Foragers on Ecosystems in Northern Malawi and Austria

Introduction

Background

This doctoral thesis focuses on questions of site formation at open-air sites and the physical environments of hunter-gatherers. Four of the five papers present collaborative work on hunter-gatherer behavior and environments in northern Malawi and the fifth, paper B, is a small-scale micromorphological study of an Upper Paleolithic cultural layer in Lower Austria. The term "geoarchaeology" generally refers to the application of techniques from the geosciences to investigate artifact contexts and anthropogenic sediments and landscapes (Canti, 2001). The central geoarchaeological technique used in this thesis is micromorphology. Micromorphological sample collection was always preceded by detailed field observations and documentation, and thin section analysis with petrographic and stereo microscopes was supplemented by cathodoluminescence microscopy, stable isotope analysis, radiocarbon dating, micro-X-ray fluorescence (μ-XRF), and micro-Fourier transform infrared spectroscopy (μ-FTIR), the latter two techniques performed by Susan Mentzer. A close collaboration existed throughout the project with landscape geoarchaeologist David Wright, allowing for an uninterrupted flow between the different scales of analysis and interpretation.

The investigated archaeological contexts in the Karonga area of northern Malawi (papers A, C, D, and E) consist of geogenic deposits which contain lithic artifacts of the Middle Stone Age (MSA). MSA assemblages are found in Africa from ~315 to 20 thousand years ago [ka] and are associated with an increase in technological complexity among hunter-gatherers, as well as developments in abstract thinking and symbolism (Richter et al., 2017; Brooks et al., 2018; Scerri et al., 2018). At present, most of the MSA archaeological

record comes from a few select regions, such as the southern coast of South Africa and the northern part of the East African Rift System (Mackay, Stewart and Chase, 2014; Wadley, 2015; Scerri, 2017; Tryon, 2019), whereas other parts of Africa remain poorly studied. The country of Malawi, situated within the southern Rift Valley in the important connecting area between eastern and southern Africa, represents one of these understudied regions (Mercader et al., 2009; Bicho et al., 2016; Thompson et al., 2018).

MSA assemblages in the Karonga area are Late Pleistocene in age as they have been dated to between ~70 and ~20 ka (Fig. 1). The open-air sites are located within remnants of a once vast alluvial fan landscape stretching along the shores of Lake Malawi (colored dark red on the geological map, see Fig. 2). These alluvial fan sediments, known as the Chitimwe Bed Formation, have long been recognized as hosting an abundance of MSA and LSA lithic artifacts which are exposed on eroded surfaces, in stream cuts, and in archaeological excavations (Dixey, 1930; Clark, 1966; Thompson et al., 2012; Wright et al., 2017; Nightingale et al., 2019). Dr. Jessica Thompson started investigations in the area in 2010 with a team of researchers and initiated the Malawi Earlier-Middle Stone Age Project (MEMSAP). MEMSAP has taken a landscape approach to be able to build a sequence of regional MSA behavior and environmental conditions, which would not have been possible when considering only a single locality. This has included surveys and test pitting in the Chitimwe Beds (Thompson et al., 2014, 2018, 2021), and more detailed archaeological excavations at specific localities such as Chaminade-I (CHA-I), Chaminade-II (CHA-II), Mwanganda´s Village (MGD), Bruce (BRU), and several others (Fig. 2) (Thompson et al., 2012; Wright et al., 2014, 2017; Nightingale et al., 2019).

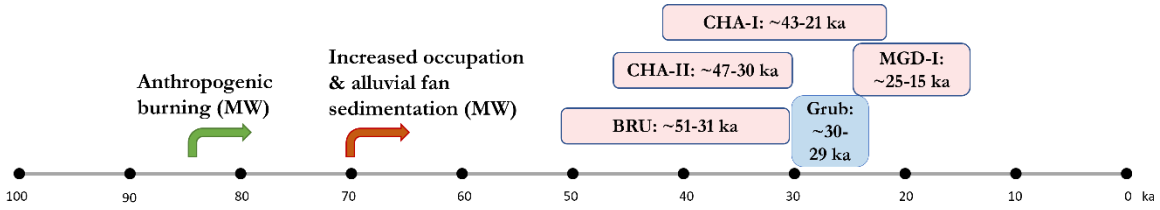

Fig. 1. Timeline showing the age ranges (thousand years [ka] BP) of in situ archaeological assemblages published with micromorphological data (more sites have been reported in other publications, e.g., in Thompson et al., [2012, 2021]). For complete OSL ages of Bruce, see Thompson et al. (2021) and Schilt et al. (2022), for Chaminade-II, see Wright et al. (2017), for Chaminade-I, see Nightingale et al. (2019), for Grub-Kranawetberg (AH4), see Zöller et al. (2013), and for Mwanganda´s Village area I (MGD-I), see Thompson et al. (2012).

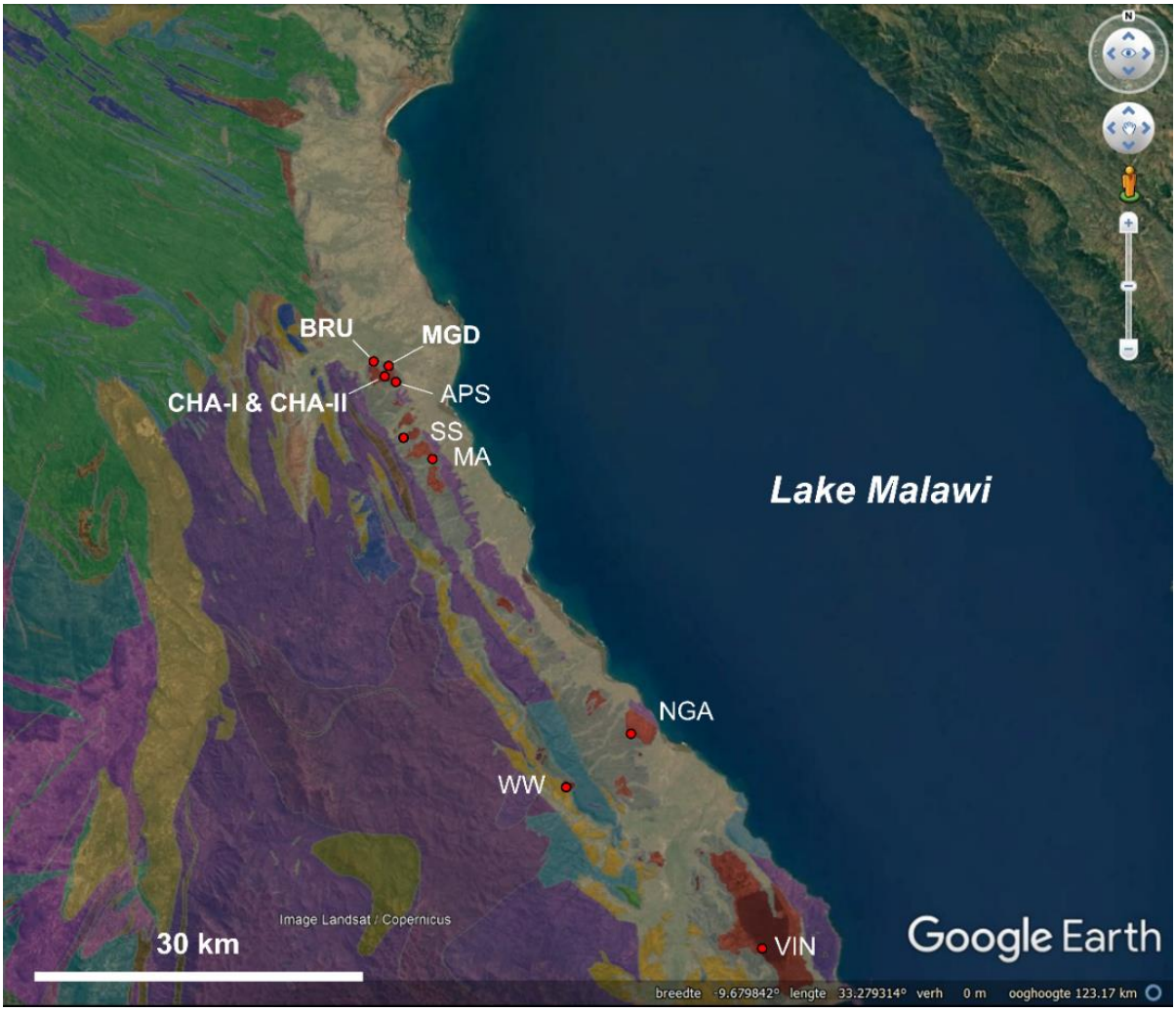

Fig. 2. Digitized geological map (J. Thompson) over Google Earth map showing remnants of Chitimwe alluvial fan (red) along the shores of lake Malawi. These deposits are rich in archaeological remains and have been focus of investigations by the Malawi Earlier-Middle Stone Age Project (MEMSAP). Site locations from which samples for micromorphology were collected before and during the doctoral research project are Mwanganda´s Village (MGD), Bruce (BRU), Chaminade-I (CHA-I), Chaminade-II (CHA-II), Airport Site (APS), Sadala South (SS), Malema (MA), Ngara (NGA), White Whale (WW), and Vinthukutu (VIN). Micromorphological studies of the first four sites, indicated in boldface on the map, have been published and are incorporated in the papers of this thesis. Recent alluvium is colored light gray, Plio-Pleistocene Chiwondo Beds dark gray, Dinosaur beds yellow, Sungwa Beds blue. Basement rocks of the Ubendian Belt (biotite gneiss with amphibolite dykes) are shown in purple. Biotite gneiss, granulites, and schists (Ubendian Belt) are shown in green.

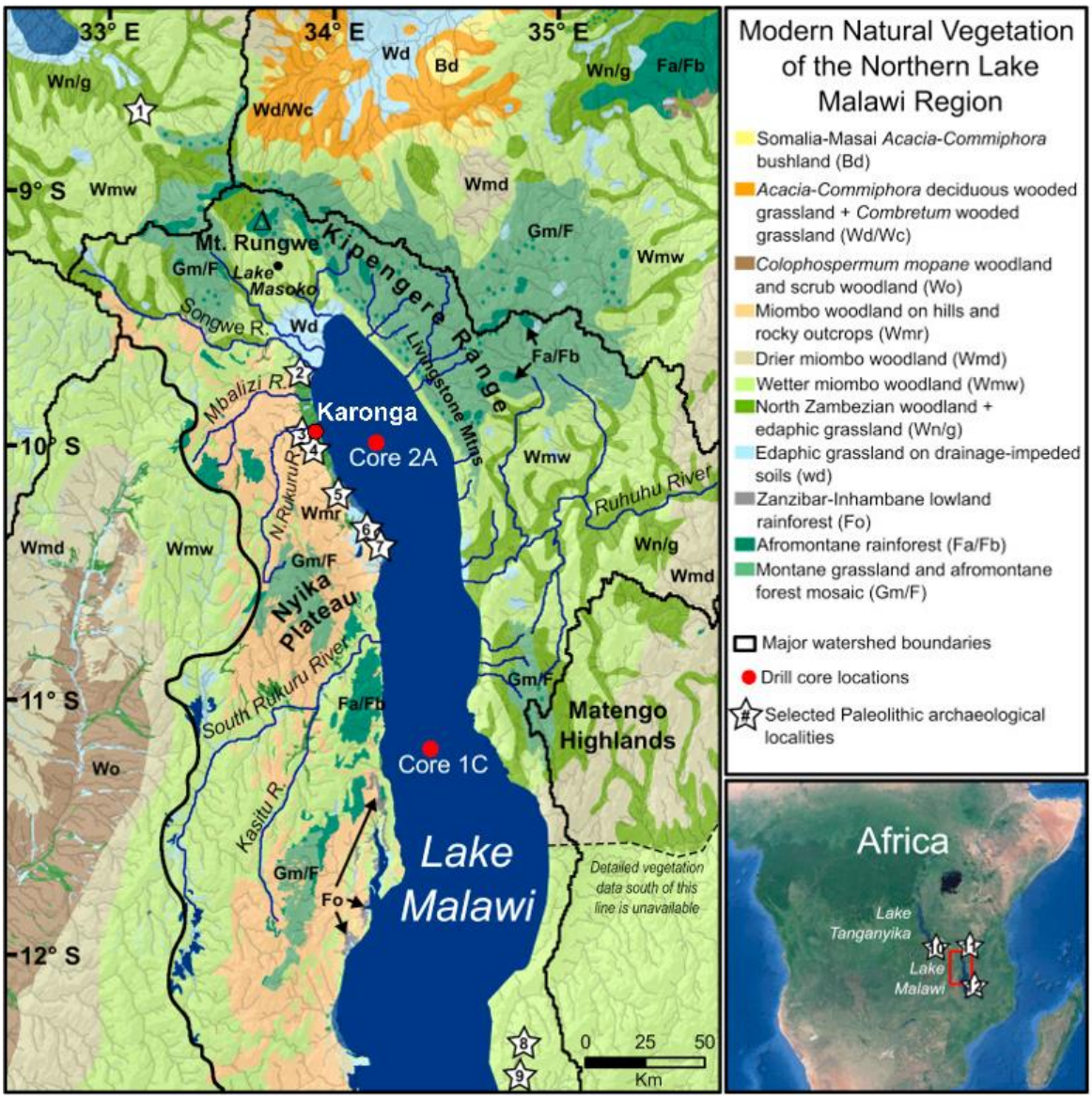

Fig. 3. Map showing potential modern vegetation of the northern Lake Malawi region with the location of two main lake cores (Scholz et al., 2006, 2011; Cohen et al., 2007; Beuning et al., 2011; Lyons et al., 2015). Karonga is situated in an area with North Zambezian woodland (Code: Wn), Miombo woodland on hills and rocky outcrops (Wmr), and patches of edaphic grassland on drainage-impeded or seasonally flooded soils and freshwater swamp (g/X). Modified after Fig. 2 in Yost et al. (2018), which uses GIS data from Potential Natural Vegetation Map of Eastern Africa Version 2.0 (van Breugel et al., 2015).

Today, the Karonga District is situated within the Zambezian Phytogeographic Zone (Fig. 3), and characterized by miombo woodlands composed of a mosaic of Brachystegia trees and variable distributions of savanna grasses, hydromorphic grasses, and evergreen taxa (White et al., 1983; Mercader et al., 2011). The climate is a tropical wet and dry climate or equatorial savanna (category Aw in the Köppen-Geiger climate classification

system) with hot, rainy summers and cool, dry winters (Kottek et al. 2006). Most of the Lake Malawi catchment has only a single rainy season, from November to April or May, because of its location on the southern margin of the Intertropical Convergence Zone. The tropical climate has stronger impacts on the sedimentary and archaeological record than in most environments in the temperate zones. Uninterrupted biological activity and intense chemical and physical weathering of sediments due to heat and moisture changes transform deposits considerably. This creates a wide range of soil formation processes and groundwater effects that may change the color of sediments, merge different deposits, and produce new minerals and precipitates. Some aspects of pedogenesis and site formation can only be viewed and distinguished in thin section, such as different types of clay illuviation, microstructures produced by soil fauna, certain redoximorphic features, and the formation of carbonate- and iron-manganese nodules (Fe-Mn nodules). Micromorphology has proven an extremely useful tool in reconstructing complex formation histories of profiles containing buried paleosols and over-thickened soil horizons, as well as profiles impacted by groundwater fluctuations and termite activity. For example, micromorphology allowed for differentiation between Fe-Mn nodules forming within the soil, redeposited nodules (e.g., as gravel), and nodule concentrations representing buried lag deposits. In combination with cathodoluminescence, micromorphology was also used to reveal the dissolution of siliceous minerals and their replacement by calcite, a critical process in the formation of nodular calcrete horizons.

A different study included in this thesis is from an Upper Paleolithic site in Lower Austria, located in primary aeolian loess deposits. The occupation of the site overlaps with the late MSA occurrences in the Karonga area (Fig. 1). Micromorphological examination of the main find layer and the bordering underlying and overlying sediments exposed anthropogenic and natural site formation processes, including climatic aspects as observed from cryogenic features in the loess deposits. Perhaps most interestingly, soil formation in the main cultural layer was attributed to the substantial input of waste materials from hunter-gatherer activity, and potential effects on the local vegetation are considered.

Evolution of the project

The title of this doctoral project originally read as follows: "A geoarchaeological investigation of Middle Stone Age human response to environmental change on the shores of Lake Malawi". Knowledge of the chronology and environmental contexts of MSA hunter-gatherers in northern Malawi was fragmentary before the beginning of this project, and because of new findings made by MEMSAP and this project, the research focus slightly shifted. When I was writing up the geoarchaeological project for the acquisition of funding from the German Research Foundation (DFG), it was expected that at least some of the sediments and archaeological sites in the Karonga area would date to the end of the Chibanian (Middle Pleistocene). Earlier investigations, first and foremost by Clark and Haynes in the 1960s (1970), had not been able to firmly date the sites but a Chibanian age was suggested for Mwanganda´s Village, based on aspects of the lithic assemblage and the belief that the site had formed in a paleosol within the Chiwondo Beds, a formation attributed to the Pliocene or Early Pleistocene (Dixey, 1927; Stephens, 1963; Clark, Stephens and Coryndon, 1966; Clark and Haynes, 1970). More recently, at the beginning of the 21. century, studies of core records from Lake Malawi showed that lakeshores had transgressed and regressed hundreds of meters in elevation through time, and that before ~85 ka, extreme arid periods of near-desiccation of the lake occurred (Scholz et al., 2006; Cohen et al., 2007; Lyons et al., 2015). Therefore, the suggested age of the site would have implied a temporal overlap between the formation of archaeological assemblages and prolonged (>10 ka) periods of megadrought. One of the original research goals was to investigate whether MSA foragers occupied the reduced lakeshores during periods of megadrought, or whether they abandoned the area. Basell (2008) and Beuning et al. (2011) had argued that during periods of prolonged aridity and tropical heat, MSA populations retreated to local refugia - such as the coastal areas of the African Rift Valley lakes – where they became fragmented and isolated from one another. An important question we intended to address in this project was therefore whether severe climatic fluctuations acted as a driving force behind demographic and behavioral changes during the Pleistocene (Basell, 2008; Blome et al., 2012).

However, extensive dating of the sediments and soils by MEMSAP has shown that the MSA from the Karonga area post-dates 92 ka, with the archaeological record becoming more evident after 70 ka (Thompson et al., 2021). Therefore, MSA activity arises only after the last megadrought and coincides with more stable climatic conditions starting around 85 ka and lasting until today. The relatively high lake levels, attributed to overall wetter conditions, may be a major reason why the region developed an abundant MSA record. Since climatic and environmental fluctuations have been more subtle after 85 ka than during the preceding millennia, the question of "human response" changed its meaning. Instead of investigating human responses to extreme climatic changes and megadroughts, we became interested in local, site-scale differences in physical environments within the larger regional context of human activity in the Karonga area.

By integrating ecological proxies with field observations and microscopic data from the (paleo)pedological and sedimentary record, we reconstructed several site formation histories and were able to integrate behavioral and environmental aspects of MSA activity. Examples of this type of collaborative work are the publications A, C, and E on the sites of Chaminade-II, Chaminade-I, Mwanganda´s Village, and Bruce (Wright et al., 2017; Nightingale et al., 2019, Schilt et al., 2022).

With regards to hunter-gatherer responses to their environment, paper D, led by Thompson, Wright, and Ivory (2021) has shown the flip side of the coin by exposing long-lasting effects of human behavior on the ecosystem. Thompson et al. (2021) were able to demonstrate the impacts of increased anthropogenic burning on plant communities and sedimentation after ~85 ka. A different kind of small-scale environmental response to human occupation emerged from a micromorphological study outside of Malawi (paper B). At the Upper Paleolithic site of Grub-Kranawetberg in Lower Austria, the main archaeological find horizon showed characteristics of an immature soil, which had formed within loess deposits as a side-effect of human occupation and the dispersal of combustion derived materials. To incorporate a study from a geographical area outside of Malawi and include the recursive relationship between hunter-gatherers and their environment, the title of this thesis now reads as follows: "Geoarchaeological investigations of Late Pleistocene

physical environments and impacts of prehistoric foragers on ecosystems in northern Malawi and Austria".

Summary of the objectives

Geoarchaeological investigations of open-air sites in the Karonga district evolved around the following central question: *"Which types of environments attracted Late Pleistocene hunter-gatherer activity in the Karonga area?"*. The reconstruction of paleoenvironments would allow us to consider any underlying factors leading to the archaeological signal and make interpretations about why foragers may have chosen certain physical environments for their activities. The first step we undertook towards answering the central question was the construction of a detailed and chronologically robust model of site formation and landscape development in the Karonga area, for which we used geoarchaeological, ecological, and chronometric methods. After generating site-scale datasets we were able to move to the second step, which consisted of linking Late Pleistocene human activity as evidenced by intact MSA artifact assemblages with physical environments, including the sedimentary environment, paleosols, and vegetation. Ultimately, we compared the on-site evidence with semi-local to regional records, both from the sites themselves (e.g., palynology) as well as from lake core records.

Each paper in this thesis addresses more specific research questions, depending on the archaeology and history of site formation of the individual site localities. However, the basic approach was always the same and consisted of (1) the reconstruction of site formation processes, (2) the reconstruction of on-site palaeoenvironments (with dates on sediments or soil precipitates wherever possible), and (3) the integration of site-scale microarchaeological data with regional environmental proxies. Micromorphology, the central technique for this thesis, was used for the reconstruction of site formation processes and artifact contexts, to optimize the application of coupled carbon and oxygen stable isotope analysis and radiocarbon dating on carbonate nodules, and to provide contextual information for optically stimulated luminescence dating.

The projected outcome of this thesis was the publication of site-scale datasets, consisting of sedimentary, micromorphological, ecological, and chronometric data combined with local to regional proxy data from pollen and phytolith samples collected at the archaeological sites, and compared with basin-wide datasets from lake core records.

The integrated data of these studies shed new light on human paleoenvironments and demonstrate benefits of detailed, multi-scale analyses of open-air tropical sites.

Results and Discussion

This chapter provides brief discussions of the five papers following three overarching themes which place the research into a broader perspective. Papers B and D fall under the first theme, *(I) Prehistoric Human Footprints – the Impact of Human Activity on the Environmental Record*, which addresses evidence of impacts of human activity on the ecosystem, in particular the effects of prehistoric forager behaviors on soil formation, vegetation, and sedimentation.

The second theme, *(II) Site Formation Processes in Alluvial Fan Deposits with Lateritic Soils* discusses the open-air MSA sites of Chaminade-II (paper A) and Chaminade-I (paper C) in northern Malawi. Both works present multi-disciplinary approaches to reconstructing human behavior and environments at stratified open-air sites. Micromorphology was essential to understanding site formation processes as well as providing context to the ecological data and OSL ages.

The last theme, *(III) Where the Alluvial Fan meets the Lagoon,* provides a review of the fifth paper (E). Here, we present data from two sites located on the fringes of the alluvial fan landscape, Mwanganda´s Village and Bruce. Due to the presence of lagoonal clay deposits and calcrete formation, we were able to employ stable isotope analysis and radiocarbon dating on pedogenic carbonate nodules in addition to micromorphology to help firmly date and reconstruct physical environments at the sites.

(I) Prehistoric Human Footprints – the Impact of Human Activity on the Environmental Record (Papers B and D)

It is widely accepted that climate and environment have been essential to human adaptation during prehistory. The effects of human occupation on natural habitats are best known from agricultural and industrial times. However, integrated evidence from archaeology, ecology, and the earth sciences has started to reveal an entanglement of humans with the evolution of their ecosystems, reaching far beyond the beginnings of agriculture and urban landscapes (Sullivan, Bird and Perry, 2017).

One example of an effect of human activity on the ecosystem is the formation of anthropogenic soils. For instance, hortic anthrosols, resulting from slash-and-burn cultivation, are well known from pre-Colombian Amazonia (Arroyo-Kalin, 2012; Glaser and Birk, 2012) and Urban Dark Earth soils commonly formed in European towns during Roman to early Medieval times. Micromorphology has been used intensively to identify the activities and processes leading to the formation of such macroscopically homogenized dark layers (Macphail, Galinié and Verhaeghe, 2003; Devos *et al.*, 2011; Macphail, 2013). Not entirely different from this phenomenon though less dark and homogenized is the archaeological horizon that formed during Upper Paleolithic occupations at Grub-Kranawetberg. This Gravettian site is located on a flat crest overlooking the Morava River valley in Lower Austria (Fig. 4). Archaeological horizons such as found here are a recurrent feature at open-air loess sites in Central and Eastern Europe and are usually recognized in the field as dark layers - contrasting with the light-colored loess - with high concentrations of artifacts as well as other anthropogenic features including hearths, remains of dwelling structures, and bone accumulations. Microscopic studies of these layers can disclose a wealth of additional information about the nature of the human occupation, site formation processes, and paleoenvironments.

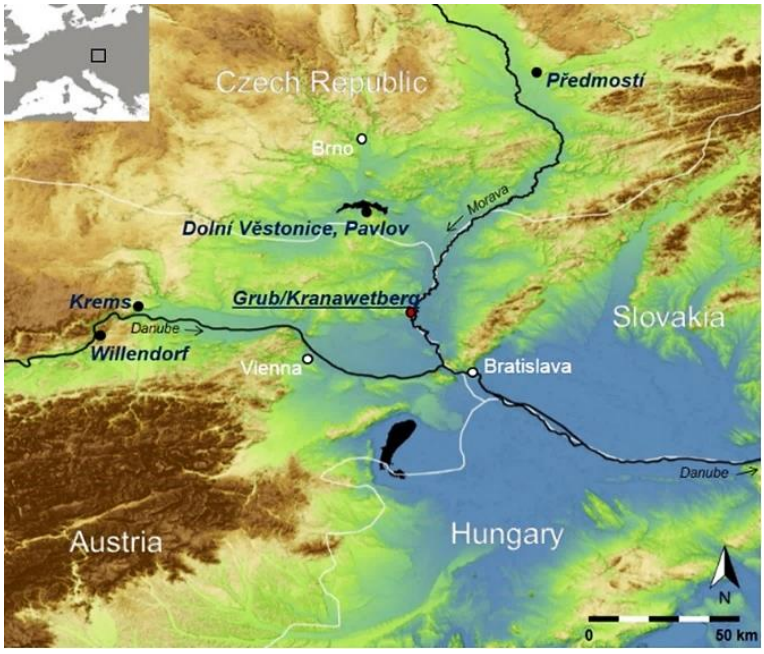

Fig. 4. Location of Grub-Kranawetberg along the Morava River. Other sites indicated on the map are Předmostí, Dolní Věstonice, Pavlov, Krems, and Willendorf. SRTM basemap from Jarvis et al. (2008).

We used a small-scale, micromorphological study of the main archaeological layer at Grub-Kranawetberg to consider cultural horizons as complex representations of the interaction between human activity and natural processes (paper B). The archaeologically sterile loess deposits underlying and overlying the archaeological layer showed impacts of frost-action and redoximorphic processes, but no soil formation except for secondary calcite features and bioturbation in relation to the cultural layer. The cultural layer itself evidenced substantial anthropogenic input of organic and mineral origin with signs of trampling. The horizon has been bioturbated by a diverse soil fauna including mollusks and earthworms. However, signs of redeposition and erosion were absent, and the occupation surface appeared to be preserved. Human waste likely influenced the diversity and composition of the plant communities by enhancing nutrient availability and soil faunal activity. This cultural layer demonstrates that waste from hunter-gatherer activity modified local ecosystems already during the Late Pleistocene and that anthropogenic soils are not limited to agricultural economies and urbanization.

Micromorphology as a technique was developed for the study of soils and urban dark earths, hortic anthrosols and cultural horizons are very suitable for analysis in thin section. However, other aspects of the environment may have been impacted by prehistoric foragers as well. The effects of human hunting on prey diversity are one example, but also the influence of anthropogenic burning on vegetation structures has received much attention. Vegetation modification resulting from the use of fire as landscape management tool has been documented as early as 50.000 years ago in Borneo (Hunt, Gilbertson and Rushworth, 2012). A recent study by Roebroeks et al. (2021) went even further back in time. Roebroeks et al. (2021) used well-preserved, fine-scale environmental records from two neighboring lake basins at Neumark-Nord to investigate the effect of intensive use of one of the two lake-shore sites by Neanderthals on vegetation structures for a period of ~2000 years during the Last Interglacial. Their comparative data suggests that the more open vegetation at the archaeological site location is attributable to Neanderthal presence. In the fourth paper of this thesis (D, Thompson et al. 2021), we looked at a similar problem but across time, combining vegetation and charcoal records from lake cores with data from the archaeological sites which provided age-constraints of MSA human activity in the Karonga area and alluvial fan aggradation. Different from Neumark-Nord, the sedimentary

and climatic context in northern Malawi does not offer a fine stratigraphy suitable for high-resolution dating. We were able to identify the earliest coupled evidence for human behavior and ecosystem transformation in the context of anthropogenic fire by linking the archaeology and geomorphology of the now extensively dated Stone Age landscape of the Karonga region to paleoenvironmental data spanning > 600 ka. The study of large-scale vegetation structures from lake core records revealed a vegetation turnover to increased human burning in the area after 85 ka, reflected by a less diverse, fire-tolerant vegetation regime. In addition, OSL ages of alluvial fan deposits at archaeological sites and test pits showed evidence of alluvial fan expansion after ~92 ka. The increase in alluvial fan sedimentation has been attributed to changes in seasonal burning as reduced tree-cover and soil stripping would have enhanced runoff and hillslope erosion. This may explain the close correlation between increased human habitation of the area and alluvial fan aggradation, resulting in multiple sites within lateritic soils in the Chitimwe Beds. In the supplementary text, detailed background is provided on the sediments and soils in the Karonga area and specifically the formation of carbonate nodules, which were sub-sampled for radiocarbon dating (appendix, pp. 213-220).

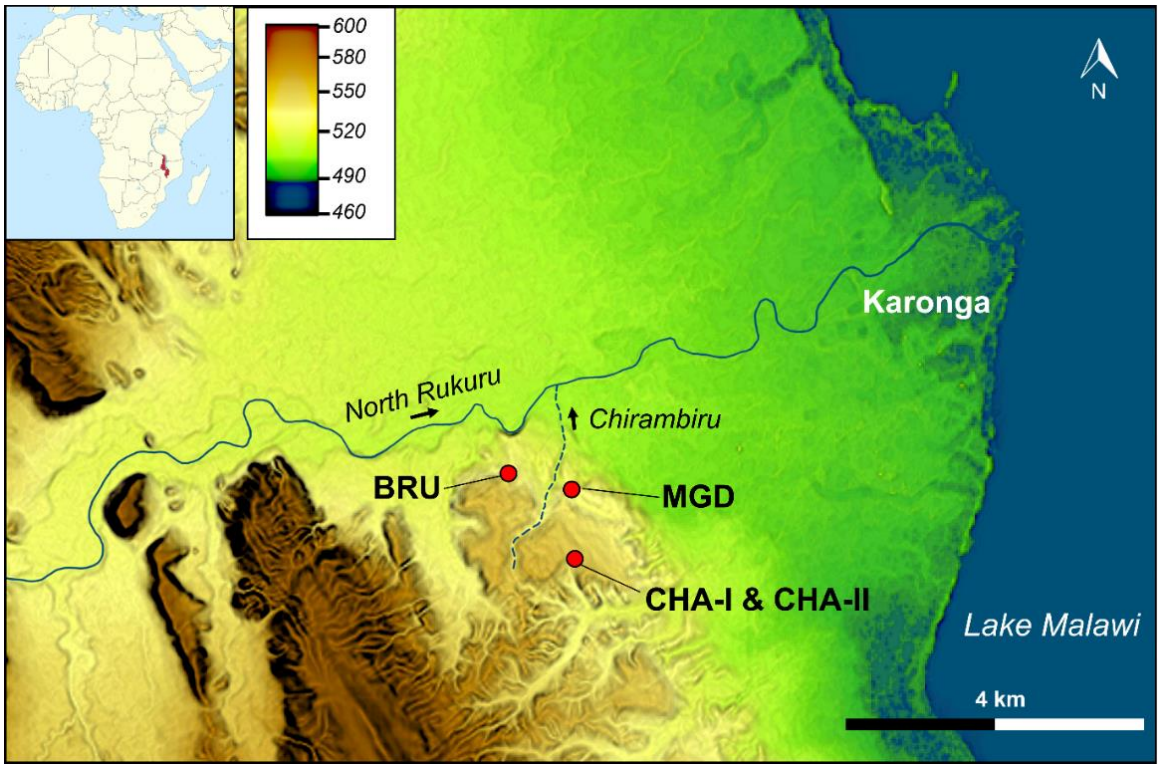

Fig. 5. Map of Map of the area west of Karonga town indicating the site locations of Bruce (BRU), Mwanganda´s Village (MGD), Chaminade-I (CHA-I), and Chaminade-II (CHA-II) (map produced with AW3D30 data).

(II) Site Formation Processes in Alluvial Fan Deposits with Lateritic Soils (Papers A and C)

Papers A and C address geoarchaeological challenges faced in the humid tropics. In these environments, the preservation of organic materials is limited, particularly in acidic sediments such as the alluvial fan deposits of the Chitimwe Formation, which have high amounts of quartz and feldspar. The only preserved archaeological finds are therefore lithics, which are eroding from the surface in many places and have been recovered in stratigraphy from multiple excavations and test pits. The high temperatures, seasonal rainfall, and uninterrupted biological activity typical for the area enhance processes of mixing and weathering, which may influence artifact distributions and transform the color, composition, and texture of sediments. Although the sites of Chaminade-I and Chaminade-II (CHA-I and CHA-II) are only 100 meters apart (Fig. 5), the sediments, formation processes, and archaeology at the two sites are very distinct. Thin section analysis was used to study the origin of iron-manganese nodules and their relation to the artifacts as well as

the impacts of termite activity, long-term mineral weathering, and groundwater fluctuations on the sedimentary and archaeological record.

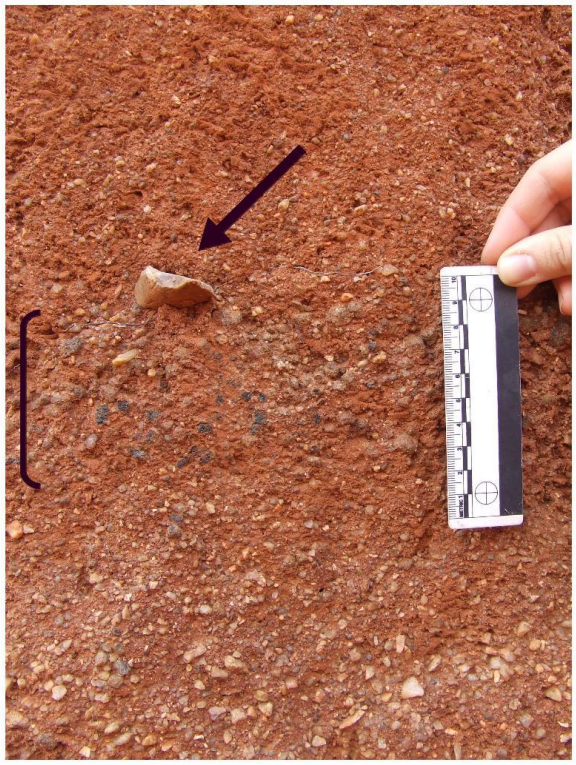

Fig. 6. Close-up of Chaminade II East Profile. Fe-Mn nodules occur at the level of the bracket and the arrow indicates a lithic artifact.

Paper A was published in a special issue of the *Journal of Archaeological Science*, edited by Mike Morley and Paul Goldberg. The journal issue brought together a series of papers under the topic of "Geoarchaeology in the Humid Tropics: Practice, Problems, Prospects". With the example of the site of CHA-II our work, headed by David Wright, presents an approach to interpreting MSA sequences from open-air sites in tropical environments, using sedimentology, micromorphology, OSL and phytolith analyses to examine the site taphonomy. Buried stone artifact assemblages at CHA-II were dated to between 47 and 30 ka. Since termites are notorious for altering the archaeological record and are important for laterite formation, micromorphology focused on post-depositional modifications in the profiles. We wanted to investigate the concentration of coarse-grained sediment and artifacts in the lower parts of a profile (Fig. 6) because while on the one hand they may

reflect human littering on a buried ground surface, they may also result from natural processes. One hypothesis, proposed by Crossley (1986) for a profile he studied nearby Chaminade Secondary School, was carefully considered. The role of termites in the formation of sediments is well documented in stone lines, especially in Australia (Smith, Ward and Moffat, 2020). Fungus-growing Macrotermitinae are widespread in Africa and are known to remove materials from deep soil horizons towards the topsoil to construct their mounds and surface-galleries (Lee and Wood, 1971). Based on granulometric analyses of the sand sheets and termite mounds in the Chaminade area, Crossley (1986) had concluded that the vertical, upward transfer of selected sand grains (max. 4 mm) by *Macrotermes falciger* termites led to the accumulation of sand sheets with concentrated larger particles (e.g., gravel) and lithic artifacts in the lower reaches of the solum. At CHA-II, however, we found no indications for this. Instead, we found that Bt horizon overthickening and the formation of vertic features associated with soil formation and groundwater variability degraded the integrity of bedding features in the profile commonly found in alluvial deposits, making the deposits appear similar to biomantles to the naked eye.

Also, the formation and movement within the soil of iron-manganese nodules received much attention. These are often reported to form as redoximorphic features in lower parts of the soil under the influence of groundwater fluctuations (Vepraskas, Wilding and Drees, 1993). At Chaminade however, the nodules formed within the upper, lateritic soil profile as pedogenic features. The incorporation of sands of different origin in the nodules during their formation provided clues for understanding potential post-depositional movement of artifacts. The reconstruction of site formation at CHA-II is illustrated in Fig. 7. With the outlined multi-disciplinary approach, we were able to reconstruct a riparian environment for MSA human activity within a grassy woodland zone.

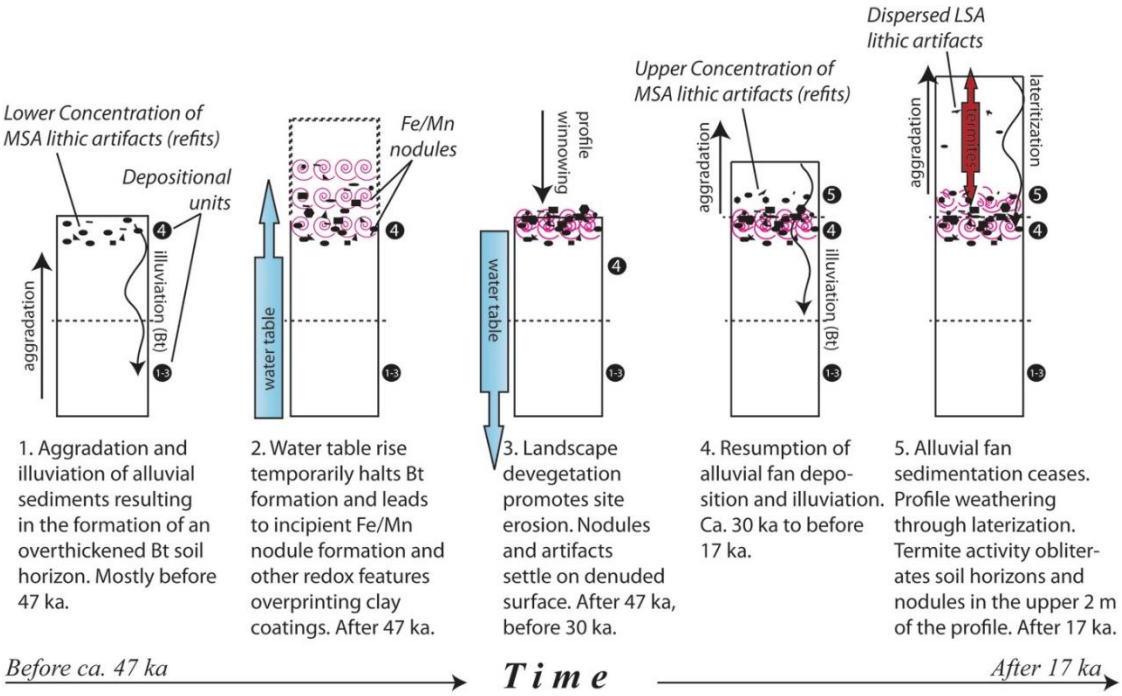

Fig. 7. Site formation model for Chaminade-II.

Underscoring this interpretation of MSA hunter-gatherers seeking out riparian environments, our other Chaminade paper (paper C), headed by lithic specialist Sheila Nightingale (2019), placed human behavior in a forested riparian context surrounded by open woodland. The paper discusses two concentrations of lithic artifacts from the late MSA (~43-21 ka) at Chaminade-I, and the reasons for their lack of elaboration in technology. The flexible and generalized approach to stone tool production challenges the linear idea that complexity always increases over time. Toolstone is abundant throughout the Karonga area, and no pieces of clear exotic origin were found. It appears that reduction efforts were not focused on extracting as many flakes from one core as possible. Through refitting, Nightingale shows that MSA people were not only visiting riparian areas for toolstone, but spent time within the active riparian system. The artifact contexts and underlying and overlying deposits were studied in thin section, supplementing detailed field observations. Fig. 8 illustrates the most relevant processes, with Fe-Mn nodules deposited as gravel in the lower artifact context and pedogenic Fe-Mn nodules forming in place at the level of the upper artifact concentration, slightly moving downward due to vertic soil processes (shrink-swell) and bioturbation. As opposed to the irregular coarse sandy nodules

at CHA-II, the Fe-Mn nodules at CHA-I are rounded and composed of concentric bands, reflecting distinct phases of formation. The smal size and concentricity of the nodules is related to the finer texture of the source sediment and to vertic activity within the soil (Delvigne, 1998).

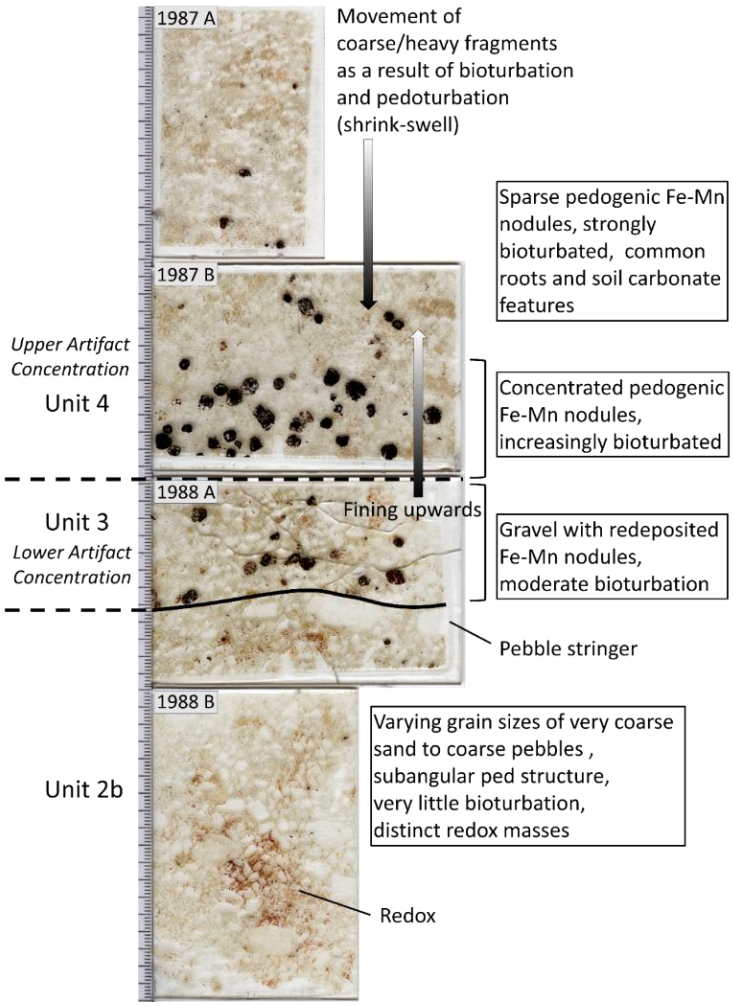

Fig. 8. Scans of thin sections from the artifact contexts and bounding deposits with summarized observations and unit boundaries indicated. The lower three thin sections are 60 x 90 mm and the topmost is 51 x 76 mm.

(III) Where the Alluvial Fan Meets the Lagoon (Paper E)

Mwanganda´s Village (MGD) and Bruce (BRU) are located on the distal end of the alluvial fan. The site complexes, each with three archaeological excavation areas and multiple test pits, have deposits dated to between 1 and 58 ka. MSA lithic assemblages at MGD date to between 15 and 25 ka, and multiple assemblages at BRU date to between 31 and 51 ka (see

Figs. 1 and 5 for site locations). Both sites were investigated by Desmond Clark and colleagues in the 1960s but the chronometric and site formation data necessary for their interpretation were still lacking. MEMSAP located and reinvestigated the sites (Thompson, Welling and Gomani Chindebvu, 2013; Wright et al., 2014) and similar to the sites of Chaminade, samples were collected for OSL dating, micromorphology, palynology, and phytolith analysis. However, the stratigraphy was different from the locations on more proximal parts of the alluvial fan. At MGD and BRU, initial alluvial fan deposition has been interrupted by the ingression of lakeshore lagoonal water, as inferred from thick deposits of finely laminated silty clay. This wetland episode and its deposits determined the types of soil that formed later at the sites. The poor permeability of the lagoonal clay created a perched water table and allowed for the formation of stage 3 nodular calcrete horizons within mixed deposits in the top of the clay unit both at MGD and in parts of BRU (Machette, 1985; Wright, 1990). We took advantage of the occurrence of these nodular calcrete paleosols and collected nodule samples, following a protocol that allowed us to study carbonate nodules in thin section before further sub-sampling for stable isotope analysis and radiocarbon dating (Mentzer and Quade, 2013). This was essential for determining the mechanism responsible for the formation of the carbonate nodules, as only pedogenic carbonates form in clear connection with a stable ground surface, while for example the formation of groundwater carbonates is unconnected to soil formation, making the interpretation of radiocarbon dates and environmental proxies from such nodules more ambiguous and possibly unrelated to any phase or landform stability.

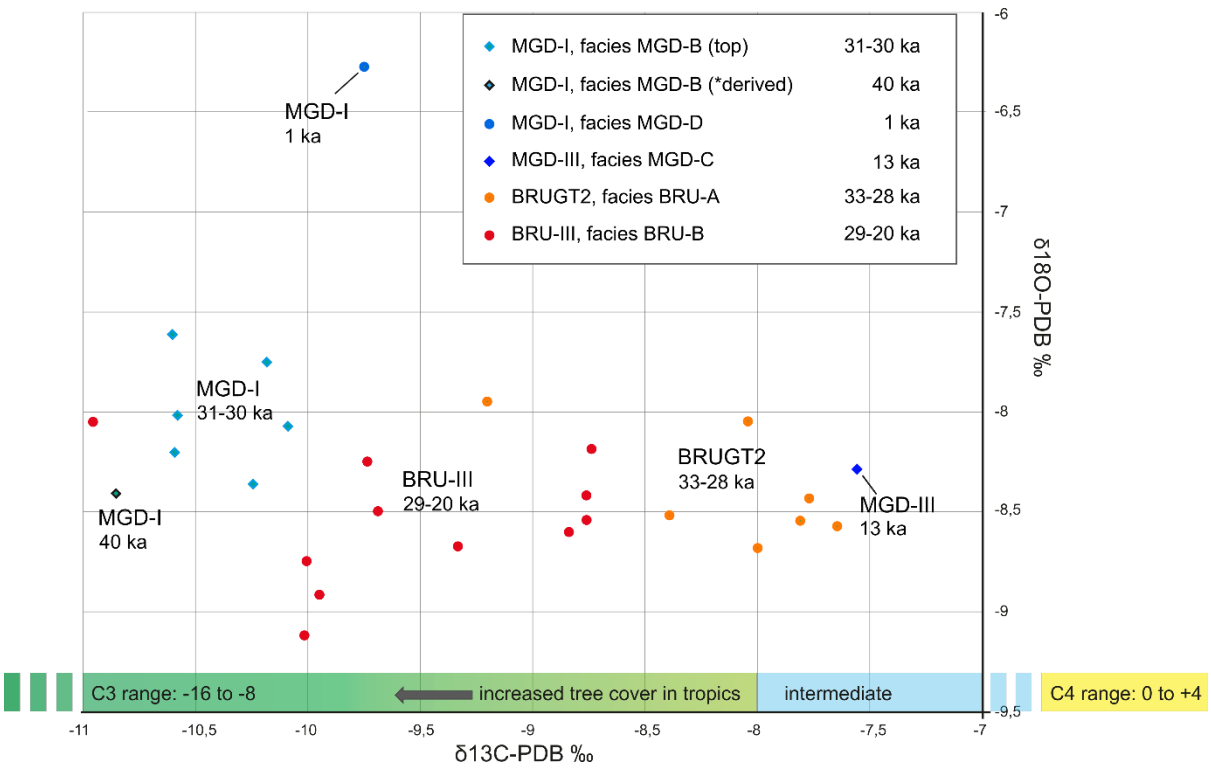

Fig. 9. Scatterplot of the $\delta^{13}C_{PC}$ and $\delta^{18}O_{PC}$ values (both presented relative to PDB) from carbonate nodules collected according to facies with the ranges of radiocarbon dates (cal BP) indicating the time of their formation, ante quem. The bar at the bottom on the x-axis shows the ranges of C_3 and C_4 vegetation, with more negative $\delta^{13}C_{PC}$ values associated with denser tree cover. The original isotopic compositions in organic matter, before carbonate formation, are between −20‰ and −35‰ for plants following the C_3 photosynthetic pathway, and between −9‰ and −17‰ or plants following the C_4 photosynthetic pathway (Cerling and Quade, 1993). Due to fractionation, pedogenic carbonates forming below C_3 vegetation have values between -16‰ and -8‰, and C_4 vegetation, shown in yellow, has values between 0‰ and +4‰. The values for C_4 vegetation lie to the right from the shown ranges on the x-axis of the scatterplot (-7‰ to -11‰ δ13C-PDB), and the distance has been truncated.

Stable carbon and oxygen isotopes were used to reconstruct aspects of vegetation and climate during soil formation (Fig. 9). Carbon stable isotopes can provide information on types of vegetation, as plants use different mechanisms for carbon fixation, making them suited for different habitats. The different mechanisms, C_3, C_4, and CAM, lead to different isotope signatures. In tropical environments, C_3 plants are common in warm areas with abundant water, so that most trees, herbs and shrubs follow the C_3 carbon fixation pathway, whereas grasses follow the C_4 pathway. In pedogenic carbonate, the carbon isotope signal is enriched by about 14 permille, because of CO_2 diffusion in the soil and equilibrium fractionation during carbonate precipitation. Oxygen stable isotopic compositions in pedogenic carbonate ($\delta^{18}O_{PC}$) derive from $\delta^{18}O$ of regional meteoric water

($\delta^{18}O_{MW}$), which is related to temperature, precipitation regimes, and evaporation (Kowler, 2007; Golubtsov et al., 2014). Enrichment of ^{18}O in pedogenic carbonates occurs with isotopic fractionation during carbonate precipitation, which is determined by soil temperature (Zanchetta et al., 2000).

Micromorphology was performed on 80 large thin sections (60 x 90 and 51 x 76 mm), and 15 small thins sections (45 x 26 mm) of carbonate samples from pedogenic carbonates and groundwater-carbonate from Chiwondo Bed deposits (Fig. 10). Using this technique, I was able to demonstrate how mixing of coarse sands from the alluvial fan into the top portion of the lagoonal clays have created loamy textures, which do not reflect the original sedimentary environment, but early stages of soil formation. Mineral weathering was observed in calcrete horizons, where carbonate physically replaced siliceous minerals during of short-term conditions of extreme alkalinity (pH >9), especially evident when using cathodoluminescence (Fig. 10a).

Thin section analysis of the sediments and textures in lateritic profiles of the alluvial fan at BRU indicates that the original clay and silt content of the alluvial fan sediments at BRU may have been negligible, and that their presence in the sediments today is primarily the result of chemical and physical weathering of feldspars and alkali granite, sandstone, and gneiss within the soil. This suggests that in granulometric or soil-chemical studies, the formation and modification of sediments and artifact concentrations by termites needs to be backed by a solid understanding of the mineral weathering processes active in the soil.

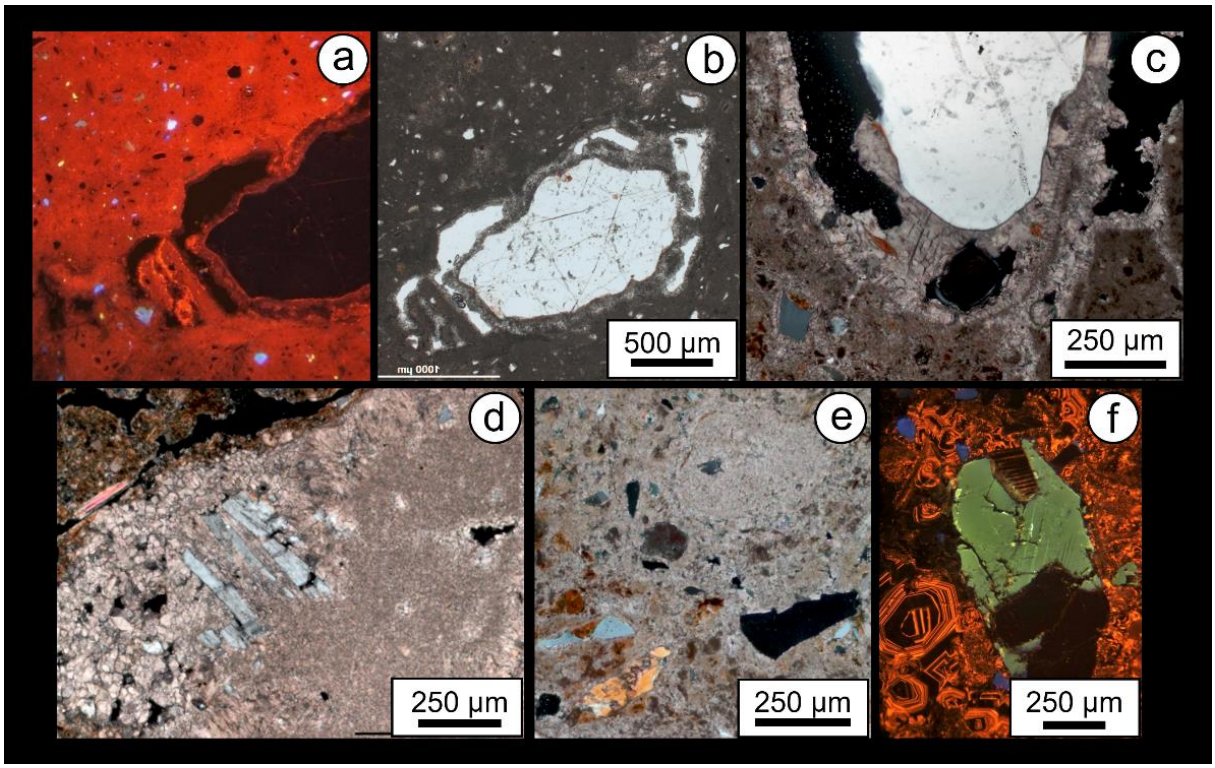

Fig. 10. Photomicrographs illustrating dissolution (a, b, c) and brecciation (d) of siliceous minerals (feldspar, clay and clay coatings, quartz) in pedogenic carbonate nodules (a-e) and groundwater carbonate (f). The upper left and lower right images are taken with cathodoluminescence, in which calcite appears red, and feldspars mostly green or yellow, and quartz mostly blue. While the calcite crystals in pedogenic carbonate (a) are small, micritic to (micro)sparitic, crystal sizes in groundwater carbonate are much larger, as seen in the rosette-shaped structures in (f). Image (b) was taken with plane polarized light, and (c-e) were taken with crossed-polarized light.

While MSA foragers repeatedly visited BRU between ~51-31 ka, an in-situ terminal MSA occupation at MGD, dating to after 26 ka, is one of the latest intact MSA assemblages known from Africa (Barton et al. 2013; Barton et al. 2016; Bader et al. 2018). The environmental reconstruction at this site enabled us to demonstrate that the MSA exploitation of forested riparian environments perpetuated into the latest Pleistocene. Our findings revealed that MSA hunter-gatherers might have chosen MGD and BRU not only due to the presence of riparian environments but also because these localities were positioned at the confluence of river and wetland areas, which serve as important corridors for the dispersal of biota (Wantzen et al. 2008). Therefore, MGD and BRU likely offered a wider range of resources to MSA people crucial for foraging and tool production.

Outlook

In geoarchaeology, we rarely get to study well-preserved anthropogenic materials and deposits such as in waterlogged or frozen contexts or, more commonly, in the protected environments of caves and rock shelters. Such sites are invaluable for our understanding of past human life. However, in many parts of the world there are no caves. More importantly, the study of open-air locations may offer different information on how people used the landscape, which we would miss if only certain types of archaeological site were investigated. My study at Grub-Kranawetberg targeted an occupation horizon in loess deposits which has acted as an anthropogenic soil. The location in central Europe and the cold conditions at the onset of the Last Glacial Maximum likely aided in the preservation of this archaeological site. In tropical environments, open-air sites can be found but do not usually preserve anthropogenic sediments. The alluvial fan landscape along the shores of Lake Malawi presents an environment where organic materials and anthropogenic deposits are lacking. Nevertheless, lithic artifact assemblages within the alluvial fan deposits show that the area was occupied by MSA hunter-gatherer populations over the course of tens of thousands of years and must have been of great significance to our Late Pleistocene ancestors. I was able to confirm the presence of stratified archaeological material across the Karonga region. By focusing on sites in different locations across a large alluvial fan remnant, I identified several processes that have impacted these stratified open-air sites, including changes in water table, the incursion of a lake lagoon onto the distal end of the alluvial fan, termite activity, lateritization, calcrete formation, and surface winnowing. Pedogenic and post-depositional processes clearly play a central role in the formation history of tropical, African open-air sites. A multi-proxy and high-resolution approach allowed me to identify these processes and directly assess their impact on the archaeological materials. Even though sediments at different locations may at first look similar due to the iron oxide-rich lateritic soils that characterize the surficial deposits of the region, our work has shown that there is no one-size-fits-all formation model for archaeological sites in the Karonga region. Different formation histories and a complex set of variables may result in the preservation of a buried paleosol in one site and its absence in a neighboring area.

Despite the different settings of Chaminade I, Chaminade II, Bruce, and Mwanganda's Village, all sites showed evidence for human exploitation of riparian and patchy environments, at times bordering marshy wetlands. These findings point toward a behavioral selection of these types of setting, possibly not just for the collection of raw material for stone tool production, but also for the extraction of food resources and for other activities. This study furthermore contributed to the discovery that the MSA humans of Karonga used fire as a means for managing and modifying the landscape surrounding the northern reaches of Lake Malawi.

This work demonstrates that the combination of a tailored set of geoarchaeological analyses with ecological proxies can be effective in creating multi-scale landscape, environmental, and behavioral reconstructions, even in a dynamic tropical landscape with limited organic preservation. Our open-air sites were positioned in riparian and wetland-adjacent physical environments, offering intact archaeological assemblages within contexts potentially preserving a wide variety of paleoenvironmental data that may be directly tied into the history of open-air hunter-gatherer occupations. Without disregarding the importance of exploring new environmental settings to increase our understanding of prehistoric forager activity throughout the landscape, future research in the tropics might target similar depositional environments.

References and Cited Sources

Arroyo-Kalin, M. (2012) 'Slash-burn-and-churn: Landscape history and crop cultivation in pre-Columbian Amazonia', *Quaternary International*, 249, pp. 4–18. doi:10.1016/J.QUAINT.2011.08.004.

Basell, L.S. (2008) 'Middle Stone Age (MSA) site distributions in eastern Africa and their relationship to Quaternary environmental change, refugia and the evolution of Homo sapiens', *Quaternary Science Reviews*, 27(27–28), pp. 2484–2498. doi:10.1016/J.QUASCIREV.2008.09.010.

Beuning, K.R.M. *et al.* (2011) 'Vegetation response to glacial-interglacial climate variability near Lake Malawi in the southern African tropics', *Palaeogeography, Palaeoclimatology, Palaeoecology*, 303(1–4), pp. 81–92. doi:10.1016/j.palaeo.2010.01.025.

Bicho, N. *et al.* (2016) 'Middle and Late Stone Age of the Niassa region, northern Mozambique. Preliminary results', *Quaternary International*, 404, pp. 87–99. doi:10.1016/j.quaint.2015.09.059.

Blome, M.W. *et al.* (2012) 'The environmental context for the origins of modern human diversity: A synthesis of regional variability in African climate 150,000–30,000 years ago', *Journal of Human Evolution*, 62(5), pp. 563–592. doi:10.1016/J.JHEVOL.2012.01.011.

van Breugel, P. *et al.* (2015*)* Potential Natural Vegetation Map of Eastern Africa (Burundi, Ethiopia, Kenya, Malawi, Rwanda, Tanzania, Uganda and Zambia)*, Forest & Landscape Denmark and World Agroforestry Centre (ICRAF).*

Brooks, A.S. *et al.* (2018) 'Long-distance stone transport and pigment use in the earliest Middle Stone Age', *Science*, 360(6384), pp. 90–94.

Canti, M. (2001) 'What is Geoarchaeology? Re-Examining the Relationship Between Archaeology and Earth Science', in Umberto Albarella (ed.) *Environmental Archaeology: Meaning and Purpose*. Springer, Dordrecht, pp. 103–112. doi:10.1007/978-94-015-9652-7_13.

Cerling, T.E. and Quade, J. (1993) 'Stable carbon and oxygen isotopes in soil carbonates', in Swart, P.K. et al. (eds) *Climate Change in Continental Isotopic Records, Volume 78*. Geophysica.

American Geophysical Uniion, pp. 217–231. doi:10.1029/gm078p0217.

Clark, J.D. (1966) 'Initial Investigation of the Archeology of Karonga District, Malawi', *American Anthropologist*, 68(2), pp. 67–87. doi:10.1525/aa.1966.68.2.02a00990.

Clark, J.D. and Haynes, C.V. (1970) 'An elephant butchery site at Mwanganda's Village, Karonga, Malawi, and its relevance for Palaeolithic archaeology', *World Archaeology*, 1(3), pp. 390–411. doi:10.1080/00438243.1970.9979455.

Clark, J.D., Stephens, E.A. and Coryndon, S.C. (1966) 'Pleistocene Fossiliferous Lake Beds of the Malawi (Nyasa) Rift: A Preliminary Report', *Source: American Anthropologist, New Series Recent Studies in Paleoanthropology*, 68(2), pp. 46–87. doi:10.1525/aa.1966.68.2.02a00960.

Cohen, A.S. *et al.* (2007) 'Ecological consequences of early Late Pleistocene megadroughts in tropical Africa.', *Proceedings of the National Academy of Sciences*, 104(42), pp. 16422–7. doi:10.1073/pnas.0703873104.

Crossley, R. (1986) 'Sedimentation by termites in the Malawi Rift Valley', *Geological Society, London, Special Publications*, 25(1), pp. 191–199. doi:10.1144/GSL.SP.1986.025.01.16.

Delvigne, J. (1998) *Atlas of Micromorphology of Mineral Alteration and Weathering*, *The canadian Mineralogist*. Available at: http://petrology.oxfordjournals.org/content/41/3/475.2.short.

Devos, Y. *et al.* (2011) 'Unravelling urban stratigraphy. The study of Brussels' (Belgium) Dark Earth. An archaeopedological perspective', *Medieval and Modern Matters*, 2, pp. 51–76. doi:10.1484/J.MMM.1.102776.

Dixey, F. (1927) 'The Geology of Nyasaland', *Quarterly Journal of the Geological Society*, 83(3), pp. 432–47.

Dixey, F. (1930) *Stone implements from the Chitimwe beds, North Nyasa. Annual Report of the Geological Survey Department, Nyasaland.*

Glaser, B. and Birk, J.J. (2012) 'State of the scientific knowledge on properties and genesis of Anthropogenic Dark Earths in Central Amazonia (terra preta de Índio)', *Geochimica et Cosmochimica Acta*, 82, pp. 39–51. doi:10.1016/J.GCA.2010.11.029.

Golubtsov, V.A. *et al.* (2014) 'Stable carbon and oxygen isotopes in pedogenic carbonate

coatings of chernozems in the Southern Cis-Baikalia as indicators of local environmental changes', *Eurasian Soil Science*, 47(10), pp. 1015–1026. doi:10.1134/S1064229314100032.

Hunt, C.O., Gilbertson, D.D. and Rushworth, G. (2012) 'A 50,000-year record of late Pleistocene tropical vegetation and human impact in lowland Borneo', *Quaternary Science Reviews*, 37, pp. 61–80. doi:10.1016/J.QUASCIREV.2012.01.014.

Jarvis, A. *et al.* (2008) *Hole-filled Seamless SRTM Data, Version 4*, *International Centre for Tropical Agriculture (CIAT)*.

Kowler, A. (2007) 'The Stable Carbon and Oxygen Isotopic Composition of Pedogenic Carbonate and its Relationship to Climate and Ecology in Southeastern Arizona', p. 57. Available at: http://www.geo.arizona.edu/Antevs/Theses/KowlerAL_07.pdf.

Lee, K.E. and Wood, T.G. (1971) *Termites and soils*. London: Academic Press, London.

Lyons, R.P. *et al.* (2015) 'Continuous 1.3-million-year record of East African hydroclimate, and implications for patterns of evolution and biodiversity', *Proceedings of the National Academy of Sciences*, 112(51), p. 201512864. doi:10.1073/pnas.1512864112.

Machette, M.N. (1985) 'Calcic soils of the southwestern United States', in, pp. 1–22. doi:10.1130/SPE203-p1.

Mackay, A., Stewart, B.A. and Chase, B.M. (2014) 'Coalescence and fragmentation in the Late Pleistocene archaeology of southernmost Africa', *Journal of Human Evolution*, 72, pp. 26–51.

Macphail, R.I. (2013) 'Reconstructing past land use from dark earth: examples from England and France', *Archéologie de l'espace urbain*, pp. 251–261. doi:10.4000/BOOKS.PUFR.7676.

Macphail, R.I., Galinié, H. and Verhaeghe, F. (2003) 'A future for Dark Earth?', *Antiquity*, 77(296), pp. 349–358. doi:10.1017/S0003598X00092334.

Mentzer, S.M. and Quade, J. (2013) 'Compositional and Isotopic Analytical Methods in Archaeological Micromorphology', *Geoarchaeology*, 28(1), pp. 87–97. doi:10.1002/gea.21425.

Mercader, J. *et al.* (2009) 'Initial excavation and dating of Ngalue Cave: A Middle Stone Age

site along the Niassa Rift , Mozambique', *Journal of Human Evolution*, 57, pp. 63–74. doi:10.1016/j.jhevol.2009.03.005.

Mercader, J. *et al.* (2011) 'Soil phytoliths from miombo woodlands in Mozambique', *Quaternary Research*, 75(1), pp. 138–150. doi:10.1016/J.YQRES.2010.09.008.

Nightingale, S. *et al.* (2019) 'Late Middle Stone Age Behavior and Environments at Chaminade I (Karonga, Malawi)', *Journal of Paleolithic Archaeology*, 2(3), pp. 258–297. doi:10.1007/s41982-019-00035-3.

Richter, D. *et al.* (2017) 'The age of the hominin fossils from Jebel Irhoud, Morocco, and the origins of the Middle Stone Age', *Nature*, 546(7657), pp. 293–296.

Roebroeks, W. *et al.* (2021) 'Landscape modification by Last Interglacial Neanderthals', *Science Advances*, 7(51), p. 5567. doi:10.1126/sciadv.abj5567.

Scerri, E.M. *et al.* (2018) 'Did our species evolve in subdivided populations across Africa, and why does it matter?', *Trends in Ecology & Evolution*, 33(8), pp. 582–584.

Scerri, E.M.L. (2017) 'The North African Middle Stone Age and its place in recent human evolution', *Evolutionary Anthropology: Issues, News, and Reviews*, 26(3), pp. 119–135.

Schilt, F.C. *et al.* (2017). Micromorphology of an Upper Paleolithic cultural layer at Grub-Kranawetberg, Austria. Journal of Archaeological Science: Reports 14:152-162. http://dx.doi.org/10.1016/j.jasrep.2017.05.041

Schilt, F.C. *et al.* (2022). Hunter-gatherer environments at the Late Pleistocene sites of Bruce and Mwanganda´s Village, northern Malawi. *Quaternary Science Reviews* 292: 107638. https://doi.org/10.1016/j.quascirev.2022.107638

Scholz, C. a. *et al.* (2006) 'The 2005 Lake Malawi Scientific Drilling Project', *Scientific Drilling*, (2, March 2006), pp. 2005–2007. doi:10.2204/iodp.sd.2.04.2006.

Scholz, C.A. *et al.* (2011) 'Scientific drilling in the Great Rift Valley: The 2005 Lake Malawi Scientific Drilling Project - An overview of the past 145,000years of climate variability in Southern Hemisphere East Africa', *Palaeogeography, Palaeoclimatology, Palaeoecology*, 303(1–4), pp. 3–19. doi:10.1016/j.palaeo.2010.10.030.

Smith, M.A., Ward, I. and Moffat, I. (2020) 'How do we distinguish termite stone lines from artefact horizons? A challenge for geoarchaeology in tropical Australia', *Geoarchaeology*, 35(2), pp. 232–242. doi:10.1002/GEA.21766.

Stephens, E.A. (1963) 'Geological Account of the Northwest Coast of Lake Malawi Between Karonga and Lion Point, Malawi', *American Anthropologist*, 68(2), pp. 50–58. doi:10.1525/aa.1966.68.2.02a00970.

Sullivan, A.P., Bird, D.W. and Perry, G.H. (2017) 'Human behaviour as a long-term ecological driver of non-human evolution', *Nature Ecology & Evolution 2017 1:3*, 1(3), pp. 1–11. doi:10.1038/s41559-016-0065.

Thompson, J.C. *et al.* (2012) 'Renewed investigations into the Middle Stone Age of northern Malawi', *Quaternary International*, 270, pp. 129–139. doi:10.1016/j.quaint.2011.12.014.

Thompson, J.C. *et al.* (2014) 'Catchment Survey in the Karonga District: a Landscape-Scale Analysis of Provisioning and Core Reduction Strategies During the Middle Stone Age of Northern Malawi', *African Archaeological Review*, 31(3), pp. 447–478. doi:10.1007/s10437-014-9167-2.

Thompson, J.C. *et al.* (2018) 'Ecological risk, demography and technological complexity in the Late Pleistocene of northern Malawi: implications for geographical patterning in the Middle Stone Age', *Journal of Quaternary Science*, 33(3), pp. 261–284. doi:10.1002/jqs.3002.

Thompson, J.C. *et al.* (2021) 'Early human impacts and ecosystem reorganization in southern-central Africa', *Science Advances*, 7(9776), pp. 1–13. Available at: https://advances.sciencemag.org/content/7/19/eabf9776.

Thompson, J.C., Welling, M. and Gomani Chindebvu, E. (2013) 'Using GIS to Integrate Old and New Archaeological Data from Stone Age Deposits in Karonga, Malawi', *International Journal of Heritage in the Digital Era*, 2(4), pp. 611–630. doi:10.1260/2047-4970.2.4.611.

Tryon, C.A. (2019) 'The Middle/Later Stone Age transition and cultural dynamics of late Pleistocene East Africa', *Evolutionary Anthropology*, 28(5), pp. 267–282. doi:10.1002/evan.21802.

Vepraskas, M.J., Wilding, L.P. and Drees, L.R. (1993) 'Aquic conditions for Soil Taxonomy: concepts, soil morphology and micromorphology', *Developments in Soil Science*, 22(C), pp. 117–131. doi:10.1016/S0166-2481(08)70402-1.

Wadley, L. (2015) 'Those marvellous millennia: the Middle Stone Age of Southern Africa', *Archaeological Research in Africa*, 50(2), pp. 155–226.

White, F. (Frank) *et al.* (1983) 'Vegetation of Africa : a descriptive memoir to accompany the Unesco/AETFAT/UNSO vegetation map of Africa', p. 356.

Wright, D.K. *et al.* (2014) 'Renewed Geoarchaeological Investigations of Mwanganda's Village (Elephant Butchery Site), Karonga, Malawi', *Geoarchaeology*, 29(2), pp. 98–120. doi:10.1002/gea.21469.

Wright, D.K. *et al.* (2017) 'Approaches to Middle Stone Age landscape archaeology in tropical Africa', *Journal of Archaeological Science*, 77, pp. 64–77. doi:10.1016/j.jas.2016.01.014.

Wright, V.P. (1990) 'A Micromorphological Classification of Fossil and Recent Calcic and Petrocalcic Microstructures', *Developments in Soil Science*, 19(C), pp. 401–407. doi:10.1016/S0166-2481(08)70354-4.

Yost, C.L. *et al.* (2018) 'Subdecadal phytolith and charcoal records from Lake Malawi, East Africa imply minimal effects on human evolution from the ~74 ka Toba supereruption', *Journal of Human Evolution*, 116, pp. 75–94. doi:10.1016/j.jhevol.2017.11.005.

Zanchetta, G. *et al.* (2000) 'Stable isotopes of pedogenic carbonates from the somma-vesuvius area,southern Italy,over the past 18 kyr: palaeoclimatic implications', *Journal of Quaternary Science*, 15(8), pp. 813–824. doi:10.1002/1099-1417(200012)15:8<813::AID-JQS566>3.0.CO;2-Z.

Zöller, L. *et al.* (2013) 'Luminescence chronology of the Grub-Kranawetberg site, Austria', *E&G Quaternary Science Journal*, 62(2), pp. 127–135. doi:10.3285/eg.62.2.04.

Appendix

A. Wright, D.K., Thompson, J.C., Schilt, F.C., Cohen, A., Choi, J.-H., Mercader, J., Nightingale, S., Miller, C.E., Mentzer, S.M., Walde, D., Welling, M., and Gomani Chindebvu, E. (2017). Approaches to Middle Stone Age landscape archaeology in tropical Africa. Special issue Geoarchaeology of the Tropics of *Journal of Archaeological Science* 77: 64-77.

B. Schilt, F. C., Verpoorte, A., Antl, W. (2017). Micromorphology of an Upper Paleolithic cultural layer at Grub-Kranawetberg, Austria. *Journal of Archaeological Science: Reports* 14:152-162.

C. Nightingale, S., Schilt, F.C., Thompson, J.C., Wright, D.K., Forman, S., Mercader, J., Moss, P., Clarke, S. Itambu, M., Gomani Chindebvu, E., Welling, M. (2019). Late Middle Stone Age Behavior and Environments at Chaminade I (Karonga, Malawi). *Journal of Paleolithic Archaeology* 2-3:258-397.

D. Thompson, J.C., Wright, D.K., Ivory, S.J., Choi, J.-H., Nightingale, S., Mackay, A., Schilt, F.C., Otárola-Castillo, E., Mercader, J., Forman, S.L., Pietsch, T., Cohen, A.S., Arrowsmith, R., Welling, M., Davis, J., Schiery, B., Kaliba, P., Malijani, O., Blome, M.W., O´Driscoll, C.A., Mentzer, S.M., Miller, C.E., Heo, S., Choi, J., Tembo, J., Mapemba, F., Simengwa, D., Gomani Chindebvu, E. (2021) Early human impacts and ecosystem reorganization in southern-central Africa, *Science Advances* 7(9776):1–13.

E. Schilt, F.C., Miller, C.E., Wright, D.K., Mentzer, S.M., Mercader, J., Moss, P., Choi, J.-H., Siljedal, G., Clarke, S., Mwambwiga, A., Thomas, K., Barbieri, A., Kaliba, P., Gomani Chindebvu, E., Thompson, J.C. (2022). Hunter-gatherer environments at the Late Pleistocene sites of Bruce and Mwanganda´s Village, northern Malawi. Manuscript under review at Quaternary Science Reviews.

Appendix: Papers with corresponding supplementary materials for the PhD thesis of Flora Schilt entitled "***Geoarchaeological investigations of Late Pleistocene physical environments and impacts of prehistoric foragers on the ecosystem in northern Malawi and Austria"***

Table of Contents

A - Approaches to Middle Stone Age Landscape Archaeology in Tropical Africa

David K. Wright [a, b, *], Jessica C. Thompson [c], Flora Schilt [d], Andrew S. Cohen [e], Jeong-Heon Choi [f], Julio Mercader [g], Sheila Nightingale [h], Christopher E. Miller [i], Susan M. Mentzer [d, j], Dale Walde [g], Menno Welling [k], Elizabeth Gomani Chindebvu [l]

[a] Department of Archaeology and Art History, Seoul National University, Seoul, 08826, South Korea. [b] University of York, Department of Archaeology, York, YO1 7EP, United Kingdom. [c] Department of Anthropology, Emory University, Atlanta, GA, 30322, USA. [d] Institute for Archaeological Sciences, University of Tübingen, Tübingen, 72070, Germany. [e] Departments of Geosciences AND Ecology and Evolutionary Biology, University of Arizona, Tucson, AZ, 85721, USA. [f] Geochronology Group, Korean Basic Science Institute, Chungbuk, 363-883, South Korea. [g] Department of Anthropology and Archaeology, University of Calgary, Calgary, AB, T2N 1N4, Canada. [h] Department of Anthropology, City University of New York, New York, NY, 10016, USA. [i] Institute for Archaeological Sciences AND Senckenberg Centre for Human Evolution and Paleoenvironment, University of Tübingen, Tübingen, 72070, Germany. [j] School of Anthropology, University of Arizona, Tucson, AZ, 85721, USA. [k] African Heritage Research and Consultancy, PO Box 622, Zomba, Malawi. [l] Malawi Ministry of Tourism, Wildlife, and Culture, Lilongwe 3, Malawi

ARTICLE INFO

Article history: Received 29 June 2015; Received in revised form 14 December 2015; Accepted 29 January 2016; Available online 19 February 2016

Keywords: Middle Stone Age; Tropical African paleoenvironments; Micromorphology; Optically Stimulated Luminescence; Phytolith analysis; Site formation processes; Alluvial fans

Full citation:

Wright, D.K., Thompson, J.C., Schilt, F.C., Cohen, A., Choi, J.-H., Mercader, J., Nightingale, S., Miller, C.E., Mentzer, S.M., Walde, D., Welling, M., and Gomani Chindebvu, E. (2017). Approaches to Middle Stone Age landscape archaeology in tropical Africa. Special issue Geoarchaeology of the Tropics of *Journal of Archaeological Science* 77: 64-77. http://dx.doi.org/10.1016/j.jas.2016.01.014

ABSTRACT

The Southern Montane Forest-Grassland mosaic ecosystem in the humid subtropics southern Rift Valley of Africa comprised the environmental context for a large area in which modern human evolution and dispersal occurred. Variable climatic conditions during the Late Pleistocene have ranged between humid and hyperarid, changing the character of the ecosystem and transforming it at different points in time into a barrier, a refuge, and a corridor between southern and eastern African populations. Alluvial fans presently blanket the areas adjacent to major river systems, which were key areas of prehistoric human habitation. These sets of variables have created conditions that are both challenging and advantageous to conduct archaeological research. Lateritic soil development has resulted in poor organic preservation and facilitated insect bioturbation, which has demanded an integrated micro-macro scale approach to building a reliable geochronology. An integrated field and analytical methodology has also been employed to identify the nature and degree of post-depositional movement in alluvial deposits, which preserve a wide range of spatial integrity levels in buried stone artifact assemblages between 47 and 30 ka in Karonga, northern Malawi. This paper describes the methodological advances taken toward understanding open-air Middle Stone Age archaeology in sub-tropical Africa, and explores the inferential potential for understanding Pleistocene human ecology in the important southern Rift Valley region.

Keywords: Middle Stone Age; Tropical African paleoenvironments; Micromorphology; Optically Stimulated Luminescence; Phytolith analysis; Site formation processes; Alluvial fans

INTRODUCTION

The Middle Stone Age (MSA) of Africa shows some of the earliest clear archaeological evidence for many behaviors that are either unique to or especially well developed in modern humans (d'Errico and Stringer, 2011; McBrearty and Brooks, 2000). As a typo-technological unit, the MSA is defined by the significant presence of prepared core technology, nascent forms of symbolic expression and the absence of large bifacial tools such as handaxes, spanning from ca. 285 thousand years ago (ka) to ca. 20 ka (Conard, 2015; Sahle et al., 2014; Tryon and Faith, 2013). Much of the evidence for the MSA comes from more temperate parts of Africa, both in the

southern (Brown et al., 2012; Henshilwood et al., 2011; Lombard, 2011; Porraz et al., 2013) and northern parts of the continent (d'Errico et al., 2009; Linstädter et al., 2012). This record is also heavily biased toward the long archives of human behavior that are found in cave or rock shelter sites.

There is a need to advance methods to understand the depositional and taphonomic context for open-air MSA sites in tropical and subtropical ecosystems. New geoarchaeological approaches are tailored for these situations and have equipped researchers with tools to investigate the environmental backdrop of cultural diversifications by MSA people that were critical in defining the trajectory of Pleistocene human evolution. Herein, we present a multi-tiered approach to the interpretation of open-air MSA archaeological sites in alluvial settings in Karonga, northern Malawi, which draws from well-vetted techniques but combines them in novel ways. High-resolution spatial analysis using 3- dimensional (3D) Geographical Information Systems (GIS) and refitting from piece-plotted archaeological excavations reveal whether archaeological deposits have been disturbed by secondary processes. Micromorphological data provide information about modes of deposition, pedogenesis and bioturbation, contextualizing their potential to alter the Optically Stimulated Luminescence (OSL) dosing environment used to estimate the ages of the sites. Integration of data from phytoliths allows for cross-referencing of macro- and micro-scale sedimentary environment observations, and developing terrestrial vegetation histories. Finally, by comparing data from archaeological contexts with a nearby high-resolution lacustrine paleoenvironmental record from Lake Malawi and adjacent regions, a model can be developed that explains human behavioral patterns in response to climatic changes throughout the Late Pleistocene. We describe these approaches to MSA sites in the tropics with specific reference to Chaminade II (CHA-II), which is typical of many archaeological sites in the Karonga District in its depositional context and artifactual composition.

BACKGROUND

The southern Rift Valley of Africa is a critical, yet little-explored geographic transition zone for understanding the evolution and diversification of MSA populations across Africa. Near the modern town of Karonga, Malawi (Fig. 1), pioneering research by Desmond Clark and Vance Haynes in the 1960s (Clark and Haynes,1970; Clark et al., 1970, 1966), followed by more intensive geoarchaeological investigations by Zefe Kaufulu (1983, 1990), demonstrated the high potential of the region's archaeological record to reveal information about the MSA in tropical and

subtropical ecosystems. However, the lack of absolute ages made it difficult to tie the human behavioral record to the significant paleoenvironmental changes the area experienced over the course of the Late Pleistocene (Cohen et al., 2007; Lane et al., 2013; Scholz et al., 2011, 2007). More recently, work by the Malawi Earlier-Middle Stone Age Project (MEMSAP) has revised interpretations of sites first studied by Clark and colleagues (Clark and Haynes, 1970; Clark et al., 1970, 1966) describing the spatial-temporal distribution and attributes of artifactual assemblages and artifact raw material sources near Karonga (Thompson et al., 2014, 2012, 2013; Wright et al., 2014; Zipkin et al., 2015).

Tropical and subtropical regions of Africa are located within the most productive biotic environments in the world (Grace et al., 2006), and, as such, present a unique cluster of opportunities and pitfalls for archaeological research. In addition to intensive and sustained agriculture and other land use practices that involve movement of sediment, bioturbation from termites (e.g., Crossley, 1986; McBrearty, 1990; Mercader et al., 2003), burrowing mammals and lizards, and fluvial winnowing (Schick, 1987; Yellen, 1996) all provide opportunity for disturbance of primary archaeological deposits. In addition, groundwater percolation (Schick, 1987; Sitzia et al., 2012; Stewart et al., 2012; Yellen, 1996), biomantle formation ("soil upbuilding"; Ahr et al., 2012; Araujo, 2013; Johnson et al., 2005; Phillips and Lorz, 2008; Van Nest, 2002) and pedogenic processes translocating minerals down the solum (Eren et al., 2014; Feathers, 2002; Gliganic et al., 2012) have been identified as potential factors affecting site taphonomy.

In northern Malawi, downwarping and fault-trough sedimentation during the Middle to Late Pleistocene (Betzler and Ring, 1995; Ebinger et al., 1993) in combination with variable climatic conditions (Crossley, 1984; Stone et al., 2011) activated alluvial fans and streams, which created riparian environments attractive to MSA people (Thompson et al., 2014, 2012; Wright et al., 2014). The remains of MSA activities in the Karonga region are embedded in remnants of an alluvial fan system known as the Chitimwe Beds (Clark and Haynes, 1970; Clark et al., 1970; Kaufulu, 1990; Wright et al., 2014). Alluvial fans can rapidly bury occupation surfaces and rework older deposits. Because many of the sediments have been subsequently modified through pedogenesis and bioturbation, artifacts can change their stratigraphic position and are often found in association with paleosols that formed at a later date. The materials and methods employed by MEMSAP were tailored to address these specific taphonomic conditions of the Karonga sites, which fall within an equatorial savanna with a dry winter (Aw) of the Köppen-Geiger classification system (Kottek et al., 2006).

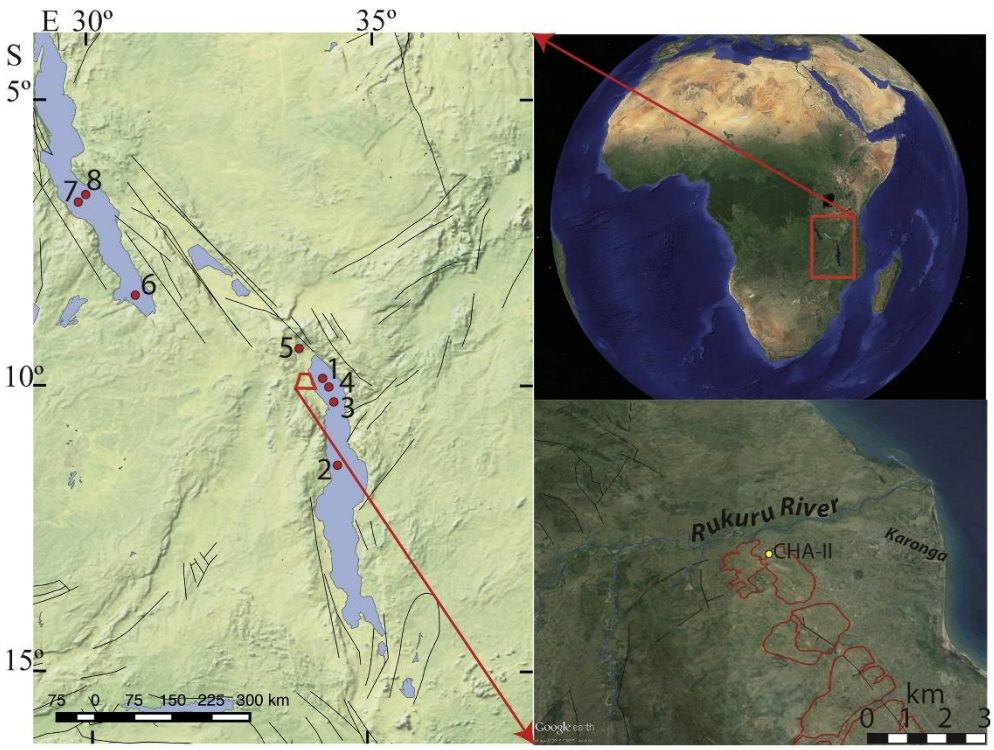

Fig. 1. Location of sites mentioned in the text. Upper right: Tropical Africa extends across the predominantly green regions. Red box denotes East-Central Africa (image from Google Earth). Left: Boxed area showing the location of paleoclimatic proxies discussed in the text. (1) Mal05e2A (Scholz et al., 2011), (2) Mal05e1C (Scholz et al., 2011), (3) M98e1P (Gasse et al., 2002; Johnson et al., 2002), (4) M98e2P (Gasse et al., 2002; Johnson et al., 2002), (5) Lake Masoko (Garcin et al., 2006; Gibert et al., 2002), (6) MPU-11 and MPU-12 (Bonnefille and Chali_e, 2000; Vincens et al., 1993), (7) KH3 (Tierney et al., 2008), (8) KH4 (Tierney et al., 2008). Fault lines are black and the red polygon denotes the study area near Karonga. Lower right: Location of Chaminade-II (CHA-II) near the modern town of Karonga, fan deposits (red outlines, Chitimwe Beds) and mapped faults. (For interpretation of the references to color in this figure legend, the reader is referred to the web version of this article.)

MATERIALS AND METHODS

Landscape-scale geomorphology and site-scale sedimentology

The focus of the geomorphologic, sedimentologic and pedologic investigation concentrated on the identification of source-to-sink processes and areas of sustained landform stability in which human activity would have been plausibly preserved. Archaeological surveys and test pitting were conducted across an alluvial fan west of the modern-day town of Karonga, Malawi, which resulted in the identification of CHA-II (Fig. 1). Recording of sedimentary lithofacies involved description of sorting, bedding features, particle sizes, inclusions, rounding properties, hardness, plasticity and unit boundaries. Pedologic recording accounted for relative degrees of weathering by recording

soil color, structure and the presence of authigenic and translocated minerals in the solum. Geomorphologic reconstruction of landform evolution was made by combining sedimentologic and pedologic analyses from numerous test units in combination with topographic maps. Sampling for OSL dating, micromorphology and phytolith analyses was performed to constrain environmental conditions within a dated context.

Excavation and artifact analysis

The CHA-II site (9.955° S, 33.892° E) was excavated in 2011 and 2012. A large eroded surface to the west of CHA-II contained 100,000s of artifacts in a series of drainage gullies that incise the Chitimwe Beds. CHA-II was mechanically excavated as a 4 x 50 m trench to a depth of 2 m, and then excavated by hand within a central 2 x 32 m area. The mechanically excavated sediments were placed in ten piles of 40 m^3 each, sieved, and found to confirm an average artifact density of 1 per m^3. The center trench was excavated in natural stratigraphic units and 1 x 1 m squares to a maximum total depth of 4.6 m, producing in total more than 10,000 stone artifacts. At the close of excavations, a geologic test pit was excavated at the southern end of the trench to a total depth of 6.6 m before the entire trench was backfilled. All artifacts, sedimentary units and samples were piece-plotted with a Nikon C-series 5" total station, and all artifacts with a discernable long axis were recorded with one point at each end.

Lithic artifacts were analyzed using complementary quantitative and qualitative methods on all plotted and sieved artifacts (sensu Mackay, 2008). When feasible, artifacts were also classified according to weathering stage (sensu Thompson et al., 2012), raw material, technological component (complete or fragmentary flakes and cores, flaking shatter, hammerstone, etc.), cortex cover and reduction method. Refits were sought to determine the extent of depositional reworking of the artifact assemblage, both horizontally and vertically. ArcGIS 10.2 was used to analyze the spatial relationships of artifacts of different sizes, raw materials, and rounding classes. The Optimized Hot Spot Analysis tool was used to identify clusters of artifacts within depositional units. Artifact orientation data were analyzed using Stereonet 9 to produce rose diagrams and establish if artifacts had preferred or random orientations in both the vertical and horizontal planes (McPherron, 2005).

Micromorphology

In 2012, seven block samples were collected from CHA-II for micromorphological analysis. The samples were oven-dried at 60 °C and impregnated with resin under vacuum. The resin was prepared with seven volume units of unpromoted polyester resin (Viscovoss N 55S), three volume

units of styrene (styrene for synthesis) and 5-6 ml/l hardener (methyl ethyl ketone peroxide, MEKP). After hardening, the blocks were sliced with a rock saw into slabs from which 6 x 9 cm sized thin-sections of 30-μm were produced. Micromorphological descriptions were conducted following analysis using a petrographic microscope with plane polarized light (PPL), crossed polarized light (XPL), blue light fluorescence and incident light at magnifications of 20x to 500x following Courty et al. (1989) and Stoops (2003).

A total of 90 microscopic Fourier transform infrared spectroscopic (m-FTIR) measurements were conducted directly on the thin sections using a Cary 610 FTIR microscope attached to a Cary 660 bench (Agilent Technologies). Spectra were collected in two modes: (1) 64 co-added scans at 4 cm^{-1} resolution in transmission mode with backgrounds collected on epoxy resin over glass under typical ambient conditions and (2) 32 co-added scans at 4 cm^{-1} resolution using a germanium crystal attenuated total reflectance (Ge-ATR) objective with backgrounds on air. The transmission measurements allowed us to characterize the absorption peaks in the region of 4000-3500 cm^{-1} (Beauvais and Bertaux, 2002; Robin et al., 2013), while the Ge-ATR measurements provided peaks from 4000 to 570 cm^{-1}. Clay-sized materials were identified to kaolin and smectite group minerals by comparing the peaks to reference spectra (Downs, 2006; Salisbury and Vergo, 1991; Van de Marel and Beutelspacher, 1976) with priority given to peaks in the OH-stretching region.

OSL geochronology

Five sediment samples were collected from the profile of CHA-II for OSL dating. Quartz grains with diameters of 180-250 μm were prepared using wet sieving, acid treatments (10% HCl, 10% H_2O_2 and 40% HF) and density separation and analyzed using a TL/OSL-DA-20 Risø reader. A dose recovery test following the Single Aliquot Regeneration (SAR) protocol (Murray and Wintle, 2000, 2003) for the lowermost sample LM12-10 determined that the measured and regenerated dose ratios were within 10% for all the preheat temperatures applied (Fig. 2). Equivalent dose (De) values were then determined in the plateau region in which the measured De was independent of the preheat temperatures (Fig. 3). Dose rates (D_r) of the samples were estimated using a Canberra BEGe 5030 low-level high-resolution gamma spectrometer. OSL signals were measured based on aliquots composed of several tens of quartz grains (Small Aliquots, SA), and the final ages were derived using the Central Age Model (Galbraith and Roberts, 2012; Galbraith et al., 1999).

Two samples, LM-3161 and LM-3162, were interpreted as potentially spurious due to high over-dispersion values generated in the SA OSL analysis (Arnold and Roberts, 2009) and were

therefore subjected to single-grain (SG) analysis. For SG dating, OSL signals in 1000 individual quartz grains from each sample were measured using a 10 mW Nd:YO_4 solid-state, diode-pumped green laser (532 nm). The optical stimulation was carried out at a readout temperature of 125 °C for 2 s, and the photon detection was through a 7-mm Hoya U-340 filter. The single grain De values were obtained using the SAR protocol (Murray and Wintle, 2000), and the feldspar grains were identified using IR depletion ratio (Duller, 2003). The OSL ages of the samples, together with dosimetry data and over-dispersion values, are given in Tables 1 and 2 and Fig. 4.

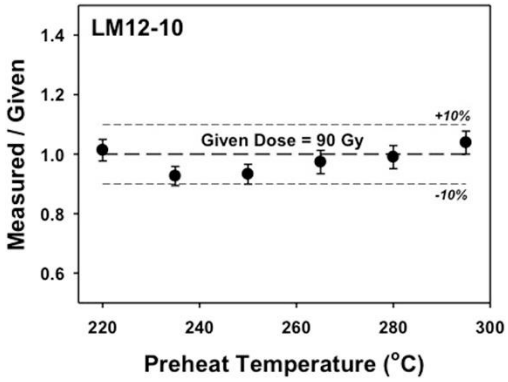

Fig. 2. Dose recovery test for LM12-10.

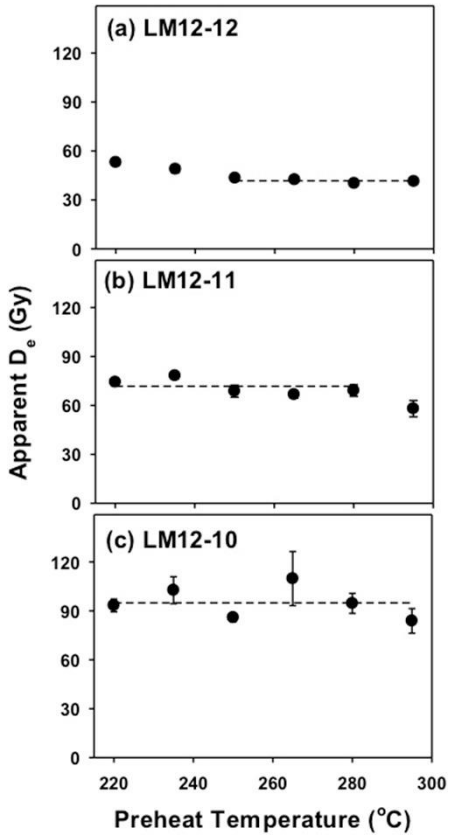

Fig. 3. Preheat plateau tests and equivalent dose (D_e) of LM12-10, LM12-11, LM12-12.

Sample	Depth[a] (cm)	Water content[b] (wt.%)	^{238}U (Bq kg^{-1})	^{226}Ra (Bq kg^{-1})	^{232}Th (Bq kg^{-1})	^{40}K (Bq kg^{-1})	Dry beta[c] (Gy ka^{-1})	Dry gamma[c] (Gy ka^{-1})	Cosmic ray[d] (Gy ka^{-1})	Total dose rate (Gy ka^{-1})	D_e (Gy)	OD[e] (%)	n	Age[f]
LM-3161	585	20 ± 10	10.0 ± 2.6	7.0 ± 0.3	24.1 ± 0.8	474 ± 9	1.40 ± 0.05	0.72 ± 0.01	0.08 ± 0.01	1.78 ± 0.13	118 ± 9	37	23	66 ± 7*
LM-3162	285	12 ± 3	8.3 ± 2.3	6.8 ± 0.3	23.6 ± 0.7	503 ± 10	1.46 ± 0.05	0.74 ± 0.01	0.13 ± 0.01	2.04 ± 0.07	174 ± 19	51	23	85 ± 10*
LM12-10	190	5 ± 2	13.2 ± 3.6	7.4 ± 0.4	30.2 ± 1.1	384 ± 10	1.23 ± 0.05	0.73 ± 0.01	0.15 ± 0.01	2.00 ± 0.06	95 ± 8	33	24	47 ± 4
LM12-11	160	5 ± 2	17.8 ± 4.8	12.9 ± 0.4	39.2 ± 1.1	417 ± 10	1.34 ± 0.06	0.86 ± 0.03	0.16 ± 0.02	2.36 ± 0.07	72 ± 3	15	20	30 ± 1
LM12-12	60	5 ± 2	17.6 ± 4.0	15.3 ± 0.3	42.8 ± 0.9	414 ± 8	1.45 ± 0.05	0.97 ± 0.02	0.19 ± 0.02	2.46 ± 0.07	42 ± 1	25	16	17 ± 1

Table 1. Equivalent dose, dose rate and Small Aliquot (SA) OSL ages of the samples.

a Depths of the samples are the vertical distance from the modern ground surface.

b Average water content of the samples during burial.

c Data from high-resolution low level gamma spectrometer were converted to infinite matrix dose rates using conversion factors given in Olley et al. (1996).

d Cosmic ray dose rates were calculated using the equations provided by Prescott and Hutton (1994).

e Over-dispersion.

f Central Age Model (CAM) ± 1σ error (also calculated for D_e).

Sample	Depth[a] (cm)	Water content (wt. %)[b]	Total dose rate (Gy ka^{-1})	$D_{e,MAM}$[c] (Gy)	$D_{e,CAM}$[d] (Gy)	O.D (%)[e]	n	MAM age[f]	CAM age[g]
LM-3161	585	20 ± 10	1.78 ± 0.13	37 ± 22	113 ± 31	69	7	21 ± 12	63 ± 18
LM-3162	285	12 ± 3	2.04 ± 0.07	27 ± 4	55 ± 6	51	24	13 ± 2	27 ± 3

Table 2. Equivalent dose and Single Grain (SG) OSL ages of the samples LM-3161 and LM-3162.

* Cosmic ray dose rates were calculated using the equations provided by Prescott and Hutton (1994) and provided in Table 1.

a Depths of the samples are the vertical distance from the modern ground surface.

b Data from high-resolution low level gamma spectrometer were converted to infinite matrix dose rates using conversion factors given in Olley et al. (1996).

c MAM = Minimum Age Model (Galbraith et al., 1999).

d CAM = Central Age Model (Galbraith et al., 1999).

e Over-dispersion.

f Minimum Age Model, ± 1σ error (4 parameters sensu Galbraith et al., 1999).

g Central Age Model, ± 1σ error (Galbraith et al., 1999).

Local paleoenvironmental reconstruction

Phytolith samples were taken as small sediment samples from the top to the base of the southeastern profile and then continuing down the same profile on the western side of the deep geological sondage. Sixteen sediment samples were processed for the purpose of creating a

vegetation landscape reconstruction. Extraction protocols were followed that were successfully employed on neighboring MSA sites (Mercader et al., 2013) and modern topsoils (Mercader et al., 2011) from the Mozambican side of the lake.

To understand the relations between specific morphotypes and taxonomic identification, the inferential baseline was grounded on the statistical analysis of local phytoliths from plants and soils (Mercader et al., 2010, 2009) and supporting references (Albert et al., 2009; Barboni and Bremond, 2009; Bremond et al., 2008; Fernandez Honaine et al., 2009; Novello et al., 2012; Piperno and Pearsall, 1998; Runge, 1999; Twiss et al., 1969). Preservation was adequate for morphometric analysis and type identification, although marked dissolution was a concern in some samples. A total of 6089 discrete phytolith shapes were classified and grouped into 59 morphotypes (Fig. 5).

THE CHAMINADE-II SEQUENCE

Lithology and site formation processes

MSA artifacts at CHA-II were entrained in alluvial fan deposits, but sedimentation of the site changed through time, reflecting different ecological conditions commonly found in tropical Africa. Site formation processes were interpreted on the basis of microscale (Supplementary Online Material 1) and macro-scale analysis of sediments and pedofeatures (Fig. 6).

Units 1 and 2 are interpreted as alluvial deposits based on the presence of horizontally laminated bedding features and well-rounded medium to coarse sandy channel sediments (Fig. 7a) in which an over-thickened Bt horizon developed during aggradation (Fig. 7b-c). These deposits are capped by either a lag channel or deflated or winnowed alluvial fan surface (Unit 3). Units 1 and 2 are culturally sterile, and Unit 3 contains only sparse and heavily rounded artifacts within the same size grade as the surrounding clasts (Fig. 8). OSL ages dating to approximately 65 ka (LM-3161) were assayed from Unit 1, but authigenic mineral formation associated with groundwater fluctuations and gleying of the sediments have likely compromised the D_r estimate as demonstrated by the results of the SG OSL analysis. SA OSL and SG OSL analyses from Unit 2 (LM-3162) do not provide reliable estimates of age of deposition of this unit based on the over-dispersion values obtained.

Within Unit 4, very poorly-sorted, coarse grained alluvial fan deposits have undergone multiple phases of Bt horizon formation, which also destroyed bedding structures that may have been present (Fig. 7d-e). Artifacts (mainly unweathered and some refitting) are concentrated in the upper 10 cm of the unit, which was deposited ca. 47 ka (LM12-10; Table 1), although authigenic iron-manganese (Fe-Mn) nodule formation would have altered the dosing environment and affected the D_r over the burial life of the sample. Additionally, multiple fluctuations in moisture initiated the shrinking and swelling of smectites present in the soils, resulting in pedoturbation and the formation of vertic features (Fig. 7f-g). Vertic processes led to the physical deformation of illuvial clay coatings, but Bt horizon formation continued, as evidenced by a later phase of coatings (Fig. 7h). At one point, Bt horizon formation ceased when the groundwater table rose significantly, which gleyed much of the lower profile and contributed to the formation of Fe-Mn nodules within the inactive Bt horizon. After the groundwater level fell, the uppermost of the nodules and large clasts (including artifacts) settled downwards forming a secondary deposit of nodules in the profile, which accommodated bulk volume changes from dewatering and winnowing of fine particulates.

Following the lowering of the Fe-Mn nodule rich horizon, deposition of finer-grained, distal alluvial fan sediments recommenced prior to 30 ka (LM12-11; Table 1) and successive formation of Bt horizons continued with clay coatings forming around lower nodules (Fig 7i) and cementation from iron leaching and accumulation within the profile. Artifact counts are highest in the bottom 30 cm of Unit 5 and are virtually absent in sediments that accumulate thereafter. Following landform stability after 17 ka (LM12-12; Table 1), lateritic soil formation pedogenically weathered quartz grains, feldspars and smectite clays top-down in Unit 5, enriching the unit in kaolinite. Additionally, termite bioturbation, associated with the formation of the laterite, occurred downwards to the top of the iron-nodule concentration (Fig. 7j).

Lithic analysis

The lithic artifacts from CHA-II form a typo-technologically generalized MSA assemblage, but provide useful data for understanding site taphonomy and land use strategies over time. Analysis of a sample of 640 piece-plotted artifacts from an area of 8 m^2 shows both dorsal and ventral sides of the artifacts were frequently coated in Fe-Mn precipitates, with only five artifacts demonstrating differential weathering on opposing sides. More detailed examination suggests that there may be two or more lenses of artifacts within this vertical concentration (Fig. 8, lower left). Vertical refits and conjoins are non-existent between designated sedimentary units. Within Unit 4 (Lower Concentration), five sets of conjoining/refitting artifacts were identified, along with eight similar sets in Unit 5 (Upper Concentration), found in discrete clusters (Fig. 9). Artifacts from CHA-II

are typically more square than elongated, so that within this sample only 125 had a maximum length:breadth ratio of ≥1.5, and thus a discernable long axis. Of these, neither the upper nor the lower lens shows a preferred orientation that would suggest winnowing (McPherron, 2005). Additionally, all artifacts are lying at angles <22° (most far flatter), indicating that they have not been post-depositionally reoriented by bioturbation (Bernatchez, 2010; Lenoble and Bertran, 2004). In total, <1% of artifacts are retouched, and over 95% of cores retain some cortex coverage, with an average 44% cortex coverage on all cores.

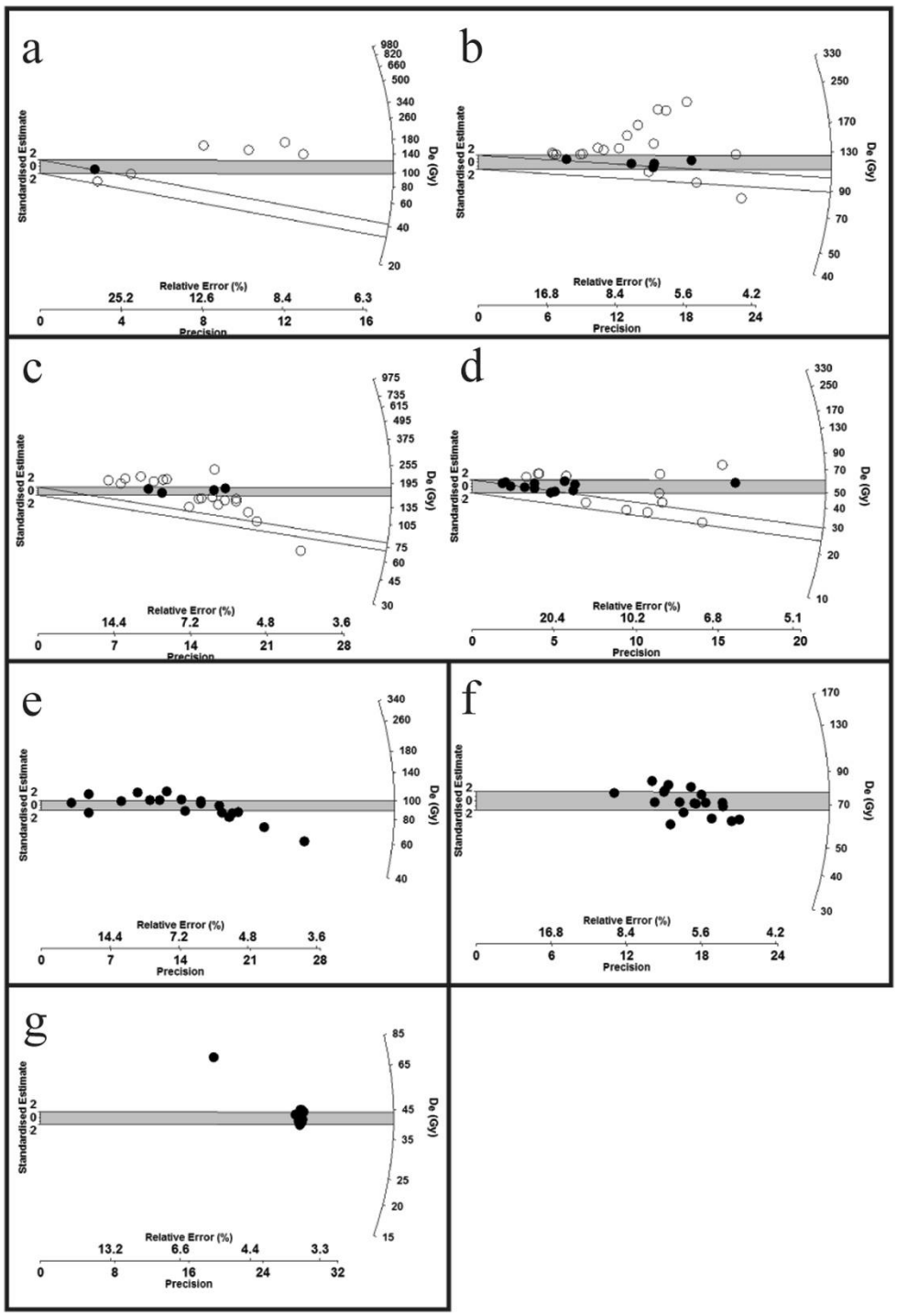

Fig. 4. Radial plots of samples from CHA-II (a) Single grain (SG) analysis of LM-3161, Central Age Model (CAM) De ¼ 113 ± 31 Gy, Over-dispersion (OD) ¼ 69%, Minimum De ¼ 37 ± 22 Gy, CAM age ¼ 63 ± 18 ka, Minimum age ¼ 21 ± 12 ka; (b) Small aliquot (SA) analysis of LM-3161, CAM De ¼ 118 ± 9 Gy, OD ¼ 37%, Min De ¼ 96 ± 13 Gy, CAM age ¼ 66 ± 7 ka, Minimum age ¼ 54 ± 8 ka; (c) LM-3162 (SG), CAM De ¼ 55 ± 6 Gy, OD ¼ 51%, Minimum De ¼ 27 ± 4 Gy, CAM age ¼ 27 ± 3 ka, Minimum age ¼ 13 ± 2 ka; (d) LM- 3162 (SA), CAM De ¼ 174 ± 19 Gy, OD ¼ 51%, Minimum De ¼ 75 ± 11 Gy, CAM age ¼ 85 ± 10 ka, Minimum age ¼ 37 ± 6 ka; (e) LM12-10 (SA), CAM De ¼ 95 ± 8 Gy, CAM age ¼ 47 ± 4 ka; (f) LM12-11 (SA), De ¼ 72 ± 3 Gy, CAM age ¼ 30 ± 1 ka; (g) LM12-12 (SA), De ¼ 42 ± 1 Gy, CAM age ¼ 17 ± 1 ka.

Phytolith analysis

Phytolith data provide an additional environmental context for the depositional and artifactual data (Supplementary Online Material 2). Phytoliths from woody (arboreal) tissue average 86.2% (range: 61.5e100%) and therefore they constitute the dominant type analyzed from CHA-II. Overall, this is indicative of a generally moist arboreal domain; however, there are cyclical peaks and drops in the abundance of arboreal phytoliths that can be classed into four vegetation phases illustrating the alternation of three wet periods with two drier ones (Fig. 6). There was no evidence for mixing of phytolith taxa between the following phases:

'Phase 1' is from Unit 1, and is likely much older than 47 ka and inferred to be ca. 65 ka based on SA OSL and SG OSL analyses with low confidence in the accuracy of this age estimate. The lower part of these sediments contains heavy arboreal representation, which transforms into fragmented woodland (arboreal phytoliths: 61.5%) in the upper part of Unit 1, where seasonal (panicoid) and wet-adapted (bambusoid) communities still abound (Poaceae phytoliths combined: >30%). This zone is interpreted as reflecting a wet woodland community.

'Phase 2' also predates 47 ka, and it yields the highest levels of arboreal phytoliths from the entire series, with grasses being minimal or absent. Phytoliths from this zone are interpreted as reflecting a forest environment, and correspond to geologic Units 2 and 3.

'Phase 3' records significant arboreal reduction starting at the stratigraphic level dated to 47 ka through 30 ka, and covering the upper solum of geologic Unit 4, and lower 30 cm of Unit 5. Phytoliths from the dry-adapted chloridoid clade peak at 58.6% for all Poaceae types. This zone is interpreted as signalling the presence of predominantly dry, grassy woodland.

'Phase 4' postdates 30 ka and extends to <17 ka. Taxa analyzed from this zone indicate a return to arboreal dominance for the remainder of the stratigraphic column, albeit with small fluctuations in seasonal-grass types. This phase is inferred as reflecting dense woodland, which is

distinct from the present-day Zambezi woodland vegetation classification of the region (White, 1983).

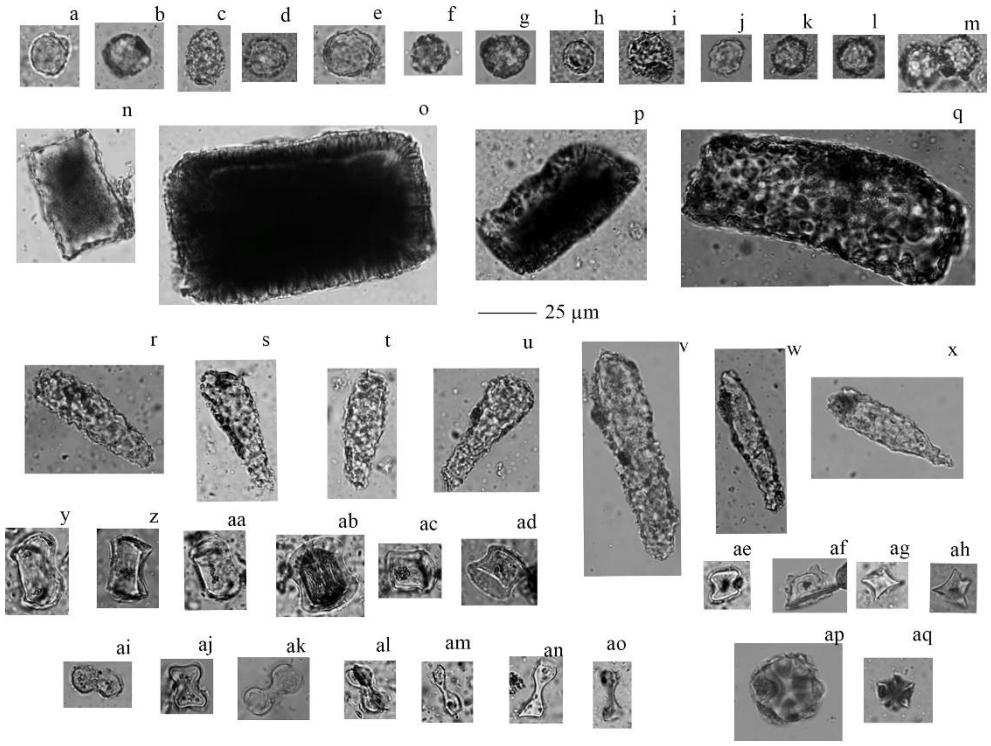

Fig. 5. Phytolith morphotypes identified from CHA-II. (aem) globular granulates derived from dicot trees and shrubs (Mercader et al., 2009; Neumann et al., 2009; Runge, 1999); (neq) blocky derived from arboreal taxa (Mercader et al., 2009); (rex) clayate granulates derived from arboreal taxa (Mercader et al., 2009); (y-ad) long saddles derived from Poaceae wet-adapted bambusoids (Mercader et al., 2010; Piperno and Pearsall, 1998); (ae) short saddles derived from xeric chloridoid grasses (Mercader et al., 2010; Twiss et al., 1969); (af-ah) towers derived from xeric chloridoid grasses (Mercader et al., 2010; Twiss et al., 1969); (ai-ao) lobates derived from tall, hydric, heliophyte panicoid grasses (Barboni and Bremond, 2009; Bremond et al., 2008; Mercader et al., 2010; Novello et al., 2012); (ap-aq) globular, 'ridged' with echinoid appearance derived from the Marantaceae family, forest-adapted taxa (de Albuquerque et al., 2013).

Comparison of CHA-II to regional paleoclimatic datasets

Terrestrial data sets present in CHA-II and other sites in the Karonga region correlate with regional climatic events documented in the Lake Malawi Drill Core and other regional proxies (Fig. 10). Terrigenous pollen consistently include miombo and bamboo forest species with some grasses throughout MIS3 (Beuning et al., 2011) with coeval supporting evidence coming from phytolith assemblages on the Mozambican side of the lake (Mercader et al., 2013). However, diatom assemblages reflect shallower water conditions between 47 and 32 ka (Stone et al., 2011),

concurrent with Phase 3 reductions in arboreal taxa from CHA-II. Regionally, the wettest conditions occur during the Early Holocene (Bonnefille and Chalie, 2000; Ivory et al., 2012; Stone et al., 2011; Tierney et al., 2008), which correlates with Phase 4 of the CHA-II phytolith sequence. Overall, the magnitude of lake level fluctuations during the last 60 ka in Lake Malawi was far less significant compared to nearby lakes Masoko and Tanganyika (Fig. 10), which may have made it a more attractive biome for persistent human habitation.

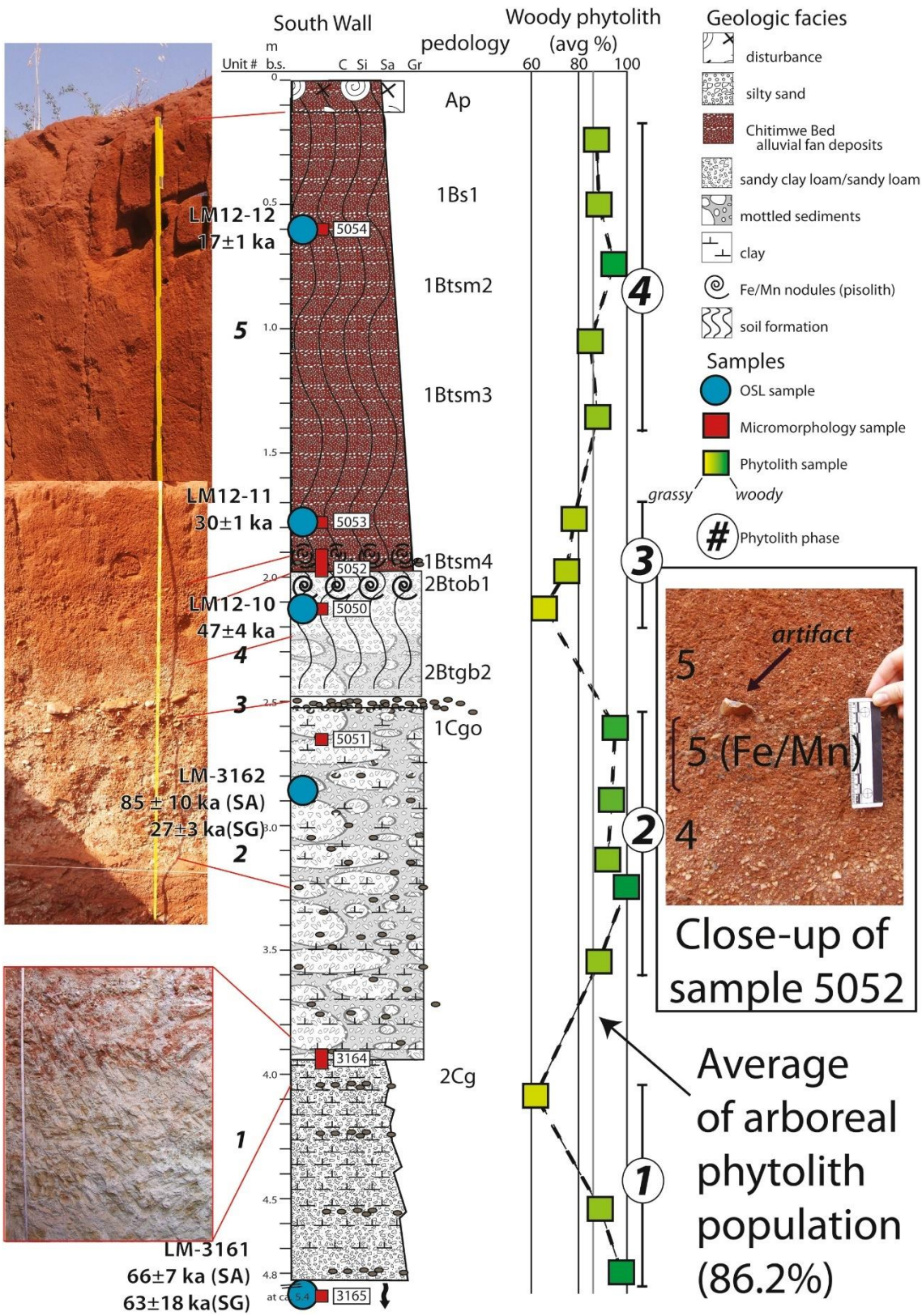

Fig. 6. South wall profile of CHA-II showing sedimentology, pedology, sampling locations and interpretation of phytolith taxa present. Sample 5052 (middle right) is shown in thin section in Fig. 7d-i and is stratigraphically associated with the densest artifact accumulations.

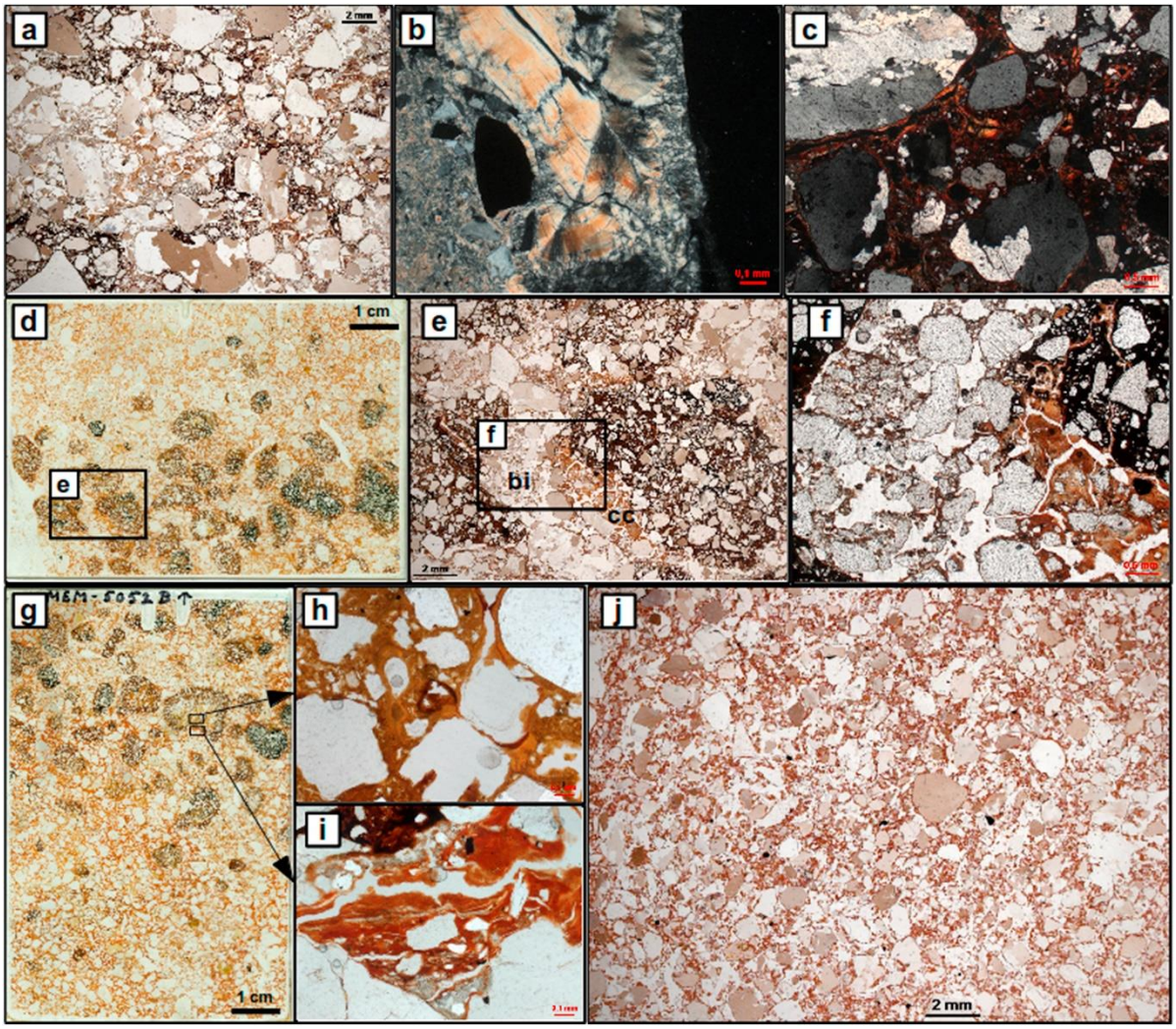

Fig. 7. Sedimentologic features of Chaminade-II through micromorphologic thin section. (a) Orthic nodules in Unit 2 underneath the concentration of iron-manganese nodules (sample MEM-5050). PPL; (b) old deformed clay coating with kink-band fabric resulting from shrink and swell (MEM-3164B). XPL; (c) fresh clay coatings from a relatively recent phase of Bt formation (MEM-5050). XPL; (d) scan of MEM-5052 thin section showing the upper half of the iron-manganese nodule concentration (6 x 9 cm); (e) anorthic iron-manganese nodules with remnants of clay coatings [c] from a Bt horizon and a bioturbated zone [bi] in between nodules. PPL; (f) framed area at higher magnification showing open bioturbated material and remnants of clay coatings on a nodule. PPL; (g) scan of thin section (6 x 9 cm) showing the lower half of the iron-manganese nodule concentration with orthic and anorthic nodules (MEM-5052B); (h) dusty clay coatings from inside an iron nodule (upper frame in [g]). Earlier phase of Bt formation pre-dating iron nodule formation; (i) iron-stained clay coatings from outside an iron nodule (lower frame in [g]), representing a later phase of Bt formation, post-dating iron nodule formation and deflation; (j) intergrain microaggregate microstructure, resulting from extensive termite activity in the laterite (MEM-5054). PPL.

DISCUSSION

The integrated paleoecological and archaeological reconstructions of CHA-II were designed to maximize the information potential of an open-air MSA site in tropical Africa. Preservation of organic remains is typically poor in tropical regions, and especially so in open-air settings, and CHA-II was no exception. However, by analyzing inorganic fossil remains of plants, sediments and artifacts, MSA environments and potential drivers of human behavior can be inferred on both a local and regional level.

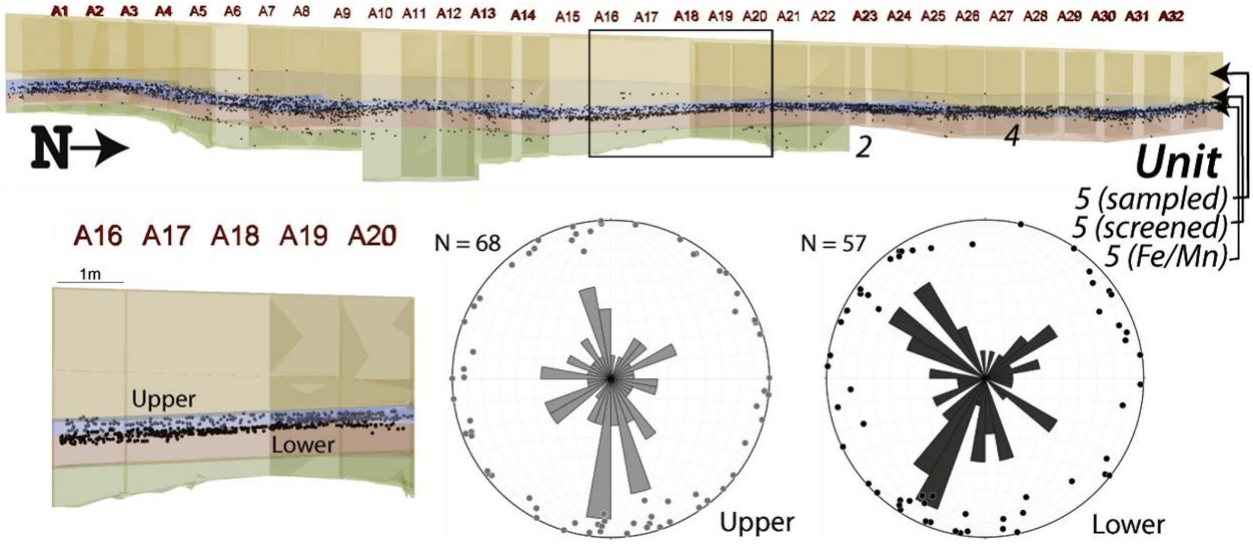

Fig. 8. CHA-II trench showing sedimentologic/pedologic units and locations of plotted finds (black points). Note that artifacts in the upper portion of Unit 5 were not piece-plotted, but that sieving showed they averaged <1/m^3. A close-up of squares A16-B20 is shown at lower left, with only artifacts in the main concentration pictured for clarity. These have been divided into two possible lenses, with a separate rose diagram at lower right given for each. The points on the rose diagrams represent the plunge of the artifacts, while the roses themselves represent their orientations.

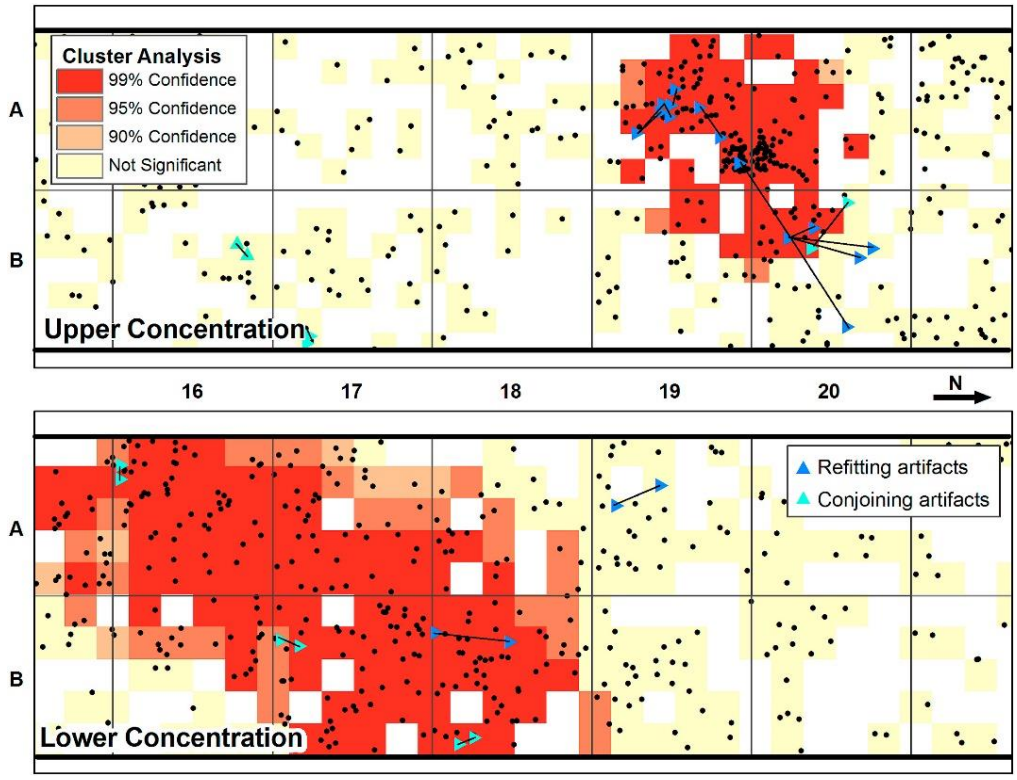

Fig. 9. Results of refitting program and GIS cluster analysis. Following Sisk and Shea (2008), "refits" are artifacts that were separated through the knapping process/conchoidal fracturing, while "conjoins" are fragments of formerly whole flakes that fit back together. In both the Upper and Lower Concentrations, refitting and conjoining artifact sets occur predominantly within cluster of artifacts identified using the Optimized Hot Spot Analysis functionality in ArcGIS 10.2. This tool identifies spatially concentrated incidences (of artifacts), and identifies the likelihood that the spatial relationships within them reject the null hypothesis of a random distribution, at increasing confidence levels.

Depositional and age models of CHA-II

In tropical environments, where rainfall tends to be heavy and seasonal, alluvial fans are typically activated during a high precipitation event following a drought severe enough to devegetate large swaths of an upland region (e.g., Kumar Singh et al., 2001; Nott et al., 2001; Thomas, 2004; Waters et al., 2010). Tectonic activity can also catalyze alluvial fan formation, but in the absence of significant upwarping or solifluction alluvial fan formation normally occurs in tandem with variable precipitation (e.g., Bull, 1977; Harvey, 2002; Kumar et al., 2007; Ritter et al., 1995; Wang et al., 2001). Erosional and depositional processes across alluvial fans are not uniform and sheetwash zones, channels and debris flows are distributed irregularly across landforms (see papers in Harvey et al., 2005 for a comprehensive review).

Based on the available evidence, sedimentation of CHA-II occurred primarily as pulses of distal alluvial fan deposits, which were sometimes reworked and deposited by intermittently occurring fluvial systems (Fig. 11). Sediment packages were poorly sorted, well mixed and do not appear to vary appreciably over the 32m exposed length of the site. Clast sizes generally range between fine and coarse sand with pockets of sediments with higher gravel fraction.

The potential for large-scale bioturbation at CHA-II is high, but the evidence suggests that such activity was localized. Groundwater fluctuations and lateritic processes facilitated the formation of the Fe-Mn nodule-rich lens that overprints bedding features from the upper portion of the sondage. Subsidence from water table depletion has been observed at CHA-II based on the uniform, undulating sediment packages observable in the profile (Fig. 8), but large accommodation zones for fine clasts to move downward do not appear to have formed. Conjoins and refits from Units 4 and 5 (Fig. 9) and clusters of chipped stone debris indicate that these are primary or minimally compressed archaeological deposits reflecting discrete activity areas. Furthermore, the micromorphology indicates that sediment mixing was restricted to distinct sedimentary zones and large-scale lateral movement of sediments decimeters from their primary depositional environment was not significant.

In addition to being a tool for dating sediment deposition, OSL is commonly used as a tool to understand bioturbation and pedoturbation within archaeological contexts (e.g., Arnold and Roberts, 2009; Gliganic et al., 2012; Guérin et al., 2015). Because the sedimentary matrix reworking at CHA-II was localized, SA OSL was employed as the method of first resort. Recent studies demonstrate that if over-dispersion is within a threshold range of <40%, it is possible to obtain accurate age estimates from SA OSL analysis as long as the skewness values within a population of aliquots are low indicating a normal or log normal distribution (Alexanderson and Murray, 2007; Armitage and King, 2013; Arnold and Roberts, 2009; Forman, 2015; Rowan et al., 2012). Radial plots of samples from CHA-II demonstrate a central tendency of the aliquots with the exceptions of LM-3161 and LM-3162 (Fig. 4), which show scattered De values indicating some sediment reworking, pedoturbation and non-solar resetting of sediments prior to deposition. Based on the combined evidence, one age is rejected (LM-3161) and two ages are considered highly uncertain (LM-3162 and LM12-10), however post-depositional effects did not significantly impact the accuracy of LM12-11 and LM12-12.

The combined sedimentary, micromorphological, artifactual, phytolith, and OSL data infer a depositional model that is inconsistent with Crossley (1986) interpretation of site taphonomies from the Chitimwe Beds. Based on granulometric analyses of the sand sheets and termite mounds

in the Chaminade area, Crossley (1986) concluded that the vertical (upward) transfer of selected (medium to coarse) sand grains by *Macrotermes falciger* termites led to the accumulation of the sand sheets and concentration of larger particles and lithic artifacts in the lower reaches of the solum. Instead, we argue that Bt horizon overthickening and the formation of vertic features associated with soil formation and groundwater variability degraded the integrity of bedding features in the profile commonly found in alluvial deposits, making the deposits appear similar to biomantles to the naked eye.

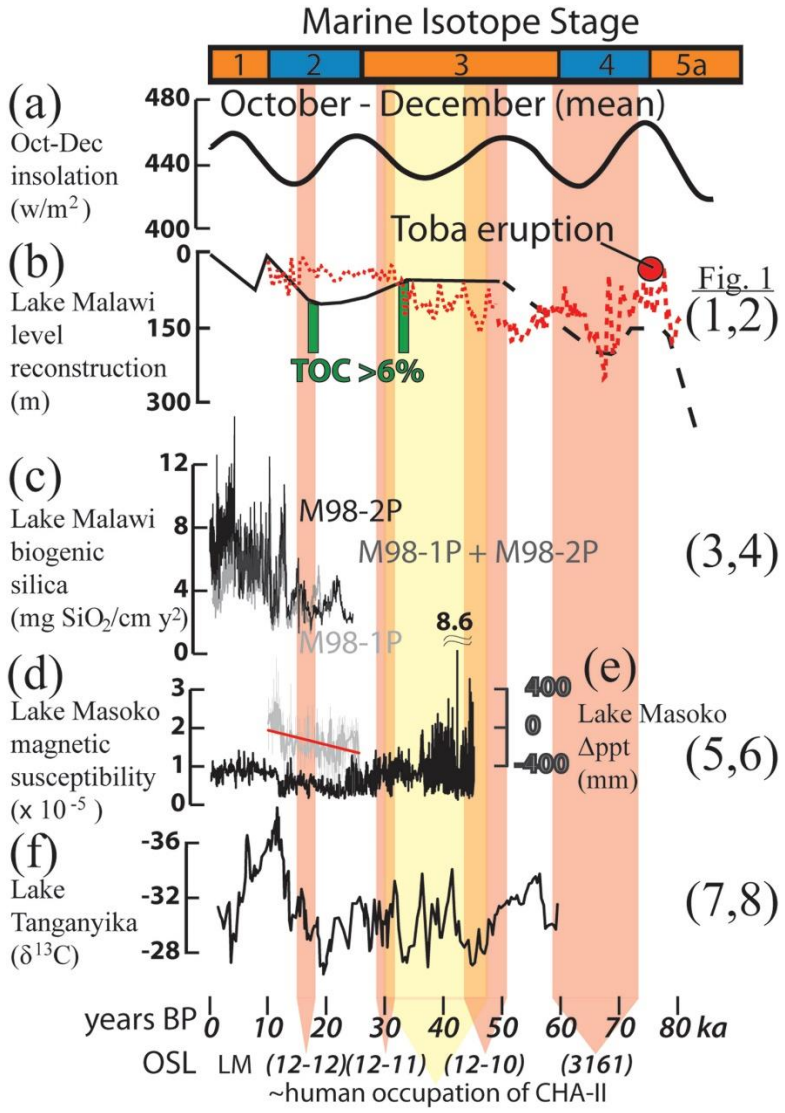

Fig. 10. Paleoclimatic proxy data from southeastern Africa. (a) Average insolation (w/m^2) at the onset of the rainy season (October-December) at 10˚S (Scholz et al., 2011); (b) Black line is the interpreted lake level based on synthesis of sediment core data (Scholz et al., 2011), red dotted line is a reconstructed lake level based on the diatom assemblage from the Lake Malawi Drill Cores (Stone et al., 2011), dashed lines after 50 ka represent age model uncertainty from

discovery of Toba Ash as reported in Lane et al. (2013); (c) Biogenic silica mass accumulation rate (mg SiO_2/cm y^2) from Lake Malawi (Johnson et al., 2002); (d) Magnetic susceptibility (x 10^{-5}) from Lake Masoko (Garcin et al., 2006); (e) Gray line shows Δppt from modern conditions (mm) from Lake Tanganyika, red line shows time-averaged linear trendline (Bonnefille and Chalié, 2000); (f) $\delta^{13}C$ of monocarboxylic fatty acids (C_{28}) vs. VPDB from Lake Tanganyika (Tierney et al., 2008). Numbers on right margin correspond to proxy points identified in Fig. 1. (For interpretation of the references to color in this figure legend, the reader is referred to the web version of this article.)

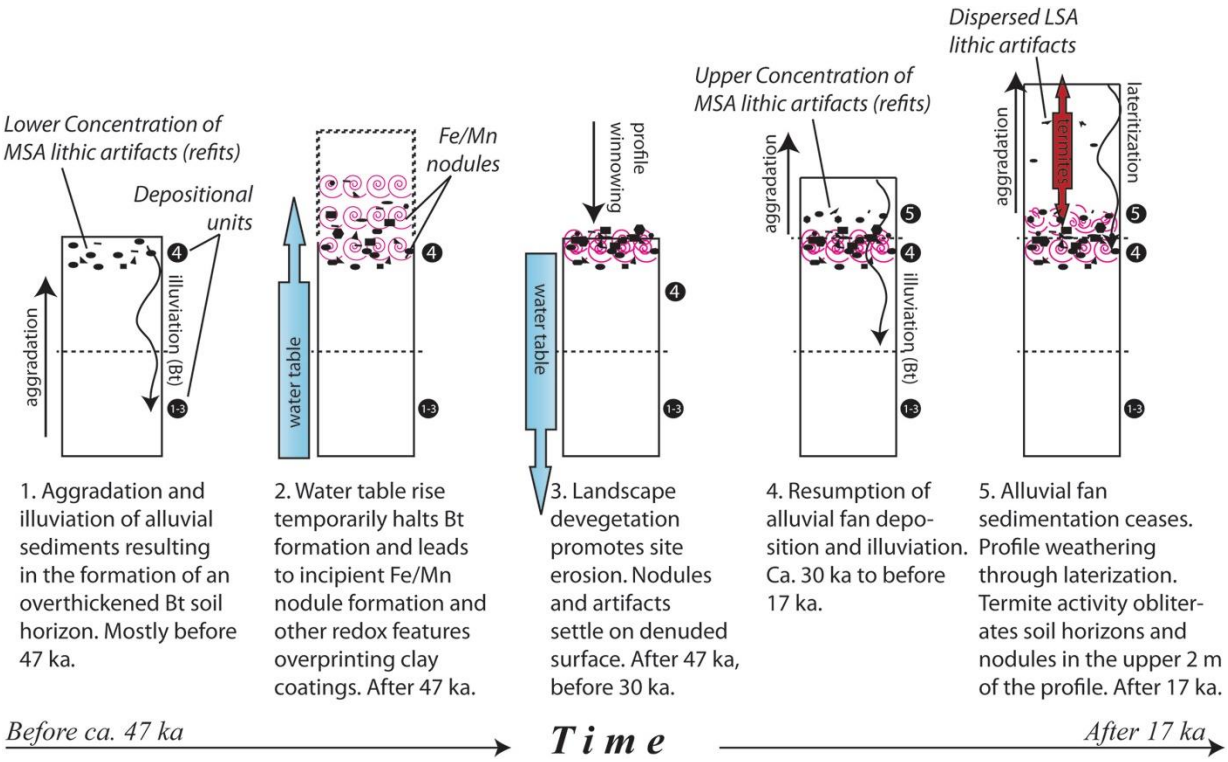

Fig. 11. Site formation model for Chaminade-II.

Landscape and behavioral models of CHA-II

Archaeological evidence from CHA-II records recurrent occupation associated with MSA foragers throughout the late MIS4 and entire MIS3 periods in the Karonga region. Diatom and geochemical proxy reconstructions of the Lake Malawi ecology indicate that site sedimentation occurs when the local environment fluctuates between mildly xeric and pluvial conditions (Finney et al.,1996; Gasse et al., 2002; Stone et al., 2011). The diatom assemblage from Lake Malawi following the eruption of Mount Toba (ca. 75 ka) and prior to 50 ka shows several prominent and rapid ecological changes (Lane et al., 2013; Stone et al., 2011), which broadly accord with the phytolith assemblage from Units 1 and 2 of CHA-II. Similarly, phytolith taxa from CHA-II connote the presence of dry, grassy woodland from this time, which are echoed in the reconstructed

paleoenvironments of the Mozambican highlands for the interval 50 to >42 ka (Mercader et al., 2013: 330). Phytoliths entrained in Units 1e3 reflect the predominance of wet woodland to forest environments, indicative of a moist precipitation regime during periods of site sedimentation. Proportions of woody vegetation drop markedly in Unit 4, which was filled by alluvial fan deposits, and then increase again through Unit 5. Occurrences of the MSA in the area are inferred prior to 47 ka by the presence of heavily-rolled artifacts in deposits associated with Unit 3 and the bottom of Unit 4. Human occupation at the site began in earnest after 47 ka and appears to have occurred during a period of profound landscape variability. Based on magnetic susceptibility of an assayed lake core at Lake Masoko (Fig. 10d), located 70 km to the north of CHA-II, the region experienced longer dry seasons and potentially stronger seasonality in precipitation compared to present conditions, but was dominated by Zambezian tree, open savannah vegetation (Garcin et al., 2006). Similarly, the environment at CHA-II became more open, which is supported by on-site grassy phytoliths and offsite diatom data from Lake Malawi reflecting higher alkalinity (Stone et al., 2011). After 30 ka, the phytolith spectra at CHA-II reflect the presence of a dense woodland community, which is in agreement with pollen and biogenic silica data derived from the Lake Malawi sediment core (Beuning et al., 2011; Johnson et al., 2011; Stone et al., 2011) and Lake Masoko (Garcin et al., 2006).

The concentration of artifacts within Unit 5 is the product of repeated occupation of the same land surface as soil aggraded over an extended period of time concurrent with slow sedimentation of the landform prior to 30 ka as the climate transitioned to wetter conditions (Fig. 11). Toolstone types and limited reduction of nodules indicate that toolstone availability was not a limiting factor. Rather, MSA foraging strategies incorporated regular visits to riparian zones for lithic raw material, which was processed and then transported outside the riparian areas for usage. Similar patterns of landscape utilization within diagenetically-altered alluvial fan sedimentary environments have been documented in the Kapthurin Formation (Tryon, 2010) and Mukogodo Hills (Pearl and Dickson, 2004) of Kenya and Jebel Gharbi in north-west Libya (Barich et al., 2006) possibly representing a generalized site taphonomy and behavioral strategy of MSA foragers operating in dynamic sedimentary and climatic environments. Artifacts entrained above the lower 30 cm of Unit 5 are relatively rare and likely bioturbated within the sediments either through termite activity or entrainment in the alluvial fan. Some artifacts from the upper portions of Unit 5, including some small pieces, can be characterized as Later Stone Age (LSA), whereas none from within the zone of artifact concentration can be assigned firmly to any typo-technological complex

other than the MSA. This adherence to cultural stratigraphy provides additional support for our interpretation of the site's formation (Fig. 11).

The micro-scale data are corroborated by lithic orientation data at CHA-II, which show most artifacts as lying horizontally, and by the lack of mixing of small LSA elements into the sediments dated >30 ka. This demonstrates that MSA behavior at both site and landscape scales can still be discerned in tropical settings that have been subsequently affected by tectonic, authigenic, pedogenic and climatic changes since the times of original artifact deposition.

CONCLUSION

Archaeological research of MSA occupation of CHA-II located on an alluvial fan in northern Malawi integrated paleoclimatologic, sedimentologic and spatial datasets to better understand human habitation patterns within a tropical to subtropical ecosystem. The primary human occupation of the landform occurred between 47 and 30 ka, concentrated on slowly aggrading alluvial fan sediments within a grassy woodland zone that was drier than during preceding and following phases of sedimentation. Although this is the driest period reflected in diatom assemblages after 70 ka (Stone et al., 2011), the magnitude of ecological variability in Lake Malawi appears to have been far less than in surrounding basins at the same time (Bonnefille and Chalie, 2000; Tierney et al., 2008). The evidence for repeated visits to the site and lack of conservation of toolstone suggests that this was a relatively attractive environment for MSA foragers. CHA-II demonstrates similar patterns in landform utilization to other MSA sites in the Karonga region (Thompson et al., 2012; Wright et al., 2014), on the Mozambican side of the lake (Bicho et al., (in press); Mercader et al., 2011, 2013) and elsewhere in Africa as cited above.

The taphonomic situation at CHA-II and other sites did not allow for the preservation of evidence for other human activities such as faunal resource exploitation or hearth construction. Much archaeology conducted in tropical ecosystems faces similar challenges due to generally poor preservation conditions in biomes with high, seasonal rainfall and rapid soil formation. Bioturbation from insects tends to be particularly severe due to the lack of cold conditions to seasonally limit tunnel construction activities. Laterite formation and highly acidic soils also degrade the integrity of organic deposits and buried A-horizons, as does redoximorphic weathering of sediments associated with fluctuating ground water levels. More specifically to the MSA, the lack of diversity in the material culture, particularly from open-air settings, limits behavioral interpretations (Sharon et al., 2014).

In spite of these limitations, archaeological studies of open-air MSA sites from tropical regions are critical for developing robust models explaining human behavioral evolution and diversity (Shea, 2011). Therefore, we advocate a multiproxy, multidisciplinary research strategy that can sufficiently tackle the challenges of working in tropical ecosystems and yield information needed to contribute to such discussions. This study shows that detailed information about MSA landscape use, lithic exploitation, and local environments can be reconstructed using multiple lines of evidence tailored to these challenging preservation conditions. Furthermore, regional paleoecological datasets augment site-scale archaeology and sedimentology, providing a broader context for deposition, soil formation and aspects of human behavior.

Acknowledgments

We thank our collaborators at the Malawi Ministry of Sports and Culture for their assistance and permission in facilitating this research. Specific thanks is given to former Deputy Director of Culture Potiphar Kaliba, current Director Chrissy Chiumia, Senior Officers Oris Malijani, Malani Chinula, and Harrison Simfukwe, and Junior Officers Frederick Mapemba, and Joseph Tembo, The 2012 Archaeological Field School run through The University of Queensland contributed a cohort of student workers in 2012, including three who stayed to volunteer additional time: Rykene Sander-Ward, James Flittner, and Megan Harris. An outstanding team of local crew worked on the CHA-II excavations, with special thanks owed to Henry Kalinga, Daudi Mwangomba, and Moses Nyondo. Liton Adhikari and Gervasio Ngumbira assisted with leadership and organization. Fieldwork and analysis were funded by National Geographic-Waitt Foundation grant W115-10 (JT), Australian Research Council Discovery Project DP110101305 (JT), The University of Queensland Archaeological Field School, and the Korean Research Foundation Global Research Network Grant 2012032907 (DW). FS, CM and SM thank Panagiotis Kritikakis for preparation of the thin sections for micromophological analysis. Funding for the micromorphological analysis and μFTIR was provided by the Deutsche Forschungsgemeinschaft (MI 1748/3-1, MI 1748/1-1, and ME 4406/1-1). AC thanks the Lake Malawi Drilling Project, NSF-Earth System History Program (NSF-EAR-0602404), DOSECC Inc. and LacCore for support. Composing this manuscript took place at the University of York, which generously hosted DW while on sabbatical from Seoul National University. Thanks to the two anonymous reviewers and organizers of this special edition of *Journal of Archaeological Science*, Mike Morley and Paul Goldberg who greatly improved the quality of this manuscript.

Appendix A. Supplementary data

Supplementary data related to this article can be found at http://dx.doi.org/10.1016/j.jas.2016.01.014.

REFERENCES

Ahr, S.W., Nordt, L.C., Driese, S.G., 2012. Assessing lithologic discontinuities and parent material uniformity within the Texas sandy mantle and implications for archaeological burial and preservation potential in upland settings. Quat. Res. 78, 60-71.

Albert, R.M., Bamford, M.K., Cabanes, D., 2009. Palaeoecological significance of palms at Olduvai Gorge, Tanzania, based on phytolith remains. Quat. Int. 193, 41-48.

Alexanderson, H., Murray, A.S., 2007. Was southern Sweden ice free at 19-25 ka, or were the post LGM glacifluvial sediments incompletely bleached? Quat. Geochronol. 2, 229-236.

Araujo, A.G.M., 2013. Bioturbation and the upward movement of sediment particles and archaeological materials: comments on Bueno et al. J. Archaeol. Sci. 40, 2124-2127.

Armitage, S.J., King, G.E., 2013. Optically Stimulated Luminescence dating of hearths from the Fazzan Basin, Libya: a tool for determining the timing and pattern of Holocene occupation of the Sahara. Quat. Geochronol. 15, 88-97.

Arnold, L.J., Roberts, R.G., 2009. Stochastic modelling of multi-grain equivalent dose (D_e) distributions: Implications for OSL dating of sediment mixtures. Quat. Geochronol. 4, 204-230.

Barboni, D., Bremond, L., 2009. Phytoliths of East African grasses: an assessment of their environmental and taxonomic significance based on floristic data. Rev. Palaeobot. Palynol. 158, 29-41.

Barich, B.E., Garcea, E.A.A., Giraudi, C., 2006. Between the Mediterranean and the Sahara: geoarchaeological reconnaissance in the Jebel Gharbi, Libya. Antiquity 80, 567-582.

Beauvais, A., Bertaux, J., 2002. In situ characterization and differentiation of kaolinites in lateritic weathering profiles using infrared microspectroscopy. Clays Clay Miner. 50, 314-330.

Bernatchez, J.A., 2010. Taphonomic implications of orientation of plotted finds from Pinnacle Point 13B (Mossel Bay, western Cape Province, South Africa). J. Hum. Evol. 59, 274-288.

Betzler, C., Ring, U., 1995. Sedimentology of the Malawi Rift: facies and stratigraphy of the Chiwondo Beds, northern Malawi. J. Hum. Evol. 28, 23-35.

Beuning, K.R.M., Zimmerman, K.A., Ivory, S.J., Cohen, A.S., 2011. Vegetation response to glacialeinterglacial climate variability near Lake Malawi in the southern African tropics. Palaeogeogr. Palaeoclimatol. Palaeoecol. 303, 81-92.

Bicho, N., Haws, J., Raja, M., Madime, O., Gonçalves, C., Cascalheira, J., Benedetti, M., Pereira, T., Aldeias, V., 2015. Middle and Late Stone Age of the Niassa region, northern Mozambique. Preliminary results. Quaternary International (in press), http://dx.doi.org/10.1016/j.quaint.2015.09.059.

Bonnefille, R., Chalie, F., 2000. Pollen-inferred precipitation time-series from Equatorial mountains, Africa, the last 40 kyr BP. Glob. Planet. Change 26, 25-50.

Bremond, L., Alexandre, A., Wooller, M.J., Hely, C., Williamson, D., Sch€afer, P.A., Majule, A., Guiot, J., 2008. Phytolith indices as proxies of grass subfamilies on East African tropical mountains. Glob. Planet. Change 61, 209-224.

Brown, K.S., Marean, C.W., Jacobs, Z., Schoville, B.J., Oestmo, S., Fisher, E.C., Bernatchez, J., Karkanas, P., Matthews, T., 2012. An early and enduring advanced technology originating 71,000 years ago in South Africa. Nature 491, 590-593.

Bull, W.B., 1977. The alluvial-fan environment. Prog. Phys. Geogr. 1, 222e270. Clark, J.D., Haynes, C.V., 1970. An elephant butchery site at Mwanganda's Village, Karonga, Malawi, and its relevance for Palaeolithic archaeology. World Archaeol. 1, 390-411.

Clark, J.D., Haynes, C.V., Mawby, J.E., Gautier, A., 1970. Interim report on palaeoanthropological investigations in the Lake Malawi Rift. Quaternaria 13, 305-354.

Clark, J.D., Stephens, E.A., Coryndon, S.C., 1966. Pleistocene fossiliferous lake beds of the Malawi (Nyasa) Rift: a preliminary report. Am. Anthropol. 68, 46-87.

Cohen, A., Stone, J.R., Beuning, K.R.M., Park, L.E., Rainthal, P.N., Dettman, D., Scholz, C.A., Johnson, T.C., King, J.W., Talbot, M.R., Brown, E.T., Ivory, S.J., 2007. Ecological consequences of early Late Pleistocene megadroughts in tropical Africa. Proc. Natl. Acad. Sci. 104, 16422-16427.

Conard, N., 2015. Cultural evolution during the Middle and Late Pleistocene in Africa and Eurasia. In: Henke, W., Tattersall, I. (Eds.), Handbook of Paleoanthropology. Springer Berlin Heidelberg, pp. 2465-2508.

Courty, M.-A., Goldberg, P., Macphail, R., 1989. Soils and Micromorphology in Archaeology. Cambridge University Press, Cambridge, UK.

Crossley, R., 1984. Controls of sedimentation in the Malawi Rift Valley, Central Africa. Sediment. Geol. 40, 33-50.

Crossley, R., 1986. Sedimentation by Termites in the Malawi Rift Valley. Geological Society, London, pp. 191-199. Special Publications 25.

d'Errico, F., Stringer, C.B., 2011. Evolution, revolution or saltation scenario for the emergence of modern cultures? Philos. Trans. R. Soc. B Biol. Sci. 366, 1060-1069.

d'Errico, F., Vanhaeren, M., Barton, N., Bouzouggar, A., Mienis, H., Richter, D., Hublin, J.-J., McPherron, S.P., Lozouet, P., 2009. Additional evidence on the use of personal ornaments in the Middle Paleolithic of North Africa. Proc. Natl. Acad. Sci. 106, 16051-16056.

de Albuquerque, E., Braga, J., Vieira, R., 2013. Morphological characterisation of silica phytoliths in Neotropical Marantaceae leaves. Plant Syst. Evol. 299, 1659-1670.

Downs, R.T., 2006. The RRUFF Project: an integrated study of the chemistry, crystallography, Raman and infrared spectroscopy of minerals. In: 19th General Meeting of the International Mineralogical Association, Kobe, Japan.

Duller, G.A.T., 2003. Distinguishing quartz and feldspar in single grain luminescence measurements. Radiat. Meas. 37, 161-165.

Ebinger, C.J., Deino, A.L., Tesha, A.L., Becker, T., Ring, U., 1993. Tectonic controls on rift basin morphology: evolution of the northern Malawi (Nyasa) Rift. J. Geophys. Res. Solid Earth 98, 17821-17836.

Eren, M.I., Durant, A.J., Prendergast, M., Mabulla, A.Z.P., 2014. Middle Stone Age archaeology at Olduvai Gorge, Tanzania. Quat. Int. 322-323, 292-313.

Feathers, J.K., 2002. Luminescence dating in less than ideal conditions: case studies from Klasies River main site and Duinefontein, South Africa. J. Archaeol. Sci. 29, 177-194.

Fernández Honaine, M., Zucol, A.F., Osterrieth, M.L., 2009. Phytolith analysis of Cyperaceae from the Pampean region, Argentina. Aust. J. Bot. 57, 512-523.

Finney, B.P., Scholz, C.A., Johnson, T.C., Trumbore, S., 1996. Late Quaternary lake-level changes of Lake Malawi. In: Johnson, T.C., Odada, E.O. (Eds.), The Limnology, Climatology, and Paleoclimatology of the East African Lakes. Gordon and Breach Publishers, Amsterdam, pp. 495-508.

Forman, S.L., 2015. Episodic eolian sand deposition in the past 4000 years in Cape Cod National Seashore, Massachusetts, USA in response to possible hurricane/ storm and anthropogenic disturbances. Front. Earth Sci. 3. http://dx.doi.org/10. 3389/feart.2015.00003.

Galbraith, R.F., Roberts, R.G., 2012. Statistical aspects of equivalent dose and error calculation and display in OSL dating: an overview and some recommendations. Quat. Geochronol. 11, 1-27.

Galbraith, R.F., Roberts, R.G., Laslett, G.M., Yoshida, H., Olley, J.M., 1999. Optical dating of single and multiple grains of quartz from jinmium rock shelter, northern Australia, part 1, Experimental design and statistical models. Archaeometry 41, 339-364.

Garcin, Y., Vincens, A., Williamson, D., Guiot, J., Buchet, G., 2006. Wet phases in tropical southern Africa during the last glacial period. Geophys. Res. Lett. 33, L07703.

Gasse, F., Barker, P., Johnson, T.C., 2002. A 24,000 yr diatom record from the northern basin of Lake Malawi. In: Odada, E.O., Olago, D.O. (Eds.), The East African Great Lakes: Limnology. Paleolimnology and Biodiversity. Kluwer Academic Publishers, Dordrecht, The Netherlands, pp. 393-414.

Gibert, E., Bergozoni, L., Massault, M., Williamson, D., 2002. AMS-C-14 chronology of 40.0 cal ka BP continuous deposits from a crater lake (Lake Massoko, Tanzania)dmodern water balance and environmental implications. Palaeogeogr. Palaeoclimatol. Palaeoecol. 187, 307-322.

Gliganic, L.A., Jacobs, Z., Roberts, R.G., Domínguez-Rodrigo, M., Mabulla, A.Z.P., 2012. New ages for Middle and Later Stone Age deposits at Mumba Rockshelter, Tanzania: Optically Stimulated Luminescence dating of quartz and feldspar grains. J. Hum. Evol. 62, 533-547.

Grace, J., Jose, J.S., Meir, P., Miranda, H.S., Montes, R.A., 2006. Productivity and carbon fluxes of tropical savannas. J. Biogeogr. 33, 387-400.

Guerin, G., Jain, M., Thomsen, K.J., Murray, A.S., Mercier, N., 2015. Modelling dose rate to single grains of quartz in well-sorted sand samples: the dispersion arising from the presence of potassium feldspars and implications for Single Grain OSL dating. Quat. Geochronol. 27, 52-65.

Harvey, A.M., 2002. The role of base-level change in the dissection of alluvial fans: case studies from southeast Spain and Nevada. Geomorphology 45, 67-87.

Harvey, A.M., Mather, A.E., Stokes, M., 2005. Alluvial Fans: Geomorphology, Sedimentology, Dynamics. Geological Society, London, pp. 1-7. Special Publications 251, London.

Henshilwood, C.S., d'Errico, F., van Niekerk, K.L., Coquinot, Y., Jacobs, Z., Lauritzen, S.-E., Menu, M., García-Moreno, R., 2011. A 100,000-year-old ochreprocessing workshop at Blombos Cave, South Africa. Science 334, 219-222.

Ivory, S.J., Lezine, A.-M., Vincens, A., Cohen, A.S., 2012. Effect of aridity and rainfall seasonality on vegetation in the southern tropics of East Africa during the Pleistocene/Holocene transition. Quat. Res. 77, 77-86.

Johnson, D.L., Domier, J.E.J., Johnson, D.N., 2005. Reflections on the nature of soil and its biomantle. Ann. Assoc. Am. Geogr. 95, 11-31.

Johnson, T.C., Brown, E.T., McManus, J., Barry, S., Barker, P., Gasse, F., 2002. A highresolution paleoclimate record spanning the past 25,000 Years in southern East Africa. Science 296, 113-132.

Johnson, T.C., Brown, E.T., Shi, J., 2011. Biogenic silica deposition in Lake Malawi, East Africa over the past 150,000-0 years. Palaeogeogr. Palaeoclimatol. Palaeoecol. 303, 103-109.

Kaufulu, Z.M., 1983. The Geological Context of Some Early Archaeological Sites in Kenya, Malawi and Tanzania: Microstratigraphy, Site Formation and Interpretation. Department of Anthropology. University of California, Berkeley, Berkeley, p. 340.

Kaufulu, Z.M., 1990. Sedimentary environments at the Mwanganda site, Malawi. Geoarchaeol. 5, 15-27.

Kottek, M., Grieser, J., Beck, C., Rudolf, B., Rubel, F., 2006. World map of the Köppen- Geiger climate classification updated. Meteorol. Z. 15, 259-263.

Kumar, R., Suresh, N., Sangode, S.J., Kumaravel, V., 2007. Evolution of the Quaternary alluvial fan system in the Himalayan foreland basin: Implications for tectonic and climatic decoupling. Quat. Int. 159, 6-20.

Kumar Singh, A., Parkash, B., Mohindra, R., Thomas, J.V., Singhvi, A.K., 2001. Quaternary alluvial fan sedimentation in the Dehradun Valley Piggyback Basin, NW Himalaya: tectonic and palaeoclimatic implications. Basin Res. 13, 449-471.

Lane, C.S., Chorn, B.T., Johnson, T.C., 2013. Ash from the Toba supereruption in Lake Malawi shows no volcanic winter in East Africa at 75 ka. Proc. Natl. Acad. Sci. 110, 8025-8029.

Lenoble, A., Bertran, P., 2004. Fabric of Palaeolithic levels: methods and implications for site formation processes. J. Archaeol. Sci. 31, 457-469.

Linstädter, J., Eiwanger, J., Mikdad, A., Weniger, G.-C., 2012. Human occupation of Northwest Africa: a review of Middle Palaeolithic to Epipalaeolithic sites in Morocco. Quat. Int. 274, 158-174.

Lombard, M., 2011. Quartz-tipped arrows older than 60 ka: further use-trace evidence from Sibudu, KwaZulu-Natal, South Africa. J. Archaeol. Sci. 38, 1918-1930.

Mackay, A., 2008. A method for estimating edge length from flake dimensions: use and implications for technological change in the southern African MSA. J. Archaeol. Sci. 35, 614-622.

McBrearty, S., 1990. Consider the humble termite: termites as agents of postdepositional disturbance at African archaeological sites. J. Archaeol. Sci. 17, 111-143.

McBrearty, S., Brooks, A.S., 2000. The revolution that wasn't: a new interpretation of the origin of modern human behavior. J. Hum. Evol. 39, 453-563.

McPherron, S.J.P., 2005. Artifact orientations and site formation processes from total station proveniences. J. Archaeol. Sci. 32, 1003-1014.

Mercader, J., Astudillo, F., Barkworth, M., Bennett, T., Esselmont, C., Kinyanjui, R., Grossman, D.L., Simpson, S.,Walde, D., 2010. Poaceae phytoliths from the Niassa Rift, Mozambique. J. Archaeol. Sci. 37, 1953-1967.

Mercader, J., Bennett, T., Esselmont, C., Simpson, S., Walde, D., 2009. Phytoliths in woody plants from the miombo woodlands of Mozambique. Ann. Bot. 104, 91-113.

Mercader, J., Bennett, T., Esselmont, C., Simpson, S., Walde, D., 2011. Soil phytoliths from miombo woodlands in Mozambique. Quat. Res. 75, 138-150.

Mercader, J., Bennett, T., Esselmont, C., Simpson, S., Walde, D., 2013. Phytoliths from Middle Stone Age habitats in the Mozambican Rift (105-29 ka). J. Hum. Evol. 64, 328-336.

Mercader, J., Marti, R., Gonzalez, I.J., Sanchez, A., Garcia, P., 2003. Archaeological site formation in rain forests: insights from the Ituri rock shelters, Congo. J. Archaeol. Sci. 30, 45-65.

Murray, A.S., Wintle, A.G., 2000. Luminescence dating of quartz using an improved single-aliquot regenerative-dose protocol. Radiat. Meas. 32, 57-73.

Murray, A.S., Wintle, A.G., 2003. The single aliquot regenerative dose protocol: potential for improvements in reliability. Radiat. Meas. 37, 377-381.

Neumann, K., Fahmy, A., Lespez, L., Ballouche, A., Huysecom, E., 2009. The Early Holocene palaeoenvironment of Ounjougou (Mali): phytoliths in a multiproxy context. Palaeogeogr. Palaeoclimatol. Palaeoecol. 276, 87-106.

Nott, J.F., Thomas, M.F., Price, D.M., 2001. Alluvial fans, landslides and Late Quaternary climatic change in the wet tropics of northeast Queensland. Aust. J. Earth Sci. 48, 875-882.

Novello, A., Barboni, D., Berti-Equille, L., Mazur, J.-C., Poilecot, P., Vignaud, P., 2012. Phytolith signal of aquatic plants and soils in Chad, Central Africa. Rev. Palaeobot. Palynol. 178, 43-58.

Olley, J.M., Murray, A., Roberts, R.G., 1996. The effects of disequilibria in the uranium and thorium decay chains on burial dose rates in fluvial sediments. Quat. Sci. Rev. 15, 751-760.

Pearl, F.B., Dickson, D.B., 2004. Geoarchaeology and prehistory of the Kipsing and Tol river watersheds in the Mukogodo Hills region of Central Kenya. Geoarchaeol. 19, 565-582.

Phillips, J.D., Lorz, C., 2008. Origins and implications of soil layering. Earth Sci. Rev. 89, 144-155.

Piperno, D.R., Pearsall, D.M., 1998. The Silica Bodies of Tropical American Grasses: Morphology, Taxonomy, and Implications for Grass Systematics and Fossil Phytolith Identification. Smithsonian Institution Press, Washington, D.C.

Porraz, G., Parkington, J.E., Rigaud, J.-P., Miller, C.M., Poggenpoel, C., Tribolo, C., Archer, W., Cartwright, C.R., Charrie-Duhaut, A., Dayet, L., Igreja, M., Mercier, N., Schmidt, P., Verna, C., Texier, P.-J., 2013. The MSA sequence of Diepkloof and the history of southern African Late Pleistocene populations. J. Archaeol. Sci. 40.

Prescott, J.R., Hutton, J.T., 1994. Cosmic ray contributions to dose rates for luminescence and ESR dating: large depths and long-term time variations. Radiat. Meas. 23, 497-500.

Ritter, J.B., Miller, J.R., Enzel, Y., Wells, S.G., 1995. Reconciling the roles of tectonism and climate in Quaternary alluvial fan evolution. Geology 23, 245-248.

Robin, V., Petit, S., Beaufort, D., Pr^et, D., 2013. Mapping kaolinite and dickite in sandstone thin sections using infrared microspectroscopy. Clays Clay Miner. 61, 141-151.

Rowan, A.V., Roberts, H.M., Jones, M.A., Duller, G.A.T., Covey-Crump, S.J., Brocklehurst, S.H., 2012. Optically Stimulated Luminescence dating of glaciofluvial sediments on the Canterbury Plains, South Island, New Zealand. Quat. Geochronol. 8, 10-22.

Runge, F., 1999. The opal phytolith inventory of soils in Central Africa - quantities, shapes, classification, and spectra. Rev. Palaeobot. Palynol. 107, 23-53.

Sahle, Y., Morgan, L.E., Braun, D.R., Atnafu, B., Hutchings, W.K., 2014. Chronological and behavioral contexts of the earliest Middle Stone Age in the Gademotta formation, main Ethiopian Rift. Quat. Int. 331, 6-19.

Salisbury, J.W., Vergo, N., 1991. Infrared (2.1-25 mm) Spectra of Minerals. John Hopkins University Press, Baltimore, Maryland.

Schick, K.D., 1987. Modeling the formation of Early Stone Age artifact concentrations. J. Hum. Evol. 16, 789-807.

Scholz, C.A., Cohen, A.S., Johnson, T.C., King, J., Talbot, M.R., Brown, E.T., 2011. Scientific drilling in the Great Rift Valley: the 2005 Lake Malawi scientific drilling project d an overview of the past 145,000 years of climate variability in southern hemisphere East Africa. Palaeogeogr. Palaeoclimatol. Palaeoecol. 303, 3-19.

Scholz, C.A., Johnson, T.C., Cohen, A.S., King, J.W., Peck, J.A., Overpeck, J.T., Talbot, M.R., Brown, E.T., Kalindekafe, L., Amoako, P.Y.O., Lyons, R.P., Shanahan, T.M., Castaneda, I.S., Heil, C.W., Forman, S.L., McHargue, L.R., Beuning, K.R., Gomez, J., Pierson, J., 2007. East African megadroughts between 135 and 75 thousand years ago and bearing on early-modern human origins. Proc. Natl. Acad. Sci. 104, 16416-16421.

Sharon, G., Zaidner, Y., Hovers, E., 2014. Opportunities, problems and future directions in the study of open-air Middle Paleolithic sites. Quat. Int. 331, 1-5.

Shea, J.J., 2011. *Homo sapiens* is as *Homo sapiens* was. Curr. Anthr. 52, 1-35.

Sisk, M.L., Shea, J.J., 2008. Intrasite spatial variation of the Omo Kibish Middle Stone Age assemblages: artifact refitting and distribution patterns. J. Hum. Evol. 55, 486-500.

Sitzia, L., Bertran, P., Boulogne, S., Brenet, M., Crassard, R., Delagnes, A., Frouin, M., Hatte, C., Jaubert, J., Khalidi, L., Messager, E., Mercier, N., Meunier, A., Peigne, S., Queffelec, A., Tribolo, C., Macchiarelli, R., 2012. The paleoenvironment and lithic taphonomy of Shi'Bat Dihya 1, a Middle Paleolithic site in Wadi Surdud, Yemen. Geoarchaeology 27, 471-491.

Stewart, B.A., Dewar, G.I., Morley, M.W., Inglis, R.H., Wheeler, M., Jacobs, Z., Roberts, R.G., 2012. Afromontane foragers of the Late Pleistocene: site formation, chronology and occupational pulsing at Melikane Rockshelter, Lesotho. Quat. Int. 270, 40-60.

Stone, J.R., Westover, K.S., Cohen, A.S., 2011. Late Pleistocene paleohydrography and diatom paleoecology of the central basin of Lake Malawi, Africa. Palaeogeogr. Palaeoclimatol. Palaeoecol. 303, 51-70.

Stoops, G., 2003. Guidelines for Analysis and Description of Soil and Regolith Thin Sections. Soil Science Society of America, Inc., Madison, Wisconsin.

Thomas, M.F., 2004. Landscape sensitivity to rapid environmental changed - a Quaternary perspective with examples from tropical areas. CATENA 55, 107-124.

Thompson, J., Mackay, A., de Moor, V., Gomani Chindebvu, E., 2014. Catchment survey in the Karonga district: a landscape-scale analysis of provisioning and core reduction strategies during the Middle Stone Age of northern Malawi. Afr. Archaeol. Rev. 31, 447-478.

Thompson, J.C., Mackay, A., Wright, D.K., Welling, M., Greaves, A., Gomani Chindebvu, E., Simengewa, D., 2012. Renewed investigations into the Middle Stone Age of northern Malawi. Quat. Int. 270, 129-139.

Thompson, J.C., Welling, M., Gomani Chindebvu, E., 2013. Using GIS to integrate old and new archaeological data from Stone Age deposits in Karonga, Malawi. Int. J. Herit. Digital Era 2, 611-630.

Tierney, J.E., Russell, J.M., Huang, Y., Damste, J.S.S., Hopmans, E.C., Cohen, A.S., 2008. Northern hemisphere controls on tropical southeast African climate during the past 60,000 years. Science 322, 252-255.

Tryon, C.A., 2010. How the geological record affects our reconstructions of Early Middle Stone Age settlement patterns: the case of an alluvial fan setting for Koimilot (Kapthurin formation), Kenya. In: Conard, N.J., Delagnes, A. (Eds.), Settlement Dynamics of the Middle Paleolithic and Middle Stone Age, Volume III Kerns Verlag, Tübingen, Germany, pp. 39-66.

Tryon, C.A., Faith, J.T., 2013. Variability in the Middle Stone Age of Eastern Africa. Curr. Anthr. 54, S234-S254.

Twiss, P.C., Suess, E., Smith, R.M., 1969. Morphological classification of grass phytoliths. Soil Sci. Soc. Am. Proc. 33, 109-115.

Van de Marel, H.W., Beutelspacher, H., 1976. Atlas of Infrared Spectroscopy of Clay Minerals and Their Admixtures. Elsevier, Amsterdam.

Van Nest, J., 2002. The good earthworm: how natural processes preserve upland Archaic archaeological sites of western Illinois, U.S.A. Geoarchaeology 17, 53-90.

Vincens, A., Chalie, F., Bonnefille, R., Tiercelin, J., 1993. Pollen-derived rainfall and temperature estimates for Lake Tanganyika and their implication for Late Pleistocene water levels. Quat. Res. 40, 343-350.

Wang, C.-y., Cheng, L.-H., Chin, C.-V., Yu, S.-B., 2001. Coseismic hydrologic response of an alluvial fan to the 1999 Chi-Chi earthquake. Taiwan. Geol. 29, 831-834.

Waters, J.V., Jones, S.J., Armstrong, H.A., 2010. Climatic controls on Late Pleistocene alluvial fans. Cyprus. Geomorphol. 115, 228-251.

White, F., 1983. The Vegetation of Africa: a Descriptive Memoir to Accompany the UNESCO/AETFAT/UNSO Vegetation Map of Africa. UNESCO, Paris.

Wright, D.K., Thompson, J., Mackay, A.,Welling, M., Forman, S.L., Price, G., Zhao, J.-x., Cohen, A.S., Malijani, O., Gomani Chindebvu, E., 2014. Renewed geoarchaeological investigations of Mwanganda's village (Elephant Butchery Site), Karonga, Malawi. Geoarchaeology 29, 98-120.

Yellen, J.E., 1996. Behavioural and taphonomic patterning at Katanda 9: a Middle Stone Age site, Kivu Province, Zaire. J. Archaeol. Sci. 6, 915-932.

Zipkin, A., Hanchar, J., Brooks, A.S., Grabowski, M.W., Thompson, J.C., Gomani Chindebvu, E., 2015. Ochre fingerprints: distinguishing among Malawian mineral pigment sources with homogenized ochre chip LA-ICPMS. Archaeometry 57, 297-317.

Supplementary Material for paper A: Wright et al. 2017

Mentzer, S. M., Miller, C. E., Schilt, F. C.

MICROMORPHOLOGICAL ATTRIBUTES OF CHAMINADE-II SAMPLES

Sample MEM-3165 (Unit 1).

This sample consists of massive, strongly gleyed sediments with a close porphyric coarse/fine-related distribution (Fig. S1). The coarse fraction consists of coarse sand to very fine gravel. A general lack of microstructure can be attributed to liquefaction of peds and aggregates by waterlogging (Kwaad and Mücher 1994, Or 1996), as well as loading from deep burial. Therefore, the original soil structure is not preserved. Also, the original depositional fabric is not visible, except for broad trends in grain size. The sediments are a mixture of sand and clay, with minor amounts of silt. The clay fraction has three sources: 1) primary clay that derives from alluvial deposition; 2) in situ weathering of biotite and muscovite, as well as feldspar; 3) translocation from higher up in the soil profile. The primary clay is present in the groundmass of the sample. Clays that formed in place are concentrated in zones in and around biotite grains.

The presence of clay translocation features suggests that this sample was formerly a Bt horizon of a soil. Translocation is evidenced by several phases of clay coating formation. From an early phase, significantly reworked (old) clay coatings, not associated with the present void system, are observed in the groundmass as papules. Some of these coatings exhibit a characteristic fabric, known as a "kink-band," that forms when Bt horizons are later impacted by vertic processes (Fig. S2; Kovda and Mermut 2010, Kühn et al. 2010, Stoops 2003). A second phase of old void coatings is observed around existing voids and some of these coatings also have a kink-band fabric. A third phase of clay coating formation, also around voids, post-dates the kink-band coatings. Some of these later coatings appear to be iron stained. Clay coatings are also present around sand grains, but it is difficult to determine their age relative to the void coatings. Clays in the matrix are striated, which is indicative of shrinking and swelling of clays (Blokhuis et al. 1990, Kovda and Mermut 2010, Nettleton and Sleeman 1985).

Micro-FTIR analysis: the clays are dominated by smectites

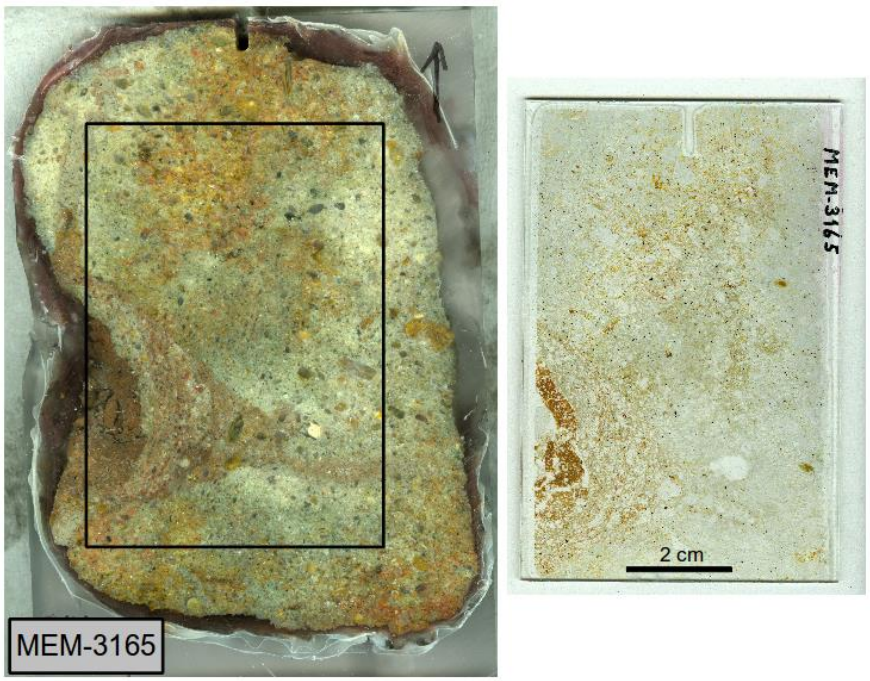

Fig. S1. Sample MEM-3165 from Unit 1. Impregnated block (left) and thin section (right), showing massive, gleyed sediment.

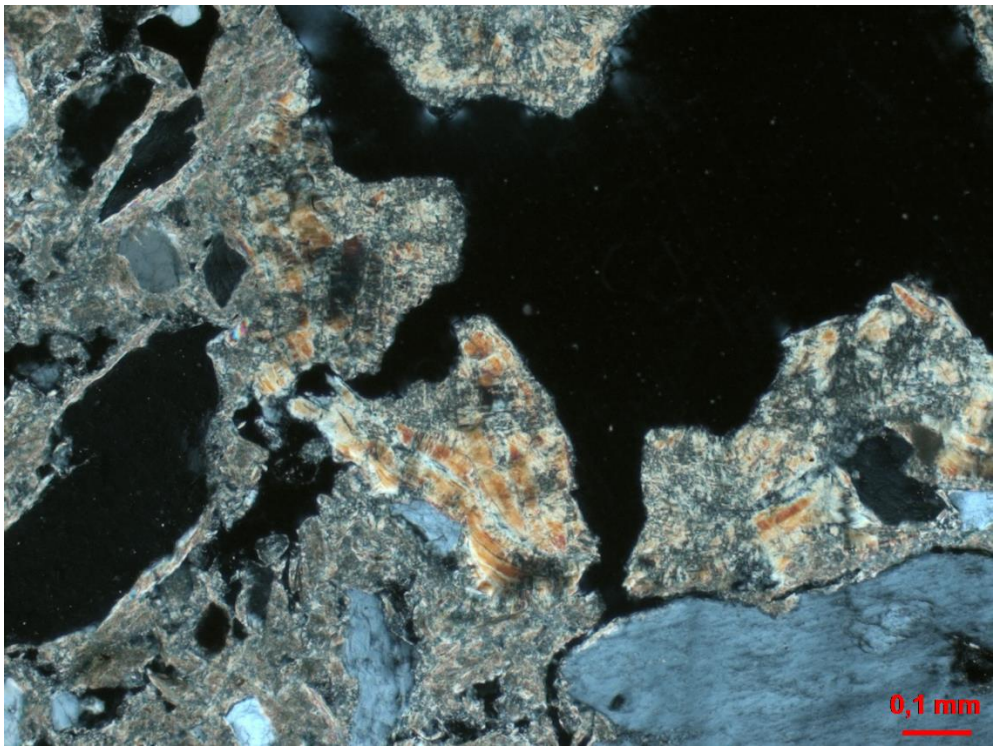

Fig. S2. Old clay coatings in MEM-3165 are deformed, fragmented and exhibit a kink-band fabric as a result of vertic processes. XPL.

Sample MEM-3164 (Unit 1-2)

MEM-3164 was collected from the transition between the pallid zone to the mottled zone, which is expressed in the field and in thin section by an abrupt increase in distinct redox masses (mottles) (Fig. S3). The sample exhibits close- to double-spaced very coarse sand to very fine gravel in a matrix of pale yellowish primary, authigenic and illuvial clay (Fig. S3). Although the sample was collected from the transition between Units 1 and 2, it appears more similar to MEM-3165 from Unit 1 than to MEM-5051, collected from the upper part of Unit 2. Many of the same features, including coatings with a kink-band fabric, are present (Fig. 6b). In this sample, the clay coatings around grains are associated with the oldest phase of clay coating formation (see description of sample MEM-3165). Despite severe bio- and pedoturbation, weak bedding is preserved (Fig. S4).

Desiccation planes, forming a weakly developed subangular ped structure, crosscut the clay coatings associated with the formation of the Bt horizon. Ped formation therefore must have occurred after completion of the first phase of Bt formation and when soil hydrology changed to periodically saturated conditions. Planes and subangular ped microstructure are observed further up the sequence until the lower half of sample MEM-5052, as are the illuvial clay coatings. Redoximorphic features post-date the illuvial clay coatings (Bt pedogenic weathering) as well as the loss of the original soil structure.

Micro-FTIR analysis: the clays are a mixture of smectites and kaolinite with positive identification of actively weathering mica as muscovite.

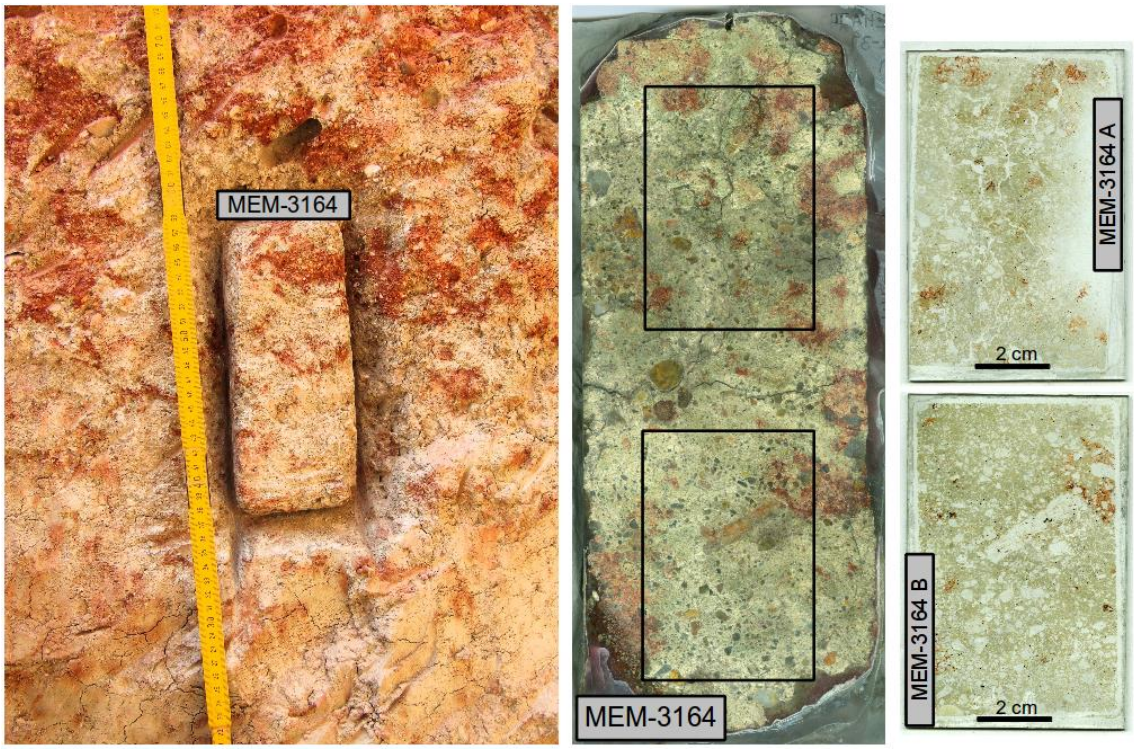

Fig. S3. Sample MEM-3164 from the transition of Unit 1 to Unit 2: in profile before sample collection (left) showing a clear change in redox; the impregnated block (middle, cracked through the middle during sampling); and the correlating thin sections (right).

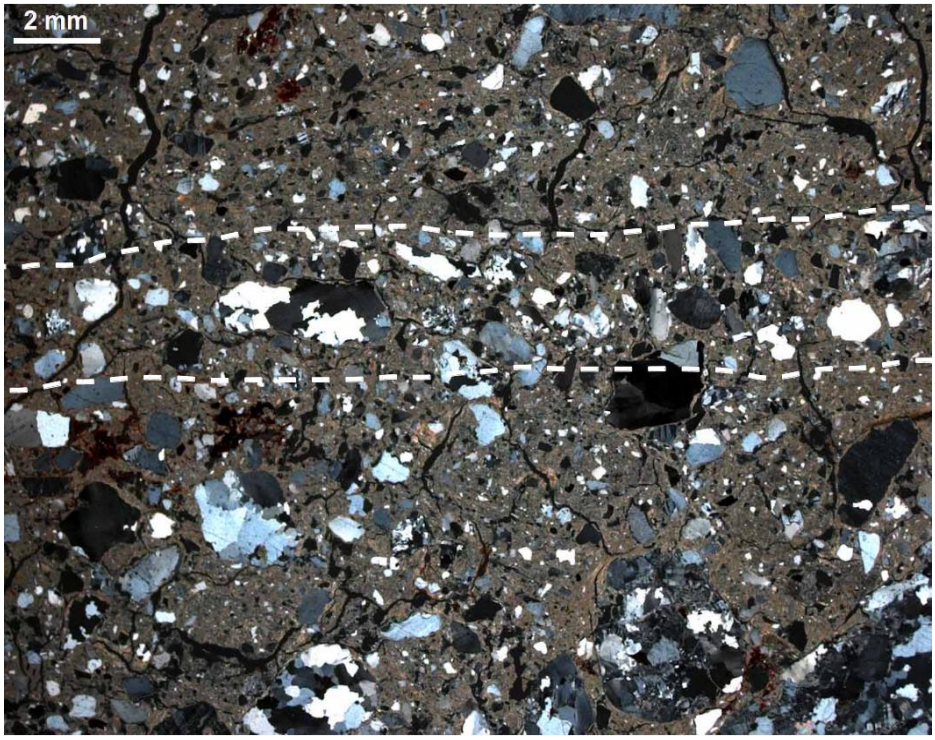

S4. Weak bedding in MEM-3164B, preserved despite extensive bio- and pedoturbation. XPL.

Sample MEM-5051 (Unit 2)

This sample, collected from the upper part of Unit 2, contains a higher proportion of coarse mineral material (primarily subangular very fine gravel) in comparison to the lower samples. The coarse fraction includes more fragments of rounded quartzite, pointing to a potential change in sediment source and higher energy deposition. In MEM-3165 and MEM-3164, primary, authigenic, and illuvial clays are equally abundant. In contrast, the clay in this sample consists predominantly of illuvial clays associated with Bt horizon formation. Older illuvial clay coatings in this sample are more deformed relative to the samples lower down in the sequence. The sample contains more mica (muscovite) that is visibly in the process of weathering, especially inside distinct redox masses (Fig. S6).

Micro-FTIR analysis: the clays are dominated by kaolinite (in illuvial clay coatings); smectites are rare but present. The relative abundance of these clays likely reflects the overall predominance of illuvial clay composed of kaolinite in this sample.

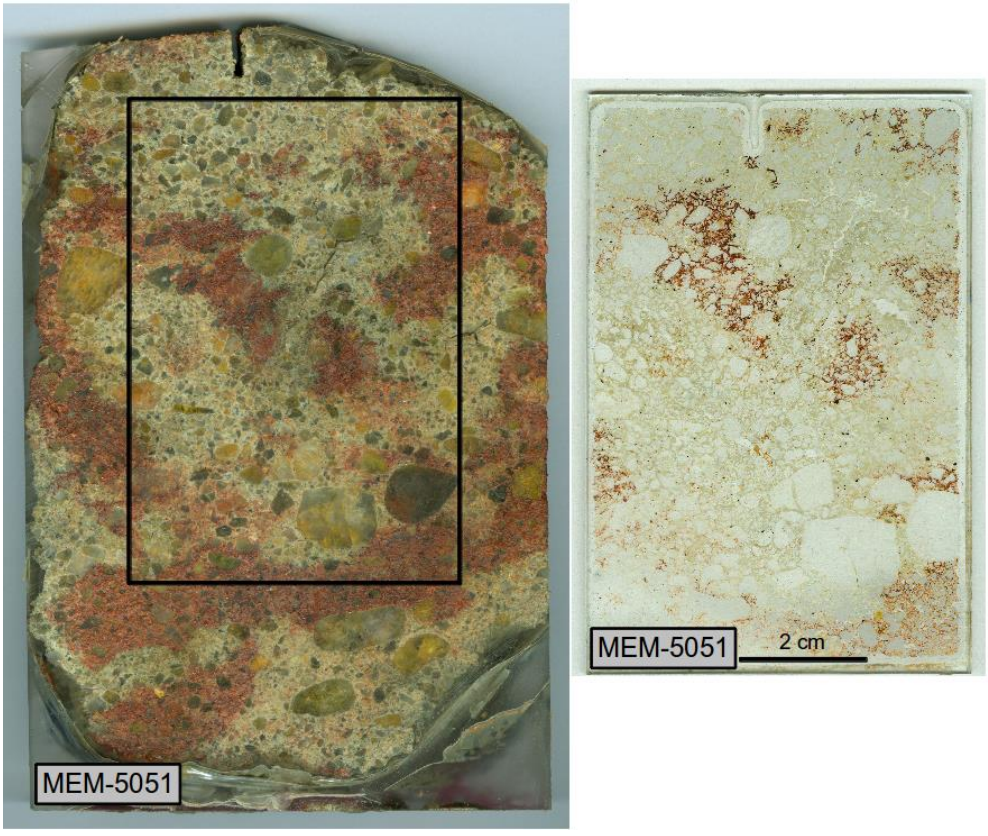

Fig. S5. Sample MEM-5051 from the upper part of Unit 2, showing distinct redox masses and rounded pebbles in the impregnated block (left) and corresponding thin section (right).

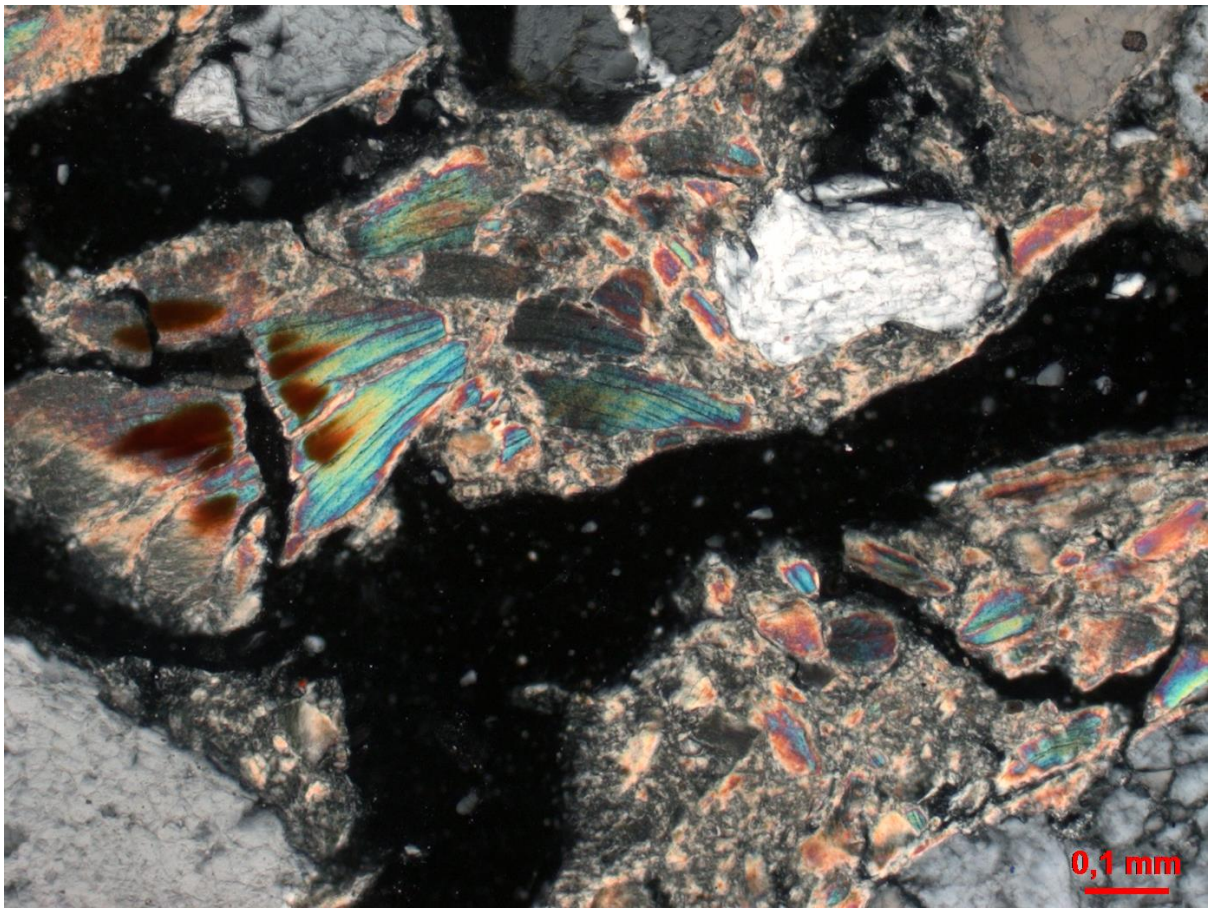

Fig. S6. Weathering mica in MEM-5051. XPL

Sample MEM-5050 (Unit 4)

The sample shows fewer gleyed areas, is for a large part oxidized (red) and contains more manganese than the samples below (Fig. S7). Multiple phases of clay coatings are present. Some in situ forming (orthic) iron manganese nodules contain old clay coatings typical of a Bt horizon (Fig. S7 and Figs. 6a and 6c). These inclusions indicate that active Bt soil formation was interrupted during a period of high groundwater levels, which allowed iron-manganese nodules to form within the former Bt horizon. The exact burial depth at the time of this higher groundwater episode is unknown but the resumption of clay illuviation in MEM-5050 after nodule formation excludes the possibility of deep burial. Older clay coatings have kink-band fabric, but overall, there is less b-fabric indicative of vertic movements.

Micro-FTIR analysis: Kaolinite dominant. Smectite in some of the younger coatings.

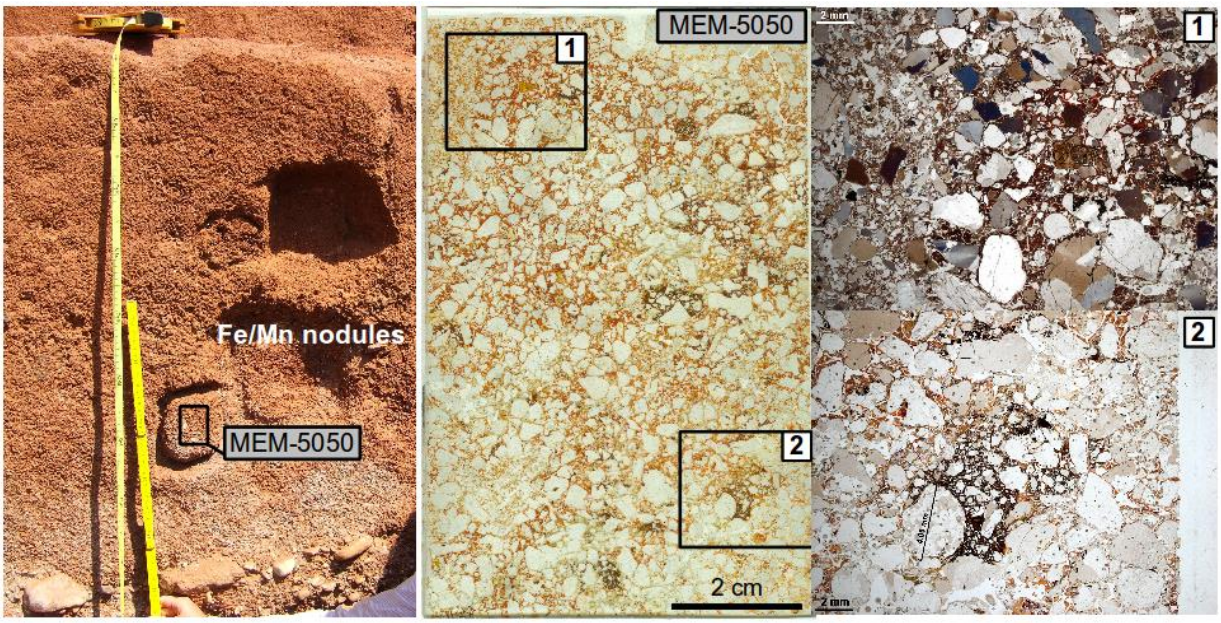

Fig. S7. Sample MEM-5050 from the artifact-bearing Unit 4, showing the sample location in the field, below the iron-nodule concentration (left); thin section (middle) showing dark, in-situ iron-manganese nodule formation, as well as slightly reworked anorthic nodules (small rounded nodule in upper right): micrograph 1 shows preserved clay coatings from a Bt horizon in the right 2/3 of the thin section, bordering open bioturbated material in the left third of the thin section. PPL; micrograph 2 shows an iron-manganese nodule forming in situ on top of a rounded, gravel-sized fragment of quartzite. PPL.

Sample MEM-5052 (Units 4 and 5)

This sample contains the contact between Units 4 and 5. The nodule zone spans this contact. The iron-manganese nodules increase in size upwards, although the grains within the nodules remain generally smaller in size than those in the sedimentary matrix, suggesting that the nodules are anorthic (formed elsewhere). The centers of some of the nodules are soft (as indicated by partial loss during thin sectioning) and contain portions of a soil that is texturally different from the soil surrounding the nodules, again indicating that these are anorthic features. The remnant soil material in the nodules contains dusty clay coatings and papules, as well as other iron nodules. As in sample MEM-5050, the clay coatings inside the nodules are indicative of Bt formation. Furthermore, the iron nodules are encased by clay coatings that formed during a second phase of Bt formation, which post-dates the formation and relocation of the nodules (Fig. S9). Bioturbation is indicated by areas with an intergrain microgranular microstructure (fine enaulic coarse/fine distribution, following Stoops 2003) indicative of termite activity, as well as a few root channels. These features increase in abundance upwards within the sample, such that the nodules at the top of the concentration are largely contained within bioturbated soil, although remnants of the

previously surrounding Bt material remains attached to the outer edges of the nodules (Fig. S8 and Figs. 6e and 6f). The increase in abundance of bioturbation features marks the transition from Unit 4 to Unit 5.

Micro-FTIR analysis: the clays are kaolinite, including the clay coatings in the centers of the nodules. Smectites are rare.

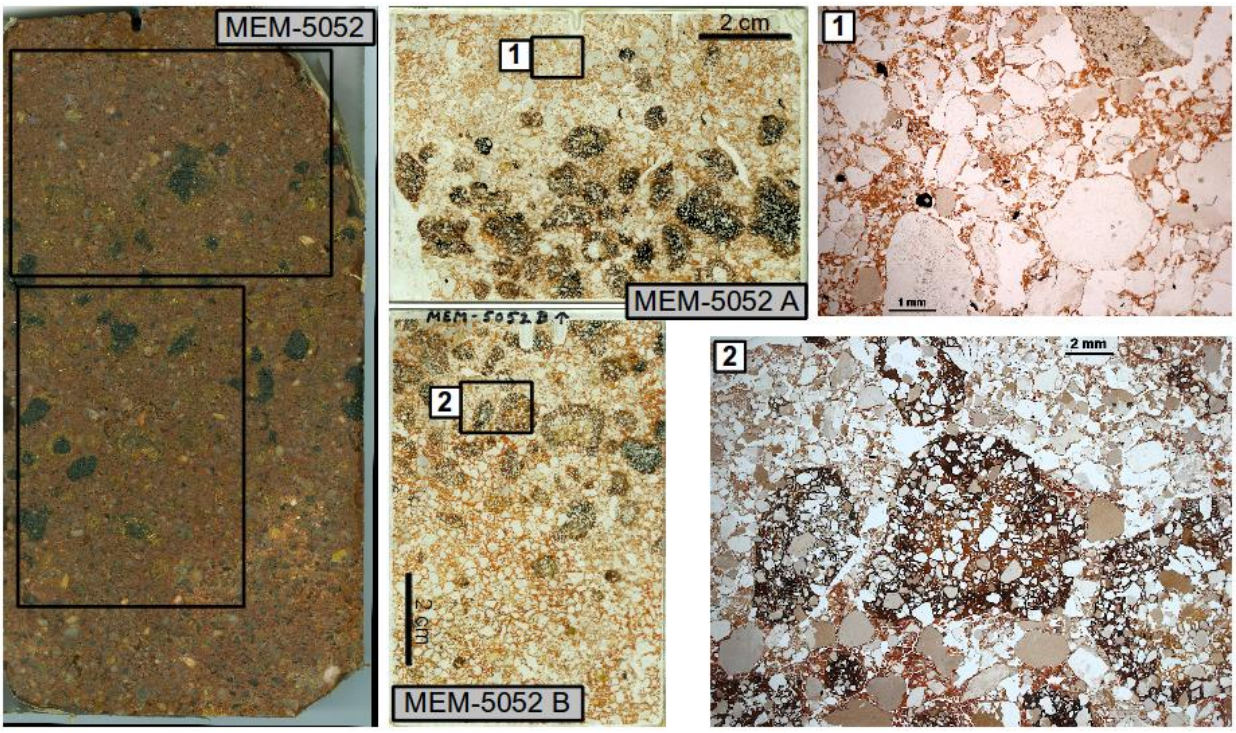

Fig. S8. Impregnated block of sample MEM-5052 (left) and the associated thin sections (middle), including the transition from Unit 4 to Unit 5 and sandy iron-manganese nodules. Micrograph 1 illustrates completely micro-aggregated fine material from termite activity in the upper part of thin section MEM-5052A. PPL. Micrograph 2 shows intact clays from the former Bt with planer voids surrounding the nodules in the lower left but more loose micro-aggregated material between the large nodules in the center and above (MEM-5052B). PPL.

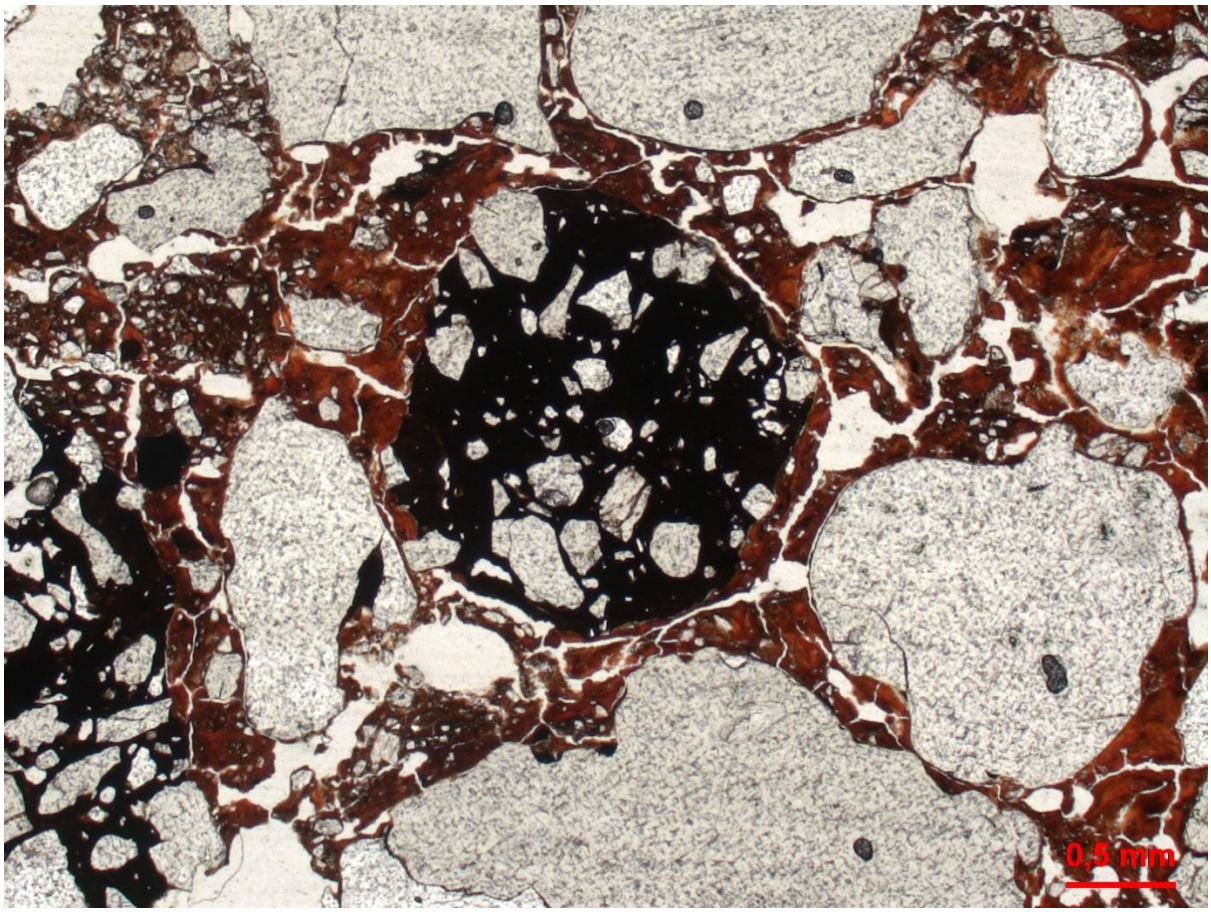

Fig. S9. Small anorthic rounded iron-manganese nodule embedded in preserved Bt material in MEM-5052B.

Samples MEM-5053 and MEM-5054 (Unit 5)

These samples are entirely from depositional Unit 5, which exhibits microscopic features that are typical of the bioturbated zone of a laterite. In the field, this unit is structureless, with a gradual reduction in texture up the sequence. Although the original depositional fabrics associated with alluvial fan sedimentation are absent, we interpret the fining upwards sequence as an artifact of shifting fan energy.

In thin section, this sample is characterized by an intergrain microaggregate microstructure, which is indicative of extensive termite activity (Jungerius et al. 1999, Lee and Wood 1971, McBrearty 1990). Mineral grains show evidence of extreme chemical weathering (Bisdom et al. 1982, Islam et al. 2002, McFarlane 1991).

Very fine gravel-sized (<4 mm) anorthic iron-manganese nodules are rare, but present in MEM-5053A and MEM-5053. These nodules are similar in size to other coarse materials within the sample. It is therefore possible that these nodules have become worked upwards from the main zone of nodules by termite activity (Araujo 2013, Lee and Wood 1971, McBrearty 1990).

Micro-FTIR analysis: the clays are kaolinite.

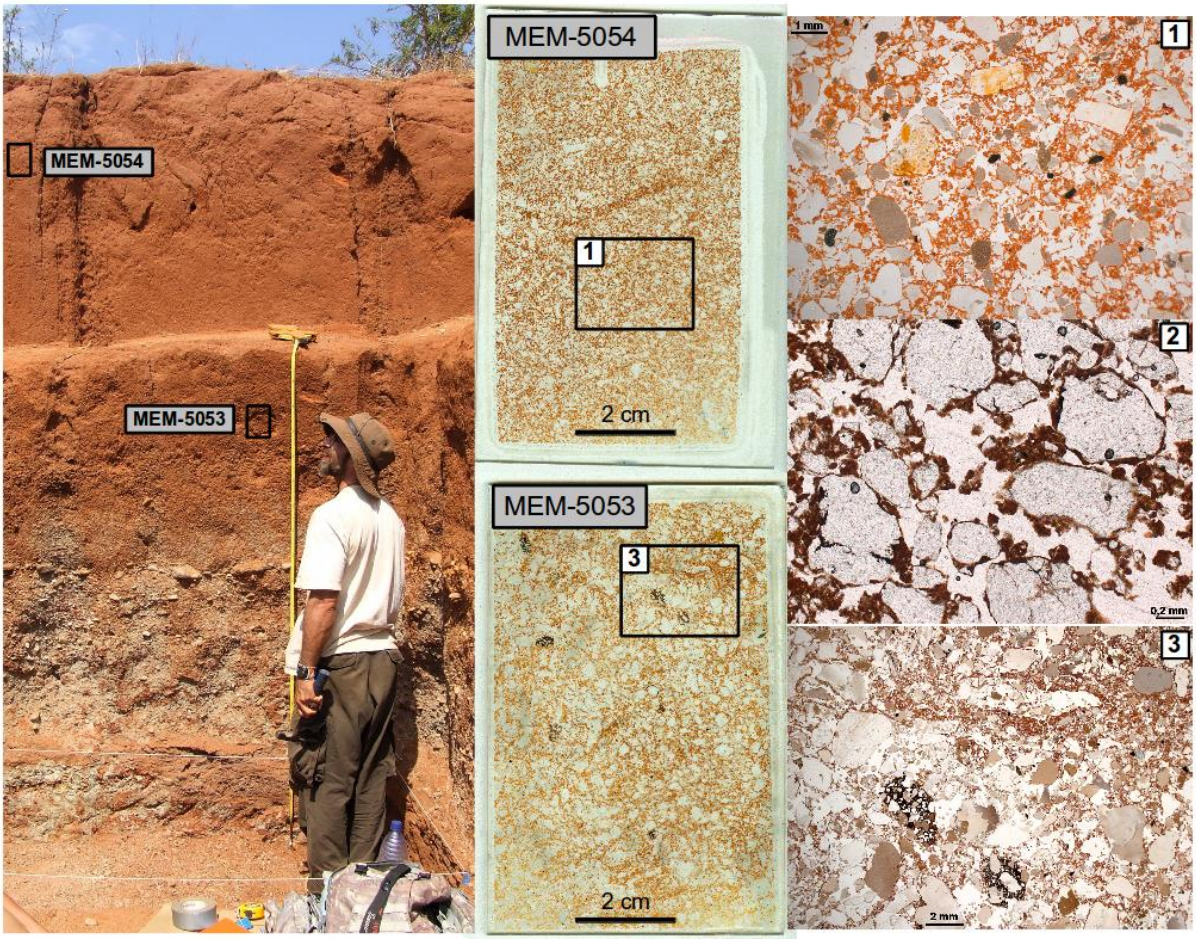

Fig. S10. Sampling locations of samples MEM-5054 and MEM-5053 from the lower and upper part of Unit 5 (left) with corresponding thin sections (middle). Micrograph 1 shows intergrain microaggregate microstructure typical for termite activity as well as small black manganese grains. PPL and oblique incident light. Micrograph 2 shows microaggregates at higher magnification in MEM-5054. PPL. Micrograph 3 shows visible bioturbation channels and fine gravel-sized anorthic iron-manganese nodules that were likely worked upwards from below by termite activity.

SYNTHESIS

We can organize our observations and interpretations of individual micromorphological samples into a series of statements about processes that impacted the CHA-II sedimentary sequence in the past, namely bioturbation, pedogenesis, and groundwater activity.

Bioturbation

In terms of visible intergrain microgranular structure and channels, bioturbation is much more apparent in the laterite represented in Unit 5 than in the underlying Units 1-4 (Fig. S10). The laterite forms the modern soil and the bioturbation observed in it likely dates to the Late Holocene. In the lower units bioturbation also occurred, but at a much earlier point in time. Crumb and granular structures are not visible, but the impacts of bioturbation, such as the development of a porphyric related distribution from a deposit that was likely laminated or bedded, are clear (Fig. S1).

At the base of the sequence, extensive bioturbation (especially visible in the upper part of sample MEM-3164A, Fig. S3) has mixed the primary finer material with the coarser grained material. Most bioturbation likely happened when the sediment in the sample was located near the surface, after which continued aggradation shifted the relative position of the sediment downwards and Bt horizon formation took over.

Pedogenesis

Buried and overthickened Bt horizons

Features typical of Bt horizons are observed in all micromorphological samples up until the lower part of the iron-manganese nodule concentration in MEM-5052B, indicating that the upward migration of the soil profile by slow aggradation of sediment has led to the formation of an overthickened Bt horizon (Schaetzl and Anderson 2005). In this scenario, surface A horizons are less likely to be preserved (Schaetzl and Anderson 2005) and are absent in the micromorphological samples of CHA-II.

Vertic soils

The buried Bt horizon(s) have been impacted by post-depositional argilloturbation. This process has yielded vertic features, but did not produce a true vertisol, possibly because the alluvial sediment is quite coarse. These features suggest that water table fluctuations or seasonal wetting and drying occurred.

At the base of the sequence, some clay coatings post-date vertic features. At the level of the Mn/Fe nodules, clay coatings post-date the formation of the nodules. These observations are consistent with fluctuations of the water table; however, it is impossible to say how many fluctuations occurred.

Clay mineralogy

The vertical trend in clay minerals as determined with micro-FTIR analysis (Fig. S11) reflects the observations and abundance of vertic features. Vertic features are most abundant at the base of the sequence where clay minerals are smectites, or a combination of smectites and kaolinite. This association is logical, given that smectite minerals (2:1 clays) shrink and swell in response to wetting and drying events, while kaolin group minerals (1:1 clays) have little capacity for swelling. Smectites form under drier conditions relative to kaolinite, with more seasonal waterlogging (Schaetzl and Anderson 2005). In some samples, illuvial clay is kaolinite, while in others it is smectite. However, we cannot determine whether the minerals in the illuvial clay coatings originally source from in situ weathering higher up within the profile or deposition from elsewhere, followed by downward translocation. Nevertheless, kaolinite formation can be indicative of high temperatures, high soil moisture, high leaching rates, and tropical forested conditions (Schaetzl and Anderson 2005). Kaolinite is typical of laterite soils, and its dominance in Unit 5 is consistent with all of the other features indicative of a laterite. Any smectites that were originally present in Unit 5 would be gone due to landscape stability and intense chemical weathering.

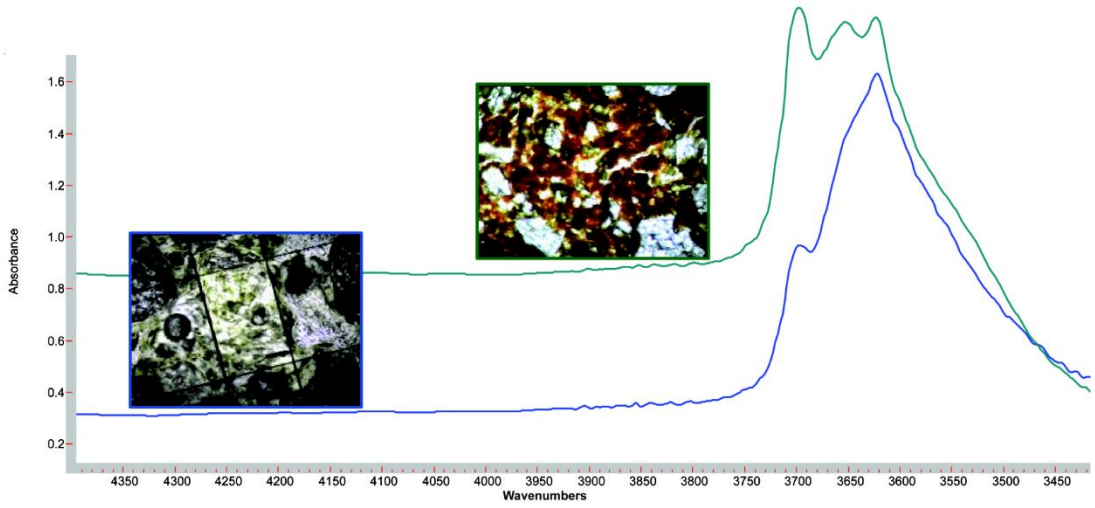

Fig. S11. Transmission spectra from yellowish clays concentrated in the groundmass of MEM-3165 (blue) and reddish clay aggregates in MEM-5054 (green) are dominated by smectite and kaolinite, respectively.

Groundwater activity

The iron-manganese nodules formed as a result of a significant rise of the groundwater table, which also led to the overprinting of illuvial clay coatings from an old Bt horizon by redoximorphic

features. In the lower half of the main iron-manganese nodule concentration the nodules are encased in illuvial clay pedofeatures, indicating that Bt formation resumed after nodule formation. Nodules in this lower portion of the iron-manganese nodule zone are generally in place (orthic), while the upper portion contains reworked, anorthic nodules, which suggests that they have moved downwards. The anorthic appearance of the nodules as well as the small grain size of the sands included in them relative to the present sedimentary matrix, suggests that they were initially more dispersed when they first formed and have since become more concentrated either through lateritization, bioturbation or winnowing. Two key observations point to the concentration of nodules by winnowing: 1) the fabric of the sediment in the center of the nodules indicates that they did not form in the overlying laterite but in a soil that contained a Bt horizon (Fig. 6h, S8); 2) although bioturbation features are present in between the nodules at the base of Unit 5, bioturbation does not extend to the base of the anorthic nodules (Fig. S8, micrograph 2). Therefore, downward movement of the nodules occurred before the onset of extensive bioturbation. It is inferred that the Mn/Fe nodule zone was originally thicker, but it cannot be determined how much thicker the nodule zone was and at what depth the nodules formed. It is likely that artifacts associated with the nodules also moved downward to some degree.

CONCLUSIONS OF MICROMORPHOLOGICAL ANALYSES

To summarize, evidence for long-term deposition of alluvial sediment with the original depositional fabric (in the micromorphological samples) largely absent due to bioturbation, pedogenesis, and groundwater activity. In extreme cases, such as the gravel channel lag (Unit 3), depositional features are preserved. Conditions were favourable for a long time for the formation of soils with Bt horizons. As the area aggraded, the zone of Bt moved upwards, resulting in an overthickened Bt horizon. Fluctuations in moisture initiated the shrinking and swelling of smectites present in the soils, resulting in pedoturbation and vertic features, but no true Vertisols. Bt horizon formation and shrinking/swelling occurred multiple times. The groundwater table rose significantly at some point, which gleyed much of the lower profile and contributed to the formation of iron-manganese nodules within the now inactive Bt horizon. After the groundwater level had dropped, profile winnowing occurred and the uppermost of the nodules settled downwards, forming a pisolith. Alluvial sedimentation continued, and Bt horizon formation resumed at the depth of the deflated nodules. At some point alluvial fan sedimentation came to a halt, the landscape stabilized, and lateritization commenced. At present, the bioturbated portion of the laterite extends down into the upper nodule zone.

When considering the environment in which MSA human activity took place, the erosion event leading to winnowing and concentration of the nodules (and artifacts) implies that the landscape had transitioned to a grassier ecosystem, which is corroborated by the abundance of grassland species in the phytolith record (Fig. 5, phase 3).

REFERENCES

Araujo, A. G. M. 2013. Bioturbation and the upward movement of sediment particles and archaeological materials: comments on Bueno et al. *Journal of Archaeological Science* 40:2124-2127.

Bisdom, E. B. A., Stoops, G., Delvigne, J., Curmi, P., Altemuller, H.-J. 1982. Micromorphology of weathering biotite and its secondary products. *Pedologie* 32-2:225-252.

Blokhuis, W. A., Kooistra, M. J., Wilding, L. P. 1990. Micromorphology of Cracking Clayey Soils (Vertisols). *Developments in Soil Science* 19:123-148.

Islam, Md. R., Stuart, R., Risto, A., Vesa, P. 2002. Mineralogical changes during intense chemical weathering of sedimentary rocks in Bangladesh. *Journal of Asian Earth Sciences* 20:889-901.

Jungerius, P. D., van den Ancker, J. A. M., Mucher, H. J. (1999). The contribution of termites to the microgranular structure of soils on the Uasin Gishu Plateau, Kenya. *Catena* 34:349–363.

Lee, K. E. and Wood, T. G. (1971). Termites and soils. Academic Press, London.

Kovda, I. and Mermut, A., 2010. Vertic features. In Stoops, G., Marcelino, V. & Mees, F. (eds.), Interpretation

of Micromorphological Features of Soils and Regoliths. Elsevier, Amsterdam, pp. 109–127.

Kühn, P., Aguilar, J., Miedema, R. (2010): Textural features and their related horizons. In: Stoops, G., Marcelino, V., Mees, F. (eds.): Interpretation of Micromorphological Features of Soils and Regoliths. Elsevier, Amsterdam pp. 217-250.

Kwaad, F.J.P.M., Mücher, H.J. 1994. Degradation of soil structure by welding — a micromorphological study, *Catena* 23, 3–4: 253-268.

McBrearty, S., 1990. Consider the humble termite: termites as agents of post-depositional disturbance at African archaeological sites. *J. Archaeol. Sci.* 17:111-143.

McFarlane, M. J. 1991. Some sedimentary aspects of lateritic weathering profile development in the major bioclimatic zones of tropical Africa. *Journal of African Earth Sciences* 12:267-282.

Nettleton, W.D. and Sleeman, J.R., 1985. Micromorphology of Vertisols. In Douglas, L.A. & Thompson, M.L. (eds.), Soil Micromorphology and Soil Classification. Soil Science Society of America Special Publication 15, SSSA, Madison, Wisconsin, pp. 165–196.

Or, D. 1996. Wetting-induced soil structural changes: The theory of liquid phase sintering. Water resources research 32-10:3041-3049.

Schaetzl, R. J. and Anderson, S. 2005. Soils. Genesis and Geomorphology. Cambridge University Press.

Stoops, G. (2003). Guidelines for Analysis and Description of Soil and Regolith Thin Sections. The Soil Science Society of America, Madison.

B - Micromorphology of an Upper Paleolithic Cultural Layer at Grub-Kranawetberg, Austria

Flora Schilt [1, 2] (corresponding author), Alexander Verpoorte [3], Walpurga Antl [4]

[1] Institute for Archaeological Sciences, Rümelinstrasse 23, 72070 Tübingen, Germany. [2] Senckenberg Centre for Human Evolution and Paleoenvironment. [3] Faculty of Archaeology, Leiden University, P.O. Box 9515, 2300 RA Leiden, The Netherlands.[4] Natural History Museum Vienna, Department of Prehistory, A-1014 Vienna, Austria

http://dx.doi.org/10.1016/j.jasrep.2017.05.041

ABSTRACT

Cultural layers are a fundamental part of open-air loess sites. As complex representations of the interaction between human activity and natural processes, we believe these layers deserve detailed investigation. In this paper we consider the impact of hunter-gatherers on sediments and soil formation and present a small-scale, micromorphological study of a cultural layer at Grub-Kranawetberg. Grub-Kranawetberg is a Gravettian site located on a flat crest overlooking the Morava river valley in Lower Austria. We used micromorphology to study the formation of the main cultural layer of the site as well as the bordering underlying and overlying deposits. The studied cultural layer of Grub-Kranawetberg shows evidence of 1) substantial anthropogenic input of organic and mineral material, 2) bioturbation by a diverse soil fauna including mollusks and earthworms, 3) translocation of carbonates, indicating soil-forming processes, 4) trampling and 5) a preserved, though bioturbated, occupation surface without signs of erosion or redeposition. By enhancing nutrient availability and soil faunal activity, the human waste influenced the diversity and composition of the plant communities. We argue that the cultural layer is best described as an anthropogenic soil, indicating that anthropogenic waste already played a role in Late Pleistocene human landscape modification.

Keywords: Cultural layer; Gravettian; micromorphology; site formation; anthropogenic soil; loess

Schilt, F.C., Verpoorte, A., Antl, W. (2017). Micromorphology of an Upper Paleolithic cultural layer at Grub-Kranawetberg, Austria. *Journal of Archaeological Science: Reports* 14:152-162.

INTRODUCTION

Soils as archives of human interaction with the environment is not a topic frequently discussed in Paleolithic archaeology (but see Brancier et al. 2014, Engovatova & Golyeva 2012, Glaser & Birk 2012, Golyeva et al. 2016). However, several studies have demonstrated the effects of early hunter-gatherers on other aspects of the environment such as vegetation and animal diversity. Palynological analyses suggest that humans impacted vegetation as early as ca. 50.000 year ago in Borneo (Hunt et al. 2012) and in Western Europe Bos and Janssen (1996) argued for early human influences during the Younger Dryas (Bos and Janssen 1996). Similarly, the hunting of animals contributed to the maintenance of prey diversity (Bird et al. 2013), but at times over-exploitation may have led to overkill and extinction events (Barnosky et al. 2004, Sandom et al. 2014 and Surovell et al. 2016, but see also Diamond 1989, Guthrie 1984, Owen-Smith 1987, MacPhee & Marx 1997 and Martin 1984). The abandonment of food refuse at campsites created plant-rich patches (Politis 1996), while some local plant and animal species benefited from human off-site use of fire (Bird et al. 2013, Scherjon et al. 2015). Stone tool use over the past 2,5 million years has also been described as resulting in a man-made lithic landscape (Foley & Lahr 2015). The influence of early hunter-gatherers on vegetation and soils may have been less intense than during agricultural times, but through the extraction of food items, raw materials and other resources, hunter-gatherers did change their local landscapes (Smith 2011, Rowley-Conwy & Layton 2011, Boivin et al. 2016). In this paper we consider the impact of hunter-gatherers on the lithosphere and present a small-scale, micromorphological study of a cultural layer. We approach the cultural layer as the complex representation of the interaction of human activity and geological processes of sedimentation, erosion and pedogenesis (Terhorst et al. 2014, Goldberg & Aldeias 2016).

Cultural layers are a characteristic feature of Upper Paleolithic open-air sites in loess and silt loam (Gribchenko 2006). At large site complexes such as Dolní Věstonice (Klíma 1963, 1969, Svoboda 1991), Pavlov (Svoboda 1994, 1997, 2005, Svoboda et al. 2016), Předmostí (Absolon & Klíma 1977, Polanska et al. 2014), Kostenki (Pietsch et al. 2014, Hoffecker et al. 2016), Willendorf (Felgenhauer 1959, Haesaerts et al. 1996, Nigst et al. 2014), Krems-Wachtberg (Einwogerer 2000, Händel et al. 2014) and Grub-Kranawetberg (Antl-Weiser 2008, Antl 2013, Antl-Weiser et al. 2010), a brown to gray horizon of up to 50 cm thick is associated with high find densities and the remains of fireplaces, dumps, and pits. Finds at smaller sites such as Jarošov (Skrdla 2005), Ollersdorf (Antl-Weiser 2008), Langenlois (Einwogerer 2008), Jaksice (Wilczyński et al. 2015) or Moravany (Hromada & Kozlowski 1995, Kozlowski 1998) are associated with less well-developed,

thinner brownish or grayish horizons. Such cultural layers are interpreted as in situ "living floors" (e.g. Händel et al. 2009, 2014), but also as "zones of occupation" with a considerable temporal spread (Hoffecker et al. 2016) and spatial and temporal palimpsests (e.g. Verpoorte 2000, Novak 2005).

Recently, several paleoenvironmental studies of loess-paleosol sequences have incorporated cultural layers into their multi-method investigations (Antoine et al. 2013, Fuchs et al. 2012, Terhorst et al. 2014, Lisá et al. 2014, Łanczont et al. 2015, Svoboda et al. 2015, Pietsch et al. 2014, Velichko et al. 2009, Haesaerts et al. 2010). These studies are extremely valuable for chronostratigraphy and environmental reconstruction but also offer insight into the climatic and paleoenvironmental contexts of human occupation. They focus on the natural conditions and processes, such as permafrost, solifluction, gleyification, vegetation and animal burrows that influenced human activities and the preservation of archaeological remains. Lisá et al. (2014) addressed the relationship between formation processes and human settlement in dry glacial landscapes by comparing three sites (Dolní Věstonice II, Předmostí and Hošálkovice) along a S-N transect in Moravia. They were able to detect differences in humidity and suggested that these differences may have been a decisive factor in the presence of Gravettian settlement by enhancing vegetation, which would have attracted animals and therefore humans.

At the site of Grub-Kranawetberg, we are able to consider humans themselves as a factor in local environmental change. This may for instance be reflected in soil formation and changes in vegetation. The anthropogenic effect on geological processes and climatic and ecological signals at Paleolithic sites has not received much attention but is just as crucial as the question of how the environment impacted human behavior and settlement dynamics. A detailed study of cultural layers offers the opportunity to gain more insight in the complex interplay between humans and their environment.

The main objectives of this paper are 1) to provide a detailed interpretation of the formation of the main cultural layer at the Gravettian site of Grub-Kranawetberg in eastern Austria 2) to discuss how human occupation influenced sedimentary deposition and soil-forming processes. We use micromorphology, combined with field observations, as the main method of investigation.

SITE DESCRIPTION

Grub-Kranawetberg is located ca. 40 km north-east of Vienna in Lower Austria near the Slovakian border (Fig. 1). The site is situated at an elevation of 196 meters above the Adriatic on a flat upland

crest overlooking the Morava river valley. Known since the 1970s for its surface finds, systematic excavations started in 1993 when a vineyard was uprooted (Antl-Weiser 1999, Antl-Weiser 2008, Ant & Fladerer 2004). Excavations continued until 2012.

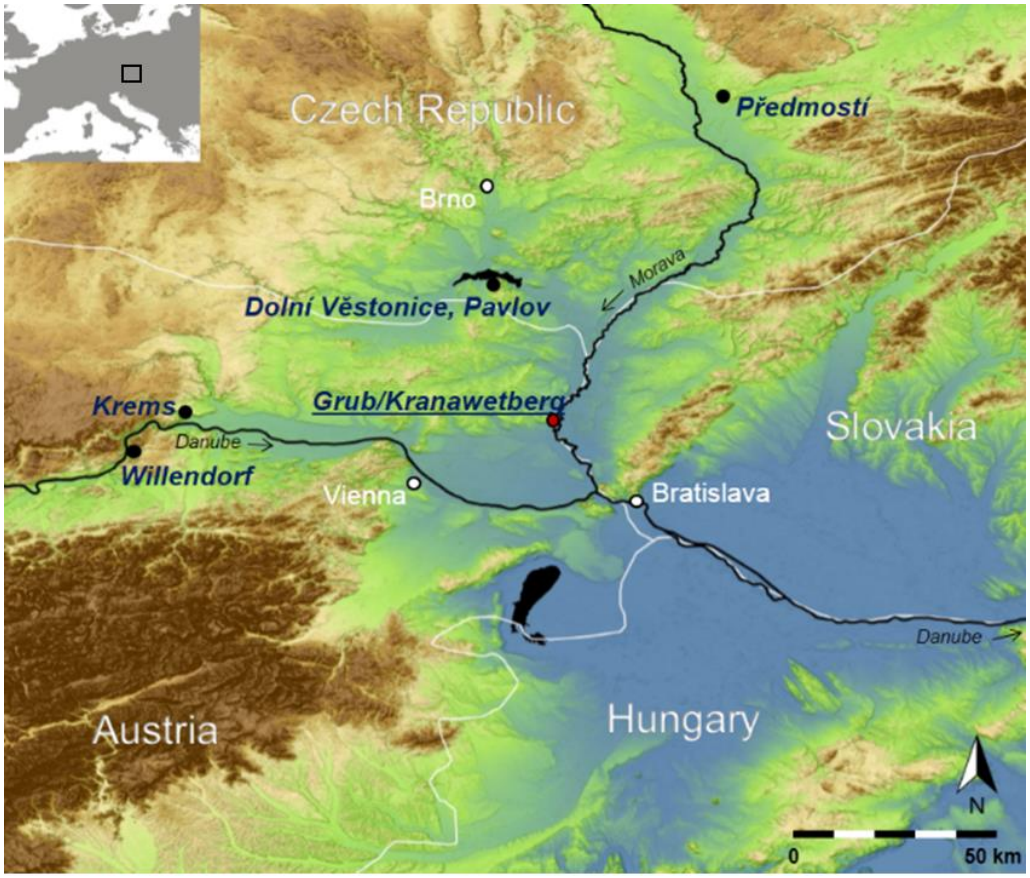

Figure 1. Location of Grub/Kranawetberg along the Morava river. Other sites mentioned in the text are Předmostí, Dolní Věstonice, Pavlov, Krems and Willendorf. SRTM basemap from Jarvis et al. (2008).

From the base to the top of the excavation, four archaeological horizons were identified: AH4 to AH1. The lowermost, AH4, represents the first occupation of the site and is regarded as the main cultural layer. In the excavated area the layer is 8-20 cm thick and light to dark brown in color (Antl 2013). In some areas, AH4 parts into two layers, separated by lenses of light colored, "clean" loess, suggesting that the layer is composed of different episodes of site use, alternated with loess deposition (Antl-Weiser et al. 2010, Antl 2013). Outside the excavated area the layer tapers completely off into the loess deposits. AH4 contained two hearth features as well as pits surrounding the hearths (Fig. 2). In the hearth features, at least four superimposed burning episodes could be identified in the field, separated by thin layers of clean, undisturbed aeolian loess. They were interpreted as a clear indication for the repeated use of the two hearths (Antl 2013).

Both combustion features were well-preserved and surrounded by a series of pits that have been interpreted as the remains of dwelling structures (Nigst 2004, Nigst & Antl-Weiser 2012). Away from these hearths not only a sharp decrease in artifact density was observed (Nigst 2004), but also "an end of the brown colored cultural layer changing to a horizon with only scattered finds" (Antl-Weiser 2008, 66).

Ca. 20 meters west from the hearths in another excavation area, concentrations of large mammal bones were uncovered (Fig. 2). The discovery of two molars of the same mammoth individual in the different excavation areas suggests contemporaneity for the main cultural layer and the bone accumulation (Antl-Weiser 2008, Antl-Weiser et al. 2010, Bosch 2009, Bosch et al. 2012). The bone concentrations are interpreted as dumping areas for the remains of animals that were butchered nearby (Antl-Weiser 2008, Antl-Weiser et al. 2010). Mammal remains in the dumping areas include mammoth, woolly rhino, reindeer, wild horse, giant deer, hare, wolf and bear (Antl et al. 1997, Antl-Weiser 2008, Antl-Weiser et al. 2010, Bosch 2009, Bosch et al. 2012). Based on zooarchaeological, taphonomic, and spatial analyses, Bosch et al. (2012, 119) conclude that "the role of fire in the Grub-Kranawetberg bone accumulation is best explained as a waste removal strategy".

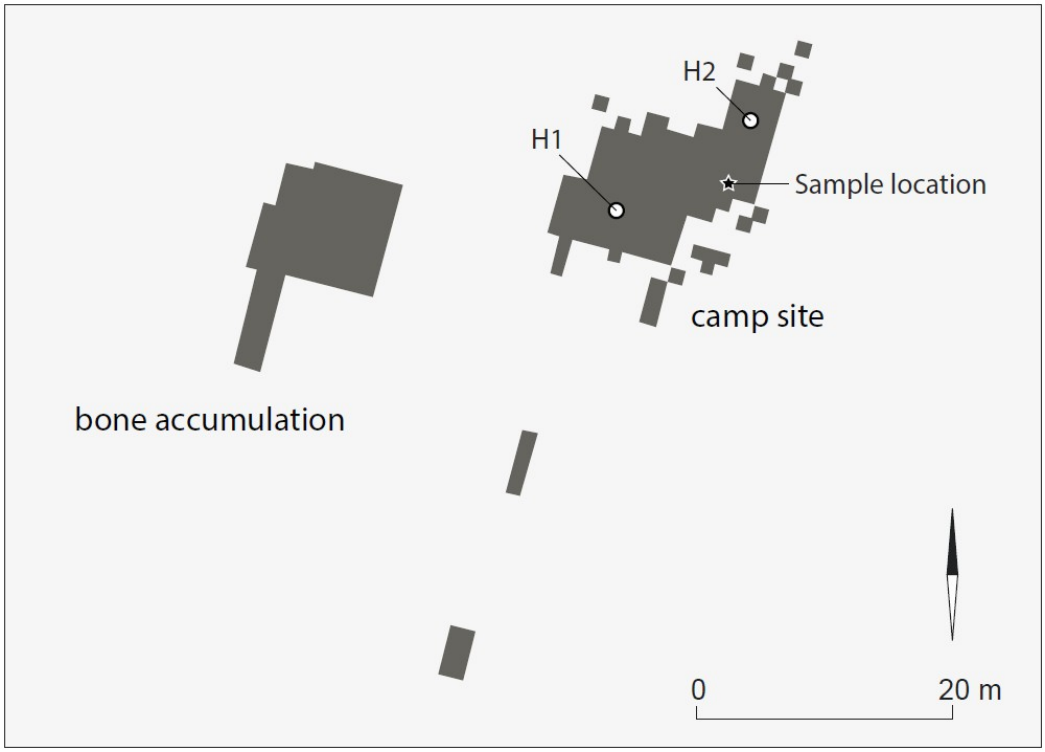

Figure 2. Site overview of the excavated areas at Grub-Kranawetberg. In the occupation area ("camp site"), the locations of the hearths are indicated (H1 and H2), as well as the sample location of the micromorphological samples.

AH3, located only ca. 8-10 cm above the main cultural and up to 16 cm thick, is lighter in color and exhibits no evident structural traces or combustion features (Antl-Weiser et al. 2010). Similar to AH4, lenses of clean loess part the layer in some places, giving a clear indication for at least one episode of abandonment. AH3 and AH4 yielded thousands of lithics and bones including some human remains, bone tools, antler, ivory beads, molluscs and ochre. Comparison of the lithics and bone material from AH4 and AH3 has led to the conclusion that these assemblages were produced and discarded by different groups of people even though the two layers are chronologically very similar (Antl 2013).

The upper two archaeological horizons, AH1 and 2, consist only of scattered finds, located ca. 5-10 cm above AH3. Antl (2013) noted that inside the ca. 80 cm in which the archaeological layers occurred extensive organic activity could be observed, while the loess above AH1 showed a marked change to "a brighter colour and higher density of the sediment" (Antl 2013, 123).

Radiocarbon dates on charcoal from AH4 and AH3 range from 25.640±160 BP (GrA-28,184: 30.354-29.354 cal BP at 95.4% modelled in OxCal v.4.2. with IntCal13) to 24.620±230 BP (GrA-9063: 29.210-28.120 cal BP at 95.4% modelled in OxCal v.4.2. with IntCal13) (Antl-Weiser et al. 2010) with a summed probability age for the main cultural layer AH4 of 30.405 to 29.162 cal BP 2σ (Zöller et al. 2013). A ca. 210 cm thick pedocomplex of brownish loess below the archaeological horizons (correlated with "Stillfried-B") is dated by Infrared Stimulated Luminescence (IRSL) and Optically Stimulated Luminescence (OSL) between ca 47 and 30 ka (Zöller et al. 2013, see also Terhorst et al. 2011, Zöller et al. 1994).

The dates place the habitation of the site at the beginning of the Alpine Last Glacial Maximum (LGM) (Heiri et al. 2014, Ivy-Ochs et al. 2008). In this period the loess landscape was covered by a forest steppe. Grasses, herbs and small shrubs formed a mosaic landscape with wooded areas of boreal trees such as birch, pine and larch (Feurdean et al. 2014; Svoboda et al. 2015). The forest steppe was inhabited by a mammoth steppe fauna including at least the large mammals found in Grub-Kranawetberg: woolly mammoth, woolly rhinoceros, horse, reindeer, giant deer, hare, wolf and bear (Bosch et al. 2012; Antl-Weiser et al. 1997).

MATERIALS AND METHODS

We employed micromorphology to investigate the deposits in detail under the petrographic microscope. Micromorphological analysis is a powerful tool to study anthropogenic as well as natural geogenic, biological, or pedogenic components at the microscopic scale (Courty et al. 1989). Soil micromorphology has been used as a standard method at Upper Paleolithic sites in the region at least since 1976, when Smoliková (1976) analyzed samples from Bohunice near Brno, and later from Dolní Věstonice II and Milovice I (Smoliková 1976, 1991, 2009, but see also Beresford-Jones et al. 2011, Łanczont et al. 2015, Lisá et al. 2014, Nigst et al. 2014, Terhorst et al. 2014, Svoboda et al. 2015).

In 2004, two micromorphological samples (5542 and 5543) were collected at Grub, using tin cans ca. 1.5 m below the modern surface from the exposed east profile of square K12, about 5 meters east from the largest hearth (Hearth I) and 6 meters south from the smaller hearth (Hearth II) (Fig. 2). Pit or hearth features are absent in this area and the three upper find-bearing layers do not visibly extend to the sample location, although a few artifacts occur at the level of AH3. The samples contained the main cultural layer (AH4) as well as the overlying and underlying units (Fig. 3). Sample collection at a peripheral part of the main archaeological horizon allowed for the study of the transitions between the cultural layer and the underlying as well as the overlying sediments in single thin sections (thin sections 5542 and 5543 B).

The samples were prepared for thin sectioning at the Institute for Archaeological Sciences at the University of Tübingen, Germany. The blocks were oven-dried for several days at 50 °C and impregnated with resin under vacuum. The resin was prepared with 7 volume units of unpromoted polyester resin (Viscovoss N 55S), 3 volume units of styrene (styrene for synthesis) and 5-6 ml/l hardener (methylethylketone peroxide, MEKP). After hardening the blocks were sliced into slabs with a rock saw from which uncovered thin sections of 6x9 cm and 30 μm thickness were produced at the laboratory of Thomas Beckmann in Braunschweig, Germany (Beckmann 1997).

The thin sections were scanned with a flat-bed scanner to observe and display macroscopic characteristics and studied under a stereoscope (0,65 - 5x magnification) and a petrographic microscope (20 - 500x magnification) using plane polarized light (PPL), crossed polarized light (XPL), blue light fluorescence and oblique incident light (Courty et al. 1989). Micromorphological description is performed following Courty et al. (1989) and Stoops et al. (2003).

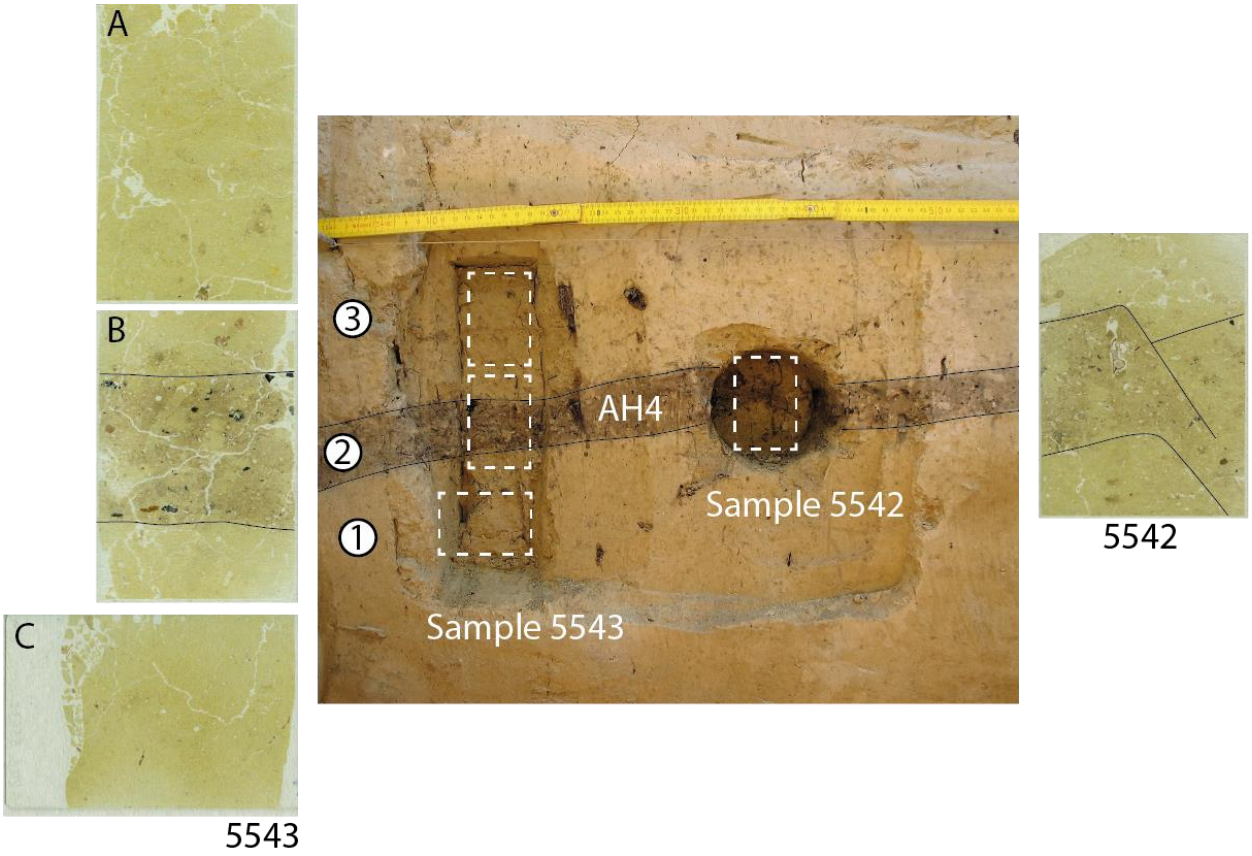

Figure 3. Photo (middle) of the sample location in the East profile of Grub-Kranawetberg, showing the two samples after collection and scans of thin sections 5543 A, B, C and 5542. The boundaries of Unit 2 (AH4) are drawn in with black lines and the units are labeled (1-3). White dashed frames indicate the location of the corresponding thin sections. Sample 5542 targeted a fault with a slight offset clearly visible in the course of Unit 2 at the sample location. A modern (vine) root disrupted the cultural layer at the same location. Thin sections are 6x9 cm.

RESULTS

Here we outline our macroscopic and microscopic observations per unit in stratigraphic order. Three distinct units were identified in thin section: the lowermost, Unit 1, comprises the loess underlying AH4, Unit 2 corresponds to the main cultural horizon of AH4, and Unit 3 consists of loess directly overlying AH4 (Fig. 3).

Unit 1

Unit 1 is included in thin section 5543C and in the lower parts of thin sections 5543B and 5542. In the field this unit was described as a homogeneous, well-sorted silt with common gray masses (iron reduced or depleted) and few weak diffuse reddish redox masses (redox concentrations),

resulting from wetting and drying (Vepraskas 1994). In the upper 10-15 cm of the unit, small carbonate nodules (< 1 cm) were observed.

The unit shows a dense light yellowish groundmass with a massive microstructure. When looking at the thin section with the naked eye a very weak iron staining can be recognized (Fig. 4a). Common ca. 1.5 mm pores are created by empty spaces inside intact mollusk shells that occur until the lower 1.5 cm of 5543C (Fig. 4b, g, h). Other void-space is in 0.5 mm wide interconnected channels of a root network that also reaches until the lower 1.5 cm of 5543C. Parts of the roots have been preserved in situ (Fig. 4a-c). Burrowing by soil fauna is restricted to common short channels and vughs (ca. 0.5 mm) that increase in abundance in the upper part of the unit toward the cultural layer. Earthworm activity is evidenced by a polycrystalline calcium carbonate granule (0.4 mm), associated with a biochannel just below (1.5 cm) the upper boundary (Canti 1998, Canti 2003a, Canti & Piearce 2003) (Fig. 4e, f).

Following common protocols for thin section description (Bullock et al. 1985, Stoops 2003), the mineral components of the deposit can be divided into a coarse fraction (> 0.01 mm) and a fine fraction (< 0.01 mm). The coarse fraction in Unit 1 consists of well-sorted silt- to very fine sand-sized subangular quartz grains with abundant mica (mainly biotite) and few volcanic minerals. Elongate coarse particles such as mica flakes have a random to vertical orientation. The fine mineral fraction is rich in microcrystalline secondary calcite (micrite), creating a crystallitic birefringence-fabric when observed under crossed polarizers (Stoops et al. 2003) (Fig. 4d). In several root channels of the aforementioned root network the plant cells, probably of a Poaceae grass species, have been replaced by spherulitic calcite crystals that now completely fill the channels (Košir 2004, Kabanov et al. 2008) (Fig. 4c, d). Similar features have been described for other open-air loess sites, e. g. at Willendorf by Mallol (Nigst et al. 2014) and at Bohunice by Smoliková (Smoliková 1976). The same spherulitic calcite crystals also occur in fresh-looking root remnants, which fits Košir´s theory that calcification occurs in living plants of pioneer communities when they colonize carbonate substrates during early phases of subaerial exposure, which he bases on observations on Paleocene calcretes (Košir 2004). Secondary carbonate formation is also reflected by calcite hypocoatings around voids, a slight cementation of the sediment by recrystallized micritic calcite and the carbonate nodules observed in the field. Under blue light fluorescence, some secondary carbonate accumulations inside root channels and in infillings of burrowed channels nearby mollusks show autofluorescence, indicating a high retention of phosphorous which may be related to the original organic substances of the roots and living animals (Altemüller & Van Vliet-Lanoë 1990, Van Vliet-Lanoë 1980) (Fig.4h).

In the upper part, a very weakly developed lenticular platy microstructure can be recognized (Fig. 4e). This microstructure is the result of ice-segregation processes especially occurring in frost-susceptible sediment such as loess and forms under periglacial conditions (Huijzer 1993, Morozova 1971, Kemp 1999, Van Vliet-Lanoë 1985, 1998, and 2010).

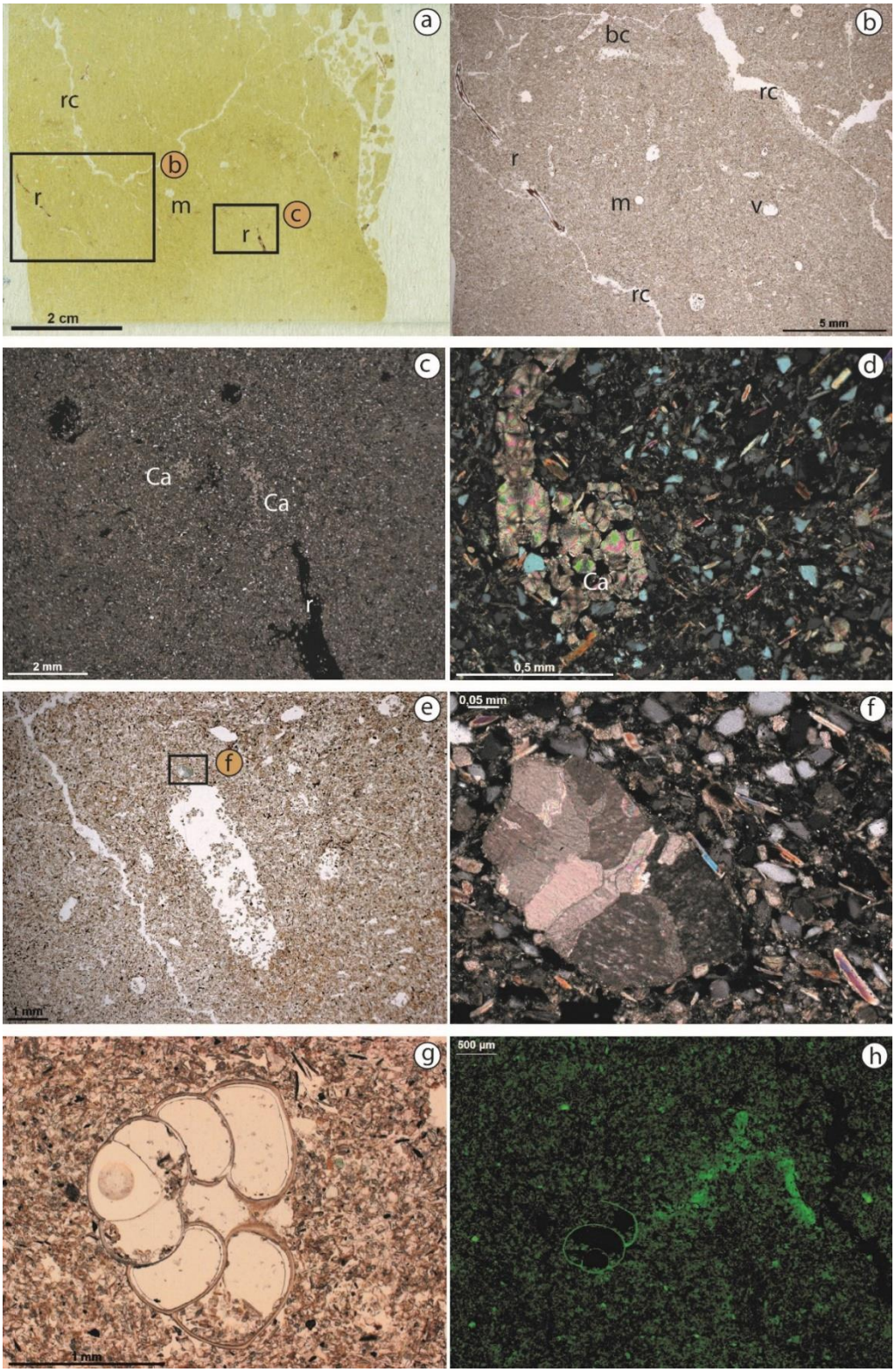

Figure 4. Unit 1. 4a: Scan of thin section 5543C showing clean loess with root remains (r), root channels (rc) and voids (v) from mollusk shells (m) or other bioturbation. 4b: Micrograph at low magnification corresponding to the left frame indicated in figure 4a, showing roots (r), root channels (rc) and bioturbation channels (bc) as well as other voids (v). Plane polarized light (PPL). 4c corresponds to the small frame in 4a and was taken with crossed polarizers (XPL) to show remains of a root (in extinction, black) and secondary carbonate (Ca) in other parts of the root network. 4d: Spherulitic carbonate crystals (Ca) in a channel. 4e: A short channel with a carbonate granule produced by an earthworm, 4f: earthworm granule at higher magnification in XPL (corresponds to the frame in 4e), 4g: complete mollusk shell in thin section, 4h: mollusk shell with a trail of autofluorescent (phosphatic) remains in a channel. Blue fluorescent light.

Unit 2

Unit 2 corresponds to the main cultural layer (AH4) and is captured in the middle part of thin sections 5543B and 5542 (Fig. 3, 5a). Between the relatively homogeneous light yellowish loess deposits of Units 1 and 3, Unit 2 stands out as a grayish brown, heterogeneous layer with very clear boundaries despite common bioturbation disturbances.

At the sample location the unit was only ca. 10 cm thick and showed a southward inclination of ca. 5°. Roots and root bioturbation from the former vineyard were noted in the field, as well as the disruption of the lower boundary of the cultural layer by smaller rootlets entering into the underlying Unit 1. At the location of sample 5542 a fault with an offset of ca. 5 cm can be observed (Fig. 3). The shape of the fault has been distorted by a modern root and other bioturbation features.

The main geogenic component of the deposit of Unit 2 is loess of similar composition as the sediment deposited in Units 1 and 3. The grayish-brown color of the unit is the result of a considerable amount of organic material, including roots, finely comminuted humified and burnt vegetal remains and few larger charcoal fragments. Rooting and bioturbation have created a much higher porosity than in the neighboring units. Sand-sized bone fragments are dispersed throughout the unit and are usually subrounded to rounded but angular pieces also occur. Most bone fragments are light yellowish to orange in PPL and have a dull color in XPL indicating burning at relatively low temperatures. A few pieces are calcined (whitish in PPL and optically isotropic in XPL), indicating that they were heated at ≥550 ºC (Macphail & Goldberg 2010, Mentzer 2012). Larger bone fragments show in situ cracking (Fig. 5f). While charred material and charcoal particles are very abundant, calcium oxalate pseudomorphs, indicative of ash, are not well-preserved and have likely been dissolved and carried out from this unit (Canti 2003b). Other components of non-aeolian origin include few well-rounded medium sand-sized quartz grains dispersed throughout

the unit as well as a fragment of weathered calcareous sandstone, chert fragments, ferruginous nodules and anorthic soil aggregates (Fig. 5a-e).

Sandwiched between light-colored, yellowish loess deposits, Unit 2 appears very distinct. However, its lower boundary is more abrupt than the upper boundary, which has become more disturbed and mixed by soil fauna (e. g. mollusks and earthworms) and roots that reach into the organic-rich unit from above. In contrast, the lower boundary is less disturbed and appears clearer because large particles of charred woody vegetal remains (ca. 5 mm) and an anorthic ferruginous nodule are horizontally aligned at the bottom of Unit 2 (Fig.3, 5a-c). This alignment and concentration of larger charcoal fragments and other anthropogenic materials at the lower boundary of Unit 2 occurs also outside the sampled area.

The root network in Unit 1 (see above) seems to originate mainly from plant-growth in and just below Unit 2. Starting just below the lower boundary of Unit 2 and continuing upwards, channels of roots join at different elevations into nodes resembling root crowns (Blair et al. 2014, Gibson 2009) (Fig. 5a). Inside Unit 2, channels are ca. 0.5-1.0 mm in diameter and become narrower when they enter Unit 1 (0.5 mm). Faunal re-use of root-channels is indicated by the slightly more rounded (burrowed) morphology of the channels. Also, contrary to Unit 1, root remains in Unit 2 are only preserved as comminuted fine vegetal material, resulting from consumption by soil fauna. Only the in situ remains of a larger root, possibly from a grapevine, can be seen in sample 5542 (Fig. 3). Soil fauna has fed on roots, charcoal fragments and other vegetal remains, producing small organic-rich excremental aggregates that are concentrated in voids (Fig. 5a, d). Most small burrows occur inside the margins of Unit 2, but a few large channels (ca. 4 mm width) clearly originate from the overlying unit because they are infilled with lighter-colored, coalesced earthworm castings (Canti 2003a), composed of clean loess (Fig. 5a). Perforated mollusks were recovered as part of the archaeological material (Antl-Weiser et al. 2010), but the few shells observed in thin section in Unit 2 look similar to the shells in Unit 1 and likely occur naturally (Fig. 5b).

In some bioturbated areas secondary carbonates as well as calcified fibrous vegetal remains show autofluorescent properties (Fig. 5g). Calcite hypocoatings are very common and well expressed in the less calcareous organic-rich matrix. Calcification of root cells and the formation of spherulitic crystals inside root remains also occur but are less abundant than in Unit 1.

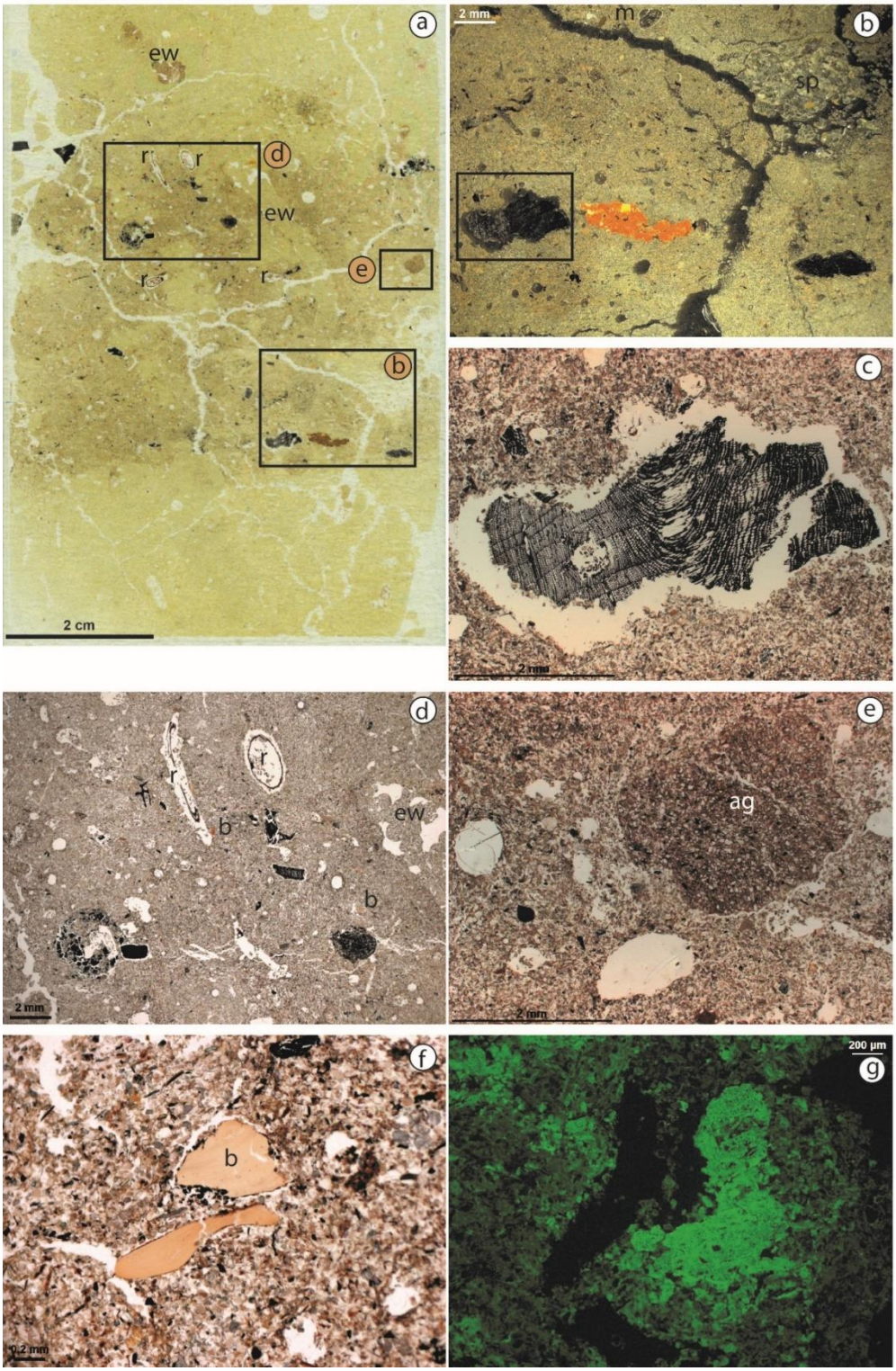

Figure 5. Unit 2, the cultural layer. 5a: Scan of thin section 5543B in which unit 2 is clearly visible as a darker band in the middle of the slide. Root remains (r) can be recognized in channels and voids, as well as earthworm infillings (ew) in burrows and charred and humified dark vegetal material. 5b: Micrograph at low magnification with oblique incident light to highlight the ferruginous clay-rich aggregate (ochre) lining the bottom of unit 2 between large vegetal remains. A mollusk (m) in the upper middle is part of the natural loess and a weathering calcitic sandstone pebble (sp) of allochthonous origin. 5c: Largely intact vegetal fragment of a coniferous tree, at higher magnification (PPL). 5d:

overview of the upper part of unit 2 with roots (r), earthworm aggregates (ew), small yellowish bone fragments (b) and reworked (charred) vegetal remains (PPL). 5e: Brown soil aggregate (allochthonous) well inside Unit 2 (PPL). 5f: Cracked bone fragments (PPL). 5g: phosphatized matrix adjacent to a biochannel (blue fluorescent light).

Unit 3

Unit 3 directly overlies the cultural layer and consists of homogeneous, well-sorted, light-yellowish clean loess of silt-sized quartz grains and a micritic (microcrystalline carbonate) fine fraction (Fig. 6a). Disturbances by modern roots and gray mottles were observed in the field throughout the unit as well as weak diffuse masses of oxidized iron in the lower part. The loess deposit is very similar to Unit 1 but shows less secondary calcium carbonate and is relatively unweathered. Compared to Unit 1 the sediment has a more open structure with less calcite hypocoatings and no complete infillings of secondary carbonate (Fig. 6e).

Characteristic for this unit are horizontal narrow voids forming a weakly developed lenticular platy microstructure, the result of ice-segregation under periglacial conditions, indicating that the ground was (at least) seasonally frozen during loess aggradation (Huijzer 1993, Van Vliet-Lanoë 2010, Lisá et al. 2014) (Fig. 6c). Ice segregation typically occurs in water-saturated materials and is a slightly different process than freeze-thaw action, which is also characteristic for periglacial conditions but leads to the formation of bands and cappings of fine material (banded fabric) (Dumanski & St. Arnaud 1966, Fedorova & Yarilova 1966). Redox features are very common in this unit and are expressed as common diffuse yellowish-orange redox masses (mottles) and few iron oxide hypocoatings around voids (ca. 1.5 mm) from cross-sections through roots (Fig. 6a, b).

Root channels are common but faunal bioturbation is relatively moderate and only few channels disrupt the lenticular platy microstructure. The anthropogenic component is completely absent and only in the lower part of the thin section bioturbation has brought in some finely comminuted vegetal remains and charcoal from the underlying cultural layer.

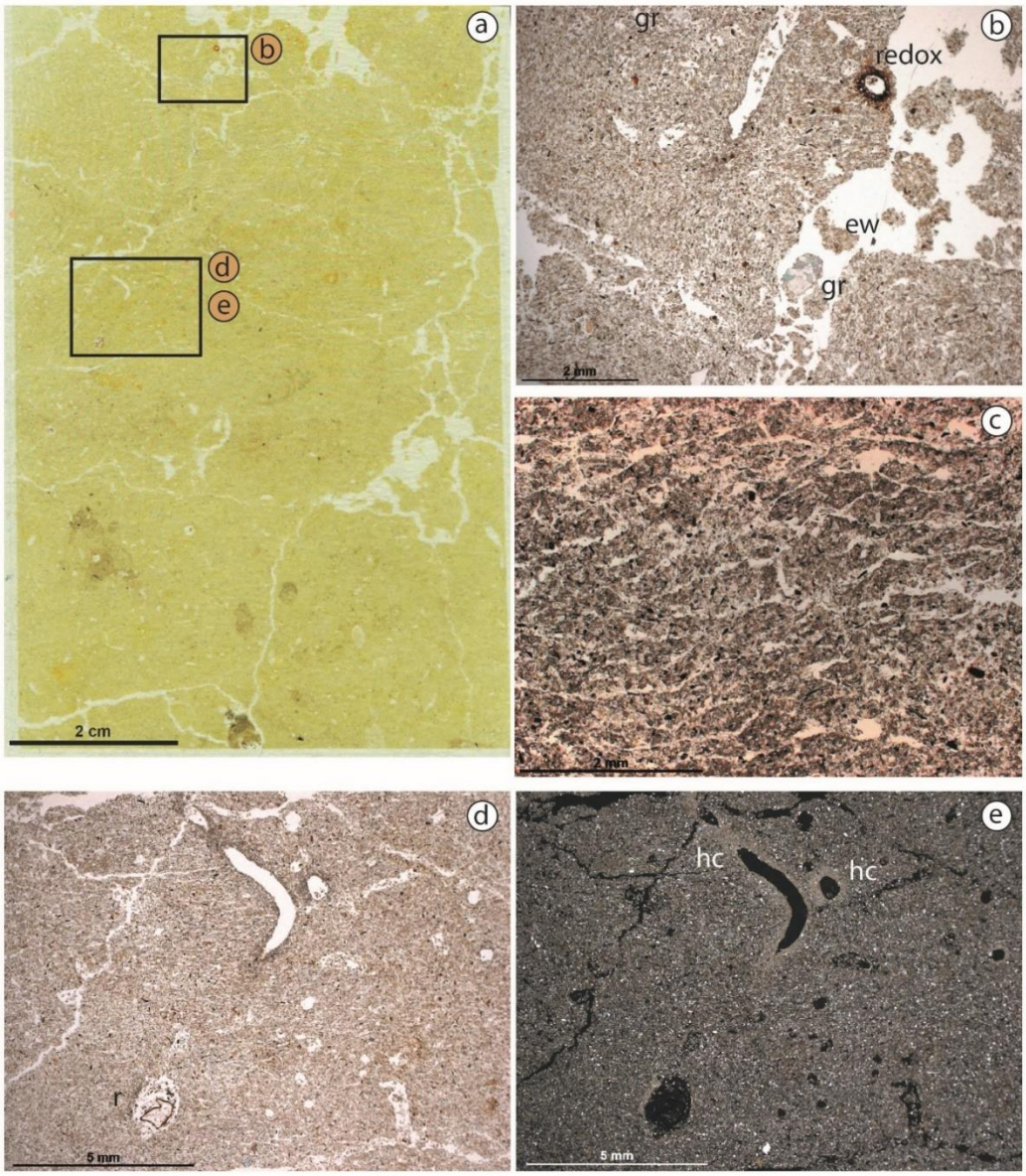

Figure 6. Unit 3. 6a: Scan of thin section 5543 A. Here, redox is clearly visible as diffuse orange-yellowish mottles. 6b: Earthworm channels (ew) and granules (gr) as well as an iron oxide hypocoating around a (root) void (PPL). 6c: Lenticular platy microstructure at a higher magnification (PPL). 6d: Channels and voids with root remains (r) disrupting the lenticular platy microstructure (PPL). 6e: Same as 6d in XPL illustrating local carbonate redistribution as hypocoatings (hc) around voids.

DISCUSSION

Based on micromorphological analysis we propose a formation model consisting of five main phases.

Phase 1 – loess deposition

Homogeneous loess reflects a relatively quick deposition in a typical periglacial environment with relatively dry and windy conditions (Pye 1995). Loess accumulation was promoted by vegetated surfaces and topography (Pye 1995). In the Middle Danube region, westerly winds dominated (Bokhorst et al. 2011). The massive microstructure of Unit 1, in which no bedding features could be detected, suggests that no or only very limited reworking and redeposition occurred (Terhorst et al. 2014). The random to vertical orientation of elongate particles such as biotite (up to 0.15 mm) also points to an aeolian origin of the loess (Le Guern and Davaud 2005) (Fig. 4d). Faunal bioturbation is very limited during this phase, as illustrated by few disturbances and the preservation of intact root remains (Fig. 4a-c). Mollusk shells are common however, and likely became incorporated into the loess deposit by shallow burrowing of land-snails (Pearce and Örstan 2006). Most of the snail shells are largely intact and the autofluorescence in a channel-filling near a mollusk may result from an individual that burrowed into the sediment just before it perished and decomposed in situ (Fig.4h). Land snail burrowing and the roots in Unit 1 may point to a slowing down of the loess accretion and the existence of a surface vegetated with some grasses and restricted biological activity. Weak lenticular platy microstructure, disrupted by later bioturbation, indicates seasonally frozen ground before the beginning of human occupation of the site.

Phase 2 – episodes of human occupation

A large amount of anthropogenic debris is introduced with human occupation of the site. The anthropogenic material became intermixed with continued (punctuated) loess deposition. Dwelling structures were erected and combustion features constructed. Thin lenses of clean loess as well as the laminations of the hearth features point to multiple episodes of site use (Antl 2013, Antl-Weiser 2008, Antl-Weiser et al. 2010). Along with the artifacts, waste material accumulated over a prolonged period of time and was redistributed during site maintenance activities (Bosch et al. 2012).

In situ root remains and excrements of soil fauna are of natural origin, even though they may have been instigated by the abundance of organic waste introduced by human activity. The bulk of the charred vegetal remains and burnt bone-fragments most likely derive from human-induced combustion. Besides bone and burnt vegetal material, other anthropogenic materials include chert fragments that are likely related to flint knapping, and an anorthic ferruginous nodule with mineral inclusions at the bottom of the cultural layer which may be part of the ochre findings reported by Antl-Weiser (2008). Coarse mineral particles, such as few well-rounded medium sand-sized quartz grains, a fragment of calcareous sandstone (5 mm) (Fig. 5b) as well as few rounded

anorthic brown soil aggregates (ca. 0.3 mm, Fig. 5e) were probably tracked into the site unintentionally by humans and animals or were adhering to vegetal materials collected for burning and other purposes (Goldberg & Bar-Yosef 1998, Goldberg et al. 2009).

Similar to observations in a cultural layer at Krems-Wachtberg (Terhorst et al. 2014), larger elongate particles are horizontally aligned at the base of the cultural layer, confirming a lack or limited extent of reworking. Among these are larger bone and charcoal fragments that appear fractured (Fig. 5f) as a result of trampling. A slight rounding of the edges of bone fragments may be caused by both trampling and soil weathering (Goldberg et al. 2009, Goldberg et al. 2012, Miller et al. 2010, Stiner et al. 1995).

Several episodes of human occupation alternated with periods during which bioturbation and soil weathering could take their course and the limited amount of root traces and bioturbation as well as the preservation of layering is indicative of sparsely vegetated stable surfaces. This phase ends when human occupation becomes more sporadic.

Phase 3 – continued bioturbation and soil formation after abandonment

The third phase of site formation is characterized by extensive post-depositional bioturbation and pedogenesis. After abandonment, the fertilized surface could have favored the colonization of mosses, grasses, and shallow rooting trees. The abundance of organic matter left by humans enhanced biological activity, leading to increased leaching and reprecipitation in and below the cultural layer (Van Vliet-Lanoë 1998). As soil leaching intensified, carbonate enrichment underneath the cultural layer (Unit 1) lead to cementation, the formation of calcite hypocoatings and calcification of root cells (Fig.5h) (Košir 2004, Kabanov et al. 2008). The cultural layer of Unit 2 has acted as an organic-rich A horizon in which patches of decalcified material as well as translocated calcite in hypocoatings can be observed.

The abundance of partially decomposed organic matter, charcoal and finely comminuted vegetal remains incorporated into the layer has made it particularly attractive for soil fauna. Most bioturbation occurred shortly after deposition of Unit 2, as illustrated by faunal bioturbation in the upper part of the cultural layer including earthworm channels infilled with aggregates of clean loess from the overlying deposit (Fig. 5a). The larger diameter of root channels in Unit 2 connected to the narrower root network in Unit 1 are a consequence of bioturbation and the re-use of root channels by soil fauna.

Phase 4 – loess sedimentation

Eventually, loess sedimentation took up again and buried the cultural layer. The organic-rich and slightly trampled and compacted cultural layer would have acted as a drainage barrier to which redoximorphic features in Unit 3 testify (Pagliai et al. 2000, Van Vliet-Lanoë 1998). Slight soil wetness may also have promoted the formation of a cryogenic lenticular platy microstructures but indications for soil saturation such as load casts are absent (Van Vliet-Lanoë 1998).

Biological activity is strongly reduced at this stage and observed as common biochannels and small voids (Fig. 6b, d, e). These channels and voids and the presence of earthworm granules are less abundant but similar to the observations made in the upper part of Unit 1. In contrast to Unit 1, mollusks are absent in Unit 3. Together with slight soil weathering as evidenced by carbonate hypocoatings the biological activity indicates that a short-lived surface existed above the sampled area. This surface may correspond with the overlying cultural layer AH3, which is located only ca. 8 cm above the main cultural layer (Antl-Weiser 2008). The moderate extent of bioturbation and soil weathering is in accordance with a relatively rapid covering of Unit 2 by loess deposition, preserving the archaeological horizon. The loess extends upwards for at least 1.5 m.

Phase 5 – later post-depositional processes

A Holocene soil formed on top of the loess, but we have no information on the soil type, soil horizons or geochemistry. Land use is unknown until the times when the field was a vineyard. Large roots of the vines were observed in the field, penetrating all three described Units. Traces of recent roots were also observed in thin section.

Based on the macroscopic and microscopic features, there are several arguments to characterize the cultural layer at Grub-Kranawetberg as an anthropogenic soil or anthrosol. First, the bulk of organic material and part of the mineral component is produced by human activities. Second, horizontal variation in the cultural layer is influenced by the effects of human occupation: following the cultural layer out of the immediate site, the layer becomes lighter and thinner, the amount of charcoal diminishes and the density of archaeological materials decreases to a scatter of finds. The soil characteristics of the cultural layer can be interpreted as the unintentional, enduring effect of human occupation.

Anthropogenic soils became widespread with the advent of agriculture. Examples are the plaggen soils in the sandy regions of Northwest Europe (Pape 1970, Blume & Leinweber 2004) and terra mulata soils in Amazonia (Arroyo-Kalin 2012). Some anthropogenic soils are associated with abandoned and re-used habitation sites such as Amazonian Dark Earths (terra preta soils) (Glaser & Birk 2012), Urban Dark Earths (Macphail et al. 2003, Golding et al. 2010, Devos et al.

2011) and cultural layers, described as "deeply transformed man-made soils", of the Early Iron Age in Central Russia (Engovatova & Golyeva 2012, Golyeva et al. 2016). These soils demonstrate that past human occupation has a lasting influence on soil characteristics and landscape variability. With the widespread adoption of agriculture and the development of urban landscapes, human modification of landscapes became ubiquitous during the Holocene (Sullivan et al. 2017).

The cultural layer of Grub-Kranawetberg shows that anthropogenic soils are not limited to agricultural economies and urbanization, but can also be the result of habitation by hunter-gatherer groups. The input of anthropogenic materials led to enhanced biological activity and influenced soil-forming processes (Curry 2004, Anderson 1988). Some studies (e.g. De Deyn et al. 2003) suggest that increased abundance of invertebrate soil fauna also influences vegetational diversity and succession. By enhancing diversity of plant communities, the impact of past hunter-gatherers contributed to the mosaic loess landscape that supported and sustained the mammoth steppe faunal community (Guthrie & Van Kolfschoten 2000). From a human behavioral point of view, it is possible that the site may have formed a vegetated patch easily recognized and re-visited over generations of Gravettian hunter gatherers.

CONCLUSION

The cultural layer of Grub-Kranawetberg shows evidence of 1) substantial anthropogenic input of organic and mineral material, 2) bioturbation by a diverse soil fauna including mollusks and earthworms, 3) translocation of carbonates, indicating soil-forming processes, 4) trampling and 5) a preserved, though bioturbated, occupation surface without signs of erosion or redeposition. We have argued that the cultural layer is best described as an anthropogenic soil. It indicates that anthropogenic waste already played a role in Late Pleistocene human modification of the landscape. By enhancing soil fauna and nutrient availability, the human waste influenced the diversity and composition of the plant communities.

Evaluating the Late Pleistocene origins of anthropogenic change is a challenging task (Boivin et al. 2016). Patterns of global colonization by modern humans have been linked to extinction of (mega)fauna, changes in fire regimes and plant ecosystem dynamics, but it remains difficult to disentangle the human factor from climatic impact. The evidence from the Upper Paleolithic site of Grub-Kranawetberg suggests that we may have to rethink the role of humans and human habitation in the dynamic mammoth steppe ecosystem of Late Pleistocene Eurasia.

Acknowledgements

We thank Christopher Miller, Susan Mentzer, Peter Kühn, Eric Verrecchia, Diego Angelucci, the editor Christopher Hunt and two anonymous reviewers for valuable input and advice and Thomas Beckmann for thin section production.

REFERENCES

Absolon, K. & B. Klíma 1977. Předmosti: ein Mammutjägerplatz in Mähren. Brno: Academia Praha.

Altemüller, H.-J. & B. Van Vliet-Lanoë. 1990. Soil thin section fluorescence microscopy. Developments in Soil Science 19, 565-579.

Anderson, J.M. 1988. Invertebrate-mediated transport processes in soils. Agriculture, Ecosystems & Environment 24 (1-3), 5-19. DOI: 10.1016/0167-8809(88)90052-7.

Antl, W. 2013. The inventories of archaeological horizons 4 and 3 and the loess section of Grub/Kranawetberg, a Gravettian site in Lower Austria. E&G Quaternary Science Journal 62(2), 120-126. DOI 10.3285/eg.62.1.03.

Antl, W. & F. A. Fladerer. 2004. Outlook to the East: the 25 ky BP Gravettian Grub/ Kranawetberg Campsite (Lower Austria). In: Svoboda, J.A., Sedlácková, L. (eds), The Gravettian along the Danube, Proceedings of the Mikulov Conference, 20-21 November, 2002. Archeologický ústav AV CR, Brno, pp. 116-130.

Antl-Weiser, W. 1999. Paläolithischer Schmuck von der Gravettienfundstelle Grub/Kranawetberg bei Stillfried, Niederösterreich, Ann. Naturhist. Mus. Wien 101-A, 23-41.

Antl-Weiser, W. 2008. Grub/Kranawetberg and Ollersdorf/Heidenberg (Lower Austria) – two Gravettian camp sites in Eastern Austria, Wiss. Mitt. Niederösterr. Landesmuseum 19, 59-78.

Antl-Weiser, W., F.A. Fladerer, P.R Nigst, P.R. & A. Verpoorte, 2010. Grub/Kranawetberg (Lower Austria) - Insights into a Gravettian micro-region in Eastern Austria. In: Neugebauer-Maresch, C., Owen, L.R. (Eds.), New Aspects of the Central and Eastern European Upper Palaeolithic: Methods, Chronology, Technology and Subsistence, Mitteilungen der Prähistorischen Kommission 72, pp. 231-243.

Antl-Weiser, W., F.A. Fladerer, R. Peticzka, F.C. Stadler, S. Verginis 1997. Ein Lagerplatz eiszeitlicher Jäger in Grub bei Stillfried. Archäologie Österreichs 8-1, 4-20.

Antoine, P., D.-D. Rousseau, J.-P. Degeai, O. Moine, F. Lagroix, S. Kreutzer, M. Fuchs, C. Hatté, C. Gauthier, J. Svoboda, and L. Lisá 2013. High-resolution record of the environmental response to climatic

variations during the Last Interglacial-Glacial cycle in Central Europe: the loess-palaeosol sequence of Dolní Vestonice (Czech Republic), Quaternary Sci. Rev. 67, 17–38

Arroyo-Kalin, M. 2012. Slash-burn-and-churn: landscape history and crop cultivation in pre-Columbian Amazonia. Quaternary International 249, 4-18. DOI: 10.1016/j.quaint.2011.08.004.

Barnosky, A.D., P.L. Koch, R.S. Feranec, S.L. Wing, A.B. Shabel 2004. Assessing the causes of Late Pleistocene extinctions on the continents. Science 306, 70-75. DOI: 10.1126/science.1101476.

Beckmann, T. 1997. Präparation bodenkundlicher Dünnschliffe für mikromorphologische Untersuchungen. In: K. Stahr (ed), Mikromorphologische Methoden in der Bodenkunde. Hohenheimer Bodenkunde 40, 89–103.

Beresford-Jones, D., S. Taylor, C. Paine, A. Pryor, J. Svoboda, and M. K. Jones 2011. Rapid Climate Change in the Upper Palaeolithic: The Record of Charcoal Conifer Rings from the Gravettian Site of Dolni Vestonice, Czech Republic. Quaternary Science Reviews. DOI:10.1016/j.quascirev.2011.04.021.

Bird, R.B., N. Tayor, B.F. Codding, D.W. Bird 2013. Niche construction and Dreaming logic: aboriginal patch mosaic burning and varanid lizards (Varanus gouldii) in Australia. Proc. R. Soc. B 280, 20132297. http://dx.doi.org/10.1098/rspb.2013.2297.

Blair, J., J. Nippert, J. Biggs 2014. Grassland Ecology. In R. Monson (ed) The Plant Sciences – Ecology and the Environment Volume 8. Springer Reference Series, Springer-Verlag, Berlin.

Blume, H.-P. & P. Leinweber 2004. Plaggen soils: landscape history, properties, and classification. J. Plant Nutr. Soil Sci. 167, 319-327. DOI: 10.1002/jpln.200420905.

Boivin, N.L., M.A. Zeder, D.Q. Fuller, A. Crowther, G. Larson, J.M. Erlandson, T. Denham, M.D. Petraglia. 2016. Ecological consequences of human niche construction: examining long-term anthropogenic shaping of global species distributions. PNAS 113-23, 6388-6396. DOI: 10.1073/pnas.1525200113

Bokhorst, M.P., J. Vandenberghe, P. Sümegi, M. Łanczont, N.P. Gerasimenko, Z.N. Matviishina, S.B. Markovic, M. Frechen. 2011. Atmospheric circulation patterns in central and eastern Europe during the Weichselian Pleniglacial inferred from loess grain-size records. Quaternary International 234, 62-74. DOI: 10.1016/j.quaint.2010.07.018.

Bos, J. A. A. and C. R. Janssen 1996. Local Impact of Palaeolithic Man on the Environment During the End of the Last Glacial in the Netherlands Journal of Archaeological Science 23, 731–739.

Bosch, M.D. 2009. Age-at-death profiles of mammoth molars in the mid-Upper Palaeolithic in the Middle Danube region. MA thesis, University of Leiden, the Netherlands.

Bosch, M., F. Fladerer, P. Nigst, W. Antl-Weiser 2012. Humans, bones and fire: zooarchaeological, taphonomic, and spatial analyses of a Gravettian mammoth bone accumulation at Grub-Kranawetberg (Austria), Quaternary International 252, 109-121. DOI: 10.1016/j.quaint.2011.08.019.

Brancier, J., C. Cammas, D. Todisco, E. Fouache 2014. A Micromorphological Assessment of Anthropogenic Features in Pre-Columbian French Guiana Dark Soils (FGDS): First Results. Zeitschrift für Geomorphologie, Supplementary Issues, 58, 1-31. DOI: 10.1127/0372-8854/2014/S-00159.

Bullock, P., N. Fedoroff, A. Jongerius, G. Stoops, T. Tursina, U. Babel 1985. Handbook for Soil Thin Section Description. Waine Research Publications.

Canti, M. 1998. Origin of calcium carbonate granules found in buried soils and Quaternary deposits. Boreas 27, 275-288. DOI: 10.1111/j.1502-3885.1998.tb01421.x.

Canti, M.G. 2003a. Earthworm Activity and Archaeological Stratigraphy: A Review of Products and Processes. Journal of Archaeological Science 30, 135-148. DOI: 10.1006/jasc.2001.0770.

Canti, M.G., 2003b. Aspects of the chemical and microscopic characteristics of plant ashes found in archaeological soils. Catena 54, 339–361. DOI:10.1016/S0341-8162(03)00127-9.

Canti, M. & T.G. Piearce 2003. Morphology and dynamics of calcium carbonate granules produced by different earthworm species. Pedobiologia 47:511-521. DOI: 10.1078/0031-4056-00221.

Courty, M.A., P. Goldberg, R. Macphail 1989. Soils and Micromorphology in Archaeology. Cambridge: Cambridge University Press.

Curry, J.P. 2004. Factors affecting the abundance of earthworms in soils. In C.A. Edwards (ed) Earthworm ecology, Boca Raton: CRC Press, 91-113.

De Deyn, G.B., C.E. Raaijmakers, H.R. Zoomer, M.P. Berg, P.C. de Ruiter, H.A. Verhoef, T.M. Bezemer, W.H. van der Putten 2003. Soil invertebrate fauna enhances grassland succession and diversity. Nature 422, 711-713. DOI: 10.1038/nature01548.

Devos, Y., L. Vrydaghs, A. Degraeve, S. Modrie. 2011. Unravelling urban stratigraphy. The study of Brussels' (Belgium) Dark Earth. An archaeopedological perspective. Medieval and Modern Matters 2, 51-76. DOI: http://dx.doi.org/10.1484/J.MMM.1.102776.

Diamond, J.M. 1989. Quaternary megafaunal extinctions: Variations on a theme by Paganini. Journal of Archaeological Science 16-2, 167–175. DOI: 10.1016/0305-4403(89)90064-2.

Dumanski, J. & St. Arnaud, R.J., 1966. A micropedological study of eluvial soil horizons. Canadian Journal of Earth Sciences 46, 287–292.

Einwögerer, T. 2000. Die jungpaläolithische Station auf dem Wachtberg in Krems, NÖ, Mitteilungen der Prähistorische Kommission 34, Vienna.

Einwögerer, T. 2008. The Upper Palaeolithic sites at the Kargl Brickyard in Langenlois (Lower Austria), Wiss. Mitt. Niederösterr. Landesmuseum 19, 79-90.

Engovatova, A. & A. Golyeva 2012. Anthropogenic soils in Yaroslavl (Central Russia): history, development, and landscape reconstruction. Quaternary International 265, 54-62. DOI: 10.1016/j.quaint.2012.02.039.

Fedorova, N.N. & E.A. Yarilova 1972. Morphology and genesis of prolonged seasonally frozen soils in western Siberia. Geoderma 7, 1–13.

Felgenhauer, F. 1959. Willendorf in der Wachau, Mitteilungen der Prähistorische Kommission 8-9, Vienna.

Feurdean, A., T. Perşoiu, S. Stevens et al. 2014. Climate variability and associated vegetation response throughout Central and Eastern Europe (CEE) between 60 and 8 ka. Quaternary Science Reviews, 106, 206-224. DOI: 10.1016/j.quascirev.2014.06.003.

Foley, R.A. & M.M. Lahr 2015. Lithic landscapes: early human impact from stone tool production on the Central Saharan environment. PloS ONE 10(3), e0116482. DOI: 10.1371/journal.pone.0116482.

Fuchs, M., S. Kreutzer, D.D. Rousseau, P. Antoine, C. Hatte, F. Lagroix, O. Moine, C. Gauthier, J. Svoboda & L. Lisá 2012. The loess sequence of Dolní Věstonice, Czech Republic: A new OSL-based chronology of the Last Climatic Cycle. Boreas, DOI: 10.1111/j.1502-3885.2012.00299.x.

Gibson, D. J. 2009. Grasses and Grassland Ecology. New York: OUP Oxford.

Glaser, B. & J.J. Birk. 2012. State of the scientific knowledge on properties and genesis of Anthropogenic Dark Earths in Central Amazonia (terra preta de Indio). Geochimica et Cosmochimica Acta 82, 39-51. DOI: 10.1016/j.gca.2010.11.029.

Goldberg, P. & O. Bar-Yosef 1998. Site formation processes in Kebara and Hayonim Caves and their significance in Levantine prehistoric caves. In T. Akazawa, K. Aoki & O. Bar-Yosef (eds). Neandertals and Modern Humans in Western Asia. Plenum, NY, 107-123.

Goldberg, P. & V. Aldeias 2016. Why does (archaeological) micromorphology have such little traction in (geo)archaeology? Archaeological and Anthropological Sciences DOI: 10.1007/s12520-016-0353-9.

Goldberg. P., C.E. Miller, S. Schiegl, B. Ligouis, F. Berna, N.J. Conard, L. Wadley 2009. Bedding, hearths, and site maintenance in the Middle Stone Age of Sibudu Cave, KwaZulu-Natal, South Africa. Archaeological and Anthropological Sciences 1, 95-122. DOI:10.1007/s12520-009-0008-1.

Goldberg, P., H. Dibble, F. Berna, D. Sandgathe, S.J.P. McPherron, and A. Turq. 2012. New Evidence on Neandertal Use of Fire: Examples from Roc de Marsal and Pech de l'Azé IV. Quaternary International 247: 325-340.

Golding, K.A., D.A. Davidson, C.A. Wilson 2010. Micromorphological evidence for the use of urban waste as a soil fertiliser in and near two historic Scottish towns. In 19th World Congress of Soil Science. Soil Solutions for a Changing World, 1-6 August 2010, Brisbane, Australia.

Golyeva, A., E. Zazovskaia, I. Turova 2016. Properties of ancient deeply transformed man-made soils (cultural layers) and their advances to classification by the example of Early Iron Age sites in Moscow Region. Catena 137, 605-610.

Gribchenko, Y.N. 2006. Lithology and stratigraphy of loess-soil series and cultural layers of Late Paleolithic campsites in Eastern Europe. Quaternary International 152-153, 153-163.

Guthrie R.D. 1984. Mosaics, allelochemicals, and nutrients: an ecological theory of Late Pleistocene megafaunal extinctions. In Quaternary extinctions: a prehistoric revolution. Martin, P.S. & Klein R.G. (eds): 259–298. Tucson, AZ:University of Arizona Press.

Guthrie, D. & T. van Kolfschoten. 2000. Neither warm and moist, nor cold and arid: the ecology of the Mid Upper Palaeolithic. In Roebroeks, W., M. Mussi, J. Svoboda, K. Fennema (eds) Hunters of the Golden Age, Leiden: Faculty of Archaeology, 13-20.

Haesaerts, P., F. Damblon, M. Bachner, G. Trnka 1996. Revised stratigraphy and chronology of the Willendorf II sequence, Lower Austria, Archaeologia Austriaca 80, 25-42.

Haesaerts, P., M. Bachner, I. Borziac, V. Chirica, F. Damblon, N. Drozdov, L. Koulakovska, S. Pirson 2010. New insights on the environmental background and the chronology of the Early Upper Palaeolithic in Central Europe. In Neugebauer-Maresch, C. & L.R. Owen (eds), New Aspects of the Central and Eastern European Upper Palaeolithic: Methods, Chronology, Technology and Subsistence, Mitteilungen der Prähistorischen Kommission 72, 9-25.

Händel, M., U. Simon, T. Einwögerer, C. Neugebauer-Maresch 2009. Loess deposits and the conservation of the archaeological record – the Krems-Wachtberg example. Quaternary International 198, 46-50.

Händel, M., T. Einwogerer, U. Simon, C. Neugebauer-Maresch 2014. Krems-Wachtberg excavations 2005-2012: main profiles, sampling, stratigraphy, and site formation. Quaternary International 351, 38-49.

Heiri, O., K.A. Koinig, C. Spötl, S. Barrett, A. Brauer, R. Drescher-Schneider, D. Gaar, S. Ivy-Ochs, H. Kerschner, M. Luetscher, A. Moran, K. Nicolussi, F. Preusser, R. Schmidt, P. Schoeneich, C. Schwörer, T. Sprafke, B. Terhorst, W. Tinner 2014. Palaeoclimate records 60-8 ka in the Austrian and Swiss Alps and their forelands, Quat. Sci. Rev. 106:185–204.

Hoffecker, J.F., V.T. Holliday, M.V. Anikovich, A.E. Dudin, N.I. Platonova, V.V. Popov, G.M. Levkovskaya, I.E. Kuz'mina, E.V. Syromyatnikova, N.D. Burova, P. Goldberg, R.I. Macphail, S.L. Forman, B.J. Carter, L.J. Crawford 2016. Kostenki 1 and the early Upper Paleolithic of Eastern Europe. Journal of Archaeological Science: Reports 5, 307-326.

Hromada, J., J.K. Kozlowski (eds) 1995. Complex of Upper Palaeolithic Sites Near Moravany, Western Slovakia: Vol. I Moravany-Zakovska (excavations 1991-1992), Krakow.

Huijzer, A.S. 1993. Cryogenic microfabrics and macrostructures: interrelations, processes and palaeoenvironmental significance. PhD-Thesis Vrije Universiteit Amsterdam.

Hunt, C.O., D.D. Gilbertson and G. Rushworth 2012. A 50,000-year record of late Pleistocene tropical vegetation and human impact in lowland Borneo. Quaternary Science Reviewers 37: 61-80.

Ivy-Ochs, S., H. Kerschner, A. Reuther, F. Preusser, K. Heine, M. Maisch, P.W. Kubik, C. Schlüchter 2008. Chronology of the last glacial cycle in the European Alps. Journal of Quaternary Science 23, 559–573. DOI: 10.1002/jqs.1202.

Jarvis A., H.I. Reuter, A. Nelson, E. Guevara 2008. Hole-filled seamless SRTM data V4, International Centre for Tropical Agriculture (CIAT), available from http://srtm.csi.cgiar.org.

Kabanov, P., P. Andanón, W. E. Krumbein 2008. Microcodium: An extensive review and a proposed non-rhizogenic biologically induced origin for its formation. Sedimentary Geology 205, 79-99. DOI: 10.1016/j.sedgeo.2008.02.003.

Kemp, R.A. 1999. Micromorphology of loess-paleosol sequences: a record of paleoenvironmental change, Catena 35(2-4), 179-196. DOI: 10.1016/S0341-8162(98)00099-X.

Klíma, B. 1963. Dolní Věstonice: vyzkum taboriste lovcu mamutu v letech 1947-1952, Monumenta Archeologica XI, Prague.

Klíma, B. 1969. Die grosse Anhäufung von Mammutknochen in Dolní Věstonice. Přírodovědné práce ústavů Československé akademie věd v Brně, III, 6. Academia Praha.

Košir, A. 2004. Microcodium revisited: root calcification products of terrestrial plants on carbonate-rich substrates. Journal of Sedimentary Research 74-6, 845-857. DOI: 10.1306/040404740845.

Kozlowski, J.K. (ed) 1998. Complex of upper palaeolithic sites near Moravany, Western Slovakia: vol. II Moravany-Lopata II (excavations 1993-1996), Krakow.

Le Guern, P. & Davaud, E. 2005. Recognition of ancient carbonate wind deposits: lessons from a modern analogue, Chrissi Island, Crete. Sedimentology 52:915–926.

Łanczont, M., T. Madeyska, P. Mroczek, M. Komar, B. Łącka, A. Bogucki, K. Sobczyk, J. Wilczyński 2015. The loess-palaeosol sequence in the Upper Palaeolithic site at Kraków-Spadzista: a palaeoenvironmental approach. Quaternary International 365, 98-113.

Lisá, L., J. Hošek, A. Bajer, T. Matys Grygar, D. Vandenberghe 2014. Geoarchaeology of Upper Palaeolithic loess sites located within a transect through Moravian valleys, Czech Republic. Quaternary International 351, 25-37. DOI: 10.1016/j.quaint.2013.08.058.

Macphail, R. I. & Goldberg, P. (2010). Archaeological materials. In G. Stoops, V. Marcelino & F. Mees (eds.), Interpretation of Micromorphological Features of Soils and Regoliths, 589-622. Amsterdam, The Netherlands: Elsevier.

Macphail, R.I., H. Galinié, F. Verhaeghe. 2003. A future for Dark Earth? Antiquity 77-296, 349-358. DOI: https://doi.org/10.1017/S0003598X00092334.

MacPhee, R.D.E. & P.A. Marx 1997. The 40 000-year plague: Humans, hyperdisease, and first-contact extinctions. In: Goodman, S.M. and Patterson, B.D. (eds.) Natural Change and Human Impact in Madagascar, 169–216. Washington, DC: Smithsonian Institution Press.

Martin, P. S. (1984). Prehistoric Overkill: The Global Model. In Quaternary Extinctions: A Prehistoric Revolution. Paul S. Martin and Richard G. Klein, eds. Pp. 354-403. Tucson: University of Arizona Press.

Mentzer, S. M. 2012. Microarchaeological approaches to the identification and interpretation of combustion features in prehistoric archaeological sites. Journal or Archaeological Method and Theory 21(3), 616–68. DOI 10.1007/s10816-012-9163-2.

Miller C. E., N.J. Conard, P. Goldberg F. Berna 2010. Dumping, Sweeping and Trampling: Experimental Micromorphological Analysis of Anthropogenically Modified Combustion Features, in Théry-Parisot I., Chabal L., Costamagno S., The taphonomy of Burned Organic Residues and Combustion Features in Archaeological Contexts, Proceedings of the round table, May 27-29 2008, CEPAM, Palethnology, 2, 25-37.

Morozova, T.D. 1971. K harakteristike lessovyh otlozheniy Central'noy Yakutii Izv. Akad. Nauk SSSR, Ser. Geogr., 5: 95–114

Nigst, P.R. 2004. Ein gravettienzeitlicher Behausungsgrundriss? Erste Beobachtungen zur räumlichen Organisation der Fundstelle Grub/Kranawetberg (Österreich). Archäologisches Korrespondenzblatt 34, 153-168.

Nigst, P.R. & W. Antl-Weiser 2012. Les structures d'occupation gravettiennes en Europe centrale: le cas de Grub/Kranawetberg, Autriche. L'Anthropologie 116(5), 639-664. DOI: 10.1016/j.anthro.2012.09.001.

Nigst, P.R., P. Haesaerts, F. Damblon, C. Frank-Fellner, C. Mallol, B. Viola, M. Götzinger, L. Niven, G. Trnka, J.-J. Hublin 2014. Early modern human settlement of Europe north of the Alps occurred 43,500 years ago in a cold steppe-type environment. PNAS 111(40), 14394-14399. DOI: 10.1073/pnas.1412201111.

Novak, M. 2005. Pavlov I - southeast. Review of spatial distributions. In Svoboda, J. (ed), Pavlov I Southeast. A Window into Gravettian Lifestyles. Brno, 53-71.

Pape, J.C. 1970. Plaggen soils in the Netherlands. Geoderma 4, 229-255. DOI: 10.1016/0016-7061(70)90005-4.

Owen-Smith, N. 1987. Pleistocene extinctions: The pivotal role of megaherbivores. Paleobiology 13, 351–362.

Pagliai, M., S. Pellegrini, N. Vignozzi, S. Rousseva, O. Grasselli 2000. The quantification of the effect of subsoil compaction on soil porosity and related physical properties under conventional to reduced management practices. Advances in Geoecology 32:305-313.

Pearce, T. A. & A. Örstan. 2006. Terrestrial Gastropoda. In C. F. Sturm, T. A. Pearce, and A. Valdés (eds), The Mollusks: A Guide to Their Study, Collection, and Preservation. American Malacological Society, 261-285.

Pietsch, D., P. Kühn, S. Lisitsyn, A. Markova, A. Sinitsyn. 2014. Krotovinas, pedogenic processes and stratigraphic ambiguities of the Upper Palaeolithic sites Kostenki and Borshchevo (Russia). Quaternary International 324, 172-179. DOI: 10.1016/j.quaint.2013.05.036.

Polanska, M., J. Svoboda, B. Hromadova, S. Sazelova 2014. Predmosti III: un site pavlovien de la Porte de Moravie (République tchèque, Europe centrale). L'Anthropologie 118, 255-291. DOI: 10.1016/j.anthro.2014.09.006.

Politis, G.G. 1996. Moving to produce: Nukak mobility and settlement patterns in Amazonia. World Archaeology 27(3), 492-511. DOI: 10.1080/00438243.1996.9980322.

Pye, K. 1995. The nature, origin and accumulation of loess. Quaternary Science Reviews 14:653-667. DOI: 10.1016/0277-3791(95)00047-X.

Rowley-Conwy, P. & R. Layton 2011. Foraging and farming as niche construction: stable and unstable adaptations. Phil.Trans. R. Soc. 366, 849-862. DOI: 10.1098/rstb.2010.0307.

Sandom, C., S. Faurby, B. Sandel, J.-C. Svenning. 2014. Global late Quaternary megafauna extinctions linked to humans, not climate change. Proc. R. Soc. B 281, 20133254. http://dx.doi.org/10.1098/rspb.2013.3254.

Scherjon, F., C. Bakels, K. MacDonald, W. Roebroeks 2015. Burning the land. An ethnographic study of off-site fire use by current and historically documented foragers and implications for the interpretation of past fire practices in the landscape. Current Anthropology 56-3, 299-326.

Skrdla, P. 2005. The Upper Paleolithic on the middle course of the Morava river, DVS 13, Brno.

Smith, B.D. 2011. General patterns of niche construction and the management of 'wild' plant and animal resources by small-scale pre-industrial societies. Phil. Trans. R. Soc. B 366, 836-848. DOI: 10.1098/rstb.2010.0253.

Smoliková, L. 1976. Mikromorphologische Untersuchung der Bodenbildung von Bohunice. In: K. Valoch (ed.): Die altsteinzeitliche Fundstelle in Brno-Bohunice. Studie AU ČSAV IV, I: 69–71. Academia, Prague.

Smoliková, L. 1991. Soil Micromorphologic Investigation of the Section at Dolní Věstonice II. In: J. Svoboda (ed.), Dolní Věstonice II – Western Slope. ERAUL 54. Liège, pp. 65-74.

Smoliková, L. 2009. Půdně-mikromorfologický výzkum na lokalitě Milovice (okr. Břeclav). In: M. Oliva, ed., Sídliště mamutího lidu u Milovic pod Pálavou. Anthropos 27, Moravské zemské muzeum, Brno, pp. 25-29.

Stiner, M.C., S. Kuhn, S. Weiner, O. Bar-Yosef 1995. Differential burning, recrystallization, and fragmentation of archaeological bone. Journal of Archaeological Science 22, 223-237. DOI: 10.1006/jasc.1995.0024.

Stoops, G.S, M.J. Vepraskas, A.G. Jongmans 2003. Guidelines for analysis and description of soil and regolith thin sections. Madison, Wisconsin, USA: Soil Science Society of America, Inc.

Sullivan, A.P., D.W. Bird, G.H. Perry 2017. Human behaviour as a long-term ecological driver of non-human evolution. Nature Ecology and Evolution 1:0065. DOI:10.1038/s41559-016-0065.

Surovell, T.A., S.R. Pelton, R. Anderson-Sprecher, A.D. Myers 2016. Test of Martin's overkill hypothesis using radiocarbon dates on extinct megafauna. PNAS 113-4:886-891. DOI: 10.1073/pnas.1504020112.

Svoboda, J. (ed) 1991. Dolní Věstonice II: The Western Slope, vol.54, ERAUL, Liège.

Svoboda, J. (ed) 1994. Pavlov I – excavations 1952-53, ERAUL Vol 66 / DVS 2, Liège.

Svoboda, J. (ed) 1997. Pavlov I-Northwest: The Upper Paleolithic burial and its settlement context, DVS 4, Brno.

Svoboda, J. (ed) 2005. Pavlov I-Southeast: a window into the Gravettian lifestyles, DVS 14, Brno.

Svoboda, J., Š. Hladilová, I. Horáček, J. Kaiser, M. Králík, J. Novák, M. Novák, P. Pokorný, S. Sázelová, L. Smolíková, T. Zikmund 2015. Dolní Věstonice IIa: Gravettian microstratigraphy, environment, and the origin of baked clay production in Moravia, Quaternary International 359-360, 195-210.

Svoboda, J., M. Novak, S. Sazelova, J. Demek. 2016. Pavlov I: a large Gravettian site in space and time. Quaternary International 406, 95-105. DOI: 10.1016/j.quaint.2015.09.015.

Terhorst, B. C. Thiel, R. Peticzka, T. Sprafke, M. Frechen, F.A. Fladerer , R. Roetzel & C. Neugebauer-Maresch 2011. Casting new light on the chronology of the loess/paleosol sequences in Lower Austria. Quaternary Science Journal 60(2–3), 270–277. DOI: 10.3285/eg.60.2-3.04

Terhorst, B., P. Kühn, B. Damm, U. Hambach, S. Meyer-Heintze, S. Sedov 2014. Paleoenvironmental fluctuations as recorded in the loess-paleosol sequence of the Upper Paleolithic site Krems-Wachtberg. Quaternary International 351, 67-82.

Van Vliet-Lanoë, B., 1980. Approche des conditions physico-chimiques favorisant l'autofluorescence des mineraux argileux. Pedologie 30-3, 369-390.

Van Vliet-Lanoë, B. 1985. Frost effects in soils. In: Boardman, J. (ed.) Soils and Quaternary Landscape Evolution. Wiley, Chichester, pp. 115–156.

Van Vliet-Lanoë, B., 1998. Frost and soils: Implications for paleosols, paleoclimates and stratigraphy. Catena 34, 157-183.

Van Vliet-Lanoë, B., 2010. Frost action. In G. Stoops, V. Marcellino & F. Mees (eds): Interpretation of micromorphological features of soils and regoliths. Elsevier, London, 81–108.

Velichko, A.A., V.V. Pisareva, S.N. Sedov, A.A. Sinitsyn, S.N. Timireva. 2009. Paleogeography of Kostenki-14 (Markina Gora). Archaeology, Ethnology & Anthropology of Eurasia 37/4, 35-50.

Vepraskas, M.J., L.P. Wilding, L.R. Drees 1994. Aquic conditions for Soil Taxonomy: concepts, soil morphology and micromorphology. In: A.J. Ringrose-Voase & G.S. Humphreys (eds), Soil Micromorphology: Studies in Management and Genesis. Proc. IX Int. Working Meeting on Soil Micromorphology, Townsville, Australia, July 1992. Developments in Soil Science 22, Elsevier, Amsterdam, pp. 117–131.

Verpoorte, A. 2000. Pavlovian reflexes and the Pompeii premise: a spatial analysis of stone artefacts from Pavlov I (Moravia, Czech Republic). Archeologicke Rozhledy 52, 577-594. DOI: 10.1163/187633002X00334.

Wilczynski, J., P. Wojtal, M. Łanczont, P. Mroczek, D. Sobieraj, S. Fedorowicz 2015. Loess, flints and bones: multidisciplinary research at Jaksice II Gravettian site (southern Poland). Quaternary International 359-360, 114-130.

Zöller, L., E.A. Oches, W.D. McCoy 1994. Towards a revised chronostratigraphy of loess in Austria with respect to key sections in the Czech Republic and in Hungary. Quaternary Science Reviews 13(5-7), 465-472.

Zöller, L., D. Richter, S. Masuth, L. Wunner, M. Fischer, W. Antl-Weiser 2013. Luminescence chronology of the Grub-Kranawetberg site, Austria. E&G Quaternary Science Journal 62 (2): 127-135. DOI: 10.3285/eg.62.5.04.

C - Late Middle Stone Age Behavior and Environments at Chaminade I (Karonga, Malawi)

Sheila Nightingale [1], Flora Schilt [2], Jessica C. Thompson [3], David K. Wright [4, 5], Steven Forman [6], Julio Mercader [7], Patrick Moss [8], Siobhan Clarke [7], Makarius Itambu [7], Elizabeth Gomani Chindebvu [9], Menno Welling [10, 11]

[1] Department of Anthropology, City University of New York, Graduate Center, New York, NY 10016, USA. [2] Institute for Archaeological Sciences, Rümelinstrasse 23, 72072 Tubingen, Germany. [3] Department of Anthropology, Yale University, New Haven, CT 06511, USA. [4] Department of Archaeology, Conservation and History, University of Oslo, N-0315 Oslo, Norway. [5] State Key Laboratory of Loess and Quaternary Geology, Institute of Earth Environment, Chinese Academy of Sciences, Xi'an 710061, China. [6] Department of Geosciences, Baylor University, Waco, TX 76790, USA. [7] Department of Anthropology and Archaeology, University of Calgary, Calgary, AB T2N 1N4, Canada. [8] School of Earth and Environmental Sciences, The University of Queensland, Queensland, Brisbane 4072, Australia. [9] Malawi Ministry of Civic Education, Culture, and Community Development, Lilongwe 3, Malawi. [10] Reinwardt Academy, Amsterdam University of the Arts, 1018 TZ Amsterdam, Netherlands. [11] African Heritage Research and Consultancy, Zomba, Malawi.

Full citation:

Nightingale, S., Schilt, F. C., Thompson, J. C., Wright, D. K., Forman, S., Mercader, J., Moss, P., Clarke, S. Itambu, M., Gomani Chindebvu, E., Welling, M. (2019). Late Middle Stone Age Behavior and Environments at Chaminade I (Karonga, Malawi). Journal of Paleolithic Archaeology 2-3:258-397. https://doi.org/10.1007/s41982-019-00035-3

ABSTRACT

The African Middle Stone Age (MSA, typical range ~ 320–30 ka) has been the subject of intense research interest in recent decades as a culture-chronological Unit associated with the emergence and dispersal of our species. Recent results of this work have shown that sites designated as "MSA" contain common approaches to lithic reduction, but that within this rubric, there is much diversity in overall assemblage characteristics and the timing of their appearance across the continent. As researchers recover more data from more sites, especially from undersampled geographic regions, this more complex picture of the MSA reveals technological and other behavioral diversity in early modern human populations that may inform about the ultimate success of our species. Here we add to this growing database by describing the environmental context and characteristics of two

concentrations of stone artifacts from the late MSA (~ 43– 21 ka) open-air locality of Chaminade-I (CHA-I), near the town of Karonga in northern Malawi. The CHA-I lithic artifacts show a flexible approach to stone tool production and use that is common to assemblages in Karonga but distinctive from MSA sites reported elsewhere. Radial and minimally reduced cores typify an unelaborated lithic assemblage, in which raw material choice is driven by toolstone clast size and shape rather than preferential use or treatment of specific materials, as found in MSA assemblages in the East African Rift, South Africa, and the North African coast. Lithic reduction at CHA-I took place within a woody, riparian context embedded within a more open woodland landscape. Most artifacts occurred in near-channel sandy deposits dated to ~ 41 ka, and were buried under alluvial fan deposits that began aggrading by at least ~ 21 ka and continued beyond ~ 5.5 ka within a grassy, open landscape. The site's late MSA age and lack of elaboration in lithic technology challenges straightforward ideas of increasing complexity in human technological behavior over time and provides important insight into the diversity of MSA technologies and the environmental conditions in which they existed.

Keywords: Site formation; East-Central Africa; Stone tools; Vegetation change

The online version of this article (https://doi.org/10.1007/s41982-019-00035-3) contains supplementary material, which is available to authorized users.

INTRODUCTION

The Middle Stone Age (MSA) of Africa is variably defined along chronological and technological terms, as both a time period in which *Homo sapiens* emerged and proliferated in Africa and by a set of behavioral adaptations documented in approaches to flaked stone tool manufacture (Clark 1982, 1988; McBrearty and Brooks 2000). Conventionally, the MSA is cited as beginning by ca. 280 ka (Douze and Delagnes 2016) and ending by ca. 40 ka (Ambrose 1998). Recent scholarship, however, has demonstrated that stone reduction strategies typical of the MSA are present beyond this time range, with earlier occurrences at ~ 320 ka in the East African Rift (Brooks et al. 2018), in association with *Homo sapiens* fossils ca. 315 ka in the Maghreb (Richter et al. 2017), and persisting into the terminal Pleistocene or even Holocene of West Africa and the Horn of Africa (Scerri et al. 2017; Tribolo et al. 2017).

The early presence of Later Stone Age (LSA) sites in both East Africa (Ambrose 1998) and South Africa (d'Errico et al. 2012; Villa et al. 2012) by ~ 40 ka highlights that shifts in foraging technologies were not uniform with respect to geography or chronology. Research, particularly over the last 20 years, has sharpened the focus on the MSA as a period marked by innovation in

both stone tool manufacture and other aspects of life that leave material traces. These include symbolic use of ochre and other materials (Henshilwood and Dubreuil 2011), regular big-game hunting using long-distance projectiles (O'Driscoll and Thompson 2018; Sahle et al. 2013), and ultimately as the period in which *Homo sapiens* dispersed out of the African continent between ca. 80 and 40 ka (Pagani et al. 2016). These observations, however, are largely based on robust datasets from areas of the continent that have historically received significant research attention: the southern tip of Africa, the East African Rift Valley, the Nile Valley, and the Maghreb. Significant spatial gaps therefore exist across the continent (Thompson et al. 2018), resulting in a patchwork understanding of behavioral differences across an environmentally varied space. Further, evidence for complex innovations is not ubiquitous across the known MSA record, even at very late-occurring MSA sites. In order to broaden the known temporal, geographic, and environmental contexts of MSA assemblages, we report stone artifacts and environmental reconstruction from Chaminade I (CHA-I, 9.956° S, 33.892° E), an open-air, late MSA site in Karonga, northern Malawi. This locality, at the southern tip of the western arm of the African Rift Valley, is one of only a few with dated MSA assemblages in east-central Africa (Mercader et al. 2009, 2012; Thompson et al. 2018; Wright et al. 2017).

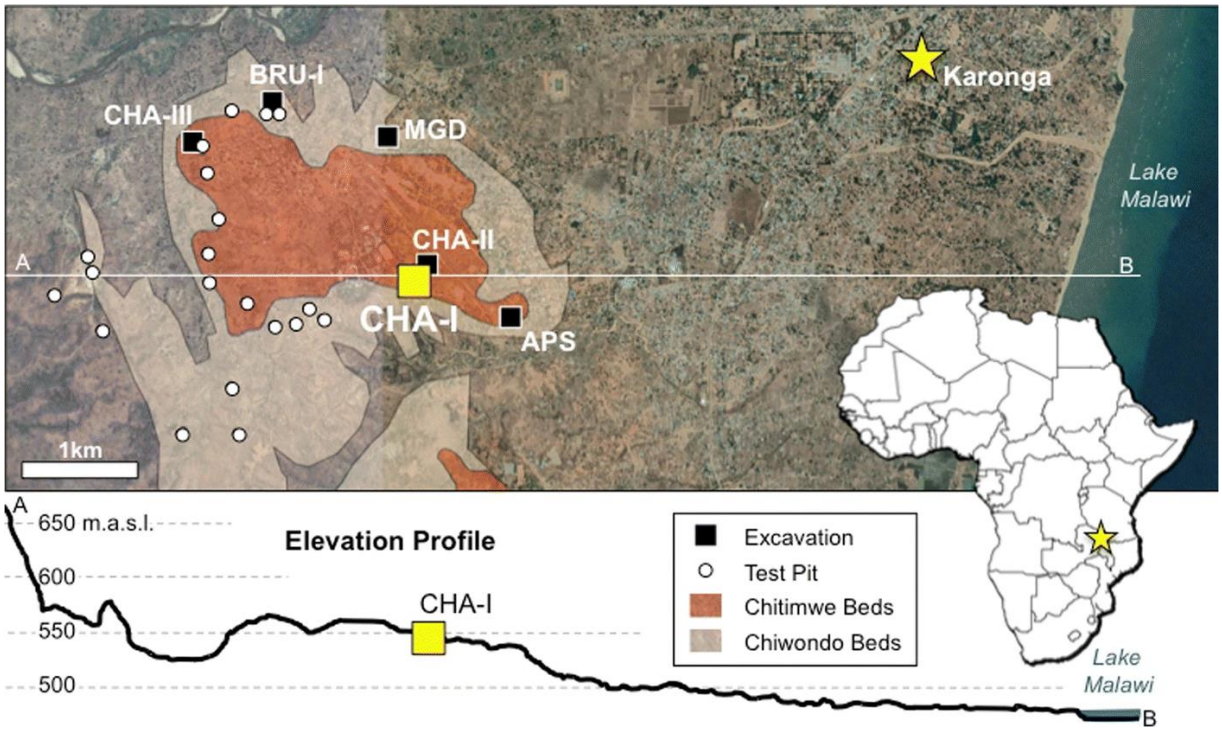

Fig. 1 Chaminade-I (CHA-I) excavation site in Karonga region of northern Malawi, with nearby MSA sites and test pits excavated by MEMSAP. MSA sites predominantly occur in remnant alluvial Chitimwe Beds (in red), which overlie archaeologically sterile Chiwondo Beds (in tan). Town of Karonga marked with yellow star. Aerial imagery from Google Earth

Near the modern town of Karonga, the Late Pleistocene Chitimwe Beds are represented by 83 km^2 of remnant alluvial fan sand and pebble/cobble deposits (4–64 mm and 64–256 mm, respectively; following Wentworth 1922), located approximately 5 km from the present shoreline of Lake Malawi (Fig. 1). Many hundreds of thousands of stone artifacts, most employing reduction styles characteristic of the MSA, erode from the Chitimwe Beds across the Karonga landscape (Thompson et al. 2014). These artifacts often derive from buried in situ sites, some of which are associated with paleoenvironmental indicators such as paleosols, phytoliths, and very occasional vertebrate fossils (Clark and Haynes 1970; Thompson et al. 2012, 2013; Wright et al. 2014, 2017). Underlying the Chitimwe Beds are the Plio-Pleistocene Chiwondo Beds, which are fossiliferous yet archaeologically sterile (Clark 1995; Juwayeyi and Betzler 1995). Extensive survey has shown that the Chitimwe Beds across the Karonga region are incised by ancient streambeds, and include dense cobble and pebble deposits; in situ archaeological occurrences are often within a few hundred meters of these ancient fluvial systems. Interpretation of site formation in the Chitimwe Beds is challenging due to preservation biases and multiple episodes of soil formation, occupation, deposition, and disturbance (Wright et al. 2017). Untangling these processes is critical to understanding the substantial human occupations responsible for the MSA artifacts that erode so abundantly from across the landscape.

The site of CHA-I preserves the techno-behavioral signatures of a late MSA population in a region of sub-Saharan Africa that has seen little detailed investigation. As a midpoint between the biogeographic regions of southern and eastern Africa, the Malawi archaeological record provides opportunities to examine variation in technological behavior and environmental preferences in the MSA. It is also a rare data point in the tropical savannas that characterized south-central Africa during the Late Pleistocene. Much emphasis has been placed on the role of climate change in mediating MSA population dynamics (Basell 2008), and the degree to which localized environments may have been buffered against extreme climate change has been explored in a synthesis by Blome et al. (2012). However, confidently dated MSA occurrences currently are exemplified by only three archaeological localities from the entire region that today encompasses Malawi, Zambia, Mozambique, Zimbabwe, and the Democratic Republic of the Congo (Blome et al. 2012). In contrast, there are several nearby high-resolution paleoclimatic datasets showing that central Africa experienced extreme fluctuations in precipitation, lake levels, and terrestrial environmental response during the Late Pleistocene (Garcin et al. 2006; Ivory et al. 2018; Johnson et al. 2016; Lyons et al. 2015; Tierney et al. 2008). This disjoin between the locations of dated and

described archaeological data and the locations of rich paleoenvironmental records has made it difficult to assess larger patterns in the relationships between MSA people and their environments.

The primary aim of this analysis is to offer a full description of an in situ MSA site in Karonga, so that robust comparisons can be made to other archaeological sites. We do this in the following ways: (1) describe the technological character of the lithic assemblage, (2) examine the relationship between raw material use and reduction strategies, (3) reconstruct the depositional and post-depositional processes that have affected site formation, (4) report the ages of the archaeological material through the results of optically stimulated luminescence (OSL) analyses, (5) provide the environmental context of the CHA-I site, and (6) contextualize CHA-I in the regional setting of the local and continental MSA.

BACKGROUND

The African Middle Stone Age

The MSA as originally defined by Goodwin (1928) is a techno-cultural industrial designation marked by prepared core reduction, the elaboration of hunting tool forms, and the absence of stone tools characteristic of either the Earlier Stone Age (i.e., large core tools) or Later Stone Age (i.e., microliths). This definition continues to evolve as researchers learn more about variation within MSA technology, as well as its temporal and geographic boundaries (Growcutt and Blinkhorn 2013). Academic discourse on the MSA since Goodwin's writing has largely focused on behavioral and biological evolutionary events and trends surrounding the emergence and spread of *Homo sapiens*, as it is generally accepted that the adaptive strategies acquired during this period enabled some, but not all, members of the *Homo* lineage to proliferate during the Middle and Later Pleistocene (Henn et al. 2011; Hublin and Klein 2011). In recent decades, MSA scholarship has centered around regionally specific reduction strategies and tools forms, evidence for increased dietary breadth, symbolic behavior, expanded foraging ranges, and in particular on specialized tool kits indicative of complex, extractive foraging strategies (Brown et al. 2012; Delagnes et al. 2016; Henshilwood and Dubreuil 2011; McCall and Thomas 2012; Sahle et al. 2014). These include the transport of raw material over considerable distances, standardization of tool forms, and evidence for composite or hafted technologies, which are strategies further expected to reflect some degree of population (i.e., cultural) cohesion or differentiation in response to regional environmental conditions and resource availability (Mackay et al. 2014).

Research in northern, eastern, and southern Africa has shown that the MSA, as a cultural/technological package, has developed discontinuously across the continent and over time (Johnson and McBrearty 2010; McBrearty and Brooks 2000; Sahle et al. 2014; Tribolo et al. 2015; Tryon and Faith 2013; Tryon et al. 2005; Van Peer et al. 2003; Wilkins and Chazan 2012), with technological hallmarks of MSA behavior both predating the minimum starting date of the MSA (~ 280 ka), and persisting in some areas into otherwise Later Stone Age periods (as recently as ~ 7.5 ka in the Horn of Africa; see Scerri et al. 2017; Tribolo et al. 2017). The diversity of behavioral repertoires evidenced in MSA contexts across Africa therefore likely reflects localized adaptations to specific environmental and cultural stimuli, rather than monolithic behavioral trends; this makes it critical to develop an understanding of MSA behavior in diverse paleoenvironmental and geographic zones (Thompson et al. 2018).

Environmental and Landscape Setting

The Karonga District of northern Malawi (Fig. 1) is situated within the Zambezian Phytogeographic Zone, characterized today by miombo woodlands containing a mosaic of tall Brachystegia trees and variable distributions of savanna grasses, hydromorphic grasses, and evergreen taxa (Mercader et al. 2011; White 1983). The climate is of an equatorial savanna (Aw in the Köppen- Geiger climate classification system), with hot, rainy summers and cool, dry winters (Kottek et al. 2006). Because it lies on the southern margin of the Intertropical Convergence Zone (ITCZ), most of the Lake Malawi catchment has only a single rainy season (November to April or May). The district is comprised of gently undulating topography on the distal end of an extensive alluvial fan system, bounded to the west by highlands of the southern Rift Valley (~ 2500 masl) and ~ 100 km to the east by Lake Malawi (~ 450 masl). To the south, the Chiweta Escarpment forms another physical boundary. In the past, these landscape features may have constrained foraging patterns for MSA populations. Rivers and streams incise the landscape, draining east into the lake, which is currently at a high-stand level.

Throughout the Pleistocene, the Lake Malawi catchment has been subject to extreme environmental variability, as seen in "megadrought" periods that have reduced lake levels by as much as 95% relative to today, transforming the local environment and subjecting human populations to changing configurations of water, vegetation, and animal resources (Cohen et al. 2007; Ivory et al. 2012; Lyons et al. 2015). The lake began to recover from the most recent extreme lowstand ca. 100 ka, and following 80 ka, lake level variability was relatively minor compared to other catchments such as Tanganyika (Bonnefille and Chalié 2000; Tierney et al. 2008) and Masoko (Garcin et al. 2006; Vincens et al. 2007). Following arid conditions of Marine Isotope Stage (MIS)

5b (87–82 ka), the overall balance of moisture has trended toward warmer and moister conditions until the Holocene (Ivory et al. 2012). Especially since ca. 60 ka, Lake Malawi has experienced an unusually long period of hydrologic overfilling (Lyons et al. 2015). Changes in orbital precession have had a limited impact on the overall distribution of rainfall since MIS 4, which ended by 57 ka (Lyons et al. 2015). All dated MSA sites in the Karonga District fall within the time of lake recovery since the last major arid period, and the majority of dated assemblages occur between 50 and 20 ka (Thompson et al. 2018). It is not clear if this increased archaeological visibility is because of an increase in population size or because of depositional factors.

Although the lake core records provide catchment-scale data on precipitation and vegetation, analysis of historical records shows that local-scale precipitation variability across the basin is high (Jury and Gwazantini 2002; Kumboyo et al. 2014; Ngongondo et al. 2001; Sene et al. 2016). This difference between catchment-scale and local proxies is also apparent in the Pleistocene. MSA sites were primarily preserved by alluvial fans that buried the sites and fluvial systems that activated within these settings created riparian zones that attracted human activity (Thompson et al. 2018;Wright et al. 2014, 2017). When Wright et al. (2017) compared phytolith assemblages from the site of Chaminade-II (CHA-II; ~ 100 m northeast of CHA-I) to vegetation proxies in the Lake Malawi Drill Core, they found that more woodland versus grassland was represented in the site and drill core records, respectively. Previous Research on the Malawian MSA Study of the Malawian MSA was initiated by J.D. Clark and colleagues in the 1950s (Clark 1954, 1956), with most focus on Karonga taking place in the 1960s (Clark 1966, 1967, 1968, 1972; Clark et al. 1966, 1970). MSA research in the region was largely discontinued afterwards with the exception of geoarchaeological work at the site of Mwanganda's Village by Kaufulu (1983, 1990). The Malawi Earlier-Middle Stone Age Project (MEMSAP) renewed study of northern Malawi in 2009 (Thompson et al. 2012), including a reinvestigation of the hypothesized Sangoan-era elephant butchery site at Mwanganda's Village (Wright et al. 2014). In addition to controlled archaeological excavation, it included extensive survey and geological trenching of MSA-bearing deposits within the alluvial fan systems comprising the Chitimwe Beds (Thompson et al. 2013, 2014, 2018; Wright et al. 2014, 2017; Zipkin et al. 2015). The CHA-I excavation was excavated in 2011 as one of the controlled excavations, as a way to establish how deeply buried artifacts were within the fan, if they were in situ, and the nature of their environmental contexts. Although overview artifact data have been published (Thompson et al. 2018; Wright et al. 2017), this study represents the first full assemblage and environmental reconstruction to be reported from a single MSA site in northern Malawi.

In addition to demonstrating a focus on past human occupation of riparian sites, prior work in Karonga has revealed a pattern in the age distributions of those sites that places all of them in the Late Pleistocene and most post-dating ca. 50 ka. These data accord with recent archaeological work on the Mozambican side of Lake Malawi, in which MSA through LSA sites are found on fluvially incised terraces and buried within fans (Bicho et al. 2016; Gonçalves et al. 2016; Mercader et al. 2012).The Malawian material suggests that although there is technological diversity in the MSA lithic artifact assemblages, there is little evidence for technological "complexity," often identified in MSA contexts by flaking or retouching methods for the production of specific tool forms, preferential raw material use or treatment, or hafted technology (Thompson et al. 2018). Detailed analysis of the CHA-I artifact assemblages allows these larger patterns in behavior to be examined at the site scale, and at the level of individual knapping events, revealing the underlying technological decision-making strategies of MSA people.

METHODS

Excavation

The CHA-I site sits on a level landscape, in a cluster of trees and shrubs surrounded by grasses in an arrangement typical of Zambezian miombo woodland. The area around it is under cultivation, and non-native *Eucalyptus* trees are in close proximity. We identified the area for excavation because of numerous typologically MSA artifacts eroding from the exposed Chitimwe Beds ~ 20 m to the west. However, because the beds typically erode into parabolic hillslopes rather than sharp exposures, stratigraphy is impossible to discern unless excavation is initiated from above the alluvial fan deposits that contain the artifacts. Excavation took place in 2011, within the exposure of a modern pit dug by area residents to access a localized deposit of gray clay for the production of bricks. Most of the upper depositional Unit of the pit had been removed prior to archaeological investigation to access the artifactually sterile clay (Fig. 2), and beneath the thick layer of modern alluvium, an artifact- and Fe-Mn nodule-bearing layer was exposed.

A 10 × 1-m excavation trench running north-south was first established and stepped into the brick pit (squares A1-A10) to assess what material might have been missing because of the brick pit excavation. With the exception of a single artifact from the middle of the long trench, all of the artifacts were recovered from the southern extent of the trench (squares A8, A9, and A10), below the base of the modern brick-clay excavation. The southern-most two meters of the trench were then extended 1 m to the east (squares B9 and B10) in order to maximize the buried artifact

sample. Therefore, although the total extent of the excavation was 12 m^2, and the upper layers yielded dating and paleoenvironmental data, only the southernmost 5 m^2 penetrated deeply enough to produce the artifacts described here. In the southwestern-most square (A10), a ~ 1-m sondage was extended beyond the closing depth of the rest of the southern excavation area to establish if further artifact-bearing deposits were below.

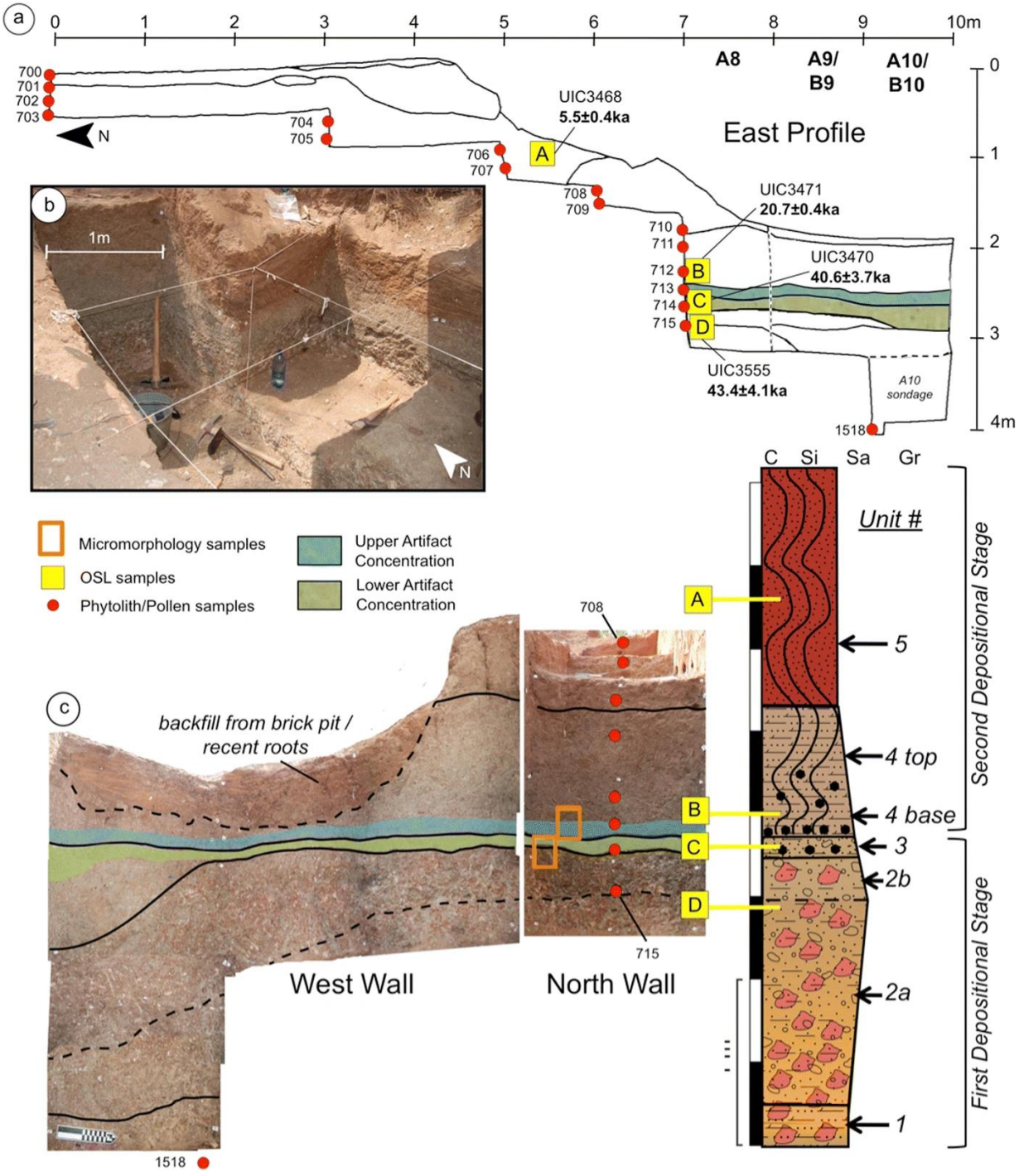

Fig. 2 a East section of CHA-I excavation, with locations of OSL, phytolith, and pollen samples and Upper and Lower Artifact Concentrations. **b** View from SW corner of excavation area. **c** West and north profile walls at CHA-I, with OSL, micromorphology, phytolith, and pollen sample locations and Upper and Lower Artifact Concentrations

Excavation was conducted according to natural stratigraphic boundaries, unless those boundaries exceeded 10 cm in maximum thickness. In those cases, the excavation proceeded in 10-cm arbitrary levels (spits). In the artifact-bearing squares of the excavation, the number of spits varied by square and depositional Unit, with a maximum of seven spits from the exposed surface of the brick pit to the base of the Unit; the artifactually sterile sondage in square A10 was excavated as a single thick level, as a geological trench. Lithic artifacts were piece-plotted during excavation using a Nikon C-series 5" total station; all sediments were then sieved through 5 mm screens to recover artifacts that were not identified during excavation. Total station-derived datasets for plotted material were incorporated into a GIS (Geographic Information System) for high-resolution mapping and spatial analysis. Flaked stone represents the only artifact class recovered at CHA-I; organic materials such as bone or shell have not been recovered from the iron oxide-rich lateritic soils that characterize the surficial deposits of the region. Indicating successive wet and dry seasons, laterites are typically acidic and thus unlikely to preserve organic material. It is only in small pockets of more calcareous sediment in the Chitimwe Beds that there is any potential for organic preservation, and none have been found at CHA-I. Ochre has the potential to preserve and has been recovered from a site reported ~ 1 km to the north, excavated in the 1960s (Clark et al. 1970). Microcharcoal may preserve in sediment samples prepared for pollen extraction, but the remains of fires and hearths do not.

At CHA-I, OSL samples were selected from the Units immediately below, containing, and above the artifact concentrations, as well as from near the top of the alluvial sequence. Micromorphology samples were taken to capture the boundaries between macroscopically visible sedimentary Units. Loose sediment samples were taken for pollen and phytolith analysis in a column from the north profile of the excavation, although because it was a step trench, some sets were offset horizontally from the next set of samples. Samples were taken every 20 cm depth or at a visible change in stratigraphy, whichever came first (Fig. 2).

Dating

OSL ages on quartz grains from sediments from CHA-I were determined by protocols similar to Wright et al. (2014; see SOM for details of sample preparation and experimental confirmation). Four samples were analyzed from fluvial contexts (point bars, bedload) at the southern extent of

the excavation; sample locations are identified in Fig. 2c. Aliquots were comprised of 100–500 grains of sand (100-355 μm) fitting within a 2-mm diameter area that was subjected to blue-light (470 ± 20 nm) excitation. Calculation of equivalent dose (D_e) by the Single Aliquot Regeneration protocols (Murray and Wintle 2003) was accomplished for 28 to 34 aliquots of the four samples tested (Table 1). A test for dose reproducibility was performed following procedures of Murray and Wintle (2003) with the initial and final regenerative dose of 6.6 Gy yielding concordant luminescence responses (at 1 − σ error) (Fig. 3). Ages are presented with 1 − σ errors.

The dose rate (D_r) is an estimate of the exposure of quartz grains to ionizing radiation with the decay of the U/Th decay series, ^{40}K, and the contribution of cosmic rays. Concentrations of U, Th, and K were determined by inductively coupled plasma mass spectrometry (ICP-MS) by Activation Laboratory Ltd., Ancaster, Ontario, Canada. The cosmic ray dose was calculated based upon the sample's location, elevation, and depth below the ground surface (Prescott and Hutton 1994).

Calculation of D_e by the single aliquot protocols was accomplished for 28 to 34 aliquots (Table 1). For all samples, 70 to 100% aliquots were used to define the final D_e distribution and age determination; aliquots were removed from analysis because the recycling ratio was not between 0.90 and 1.10, the zero dose was > 5% of the natural emissions, or the error in equivalent dose determination is > 10%. D_e distributions were log normal and exhibited a range of overdispersion values from 24 to 14% (Table 1). An overdispersion percentage of a D_e distribution is an estimate of the relative standard deviation from a central D_e value in context of a statistical estimate of errors (Galbraith and Roberts 2012; Galbraith et al. 1999). A zero overdispersion percentage indicates high internal consistency in D_e values with 95% of the D_e values within 2σ errors. Overdispersion values ≤ 25% are routinely assessed for small aliquots of quartz grains that are well solar reset, like eolian sands (Meier et al. 2013; Olley et al. 2004; Wright et al. 2011), and this value is considered a threshold metric for calculation of a D_e value using the central age model of Galbraith et al. (1999).

Sample	Unit	Depth (m below surface)	Grain size (μm)	Aliquots	Equivalent dose (Gy)[a]	Overdispersion (%)[b]	U (ppm)[c]	Th (ppm)[c]	K (%)[c]	H_20 (%)	Cosmic dose (mGy/year)[d]	Dose rate (mGy/year)	OSL age (ka)[e]
UIC3468 (A)	5	1.20	100–150	30/30	14.37 ± 0.76	22.1 ± 3.2	1.6 ± 0.1	13.1 ± 0.1	1.41 ± 0.02	10 ± 3	0.19 ± 0.02	2.63 ± 0.13	5.5 ± 0.4
UIC3471 (B)	4 base	2.50	250–355	29/30	45.33 ± 1.93	14.3 ± 2.1	1.5 ± 0.1	10.4 ± 0.1	1.29 ± 0.02	10 ± 3	0.16 ± 0.02	2.19 ± 0.11	20.7 ± 1.5
UIC3470 (C)	3	2.75	250–355	28/30	75.82 ± 3.76	19.1 ± 2.7	0.9 ± 0.1	7.1 ± 0.1	1.34 ± 0.02	10 ± 3	0.14 ± 0.01	1.87 ± 0.09	40.6 ± 3.7
UIC3555 (D)	2a	3.05	100–150	34/44	74.94 ± 4.28	23.6 ± 3.5	0.7 ± 0.1	6.0 ± 0.1	1.34 ± 0.02	15 ± 5	0.12 ± 0.01	1.73 ± 0.09	43.4 ± 4.1

Table 1 Optically stimulated luminescence (OSL) ages on quartz grains from CHA-I, Karonga, Malawi

a Quartz fraction (2 mm plate area) analyzed under blue-light excitation (470 ± 20 nm) by single aliquot regeneration protocol (Murray and Wintle 2003)

bValues reflect precision beyond instrumental errors; values of ≤ 20% indicate low spread in equivalent dose values with an unimodal distribution

c U, Th, and K20 content analyzed by inductively coupled plasma-mass spectrometry analyzed by Activation Laboratory LTD, Ontario, Canada

d From Prescott and Hutton (1994)

e Ages calculated using the central age model of Galbraith et al. (1999), with overdispersion values < 20% at two sigma errors

All errors are at 1 sigma and include random and systematic errors calculated in a quadrature. Ages calculated from the reference year AD 2010

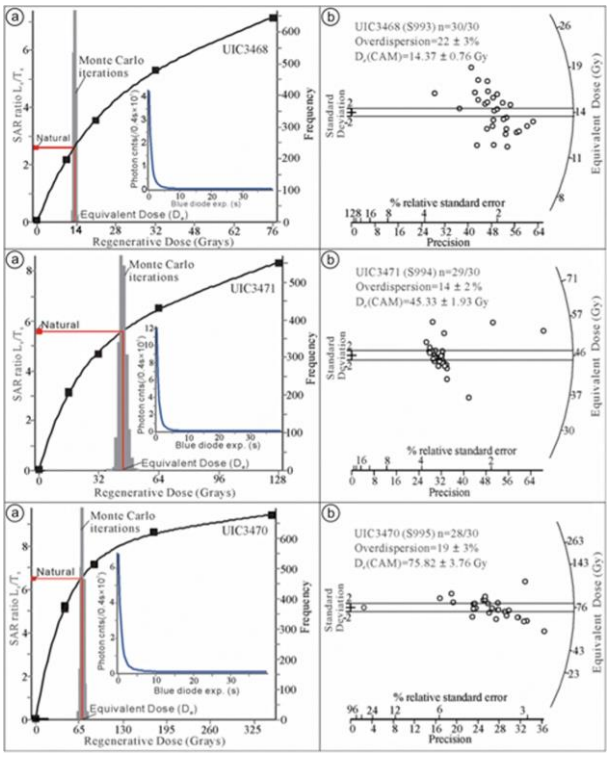

Fig. 3 a OSL regenerative growth curves for aliquots of quartz grains of UIC3468, UIC3471, and UIC3470 with inset figure showing representative shine-down curve for a natural emission. **b** Radial plots of equivalent dose (D_e) values for aliquots. Shown is the two sigma D_e range for the Central Age Model (CAM) (after Galbraith and Roberts, 2012)

Micromorphology

Four micromorphological samples were taken from the north wall of the step-trench, three of which were aligned with OSL samples to aid in the evaluation and integration of results of both analyses. Thin sections from two of the oriented blocks were studied following methodology details in the SOM Section 2. Micromorphological description included sediment microstructure,

mineralogy and grain size of the coarse fraction (> 100 μm), characteristics of the fine fraction (< 100 μm), porosity, nature and degree of bioturbation, spatial relationships of components, redoximorphic features, organic materials, clay coatings, and other attributes following Courty et al. (1989) and Stoops (2003). This methodology enables the study of sedimentary constituents and processes of deposition, as well as post-depositional alterations of the sediments resulting from soil formation, bioturbation, or groundwater fluctuations.

Paleoecology Analysis

Sixteen paired phytolith and palynology samples were taken from the stepped north wall of the excavation, and one sample was taken from the base of the sondage wall at the southern extent of the trench. Phytolith extraction followed protocols established in Mercader et al. (2011) and is described in the SOM Section 3. An average of 451 phytoliths was tallied per sample in adjacent, non-overlapping lines across the cover slip (20 × 40 mm). Poaceae short cells were counted to > 200 cells. System microscopy was conducted at × 40 magnification (Motic BA410E; image software: Images Plus).

Quantitative phytolith taxonomies from Zambezian woodlands establish that their woody species leave behind blocky, cylindroid, globular, and tabular phytoliths (Mercader et al. 2009). In addition, taphonomically normalized assemblages from modern soils under miombos consist of globular, blocky, cylindroid, lobate, tabular, and tower phytoliths (Mercader et al. 2011). With this baseline in mind, we have considered globular granulates (Fig. 4a, b), blocky (Fig. 4c, d), tabular (Fig. 4e, f), and cylindroids (Fig. 4g) to come from the bark tissue from woody dicots (Neumann et al. 2009; Runge 1999). Globular psilates (Fig. 4h), from Zambezian soils, group along with arboreal phytoliths (Mercader et al. 2011). Zambezian clavate granulates (Fig. 4i, j) represent the arboreal species of the *Dipterocarpaceae* (Mercader et al. 2009). As for the grasses that coexist amidst Zambezian woody taxa (Mercader et al. 2010), they are recognized through tall, hydric, and heliophyte panicoids (lobates; Fig. 4k–m), wet-loving bambusoids (long saddle; Fig. 4n), cool-adapted pooids (rondels, towers; Fig. 4o–q), and xeric chloridoids (short saddles; Fig. 4r, s).

Palynomorphs (predominantly pollen and spores) and microcharcoal (particles < 125 μm) were extracted using the method developed by van der Kaars (1991) and discussed in depth by Moss (2013); details of extraction are provided in the SOM Section 4. Following extraction, pollen concentrate materials were slide-mounted in glycerol for analysis. The pollen sum consisted of a minimum of 200 palynomorphs or two completely counted slides, while the microcharcoal analysis involved counting all black angular fragments > 5 μm across three evenly spaced transects across

all samples. Pollen and charcoal concentrations were determined from counts of exotic *Lycopodium* marker spores, which were added as a tablet (i.e., at the start of the analysis) with a known concentration of *L. clavatum* (Stockmarr 1971; Wang et al. 1999).

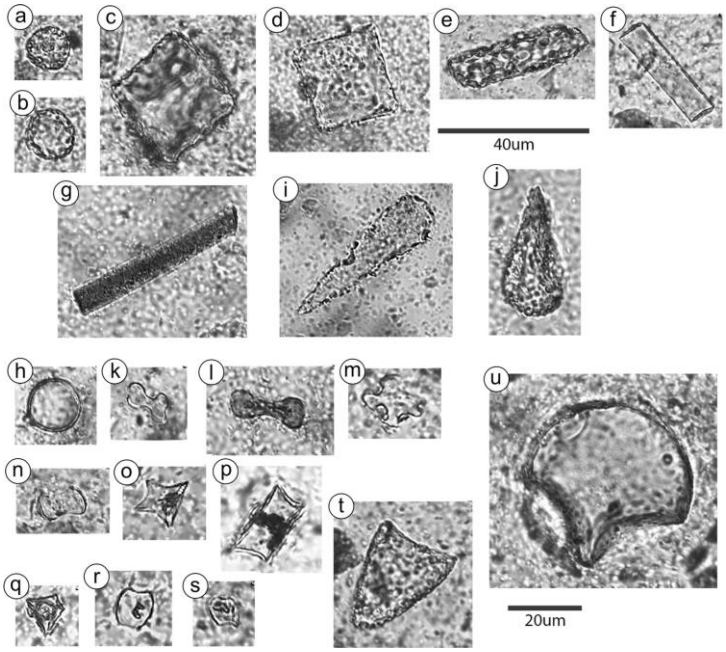

Fig. 4 Key phytolith types identified at CHA-I. **a, b** Globular granulate. **c, d** Blocky. **e** Tabular cavate. **f** Tabular elongate. **g** Cylindrical. **h** Globular psilate. **i, j** Clavate. **k** Bilobate, short concave. **l** Bilobate, long concave. **m** Lobate, cross. **n** Saddle, long. **o** Tower, horned. **p** Rondel. **q** Tower. **r, s** Saddle, short. **t** Scutiform. **u** Bulliform. Scutiforms (**u**) and bulliforms (**t**) come from undetermined grasses. Globular psilates (**h**) abound in wooded environments (Mercader, et al., 2011)

Lithic Analysis

The stone tool assemblage from CHA-I was analyzed on metric and descriptive characteristics, based on the data collection methods established for previous MEMSAP excavations (Thompson et al. 2012). All objects were classed according to basic characteristics including: raw material, grain size, weight, maximum dimension, relative amount of cortex preserved, and technological component (core, flake, unidentifiable debitage or shatter, etc.). The degree of edge-rounding on each artifact was also quantified (following Thompson et al. 2012) to assess the possibility of post-depositional fluvial transport or subaerial exposure. Divided into four classes, artifacts were described as follows: 0, no edge rounding (i.e., in fresh/sharp condition); 1, slight edge rounding visible to the naked eye; 2, edge rounding to the degree that smaller features such as conchoidal ripples were obscured, though general artifact morphology and reduction characteristics are evident; 3, edge rounding significant enough to obscure major reduction characteristics or to

modify artifact morphology. Metric measurements on cores, flakes, and other debitage captured size and shape characteristics and qualitative description permitted analysis of reduction strategies and trends in raw material use. Retouching location and invasiveness (the relative depth of a retouch scar across the surface of an artifact) were recorded when found (following Clarkson 2002), as was the presence of specialized tool forms such as points or blades.

Radial (or discoidal) cores were defined by centripetal flaking around a perimeter and onto one or both opposed hemispheres. Throughout MSA literature, the terms "radial" and "discoid" are used in various ways: (1) to differentiate cross-sectional attributes of cores (radial cores have thick cross-sections, while discoidal cores have flat cross-sections; Willoughby 2009), (2) according to the preferences of the analyst (for example, McCall (2006) and Tryon et al. (2012) consistently use "discoidal," while Pleurdeau (2006) and Mackay et al. (2014) use "radial"), (3) to group non-Levallois radially flaked cores (discoids) and centripetal Levallois cores under the organizational rubric of "radial" (Villa et al. 2005), or (4) more-or-less interchangeably (McBrearty and Brooks 2000). Levallois cores are centripetally flaked and are distinguished on the basis of an asymmetry of hemisphere volumes, preparation of the preferential flake platform, and shaping of the Levallois surface for the removal of a preferential flake (Boëda 1995).

All artifacts were assessed for conjoins (ancient, unintentional breaks that did not result from the flaking process) and refits (sets of subsequent flake removals or flake-and-core sets; the distinction follows Sisk and Shea 2009). Refitting allows for a more complete understanding of reduction methods, the equifinality of multiple flaking schemes, and of the relative use-life of reduced stones. Refitting also permits an assessment of the degree of post-depositional disturbance or winnowing to which an assemblage may have been subjected; a high incidence of refitting artifacts suggests that little post-depositional reworking has modified the assemblage, whereas highly disturbed contexts are unlikely to preserve high frequencies of refitting pieces (Schick 1987).

Spatial Analysis

Artifact attribute data resulting from lithic analysis were joined with total-station derived spatial data into a GIS, using ESRI ArcMap 10.2; full artifact data, including coordinate data, are provided as a supplementary database. GIS analysis consisted of three nested approaches: (1) map the distribution of raw material types and reduction strategies, (2) map refitting and conjoining artifacts, and (3) identify non-random clusters of artifacts using the ArcGIS Optimized Hot Spot Analysis (OHSA) functionality, similar to the analysis conducted for the nearby site of CHA-II (Wright et al. 2017). The OHSA tool analyzes two-dimensional datasets for spatial clustering along

a third attribute; in this case, elevation was used as a third attribute, meaning that the tool identifies data points that are closely grouped on *x*-, *y*-, and *z*-axes. The resulting data layer identifies artifacts with high statistical significance, at 99%, 95%, and 90% confidence intervals, for both high and low *z* (elevation) values, as well as areas of no significant clustering. Given the small excavation area and limited depth (~ 5– 10 cm) and slope of the artifact concentrations, it was unnecessary to normalize the z value data, as it might be necessary for datasets with wide ranges in elevation that could obscure mid-elevation clustering.

RESULTS

Dating and Stratigraphy

We document two stages of sediment aggradation at CHA-I (Fig. 2). The first stage is represented in Units 1–3 in which poorly sorted sediments vary in size from coarse sand to cobbles, reflecting a high-energy depositional environment and deposition of fluvial bedload (Table 2). These lower strata are characterized by redoximorphic features such as low chroma colors (gley) and reddish redox masses (mottles) (Vepraskas et al. 1993). The base of the sequence (Unit 1) is archaeologically sterile, and artifacts increase in density through Unit 2a (n = 47) and Unit 2b (n = 75), with their highest numbers in Unit 3 ("Lower Artifact Concentration," n = 323). A break in sedimentation following Unit 3 marks the second stage of sediment deposition at the site, and it is during this break that the majority of artifacts were deposited ("Upper Artifact Concentration," n = 893), dating maximally to between ~ 43.4 and 40.6 ka (OSL samples D and C, respectively) and minimally to ~ 21 ka (OSL sample B). The artifacts were deposited during a lower-energy phase of this sequence, in a sandy and very fine gravel matrix representing alluvial fan aggradation.

Texture	Consistency	Sediment color	Inclusions	Lower boundary	Lithic assemblage	OSL sample and results
Unit 5: sandy alluvial fan deposits/laminated fill						
Poorly sorted, subangular to subrounded medium to coarse sand fining up to a fine to medium sand	Soft, loose, nonsticky, nonplastic	2.5YR5/8-d (bottom), 2.5YR5/6-d (top)	Many root and insect disturbances	Merging, continuous boundary	*n* = 3 Minimal scatter, artifacts out of context	UIC3468 = 5470 ± 430 "A" in figs.
Unit 4 (top): gray clay/"brick pit"						
Poorly sorted medium to very coarse, angular sandy clay loam	Soft, slightly friable, sticky, very plastic	7.5YR4/4-w, 10YR5/3-w, 10YR6/3-d, 10YR7/4-d	cm-scale intraclasts of moderately well sorted fine to medium sand; 1–2% 2–5-mm Fe-Mn nodules; many root and insect disturbances	Abrupt boundary	*n* = 0 Artifactually sterile	
Unit 4 (base): Fe-Mn nodules/alluvial fan deposits						
Poorly sorted angular to subangular coarse to very coarse sand and fine gravel fining upwards to very fine gravel/coarse sand	Slightly hard, friable, non-sticky, non-plastic	2.5Y6/2-w, 10YR7/4-d; weak redoximorphic mottling (10R6/6)	Discontinuously distributed 5–20% 0.5–2-mm Fe-Mn nodules; many root and insect disturbances	Abrupt boundary	*n* = 893 Upper Artifact Concentration; ~ 92% of artifacts show little or no weathering; several refit/ conjoin sets	UIC3471 = 20,660 ± 1500 "B" in figs.
Unit 3: cobbles in fine gravel/stream channels						
Poorly sorted, sporadically imbricated semi-prismoidal to semi-discoidal, rounded to well-rounded very coarse pebbles and cobbles in a matrix of poorly sorted angular to subangular coarse to very coarse sand and fine gravels; massive	Hard, friable, non-sticky, non-plastic	2.5Y6/2-w, 10YR7/4-d; cm-scale weak redoximorphic mottles (10R4/8)	2–5% dispersed Fe-Mn nodules (0.5-2 mm) and concentrated just above cobbles	Abrupt boundary dipping to the south	*n* = 323 Lower Artifact Concentration; ~ 87% of artifacts show little to no weathering; several refit/ conjoin sets	UIC3470 = 40,560 ± 3230 "C" in figs.
Unit 2b: pebble gravel						
Poorly sorted angular to subangular coarse to very coarse sand to fine gravel (matrix supported); massive	Hard, friable, non-sticky, non-plastic	2.5YR5/4-w, 10YR7/4-d; weak mm- to cm-scale redoximorphic mottles (2.5YR6/8	Few root disturbances	Merging, continuous boundary	*n* = 75 Artifacts more diffuse and slightly more weathered than units above; no refit/conjoin sets	
Unit 2a: gleyed clayey gravel						
Poorly sorted, angular to subangular very coarse sand to medium gravel with 5–10% coarse rounded gravel; massive	Hard, friable, non-sticky, non-plastic	2.5YR4/8-w, 5Y7/1-w, 10YR6/3-d; weak mm- to cm-scale redoximorphic mottles (2.5YR5/8)	Many root disturbances	Merging, continuous boundary	*n* = 47 Artifacts more diffuse than units above; variable degrees of weathering; no refit/conjoin sets	UIC3555 = 43,390 ± 4125 "D" in figs.
Unit 1: fine gravel						
Very poorly sorted, angular to subangular very coarse sand to fine gravel (matrix supported); massive; cm-scale intraclasts of poorly sorted medium- to coarse sand	Hard, friable, non-sticky, non-plastic	5YR4/2-w, 2.5Y7/3-d; weak mm- to cm-scale redoximorphic mottles (2.5YR5/8)	Common root disturbances	N/A	*n* = 0 Artifactually sterile	

Table 2 CHA-I stratigraphic description, artifact distribution, and OSL results

Alluvial fan deposits are documented based on sediment texture and sorting characteristics (SOM Section 2) beginning prior to ~ 20.7 ka (OSL sample B). This constrains the upper age of all artifact deposition at the site (except for the artifact recovered from the top of Unit 5 that was likely introduced during a period of more recent alluvial activity). An abrupt depositional boundary was identified within the second stage of site formation, between Units 4 and 5, after which more alluvial fan deposits aggraded until they ceased sometime after ~ 5.5 ka (OSL sample A). Lateritic soil formation ensued after the cessation of alluvial fan deposition and contributed via pedogenic weathering and bioturbation to homogenization of the profile in Units 4 and 5; bedding structures and distinct sedimentation zones that may have been present during the initial sedimentation of the site were disturbed and overprinted. Laterite (plinthite) formation is typical of the Chitimwe

Bed alluvial fan deposits in the Karonga area and has been described for the nearby excavation of CHA-II (Wright et al. 2014, 2017).

Micromorphology Results

Micromorphological analysis was performed on samples from the contact of Unit 2b with Unit 3 (sample 1988) and from the base of Unit 4 (sample 1987), encompassing the contexts of the lower and upper lithic artifact concentrations (Fig. 5; for greater detail on the micromorphological analysis, see SOM Section 2). The upper part of Unit 2b, as captured in the lowermost sample 1988 (Fig. 5e), is marked by variability in grain sizes changing from medium to coarse pebbles in the lower part to very coarse sand to fine gravel in the upper part of the Unit. A discontinuous lens of well-rounded, sub-discoidal medium pebbles caps the sequence (Fig. 5e). The fine matrix of Unit 2b consists of pale yellowish, black-speckled clay. The coarse and fine material of Unit 2b is organized in a blocky subangular microstructure. Thick multi-phased compound clay coatings formed in the unit, as well as distinct redox masses (Fig. 5f). The clay coatings have been deformed by shrink-swell activity, and in some of them, a kink-band fabric (Fig. 5h) can be observed.

Unit 3 is contained in the upper part of sample 1988 (Fig. 5e) and consists of very fine to fine gravels among which are subrounded iron-manganese (Fe-Mn) nodules of fine gravel size (Fig. 5e, g). The fine fraction consists of pale yellowish, black-speckled, limpid clay, similar to Unit 2b. Few bioturbation features (roots; Fig. 5c) disrupt the subangular blocky microstructure, and locally, the clay is arranged in a very weak grano-striated b-fabric. Similar to Unit 2b, this Unit contains compound clay coatings, which have been deformed by vertic activity. Redox masses are more diffused compared to Unit 2b.

The deposition of Unit 4 initiates with somewhat coarser sediment than Unit 3, which fines upwards to a coarse sandy clay loam in the upper part of sample 1987 (Fig. 6b). The very coarse sand to fine gravel at the lower boundary of the unit contains inclusions of medium gravel and well-rounded concentric Fe-Mn nodules of sizes ranging from fine to medium gravel (Fig. 6b, d). Unit 4 shows a strong increase in bioturbation and the coarse and fine constituents form a medium separated, granular microstructure. Common carbonate features occur in association with bioturbation features in which root remains, termite excrement, and organic material modified by termites and fungal hyphae appear to play a role in the formation of biogenic secondary carbonates. The full formation sequence is illustrated and summarized in SOM Figure S4.

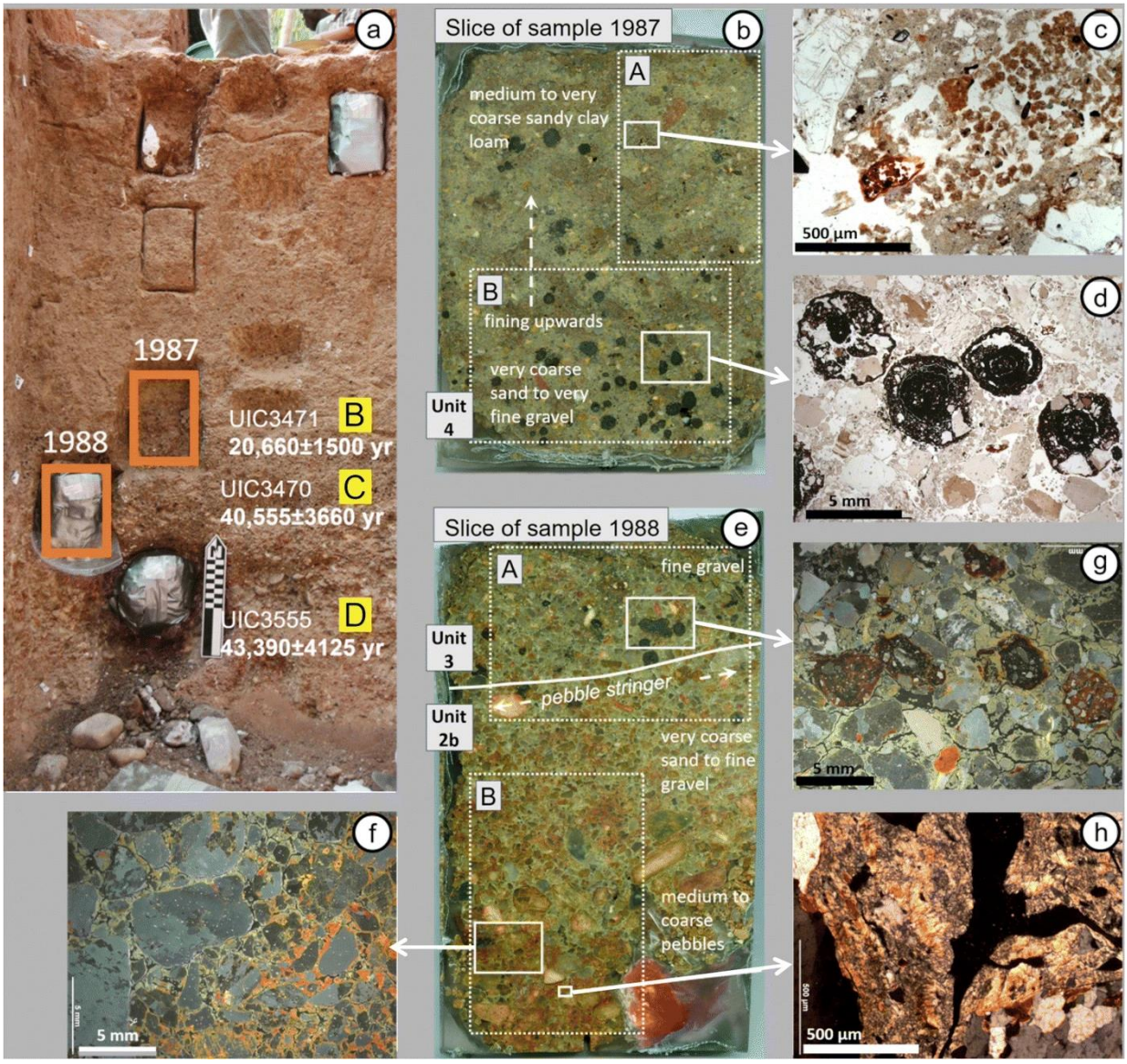

Fig. 5 Micromorphology samples from CHA-I north profile. **a** North profile with the location of the samples 1987 and 1988 (orange frames), as well as the locations of the three OSL samples and their resulting dates. **b** Slice of the impregnated and hardened sample 1987. The dotted frames indicate the approximate locations of the thin sections (A and B) produced from this sample. The sample comprises the lowermost part of Unit 4, which extends further upward. **c** Channel infilled with root remains and microaggregates (agg) of masticated and excremental material (PPL) (100×). **d** Concentric iron-manganese nodules in Unit 4. Note the sand-sized inclusions in the outermost bands and fissures from physical damage and dissolution (PPL) (8×). **e** Slice of the impregnated and hardened sample 1988. The dotted frames indicate the approximate locations of the thin sections (A and B) produced from this sample. The sample includes the upper part of Unit 2b and a large part of Unit 3. **f** Redox concentration (lower right) and depletion (upper left). Micrograph taken with crossed polarizers (XPL) and oblique incident light (OIL) to show the distribution of iron oxides (6.5×). **g** Very fine gravel and horizontally aligned, redeposited iron-manganese nodules in a subangular ped microstructure in Unit 3 (XPL and OIL) (6.5×). **h** Thick deformed compound clay coatings with fine sand-sized inclusions showing multiple episodes of clay translocation. Earlier clay coatings are more iron stained, and deformation from shrink-swell activity has led to a kink-band fabric (XPL) (100×)

Paleoecology Results

Sixteen paired sediment samples from the stratigraphic sequence were processed for phytolith and palynology analysis (nos. 700-715), and one phytolith sample was analyzed at the base of the sondage wall in square A10 (no. 1518). In both sets of samples, no. 715 did not produce sufficient phytolith or pollen counts to be included in analysis; two further samples (nos. 706, 713) also did not produce enough pollen for analysis, though all samples did produce microcharcoal.

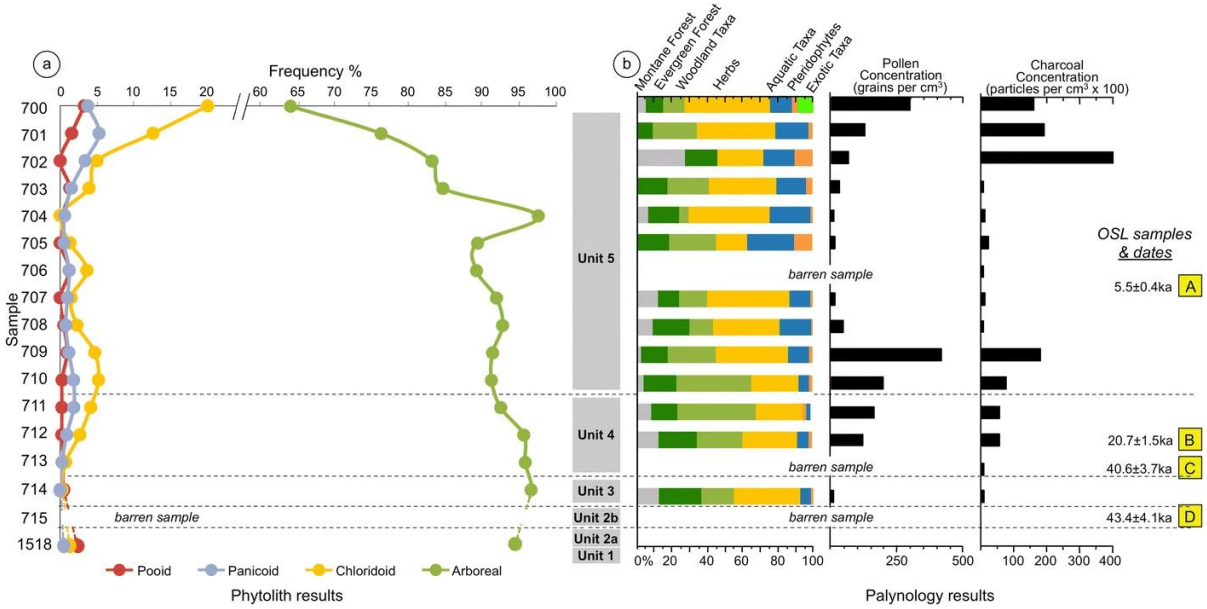

Fig. 6 a Phytolith frequencies from CHA-I sequence (indeterminate types not represented), full dataset represented in SOM Table S2. **b** Pollen and microcharcoal frequencies from CHA-I sequence, frequencies of all 28 recovered pollen taxa represented in SOM Figure S9

A total of 7649 phytoliths were counted throughout the sequence, with a mean phytolith tally of 451 per sample. Preservation was adequate for morphometric analysis and type identification, and a total of 28 morphotypes were classified. The complete dataset appears in SOM Table S2; Fig. 6a illustrates the relative frequency of phytolith types through the CHA-I sequence.

Overall, the sampled sequence is dominated by arboreal morphotypes from bark tissue (Fig. 6a). The mean percentage of woody phytoliths throughout the column is 89% (min 63.93% [sample no. 700]; max 97.54% [sample no. 704]), reflecting a significant and consistent woody plant component around CHA-I that gradually increases through the lower, artifact-bearing Units. Grass clades are only minimally represented in the phytolith samples, typically at ~ 5% of overall phytolith totals. Variance in the relative frequency of woody and grass phytoliths support a division of the sequence into two main zones: an upper zone (sample nos. 700–703) in upper Unit 5, where

woody phytoliths have a mean frequency of 77%, and a lower zone (sample nos. 704–714, 1518) running from lower Unit 5 to Unit 2b, in which woody phytoliths account for an average of 93% of the recovered samples. The upper zone marks an upward change toward tree cover contraction and spread of grasses. The most prominent change occurs in the youngest part of the column (sample nos. 700, 701) when cool-adapted pooids reach ~ 16.2%, and seasonally wet-adapted panicoids and xeric chloridoids also peak, albeit at low percentages; these increases are concomitant with a decrease in arboreal values. In the lower zone there are two arboreal hyperabundance (> 90%) phases, at the middle of Unit 5 (sample no. 704) and Unit 3 (sample no. 714). The grasses from this phytolith zone, although uncommon, do reflect fluctuations with alternating higher and lower frequencies. They concurrently peak at sample no. 706 (mid-Unit 5) and sample nos. 709–711 (lower Unit 5/upper Unit 4) while the intervening values are relatively low. Samples 713 and 714 are associated with the majority of the MSA artifacts, and represent a time between ca. 40.6–20.7 ka when the relative abundance of arboreal phytoliths was at one of its highest points.

Sixteen palynology samples were taken in tandem with phytolith samples (nos. 700– 715) but did not sample the base of the excavation/sondage. Three of the samples (706, 713, 715) did not produce sufficient pollen counts to be included in the analysis, though all samples did produce microcharcoal. Pollen from 32 taxa was recovered from the sequence, which we divide into seven groups: montane forest, evergreen forest, woodland taxa, herbaceous taxa, aquatic taxa, pteridophytes (ferns), and exotic taxa (*Eucalyptus*). Relative and absolute frequencies of recovered microcharcoal and pollen grains from the seven main groups are reported in Fig. 6b, and the full sequence of all 28 identified taxa are in SOM Figure S9.

In contrast to the phytolith samples where woody dicots are most common, herbs are the most commonly recovered pollen types throughout the sequence, accounting for ~ 15–50% of each sample (mean = ~ 35%). Arboreal taxa are the next most common, with an average frequency of ~ 20% through the sequence, followed by evergreen and montane taxa. Aquatic taxa and pteridophytes (ferns) are present throughout but show an increase in frequency in the upper half of the sequence. Absolute pollen and microcharcoal frequencies are low at the base of the excavation (Unit 2b), gradually increasing throughout Units 3 and 4 and into basal Unit 5, where frequencies again drop to barren levels and then increase to the surface. The changes in pollen and microcharcoal frequencies between samples indicate that bioturbation was limited to localized activity and did not homogenize the entire profile.

Lithic Analysis

Assemblage Composition

A total of 1341 lithic artifacts were recovered at CHA-I. The majority of these artifacts lie within either the "Upper Artifact Concentration" (n = 893) from the basal ~ 5 cm of Unit 4 or immediately below in the "Lower Artifact Concentration" (n = 323) at the top of Unit 3. Approximately 45% of the artifacts from these two concentrations are in fresh condition, and another 45% show only slight signs of mechanical or chemical weathering. Diffuse scatters of variably weathered artifacts were recovered in Units both above and below the two artifact concentrations (Table 2), though the very base of the excavation trench (Unit 1, in the square A10 sondage) was archaeologically sterile. We focus analysis of the lithic assemblages at CHA-I on the Upper and Lower Artifact Concentrations.

Like other Karonga MSA assemblages, the CHA-I assemblage is produced primarily on fine-grained quartzite and coarse-grained quartz; both materials derive from locally abundant river cobbles. Quartzite artifacts are more common in both the Upper and Lower Artifact Concentrations, at 62% and 78%, respectively. Artifacts made on chert and other fine-grained siliceous materials are present but rare in Units 4 and 3 (n = 6 and 1, respectively). Primary sources have not been identified in the Karonga region nor are these clasts common within sampled cobble beds.

A layer of small cobbles was excavated below the artifact concentrations (in unit 2b). Based on observations around CHA-I and other sites in Karonga, it is likely that cobble beds would have been exposed nearby, though it is not currently possible to determine an exact distance to such beds. The small cobbles from CHA-I were not collected at the time of excavation.

Upper Artifact Concentration

The majority of flaking at CHA-I was conducted via free-hand, hard hammer percussion, though occasional examples of bipolar reduction are present. The assemblages from both artifact concentrations show similar approaches to toolstone reduction; Figs. 7 and 8 show a selection of artifacts recovered from these Units, and the full core dataset is reported in SOM Table S3. In the Upper Artifact Concentration, which dates maximally to ~ 43.4–40.6 ka, no single reduction strategy dominates, though radial and Levallois methods are the most common (Table 3), at 34.3% and 25.7% of cores, respectively. They are typically made on rounder (rather than oblong) cobbles.

At least three of the Levallois cores in the Upper Artifact Concentration were made on sizable primary flakes, which provided the natural convexity to the hemispheres variably exploited

in Levallois reduction and minimized the degree of preparation on both surfaces for platform shaping or preferential removals. Radial and Levallois cores do not show significant differences in reduction intensity, as seen in the average number of flakes scars per core (~ 12) or the amount of cortex remaining (~ 0% and ~ 50–60% on opposed surfaces). However, radial cores are on average larger than Levallois cores (avg. L. 56.66 mm vs. 46.34 mm, respectively), suggesting that radial cores are slightly less reduced than Levallois cores relative to their size. The next most common core type is the "casual" or "minimally reduced" core, defined as a core with five or fewer flake scars. Because this definition is based on reduction intensity and not typology or technological organization, casual cores exhibit a range of reduction styles, and the difference between casual and other core types is often a matter of degree rather than kind. The casual cores in the Upper Artifact Concentration have an average length of 56.94 mm and most are reduced unifacially along a single platform edge (Fig. 7b), leaving a bulk of the cobble unmodified. Single platform core reduction is also typically focused on the smaller faces of more rectangular clasts while leaving the bulk of the cobble unmodified; the average single platform core has only six flake scars, retains ~ 67% cortex coverage, and is 56.5 mm in length. Multi-platform cores are more reduced than single platform cores, with an average of ten preserved flake scars and 30% remaining cortex coverage.

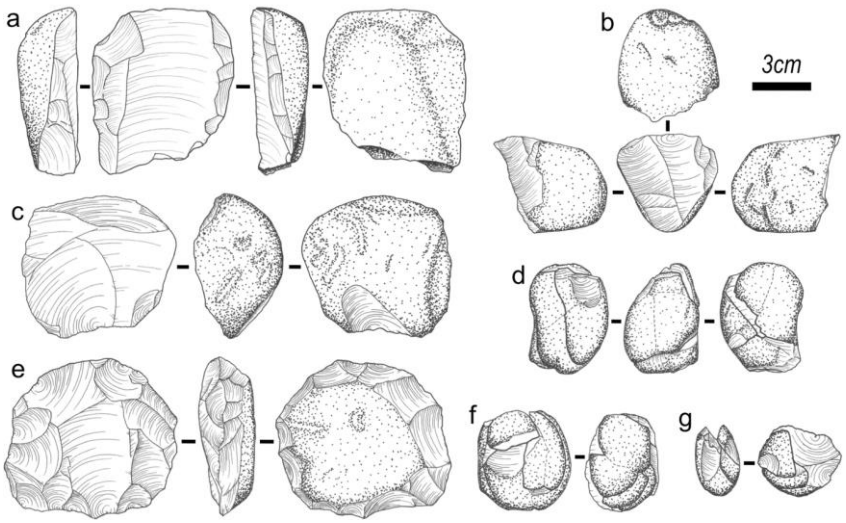

Fig. 7 Selected artifacts from CHA-I. **a, c** Minimally reduced cores-on-flakes. **b** Casual single platform core. **e** Radially flaked core. **d, f** Flaked quartz crystal nodules with refitting flakes (refit groups 012 and 011, respectively). **g** Quartzite casual core with refitting flakes (refit group 005)

Fig. 8 Selected artifacts from CHA-I. **a** Retouched Levallois quartzite flake. **b** Radial quartzite core. **c** Casual quartzite core. **d** Levallois quartz core with refitting flake. **e, i** Flaked quartz crystal nodules with refitting flakes (refit groups 011 and 012, respectively). **f** Levallois quartzite core. **g** Four refitting quartzite flakes (refit group 03). **h** Levallois quartz core-on-flake. **j** Quartzite casual core with refitting flakes (refit group 05)

Complete flakes comprise only a small fraction of the Upper Artifact Concentration (n = 48, 46 of which are non-diagnostic). As with the cores from CHA-I, flakes show a variability of reduction styles and platform preparations, and the combination of these characteristics does not cluster in significant patterns; full data for complete flakes, including metric measurements, cortex coverage, and dorsal flake scar patterns and counts, are in SOM Table S4. In total, 22 of the 48 complete flakes (46%) retain cortex on the dorsal surface, with an average of 66.4% cortex coverage between them. Cortical platforms are the most common (29.2%), and five of the flakes are from primary core reduction. Plain and dihedral platforms (27.1% and 25%) are also common. Centripetal flake scars are the most common pattern (33.3%), followed by unidirectional flake scars (25%). Centripetal flakes preserve the greatest average number of dorsal scars (4.2) and the least amount of cortex (mean = 6.6% coverage), while unidirectional flakes have fewer dorsal scars (2.6) and greater cortex coverage (mean = 35%). This corresponds well to the core assemblage,

where radially flaked cores are the most reduced and platform cores with parallel flake removals are among the least reduced. Only two flakes (one complete and one fragmentary) from the Upper Artifact Concentration bear the hallmarks of preferential Levallois flake reduction. This number likely underrepresents the true number of Levallois products, however, due to the equifinality of form between radial and Levallois core removals.

Other "specialized" forms, such as points or blades, are similarly rare within the Upper Artifact Concentration. Only two point-shaped flakes were recovered in the Upper 4, both of which were produced through unidirectional flaking. Given the paucity of this particular flake shape and the non-specific reduction method, we consider these "points" to be coincidental forms and not indicative of intentional point-production efforts. There is also no evidence for blade production at the site. The average length:width ratio for complete flakes in Unit 5 is 1.05 (σ = 0.28, CV= 27.0%), indicating that flakes are primarily short and broad and do not show great variance around this trend. Indeed, not a single flake from either Unit has a length:width ratio of 2:1, a discriminating characteristic of blades or "elongated" flakes. The most elongated flakes in the assemblage are those produced through platform reduction, featuring plain platforms and unidirectional flake scars (avg. L. 52.86 mm, avg. W. 37.76 mm, avg. L:W ratio 1.31). Modification of flake blanks into formalized tool types is also absent. Only three fragmentary retouched flakes were recovered, accounting for 0.4% of all artifacts Upper Artifact Concentration. The location and minimal intensity of retouch on these pieces does not appear to have been aimed at a specific, formalized tool type. No evidence of hafting residue or impact damage was noted in the assemblage. The Upper Artifact Concentration displays a high degree of fragmentation. Of the flake fraction, fragmentary flakes are nearly eight times more common than complete flakes, and angular shatter comprises ~ 47% of the total assemblage.

Lower Artifact Concentration

The Lower Artifact Concentration, although more diffuse than the assemblage above, has similar overall characteristics to the Upper Artifact Concentration. Cores are slightly less common (1.5% of total Lower assemblage, compared to 3.9% in the Upper assemblage) and slightly larger, though the length of each of the complete cores remains within one standard deviation of the mean length in the Upper concentration. Complete and fragmentary flakes are represented at similar proportions compared to the Upper Concentration. However, cortical platforms are much less common in the Lower concentration (only one of the 19 complete flakes [5%], versus 14 of 48 [29.2%] in the Upper assemblage); plain platforms account for 47% of the complete flakes, and the unidirectional flaking more common in the Upper concentration is only found on one of the

19 (5%) complete flakes. Cortex on flakes is also less common in the Lower Artifact Concentration: only four of the 19 complete flakes (21%) have cortex on the dorsal surface, with an average of 37.5% coverage between them.

As with the Upper concentration, the assemblage from the Lower Artifact Concentration lacks specialized or diagnostic tool forms: neither points, blades, nor retouched pieces were recovered, and only two fragmentary Levallois flakes were identified.

	Upper Artifact Concentration Unit 4		Lower Artifact Concentration Unit 3	
	n	%	*n*	%
Cores[1]				
Radial	12	34.3	2	40.0
Levallois	9	25.7	1	20.0
Single platform	3	8.6	–	–
Multi-platform	3	8.6	–	–
Casual	8	22.8	1	20.0
Indet.	–	–	1	20.0
Subtotal (of assemblage)	35	100	5	100
	35	3.9	5	1.5
Flakes				
Complete (non-diagnostic)	46	5.2	18	5.6
Fragmentary (non-diagnostic)	384	43.0	135	41.8
Levallois flakes[2]	2[3]	0.2	1	0.3
Points	2	0.2	–	–
Blades	–	–	–	–
Retouched	2	0.2	–	–
Angular shatter	422	47.3	164	50.7
Total	893	100	323	100

Table 3 Lithic artifact assemblages composition, from the Upper Artifact Concentration (Unit 4) and Lower Artifact Concentration (Unit 3) at CHA-I

[1] Counts include complete and broken cores

[2] Counts of Levallois flakes, points, blades, and retouched flakes include complete and fragmentary flakes

[3] One Levallois flake is also retouched, not included in the count of retouched flakes

Refitting and Conjoining Artifacts

The refitting program initiated on the CHA-I artifacts produced a total of 24 sets of refitting or conjoining pieces (SOM Table S5); the location of these refit and conjoin sets are shown in Fig. 9. Sixteen sets were identified in Unit 4 (seven conjoining, seven refitting, and two that included both conjoins and refits) and eight in Unit 3 (five conjoining and three refitting). Conjoining fragments in both layers show ancient breaks of flakes, cores, and indeterminate debitage. Refitting sets are generally comprised of only two or three pieces, and full sequences of flaking cannot be analyzed. Nevertheless, the refitting of flakes, and in particular of flakes onto cores, shows that cores are only minimally reduced, and that "exhausted" cores are not common at CHA-I. For example, refit

group 005 (Fig. 7g) includes a small (40.22 mm) radially flaked quartzite core and three proximal flake fragments; two of the flake fragments preserve cortical platforms and cortex on their dorsal surfaces, while the third flake fragment has a plain platform. The preservation of cortex on the flake fragments indicates early stage reduction of the core, but these flakes are also among the last to have been removed, demonstrating that knapping was not focused on exploiting the full volume of the core before finalizing the sequence.

Two of the refitting groups are particularly worthy of note: refit groups 011 and 012 (Fig. 8) are both small quartz crystal cobbles (< 50 mm) that were likely flaked through initial hammer and anvil bipolar reduction, but suffered fracturing failures and ultimately shattered after two or three strikes each (Fig. 7d, f). These refit groups highlight several considerations that likely affected the reduction of various raw materials in this area: (1) while flaking quartz crystal can produce very sharp, durable cutting edges, flaking failure is fairly common, and may end in the complete obliteration of the toolstone clast and (2) the size and relative frequency of quartz crystal cobbles in the Chitimwe cobble beds (e.g., small and rare) results in minimal use of this particular material.

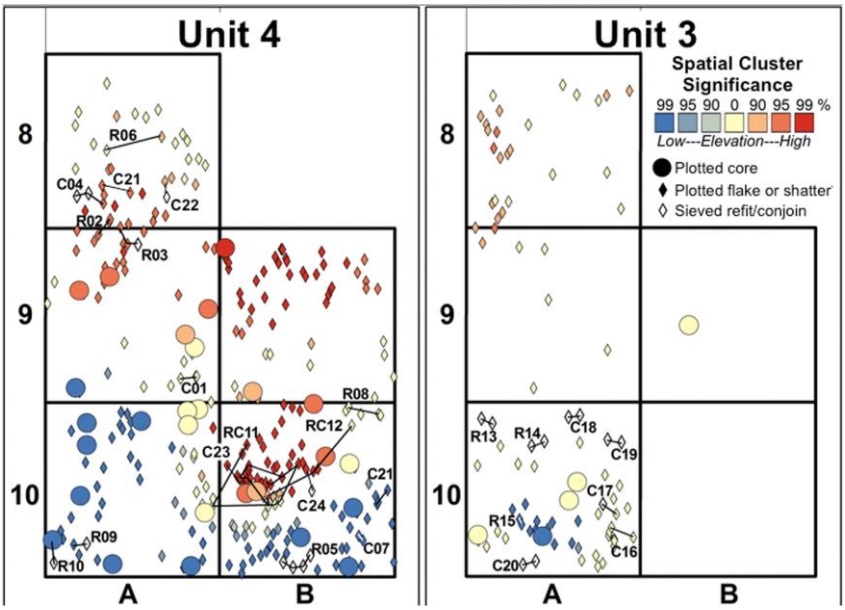

Fig. 9 Optimized Hot Spot Analysis (OHSA) and refitting and conjoining artifacts from the main artifact concentrations at CHA-I. R refit, C conjoin, RC refits and conjoins. Spatial clusters are identified at 90%, 95%, and 99% statistical significance for both high and low elevations

Spatial Analysis

Artifact attributes such as raw material or reduction strategy did not map in spatially significant patterns. Quartz and quartzite artifacts are evenly distributed across excavation squares, and

neither core nor flake characteristics appear in meaningful clusters. When mapped into the GIS, refit and conjoin groups cluster spatially and do not transgress across depositional layers. Several artifacts that comprise the refit and conjoin sets were recovered from the sieved artifact fraction and could only be mapped to the resolution of the excavation square. Nevertheless, most refitting and conjoining artifacts tend to occur within ~ 10–20 cm of each other.

Optimized Hot Spot Analysis (OHSA) was run on plotted artifacts from the two main artifact concentrations. Figure 9 shows the results of the OHSA for the Lower and Upper Artifact Concentrations, with clustering of artifacts around *x*-, *y*-, and *z*-axes for both low (blue) and high (red) elevations at three levels of statistical significance. The Lower Artifact Concentration (Unit 3) shows significant clustering at 90% and 95% confidence intervals in the northern area of the main excavation. A group of artifacts cluster at a 99% confidence interval in the southern extent of the excavation, where the largest number of refitting and conjoining artifacts in the Unit was also found. In the Upper Artifact Concentration (Unit 4), at least four areas of significant spatial clustering can be identified. In the southern excavation squares, artifacts cluster at both high and low relative elevations at 99% confidence, and refit groups often lie within these clusters.

When refit and conjoin data are mapped on to the OHSA results, refit groups occur most commonly in significantly associated artifact clusters. That sets of refitting and conjoining artifacts sit within non-random clusters of artifacts suggests that despite some post-depositional reworking and landform subsidence, discrete flaking and depositional events are preserved within the CHA-I assemblage.

DISCUSSION

The open-air setting and complex sedimentation and post-depositional history of CHA-I present challenges to interpreting how the site formed. Our reconstruction of the environmental setting and site formation processes combined field documentation with micromorphology, phytolith and palynology analysis, OSL dating, and the spatial analysis of recovered artifacts.

Site Formation

In the first depositional stage, the lowest Units of the site (Unit 1–3) document repeated stream alluvial deposition, particularly in Unit 2b (chronologically constrained between 40.6 ± 3.7 ka and 43.4 ± 4.1 ka). A lens of well-rounded pebbles caps Unit 2b, marking its boundary with Unit 3 (Fig. 5e). This pebble lens may represent the winnowed lag of a migrating channel, indicating the

preservation of an exposed land surface at this position in the sequence. However, cut-and-fill processes or changes in depositional regimes could also explain the presence of these pebbles (Blair and McPherson 2009). Unit 2b is characterized by low porosity sediments with distinct redox masses and thick laminated (compound) clay coatings, reflecting partially saturated soil conditions alternating with drier periods during which clay illuviation could occur (Fig. 5e, f, h).

Unit 3 caps the first stage of deposition at CHA-I. The subrounded Fe-Mn nodules of Unit 3 (Figs. 5e, g) likely derive from surfaces eroded elsewhere and were subsequently redeposited together with the other very fine gravels of the Unit. As a result of their redeposition, the nodules are somewhat horizontally aligned Figs. 5e, g). The occurrence of reworked Fe-Mn nodules among the reworked gravels of Unit 3 reflects a change in sediment source as compared to the underlying Units. Distinct redox masses reach their maximum height in Unit 3, indicating that these lower strata have been impacted by fluctuating groundwater levels (sensu Vepraskas 1994) and are interpreted to have resulted in sediment compaction, landform subsidence, and a slight downward movement of sediment and associated artifacts. As redox features extend down the profile, there are no indications of persistent dry conditions in the lowermost three Units (Units 1–3) of the CHA-I sequence. Micromorphological observations indicate that both unit 2b and Unit 3 were still subject to seasonal fluctuations of the current water table. Woody dicot phytoliths and pollen from forest and woodland taxa are most common in the lower (older) depositional Units, and cobble beds present within and near the excavation area point to a wooded, riparian environment in which humans were making and discarding stone tools (Lower Artifact Concentration). Unit 3 ended with a break in sedimentation, after which a gravel surface was exposed for a length of time.

Although sparse artifact scatters exist throughout the lower portion of the sequence (Units 1-2b), and these show greater evidence of post-depositional weathering (and thus may be part of channel clast material), it is at the end of this depositional episode (in Unit 3) that substantial numbers of artifacts were deposited. A large component of the artifact assemblage is therefore likely in situ. After deposition of Unit 3 ceased, the Upper Artifact Concentration represents a scatter of lithic artifacts that likely accumulated on an exposed surface of gravels through manufacture and discard. This is indicated by the change in sedimentation between Units 3 and 4 from stream channel deposits to alluvial fan aggradation and the position of the artifacts at the base of Unit 4. Buried by accreting alluvial fan sediments prior to 20.7 ± 1.5 ka, these artifacts thus sit within Unit 4 but largely date to a preceding depositional hiatus between Units 3 and 4.

The existence of a former stable land surface somewhere above Unit 3 is evidenced by laminated (compound) clay coatings in both Units 2b and 3, as multiple phases of clay illuviation

point to soil formation taking place over a prolonged period of time. The well-rounded, concentric Fe-Mn nodules found at the base of Unit 4 are endogenous pedogenic features (Fig. 5b, d), forming within the Unit 4 alluvium rather than being redeposited from elsewhere as were the Fe-Mn nodules in the Unit 3. Most likely, they started forming higher in the Unit. Angular sand inclusions of changing grain sizes in the concentric bands of the nodules point to a long history of formation during which the nodules moved downward and became concentrated at the base of the Unit. Factors contributing to their downward movement include shrink-and-swell processes, bioturbation, and the weight of the metallic Fe-Mn nodules.

It is difficult to infer the way phytoliths and pollen may have moved in the soil from the observation of large objects such as rounded Fe-Mn nodules, but it is possible that some of the lithic artifact assemblage in basal Unit 4 originally derived from somewhat higher in the Unit. This would date them to after the initiation of alluvial fan formation ca. 20.7 ka. However, the presence of refitting artifact groups in close spatial association, both vertical and horizontal, suggests that any movement of the artifact assemblage after initial deposition was minimal and that the majority of artifacts were recovered from a near-original depositional context, being buried by the sediment of Unit 4. The downward movement of coarse components of the sediment in Unit 4 may have also affected the pollen and phytolith records, though absolute counts in the samples from the Unit show that both pollen and phytoliths were recovered in greater numbers in the upper portion of the Unit. The pollen sample from the base of Unit 4 (sample no. 713) produced so few pollen grains that it was considered a barren sample. Had the downward movement of sediment in the Unit significantly repositioned pollen or phytoliths, they would likely also be concentrated at the base of the Unit, and exotic pollen (*Eucalyptus*) should not be restricted to only the top of the sequence.

Unit 4 has an increasingly open, better-aerated and mixed (bioturbated) microstructure, indicating that the vadose zone was reached (Fig. 5b–d). The sediments quickly fine upward from very coarse sand/very fine gravel with a large coarse fraction to a loamier coarse sand and fine gravel texture (Fig. 5b). At least part of the fining-up of the sediment is attributable to termite bioturbation, which is more pronounced in Unit 4 than in underlying sediments, and would have preferentially moved finer grained particles upward and coarse, heavy fragments downward (Crossley 1986).

Woody phytoliths remained dominant throughout the deposition of Unit 4, suggesting a relatively consistent tree cover in the area despite the possibility of taphonomic preservation bias (Albert et al. 2006; Garnier et al. 2012; Tsartsidou et al. 2007). We note variance between the

phytolith and pollen records in regard to woody dicot vs. monocot grass cover at CHA-I and interpret this as reflecting different scales of influence, from site to catchment levels. The phytolith record is likely more relevant to the immediate area of the site while the pollen record samples the more regional environment. We also acknowledge the possibility of a taphonomic bias in terms of an underrepresentation of monocot grass phytoliths (Mercader et al. 2018). The combination of phytolith and pollen analyses highlights the vegetation mosaic typical of a miombo setting, with a strong signal of riparian and woody plants in the broader grassland environment. Nevertheless, the high frequency of herbs and woodland taxa pollen throughout the CHA-I sequence indicates primarily savanna-woodland conditions around the site as a result of either landscape clearance practices (e.g., burning, coppicing) or climate-induced vegetation change. Evergreen and montane forests are indicated in the pollen record at the sub-regional and regional scales, respectively. Higher rates of aquatic taxa and pteridophytes (ferns) toward the top of the sequence point to increasingly wetter conditions through the Holocene. Alluvial deposition at the site continued until ~ 5.5 ka, after which laterite soil formation intensified, and a reduction of tree cover is associated with the expansion of grass in the latest part of the sequence, mirroring modern conditions.

Stone Tool Systems

The lithic artifact assemblage from CHA-I reflects a flexible and generalized approach to stone tool production. Regional survey has demonstrated the abundance of toolstone throughout the Karonga region, and these locally available toolstone resources were targeted for stone tool making; to date, no artifacts have been recovered from MSA contexts around Karonga that have a clear exotic origin. The degree of cobble cortex and preserved flake scars on discarded cores shows that reduction efforts were not focused on extracting the maximum amount of flakes per unit of toolstone. In situ knapping events are documented at localities like CHA-I through refitting sets of artifacts, showing that MSA people were not visiting riparian areas solely to acquire cobbles for toolmaking. They spent time in active riparian systems, as shown by the arboreal phytolith signature in what catchment-scale data show was a mosaic and largely open environment with abundant grass (Ivory et al. 2018). The relatively high incidence of fragmentation found in the lithic artifact assemblage at CHA-I may further indicate that MSA foragers engaged in prolonged episodes of activity in these riparian zones, as trampling knapped stone has the documented effect of inducing significant breakage beyond that typical of knapping events (Driscoll et al. 2015; McBrearty et al. 1998).

Observations from other excavations and survey around Karonga show that raw material choice in the area is largely driven by availability and clast size and perhaps also clast shape

(Thompson et al. 2014). Cobbles found during excavations at the Airport Site (APS; ~ 600 m away) (Thompson et al. 2012) and Bruce (BRU; ~ 2000 m away) were collected to assess the frequency of the various raw materials in the local cobble beds. At both sites, cobbles ≥ 20 mm were measured and classed to raw material (Table 4). Quartzite is the most common material in both samples, at 54% from APS and 70% at BRU. These frequencies broadly track with the relative representation of quartzite within the CHA-I artifact assemblage: 62.2% in the Upper Artifact Concentration and 78.0% in the Lower Artifact Concentration. Quartzite artifacts are, on average, larger than quartz artifacts in each Unit, though cores on each material vary considerably in their dimensions (SOM Table S3). The mean maximum dimension of cores of all types found at CHA-I is 63.02 mm (σ = 21.58), and the smallest cores are among the more extensively worked, with maximum dimensions falling just below ~ 40 mm. We can thus set 40 mm as a threshold for the minimum cobble length selected for most knapping endeavors, allowing for considerations of which toolstones may have been targeted by MSA tool makers. In the BRU sample, for instance, only ~ 30% of cobbles are ≥ 40 mm in maximum dimension. Of these, 70% are quartzite, 29% are quartz (including quartz crystal), and 1.2% are other stone types.

		Quartzite	Quartz	Other[1]
CHA-I				
Upper (Unit 4)	*n* · %	555 62.2%	332 37.2%	6 0.6%
Lower (Unit 3)	*n* · %	252 78.0%	70 21.7%	1 0.3%
APS				
≥ 20 mm cobbles	*n* · %	267 54%	206 41%	23 5%
Mean max. dimension		51.6 mm	45.7 mm	
BRU				
≥ 20 mm cobbles	*n* · %	2610 70%	1088 29%	42 1%
≥ 40 mm cobbles	*n* · %	675 71%	267 28%	11 1%
Mean max. dimension		37.5 mm	36.7 mm	

Table 4 Raw material frequencies of CHA-I Upper Artifact Concentration (Unit 4) and Lower Artifact Concentration (Unit 3), and sampled cobbles from nearby sites APS and BRU

[1] Includes chert, ferricrete, and unidentified fine-grained siliceous rocks

	Dorsal flake scar pattern						
		Cortical	Unidirectional	Bidirectional	Centripetal	Indeterminate	Total
	Upper Artifact Concentration (Unit 4)						
Platform type	Cortical	5	5	1	2	1	14
	Plain	1	5		4	3	13
	Dihedral	2	2	2	5	1	12
	Polyhedral	–	–	1	1*	1	3
	Faceted	–	–	–	1	–	1
	Punctiform	–	–	–	–	–	–
	Indeterminate	–	–	2	3	–	5
	Total	8	12	6	16	6	48
	Lower Artifact Concentration (Unit 3)						
	Cortical	–	–	–	1	–	1
	Plain	–	1	2	1	5	9
	Dihedral	–	–	3	1	1	5
	Polyhedral	–	–	–	–	–	–
	Faceted	–	–	–	1*	–	1
	Punctiform	–	–	1	–	–	1
	Indeterminate	–	–	–	2	–	2
	Total	0	1	6	6	6	19

Table 5 Platform and dorsal scar pattern attributes for complete flakes from the Upper and Lower Artifact Concentrations

*Levallois flakes

When taken with the greater frequency of quartzite artifacts in both Upper and Lower Artifact Concentrations at CHA-I, the implication is that cobble size is a first-stage determinant of raw material choice; there are fewer appropriately sized quartz cobbles from which to select, and therefore, quartzite becomes the material most likely to be used (Table 4). This finding further suggests that other aspects related to raw material choice (i.e., quality of material, predictability of fracture surfaces or edges, matrix homogeneity) may have had less demonstrable utility to the Karonga knappers, insofar as clasts appear to have been selected from cobble beds in relative proportion to their abundance above a minimum size. Quartz crystal cobbles sampled at BRU typically fall below 40 mm in maximum dimension. Thus, despite the advantages of quartz crystal in maintaining sharp cutting edges, it likely represented a relatively inefficient expenditure of time and energy when larger, more common, and more reliable toolstone clasts were available for the reduction strategies of the time. In spite of this, occasional attempts were made to exploit it even when there was apparently an abundance of other toolstone options in the immediate area. Upper size limits likely also influence raw material choice, because though very large (avg. 145 mm) quartzite cobbles exist in abundance across northern Malawi (Thompson et al. 2014), the majority of cores from CHA-I are less than half that size in maximum dimension, and retain sufficient cortex coverage to show that they had not been heavily reduced from a significantly greater size.

The high incidence of cortex coverage on discarded cores (most cores retain at least 50% cobble cortex) and the relatively low number of preserved flake scars (avg. 8.5 scars per core) also indicates that stone reduction efforts at CHA-I were not focused on efforts to produce the most useable flake blanks per Unit of toolstone. This is mirrored in a core to flake ratio of 1:14, a lower degree of exploitation than documented in published data from MSA sites such as Porc Epic (~ 1:20; Pleurdeau 2006), Pinnacle Point (~ 1:29; Thompson et al. 2010), or Klipdrift (~ 1:30; Henshilwood et al. 2014). Rather, flaking strategies are loosely linked to stone clast size as well as shape. Rounded clasts are more commonly reduced through radial or Levallois methods, whereas rectangular clasts typically feature platform reduction. Although the majority of clasts sampled in the Karonga region are rounded or sub-rounded, rectangular clasts are more commonly quartzite, which is reflected in their more common use as platform cores. Thus, the core assemblage at CHA-I shows that reduction strategies are at least in part influenced by clast shape. An alternative explanation could be that clasts of particular sizes or shapes were selected according to the toolmaker's intended final result. However, the short, broad flakes typical of the CHA-I debitage occur across reduction methods. That is, particular styles of core reduction are not linked to distinct flake morphologies, with the single exception of some platform core flakes that are slightly elongated (avg. L:W ratio 1.27) relative to the whole flake sample (avg. L:W ratio 1.06). Table 5 shows the relationship of flake platforms and dorsal scar types in both artifact concentrations, illustrating that flake characteristics do not cluster around certain trends as might be expected if flake morphology were a primary factor in reduction efforts.

That platform cores are among the least reduced (avg. six scars) of the cores undercuts the idea that slightly elongated flakes were a targeted goal for most reduction efforts. Similarly, there is no obvious intentionality behind producing the squat flake blanks seen in the CHA-I assemblages. The flakes lack evidence for retouch needed to produce formalized "tool" types or for resharpening of cutting edges. Therefore, technological strategies at CHA-I are neither focused on maximization of toolstone clasts nor are they reflections of strict techno-cultural rules for the production of particularly shaped or sized flake blanks. A similar pattern was found during extensive surface survey (Thompson et al. 2014) and at nearby CHA-II (Wright et al. 2017). Apart from the factors of size and shape of raw material packages that may have influenced the use of certain raw materials or reduction methods over others, specific flaking methods do not appear linked to differential raw material use.

The most notable characteristic of the CHA-I stone tools is the rarity of formal or standardized flake production. Flakes in the CHA-I assemblage were not modified to facilitate

hafting into compound or composite tools, though this does not preclude the hafting of unmodified flakes. The lack of specialized forms such as blades and points— the latter considered in most MSA contexts to have required hafting for intended and effective use (McBrearty and Brooks 2000)—may further suggest that multicomponent technology was limited in the Karonga region. Retouched pieces are extremely rare, and specialized forms (such as points or blades) are non-existent at CHA-I. The absence of these tool forms from a late MSA context requires explanation.

One scenario might be that CHA-I samples a specific activity area that is not indicative of the whole suite of forager technologies in the Karonga area. Refitting artifacts in both the Upper and Lower Artifact Concentrations document discrete on-site knapping events, perhaps indicative of a workshop area situated to make best use of riparian resources. The relatively high incidence of Levallois cores to Levallois debitage may indicate on-site reduction and subsequent transport of flakes for use elsewhere; further supporting this idea is the fact that Levallois cores are more common at CHA-I (~ 25% of all cores) than at other Chaminade area sites (~ 5%) or sites further south (~ 6% in Sadala South study area; 0% in Ngara study area; Thompson et al. 2018). Alternatively, the apparent low frequency of Levallois flakes in the CHA-I assemblage may be a consequence of the minimal degree of preparation given to Levallois cores, as seen in the core sample recovered from CHA-I.

The lack of retouched or formalized tool types at CHA-I may alternatively reflect off-site modification of flake blanks. If this were the case, we would expect other sites in the area to produce typologically or technologically distinct lithic assemblages, and yet, the results of the lithic analysis at CHA-I are consistent with those from the Airport Site (Thompson et al. 2012), CHA-II (Wright et al. 2017), Mwanganda's Village (Wright et al. 2014), and other sites in Karonga (Thompson et al. 2018). Throughout the Karonga region, formalized tool types, blades, and pointed forms are rare (Thompson et al. 2014, 2018), indicating that while the riparian resources at CHA-I likely provided an opportune locale for stone acquisition and reduction, the characteristics of the lithic assemblage reflect region-wide approaches to tool production and use. A broader survey of raw material use and core exploitation in the Karonga region holds to the trends witnessed at CHA-I, in particular the non-exhaustive use of locally available toolstone and technological flexibility in reduction strategies (Thompson et al. 2014). Taken together, these data show that stone tool manufacture at and around CHAI in the later MSA of Malawi is not oriented toward strict technological end-goals. Rather, it seems the functional needs of late MSA foragers at Karonga were satisfied without complex or elaborated tool systems.

CHA-I in Larger Context

MSA foragers met their technological needs through varied means, in response to environmental and social conditions (Tryon and Faith 2016). Among these conditions are questions of hominin cognitive ability, population size and interaction, and subsistence risk. Thompson et al. (2018) reviewed these factors as they are predicted to affect forager technologies across the African MSA and found relative subsistence risk to offer the most compelling explanation for broader patterns observable across the continent. In this model, patchy or inconsistent resources are likely to result in a higher investment in technological systems, whereas predictable and abundant resources relax the need to develop complex technologies. The lithic artifact assemblages from CHA-I show little significant investment in complex technological design that is commonly found in other areas of Africa. In northeastern Africa, for example, points were predominantly produced through Nubian Levallois reduction methods, in which the shapes of flakes are predetermined through preparatory flaking of cores (Van Peer 1998). In northwestern Africa, the Aterian tradition documents the modification of flake blanks into tanged pieces, presumably to be inset in composite tools (Scerri 2013). The regular use of these strategies implies a link between specialized tool forms and specific activities—such as intercept hunting—within these forager populations. East African lithic assemblages often feature long-distance procurement of raw materials, blade production, bifacially retouched points, and early instances of microlithic implements (Ambrose 1998; Gliganic et al. 2012; Pleurdeau 2006; Tryon et al. 2012). The southern African record has produced a robust dataset of precocious time-constrained industries in which flake or blade blanks were retouched to create near-microlithic tool insets, again linked to specific environmental and demographic pressures (Brown et al. 2012; McCall 2007). In these examples, time and energy investments in stone tool technologies were oriented toward specific goals.

In the more immediate region of East-Central Africa, at the Songwe River Valley (Tanzania) (Willoughby 2001; Willoughby and Sipe 2002), and across Lake Malawi at the Mozambican sites of Ngalue Rockshelter, Mvumu, and other open-air localities in the Niassa Region (Bicho et al. 2016; Mercader et al. 2009, 2012), MSA assemblages are reported showing radial approaches to toolstone reduction, similar in style, frequency, and degree of exploitation to those seen at CHA-I. Notably, however, sites in both southern Tanzania and Mozambique also produced formalized, retouched tools such as scrapers, points, bifaces, and awls, in greater numbers than seen in any Karonga assemblages, as well as "heavy duty" tools such as choppers and core-axes, and grinding stones, all of which have been identified as expected components in the generalized MSA forager's toolkit (Tryon and Faith 2013). All of these are absent from the

CHA-I assemblage, and extensive survey and test-pitting have only identified them sporadically across the Karonga landscape (Thompson et al. 2018). From the perspective of the highly or even overdesigned toolkits in the northern and southern extremes of the continent, the lithic assemblages of Mozambique and southern Tanzania appear much more oriented toward a flexible foraging strategy, and the CHA-I assemblage extends this trend of diminishing technological investment.

CONCLUSIONS

The late persistence and expedient, unelaborated nature of the lithic technology at CHA-I is ostensibly at odds with a view of the MSA as a techno-chronological Unit that shows increasing behavioral and cognitive complexity following the emergence of *Homo sapiens*. Instead, it fits with an emerging disciplinary understanding of the many factors that influenced diversity in MSA forager behavior and technological choices. Compared to other regions across Africa from MIS4 to MIS2, northern Malawi enjoyed relatively stable and pluvial aggregate environmental conditions throughout its inhabitation by late MSA populations (Scholz et al. 2011). The datasets produced by excavation at CHA-I and nearby CHA-II (Wright et al. 2017) indicate the preservation of woody phytolith taxa during the LGM, suggesting perpetuation of a relatively moist climatic regime even as the northern portions of the continent faced severe aridification (Blome et al. 2012). Successive cycles of wetting and drying of the landscape, as documented through micromorphological analysis, further support this interpretation. The CHA-I excavation documents a riparian environment, where toolstone and food resources would have been regularly accessible; lithic raw materials were likely selected from the immediate environment, reduced and discarded on-site. In the context of broader patterns in the MSA, the late age of CHA-I shows that by ~ 40 ka, not all African populations were making substantial changes to their technological or behavioral patterns that archaeologists identify with the start of the LSA. Instead, in the relatively stable environments of the Lake Malawi basin, flexibility and expediency in lithic technology continued to provide the necessary means to meet daily foraging requirements.

Acknowledgments

We thank our collaborators at the Malawi Ministry of Civic Education, Culture, and Community Development for their assistance and permission in facilitating this research. The CHA-I field season was executed in 2011, and special thanks are given to Potiphar Kaliba (Deputy Director of Culture at the time), Oris Malijani (Senior Antiquities Officer), and an outstanding team of local

crew—many of whom continue to work with us today. These include Moses Nyondo, Kondwani Mwafulirwa, Henry Kalinga, and Daudi Mwangomba. Flora Schilt thanks Prof. Dr. Christopher Miller and Dr. Susan Mentzer for their supervision, as well as Panagiotis Kritikakis for preparation of the thin sections for micromorphological analysis. We also thank the editors and six anonymous reviewers, whose thoughtful comments contributed substantially to the improvement of this manuscript.

Funding Information Fieldwork and analysis were funded by National Geographic-Waitt Foundation grant W115-10 and the Australian Research Council Discovery Project DP110101305. Funding for the micromorphological analysis was provided by the Deutsche Forschungsgemeinschaft (MI 1748/3-1, MI 1748/1-1, and ME 4406/1-1).

Compliance with Ethical Standards: Conflict of Interest The authors declare that there is no conflict of interest.

REFERENCES

Albert, R. M., Bamford, M. K., & Cabanes, D. (2006). Taphonomy of phytoliths and macroplants in different soils from Olduvai Gorge (Tanzania) and the application to Plio-Pleistocene palaeoanthropological samples. Quaternary International, 148, 78–94. https://doi.org/10.1016/j.quaint.2005.11.026.

Ambrose, S. (1998). Chronology of the Later Stone Age and food production in East Africa. Journal of Archaeological Science, 25, 377–392.

Basell, L. S. (2008). Middle Stone Age (MSA) site distributions in eastern Africa and their relationship to Quaternary environmental change, refugia and the evolution of *Homo sapiens*. Quaternary Science Reviews, 27, 2484–2498. https://doi.org/10.1016/j.quascirev.2008.09.010.

Bicho, N., Haws, J., Raja, M., Madime, O., Gonçalves, C., Cascalheira, J., Benedetti, M., Pereira, T., & Aldeias, V. (2016). Middle and Late Stone Age of the Niassa region, northern Mozambique. Preliminary results. Quaternary International, 404, 87–99. https://doi.org/10.1016/j.quaint.2015.09.059.

Blair, T. C., & McPherson, J. G. (2009). Processes and forms of alluvial fans. In A. J. Parson & A. D. Abrahams (Eds.), Geomorphology of desert environments (2nd ed., pp. 413–467). New York: Springer.

Blome, M.W., Cohen, A. S., Tryon, C. A., Brooks, A. S., & Russell, J. (2012). The environmental context for the origins of modern human diversity: a synthesis of regional variability in African climate 150,000-30,000 years ago. Journal of Human Evolution, 62(5), 563–592. https://doi.org/10.1016/j.jhevol.2012.01.011.

Boëda, E. (1995). Levallois: a volumetric construction, methods, a technique. In The definition and interpretation of Levallois technology. (Vol. 23, pp. 41-65): Prehistory Press Madison.

Bonnefille, R.,&Chalié, F. (2000). Pollen-inferred precipitation time-series from equatorial mountains, Africa, the last 40 kyr BP. Global and Planetary Change, 26(1), 25–50. https://doi.org/10.1016/S0921-8181(00)00032-1.

Brooks, A. S., Yellen, J. E., Potts, R., Behrensmeyer, A. K., Deino, A. L., Leslie, D. E., Ambrose, S. H., Ferguson, J. R., d'Errico, F., Zipkin, A. M., Whittaker, S., Post, J., Veatch, E. G., Foecke, K., & Clark, J. B. (2018). Long-distance stone transport and pigment use in the earliest Middle Stone Age. Science, 360(6384), 90–94.

Brown, K. S., Marean, C. W., Jacobs, Z., Schoville, B. J., Oestmo, S., Fisher, E. C., Bernatchez, J., Karkanas, P., & Matthews, T. (2012). An early and enduring advanced technology originating 71,000 years ago in South Africa. Nature, 491(7425), 590–593. https://doi.org/10.1038/nature11660.

Clark, J. D. (1954). Upper Sangoan industries from northern Nyasaland and the Luangwa Valley: a case of environmental differentiation? South African Journal of Science, 50(8), 201–208 http://hdl.handle.net/10520/AJA00382353_2810.

Clark, J. D. (1956). Prehistory in Nyasaland. The Nyasaland Journal, 9(1), 92–119.

Clark, J. D. (1966, The Society of Malawi Journal). Archaeology in Malawi., 19(2), 15–25 www.jstor.org/stable/29778138.

Clark, J. D. (1967). Notes on archaeological work carried out during 1966 in northern Malawi. The Society of Malawi Journal, 20(2), 12–16 www.jstor.org/stable/29778158.

Clark, J. D. (1968). Antiquities programme: Malawi - (mission) 19 July-15 September 1968. UNESCO Document (pp. 73). Paris.

Clark, J. D. (1972). Archaeological mission: Malawi - (mission) July-September 1972. UNESCO Document (pp. 17). Paris.

Clark, J. D. (1982). The cultures of the Middle Palaeolithic/Middle Stone Age. In J. D. Clark (Ed.), The Cambridge history of Africa: from the earliest times to c. 500 BC (pp. 248–341). Cambridge: Cambridge University Press.

Clark, J. D. (1988). The Middle Stone Age of East Africa and the beginnings of regional identity. Journal of World Prehistory, 2(3), 235–305. https://doi.org/10.1007/BF00975618.

Clark, J. D. (1995). Introduction to research on the Chiwondo Beds, northern Malawi. Journal of Human Evolution, 28, 3–5.

Clark, J. D., & Haynes, C. V. (1970). An elephant butchery site at Mwanganda's Village, Karonga, Malawi, and its relevance for Palaeolithic archaeology. World Archaeology, 1(3), 390–411. https://doi.org/10.1080/00438243.1970.9979455.

Clark, J. D., Haynes, C. V., Mawby, J. E., & Gautier, A. (1970). Interim report on palaeoanthropological investigations in the Lake Malawi Rift. Quaternaria, 13, 305–354.

Clark, J. D., Stephens, E. A., & Coryndon, S. C. (1966). Pleistocene fossiliferous lake beds of the Malawi (Nyasa) Rift: a preliminary report. American Anthropologist, 68(2, Part 2: Recent Studies in Paleoanthropology), 46-87, https://doi.org/10.1525/aa.1966.68.2.02a00960.

Clarkson, C. (2002). An index of invasiveness for the measurement of unifacial and bifacial retouch: a theoretical, experimental and archaeological verification. Journal of Archaeological Science, 29(1), 65– 75. https://doi.org/10.1006/jasc.2001.0702.

Cohen, A., Stone, J. R., Beuning, K. R. M., Park, L. E., Rainthal, P. N., Dettman, D., Scholz, C. A., Johnson, T. C., King, J. W., Talbot, M. R., Brown, E. T., & Ivory, S. J. (2007). Ecological consequences of early Late Pleistocene megadroughts in tropical Africa. Proceedings of the National Academy of Science, 104, 16422–16427. https://doi.org/10.1073/pnas.0703873104.

Courty, M. A., Goldberg, P., & Macphail, R. I. (1989). Soils and micromorphology in archaeology. Cambridge: Cambridge University Press.

Crossley, R. (1986). Sedimentation by termites in the Malawi Rift Valley. Geological Society, London, Special Publications, 25(1), 191–199. https://doi.org/10.1144/GSL.SP.1986.025.01.16.

d'Errico, F., Backwell, L. R., & Wadley, L. (2012). Identifying regional variability in Middle Stone Age bone technology: the case of Sibudu Cave. Journal of Archaeological Science, 39(7), 2479–2495. https://doi.org/10.1016/j.jas.2012.01.040.

Delagnes, A., Schmidt, P., Douze, K., Wurz, S., Bellot-Gurlet, L., Conard, N. J., Nickel, K. G., Van Niekerk, K. L., & Henshilwood, C. S. (2016). Early evidence for the extensive heat treatment of Silcrete in the Howiesons Poort at Klipdrift Shelter (layer PBD, 65 ka), South Africa. PLoS One, 11(10), e0163874. https://doi.org/10.1371/journal.pone.0163874.

Douze, K., & Delagnes, A. (2016). The pattern of emergence of a Middle Stone Age tradition at Gademotta and Kulkuletti (Ethiopia) through convergent tool and point technologies. Journal of Human Evolution, 91, 93–121. https://doi.org/10.1016/j.jhevol.2015.11.006.

Driscoll, K., Alcaina, J., Egüez, N.,Mangado, X., Fullola, J.-M., & Tejero, J.-M. (2015). Trampled under foot: a quartz and chert human trampling experiment at the Cova del Parco rock shelter, Spain. Quaternary International, 424, 130–142.

Galbraith, R. F., & Roberts, R. G. (2012). Statistical aspects of equivalent does and error calculation and display in OSL dating: an overview and some recommendations. Quaternary Geochronology, 11, 1–27. https://doi.org/10.1016/j.quageo.2012.04.020.

Galbraith, R. F., Roberts, R. G., Laslett, G.M., Yoshida, H., & Olley, J.M. (1999). Optical dating of single and multiple grains of quartz from Jinmium rock shelter, northern Australia, part 1, experimental design and statistical models. Archaeometry, 41, 339–364. https://doi.org/10.1111/j.1475-4754.1999.tb00987.x.

Garcin, Y., Williamson, D., Taieb, M., Vincens, A., Mathé, P. E., & Majule, A. (2006). Centennial to millennial changes in maar-lake deposition during the last 45,000 years in tropical Southern Africa (Lake Masoko, Tanzania). Palaeogeography, Palaeoclimatology, Palaeoecology, 239(3), 334–354. https://doi.org/10.1016/j.palaeo.2006.02.002.

Garnier, A., Neumann, K., Eichhorn, B., & Lespez, L. (2012). Phytolith taphonomy in the middle- to late-Holocene fluvial sediments of Ounjougou (Mali, West Africa). The Holocene, 23(3), 416–431.

Gliganic, L. A., Jacobs, Z., Roberts, R. G., Dominguez-Rodrigo, M., & Mabulla, A. Z. (2012). New ages for Middle and Later Stone Age deposits at Mumba rockshelter, Tanzania: optically stimulated luminescence dating of quartz and feldspar grains. Journal of Human Evolution, 62(4), 533–547. https://doi.org/10.1016/j.jhevol.2012.02.004.

Gonçalves, C., Raja, M., Madime, O., Cascalheira, J., Haws, J., Matos, D., & Bicho, N. (2016). Mapping the Stone Age of Mozambique. African Archaeological Review, 33(1), 1–12. https://doi.org/10.1007/s10437-016-9212-4.

Goodwin, A. J. H. (1928). An introduction to the Middle Stone Age in South Africa. South African Journal of Science, 25, 410–418.

Growcutt, H. S., & Blinkhorn, J. (2013). The Middle Palaeolithic in the desert and its implications for understanding hominin adaptation and dispersal. Quaternary International, 300, 1–12.

Henn, B. M., Bustamante, C. D., Mountain, J. L., & Feldman, M. W. (2011). Reply to Hublin and Klein: locating a geographic point of dispersion in Africa for contemporary humans. Proceedings of the National Academy of Sciences, 108(28), E278–E278. https://doi.org/10.1073/pnas.1107300108.

Henshilwood, C. S., & Dubreuil, B. (2011). The Still Bay and Howiesons Poor, 77-59ka: symbolic material culture and the evolution of the mind during the AfricanMiddle Stone Age. Current Anthropology, 52(3), 361–400.

Henshilwood, C. S., van Niekerk, K. L., Wurz, S., Delagnes, A., Armitage, S. J., Rifkin, R. F., Douze, K., Keene, P., Haaland,M.M., Reynard, J., Discamps, E., & Mienies, S. S. (2014). Klipdrift Shelter, southern Cape, South Africa: preliminary report on the Howiesons Poort layers. Journal of Archaeological Science, 45, 284–303. https://doi.org/10.1016/j.jas.2014.01.033.

Hublin, J.-J., & Klein, R. G. (2011). Northern Africa could also have housed the source population for living humans. Proceedings of the National Academy of Sciences, 108(28), E277–E277. https://doi.org/10.1073 /pnas.1105710108.

Ivory, S. J., Lézine, A.-M., Vincens, A., & Cohen, A. S. (2012). Effect of aridity and rainfall seasonality on vegetation in the southern tropics of East Africa during the Pleistocene/Holocene transition. Quaternary Research, 77(1), 77–86. https://doi.org/10.1016/j.yqres.2011.11.005.

Ivory, S. J., Lézine, A.-M., Vincens, A., & Cohen, A. S. (2018). Waxing and waning of forests: Late Quaternary biogeography of southeast Africa. Global Change Biology, 24(7), 2939–2951.

Johnson, C. R., & McBrearty, S. (2010). 500,000 year old blades from the Kapthurin Formation, Kenya. Journal of Human Evolution, 58, 193–200. https://doi.org/10.1016/j.jhevol.20.

Johnson, T. C., Werne, J. P., Brown, E. T., Abbott, A., Berke, M., Steinman, B. A., Halbur, J., Contreras, S., Grosshuesch, S., Deino, A., & Scholz, C. A. (2016). A progressively wetter climate in southern East Africa over the past 1.3 million years. Nature, 537(7619), 220–224. https://doi.org/10.1038/nature19065.

Jury, M. R., & Gwazantini, M. E. (2002). Climate variability in Malawi, part 2: sensitivity and prediction of lake levels. International Journal of Climatology, 22(11), 1303–1312. https://doi.org/10.1002/joc.772.

Juwayeyi, Y. M., & Betzler, C. (1995). Archaeology of the Malawi Rift: the search continues for Early Stone Age occurrences in the Chiwondo Beds, northern Malawi. Journal of Human Evolution, 28, 115–116.

Kaufulu, Z. M. (1983). The geological context of some early archaeological sites in Kenya, Malawi, and Tanzania: microstratigraphy, site formation and interpretation. Berkeley: University of California.

Kaufulu, Z. M. (1990). Sedimentary environments at the Mwanganda Site, Malawi. Geoarchaeology, 8(1), 15–27. https://doi.org/10.1002/gea.3340050103.

Kottek, M., Grieser, J., Beck, C., Rudolf, B., & Rubel, F. (2006). World map of the Köppen-Geiger climate classification updated. Meteorologische Zeitschrift, 15, 259–263.

Kumboyo, C. P., Yasuda, H., Kitamura, Y., & Shimizu, K. (2014). Fluctuation of rainfall time series in Malawi: an analysis of selected areas. Geofizika, 31(1), 13–28. https://doi.org/10.15233/gfz.2014.31.1.

Lyons, R. P., Scholz, C. A., Cohen, A. S., King, J.W., Brown, E. T., Ivory, S. J., Johnson, T. C., Deino, A. L., Reinthal, P. N., & McGlue, M. M. (2015). Continuous 1.3-million-year record of East African hydroclimate, and implications for patterns of evolution and biodiversity. Proceedings of the National Academy of Sciences, 201512864, https://doi.org/10.1073/pnas.1512864112.

Mackay, A., Stewart, B. A., & Chase, B. M. (2014). Coalescence and fragmentation in the late Pleistocene archaeology of southernmost Africa. Journal of Human Evolution, 72, 26–51. https://doi.org/10.1016/j. jhevol.2014.03.003.

McBrearty, S., Bishop, L. C., Plummer, T., Dewar, R., & Conard, N. (1998). Tools underfoot: human trampling as an agent of lithic artifact edge modification. American Antiquity, 63(1), 108–129.

McBrearty, S., & Brooks, A. S. (2000). The revolution that wasn't: a new interpretation of the origin of modern human behavior. Journal of Human Evolution, 39(5), 453–563. https://doi.org/10.1006 /jhev.2000.0435.

McCall, G. S. (2006). Multivariate perspectives on change and continuity in the Middle Stone Age lithics from Klasies River Mouth, South Africa. Journal of Human Evolution, 51(4), 429–439. https://doi.org/10.1016 /j.jhevol.2006.06.003.

McCall, G. S. (2007). Behavioral ecological models of lithic technological change during the later Middle Stone Age of South Africa. Journal of Archaeological Science, 34(10), 1738–1751. https://doi. org/10.1016/j.jas.2006.12.015.

McCall, G. S., & Thomas, J. T. (2012). Still Bay and Howiesons Poort foraging strategies: recent research and models of culture change. African Archaeological Review, 29(1), 7–50. https://doi.org/10.1007/s10437- 012-9107-y.

Meier, H. A., Nordt, L. C., Forman, S. L., & Dreise, S. G. (2013). Late Quaternary alluvial history of the middle Owl Creek drainage basin in central Texas: a record of geomorphic response to environmental change. Quaternary International, 306, 24–41. https://doi.org/10.1016/j.quaint.2013.07.010.

Mercader, J., Akeju, T., Brown, M., Bundala, M., Collins, M. J., Copeland, L., Crowther, A., Dunfield, P., Henry, A., Inwood, J., Itambu, M., Kim, J.-J., Larter, S., Longo, L., Oldenburg, T., Patalano, R., Sammynaiken, R., Soto, M., Tyler, R., & Xhauflair, H. (2018). Exaggerated expectations in ancient starch research and the need for new taphonomic and authenticity criteria. Facets, 3, 777–798. https://doi. org/10.1139/facets-2017-0126.

Mercader, J., Asmerom, Y., Bennett, T., Raja, M., & Skinner, A. (2009). Initial excavation and dating of Ngalue Cave: a Middle Stone Age site along the Niassa Rift, Mozambique. Journal of Human Evolution, 57(1), 63–74. https://doi.org/10.1016/j.jhevol.2009.03.005.

Mercader, J., Astudillo, F., Barkworth, M., Bennet, T., Esselmont, C., Kinyanjui, R., Grossman, D. L., Simpson, S., & Walde, D. (2010). Poaceae phytoliths from the Niassa Rift, Mozambique. Journal of Archaeological Science, 37(8), 1953–1967.

Mercader, J., Bennet, T., Esselmont, C., Simpson, S., & Walde, D. (2011). Soil phytoliths from miombo woodlands in Mozambique. Quaternary Research, 75(1), 138–150.

Mercader, J., Gosse, J. C., Bennett, T., Hidy, A. J., & Rood, D. H. (2012). Cosmogenic nuclide age constraints on Middle Stone Age lithics from Niassa, Mozambique. Quaternary Science Reviews, 47, 116–130. https://doi.org/10.1016/j.quascirev.2012.05.018.

Moss, P. T. (2013). Palynology and its applications to geomorphology. In J. F. Schroder (Ed.), Treatise in geomorphology (pp. 315–325). San Diego: Academic Press.

Murray, A. S., & Wintle, A. G. (2003). The single aliquot regenerative dose protocol: potential for improvements in reliability. Radiation Measurements, 37, 377–381. https://doi.org/10.1016/S1350-4487(03)00053-2.

Neumann, K., Fahmy, A., Lespez, L., Ballouche, A., & Huysecom, É. (2009). The Early Holocene palaeoenvironment of Ounjougou (Mali): phytoliths in a multiproxy context. Palaeogeography, Palaeoclimatology, Palaeoecology, 276(1–4), 87–106.

Ngongondo, C., Xu, C. Y., Gottschalk, L., & Alemaw, B. (2001). Evaluation of spatial and temporal characteristics of rainfall in Malawi: a case of data scarce region. Theoretical and Applied Climatology, 106(1–2), 79–93. https://doi.org/10.1007/s00704-011-0413-0.

O'Driscoll, C., & Thompson, J. C. (2018). The origins and early elaboration of projectile technology. Evolutionary Anthropology, 27(1), 30–45.

Olley, J. M., Pietsch, T., & Roberts, R. G. (2004). Optical dating of Holocene sediments from a variety of geomorphic settings using single grains of quartz. Geomorphology, 60(3), 337–358. https://doi. org/10.1016/j.geomorph.2003.09.020.

Pagani, L., Lawson, D. J., Jagoda, E., Mörseburg, A., Eriksson, A., Mitt, M., Clemente, F., Hudjashov, G., DeGiorgio, M., Saag, L., Wall, J. D., Cardona, A., Mägi, R., Sayres, M. A. W., Kaewert, S., Inchley, C., Scheib, C. L., Järve, M., Karmin,M., Jacobs, G. S., Antao, T., Iliescu, F. M., Kushniarevich, A., Ayub, Q., Tyler-Smith, C., Xue, Y., Yunusbayev, B., Tambets, K., Mallick, C. B., Saag, L., Pocheshkhova, E., Andriadze, G., Muller, C., Westaway, M. C., Lambert, D. M., Zoraqi, G., Turdikulova, S., Dalimova, D., Sabitov, Z., Sultana, G. N. N., Lachance, J., Tishkoff, S., Momynaliev, K., Isakova, J., Damba, L. D., Gubina, M., Nymadawa, P., Evseeva, I., Atramentova, L., Utevska, O., Ricaut, F.-X., Brucato, N., Sudoyo, H., Letellier, T., Cox, M. P., Barashkov, N. A., Skaro, V., Mulahasanovic, L., Primorac, D., Sahakyan, H., Mormina, M., Eichstaedt, C. A., Lichman, D. V., Abdullah, S., Chaubey, G.,Wee, J. T. S., Mihailov, E., Karunas, A., Litvinov, S., Khusainova, R., Ekomasova, N., Akhmetova, V., Khidiyatova, I., Marjanović, D., Yepiskoposyan, L., Behar, D. M., Balanovska, E., Metspalu, A., Derenko, M., Malyarchuk, B., Voevoda, M., Fedorova, S. A., Osipova, L. P., Lahr, M. M., Gerbault, P., Leavesley, M., Migliano, A. B., Petraglia, M., Balanovsky, O., Khusnutdinova, E. K., Metspalu, E., Thomas, M. G., Manica, A., Nielsen, R., Villems, R., Willerslev, E., Kivisild, T., & Metspalu, M. (2016). Genomic analyses inform on migration events during the peopling of Eurasia. [Letter]. Nature, 538(7624), 238. https://doi.org/10.1038/nature19792.

Pleurdeau, D. (2006). Human technical behavior in the African Middle Stone Age: the lithic assemblage of Porc-Epic Cave (Dire Dawa, Ethiopia). African Archaeological Review, 22(4), 177–197. https://doi. org/10.1007/s10437-006-9000-7.

Prescott, J. R., & Hutton, J. T. (1994). Cosmic ray contributions to dose rates for luminescence and ESR dating: large depths and long-term time variations. Radiation Measurements, 23, 497–500. https://doi.org/10.1016/1350-4487(94)90086-8.

Richter, D., Grün, R., Joannes-Boyau, R., Steele, T. E., Amani, F., Rué, M., Fernandes, P., Raynal, J.-P., Geraads, D., Ben-Ncer, A., Hublin, J.-J., & McPherron, S. P. (2017). The age of the hominin fossils from Jebel Irhoud, Morocco, and the origins of the Middle Stone Age. Nature, 546, 293–296. https://doi.org/10.1038/nature22335.

Runge, F. (1999). The opal phytolith inventory of soils in central Africa—quantities, shapes, classification, and spectra. Review of Palaeobotony and Palynology, 107(1–2), 23–53.

Sahle, Y., Hutchings, W. K., Braun, D. R., Sealy, J. C., Morgan, L. E., Negash, A., & Atnafu, B. (2013). Earliest stone-tipped projectiles from the Ethiopian Rift date to >279,000 years ago. PLoS One, 8(11), e78092. https://doi.org/10.1371/journal.pone.0078092.

Sahle, Y., Morgan, L. E., Braun, D. R., Atnafu, B., & Hutchings, W. K. (2014). Chronological and behavioral contexts of the earliest Middle Stone Age in the Gademotta Formation, Main Ethiopian Rift. Quaternary International, 331, 6–19. https://doi.org/10.1016/j.quaint.2013.03.010.

Scerri, E. M., Blinkhorn, J., Niang, K., Bateman, M. D., & Groucutt, H. S. (2017). Persistence of Middle Stone Age technology to the Pleistocene/Holocene transition supports a complex hominin evolutionary scenario inWest Africa. Journal of Archaeological Science: Reports, 11, 639–646. https://doi.org/10.1016/j.jasrep.2017.01.003.

Scerri, E. M. L. (2013). The Aterian and its place in the North African Middle Stone Age. Quaternary International, 300, 111–130. https://doi.org/10.1016/j.quaint.2012.09.008.

Schick, K. D. (1987). Experimentally-derived criteria for assessing hydrologic disturbance of archaeological sites. Natural formation processes and the archaeological record, 352, 86–107.

Scholz, C. A., Cohen, A. S., Johnson, T. C., King, J., Talbot, M. R., & Brown, E. T. (2011). Scientific drilling in the Great Rift Valley: the 2005 Lake Malawi Scientific Drilling Project—an overview of the past 145, 000 years of climate variability in Southern Hemisphere East Africa. Palaeogeography, Palaeoclimatology, Palaeoecology, 303, 3–19. https://doi.org/10.1016/j.palaeo.2010.10.030.

Sene, K., Piper, B., Wykeham, D., McSweeney, R. T., Tyce,W., & Beven, K. (2016). Long-term variations in the net inflow record for Lake Malawi. Hydrology Research, 48(3), 851–866. https://doi.org/10.2166/nh.2016.143.

Sisk, M. L., & Shea, J. J. (2009). Experimental use and quantitative performance analysis of triangular flakes (Levallois points) used as arrowheads. Journal of Archaeological Science, 36(9), 2039–2047. https://doi.org/10.1016/j.jas.2009.05.023.

Stockmarr, J. (1971). Tablets with spores used in absolute pollen analysis. Pollen et Spores, 13, 615–621.
Stoops, G. (2003). Guidelines for analysis and description of soil and regolith thin sections. Madison, Wisconsin: Soil Science Society of America, Inc..

Thompson, E.,Williams, H. M., & Minichillo, T. (2010). Middle and late Pleistocene Middle Stone Age lithic technology from Pinnacle Point 13B (Mossel Bay, Western Cape Province, South Africa). Journal of Human Evolution, 59(3–4), 358–377. https://doi.org/10.1016/j.jhevol.2010.07.009.

Thompson, J. C., Mackay, A., de Moor, V., & Gomani Chindebvu, E. (2014). Catchment survey in the Karonga District: a landscape-scale analysis of provision and core reduction strategies during the Middle Stone Age of northern Malawi. African Archaeological Review, 31, 447–478. https://doi.org/10.1007 /s10437-014-9167-2.

Thompson, J. C., Mackay, A., Nightingale, S., Wright, D. K., Choi, J.-H., Blackmore, H., Welling, M., & Gomani Chindebvu, E. (2018). Ecological risk, demography, and geographic patterning of technological complexity in the Late Pleistocene of Africa. Journal of Quaternary Science, 33(3), 261–284. https://doi. org/10.1002/jqs.3002.

Thompson, J. C., Mackay, A.,Wright, D. K.,Welling, M., Greaves, A., Gomani Chindebvu, E., & Simengwa, D. (2012). Renewed investigations into the Middle Stone Age of northern Malawi. Quaternary International, 270, 129–139. https://doi.org/10.1016/j.quaint.2011.12.014.

Thompson, J. C., Welling, M., & Gomani Chindebvu, E. (2013). Using GIS to integrate old and new archaeological data from Stone Age deposits in Karonga, Malawi. International Journal of Heritage in the Digital Era, 2(4), 611–630. https://doi.org/10.1260/2047-4970.2.4.611.

Tierney, J. E., Russell, J. M., Huang, Y., Damsté, J. S. S., Hopmans, E. C., & Cohen, A. S. (2008). Northern hemisphere controls on the tropic southeast African climate during the past 60,000 years. Science, 322(5899), 252–255. https://doi.org/10.1126/science.1160485.

Tribolo, C., Asrat, A., Bahain, J.-J., Chapon, C., Douville, E., Fragnol, C., Hernandez, M., Hovers, E., Leplongeon, A., & Martin, L. (2017). Across the gap: geochronological and sedimentological analyses from the Late Pleistocene-Holocene sequence of Goda Buticha, Southeastern Ethiopia. PLoS One, 12(1), e0169418. https://doi.org/10.1371/journal.pone.0169418.

Tribolo, C., Rasse, M., Soriano, S., & Huysecom, E. (2015). Defining a chronological framework for the Middle Stone Age in West Africa: comparison of methods and models for OSL ages at Ounjougou (Mali). Quaternary Geochronology, 29, 80–96. https://doi.org/10.1016/j.quageo.2015.05.013.

Tryon, C. A., & Faith, J. T. (2013). Variability in the Middle Stone Age of Eastern Africa. Current Anthropology, 54(S8), S234–S254. https://doi.org/10.1086/673752.

Tryon C. A., & Faith J. T. (2016) A demographic perspective on theMiddle to Later Stone Age transition from Nasera rockshelter, Tanzania. Phil. Trans. R. Soc. B 371:20150238.

Tryon, C., McBrearty, S., & Texier, P.-J. (2005). Levallois lithic technology from the Kapthurin formation, Kenya: Acheulian origin and Middle Stone Age diversity. African Archaeological Review, 22(4), 199– 229. https://doi.org/10.1007/s10437-006-9002-5.

Tryon, C. A., Peppe, D. J., Tyler Faith, J., Van Plantinga, A., Nightingale, S., Ogondo, J., & Fox, D. L. (2012). Late Pleistocene artefacts and fauna from Rusinga and Mfangano islands, Lake Victoria, Kenya. Azania: Archaeological Research in Africa, 47(1), 14–38. https://doi.org/10.1080/0067270x.2011.647946.

Tsartsidou, G., Lev-Yadun, S., Albert, R. M., Miller-Rosen, A., Efstratiou, N., & Weiner, S. (2007). The phytolith archaeological record: strengths and weaknesses evaluated based on a quantitative modern reference collection from Greece. Journal of Archaeological Science, 34(8), 1262–1275.

van der Kaars, W. A. (1991). Palynology of eastern Indonesian marine piston cores: a Late Quaternary vegetational and climatic record from Australia. Palaeogeography, Palaeoclimatology, Palaeoecology, 85, 239–302. https://doi.org/10.1016/0031-0182(91)90163-L.

Van Peer, P. (1998). The Nile Corridor and the Out-of-Africa model: an examination of the archaeological record. Current Anthropology, 39(S1, Special Issue: The Neanderthal Problem and the Evolution of Human Behavior.), S115-S140, doi: https://doi.org/10.1086/204692.

Van Peer, P., Fullagar, R., Stokes, S., Bailey, R. M., Moeyersons, J., Steenhoudt, F., Geerts, A., Vanderbeken, T., De Dapper, M., & Geus, F. (2003). The Early to Middle Stone Age transition and the emergence of modern human behaviour at site 8-B-11, Sai Island, Sudan. Journal of Human Evolution, 45(2), 187–193. https://doi.org/10.1016/s0047-2484(03)00103-9.

Vepraskas, M. J. (1994). Redoximorphic features for identifying aquic conditions. North Carolina Agricultural Research Service, Raleight, North Carolina., Technical Bulletin, 301, 33.

Vepraskas, M. J., Wilding, L. P., & Drees, L. R. (1993). Aquic conditions for soil taxonomy: concepts, soil morphology and micromorphology. In A. J. Ringrose-Voase & G. S. Humphreys (Eds.), Developments in soil science (Vol. 22, pp. 117–131). Amsterdam: Elsevier.

Villa, P., Delagnes, A., & Wadley, L. (2005). A late Middle Stone Age artifact assemblage from Sibudu (KwaZulu-Natal): comparisons with the EuropeanMiddle Paleolithic. Journal of Archaeological Science, 32(3), 399–422. https://doi.org/10.1016/j.jas.2004.11.007.

Villa, P., Soriano, S., Tsanova, T., Degano, I., Higham, T. F. G., d'Errico, F., Backwell, L., Lucejko, J. J., Colombini, M. P., & Beaumont, P. B. (2012). Border Cave the the beginning of the Later Stone Age in South Africa. Proceedings of the National Academy of Science, 109(33), 13208–13213.

Vincens, A., Garcin, Y., & Buchet, G. (2007). Influence of rainfall seasonality on African lowland vegetation during the Late Quaternary: pollen evidence from Lake Masoko, Tanzania. Journal of Biogeography, 34, 1274–1288. https://doi.org/10.1111/j.1365-2699.2007.01698.x.

Wang, X., van der Kaars, S., Kershaw, P., Bird, M., & Jansen, F. (1999). A record of fire, vegetation and climate through the last three glacial cycles from Lombok Ridge core G6-4, eastern Indian Ocean, Indonesia. Palaeogeography, Palaeoclimatology, Palaeoecology, 147, 241–256. https://doi.org/10.1016/S0031-0182(98)00169-2.

Wentworth, C. K. (1922). A scale of grade and class terms for clastic sediments. The Journal of Geology, 30(5), 377–392.

White, F. (1983). The vegetation of Africa: a descriptive memoir to accompany the UNESCO/AETFAT/UNSO vegetation map of Africa. Natural Resources Research Report XX, UNESCO. Paris.

Wilkins, J., & Chazan, M. (2012). Blade production 500 thousand years ago at Kathu Pan 1, South Africa: support for a multiple origins hypothesis for early Middle Pleistocene blade technologies. Journal of Archaeological Science, 39(6), 1883–1900. https://doi.org/10.1016/j.jas.2012.01.031.

Willoughby, P. R. (2001). Middle and Later Stone Age technology from the Lake Rukwa Rift, Southwestern Tanzania. The South African Archaeological Bulletin, 56(173/174), 34–45 www.jstor.org/stable/3889026.

Willoughby, P. R. (2009). From the Middle to the Later Stone Age in Eastern Africa. In M. Camps & P. Chauhan (Eds.), Sourcebook of Paleolithic transitions: methods, theories, and interpretations (pp. 301–314). New York: Springer.

Willoughby, P. R., & Sipe, C. G. (2002). Stone Age prehistory of the Songwe River Valley, Lake Rukwa Basin, Southwestern Tanzania. The African Archaeological Review, 19(4), 203–221. https://doi.org/10.1023/A:1021211120581.

Wright, D. K., Forman, S. L.,Waters, M. R., & Ravesloot, J. C. (2011). Holocene eolian activation as a proxy for broad-scale landscape change on the Gila River Indian Community, Arizona. Quaternary Research, 76(1), 10–21. https://doi.org/10.1016/j.yqres.2011.04.008.

Wright, D. K., Thompson, J. C., Mackay, A., Welling, M., Forman, S. L., Price, G., Zhao, J.-x., Cohen, A. S., Malijani, O., & Gomani Chindebvu, E. (2014). Renewed geoarchaeological investigations of Mwanganda's Village (Elephant Butchery Site), Karonga, Malawi. Geoarchaeology, 29, 98–120. https://doi.org/10.1002/gea.21469.

Wright, D. K., Thompson, J. C., Schilt, F., Cohen, A. S., Choi, J.-H., Mercader, J., Nightingale, S., Miller, C. E., Mentzer, S. M., Walde, D., Welling, M., & Gomani Chindebvu, E. (2017). Approaches to Middle Stone Age landscape archaeology in tropical Africa. Journal of Archaeological Science, 77, 64–77. https://doi.org/10.1016/j.jas.2016.01.014.

Zipkin, A. M., Hanchar, J. M., Brooks, A. S., Grabowski, M.W., Thompson, J. C., & Gomani Chindebvu, E. (2015). Ochre fingerprints: distinguishing among Malawian mineral pigment sources with Homogenized Ochre Chip LA-ICPMS. Archaeometry, 57(2), 297–317. https://doi.org/10.1111/arcm.12090.

Supplementary Material for paper C: Nightingale et al. 2019

SOM SECTION 1: OPTICALLY STIMULATED LUMINESCENCE (OSL)

Sample preparation

Four OSL samples were taken from the north wall at the southern end of the stepped trench. Samples were prepared according to protocols established in Wright et al. (2014). Material for Dr calculations were extracted from the ends of the sediment tubes adjacent to where the sample was extracted for density separation (and, ultimately, dating). The Dr-calculated material was homogenized using a mortar and pestle prior to sending it to the laboratory for analysis. The Single Aliquot Regeneration (SAR) method (Murray and Wintle 2003) was used to averaged equivalent does values (D_e) for 28 to 34 aliquots of 100-150, 150–250 or 250-355 μm sized quartz grains. A series of experiments was performed to evaluate the effect of preheating at 180, 200, 220, 240 and 260 °C on isolating the most robust time-sensitive emissions and thermal transfer of the regenerative signal prior to the application of SAR dating protocols (see Murray and Wintle 2003). These experiments entailed giving a known dose (25 Gy) and evaluating which preheat resulted in recovery of this dose. There was concordance with the known dose (25 Gy) for preheat temperatures above 200 °C with an initial preheat temperature used of 220 °C for 10 s in the SAR protocols. A "cut heat" at 160 °C for 10 s was applied prior to the measurement of the test dose and a final heating at 260 °C for 40 s was applied to minimize carryover of luminescence to the succession of regenerative doses. A test for dose reproducibility was also performed following procedures of Murray and Wintle (2003) with the initial and final regenerative dose of 6.6 Gy yielding concordant luminescence responses (at one-sigma error) (Fig. 3).

Results

OSL dating was performed using the Single Aliquot Regeneration (SAR) method following protocols developed by Murray and Wintle (2003) (Table S1). Depending on the available sediment grain size, aliquots of 100–150, 150–250 or 250–355 μm diameter were selected using density separation. Experiments were performed to evaluate the effect of preheating at 180, 200, 220, 240 and 260 °C to isolate the most robust time-sensitive emissions and thermal transfer of the regenerative signal prior to the application of SAR dating protocols (Murray and Wintle 2003). These experiments entailed subjecting the sample to a fixed dose of beta-radiation (25 Gy) and evaluating which preheat resulted in the recovery of this dose. There was concordance with the known dose (25 Gy) for preheat temperatures above 200 °C with an initial preheat temperature used of 220 °C for 10 s in the SAR protocols. A "cut heat" at 160 °C for 10 s was applied prior to

the measurement of the test dose and a final heating at 260 °C for 40 s was applied to minimize carryover of luminescence to the succession of regenerative doses. For all samples, between 70 and 100% of the aliquots were used to define the final equivalent dose (D_e) distribution and age determination. Of those aliquots not used in the final calculation, removal was made on the basis that the recycling ratio was not between 0.90 and 1.10, the zero dose was > 5% of the natural emissions, or the error in D_e determination was >10%.

Step	Treatment
1	Natural dose or give beta dose
2	Preheat 220 °C for 10 s
3	Stimulate with blue light (470 nm) for 40 s at 125 °C
4	Give beta test dose (6.6 Gy)
5	Preheat 220 °C for 10 s
6	Stimulate with blue light (470 nm) for 40s at 125 °C
7	Stimulate with blue light for 40 s at 260 °C
8	Return to step 1

Table S1. Single Aliquot Regeneration protocols.

All D_e distributions were lognormal and exhibited a range of overdispersion values from 14 to 24% (Table 1). The overdispersion percentage of a D_e distribution is an estimate of the relative standard deviation from a central D_e value in context of a statistical estimate of errors (Galbraith et al. 1999; Galbraith and Roberts 2012). A zero overdispersion percentage indicates the highest internal consistency in D_e values with 95% of the D_e values within 2-σ errors. Overdispersion values ≤ 25% are routinely assessed for small aliquots of quartz grains that are well solar reset, like eolian sands (Meier et al. 2013; Olley et al. 2004; Wright et al. 2011) and this value is considered a threshold metric for calculation of a D_e value using the central age model (CAM) of Galbraith et al. (1999). In circumstances with symmetrical overdispersion values between 20 and 32% (such as sample S993), CAM is considered a robust statistical model because such variability is often the result of microdosimetry and/or small-scale sedimentary mixing processes (Arnold and Roberts 2009).

The dose rate (D_r) is an estimate of the exposure of quartz grains to ionizing radiation with the decay of the U/Th decay series, ^{40}K, and the contribution of cosmic rays. Concentrations of U, Th, and K were determined by inductively coupled plasma mass spectrometry (ICP-MS) by Activation Laboratory Ltd, Ancaster, Ontario, Canada. The cosmic ray dose was calculated based

upon the sample's location, elevation, and depth below the ground surface (Prescott and Hutton 1994). Additionally, the attenuation of radiation within sedimentary rocks is amplified by its relative water content. Since 2009, numerous tests of water content have been performed on OSL samples from Karonga. These tests involve weighing samples upon arrival in the laboratory, drying the samples in a low-heat oven for several days, then weighing the samples again. In general, water content from samples from alluvial fan contexts in the Karonga region range between 5 and 15% with lower elevation sites having the highest water content due to their proximity to a permanent water body and the water table.

SOM SECTION 2: MICROMORPHOLOGY

Sample preparation

During excavations in 2011, five micromorphological samples were collected at Chaminade Area I, two of which were suitable for analysis and processed and analyzed at the Laboratory of Soil Science and Geoecology at the Institute for Archaeological Sciences in Tübingen, Germany (Fig. S1). The two block samples were collected as a consecutive column within the portion of the sequence where a majority of the artifacts are concentrated and yielded three oversized petrographic thin sections of 60x90 mm and one of 51x76 mm (Figure S1). The block samples were oven dried at 60°C for several days and impregnated with resin under vacuum. The resin was prepared with 7 volume units of unpromoted polyester resin (Viscovoss N 55S), 3 units of styrene (styrene for synthesis) and 5-6ml/l hardener (methylethylketone peroxide, MEKP). After hardening, the blocks were sliced with a machine rock saw into slabs from which thin-sections of 30 μm in thickness were produced. Thin-sections were viewed under a stereoscope (6.5x to 50x) and a petrographic microscope (20x to 500x), using plane polarized light (PPL), crossed polarized light (XPL), and oblique incident light (OIL).

Results

Below are descriptions of the sediment visible in the impregnated blocks and micromorphological thin sections in the order of deposition with terminology following Stoops (2003).

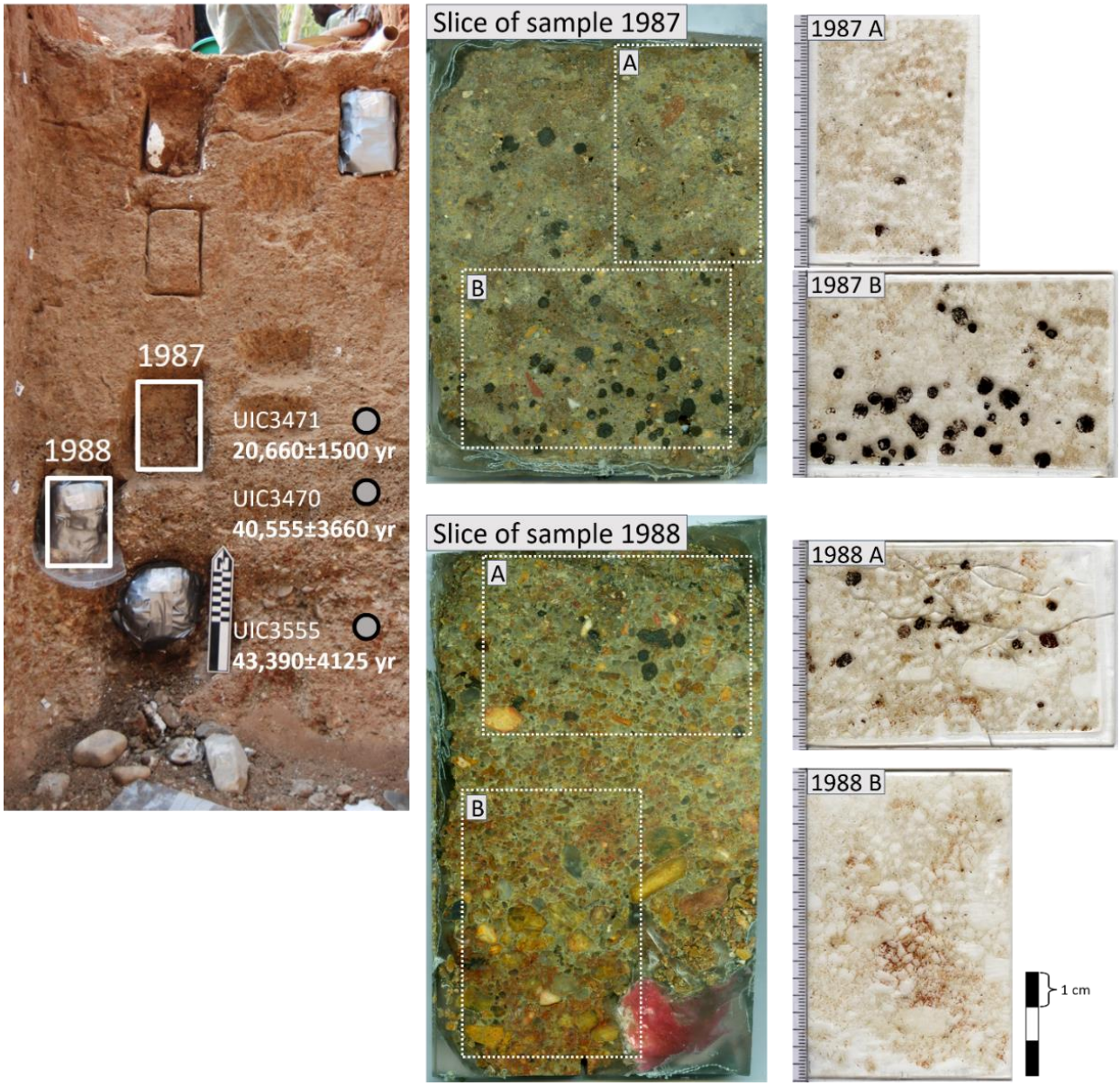

Figure S1: Left: The north profile with sample locations of MEM-1987 and MEM-1988 indicated (white boxes). The three samples visible at the top of the profile and the one underneath were not suitable for analysis. Approximate locations of the OSL samples are indicated as well. Middle: Impregnated slices of sediment that were cut from the corresponding samples 1987 and 1988. Boxes indicate the locations of thin sections. Right: Thin sections MEM-1987 A (51x76 mm), MEM-1987 B, MEM-1988 A and MEM-1988 B (60x90 mm).

Sample MEM-1988 (Units 2b-3)

Sample MEM-1988 contains the transition from Unit 2b to Unit 3. The sliced section of the block sample (Fig. S2) shows a variability in grain sizes within the subunit 2b. The lower part of the sample contains medium to coarse pebbles, followed by a 5-6 cm-thick lens of very coarse sand to fine gravel topped by a discontinuous stringer of pebbles. The upper third of the block sample represents Unit 3, which is the context of the lowermost artifacts (lower artifact concentration)

found in the excavation. In the sample, this unit contains slightly coarser sediment than below, with predominantly fine gravel, including fine gravel-sized black Fe-Mn nodules with sand inclusions.

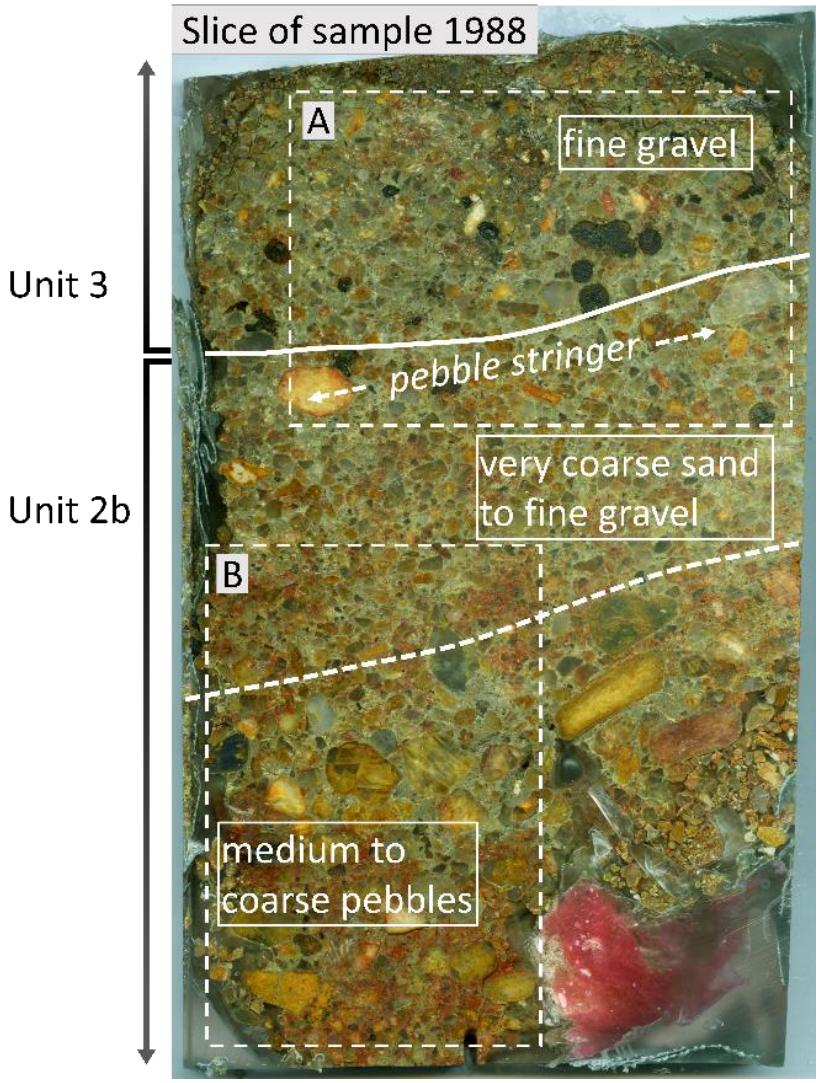

Figure S2: Sliced section from block sample MEM-1988 showing variability in grain sizes within Unit 2b and the relation of the units to sediment captured in the two thin sections MEM-1988 A and B (dashed frames). Thin section MEM-1988 B includes the two subunits of Unit 2b, while MEM-1988 A contains the transition to Unit 3 (S1 and S2).

Thin section MEM-1988 B

Constituents and microstructure: The sediment in this thin section has a coarse fraction of subrounded to well-rounded, very fine to fine gravel of mostly quartz and ca. 5% feldspars (Fig. S5-a, b). Additionally, the lower 2/3rd of the thin section contains ca. 20% medium to coarse rounded to well-rounded pebbles (Figs. S2, S5-c). Many grains show signs of weathering, such as mineral alterations, fracturing, and iron staining inside fractures (Figs. S5-a, b, g). The fine fraction consists

of a pale yellowish black-speckled clay. The clay exhibits a weak grano-striated b-fabric under crossed polarized light (XPL) (Fig. S5-d). Planar voids organize the sediment in a subangular blocky microstructure, with moderately to highly separated peds and strongly developed pedality, defined as follows in Stoops (2003, p. 62): "the soil material is divided into a number of units each of which is entirely surrounded by features pointing to a surface of weakness" (Fig. S5-a, b, c). Most peds consist of a single gravel-sized fragment with clay domains adhering to it, face to face with the clay domains of neighboring peds. The relative abundances of pore space, coarse fraction and fine fraction are estimated as follows:

Pore space: 5 %, Coarse: 80 %, Fine: 15 %

Pedofeatures: Clay coatings of planes are 200-400 µm thick and multi-layered (compound). They are often fragmented, appear lacerated and are slightly displaced (Fig. S5-e, g). Some clay coatings show a kink-band fabric under crossed polarizers (Fig. S5-f, h). Distinct cm-scale red redox masses occur in proportions of ca. 50 % in a reduced (gleyed) greenish-grey matrix (Fig. S5-a, c). Carbonate features are absent except in the upper part of the thin section where equant, sparitic carbonate crystals precipitated inside desiccation planes nearby a fragment of decomposed vegetal material, likely part of a root (Fig. S5-d).

Thin section MEM-1988 A

Constituents and microstructure: The coarse fraction in thin section A consists of randomly oriented, subangular to rounded, very fine to fine gravel-sized fragments of mainly (polycrystalline) quartz and quartzite with very few feldspars, similar to thin section MEM-1988 B (Fig. S6-a, b, c). Rounded, medium to coarse pebbles (ca. 10 %) are horizontally aligned in the lower-middle part of the thin section (Fig. S6-a, b). Many pebbles have iron staining inside fissures, and show mineral weathering. A few pebbles are cracked in situ (Fig. S6-g). Dark red to black, aggregated, subrounded anorthic iron-manganese nodules (3-5 mm) are concentrated above these rounded pebbles (Figure S6-h). The nodules themselves conform in size with the surrounding sediment (very fine to fine gravel) and they contain inclusions of poorly sorted, angular, medium to coarse quartz sand. The fine fraction consists of a pale yellowish, black-speckled, limpid clay. The clay is arranged only locally in a very weak grano-striated b-fabric. The microstructure can be characterized as subangular blocky (Fig. S6-a, b, c), with common disturbances of channels derived from the activities of roots and burrowing soil fauna (Fig. S6-c, e, f).

Porosity: 10 %, Coarse: 70 %, Fine: 20 %

Pedofeatures: Multi-layered (compound) clay coatings of 200-400 μm occur but are frequently deformed and fragmented, sometimes showing a kink-band fabric. Redox masses are more diffuse than below in MEM-1988 B and instead, reddish-brown bioturbation features become more common, especially above the stringer of medium to coarse pebbles. The bioturbation features derive from both roots and soil fauna, and a few channels contain degraded root remains. Micritic secondary carbonate features often occur in association with bioturbation features (Fig. S6-e, f). The occurrence of a very small (0.5 mm), orthic, nucleic iron-manganese nodule in the upper part of the thin section above the pebble stringer indicates that the soil conditions permitted in situ nodule formation (Fig. S6-d).

Sample MEM-1987 (Unit 4)

Sample MEM-1987 was collected from the lowermost part of Unit 4, which formed the context of the upper artifact concentration. Its lower part consists of somewhat coarser sediment than below in the top of Unit 3, and rapidly fines upwards to a coarse sandy clay loam in the upper part of the sample (Figure S3). Among the very coarse sands and fine gravel at the bottom are inclusions of medium gravel and of abundant concentric fine to medium gravel-sized Fe-Mn nodules which are slightly larger than the non-concentric and less rounded nodules in Unit 3. The sediment has been strongly bioturbated. Still, in the block (Figure S3), discrete reddish-brown bioturbation features of several centimeters can be distinguished, indicating that bioturbation did not lead to a complete homogenization of the sediment in this part of Unit 4.

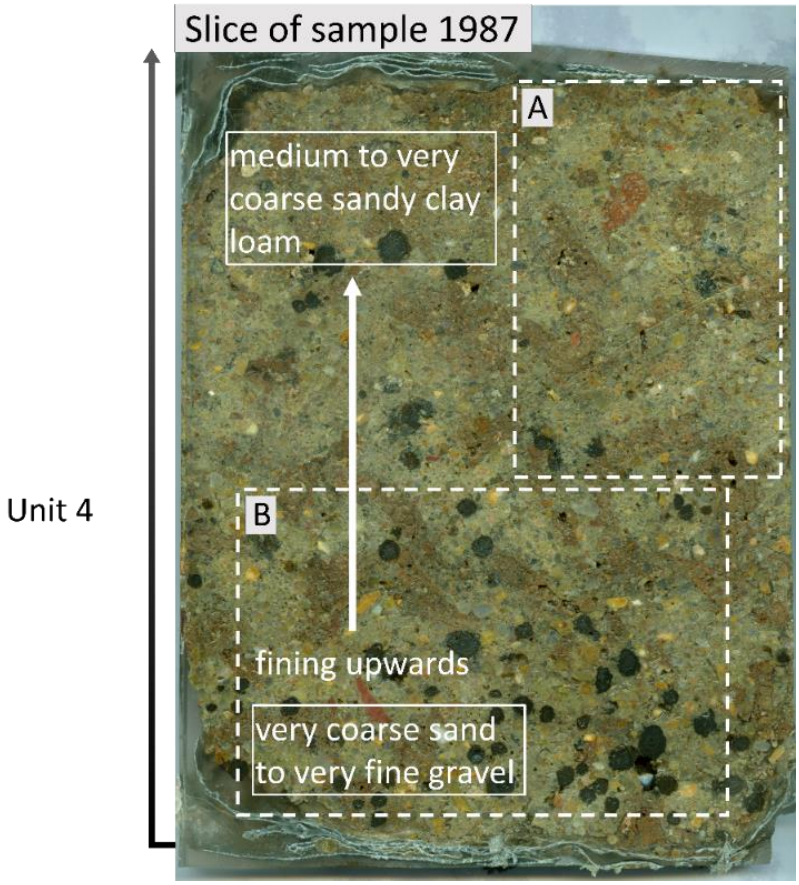

Figure S3: Sliced section from block sample MEM-1987, showing the location of the thin sections MEM-1987 A and B (dashed frames) and general textures contained in the sample. Bioturbation features contrast with the surrounding sediment and can be easily recognized from their reddish-brown color.

Thin section MEM-1987 B (Unit 4)

Constituents and microstructure: The coarse fraction consists of moderately sorted, subangular to rounded, very coarse sand to very fine gravel with few inclusions of medium gravel (Fig. S7-c, d). Many grains show signs of weathering (Fig. S7-i, j). Fragments of quartz and quartzite are present throughout, but feldspars (mostly microcline) as well as few other minerals (olivine) increase in abundance and are common in the upper half of the thin section. Abundant silt-sized opaque grains with a black luster when observed under oblique incident light are likely Mn oxides. The fine fraction is a very pale yellowish, limpid, black-speckled clay (Fig. S7-g, h). In the lower part, the clay is locally organized in a weakly developed grano-striated b-fabric (Fig. S7-h) and in the upper part in a stipple speckled b-fabric. The coarse and fine constituents form a medium separated, granular microstructure (Fig. S7-d), with a very weak subangular ped structure in a few zones within the lowermost part (Fig. S7-a, g, h).

Porosity: 20%, Coarse: 60%, Fine: 30%

Pedofeatures: This sample is strongly bioturbated by soil meso- and macro- faunal activity as well as root action. With the naked eye, irregular bioturbation zones can be recognized by their reddish brown color, which is due to finely comminuted organic material included in them and redox resulting from aeriation and organic material related to burrowing and rooting activity (Figs. S1, S3) (Le Roux and De Preez 2008). Black iron-manganese nodules of 3-7 mm in diameter are concentrated in the lower 2 cm of the thin section and are more sparsely dispersed above (Figs. S1, S7-a, b, c, d, e). The nodules are concentric and consist of a nucleus with at least three and up to eight distinguishable bands. Some concentric bands have no inclusions, and other bands contain sorted inclusions and voids (left by dissolved grains) of size classes ranging from very fine to coarse sand (Fig. S7-a, b, c, d, e). The sand grains are angular almost without exception. Naturally, each nodule shows a different cross section in thin section, according to its position in the sample and the location of the thin section (Stoops 2003). It is nevertheless noted, that in many nodules the outermost band contains coarse sand-sized quartz grains rather than finer grains and voids or no inclusions (Fig. S7-b, c). Many nodules show signs of damage. Fissures opening up the nodules between concentric bands (Fig. S7-b, c, d) and fragments of nodule cortex that have become completely separated from the nodule and assimilated in the matrix are indications of physical destruction and chemical dissolution of iron (Delvigne 1998). Isolated fragments of Fe-Mn nodules are common (Fig. S7-b, c). In some iron-manganese nodules, micritic to microsparitic carbonate has precipitated in fissures between concentric bands that have opened as a result of dissolution and/or damage (Fig. S7-e). Secondary carbonate features also commonly occur as small micritic nodules or infillings and are often associated with bioturbation features (Fig. S7-d, f).

Thin section MEM-1987 A (Unit 4)

Constituents and microstructure: the coarse fraction is slightly finer than in MEM-1987 B and consists of a poorly sorted subangular to subrounded coarse sand to fine gravel. The coarse grains have a diverse mineralogy and are very weathered. Fractures are common, turning originally rounded larger grains into smaller angular fragments. Black fine sand-sized fragments of humified vegetal remains or charcoal are common. The fine fraction takes up a larger portion than below in the same sample and locally includes more finely comminuted vegetal remains besides pale yellowish to light orange, limpid, black-speckled clay. A weak grano-striated b-fabric can locally be recognized in zones with less bioturbation. The coarse and fine constituents form a medium separated, granular microstructure.

Porosity: 20%, Coarse: 50%, Fine: 40%

Pedofeatures: this part of the sample shows increased bioturbation with roots preserved in the upper part of the thin section. Common micritic or radial fibrous carbonate features are found in association with bioturbation features. The thin section contains very few pale yellowish clay coatings and fragments of clay coatings (papules) reworked in the matrix. The few Fe-Mn nodules are smaller than below (2-5 mm). They are damaged and fragmented but show a concentricity similar to the nodules in MEM-1987 B.

Interpretation: the depositional history of CHA-I

In sample MEM-1988, the upper part of Unit 2b is marked by coarse sediment likely representing the end of an episode of higher energy channel deposition. This episode ends with the deposition of finer gravels topped by a discontinuous stringer of horizontally aligned pebbles (Figs. S2 and S4). This pebble stringer demarcates the boundary between Units 2b and 3. It may represent the winnowed lag of a migrating channel, which would imply that an exposed land surface has been preserved at this position in the sequence. However, the observations are limited to a very small area and changes in deposition between the units may also be caused by cut-and-fill processes, possibly related to a change in depositional regime at this location in the alluvial fan (Blair and McPherson 2009).

The subrounded Fe-Mn nodules in Unit 3 likely derive from a soil eroded elsewhere and were redeposited together with the other very fine gravel of Unit 3. They are to some extent horizontally aligned and lack the well-expressed concentric rings exhibited by the nodules in Unit 4. The redeposition of Fe-Mn nodules from a soil with close affinity to Unit 3 may indicate a break in deposition and a change in sediment source between Units 2b and 3.

Unit 4 represents long-term accretion of alluvial fan sediment. While Unit 2 has low porosity, very little bioturbation and signs of prolonged and repeated saturation and Unit 3 has only few bioturbation features disrupting the ped soil structure, Unit 4 has an increasingly open, better-aerated and mixed (bioturbated) microstructure, indicating that the vadose zone has been reached. Unit 4 quickly fines upward from very coarse sand/very fine gravel with a large coarse fraction to a loamier coarse sand and fine gravel texture. As coarse and heavy fragments generally move downwards with bioturbation, at least some of the fining up of the sediment is attributable to bioturbation, especially termite activity.

Post-depositional processes and Fe-Mn nodules

Besides bioturbation, post-depositional processes observed at Chaminade I include clay translocation, vertic activity, redox reactions and Fe-Mn nodule formation, mineral weathering, the concentration of Fe-Mn nodules, and precipitation of secondary carbonates.

Thick clay coatings in MEM-1988 reflect multiple phases of clay illuviation (Fig. S5-e-h). Together with distinct redox masses (Fig. S5-a, c) they form a redoximorphic Bt horizon, also known as a "dynamic B horizon" in Unit 2b, in which intense clay illuviation, requiring periodically well-drained conditions, was alternated with hydromorphic processes (Kühn et al. 2010; Mücher and Coventry 1994). Shrink-swell activity (argilloturbation) has led to the formation of a subangular blocky microstructure as well as some fragmentation and deformation of clay coatings (Fig. S5-a, b, e-h). Based on field observations, redox features extend down the profile until the bottom of the excavated sequence. No indications for persistent dry conditions, such as secondary carbonate features or roots, are found in Unit 2b, suggesting that the observed redox concentrations and depletions (mottles) are not relict but still reflect the zone in which the modern groundwater causes near-saturation for extended periods of time. The sudden increase in bioturbation features in Unit 3 and Unit 4 indicates that the upper limit of the modern groundwater table generally reaches until Unit 3, taking into account considerable fluctuations between the dry and the wet season (Dangerfield et al. 1998; Mujinya et al. 2011).

Slight differences are observed between the mineralogy and roundness of grains in Unit 2b and the units above. While the coarse fraction in Unit 2b is mostly subrounded to well-rounded, grains are more (sub-)angular in the overlying units. Unit 2b also shows a lower abundance of feldspars and very few easily weathered minerals. This may be explained by strong mineral weathering in this unit and the preferential mineral weathering of feldspars as opposed to quartz, however a difference in sediment source may also be responsible.

Just a few centimeters above the redeposited nodules of Unit 3, concentric, pedogenic Fe-Mn nodules are concentrated at the bottom of Unit 4 and continue to occur more dispersed in the higher regions of the unit. These nodules consist of a nucleus with multiple concentric bands that contain inclusions of sorted grains of size-classes varying per band. Mineralogical differences between bands may give information on the matrix in which they formed (Delvigne 1998). However, the sands and gravels of the Chitimwe Beds are mineralogically rather homogeneous and changes between concentric bands and the modern matrix could not be detected. Up to eight concentric bands can be distinguished. Most nodules show signs of destruction and partial dissolution. The damage, together with the changing grain sizes of inclusions in the bands and the angularity of inclusions compared to the surrounding sediment clearly illustrates a long history of

formation and further accretion of nodule bands as well as movement through the deposit. Most mineral grains are protected from mineral weathering once they are enclosed by sequioxides in Fe-Mn nodules (Delvigne 1998). Sand and silt inclusions inside the Fe-Mn nodules of both Unit 3 and 4 are angular. Assuming that the nodules in Unit 4 formed inside that same unit, even though they were moved from where they initially formed, the angularity of inclusions in the Fe-Mn nodules compared to their surrounding matrix points to a high maturity of the sediment and to an old age of both the redeposited Fe-Mn nodules in Unit 3 and the pedogenic ones in Unit 4 (Stoops et al. 2010).

While the nodules most likely formed somewhere in the solum of Unit 4, they have been continuously displaced during the history of their formation and partial destruction. The nodules probably became concentrated near the bottom of the unit as a result of pedo- and bioturbation, leading to a general downward movement of relatively large and heavy components (Stoops and Buol 1985). Their downward movement would have come to a halt due to two factors: the presence of similar-sized and closely packed gravel and a reduction in bioturbation intensity.

The concentric bands of the Fe-Mn nodules are also indicative of shrinking and swelling. Concentric nodules typically form in the vadose zone of soils with wet-dry cycles (Kovda and Mermut 2010; Stiles et al. 2001). The concentricity is favored in vertic horizons by centrifugal cortification (Delvigne 1998) and the bands are believed to form as a response to seasonal changes in soil moisture relative to phase saturation (Stiles et al. 2001). According to Delvigne (1998), the bands represent phases of accretion that likely took place during dry phases when shrinkage lead to the formation of fissures around the nodules, allowing for new ferruginous cortex to form by centrifugal action of the nodule in its matrix (Delvigne 1998).

Extensive bioturbation in Unit 4 has resulted in a granular microstructure of bioturbation aggregates. Remnants of peds in the lowermost, coarser regions of Unit 4 as well as a weakly developed grano-striated b-fabric in the finer and loamier sediment, show that shrink-swell also impacted this part of the sequence.

The occurrence of secondary carbonate features inside fissures of damaged Fe-Mn nodules, shows that the main phase of formation of these nodules lies far back in time during a period with wetter soil conditions. Subsequently, considerably dryer soil conditions allowed for the precipitation of carbonates in the fissures of damaged Fe-Mn nodules.

The formation sequence is illustrated and summarized in Figure S4.

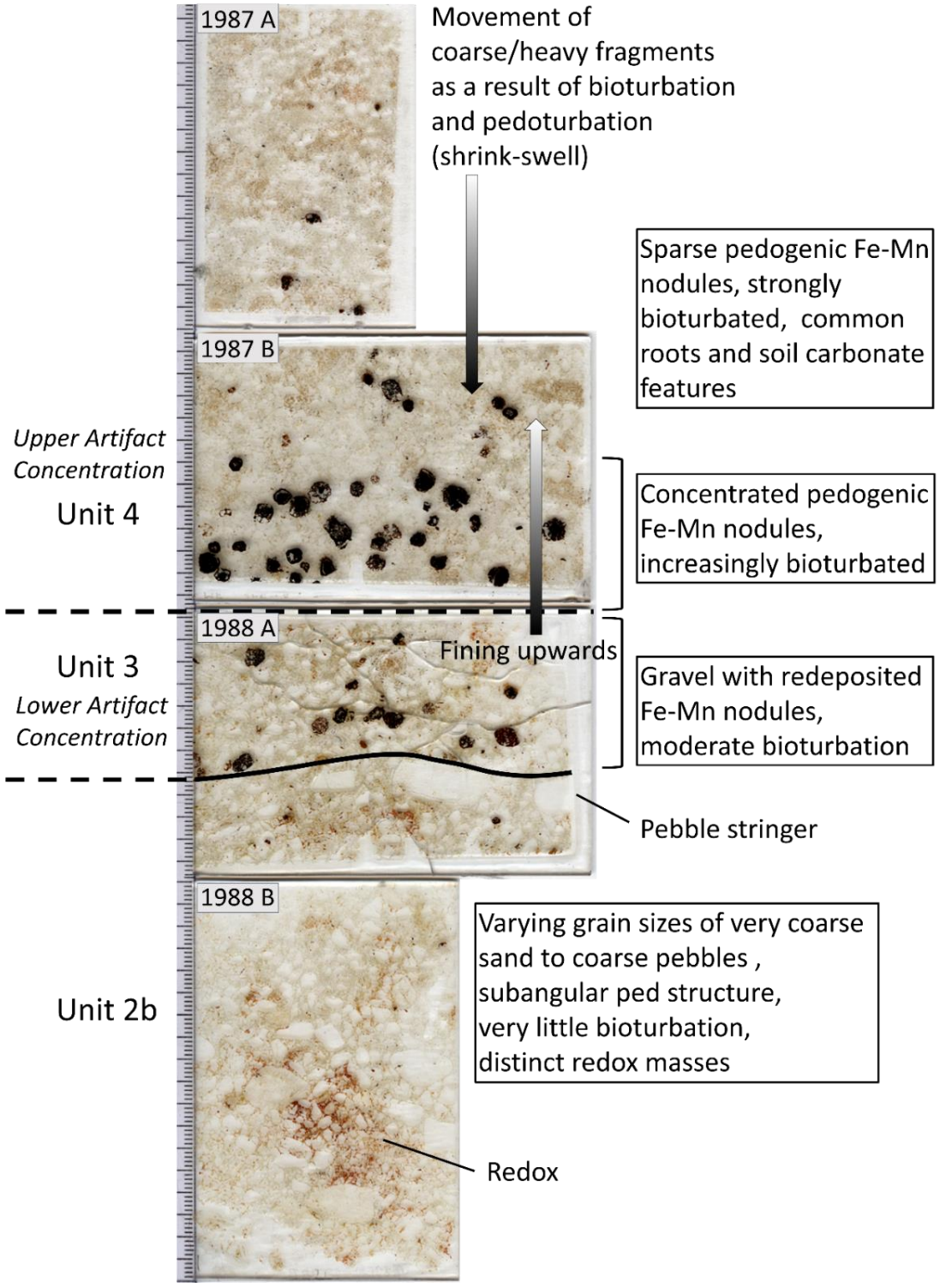

Figure S4: Scans of thin section MEM-1988 B, MEM-1988 A, MEM-1987 B and MEM-1987 A with summarized observations and unit boundaries indicated. Thin sections are 60x90mm and 51x76 mm (MEM 1987 A).

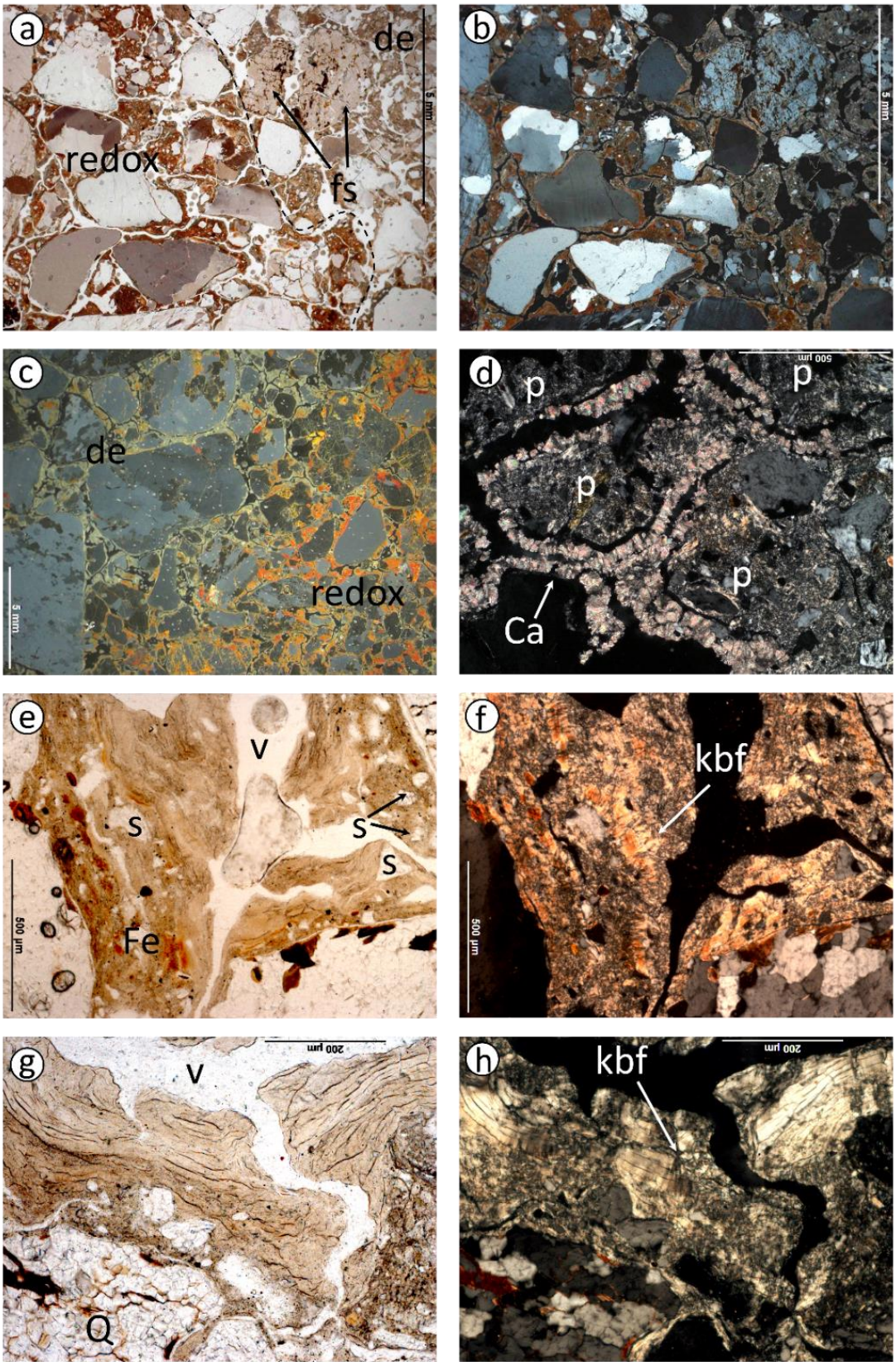

Figure S5: Microphotographs of MEM-1988 B. a) Subangular blocky microstructure in a redox concentration (redox) and depletion (de) with a strongly weathered and fractured feldspar gravel (fs) in the upper right (12.5x), plane polarized light (PPL). b) Same as a) in crossed polarized light (XPL). c) Redox concentration (redox) and depletion

(de) (6.5x). Micrograph taken with crossed polarizers (XPL) and oblique incident light (OIL) to show the distribution of iron oxides. d) CaCO3 feature of sparitic crystals (Ca) around soil peds (p) (100x) (XPL). e) Thick deformed and fragmented compound clay coatings with fine sand (s) inclusions showing multiple episodes of clay translocation. Earlier clay coatings are iron stained (Fe) (100x) (PPL). During preparation of the thin section some air bubbles were artificially trapped in the thin section. f) The same as e) with crossed polarizers, showing deformations and kinkband fabric (kbf) in the clay coatings. g) Thick and deformed compound clay coating with a slightly more iron-stained first phase followed by illuviation of very pale yellow limpid clay. In the lower left a quartz fragment (Q) with fissures filled by sesquioxides (200x) (PPL). h) same as g) but with crossed polarizers showing deformations in the clay coatings and kinkband fabric (kbf) (XPL).

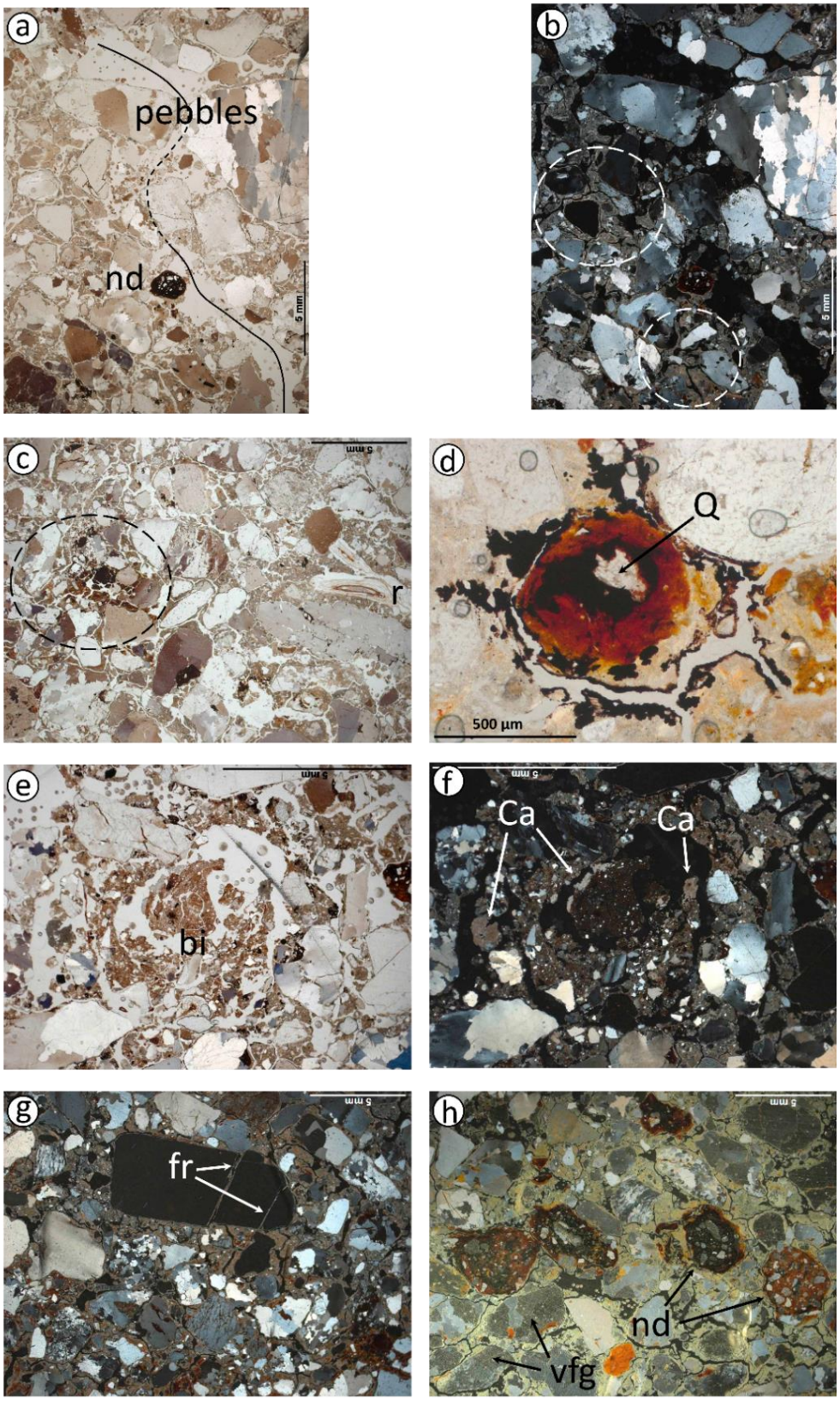

Figure S6: Microphotographs of MEM-1988 A. a) Overview at low magnification showing the unit boundary between Units 2b and 3. A biochannel (line) through the pebble stringer probably permitted a small relic Fe-Mn nodule to pass through to unit 2b (6.5x) (PPL). b) Same as a) with crossed polarized light (XPL). Zones with evident subangular ped

structure are encircled. c) Gravel in a subangular blocky microstructure with a clear mottle (encircled). Root remains (r) in a channel in the right part (6.5x) (PPL). d) Small orthic (in situ) nucleic Fe-Mn nodule around a quartz sand grain (Q) (100x) (PPL). e) Spiral bioturbation feature (bi) with micritic nodular CaCO3 precipitated in associated circumferential channels (12.5x) (XPL). f) Same as e) but with crossed polarized light showing carbonate features (Ca) (XPL). g. Fractured pebble (6.5x) (XPL). h) Very fine gravel and horizontally aligned Fe-Mn nodules in a subangular ped microstructure in Unit 3, (XPL and OIL).

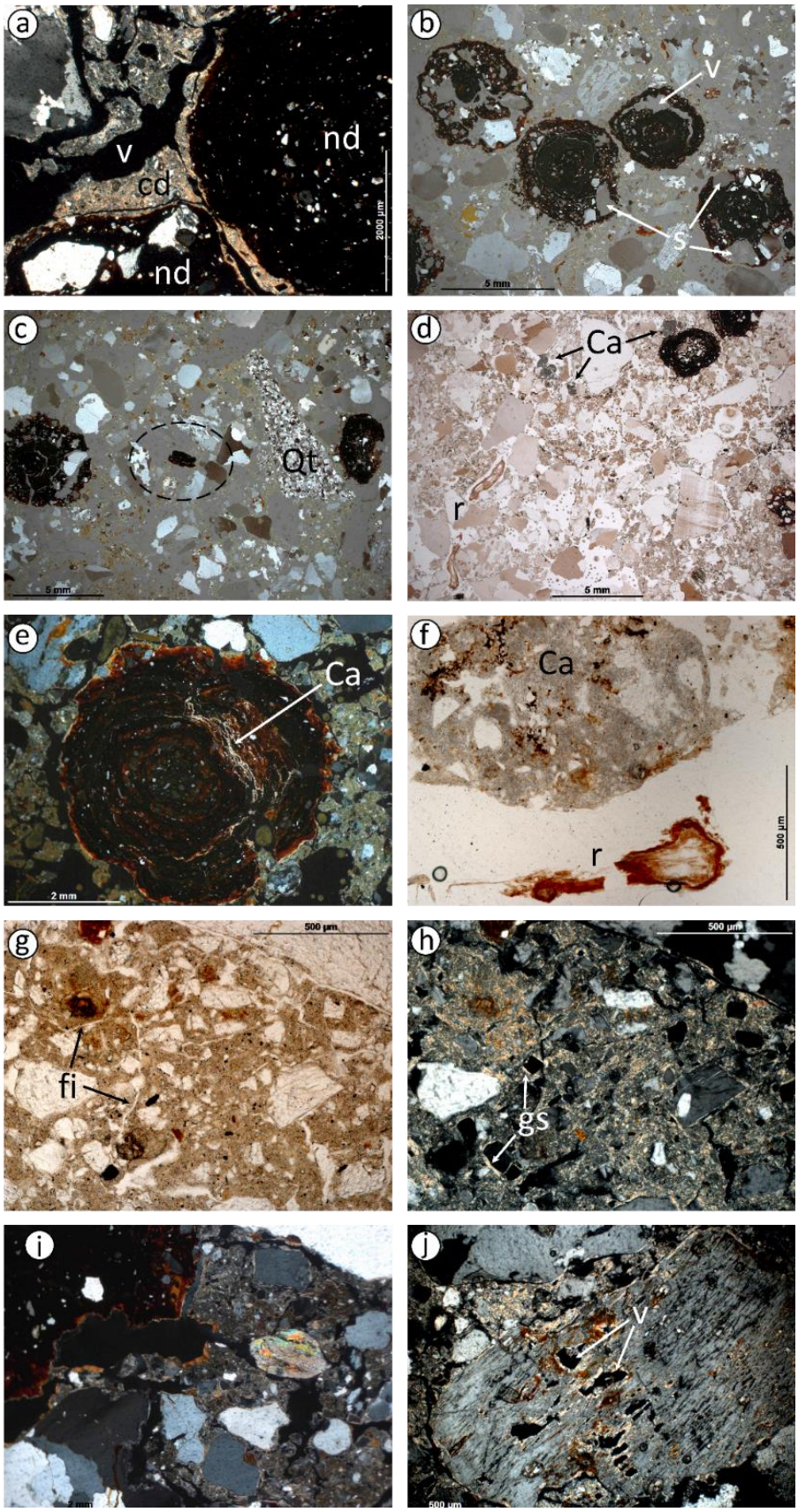

Figure S7: Microphotographs of MEM-1987 B. a) Fragments of clay domains (cd) adhering to Fe-Mn nodules (nd) in the lowermost part of the thin section (25x) (XPL). b) Damaged concentric Fe-Mn nodules in an open bioturbated

matrix of gravel. Plane polarized light (PPL) with oblique incident light (OIL) (8x). c) Elongate, oblique to vertically oriented quartzite fragment (Qt) and an isolated fragment of an Fe-Mn nodule cortex (encircled) in very fine gravel matrix between two concentric Fe-Mn nodules. (6.5x) (PPL and OIL). d) Root fragments (r) in a channel and aggregated bioturbated fine matrix with small CaCO3 nodules (Ca) (6.5x) (PPL). e) Strongly weathered and damaged Fe-Mn nodule with thin coatings of micritic secondary carbonate in the fissures (20x) (XPL). f) Micritic CaCO3 nodule with sand inclusions and stained by humic substances. The carbonate feature is likely related to root remains (r) in the adjacent channel. (100x) (PPL). g) Relatively undisturbed area in lowermost part of the thin section showing a black speckled fine matrix, subangular to angular fine sand grains and desiccation fissures (fi) (100x) (PPL). h) Same as g) but with crossed polarized light, illustrating a grano-striated b-fabric (gs). i) Example of mineral weathering on an olivine grain (100x) (XPL) j) Pores (v) in a weathered feldspar grain (50x) (XPL).

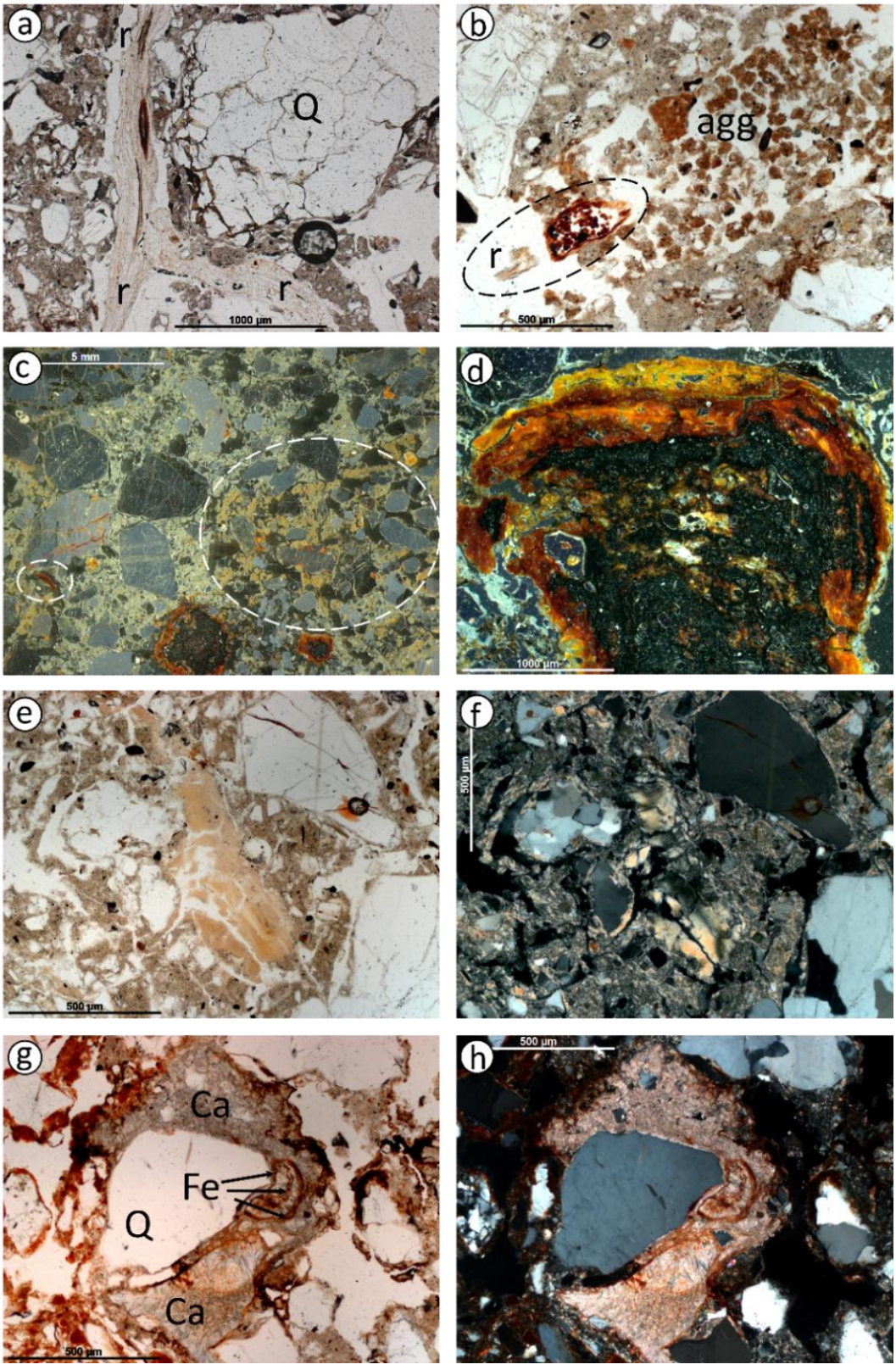

Figure S8: Microphotographs of MEM-1987 A. a) Section of intact root remains (r) in a channel running along a quartz (Q) grain with iron staining inside its fissures (50x), (PPL). The round black feature in the lower right is an artifact from thin sectioning. b) Channel infilled with root remains (lower left, encircled) and microaggregates (agg) of masticated or excremental material (100x) (PPL). c) Diffuse redox in a bioturbation feature (large circle) and two Fe-

Mn nodules as well as a cortex fragment in the lower left (small circle) (10x), (XPL with OIL). d) Upper half of a Fe-Mn nodule showing damage on its left side and preserved concentric bands with different iron and manganese phases in oblique incident light (50x) (OIL). e) Reworked light yellowish limpid clay coating (100x), (PPL). f) Same as e, in XPL. g) Pedogenic carbonate feature of fibrous radial calcite (Ca) with different growth phases demarcated by reddish-brown iron staining (Fe) (100x) (PPL). h) Same as g, in XPL.

SOM SECTION 3: PHYTOLITH ANALYSIS

Sample preparation

Phytoliths were extracted using a four-step process: 1) clay dispersion using 0.1% pre-boiled solution of sodium hexametaphosphate $(NaPO_3)_6$, with sonication (15 minutes) and orbital shaking overnight; 2) inorganic mineral removal with 3N hydrochloric acid (HCl) and nitric acid (HNO_3); 3) organics removal with hydrogen peroxide (H_2O_2); 4) phytolith separation with pre-boiled sodium polytungstate ($2Na_2WO_4 \bullet 9WO_3 \bullet H_2O$) at specific gravity 2.4, with sample rinsing, centrifugation (3000rpm for 5 minutes) and drying following. For microscopy, a fixed aliquot of 0.001g was mounted onto a microscope slide with Entellan New after proper mixing. An average of 451 phytoliths were tallied per sample in adjacent, non-overlapping lines across the cover slip (20x40mm). Poaceae short cells were counted to >200 cells. System microscopy was conducted at 40x magnification (Motic BA410E; image software: Images Plus). Full results are shown in Table S2.

SOM SECTION 4: PALYNOLOGY ANALYSIS

Sample preparation

Sediment samples were disaggregated using sodium pyrophosphate (10% and heated to 100 °C), after which the samples were sieved using an 8-μm mesh (to remove clays) and a 125-μm sieve (to screen sand/gravels). The silt-size fraction (including palynomorphs and micro-charcoal particles) then underwent heavy liquid separation using sodium polytungstate (specific gravity, 2.0), which separated the organic fraction from the mineral component of the samples. The organic portion then underwent acetolysis in which a 9:1 acetic anhydride and concentrated sulphuric solution was utilized to remove excess humic material and stain the pollen grains a golden color. The pollen concentrate material was then mounted on slides for counting in glycerol. The pollen sum consisted of a minimum of 200 palynomorphs or two completely counted slides, while the micro-charcoal analysis involved counting all black angular fragments >5 μm across three evenly spaced transects across all samples. Pollen and charcoal concentrations were determined from counts of exotic *Lycopodium* marker spores, which were added as a tablet (i.e. at the start of the analysis) with a known concentration of *L. clavatum* (Stockmarr 1971; Wang et al. 1999).

		sample nos.																
		700	**701**	**702**	**703**	**704**	**705**	**706**	**707**	**708**	**709**	**710**	**711**	**712**	**713**	**714**	**716**	**N**
Panicoids	Bilobate –long, concave									1						1		2
	Bilobate – long, flat	1																1
	Bilobate – long, notched	4																4
	Bilobate – short, concave	24	11		5						1	1	1	1		1	2	47
	Bilobate – short, convex	4	2			1		4							1		2	14
	Bilobate – short, flat	1									1				1		3	6
	Cross										2							2
	Polylobate	1			1					1							2	5
Pooids	Rondel	143	64	20	12		2	5	4	5	13	12	10	7	3		3	303
	Tower	56	37	8	6		3	7	2	4	6	8	7	4		1	2	151
	Tower – beveled	2	1															3
	Tower – horned	13	3								1		1	1				19
Chloridoids	Saddle - short	40	44	19	7	2	2	4	4	3	5	7	8	4	1		2	152
Bambusoids	Saddle – long	1	2							1	2	2	1	1		2		12
Grass, Undetermined	Bulliform	24	8		14	3	23	8	12	5	4	1	4	2	7	5	3	123
	Scutiform	11			9	2	8	7	11	8	2	2	1		4	1		66
Other	Globular – echinate																1	1
	Globular – psilate	62	27	48	17		2	1		1		1				3		162
Dicot, Woody	Blocky	71	126	108	53	161	53	49	91	69	89	91	69	109	120	133	103	1495
	Clavate	18	3		8	1	12	1		3	1			1		2		50
	Cylindrical	17	2		2			11	6	9	4	2	8	3	4	1	10	79
	Globular – granulate	337	176	165	113	48	124	135	124	159	145	122	135	156	134	138	138	2349
	Tabular – cavate		156	88	106	31	99	55	87	77	87	70	97	67	59	46	13	1138
	Tabular – crenate	3	2	3	3				1	1	1	2	1	2		1	4	24
	Tabular – dendriform	8	1		1					1	2	1	4	5				23
	Tabular – elongate	95	16	8	4	19	5	12	11	7	13	9	11	17	4	7	20	258
	Tabular – scrobiculate	135	156	96	100	57	41	33	53	42	48	55	79	72	64	66	61	1158
	Vessel	2																2
Sample Total		**243**	**665**	**104**	**407**	**76**	**46**	**45**	**64**	**369**	**390**	**261**	**335**	**432**	**68**	**73**	**81**	**7649**

Table S2: Phytoliths recovered from CHA-I sequence, by sample and type.

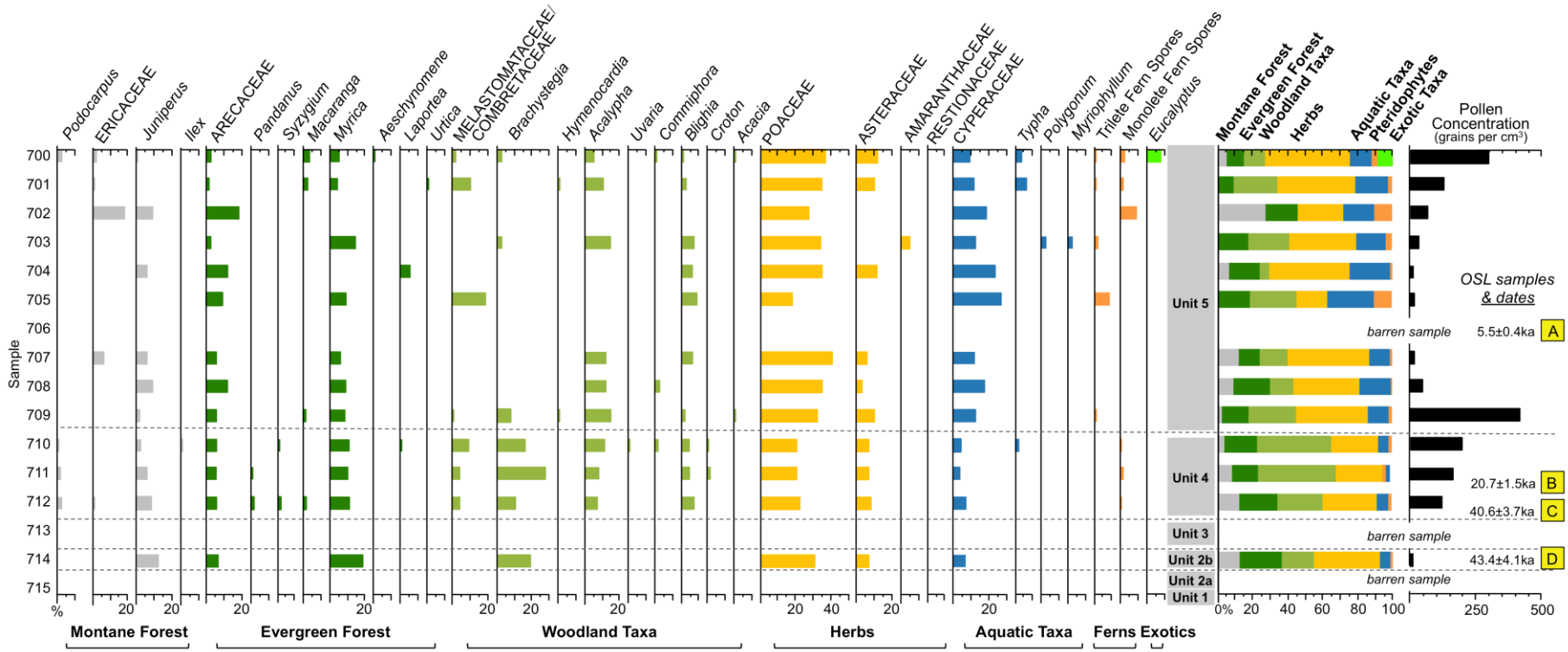

Figure S9: Pollen analysis results showing frequency rates for the 28 recovered taxa, sorted into seven main groups.

SOM SECTION 5: LITHIC ANALYSIS

Methods

All methods are detailed in the main body of the text.

Results

Full results of the lithic analysis are shown in Tables S3, S4, S5, and the attached Datasheet S1 with full spatial and artifact data.

Lithic analysis

	Core Type	Material	Core dimensions (mm)[1] L.	W.	Th.	Cortex %[2]	Flake scars *n*[3] ≥15mm	≥20% core L.
Upper Artifact Concentration (Unit 4)	radial	quartzite	40.02	36.71	20.1	15 • 50	8	11
	radial	quartzite	42.29	59.60	24.62	0 • 55	13	13
	radial	quartzite	50.93	51.43	25.85	0 • 80	10	17
	radial	quartzite	60.08	56.66	38.28	0 • 20	13	13
	radial	quartz	32.08	40.36	14.48	0 • 50	6	12
	radial	quartz	81.23	65.54	36.41	0 • 100	7	7
	radial	quartz	90.00	75.39	58.26	0 • 65	10	10
	average		**56.66**	**55.10**	**31.14**	**2 • 60**	**9.6**	**11.9**
	Levallois	quartzite	46.36	46.94	27.18	0 • 60	8	10
	Levallois	quartzite	50.39	62.99	23.76	0 • 0	8	12
	Levallois	quartzite	55.77	54.96	39.91	0 • 10	15	18
	Levallois	quartzite	78.33	87.48	26.41	0 • 60	20	19
	Levallois	quartz	32.24	38.05	15.82	0 • 25	7	9
	Levallois	quartz	32.64	25.87	12.61	0 • 80	1	8
	Levallois	quartz	36.54	33.65	12.85	0 • 80	3	10
	Levallois	quartz	38.43	36.91	12.76	0 • 95	5	6
	average		**46.34**	**48.36**	**21.41**	**0 • 51**	**8.4**	**11.5**
	platform	quartzite	42.76	65.47	69.05	80	5	6
	platform	quartzite	53.97	68.03	92.07	40	6	7
	platform	quartzite	72.77	58.28	32.58	80	6	6
	average		**56.50**	**63.93**	**64.57**	**66.7**	**5.7**	**6.3**
	multiplatform	quartzite	32.48	77.82	50.85	80	9	11
	multiplatform	quartzite	47.71	37.79	26.25	0	6	11
	average		**40.10**	**57.81**	**38.55**	**40**	**7.5**	**11**
	casual	quartzite	41.09	35.39	22.16	30 • 50	3	3
	casual	quartzite	45.3	38.07	21.49	25	1	1
	casual	quartzite	69.79	76.03	36.04	0 • 90	4	4
	casual	quartzite	74.64	92.62		0 • 85	5	5
	casual	quartzite	113.01	73.23	37.22	60 • 80	3	3
	casual	quartz	31.55	34.87	11.18	0 • 100	2	2
	casual	quartz	33.35	40.77	15.54	0 • 85	1	3
	casual	quartz	46.8	48.91	58.17	0	3	4
	average		**56.94**	**54.99**	**28.83**	**43.4**	**2.8**	**3.1**
	broken cores: radial	1 quartzite, 4 quartz						
	Levallois	1 quartzite						
	multiplatform	1 quartzite						
Lower Artifact Concent	radial	quartz	67.83	76.48	30.77	0 • 45	15	16
	casual	quartzite	82.84	64.45	19.75	0 • 80	2	2
	broken cores: radial	1 quartzite						

Levallois	1 quartzite
indeterminate	1quartz

[1]Core dimensions measured are length (L.), width (W.) and thickness (Th.).

[2]Cortex estimated on cores to 5%; two measures are recorded for the opposed surfaces of hemispherically organized cores (radial, Levallois), single measures are recorded for other core types (platform, multiplatform, casual, indeterminate).

[3]Flake scars were counted two ways: all scars greater than or equal to 15mm in length, and all scars greater than or equal to 20% of the length of the core

Table S3: Characteristics of the cores from the CHA-I Upper Artifact Concentration (Unit 4) and Lower Artifact Concentration (Unit 3).

	Platform	Dorsal Scar Pattern	Material	Flake dimensions[1] L.	W.	Th.	Platform dimensions W.	Th.	L:W ratio[2]	Dorsal Scar #	Dorsal Cortex %[3]	Termination
Upper Artifact Concentration (Unit 4 40.6 ±3.7 ka, *terminus ante quem* 20.7 ±1.5 ka	cortical	cortical (primary)	quartzite	10.37	16.05	4.95	15.45	4.03	0.6	0	100	feather
	cortical	cortical (primary)	quartzite	32.39	31.36	13.19	24.57	11.17	1.0	0	100	feather
	cortical	cortical (primary)	quartzite	51.33	54.61	18.27	50.23	16.2	0.9	0	100	feather
	cortical	cortical (primary)	quartzite	59.37	47.01	17.84	24.77	12.83	1.3	0	100	feather
	cortical	cortical (primary)	quartz	19.89	19.72	5.83	14.67	3.99	1.0	0	100	feather
	cortical	unidirectional	quartz	11.51	11.92	5.49	11.91	5.52	1.0	2	0	feather
	cortical	unidirectional	quartz	14.49	16.03	6.05	14.41	6	0.9	2	0	feather
	cortical	unidirectional	quartz	50.21	33.75	16.41	14.79	8.38	1.5	1	65	feather
	cortical	unidirectional, convergent	quartz	17.75	11.83	3.12	11.86	3.32	1.5	3	0	feather
	cortical	bidirectional, orthogonal	quartz	31.97	47.8	20.54	28.39	13.54	0.7	3	30	feather
	cortical	centripetal	quartzite	45.74	45.05	17.63	20.61	12.27	1.0	2	50	feather
	cortical	centripetal	quartz	12.7	18.99	4.77	13.6	4.4	0.7	3	0	feather
	cortical	indet.	quartz	11.08	12.27	5.3	12.26	5.12	0.9	2	0	feather
	cortical (crushed)	unidirectional	quartzite	62.44	46.02	21.94	indet.	indet.	1.4	3	40	feather
	plain	cortical	quartzite	16.27	30.55	4.96	22.51	5.95	0.5	0	100	feather
	plain	unidirectional	quartzite	20.85	19.18	5.2	11.3	2.6	1.1	1	90	feather
	plain	unidirectional	quartzite	32.34	27.91	10.36	24.29	9.99	1.2	1	56	feather
	plain	unidirectional	quartz	32.34	29.38	10.27	15.99	7.5	1.1	1	40	feather
	plain	unidirectional	quartz	84.69	61.38	30.51	22.76	14.9	1.4	3	65	feather
	plain	unidirectional, convergent	quartzite	94.08	50.94	15.25	23.5	13.53	1.8	9	0	feather
	plain	centripetal	quartzite	15.89	17.19	4.06	9.47	3.15	0.9	3	0	feather
	plain	centripetal	quartzite	23.14	21.72	9.14	13.8	10.5	1.1	3	0	feather
	plain	centripetal	quartzite	35.12	20.55	10.9	17.48	7.89	1.7	5	0	feather
	plain	centripetal	quartzite	24.91	19.37	8.37	12.84	7.2	1.3	4	0	feather
	plain	indet.	quartzite	12.94	14.98	4.34	12.79	4.86	0.9	2	0	feather
	plain	indet.	quartzite	9.23	8.49	2.68	8.44	2.72	1.1	0	0	feather
	plain	indet.	quartz	23.35	16.83	9.14	11.05	8.43	1.4	2	0	feather
	faceted	centripetal	quartzite	24.76	32.84	10.55	31.41	11.08	0.8	3	0	feather

	Platform	Dorsal Scar Pattern	Material	Flake dimensions L.	Flake dimensions W.	Flake dimensions Th.	Platform dimensions W.	Platform dimensions Th.	L:W ratio	Dorsal Scar #	Dorsal Cortex %	Termination
Upper Artifact Concentration (Unit 4)	dihedral	cortical	quartz	21.4	26.61	10.24	26.46	10.21	0.8	0	100	feather
	dihedral	cortical	quartz	28.68	22.8	8.2	18.49	5.47	1.3	0	100	feather
	dihedral	unidirectional	quartzite	20.79	26.24	6.28	18.7	3.21	0.8	1	65	feather
	dihedral	unidirectional	quartzite	29.63	42.9	13.47	30.4	13.49	0.7	4	0	feather
	dihedral	bidirectional, orthogonal	quartzite	23.91	26.59	9.69	26.29	9.71	0.9	2	0	feather
	dihedral	bidirectional, opposed	quartz	32.26	26.66	9.83	23.49	6.02	1.2	3	0	feather
	dihedral	centripetal	quartzite	9.82	15.85	2.82	8.37	2.74	0.6	3	0	feather
	dihedral	centripetal	quartzite	21.18	15.77	5.88	14.73	3.99	1.3	3	0	feather
	dihedral	centripetal	quartzite	30.02	24.53	7.66	22.59	7.13	1.2	3	0	feather
	dihedral	centripetal	quartzite	32.4	24.06	7.33	15.17	3.77	1.3	4	0	feather
	dihedral	centripetal	quartz	20.09	22.32	6.13	12.62	5.49	0.9	7	0	feather
	dihedral	indet.	quartzite	8.49	11.13	2.42	10.77	2.4	0.8	3	0	feather
	polyhedral	bidirectional, orthogonal	quartzite	35.22	43.33	22.87	43.53	22.8	0.8	4	0	feather
	polyhedral	Levallois, centripetal	quartz	47.59	45.89	11.98	33.52	11.18	1.0	5	0	feather
	polyhedral	indet.	quartzite	39.19	38.63	10.6	24.41	9.41	1.0	2	0	feather
	indet. (crushed)	bidirectional, orthogonal	quartzite	52.73	41.51	20.32	28.69	indet.	1.3	1	65	feather
	indet. (crushed)	bidirectional, opposed	quartz	17.37	15.24	5.2	12.33	3.33	1.1	2	40	feather
	indet. (crushed)	centripetal	quartzite	36.74	36.91	9.29	6.31	indet.	1.0	5	5	feather
	indet. (crushed)	centripetal	quartz	22.67	20.99	7.82	13.41	3.9	1.1	3	25	feather
	indet.	centripetal	quartz	36.06	41.02	15.2	21.28	10	0.9	11	25	feather
Lower Artifact	cortical	centripetal	quartzite	69.66	42.88	21.1	25.62	18.3	1.6	5	0	hinge
	plain	unidirectional	quartzite	59.46	47.33	16.78	18.69	3.9	1.3	1	80	feather
	plain	bidirectional, orthogonal	quartzite	32.79	32.31	6.48	12.14	4.42	1.0	2	0	feather

	plain	bidirectional, orthogonal	quartzite	35.7	35.31	14.31	29.48	13.28	1.0	3	35	feather
	plain	centripetal	quartz	16.87	15.06	4.81	10.49	3.37	1.1	5	0	feather
	plain	indet.	quartzite	7.73	10.01	3.68	9.09	3.68	0.8	2	0	feather

				Flake dimensions			Platform dimensions					
	Platform	**Dorsal Scar Pattern**	**Material**	**L.**	**W.**	**Th.**	**W.**	**Th.**	**L:W ratio**	**Dorsal Scar #**	**Dorsal Cortex %**	**Termination**
Lower Artifact Concentration (Unit 3)	plain	indet.	quartzite	10.4	13.8	4.75	13.34	4.77	0.8	2	0	feather
	plain	indet.	quartzite	17.2	9.88	2.33	6.26	1.96	1.7	2	0	feather
	plain	indet.	quartzite	21.91	29.91	10.63	29.26	9.72	0.7	3	0	hinge
	plain	indet.	quartzite	31.17	33.04	17.25	28.58	10.61	0.9	3	0	hinge
	faceted	Levallois, centripetal	quartzite	47.56	60.34	13.42	56.95	15.59	0.8	4	0	feather
	dihedral	bidirectional, orthogonal	quartzite	14.76	23.73	7.21	23.73	7.14	0.6	3	0	feather
	dihedral	bidirectional, orthogonal	quartzite	24.34	18.16	5.68	12.2	4.81	1.3	2	10	overshot
	dihedral	Levallois, centripetal	quartzite	43.9	44.38	13.88	34.59	11.44	1.0	3	0	feather
	dihedral	indet.	quartz	21.66	21.35	5.71	19.79	5.71	1.0	3	0	overshot
	dihedral (cortical)	bidirectional, orthogonal	quartz	29.67	35.52	10.34	25.87	9.48	0.8	1	25	feather
	punctiform	bidirectional, orthogonal	quartzite	21.43	24.1	5.38	9.87	4.69	0.9	6	0	feather
	indet.	centripetal	quartzite	23.7	20.04	8.24	17.54	6.77	1.2	3	0	feather
	indet. (crushed)	centripetal	quartz	25.02	17.02	8.05	13.11	indet.	1.5	3	0	feather

[1]Flake dimensions measured are length (L.), width (W.), and thickness (Th.); flake platform dimensions measured are width (W.) and thickness (Th.)

[2]Ratio of flake length to flake width is recorded as "L:W ratio"; a L:W ratio <1 represents flakes wider than they are long and a L:W ratio >1 represents flake longer than they are wide; elongated flakes have L:W ratio ≥2.

[3]Cortex coverage on dorsal flake surface is estimated to 5%; cortex on platform is not included in this number.

Table S4: Characteristics of the flakes from the CHA-I Upper Artifact Concentration (Unit 4) and Lower Artifact Concentration (Unit 3).

	Refit Group	Set type; # artifacts	Stone type	Description
Upper Artifact Concentration (Unit 4)	01	Conjoin; 2	quartzite	Two conjoining pieces of a flake fragment (portion of flake still missing); flake is one of the two retouched pieces in the CHA-I assemblage.
	02	Refit; 2	quartzite	Two refitting proximal flake fragments.
	03	Refits; 4	quartzite	Three proximal flake fragments and one complete flake, all with plain platforms (likely single platform reduction).
	04	Conjoin; 3	quartzite	Three conjoining pieces of a flake fragment.
	05	Refits; 4	quartzite	Radial core (#12566) with two refitting proximal flake fragments, one with plain platform and one with a cortical platform; a third flake fragment did not directly refit but was from the same clast.
	06	Refit; 2	quartzite	Complete primary flake and refitting proximal flake fragment that sits below; both pieces show evidence of having been burned prior to flaking.
	07	Conjoin; 2	quartz	Two pieces of a fragmentary flake.
	08	Refit; 2	quartzite	One complete and one fragmentary flake.
	09	Refit; 2	quartz	One complete and one fragmentary flake, both with cortical platforms.
	10	Refit; 2	quartz	Radial core and refitting complete flake.
	11	Conjoins & Refits; 8	quartz crystal	Small quartz crystal cobble that shattered during the flaking process; many portions still missing. #12478, 12478, and 12499 all comprise conjoin to form the first flake removed (though portion still missing); #11080 and 12405 conjoin to form the second removal (portions still missing); #12406, 12441 are flaking debris, and #5943 forms part of the nucleus or core of the cobble.
	12	Conjoins & Refits; 8	quartz crystal	Small quartz crystal cobble that shattered during the flaking process; many portions still missing. #12403 and 11090 conjoin to form a primary flake fragment; #12408 is a fragment of the second attempted flake removal; #11089, 12419, 12426: conjoin to form half of the nucleus or core of the cobble; #11073 and 11075 conjoin to form the other half of the nucleus.
	21	Conjoin; 2	quartzite	Two conjoining flake fragments.
	22	Conjoin; 2	quartz	Two conjoining split flake fragments.
	23	Conjoin; 2	quartz	Two conjoining proximal flake fragments.
	24	Conjoin; 2	quartz	Two conjoining primary flake fragments, siret break.
Lower Artifact Concentration (Unit ?)	13	Refit; 2	quartzite	Two refitting proximal flake fragments.
	14	Refit; 2	quartzite	Two refitting proximal flake fragments.
	15	Refit; 2	quartz	Two refitting debitage fragments; indeterminate technological class.
	16	Conjoin; 2	quartzite	Two conjoining pieces of a distal flake fragment.
	17	Conjoin; 2	quartzite	Two conjoining pieces of a proximal flake fragment.
	18	Conjoin; 2	quartzite	Two conjoining debitage fragments; indeterminate technological class.
	19	Conjoin; 2	quartzite	Two conjoining debitage fragments; indeterminate technological class.
	20	Conjoin; 2	quartzite	Two conjoining pieces of a split flake fragment.

Table S5: CHA-I refitting and conjoining artifact sets from the Upper and Lower Artifact Concentrations.

REFERENCES

Arnold, L. J., & Roberts, R. G. (2009). Stochastic modelling of multi-grain equivalent dose (De) distributions: Implications for OSL dating of sediment mixtures. Quaternary Geochronology, 4(3), 204-230.

Blair, T. C., & McPherson, J. G. (2009). Processes and Forms of Alluvial Fans. In A. J. Parson, & A. D. Abrahams (Eds.), Geomorphology of Desert Environments (2nd ed., pp. 413-467). New York: Springer.

Dangerfield, J. M., McCarthy, T. S., & Ellery, W. N. (1998). The mound-building termite Macrotermes michaelseni as an ecosystem engineer. . Journal of Tropical Ecology, 14, 507-520, doi:http://www.jstor.org/stable/2559880.

Delvigne, J. E. (1998). Atlas of Micromorphology of Mineral Alteration and Weathering. (Vol. No. 549 A5). Ontario, Canada: Mineralogical Association of Canada.

Galbraith, R. F., & Roberts, R. G. (2012). Statistical aspects of equivalent does and error calculation and display in OSL dating: An overview and some recommendations. . Quaternary Geochronology, 11, 1-27, doi:https://doi.org/10.1016/j.quageo.2012.04.020.

Galbraith, R. F., Roberts, R. G., Laslett, G. M., Yoshida, H., & Olley, J. M. (1999). Optical dating of single and multiple grains of quartz from Jinmium rock shelter, northern Australia, part 1, Experimental design and statistical models. Archaeometry, 41, 339-364, doi:doi: 10.1111/j.1475-4754.1999.tb00987.x.

Kovda, I., & Mermut, A. R. (2010). Vertic Features. In G. Stoops, V. Marcelino, & F. Mees (Eds.), Interpretation of Micromorphological Features of Soils and Regoliths. (pp. 109-127): Elsevier.

Kühn, P., Aguilar, J. A., & Miedema, R. (2010). Textural pedofeatures and related horizons. In G. Stoops, V. Marcelino, & F. Mees (Eds.), Interpretation of Micromorphological Features of Soils and Regoliths. (pp. 217-250): Elsevier.

Le Roux, P. A. L., & De Preez, C. C. (2008). Micromorphological evidence of redox activity in the soft plinthic B horizon of a soil of the Bainsvlei form in an arid bioclimate. South African Journal of Plant Soil, 25(2), 84-91.

Meier, H. A., Nordt, L. C., Forman, S. L., & Dreise, S. G. (2013). Late Quaternary alluvial history of the middle Owl Creek drainage basin in central Texas: A record of geomorphic response to environmental change. Quaternary International, 306, 24-41, doi:https://doi.org/10.1016/j.quaint.2013.07.010.

Mücher, H. J., & Coventry, R. J. (1994). Soil and landscape processes evident in a hydromorphic grey earth (Plinthusalf) in semiarid tropical Australia. In A. J. Ringrose-Voase, & G. S. Humphreys (Eds.), Soil Micromophology: Studies in Management and Genesis. Roc. IX Int. Working Meeting on Soil

Micromorphology, Townsville, Australia, July 1992 (pp. 221-231, Vol. Developments in Soil Science 22). Amsterdam: Elsevier.

Mujinya, B. B., Mees, F., Boeckx, P., Bodé, S., Baert, G., Erens, H., Delefortrie, S., Verdoodt, A., Ngongo, M., & Van Ranst, E. (2011). The origin of carbonates in termite mounds of the Lubumbashi area, D.R. Congo. . Geoderma, 165, 95-105, doi:https://doi.org/10.1016/j.geoderma.2011.07.009.

Murray, A. S., & Wintle, A. G. (2003). The single alquiot regenerative dose protocol: potential for improvements in reliability. Radiation Measurements, 37, 377-381, doi:https://doi.org/10.1016/S1350-4487(03)00053-2.

Olley, J. M., Pietsch, T., & Roberts, R. G. (2004). Optical dating of Holocene sediments from a variety of geomorphic settings using single grains of quartz. Geomorphology, 60(3), 337-358, doi:https://doi.org/10.1016/j.geomorph.2003.09.020.

Prescott, J. R., & Hutton, J. T. (1994). Cosmic ray contributions to dose rates for luminescence and ESR dating: large depths and long-term time variations. . Radiation Measurements, 23, 497-500, doi:https://doi.org/10.1016/1350-4487(94)90086-8.

Stiles, C. A., Mora, C. I., & Driese, S. G. (2001). Pedogenic iron-manganese nodules in Vertisols: A new proxy for paleoprecipitation? Geology, 29(10), 943-946.

Stockmarr, J. (1971). Tablets with spores used in absolute pollen analysis. Pollen et Spores, 13, 615-621.

Stoops, G. (2003). Guidelines for analysis and description of soil and regolith thin sections. Madison, Wisconsin: Soil Science Society of America, Inc.

Stoops, G., Marcelino, V., & Mees, F. (2010). Micromorphological Features and Their Relation to Processes and Classification: General Guidelines and Keys. In G. Stoops, V. Marcelino, & F. Mees (Eds.), Interpretation of Micromorphological Features of Soils and Regoliths (pp. 15-35): Elsevier.

Stoops, G. J., & Buol, S. W. (1985). Micromorphology of Oxisols. In L. A. Douglas, & M. L. Thompson (Eds.), Soil Micromorphology and Soil Classification. (Vol. 15, pp. 105-119). Madison, Wisconsin: Soil Science Society of America Special Publication.

Wang, X., van der Kaars, S., Kershaw, P., Bird, M., & Jansen, F. (1999). A record of fire, vegetation and climate through the last three glacial cycles from Lombok Ridge core G6-4, eastern Indian Ocean, Indonesia. Palaeogeography, Palaeoclimatology, Palaeoecology, 147, 241-256, doi:https://doi.org/10.1016/S0031-0182(98)00169-2.

Wright, D. K., Forman, S. L., Waters, M. R., & Ravesloot, J. C. (2011). Holocene eolian activation as a proxy for broad-scale landscape change on the Gila River Indian Community, Arizona. Quaternary Research, 76(1), 10-21, doi:https://doi.org/10.1016/j.yqres.2011.04.008.

Wright, D. K., Thompson, J. C., Mackay, A., Welling, M., Forman, S. L., Price, G., Zhao, J.-x., Cohen, A. S., Malijani, O., & Gomani Chindebvu, E. (2014). Renewed geoarchaeological investigations of Mwanganda's Village (Elephant Butchery Site), Karonga, Malawi. Geoarchaeology, 29, 98-120, doi:doi: 0.1002/gea.21469.

D - Early Human Impacts and Ecosystem Reorganization in Southern-Central Africa

Jessica C. Thompson [1, 2*†], David K. Wright [3, 4*†], Sarah J. Ivory [5*†], Jeong-Heon Choi [6], Sheila Nightingale [7], Alex Mackay [8], Flora Schilt [9, 10], Erik Otárola-Castillo [11], Julio Mercader [12, 13, 14], Steven L. Forman [15], Timothy Pietsch [16], Andrew S. Cohen [17], J. Ramón Arrowsmith [18], Menno Welling [19, 20], Jacob Davis [21], Benjamin Schiery [22], Potiphar Kaliba [23], Oris Malijani [23], Margaret W. Blome [24], Corey A. O'Driscoll [8], Susan M. Mentzer [9, 25], Christopher Miller [9, 26], Seoyoung Heo [6], Jungyu Choi [27], Joseph Tembo [23], Fredrick Mapemba [23], Davie Simengwa [28], Elizabeth Gomani Chindebvu [29]

[1] Department of Anthropology, Yale University, New Haven, CT, USA. [2] Institute of Human Origins, P.O. Box 874101, Tempe, AZ 85287, USA. [3] Department of Archaeology, Conservation and History, University of Oslo, Oslo, Norway. [4] State Key Laboratory of Loess and Quaternary Geology, Institute of Earth Environment, Chinese Academy of Sciences, Xian, China. [5] Department of Geosciences and Earth and Environmental Systems Institute, Pennsylvania State University, University Park, PA, USA. [6] Department of Earth and Environmental Sciences, Korea Basic Science Institute, Ochang, Republic of Korea. [7] Department of Anthropology, City University of New York, Graduate Center, New York, NY, USA. [8] Centre for Archaeological Science, School of Earth, Atmospheric and Life Sciences, University of Wollongong, Wollongong, NSW, Australia. [9] Institute for Archaeological Sciences and Senckenberg Centre for Human Evolution and Palaeoenvironment, University of Tübingen, Tübingen, Germany. [10] Universidade do Algarve, Interdisciplinary Center for Archaeology and Evolution of Human Behavior (ICArEHB), FCHS, Campus Gambelas, J27, Faro 8005-139, Portugal. [11] Department of Anthropology, Purdue University, West Lafayette, IN, USA. [12] Department of Anthropology and Archaeology, University of Calgary, Calgary, AB, Canada. [13] Max Planck Institute for the Science of Human History, Jena, Germany. [14] Institut Català de Paleoecologia Humana i Evolució Social (IPHES), Zona Educacional, 4– Campus Sescelades URV (Edifici W3), 43007 Tarragona, Spain. [15] Department of Geosciences, Baylor University, Waco, TX, USA. [16] Australian Rivers Institute, Griffith University, Brisbane, QLD, Australia. [17] Department of Geosciences, University of Arizona, Tucson, AZ, USA. [18] School of Earth and Space Exploration, Arizona State University, Tempe, AZ, USA. [19] Reinwardt Academy, Amsterdam University of the Arts, Amsterdam, Netherlands. [20] African Heritage Ltd., Box 622, Zomba, Malawi. [21] Independent Researcher, New Haven, CT, USA. [22] Biostatistics Department, Medpace Inc., Cincinnati, OH, USA. [23] Malawi Department of Museums and Monuments, Lilongwe, Malawi. [24] Department of Geological Sciences, East Carolina University, Greenville, NC, USA. [25] School of Anthropology, University of Arizona, Tucson, AZ, USA. [26] SFF Centre for Early Sapiens Behaviour (SapienCE), University of Bergen, Bergen, Norway. [27] Gyeongju National Research Institute of Cultural Heritage, Gyeongju, Republic of Korea. [28] Lanujos Social Research and Consultancy, Blantyre, Malawi. [29] Ministry of Civic Education and National Unity, Lilongwe, Malawi.

*Corresponding author. Email: jessica.thompson@yale.edu (J.C.T); david.wright@iakh.uio.no (D.K.W.); sji15@psu.edu (S.J.I.)

†These authors contributed equally to this work.

https://advances.sciencemag.org/content/7/19/eabf9776

ABSTRACT

Modern *Homo sapiens* engage in substantial ecosystem modification, but it is difficult to detect the origins or early consequences of these behaviors. Archaeological, geochronological, geomorphological, and paleoenvironmental data from northern Malawi document a changing relationship between forager presence, ecosystem organization, and alluvial fan formation in the Late Pleistocene. Dense concentrations of Middle Stone Age artifacts and alluvial fan systems formed after ca. 92 thousand years ago, within a paleoecological context with no analog in the preceding half-million-year record. Archaeological data and principal coordinates analysis indicate that early anthropogenic fire relaxed seasonal constraints on ignitions, influencing vegetation composition and erosion. This operated in tandem with climate-driven changes in precipitation to culminate in an ecological transition to an early, pre-agricultural anthropogenic landscape.

INTRODUCTION

Modern humans act as powerful agents of ecosystem transformation. They have extensively and intentionally modified their environments for tens of millennia, leading to much debate about when and how the first human-dominated ecosystems arose (1). A growing body of archaeological and ethnographic evidence shows substantial, recursive interactions between foragers and their environments that suggest that these behaviors were fundamental to the evolution of our species (2–4). Fossil and genetic data indicate that *Homo sapiens* were present in Africa by ~315 thousand years (ka) ago, and archaeological data show notable increases in the complexity of behavior that

took place across the continent within the past ~300- to 200-ka span at the end of the Middle Pleistocene (Chibanian) (5). Since our emergence as a species, humans have come to rely on technological innovation, seasonal scheduling, and complex social cooperation to thrive. These attributes have enabled us to exploit previously uninhabited or extreme environments and resources, so that today humans are the only pan-global animal species (6). Fire has played a key role in this transformation (7).

Biological models suggest that adaptations for cooked food extend back at least 2 million years, but regular archaeological evidence for controlled use of fire does not appear until the end of the Middle Pleistocene (8). A marine core with a dust record drawn from a wide swath of the African continent shows that over the past million years, peaks in elemental carbon occurred after ~400 ka, predominately during shifts from interglacial to glacial conditions, but also during the Holocene (9). This suggests that fire was less common in sub-Saharan Africa before ~400 ka and that by the Holocene, there was a substantial anthropogenic contribution (9). Fire is a tool that has been used by pastoralists to open and maintain grasslands throughout the Holocene (10). However, detecting the contexts and ecological impacts of fire use by Pleistocene early hunter-gatherers is more complex (11).

Fire is known both ethnographically and archaeologically as an engineering tool for resource manipulation, including improvement of subsistence returns or modification of raw materials, with these activities often associated with communal planning and requiring substantial ecological knowledge (2, 12, 13). Landscape-scale fires allow hunter-gatherers to drive game, control pests, and enhance productivity of habitat (2). On-site fire facilitates cooking, warmth, predator defense, and social cohesion (14). However, there is substantial ambiguity regarding the extent to which fires by hunter-gatherers can reconfigure components of a landscape, such as ecological community structure and geomorphology (15, 16).

Understanding the development of human-induced ecological change is problematic without well-dated archaeological and geomorphic data from multiple sites, paired with continuous environmental records. Long lacustrine sedimentary records from the southern African Rift Valley, coupled with the antiquity of the archaeological record in this region, make it a place where anthropogenically induced ecological impacts may be investigated into the Pleistocene. Here, we report the archaeology and geomorphology of an extensively dated Stone Age landscape in southern-central Africa. We then link it to paleoenvironmental data spanning >600 ka to identify the earliest coupled evidence for human behavior and ecosystem transformation in the context of anthropogenic fire.

RESULTS

Geochronology and geomorphology

We provide previously unreported age constraints for the Chitimwe Beds of the Karonga District that lie at the northern end of Lake Malawi in the southern portion of the African Rift Valley (Fig. 1) (17). These beds are composed of lateritic alluvial fan and stream deposits that cover ~83 km^2, containing millions of stone artifacts, but do not have preserved organic remains such as bone (Supplementary Text) (18). Our optically stimulated luminescence (OSL) data from terrestrial records (Fig. 2 and tables S1 to S3) revise the age of the Chitimwe Beds to the Late Pleistocene, with the oldest age for both alluvial fan activation and burial of Stone Age sites ca. 92 ka (18, 19). The alluvial and fluvial Chitimwe Beds overlie Plio-Pleistocene Chiwondo Beds of lacustrine and fluvial origin in a low, angular unconformity (17). These sedimentary packages are in fault-bounded wedges along the lake margin. Their configuration indicates interactions between lake level fluctuations and active faulting extending into the Pliocene (17). Although tectonism may have affected regional relief and piedmont slopes over an extended time, fault activity in this region likely slowed since the Middle Pleistocene (20). After ~800 ka until shortly after 100 ka, the hydrology of Lake Malawi became primarily climate driven (21). Therefore, neither is likely the sole explanation for Late Pleistocene alluvial fan formation (22).

Landscape stability after (Chitimwe) fan formation is indicated by formation of laterites and pedogenic carbonates, which cap fan deposits across the study region (Supplementary Text and table S4). The formation of alluvial fans in the Late Pleistocene of the Lake Malawi basin is not restricted to the Karonga region. About 320 km to the southeast in Mozambique, terrestrial cosmogenic nuclide depth profiles of 26Al and 10Be constrain formation of the alluvial, lateritic Luchamange Beds to 119 to 27 ka (23). This broad age constraint is consistent with our OSL chronology for the western Lake Malawi basin and indicates regional alluvial fan expansion in the Late Pleistocene. This is supported by data from lake core records, which suggest a higher sedimentation rate accompanied by increased terrigenous input after ca. 240 ka, with particularly high values at ca. 130 and 85 ka (Supplementary Text) (21).

Archaeology

The earliest evidence for human occupation in the region is tied to the Chitimwe sedimentary deposits identified at ~92 ± 7 ka. This result is based on 605 m^3 of excavated sediment from 14 archaeological excavations with subcentimeter spatial control, and 147 m^3 of sediment from 46

archaeological test pits with 20-cm vertical and 2-m horizontal control (Supplementary Text and figs. S1 to S3). In addition, we have surveyed 147.5 linear km, emplaced 40 geological test pits, and analyzed over 38,000 artifacts from 60 of these localities (tables S5 and S6) (18). These extensive surveys and excavations show that while hominins, including early modern humans, may have inhabited the region before ~92 ka, depositional aggradation associated with rising and then stabilized Lake Malawi levels did not preserve archaeological evidence until formation of the Chitimwe Beds.

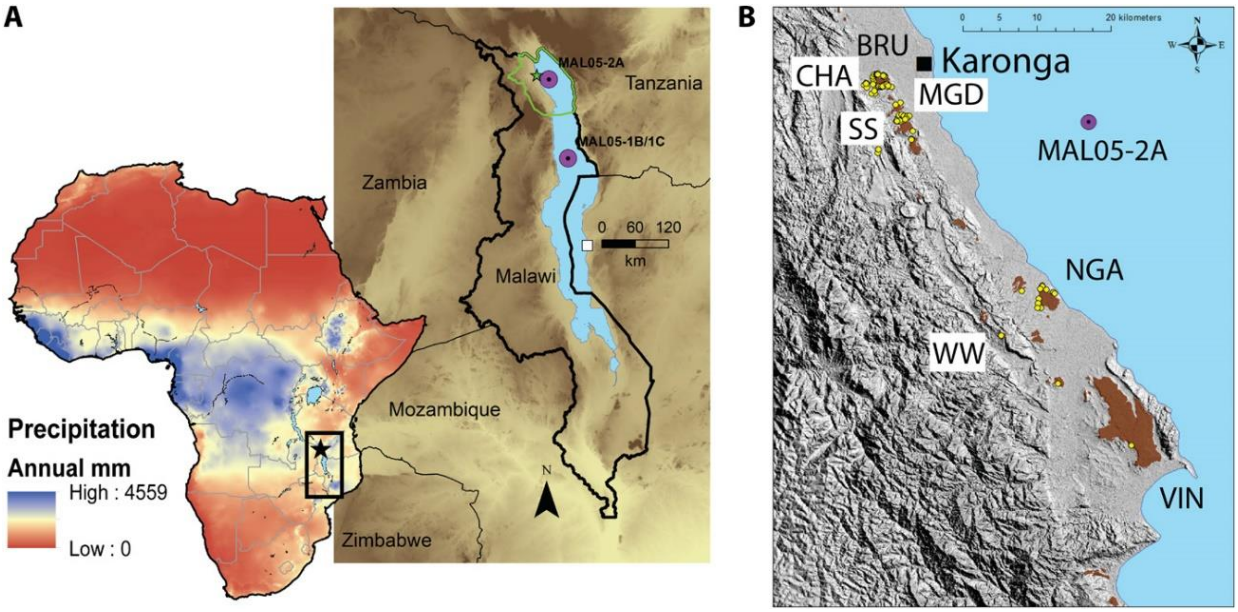

Fig. 1. Map of region, geology, and excavation sites. (**A**) Location of sites in Africa (star) relative to modern precipitation; blue is wetter and red is more arid (73); boxed area at left shows location of the MAL05-2A and MAL05-1B/1C cores (purple dots) in Lake Malawi and surrounding region, with the Karonga District highlighted as a green outline and location of Luchamange Beds as a white box. (**B**) Northern basin of Lake Malawi showing the hillshaded topography, remnant Chitimwe Beds (brown patches), and Malawi Earlier-Middle Stone Age Project (MEMSAP) excavation locations (yellow dots), relative to the MAL05-2A core; CHA, Chaminade; MGD, Mwanganda's Village; NGA, Ngara; SS, Sadala South; VIN, Vinthukutu; WW, White Whale.

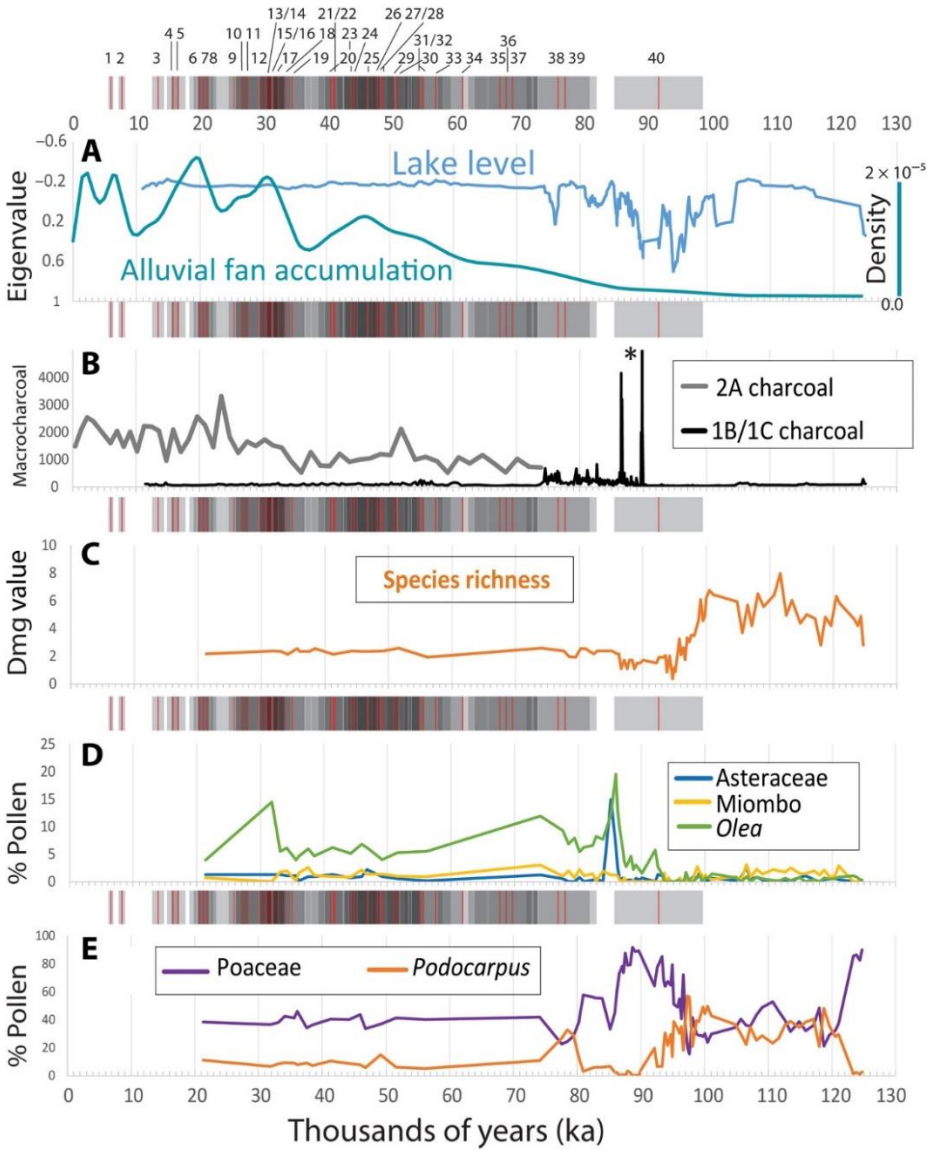

Fig. 2. Ages of archaeological sites with geomorphic and paleoenvironmental data. OSL central age (red lines) and error ranges at 1-σ (25% gray) for all OSL ages associated with in situ artifact occurrences in Karonga. Ages are shown against the past 125 ka of data for (**A**) Kernel density estimate of all OSL ages from alluvial fan deposits indicating sedimentation/alluvial fan accumulation (teal), and lake level reconstructions based on eigenvalues of a principal components analysis (PCA) of aquatic fossils and authigenic minerals from the MAL05-1B/1C core (21) (blue). (**B**) Counts of macrocharcoal per gram normalized by sedimentation rate, from the MAL05-1B/1C core (black, one value near 7000 off scale with asterisk) and MAL05-2A core (gray). (**C**) Margalef's index of species richness (Dmg) from fossil pollen of the MAL05-1B/1C core. (**D**) Percentages of fossil pollen from Asteraceae, miombo woodland, and *Olea*, and (**E**) percentages of fossil pollen from Poaceae and *Podocarpus*. All pollen data are from the MAL05-1B/1C core. Numbers at the top refer to individual OSL samples detailed in tables S1 to S3. Differences in data availability and resolution are due to different sampling intervals and material availability in the core. Figure S9 shows the two macrocharcoal records converted to z scores.

The archaeological data support the inference that during the Late Quaternary, fan expansion and human activities in northern Malawi were substantial, and artifacts were of a type associated elsewhere in Africa with early modern humans. The majority of artifacts were created from quartzite or quartz river cobbles and featured radial, Levallois, platform, and casual core reduction (fig. S4). Morphologically diagnostic artifacts can be predominantly attributable to Levallois-type technologies characteristic of the Middle Stone Age (MSA), known to date from at least ~315 ka in Africa (24). The uppermost Chitimwe Beds, which continue into the Early Holocene, contain sparsely distributed Later Stone Age occurrences, found in association with terminal Pleistocene and Holocene hunter-gatherers across Africa. In contrast, stone tool traditions typically associated with the Early and Middle Pleistocene, such as large cutting tools, are rare. Where these do occur, they are found within MSA-bearing deposits dated to the Late Pleistocene, not an earlier phase of sedimentation (table S4) (18). Although sites are present from ~92 ka, the most well-represented period of both human activity and alluvial fan deposition occurs after ~70 ka, well defined by a cluster of OSL ages (Fig. 2). We confirm this pattern with 25 published and 50 previously unpublished OSL ages (Fig. 2 and tables S1 to S3). These show that of a total of 75 age determinations, 70 were recovered from sediment that postdates ~70 ka. The 40 ages associated with in situ MSA artifacts are shown in Fig. 2, relative to major paleoenvironmental indicators published from the MAL05-1B/1C central basin lake core (25) and previously unpublished charcoal from the MAL05-2A northern basin lake core (adjacent to the fans that produced the OSL ages).

Paleoclimate and environment reconstruction

Climate and environmental conditions coeval with MSA human occupation at Lake Malawi were reconstructed using freshly generated data from phytoliths and soil micromorphology from archaeological excavations and published data from fossil pollen, macrocharcoal, aquatic fossils, and authigenic minerals from the Lake Malawi Drilling Project cores (21). The latter two proxies are the primary basis of the reconstruction of relative lake depth dating back over 1200 ka (21) and are matched to pollen and macrocharcoal samples taken from the same places in the core that span the past ~636 ka (25). The longest cores (MAL05-1B and MAL05-1C; 381 and 90 m, respectively) were collected ~100 km southeast of the archaeological project area. A shorter core (MAL05-2A; 41 m) was collected ~25 km east, offshore from the North Rukuru River (Fig. 1). The MAL05-2A core reflects terrigenous paleoenvironmental conditions of the Karonga region, whereas the MAL05-1B/1C cores did not receive direct riverine input from Karonga and thus are more reflective of regional conditions.

Sedimentation rates recorded in the MAL05-1B/1C composite drill core began to increase starting ~240 ka from a long-term average of 0.24 to 0.88 m/ka (fig. S5). The initial increase is associated with changes in orbitally modulated insolation, which drive high amplitude changes in lake level during this interval (25). However, when orbital eccentricity decreased and climate stabilized after 85 ka, sedimentation rates remained high (0.68 m/ka). This is concurrent with the terrestrial OSL record, which shows extensive evidence for alluvial fan expansion after ~92 ka, and congruent with magnetic susceptibility data that show a positive relationship between erosion and fire after 85 ka (Supplementary Text and table S7). Given the error ranges of available geochronological controls, it is not possible to tell whether this set of relationships evolved slowly from a progression of recursive processes or occurred in rapid bursts as tipping points were reached. On the basis of geophysical models of basin evolution, rift extension and associated subsidence have slowed since the Middle Pleistocene (20) and, therefore, are not the primary cause of extensive fan formation processes we have dated to mainly after 92 ka.

Climate has been the dominant control of lake level since the Middle Pleistocene (26). Specifically, uplift in the northern basin closed an existing outlet ca. 800 ka, allowing the lake to deepen until reaching the sill elevation of the modern outlet (21). This outlet, located at the southern end of the lake, provides an upper limit on lake levels during wet intervals (including the present day), but allows the basin to close as lake levels drop during periods of aridity (27). Lake level reconstructions show alternating wet-dry cycles over the past 636 ka. On the basis of evidence from fossil pollen, periods of extreme aridity (>95% decrease in total water volume) linked to lows in summer insolation resulted in the expansion of semidesert vegetation with trees restricted to permanent waterways (27). These (lake) lowstands were associated with pollen spectra showing high proportions of grass (80% or more) and xerophytic herbs (Amaranthaceae) at the expense of tree taxa and low overall species richness (25). In contrast, when the lake was near the modern level, vegetation with strong affinities to Afromontane forest typically expanded to the lakeshore [~500 m above sea level (masl)]. Today, Afromontane forests only occur in small, discontinuous patches above ~1500 masl (25, 28).

The most recent period of extreme aridity occurred from 104 to 86 ka, after which open miombo woodland with substantial grass and herbaceous components became widespread, despite recovery of the lake level to high-stand conditions (27, 28). Afromontane forest taxa, most notably *Podocarpus*, never recovered after 85 ka to values similar to previous periods of high lake levels (10.7 ± 7.6% after 85 ka versus 29.8 ± 11.8% during analogous lake level before 85 ka). Margalef's index (Dmg) also shows that the past 85 ka has been marked by species richness 43% lower than during

previous sustained periods of high lake level (2.3 ± 0.20 versus 4.6 ± 1.21, respectively), for example, in the high lake period between ca. 420 and 345 ka (Supplementary Text and figs. S5 and S6) (25). Pollen samples from the period ca. 88 to 78 ka also contain high percentages of Asteraceae pollen, which can be indicative of vegetation disturbance and is within the error range of the oldest date for human occupation of the area.

Paleoenvironmental analysis

We use a climate anomaly approach (29) to analyze paleoecological and paleoclimatic data from the drill cores before and after 85 ka and test the hypothesis that the ecological relations among vegetation, species richness, and precipitation became decoupled from predictions derived from the presumably purely climate-driven baseline pattern of the preceding ~550 ka. This transformed ecological system was influenced by both lake infilling precipitation conditions and fire occurrence, as reflected in a species-poor and novel vegetation assemblage. Only some forest elements recovered after the last arid period, and these included fire-tolerant components of the Afromontane forest such as *Olea*, and hardy components of tropical seasonal forest such as *Celtis* (Supplementary Text and fig. S5) (25). To test this hypothesis, we model lake level derived from ostracode and authigenic mineral proxies as the independent variable (21) versus dependent variables such as charcoal and pollen that could have been affected by increased fire frequency (25).

To examine how similar or dissimilar the assemblages were to one another at different times, we conducted a principal coordinates analysis (PCoA) using pollen from *Podocarpus* (evergreen tree), Poaceae (grasses), *Olea* (a fire-tolerant component of Afromontane forest), and miombo (the dominant woodland component today). By mapping the PCoA on top of an interpolated surface that represents lake level at the time each assemblage was formed, we examine how pollen assemblages changed relative to precipitation and how this relationship changed after 85 ka (Fig. 3 and fig. S7). Before 85 ka, samples dominated by Poaceae cluster toward drier conditions, while samples dominated by *Podocarpus* cluster toward wetter conditions. In contrast, samples dating to after 85 ka cluster away from the majority of pre-85-ka samples and have a different average value, showing that their composition is unusual for similar precipitation conditions. Their position in the PCoA reflects the influence of Olea and miombo, both of which are favored under more fire-prone conditions. Of the post-85-ka samples, *Podocarpus* is only abundant in three successive samples, which occurred just after the onset of this interval between 78 and 79 ka. This suggests that after initial rainfall increase, forests appear to make a brief recovery before eventual collapse.

To investigate the relations among the pollen, lake levels, and charcoal, we used a nonparametric multivariate analysis of variance (NP-MANOVA) to compare the total "environment" (represented by a data matrix of pollen, lake levels, and charcoal), before and after the transition at 85 ka. We found that variation and covariation found in this data matrix are statistically significantly different before and after 85 ka (Table 1).

Our terrestrial paleoenvironmental data from phytoliths and soils on the western lake margins agree with interpretations based on proxies from the lake. These show that despite high lake levels, the landscape had transitioned to one dominated by open canopy woodland and wooded grassland, much as today (25). All localities analyzed for phytoliths on the western margin of the basin date to after ~45 ka and show substantial arboreal cover that reflect wet conditions. However, they suggest that much of that cover is in the form of open woodlands in cohort with bambusoid and panicoid grasses. On the basis of phytolith data, fire-intolerant palms (Arecaceae) were present exclusively by the lake shoreline and rare or absent from inland archaeological sites (table S8) (30).

In general, wet but open conditions in the later part of the Pleistocene are also inferred from terrestrial paleosols (19). Lagoonal clay and palustrine-pedogenic carbonates from the vicinity of the Mwanganda's Village archaeological site date between 40 and 28 cal ka BP (calibrated kiloanni before present) (table S4). Carbonate soil horizons within the Chitimwe Beds are typically nodular calcretes (Bkm) and argillic and carbonate (Btk) horizons, which indicate locations of relative landform stability with slow sedimentation derived from distal alluvial fan progradation by ca. 29 cal ka BP (Supplementary Text). Eroded, indurated laterite soils (petroplinthites) formed on remnants of paleofans are indicative of open landscape conditions (31) with strongly seasonal precipitation (32), illustrating the ongoing legacy of these conditions on the landscape.

Support for the role of fire in this transformation comes from the paired macrocharcoal records from the drill cores, which from the central basin (MAL05-1B/1C) show an overall increase in charcoal influx starting ca. 175 ka. Substantial peaks follow between ca. 135 and 175 ka and 85 and 100 ka, after which time lake levels recover but forest trees and species richness do not (Supplementary Text, Fig. 2, and fig. S5). The relationship between charcoal influx and magnetic susceptibility of lake sediments can also show patterns in long-term fire history (33). Using data from Lyons et al. (34), ongoing erosion of burned landscapes after 85 ka is implied at Lake Malawi by a positive correlation (Spearman's $Rs = 0.2542$ and $P = 0.0002$; table S7), whereas older sediments show an inverse relationship ($Rs = -0.2509$ and $P < 0.0001$). In the northern basin, the shorter MAL05-2A core has its deepest chronological anchor point with the Youngest Toba Tuff

at ~74 to 75 ka (35). Although it lacks the longer-term perspective, it receives input directly from the catchment from which the archaeological data derive. The north basin charcoal record shows a steady increase in terrigenous charcoal input since the Toba crypto-tephra marker, over the period where archaeological evidence is most prevalent (Fig. 2B).

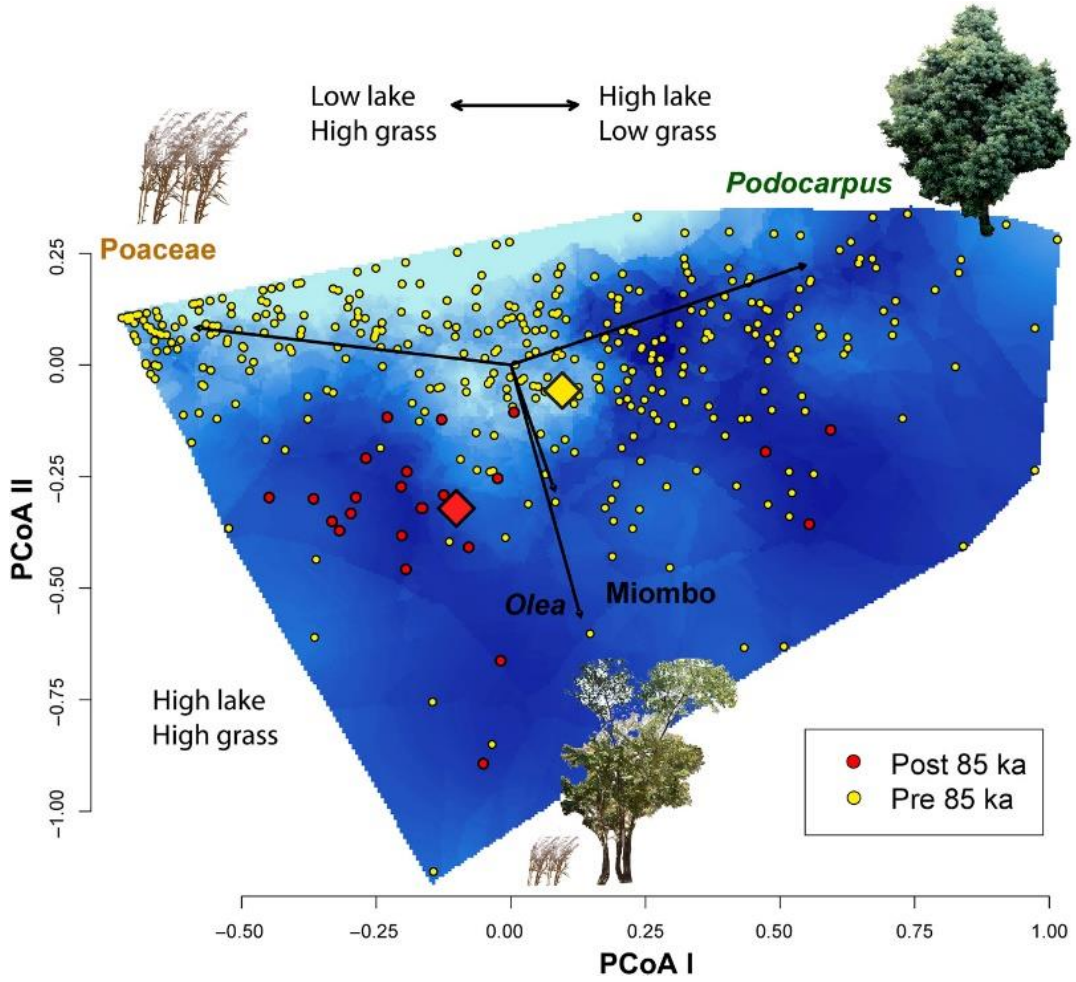

Fig. 3. PCoA analysis of pollen from Lake Malawi core MAL05-1B/1C (25). Each dot represents a single pollen sample at a given point in time, using the age model in the Supplementary Text and fig. S8. Vectors show the direction and gradient of change, with longer vectors representing a stronger trend. The underlying surface represents lake levels as a proxy for precipitation; darker blue is higher. A mean value for the PCoA eigenvalues is provided for the post-85-ka data (red diamond) and all pre-85-ka data from analogous lake levels (yellow diamond). "Analogous lake levels" are between −0.130-σ and −0.198-σ around the mean eigenvalue of the lake level PCA using the entire 636 ka of data.

Table 1. Results of MANOVA using *Podocarpus*, Poaceae, *Olea*, miombo, charcoal, and lake level as proxies for the environment. DF, degrees of freedom.

	DF	SumSquares	MeanSquares	F. model	R^2	*Pr* (>*F*)
Age > 85 ka	1	3.337	3.3374	13.603	0.0326	<0.0001
Residuals	404	99.121	0.2453		0.9674	
Total	405	102.458			1.0000	

DISCUSSION

Evidence for anthropogenic fire may reflect intentional use at the landscape scale, widespread populations creating more or larger on-site ignitions, alteration of fuel availability through harvesting of the understory, or a combination of these activities. Modern hunter-gatherers use fire to actively modify foraging returns (2). Their activities increase prey abundances, maintain mosaic landscapes, and increase pyrodiversity and succession stage heterogeneity (13). Fire is also important for on-site activities such as heat, cooking, defense, and socialization (14). Even small differences in the deployment of fire outside of natural lightning strikes can alter patterns of forest succession, fuel availability, and seasonality of ignitions. Reductions in arboreal cover and woody understory have the most potential to enhance erosion, while loss of species diversity in this region is tightly tied to loss of Afromontane forest communities (25).

Human control of fire is well established in the archaeological record from before the start of the MSA (15), but its use as a landscape management tool has only so far been documented in a few Paleolithic contexts. These include in Australia ca. 40 ka (36), Highland New Guinea ca. 45 ka (37), and ca. 50 ka at Niah Cave in lowland Borneo (38). In the Americas, anthropogenic ignitions have been implicated as major factors in the reconfiguration of faunal and floral communities as humans first entered these ecosystems, especially within the past 20 ka (16). These conclusions are necessarily based on correlative evidence, but the argument for a cause-and-effect relationship is strengthened where there is direct overlap of archaeological, geochronological, geomorphic, and paleoenvironmental data. Although marine core data offshore of Africa have previously provided evidence of altered fire regimes over the past ~400 ka (9), here, we provide evidence of anthropogenic impacts that draw from correlated archaeological, paleoenvironmental, and geomorphic datasets.

Identifying anthropogenic fire in the paleoenvironmental record requires evidence of temporal or spatial changes in fire activity and vegetation, demonstration that these changes are not predicted by climate parameters alone, and temporal/spatial coincidence between fire regime changes and changes in the human record (29). Here, the first evidence for extensive MSA occupation and alluvial fan formation in the Lake Malawi basin occurred alongside a major reorganization of regional vegetation that began ca. 85 ka. Charcoal abundances in the MAL05-1B/1C core are reflective of regional trends in charcoal production and sedimentation that show substantial differences after ca. 150 ka when compared to the rest of the 636-ka record (figs. S5, S9, and S10). This transition shows an important contribution of fire for shaping ecosystem composition that cannot be explained by climate alone. In natural fire regimes, lightning ignitions

typically occur at the end of the dry season (39). Anthropogenic fires, however, may be ignited at any time if fuels are sufficiently dry. On a site scale, humans can alter fire regimes continuously through collection of firewood from the understory. The net result of anthropogenic fire of any kind is that it has the potential to result in more consumption of woody vegetation, continuously throughout the year, and at a variety of scales.

In South Africa, fire was used in the heat treatment of stone for tool manufacture as early as 164 ka (12) and as a tool for cooking starchy tubers as early as 170 ka (40), taking advantage of resources that thrived in ancient fire-prone landscapes (41). Landscape fires reduce arboreal cover and are crucial tools in maintaining grassland and forest patch environments, which are defining elements of anthropogenically mediated ecosystems (13). If modification of vegetation or prey behavior was the intent of increased anthropogenic burning, then this behavior represents an increase in the complexity with which early modern humans controlled and deployed fire in comparison to earlier hominins and shows a transformed interdependency in our relationship with fire (7). Our analysis offers an additional avenue for understanding how human use of fire changed in the Late Pleistocene and what impacts these changes had on their landscapes and environments.

The expansion of alluvial fans during the Late Quaternary in the Karonga region may be attributable to changes in seasonal burning cycles under higher-than-average rainfall conditions, which resulted in enhanced hillslope erosion. The mechanism through which this occurred was likely by driving watershed-scale responses from fire-induced disturbance with enhanced and sustained denudation in the upper portions of the watersheds, and alluvial fan expansion in the piedmont environments adjacent to Lake Malawi. These responses likely included changes in soil properties to decrease infiltration rates, diminished surface roughness, and enhanced runoff as high precipitation conditions combined with reduced arboreal cover (42). Sediment availability is enhanced initially by the stripping of cover material and over longer time scales potentially by loss of soil strength from heating and from decreased root strength. The stripping of topsoil increased sediment flux, which was accommodated by fan aggradation downstream and accelerated laterite formation on the fans.

Many factors can control the landscape response to changing fire regime, and most of them operate at short time scales (42–44). The signal we associate here is manifest at the thousand-year time scale. Analytical and landscape evolution models have shown notable denudation rate changes over thousand-year time scales with recurrent wildfire-induced vegetation disturbances (45, 46). A lack of regional fossil records contemporaneous with the observed changes in charcoal and vegetation records impedes reconstruction of the impacts of human behavior and

environmental change on herbivore community composition. However, large grazing herbivores that inhabit landscapes that are more open play a role in maintaining them and in keeping woody vegetation from encroaching (47). Evidence of change across different components of the environment should not be expected to be simultaneous, but rather viewed as a series of cumulative effects that may have occurred over a prolonged period (11). Using a climate anomaly approach (29), we attribute human activity as a key driver in shaping the landscape of northern Malawi over the course of the Late Pleistocene. However, these impacts may be built on an earlier, less visible legacy of human-environment interactions. Charcoal peaks that appear in the paleoenvironmental record before the earliest archaeological dates may include an anthropogenic component that did not result in the same ecological regime change that is documented later in time and that did not involve sedimentation sufficient to confidently indicate human occupation.

Short sediment cores, such as that from the adjacent Lake Masoko basin in Tanzania, or shorter cores within Lake Malawi itself, show changes in the relative pollen abundances of grass to woodland taxa that have been attributed to natural climate variability over the past 45 ka (48–50). However, it is only with the longer perspective of the >600-ka pollen record of Lake Malawi, accompanied by the extensively dated archaeological landscape next to it, that it is possible to understand the longer-term associations between climate, vegetation, charcoal, and human activity. Although humans were likely present in the northern Lake Malawi basin before 85 ka, the density of archaeological sites after ca. 85 ka, and especially after 70 ka, indicates that the region was attractive for human occupation after the last major arid period ended. At this time, novel or more intensive/frequent usage of fire by humans apparently combined with natural climate shifts to restructure a >550- ka ecological relationship, ultimately generating an early preagricultural anthropogenic landscape (Fig. 4). Unlike during earlier time periods, the depositional nature of this landscape preserved MSA sites as a function of the recursive relationship between environment (resource distributions), human behavior (activity patterns), and fan activation (sedimentation/site burial).

The Anthropocene represents the accumulation of niche construction behaviors that have developed over millennia, at a scale unique to modern H. sapiens (1, 51). In the modern context, anthropogenic landscapes persist and have intensified following the introduction of agriculture, but they are extensions, not disconnections, of patterns established during the Pleistocene (52). Data from northern Malawi show that periods of ecological transition can be prolonged, complex, and iterative. Transformations of this scale reflect complex ecological knowledge by early modern humans and illustrate their transition to the globally dominant species we are today.

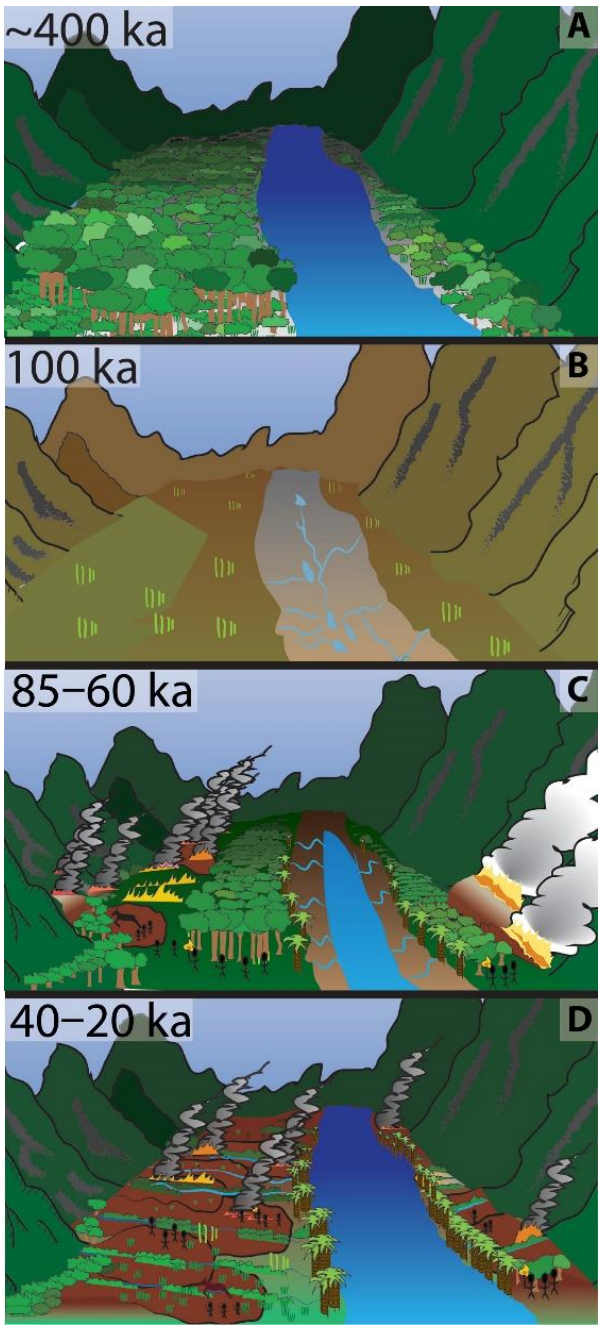

Fig. 4. Landscape evolution and ecology of the northern Lake Malawi basin. (**A**) ca. 400 ka: No detectable human presence. Wet conditions similar to today with high lake level. Diverse, non–fire-tolerant arboreal cover. (**B**) ca. 100 ka: No archaeological record, but human presence possibly detected by charcoal influx. Extremely arid conditions occur in a desiccated watershed. Commonly exposed bedrock, limited surface sediment. (**C**) ca. 85 to 60 ka: Lake level is increasing with higher precipitation. Human presence archaeologically detectable after 92 ka and concentrated after 70 ka. Burning of uplands and alluvial fan expansion ensue. Less diverse, fire-tolerant vegetation regime emerges. (**D**) ca. 40 to 20 ka: Ambient charcoal input in the northern basin increases. Alluvial fan formation continues but begins to abate toward the end of this period. Lake levels remain high and stable relative to the preceding 636-ka record.

MATERIALS AND METHODS

Fieldwork survey, excavation, and profile documentation

Site survey and recording of artifact and cobble characteristics on survey tracts followed protocols described in Thompson et al. (53). Test pit emplacement and main site excavation, including micromorphology and phytolith sampling, followed protocols described in Thompson et al. (18) and Wright et al. (19). Our Geographic Information System (GIS) maps based on Malawi geological survey maps of the region show a clear association between the Chitimwe Beds and archaeological sites (fig. S1). Placement of geologic and archaeological test pits in the Karonga region was spaced to capture the broadest representative sample possible (fig. S2). Geomorphic, geochronometric, and archaeological investigations of Karonga involved four main field approaches: pedestrian survey, archaeological test pitting, geological test pitting, and detailed site excavations. Together, these techniques allowed major exposures of the Chitimwe Beds to be sampled in the northern, central, and southern parts of Karonga (fig. S3).

Site survey and recording of artifact and cobble characteristics on pedestrian survey tracts followed protocols described in Thompson et al. (53). This approach had two main goals. The first was to identify localities where artifacts were actively eroding, and then place archaeological test pits upslope at those localities to recover artifacts in situ from buried contexts. The second goal was to formally document the distribution of artifacts, their characteristics, and their relationship to nearby sources of lithic raw material (53). For this work, a crew comprising three people walked at 2- to 3-m spacing for a combined total of 147.5 linear km, transecting across most of the mapped Chitimwe Beds (table S6).

Work concentrated first on the Chitimwe Beds to maximize the sample of observed artifacts, and second on long linear transects from the lakeshore to the uplands that crosscut different sedimentary units. This confirmed the key observation that artifacts located between the western highlands and the lakeshore are exclusively associated with the Chitimwe Beds or more recent Late Pleistocene and Holocene deposits. Artifacts found in other deposits are ex situ and have been relocated from elsewhere on the landscape, as revealed by their abundances, sizes, and degree of weathering.

Archaeological test pit emplacement and main site excavation, including micromorphology and phytolith sampling, followed protocols described in Thompson et al. (18, 54) and Wright et al. (19, 55). The primary aim was to understand the subsurface distribution of artifacts and fan deposits across the larger landscape. Artifacts are typically deeply buried within the Chitimwe Beds

in all places except at the margins, where erosion has begun to remove the top part of the deposit. During informal survey, two people walked across Chitimwe Beds that appear as mapped features on Government of Malawi geological maps. As these people encountered the shoulders of Chitimwe Bed deposits, they began to walk along the margins where they could observe artifacts eroding from the deposits. By placing excavations slightly (3 to 8 m) upslope from actively eroding artifacts, excavations could reveal their in situ locations relative to their containing sediments, without the necessity of laterally extensive excavations. Test pits were emplaced so that they would be 200- to 300-m distant from the next-nearest pit and thus capture the variation across Chitimwe Bed deposits and the artifacts they contained. In some cases, test pits revealed localities that later became the sites of full excavations.

All test pits began as 1 × 2 m squares, oriented north-south, and excavated in 20-cm arbitrary units, unless there was a noticeable change in sediment color, texture, or inclusions. Sedimentologic and pedologic attributes were recorded for all excavated sediment, which was passed uniformly through a 5-mm dry sieve. If deposit depth continued beyond 0.8 to 1 m, then excavation ceased in one of the two square meters and continued in the other, thus creating a "step" so that the deeper layers could be safely accessed. Excavation then continued until bedrock was reached, at least 40 cm of archaeologically sterile sediment had been reached below a concentration of artifacts, or excavation became too unsafe (deep) to proceed. In some cases, deposit depth required extension of the test pit into a third square meter, with two steps into the trench.

Geologic test pits had previously revealed that the Chitimwe Beds often appear on geologic maps because of a distinctive reddish color, when they include a wide range of stream and river deposits, alluvial fan deposits, and do not always present as red in color (19). Geologic test pits were excavated as simple pits designed to clean off mixed upper sediments to reveal the subsurface stratigraphy of deposits. This was necessary because the Chitimwe Beds erode as parabolic hillslopes with slumped sediments coating the slope and do not typically form clear natural sections or cuts. These excavations thus occurred either at the tops of Chitimwe Beds, where there was an inferred subsurface contact between the Chitimwe Beds and the underlying Pliocene Chiwondo Beds, or where river terrace deposits required dating (55).

Full archaeological excavations proceeded at localities that promised large assemblages of in situ stone artifacts, typically based on test pits or where artifacts could be seen eroding in large quantities from a slope. Artifacts from the main excavations were recovered from sedimentary units that were excavated separately in 1 × 1 m squares. Units were excavated as spits of either 10

or 5 cm if artifact densities were high. All stone artifacts, fossil bone, and ochre were piece plotted at each main excavation, with no size cutoff. The sieve size was 5 mm. Artifacts were assigned unique barcoded plotted find numbers if they were recovered during excavation, and find numbers within the same series were assigned to sieved finds. Artifacts were labeled with permanent ink, placed in a bag with their specimen label, and bagged together with other artifacts from the same context. After analysis, all artifacts were stored at the Cultural and Museum Centre, Karonga.

All excavation was conducted according to natural layers. These were subdivided into spits, with spit thickness dependent on artifact density (e.g., spit thickness would be high if artifact density was low). Context data (e.g., sediment attributes, context relationships, and observations about disturbances and artifact densities) were recorded in an Access database. All coordinate data (e.g., piece-plotted finds, context elevations, square corners, and samples) are based on Universal Transverse Mercator (UTM) coordinates (WGS 1984, Zone 36S). At main sites, all points were recorded using a Nikon Nivo C-series 5" total station that was established within a local grid oriented as closely as possible to UTM north. The location of the northwest corner of each excavated site and the volume of sediment removed for each are given in table S5.

Profiles of sedimentologic and pedologic features were documented from all excavation units using the U.S. Department of Agriculture classification scheme (56). Sedimentologic units were designated on the basis of grain sizes, angularity, and bedding features. Anomalous inclusions and disturbances relative to the sediment unit were noted. Soil development was determined on the basis of subsurface accumulation of sesquioxides or carbonates in the subsoils. Subaerial weathering (e.g., redox, residual Mn nodule formation) was also commonly documented.

OSL dating

Collection points for OSL samples were determined on the basis of an estimation of which facies were likely to yield the most reliable estimation of sediment burial age. At sample locations, trenches were made to expose authigenic sediment layers. All samples for OSL dating were collected by inserting light-tight steel tubes (approximately 4 cm in diameter and 25 cm in length) into the sediment profiles.

OSL dating measures the size of the population of trapped electrons within crystals such as quartz or feldspar arising from exposure to ionizing radiation. The bulk of this radiation originates from the decay of radioactive isotopes within the environment with a minor additional component in the tropical latitudes coming in the form of cosmic radiation. Trapped electrons are released upon exposure of the crystals to light, which occurs either during transport (the zeroing

event) or in the laboratory, where illumination occurs beneath a sensor (for example, a photomuliplier tube or charged couple device camera) that can detect photons emitted when the electrons return to their ground state. Quartz grains measuring between 150 and 250 μm were isolated through sieving, acid treatments and density separations, and analyzed either as small aliquots (<100 grains) mounted to the surface of aluminum disks or as single grains held within 300 by 300 mm wells drilled into an aluminum disc. Burial doses were typically estimated using single aliquot regeneration methods (57). In addition to assessment of the radiation dose received by grains, OSL dating also requires estimation of the dose rate through measurements using gamma spectrometry or neutron activation analysis of radionuclide concentrations within the sediments from which the sample was collected, along with determination of a cosmic dose rate by reference to the sample location and burial depth. Final age determination is achieved by dividing the burial dose by the dose rate. However, statistical modeling is required to determine an appropriate burial dose to use when there is a variation in the doses measured for individual grains or groups of grains. Burial doses were calculated here using the Central Age Model, in the case of single aliquot dating, or the finite mixture model in the case of single grain dating (58).

Three separate laboratories performed OSL analysis for this study. Detailed individual methods for each laboratory are presented below. In general, we applied OSL dating using regenerative-dose methods to small aliquots (tens of grains) rather than using single grain analysis. This is because small aliquots of samples had low recuperation ratios (<2%) during regenerative growth experiments and the OSL signals were not saturated at the levels of natural signals. Interlaboratory consistency of age determinations, consistent harmony of results within and between stratigraphic sections tested, and parity with geomorphic interpretations of ^{14}C ages from carbonates were the primary basis of this assessment. Single grain protocols were evaluated or performed at each laboratory, but independently determined to be inappropriate for use in this study. Detailed methods and analytical protocols followed by individual laboratories are provided in Supplementary Materials and Methods.

Lithic analysis

Lithic artifacts recovered from controlled excavations (BRU-I; CHA-I, CHA-II, and CHA-III; MGD-I, MGD-II, and MGD-III; and SS-I) were analyzed and described according to metric and qualitative characteristics. Weight and maximum dimension were measured for each artifact (weight was measured to 0.1 g using a digital scale; all dimensions measured to 0.01 mm with Mitutoyo digital calipers). All artifacts were also classified according to raw material (quartz, quartzite, chert, and other), grain size (fine, medium, and coarse), grain size homogeneity, color,

cortex type and coverage, weathering/edge rounding, and technological class (complete or fragmentary core or flake, flake piece/angular shatter, hammerstone, manuport, and other).

Cores were measured along their maximum length; maximum width; width at 15, 50, and 85% of length; maximum thickness; and thickness at 15, 50, and 85% of length. Measurements were also taken to assess the volumetric attributes of hemispherically organized (radial and Levallois) cores. Both complete and broken cores were classified according to reduction method (single or multiplatform, radial, Levallois, and other), and flake scars were counted at both ≥15 mm and at ≥20% of core length. Cores with five or fewer scars 15 mm were classified as "casual." Cortex coverage was recorded for the total core surface, and on hemispherically organized cores, the relative cortex coverage was recorded for each side.

Flakes were measured along their maximum length; maximum width; width at 15, 50, and 85% of length; maximum thickness; and thickness at 15, 50, and 85% of length. Fragmentary flakes were described according to the portion preserved (proximal, medial, distal, split right, and split left). Elongation was calculated by dividing maximum length by maximum width. Platform width, thickness, and exterior platform angle were measured on complete flakes and proximal flake fragments, and platforms were classified according to degree of preparation. Cortex coverage and location were recorded on all flakes and fragments. Distal edges were classified according to termination type (feather, hinge, and overshot). On complete flakes, the number and orientation of prior flake scars were recorded. When encountered, retouch location and invasiveness were recorded following the protocol established by Clarkson (59). Refitting programs were initiated for most of the excavated assemblages to assess reduction methods and site depositional integrity.

Lithic artifacts recovered from test pits (CS-TP1-21, SS-TP1-16, and NGA-TP1-8) were described according to a simpler scheme than those from controlled excavations. For each artifact, the following characteristics were recorded: raw material, grain size, cortex coverage, size class, weathering/edge damage, technological component, and preserved portion of fragmentary pieces. Descriptive notes were recorded for diagnostic features of flakes and cores.

Micromorphology and carbonate dating

Intact blocks of sediment were cut from profiles exposed in excavations and geological trenches. These blocks were stabilized in the field, using either plaster-of-Paris bandages or toilet paper and packaging tape, and transported to the Geoarchaeology Laboratory at the University of Tübingen, Germany. There, the samples were dried at 40°C for at least 24 hours. They were then indurated under vacuum, using a mixture of unpromoted polyester resin and styrene at a ratio of 7:3.

Methyethylketone peroxide was used as the catalyst, with resin-styrene mixture (3 to 5 ml/liter). Once the resin mixture had gelled, the samples were heated at 40°C for at least 24 hours to completely harden the mixture. The hardened samples were cut with a tile saw into chips measuring 6 × 9 cm, which were glued to a glass slide and ground to a thickness of 30 μm. The resulting thin sections were scanned using a flatbed scanner and analyzed under the naked eye and under magnification (×50 to ×200) using plane-polarized light, cross-polarized light, oblique incident light, and blue-light fluorescence. Terminology and descriptions of the thin sections follow guidelines published by Stoops (60) and Courty et al. (61).

Pedogenic carbonate nodules, collected from a depth of >80 cm, were sliced in half so that one half could be impregnated and studied in thin section (4.5 × 2.6 cm), using standard stereoscopic and petrographic microscopes, as well as cathodoluminescence (CL) microscopy. Control on the type of carbonate was given much care, as pedogenic carbonates form in connection to a stable ground surface, while groundwater carbonates form independently from a ground surface or soil.

Samples were drilled from the cut faces of pedogenic carbonate nodules, which were halved to be used for various analyses. The thin sections were studied by F.S. with standard stereo and petrographic microscopes of the working group for geoarchaeology and with a CL microscope at the working group for experimental mineralogy, both in Tübingen, Germany. Subsamples for radiocarbon dating were drilled with a precision drill from designated areas of ca. 3 mm in diameter in the opposing half of the nodule, avoiding zones with late recrystallization, abundant mineral inclusions, or great variability in calcite crystal sizes. The same protocol could not be followed for samples MEM-5038, MEM-5035, and MEM-5055 A, which were selected from loose sediment samples and too small to be cut in half for thin sectioning. However, corresponding micromorphological samples of the adjacent sediment, including carbonate nodules, were studied in thin section.

We submitted samples for ^{14}C dating to the Center for Applied Isotope Studies (CAIS), at the University of Georgia, Athens, USA. The carbonate samples were reacted with 100% phosphoric acid in evacuated reaction vessels to produce CO_2. CO_2 samples were cryogenically purified from the other reaction products and catalytically converted to graphite. Graphite 14C/13C ratios were measured using a 0.5-MeV accelerator mass spectrometer. The sample ratios were compared to the ratio measured from the oxalic acid I standard (NBS SRM 4990). Carrara marble (IAEA C1) was used as the background, and travertine (IAEA C2) was used as a secondary standard. The results are presented as percent modern carbon, and the quoted uncalibrated dates

are given in radiocarbon years before 1950 (years BP), using the ^{14}C half-life of 5568 years. The error is quoted as 1-σ and reflects both statistical and experimental errors. The dates have been corrected for isotope fractionation based on the isotope-ratio mass spectrometry–measured $\delta^{13}C$ values reported by C. Wissing at the laboratory for Biogeology in Tübingen, Germany, except in the case of UGAMS-35944r, which was measured at CAIS. Sample 6887B was analyzed in duplicate. A second subsample was drilled from the nodule for this purpose (UGAMS-35944r) from the sampling region indicated on the cut surface. All samples were corrected for atmospheric fractionation of 14C to 2-□ using the southern hemisphere application of the INTCAL20 calibration curve (table S4) (62).

Phytolith analysis

Sample (sediment, 0.7 g) was mixed with 0.1% preboiled solution of sodium hexametaphosphate $Na_6[(PO_3)_6]$ and sonicated (5 min). Orbital shaking took place overnight at 200 rpm. After clay dispersal, 3 N hydrochloric and nitric acids (HCl) (HNO_3) plus hydrogen peroxide (H_2O_2) were added. Then, sodium polytungstate ($3Na_2WO_4 \cdot 9WO_3 \cdot H_2O$) (Poly-Gee) at specific gravity 2.4 (preboiled) separated out phytoliths. This was followed by rinsing and centrifugation of samples at 3000 rpm for 5 min. Aliquots (15 μl) were mounted on boiled microscope slides with Entellan New (cover, 20 × 40 mm = inspected area). System microscopy was performed at 40× (Olympus BX41, Motic BA410E). Classification nomenclature followed the International Code for Phytolith Nomenclature (63). The referential baseline included modern plants from several African ecoregions (64) and local soils (65), as well as archaeological localities in the Malawi basin (19, 66).

Statistical methods

The OSL data from the landscape and paleoecological data from the Lake Malawi 1B/1C core were subjected to statistical analyses to examine how they changed before and after ~85 ka. Kernel density estimates (KDEs) of sedimentation were constructed following protocols developed in Vermeesch (67) and Kappler et al. (68) from 72 luminescence ages interpreted as originating from alluvial fan deposits (tables S1 to S3). KDEs provide reliable distributions of age occurrences when standard errors (SEs) overlap or the analytical imprecision of the true age is high (67). For the present analysis, each age was replotted 10,000 times along a normal distribution using the rnorm command in R based on the laboratory generated mean and 1-σ SE. The KDE was created in the "kde1d" package in R (69). Bandwidth was set to default, with data-derived parameters developed by Sheather and Jones (70).

To characterize the biotic environment, we used proportions of pollen from Poaceae, *Podocarpus*, miombo, and *Olea*. We used lake levels to characterize the abiotic environment. Over the ~636 ka span of the MAL05-1B/1C core for which pollen data are available, there have been several periods when lake level was equivalent to modern conditions. We have defined these analogous conditions by downsampling the published lake level data (21) to fit the pollen sample intervals (25), and then calculating the statistical mean of the principal components analysis (PCA) eigenvalue for all lake level proxies over the past 74 ka to represent "modern-like" lake conditions. The pollen sampling intervals effectively make this the statistical mean of lake levels between 21.4 and 56.2 ka [−0.130-σ and −0.198-σ (25)] and enable us to compare recent vegetation composition to its composition during older, analogous precipitation regimes.

To evaluate whether there were differences in the regional environmental structure before and after 85 ka, we conducted a NP-MANOVA (71). However, vegetation and lake level proxies are inherently different data types [pollen proportions (25) and the first principal component of all lake level proxies (21), respectively]. To conduct the MANOVA, these data must be the same type. Pollen, lake level proxies, and macrocharcoal were also sampled at different densities and intervals in the cores. To properly adjust the data so that once a single pollen sample and its age are matched to a single charcoal and lake level sample, we conducted a series of transformations. Because the pollen data were the most sparsely sampled, we used a spline to fit and downsample the lake level and charcoal data to match them. To make the pollen and lake level data equivalent, we conducted a PCoA using R software (72). PCoA is similar to the widely known PCA in that PCoA conducts a decomposition of a data matrix to obtain eigenvalues and their corresponding eigenvectors. The difference is that while PCA decomposes the variance-covariance matrix, PCoA solves for the eigenvalues of a distance matrix of the original data. To create the distance matrix, we used the X^2 distance, which is appropriate for proportion data, like pollen. The PCoA results in a set of scores, representing the original data, which can be plotted similar to PCA. In our case, these scores are not only useful for graphic illustration, but as they are normalized and Euclidean, they are identical to the lake level data and maintain all information contained by the original pollen dataset. This procedure allowed us to use the PCoA pollen scores in conjunction with lake level variable in the NP-MANOVA to test whether there was a difference in environment before and after 85 ka. For the Supplementary Materials statistics, biplots of species richness and lake level were constructed using the "ggplot2" package of R. Box and whiskers quartiles used the "boxplot" command in base R.

REFERENCES

1. N. L. Boivin, M. A. Zeder, D. Q. Fuller, A. Crowther, G. Larson, J. M. Erlandson, T. Denham, M. D. Petraglia, Ecological consequences of human niche construction: Examining long-term anthropogenic shaping of global species distributions. Proc. Natl. Acad. Sci. U.S.A. 113, 6388–6396 (2016).

2. F. Scherjon, C. Bakels, K. MacDonald, W. Roebroeks, Burning the land: An ethnographic study of off-site fire use by current and historically documented foragers and implications for the interpretation of past fire practices in the landscape. Curr. Anthropol. 56, 299–326 (2015).

3. S. White, Grass páramo as hunter-gatherer landscape. Holocene 23, 898–915 (2013).

4. R. Bliege Bird, C. McGuire, D. W. Bird, M. H. Price, D. Zeanah, D. G. Nimmo, Fire mosaics and habitat choice in nomadic foragers. Proc. Natl. Acad. Sci. U.S.A. 117, 12904–12914 (2020).

5. E. M. L. Scerri, M. G. Thomas, A. Manica, P. Gunz, J. T. Stock, C. Stringer, M. Grove, H. S. Groucutt, A. Timmermann, G. P. Rightmire, F. d'Errico, C. A. Tryon, N. A. Drake, A. S. Brooks, R. W. Dennell, R. Durbin, B. M. Henn, J. Lee-Thorp, P. deMenocal, M. D. Petraglia, J. C. Thompson, A. Scally, L. Chikhi, Did our species evolve in subdivided populations across Africa, and why does it matter? Trends Ecol. Evol. 33, 582–594 (2018).

6. P. Roberts, B. A. Stewart, Defining the 'generalist specialist' niche for Pleistocene *Homo sapiens*. Nat. Hum. Behav. 2, 542–550 (2018).

7. R. Biggs, W. Boonstra, G. Peterson, M. Schlüter, The domestication of fire as a social-ecological regime shift. PAGES—Past Global Chang. Mag. 24, 22–23 (2016).

8. J. A. J. Gowlett, The discovery of fire by humans: A long and convoluted process. Philos. Trans. R. Soc. Lond. B Biol. Sci. 371, 20150164 (2016).

9. M. I. Bird, J. A. Cali, A million-year record of fire in sub-Saharan Africa. Nature 394, 767–769 (1998).

10. C. W. Marean, Implications of late Quaternary mammalian fauna from Lukenya Hill (south-central Kenya) for paleoenvironmental change and faunal extinctions. Quatern. Res. 37, 239–255 (1992).

11. J. C. Thompson, D. K. Wright, S. J. Ivory, The emergence and intensification of early hunter-gatherer niche construction. Evol. Anthropol. 30, 17–27 (2021).

12. K. S. Brown, C. W. Marean, A. I. R. Herries, Z. Jacobs, C. Tribolo, D. Braun, D. L. Roberts, M. C. Meyer, J. Bernatchez, Fire as an engineering tool of early modern humans. Science 325, 859–862 (2009).

13. R. Bliege Bird, D. W. Bird, L. E. Fernandez, N. Taylor, W. Taylor, D. Nimmo, Aboriginal burning promotes fine-scale pyrodiversity and native predators in Australia's Western Desert. Biol. Conserv. 219, 110–118 (2018).

14. P. W. Wiessner, Embers of society: Firelight talk among the Ju/'hoansi Bushmen. Proc. Natl. Acad. Sci. 111, 14027–14035 (2014).

15. A. Glikson, Fire and human evolution: The deep-time blueprints of the Anthropocene. Anthropocene 3, 89–92 (2013).

16. N. Pinter, S. Fiedel, J. E. Keeley, Fire and vegetation shifts in the Americas at the vanguard of Paleoindian migration. Quat. Sci. Rev. 30, 269–272 (2011).

17. U. Ring, C. Betzler, Geology of the Malawi Rift: Kinematic and tectonosedimentary background to the Chiwondo Beds, northern Malawi. J. Hum. Evol. 28, 7–21 (1995).

18. J. C. Thompson, A. Mackay, S. Nightingale, D. Wright, J. H. Choi, M. Welling, H. Blackmore, E. Gomani Chindebvu, Ecological risk, demography and technological complexity in the Late Pleistocene of northern Malawi: Implications for geographical patterning in the Middle Stone Age. J. Quat. Sci. 33, 261–284 (2018).

19. D. K. Wright, J. C. Thompson, F. Schilt, A. S. Cohen, J.H. Choi, J. Mercader, S. Nightingale, C. E. Miller, S. M. Mentzer, D. Walde, M. Welling, E. Gomani Chindebvu, Approaches to Middle Stone Age landscape archaeology in tropical Africa. J. Archaeol. Sci. 77, 64–77 (2017).

20. E. Mortimer, D. A. Paton, C. A. Scholz, M. R. Strecker, P. Blisniuk, Orthogonal to oblique rifting: Effect of rift basin orientation in the evolution of the North basin, Malawi Rift, East Africa. Basin Res. 19, 393–407 (2007).

21. S. J. Ivory, M. W. Blome, J. W. King, M. M. McGlue, J. E. Cole, A. S. Cohen, Environmental change explains cichlid adaptive radiation at Lake Malawi over the past 1.2 million years. Proc. Natl. Acad. Sci. U.S.A. 113, 11895–11900 (2016).

22. D. Delvaux, Peri-Tethys Memoir: PeriTethyan Rift/Wrench Basins and Passive Margins, P. A. Ziegler, W. Cavazza, A. H. F. Robertson, S. Crasquin-Soleau, Eds. (Memoirs of the National Museum of Natural History, Paris 2001), pp. 545–567.

23. J. Mercader, J. C. Gosse, T. Bennett, A. J. Hidy, D. H. Rood, Cosmogenic nuclide age constraints on Middle Stone Age lithics from Niassa, Mozambique. Quat. Sci. Rev. 47, 116–130 (2012).

24. D. Richter, R. Grün, R. Joannes-Boyau, T. E. Steele, F. Amani, M. Rué, P. Fernandes, J. P. Raynal, D. Geraads, A. Ben-Ncer, J. J. Hublin, S. P. McPherron, The age of the hominin fossils from Jebel Irhoud, Morocco, and the origins of the Middle Stone Age. Nature 546, 293–296 (2017).

25. S. J. Ivory, A.-M. Lézine, A. Vincens, A. Cohen, Waxing and waning of forests: Late Quaternary biogeography of southeast Africa. Glob. Chang. Biol. 24, 2939–2951 (2018).

26. C. A. Scholz, T. C. Johnson, A. S. Cohen, J. W. King, J. A. Peck, J. T. Overpeck, M. R. Talbot, E. T. Brown, L. Kalindekafe, P. Y. O. Amoako, R. P. Lyons, T. M. Shanahan, I. S. Castaneda, C. W. Heil, S. L. Forman, L. R. McHargue, K. R. Beuning, J. Gomez, J. Pierson, East African megadroughts between 135 and 75 thousand years ago and bearing on early-modern human origins. Proc. Natl. Acad. Sci. U.S.A. 104, 16416–16421 (2007).

27. R. P. Lyons, C. A. Scholz, A. S. Cohen, J. W. King, E. T. Brown, S. J. Ivory, T. C. Johnson, A. L. Deino, P. N. Reinthal, M. M. McGlue, M. W. Blome, Continuous 1.3-million-year record of East African hydroclimate, and implications for patterns of evolution and biodiversity. Proc. Natl. Acad. Sci. U.S.A. 112, 15568–15573 (2015).

28. S. J. Ivory, R. Early, D. F. Sax, J. Russell, Niche expansion and temperature sensitivity of tropical African montane forests. Glob. Ecol. Biogeogr. 25, 693–703 (2016).

29. D. M. J. S. Bowman, J. Balch, P. Artaxo, W. J. Bond, M. A. Cochrane, C. M. D'Antonio, R. Defries, F. H. Johnston, J. E. Keeley, M. A. Krawchuk, C. A. Kull, M. Mack, M. A. Moritz, S. Pyne, C. I. Roos, A. C. Scott, N. S. Sodhi, T. W. Swetnam, R. Whittaker, The human dimension of fire regimes on Earth. J. Biogeogr. 38, 2223–2236 (2011).

30. J. Mercader, F. Astudillo, M. Barkworth, T. Bennett, C. Esselmont, R. Kinyanjui, D. L. Grossman, S. Simpson, D. Walde, Poaceae phytoliths from the Niassa Rift, Mozambique. J. Archaeol. Sci. 37, 1953–1967 (2010).

31. N. van Breemen, P. Buurman, Soil Formation, N. van Breemen, P. Buurman, Eds. (Springer Netherlands, Dordrecht, 1998), pp. 291–312.

32. B. P. Finney, T. C. Johnson, Sedimentation in Lake Malawi (East Africa) during the past 10,000 years: A continuous paleoclimatic record from the southern tropics. Palaeogeogr. Palaeoclimatol. Palaeoecol. 85, 351–366 (1991).

33. C. Whitlock, C. Larsen, Charcoal as a fire proxy, in Tracking Environmental Change Using Lake Sediments: Terrestrial, Algal, and Siliceous Indicators, J. P. Smol, H. J. B. Birks, W. M. Last, R. S. Bradley, K. Alverson, Eds. (Springer Netherlands, 2001), pp. 75–97.

34. R. P. Lyons, C. A. Scholz, M. R. Buoniconti, M. R. Martin, Late Quaternary stratigraphic analysis of the Lake Malawi Rift, East Africa: An integration of drill-core and seismic-reflection data. Palaeogeogr. Palaeoclimatol. Palaeoecol. 303, 20–37 (2011).

35. C. L. Yost, L. J. Jackson, J. R. Stone, A. S. Cohen, Subdecadal phytolith and charcoal records from Lake Malawi, East Africa imply minimal effects on human evolution from the ~74 ka Toba supereruption. J. Hum. Evol. 116, 75–94 (2018).

36. S. van der Kaars, G. H. Miller, C. S. M. Turney, E. J. Cook, D. Nürnberg, J. Schönfeld, A. P. Kershaw, S. J. Lehman, Humans rather than climate the primary cause of Pleistocene megafaunal extinction in Australia. Nat. Commun. 8, 14142 (2017).

37. G. R. Summerhayes, M. Leavesley, A. Fairbairn, H. Mandui, J. Field, A. Ford, R. Fullagar, Human adaptation and plant use in highland New Guinea 49,000 to 44,000 years ago. Science 330, 78–81 (2010).

38. C. O. Hunt, D. D. Gilbertson, G. Rushworth, A 50,000-year record of late Pleistocene tropical vegetation and human impact in lowland Borneo. Quat. Sci. Rev. 37, 61–80 (2012).

39. Y. Le Page, D. Oom, J. M. N. Silva, P. Jönsson, J. M. C. Pereira, Seasonality of vegetation fires as modified by human action: Observing the deviation from eco-climatic fire regimes. Glob. Ecol. Biogeogr. 19, 575–588 (2010).

40. L. Wadley, L. Backwell, F. d'Errico, C. Sievers, Cooked starchy rhizomes in Africa 170 thousand years ago. Science 367, 87–91 (2020).

41. T. Kraaij, F. Engelbrecht, J. Franklin, R. M. Cowling, A fiery past: A comparison of glacial and contemporary fire regimes on the Palaeo-Agulhas Plain, Cape Floristic Region. Quat. Sci. Rev. 235, 106059 (2020).

42. J. A. Moody, R. A. Shakesby, P. R. Robichaud, S. H. Cannon, D. A. Martin, Current research issues related to post-wildfire runoff and erosion processes. Earth Sci. Rev. 122, 10–37 (2013).

43. R. A. DiBiase, M. P. Lamb, Vegetation and wildfire controls on sediment yield in bedrock landscapes. Geophys. Res. Lett. 40, 1093–1097 (2013). 44. S. J. Ivory, M. M. McGlue, G. S. Ellis, A. M. Lézine, A. S. Cohen, A. Vincens, Vegetation controls on weathering intensity during the last deglacial transition in Southeast Africa. PLOS ONE 9, e112855 (2014).

45. E. Istanbulluoglu, R. L. Bras, Vegetation-modulated landscape evolution: Effects of vegetation on landscape processes, drainage density, and topography. J. Geophys. Res. Earth 110, F02012 (2005).

46. C. A. Orem, J. D. Pelletier, The predominance of post-wildfire erosion in the long-term denudation of the Valles Caldera, New Mexico. J. Geophys. Res. Earth 121, 843–864 (2016).

47. I. P. J. Smit, H. H. T. Prins, Predicting the effects of woody encroachment on mammal communities, grazing biomass and fire frequency in African savannas. PLOS ONE 10, e0137857 (2015).

48. Y. Garcin, A. Vincens, D. Williamson, G. Buchet, J. Guiot, Abrupt resumption of the African Monsoon at the Younger Dryas—Holocene climatic transition. Quat. Sci. Rev. 26, 690–704 (2007).

49. S. J. Ivory, A.-M. Lézine, A. Vincens, A. S. Cohen, Effect of aridity and rainfall seasonality on vegetation in the southern tropics of East Africa during the Pleistocene/Holocene transition. Quatern. Res. 77, 77–86 (2012).

50. G. H. DeBusk, A 37,500-year pollen record from Lake Malawi and implications for the biogeography of afromontane forests. J. Biogeogr. 25, 479–500 (1998).

51. E. C. Ellis, Anthropogenic transformation of the terrestrial biosphere. Philos. Trans. R. Soc. A Math. Phys. Eng. Sci. 369, 1010–1035 (2011).

52. A. M. Bauer, E. C. Ellis, The anthropocene divide: Obscuring understanding of social-environmental change. Curr. Anthropol. 59, 209–227 (2018).

53. J. C. Thompson, A. Mackay, V. de Moor, E. Gomani Chindebvu, Catchment survey in the Karonga District: A landscape-scale analysis of Provisioning and core reduction strategies during the Middle Stone Age of northern Malawi. African Archaeol. Rev. 31, 447–478 (2014).

54. J. C. Thompson, A. Mackay, D. K. Wright, M. Welling, A. Greaves, E. Gomani Chindebvu, D. Simengwa, Renewed investigations into the Middle Stone Age of northern Malawi. Quatern. Int. 270, 129–139 (2012).

55. D. K. Wright, J. Thompson, A. Mackay, M. Welling, S. L. Forman, G. Price, J. X. Zhao, A. S. Cohen, O. Malijani, E. Gomani Chindebvu, Renewed geoarchaeological investigations of Mwanganda's Village (Elephant Butchery Site), Karonga, Malawi. Geoarchaeology 29, 98–120 (2014).

56. P. J. Schoeneberger, D. A. Wysocki, E. C. Benham; Soil Survey Staff, Field Book for Describing and Sampling Soils, Version 3.0 (Natural Resources Conservation Service, National Soil Survey Center, 2012).

57. A. S. Murray, A. G. Wintle, The single aliquot regenerative dose protocol: Potential for improvements in reliability. Radiat. Meas. 37, 377–381 (2003).

58. R. F. Galbraith, R. G. Roberts, Statistical aspects of equivalent dose and error calculation and display in OSL dating: An overview and some recommendations. Quat. Geochronol. 11, 1–27 (2012).

59. C. Clarkson, An index of invasiveness for the measurement of unifacial and bifacial retouch: A theoretical, experimental and archaeological verification. J. Archaeol. Sci. 29, 65–75 (2002).

60. G. Stoops, Guidelines for Analysis and Description of Soil and Regolith Thin Sections (Soil Science Society of America, Inc., 2003).

61. M. A. Courty, P. Goldberg, R. Macphail, Soils and Micromorphology in Archaeology (Cambridge Manuals in Archaeology, Cambridge Univ. Press, 1989).

62. A. G. Hogg, T. J. Heaton, Q. Hua, J. G. Palmer, C. S. M. Turney, J. Southon, A. Bayliss, P. G. Blackwell, G. Boswijk, C. B. Ramsey, C. Pearson, F. Petchey, P. Reimer, R. Reimer, L. Wacker, SHCal20 southern hemisphere calibration, 0–55,000 years Cal BP. Radiocarbon, 759–778 (2020).

63. M. Madella, A. Alexandré, T. Ball, International code for phytolith nomenclature 1.0. Ann. Bot. 96, 253–260 (2005).

64. F. Runge, The opal phytolith inventory of soils in central Africa—Quantities, shapes, classification, and spectra. Rev. Palaeobotany Palynol. 107, 23–53 (1999).

65. J. Mercader, T. Bennett, C. Esselmont, S. Simpson, D. Walde, Soil phytoliths from miombo woodlands in Mozambique. Quatern. Res. 75, 138–150 (2011).

66. J. Mercader, T. Bennett, C. Esselmont, S. Simpson, D. Walde, Phytoliths from Middle Stone Age habitats in the Mozambican Rift (105-29 ka). J. Hum. Evol. 64, 328–336 (2013).

67. P. Vermeesch, On the visualisation of detrital age distributions. Chem. Geol. 312-313, 190–194 (2012).

68. C. Kappler, K. Kaiser, M. Küster, A. Nicolay, A. Fülling, O. Bens, T. Raab, Late Pleistocene and Holocene terrestrial geomorphodynamics and soil formation in northeastern Germany: A review of geochronological data. Phys. Geogr. 40, 405–432 (2019).

69. G. Geenens, C. Wang, Local-likelihood transformation Kernel Density Estimation for positive random variables. J. Comput. Graph. Stat. 27, 822–835 (2018).

70. S. J. Sheather, M. C. Jones, A reliable data-based bandwidth selection method for Kernel Density Estimation. J. R. Stat. Soc. B. Methodol. 53, 683–690 (1991).

71. E. Otárola-Castillo, M. G. Torquato, H. C. Hawkins, E. James, J. A. Harris, C. W. Marean, S. P. McPherron, J. C. Thompson, Differentiating between cutting actions on bone using 3D geometric morphometrics and Bayesian analyses with implications to human evolution. J. Archaeol. Sci. 89, 56–67 (2018).

72. R Core Team, R: A Language and Environment for Statistical Computing (R Foundation for Statistical Computing, 2020).

73. R. J. Hijmans, S. E. Cameron, J. L. Parra, P. G. Jones, A. Jarvis, Very high resolution interpolated climate surfaces for global land areas. Int. J. Climatol. 25, 1965–1978 (2005).

74. A. S. Murray, A. G. Wintle, Luminescence dating of quartz using an improved singlealiquot regenerative-dose protocol. Radiat. Meas. 32, 57–73 (2000).

75. A. G. Wintle, A. S. Murray, A review of quartz optically stimulated luminescence characteristics and their relevance in single-aliquot regeneration dating protocols. Radiat. Meas. 41, 369–391 (2006).

76. R. F. Galbraith, R. G. Roberts, G. M. Laslett, H. Yoshida, J. M. Olley, Optical dating of single and multiple grains of quartz from Jinmium Rock Shelter, Northern Australia: Part I, Experimental design and statistical models. Archaeometry 41, 339–364 (1999).

77. J. M. Olley, A. Murray, R. G. Roberts, The effects of disequilibria in the uranium and thorium decay chains on burial dose rates in fluvial sediments. Quat. Sci. Rev. 15, 751–760 (1996).

78. D. W. Zimmerman, Thermoluminescent dating using fine grains from pottery. Archaeometry 13, 29–52 (1971).

79. J. R. Prescott, J. T. Hutton, Cosmic ray contributions to dose rates for luminescence and ESR dating: Large depths and long-term time variations. Radiat. Meas. 23, 497–500 (1994).

80. V. Mejdahl, H. H. Christiansen, Procedures used for luminescence dating of sediments. Quat. Sci. Rev. 13, 403–406 (1994).

81. L. Bøtter-Jensen, E. Bulur, G. A. T. Duller, A. S. Murray, Advances in luminescence instrument systems. Radiat. Meas. 32, 523–528 (2000).

82. L. J. Arnold, R. G. Roberts, Stochastic modelling of multi-grain equivalent dose (De) distributions: Implications for OSL dating of sediment mixtures. Quat. Geochronol. 4, 204–230 (2009).

83. A. C. Londoño, S. L. Forman, T. Eichler, J. Pierson, Episodic eolian deposition in the past ca. 50,000years in the Alto Ilo dune field, southern Peru. Palaeogeogr. Palaeoclimatol. Palaeoecol. 346-347, 12–24 (2012).

84. J. Fain, S. Soumana, M. Montret, D. Miallier, T. Pilleyre, S. Sanzelle, Luminescence and ESR dating beta-dose attenuation for various grain shapes calculated by a Monte-Carlo method. Quat. Sci. Rev. 18, 231–234 (1999).

85. W. R. Van Schumus, Natural radioactivity in crust and mantle, in Global Earth Physics: A Handbook of Physical Constants, T. J. Ahrens, Ed. (American Geophysical Union, 1995), pp. 283–291.

86. M. J. Aitken, An Introduction to Optical Dating: The Dating of Quaternary Sediments by the Use of Photon-Stimulated Luminescence (Oxford Univ. Press, 1998).

87. J. M. Olley, T. Pietsch, R. G. Roberts, Optical dating of Holocene sediments from a variety of geomorphic settings using single grains of quartz. Geomorphology 60, 337–358 (2004).

88. R. G. Roberts, R. F. Galbraith, H. Yoshida, G. M. Laslett, J. M. Olley, Distinguishing dose populations in sediment mixtures: A test of single-grain optical dating procedures using mixtures of laboratory-dosed quartz. Radiat. Meas. 32, 459–465 (2000).

89. S. Stokes, S. Ingram, M. J. Aitken, F. Sirocko, R. Anderson, D. Leuschner, Alternative chronologies for Late Quaternary (Last Interglacial–Holocene) deep sea sediments via optical dating of silt-sized quartz. Quat. Sci. Rev. 22, 925–941 (2003).

90. V. Mejdahl, Thermolumiscence dating: Beta-dose attenuation in quartz grains. Archaeometry 21, 61–72 (1997).

91. M. Jain, L. Bøtter-Jensen, A. Singhvi, Dose evaluation using multiple-aliquot quartz OSL: Test of methods and a new protocol for improved accuracy and precision. Radiat. Meas. 37, 67–80 (2003).

92. J. D. Clark, C. V. Haynes Jr., An elephant butchery site at Mwanganda's Village, Karonga, Malawi, and its relevance for Palaeolithic archaeology. World Archaeol. 1, 390–411 (1970).

93. C. B. Ramsey, M. Scott, J. van der Plicht, Calibration for archaeological and environmental terrestrial samples in the time range 26–50 ka cal BP. Radiocarbon 55, 2021–2027 (2013).

94. C. Betzler, U. Ring, Sedimentology of the Malawi Rift: Facies and stratigraphy of the Chiwondo Beds, northern Malawi. J. Hum. Evol. 28, 23–35 (1995).

95. F. Dixey, The Tertiary and post-Tertiary lacustrine sediments of the Nyasan Rift-Valley. Quat. J. Geol. Soc. Lond. 83, 432–442 (1927).

96. A. M. Alonso-Zarza, V. P. Wright, Calcretes, in Carbonates in Continental Settings: Facies, Environments and Processes, Developments in Sedimentology, A. M. Alonso-Zarza, L. H. Tanner, Eds. (Elsevier, 2010), vol. 61, pp. 225–267.

97. G. M. Ashley, D. M. Deocampo, J. Kahmann-Robinson, S. G. Driese, Groundwater-fed wetland sediments and paleosols: It's all about water table, in New Frontiers In Paleopedology And Terrestrial Paleoclimatology, S. G. Driese, L. C. Nordt, Eds. (SEPM Society for Sedimentary Geology, 2013), vol. 104, pp. 47–61.

98. K. Zamanian, K. Pustovoytov, Y. Kuzyakov, Pedogenic carbonates: Forms and formation processes. Earth Sci. Rev. 157, 1–17 (2016). 99. M. N. Machette, Calcic Soils of the Southwestern United States, in Soils and Quaternary Geology of the Southwestern United States: Geological Society of America Special Paper, D. L. Weide, M. L. Faber, Eds. (Geological Society of America, 1985), vol. 203, pp. 1–21.

100. Z. Naiman, J. Quade, P. J. Patchett, Isotopic evidence for eolian recycling of pedogenic carbonate and variations in carbonate dust sources throughout the southwest United States. Geochim. Cosmochim. Acta 64, 3099–3109 (2000).

101. J. Quade, A. R. Chivas, M. T. McCulloch, Strontium and carbon isotope tracers and the origins of soil carbonate in South Australia and Victoria. Palaeogeogr. Palaeoclimatol. Palaeoecol. 113, 103–117 (1995).

102. C. V. Haynes, Interim report on the Quaternary geology of northern Malawi and southern Tanzania. Quaternaria 13, 307–318 (1970).

103. Z. M. Kaufulu, Sedimentary environments at the Mwanganda site, Malawi. Geoarchaeology 5, 15–27 (1990).

104. E. A. Stephens, Geological account of the northwest coast of Lake Malawi between Karonga and Lion Point, Malawi. Am. Anthrop. 68, 50–58 (1966).

105. A. M. Alonso-Zarza, V. P. Wright, Palustrine carbonates, in Carbonates in Continental Settings: Facies, Environments and Processes, Developments in Sedimentology A. M. Alonso-Zarza, L. H. Tanner, Eds. (Elsevier, 2010), vol. 61, pp. 103–131.

106. P. Freytet, E. P. Verrecchia, Lacustrine and palustrine carbonate petrography: An overview. J. Paleolimnol. 27, 221–237 (2002).

107. A. S. Goudie, Calcrete, in Chemical Sediments and Geomorphology, A. S. Goudie, K. Pye, Eds. (Academic Press, 1983), pp. 93–131.

108. E. P. Verrecchia, Litho-diagenetic implications of the calcium oxalate-carbonate biogeochemical cycle in semiarid Calcretes, Nazareth, Israel. Geomicrobiol. J. 8, 87–99 (1990).

109. R. Amit, Biogenic calcic horizon development under extremely arid conditions, Nizzana Sand Dunes, Israel. Adv. GeoEcol. 28, 65–88 (1995).

110. R. J. Schaetzl, S. Anderson, Soil Genesis and Geomorphology (Cambridge Univ. Press, 2005).

111. J. L. Slate, G. A. Smith, Y. Wang, T. E. Cerling, Carbonate-paleosol genesis in the Plio- Pleistocene St. David Formation, southeastern Arizona. J. Sediment. Res. 66, 85–94 (1996).

112. V. P. Wright, Calcrete, in Geochemical Sediments and Landscapes, D. J. Nash, S. J. McLaren, Eds. (Blackwell Publishing, 2007), pp. 10–45.

113. P. Alonso, C. Dorronsoro, J. A. Egido, Carbonatation in palaeosols formed on terraces of the Tormes river basin (Salamanca, Spain). Geoderma 118, 261–276 (2004).

114. G. Taylor, R. A. Eggleton, Regolith Geology and Geomorphology (John Wiley & Sons, Chicester, 2001).

115. V. P. Wright, Soil Micromorphology: A Basic and Applied Science, L. A. Douglas, Ed. (Elsevier, 1990), pp. 401–407.

116. G. Cailleau, E. P. Verrecchia, O. Braissant, L. Emmanuel, The biogenic origin of needle fibre calcite. Sedimentology 56, 1858–1875 (2009).

117. E. P. Verrecchia, K. E. Verrecchia, Needle-fiber calcite; A critical review and a proposed classification. J. Sediment. Res. 64, 650–664 (1994).

118. M. Wieder, D. H. Yaalon, Micromorphological fabrics and developmental stages of carbonate nodular forms related to soil characteristics. Geoderma 28, 203–220 (1982).

119. R. Crossley, Controls of sedimentation in the Malawi rift valley, Central Africa. Sediment. Geol. 40, 33–50 (1984).

120. J. R. Stone, K. S. Westover, A. S. Cohen, Late Pleistocene paleohydrography and diatom paleoecology of the central basin of Lake Malawi, Africa. Palaeogeogr. Palaeoclimatol. Palaeoecol. 303, 51–70 (2011).

121. M. J. Vepraskas, L. P. Wilding, L. R. Drees, Aquic conditions for Soil Taxonomy: Concepts, soil morphology and micromorphology, in Developments in Soil Science, A. J. Ringrose-Voase, G. S. Humphreys, Eds. (Elsevier, 1993), vol. 22, pp. 117–131.

122. M. J. McFarlane, Laterite and Landscape (Academic Press, 1976). 123. M. J. McFarlane, Mechanisms for lateritisation and the formation of erosion surfaces in parts of east and southern Africa. Bulletin de la Société Géographique de Liège 27, 149–155 (1991).

124. S. Nightingale, F. Schilt, J. C. Thompson, D. K. Wright, S. Forman, J. Mercader, P. Moss, S. Clarke, M. Itambu, E. Gomani Chindebvu, M. Welling, Late Middle Stone age behavior and environments at chaminade I (Karonga, Malawi). J. Paleolithic Archaeol. 2, 258–297 (2019).

125. J. E. Delvigne, Atlas of Micromorphology of Mineral Alteration and Weathering (Mineralogical Association of Canada, 1998).

126. I. Kovda, A. R. Mermut, Vertic features, in Interpretation of Micromorphological Features of Soils and Regoliths, G. Stoops, V. Marcelino, F. Mees, Eds. (Elsevier, 2010), pp. 109–127.

127. C. A. Stiles, C. I. Mora, S. G. Driese, Pedogenic iron-manganese nodules in Vertisols: A new proxy for paleoprecipitation? Geology 29, 943–946 (2001).

128. M. J. McFarlane, D. J. Bowden, Mobilization of aluminium in the wathering profiles of the African surface in Malawi. Earth Surf. Process. Landf. 17, 789–805 (1992).

129. E. Fritsch, C. R. Montes-Lauar, R. Boulet, A. J. Melfi, E. Balan, P. Magat, Lateritic and redoximorphic features in a faulted landscape near Manaus, Brazil. Eur. J. Soil Sci. 53, 203–217 (2002). 130. Y. Tardy, Petrology of Laterites and Tropical Soils (A. A. Balkema Publishers, 1997).

131. S. H. Ambrose, Chronology of the Later Stone Age and food production in East Africa. J. Archaeol. Sci. 25, 377–392 (1998).

132. K. Douze, A. Delagnes, The pattern of emergence of a Middle Stone Age tradition at Gademotta and Kulkuletti (Ethiopia) through convergent tool and point technologies. J. Hum. Evol. 91, 93–121 (2016).

133. S. McBrearty, A. S. Brooks, The revolution that wasn't: A new interpretation of the origin of modern human behavior. J. Hum. Evol. 39, 453–563 (2000).

134. C. R. Johnson, S. McBrearty, 500,000 year old blades from the Kapthurin Formation, Kenya. J. Hum. Evol. 58, 193–200 (2010).

135. J. Wilkins, M. Chazan, Blade production ~500 thousand years ago at Kathu Pan 1, South Africa: Support for a multiple origins hypothesis for early Middle Pleistocene blade technologies. J. Archaeol. Sci. 39, 1883–1900 (2012).

136. E. M. Scerri, J. Blinkhorn, K. Niang, M. D. Bateman, H. S. Groucutt, Persistence of Middle Stone Age technology to the Pleistocene/Holocene transition supports a complex hominin evolutionary scenario in West Africa. J. Archaeol. Sci. Rep. 11, 639–646 (2017).

137. C. Tribolo, A. Asrat, J. J. Bahain, C. Chapon, E. Douville, C. Fragnol, M. Hernandez, E. Hovers, A. Leplongeon, L. Martin, D. Pleurdeau, O. Pearson, S. Puaud, Z. Assefa, Across the gap: Geochronological and sedimentological analyses from the Late Pleistocene- Holocene sequence of Goda Buticha, Southeastern Ethiopia. PLOS ONE 12, e0169418 (2017).

138. A. J. H. Goodwin, An introduction to the Middle Stone Age in South Africa. S. Afr. J. Sci. 25, 410–418 (1928).

139. A. J. H. Goodwin, C. Van Riet Lowe, The Stone Age cultures of South Africa. Ann. S. Afr. Mus. 27, 1–289 (1929).

140. J. D. Clark, C. V. Haynes, J. E. Mawby, A. Gautier, Preliminary investigations in Malawi. Quaternaria, 305–354 (1970).

141. K. Faegri, J. Iversen, P. E. Kaland, K. Krzywinski, Textbook of Pollen Analysis (Blackburn Press, ed. 4th, 1989).

142. J. Maley, Contributions a l'etude du Bassin tchadien Atlas de pollens du Tchad. Bull. Jard. Bot. Nat. Belg. 40, 29–48 (1970).

143. R. Bonnefille, G. Riollet, Pollens de Savanes d'Afrique Orientale (Éditions du Centre national de la recherche scientifique, Paris, 1980).

144. E. C. Grimm, Tilia and Tiliagraph (Illinois State Museum, 1991).

145. E. C. Grimm, CONISS: A FORTRAN 77 program for stratigraphically constrained cluster analysis by the method of incremental sum of squares. Comput. Geosci. 13, 13–35 (1987).

146. R. Margalef, Information theory in ecology. Int. J. Gen. Syst. 3, 36–71 (1958).

147. J. Mercader, T. Bennett, C. Esselmont, S. Simpson, D. Walde, Phytoliths in woody plants from the miombo woodlands of Mozambique. Ann. Bot. 104, 91–113 (2009).

148. R. M. Albert, M. K. Bamford, D. Cabanes, Taphonomy of phytoliths and macroplants in different soils from Olduvai Gorge (Tanzania) and the application to Plio-Pleistocene palaeoanthropological samples. Quatern. Int. 148, 78–94 (2006).

149. B. M. Campbell, The Miombo in transition: Woodlands and welfare in Africa (Bogor, Indonesia, Center for International Forestry Research, 1996).

150. C. M. Ryan, M. Williams, How does fire intensity and frequency affect miombo woodland tree populations and biomass? Ecol. Appl. 21, 48–60 (2011).

151. W. A. Hoffmann, E. L. Geiger, S. G. Gotsch, D. R. Rossatto, L. C. R. Silva, O. L. Lau, M. Haridasan, A. C. Franco, Ecological thresholds at the savanna-forest boundary: How plant traits, resources and fire govern the distribution of tropical biomes. Ecol. Lett. 15, 759–768 (2012).

152. C. A. Scholz, A. S. Cohen, T. C. Johnson, J. King, M. R. Talbot, E. T. Brown, Scientific drilling in the Great Rift Valley: The 2005 Lake Malawi Scientific Drilling Project—An overview of the past 145,000 years of climate variability in Southern Hemisphere East Africa. Palaeogeogr. Palaeoclimatol. Palaeoecol. 303, 3–19 (2011).

153. J. Jouzel, V. Masson-Delmotte, O. Cattani, G. Dreyfus, S. Falourd, G. Hoffmann, B. Minster, J. Nouet, J. M. Barnola, J. Chappellaz, H. Fischer, J. C. Gallet, S. Johnsen, M. Leuenberger, L. Loulergue, D. Luethi, H. Oerter, F. Parrenin, G. Raisbeck, D. Raynaud, A. Schilt, J. Schwander, E. Selmo, R. Souchez, R. Spahni, B. Stauffer, J. P. Steffensen, B. Stenni, T. F. Stocker, J. L. Tison, M. Werner, E. W. Wolff, Orbital and millennial Antarctic climate variability over the past 800,000 years. Science 317, 793–796 (2007).

154. A. Berger, M.-F. Loutre, Insolation values for the climate of the last 10 million years. Quat. Sci. Rev. 10, 297–317 (1991).

Acknowledgments: We thank our collaborators at the Malawi Ministry of Youth, Sports, and Culture, and the Karonga community for assistance and permission in facilitating this research. An outstanding team of local crew worked on all excavations along with their cohorts at the Catholic University of Malawi. Many students, particularly of the University of Queensland Archaeological Field School, participated in fieldwork. We thank W. Fadillah for assistance with charcoal counting of MAL05-2A. We thank African Heritage Ltd. for logistical support during field operations. **Funding:** This work was supported by the National Geographic-Waitt Foundation grant W115-785 10 (to J.C.T., M.W., and E.G.-C.); the Australian Research Council Discovery Project DP110101305 (to J.C.T., A.S.C., and J.R.A.); Wenner-Gren Foundation grant 8539 (to J.C.T.); the University of Queensland Archaeological Field School (to J.C.T.); Korean Research Foundation Global Research Network Grant 2012032907 (to D.K.W. and J.-H.C.); Deutsche Forschungsgemeinschaft grants MI 1748/3-1 (to C.M.) and ME 4406/1-1 (to S.M.M.); Emory University (J.C.T.); Belmont Forum award number 1929563 (to S.J.I.); and Purdue University (to E.O.-C. and B.S.). C.M. is partially supported by the Research Council of Norway, through its Centres of Excellence funding scheme, SFF Centre for Early Sapiens Behaviour (SapienCE), project number 262618. Lake Malawi drill core analysis was supported by NSF-EAR-0602350 and the International Continental Scientific Drilling Program. J.M.'s laboratory work for this paper was made possible by the Canadian Social Sciences and Humanities Research Council under its Partnership Grant Program No. 895-2016-1017. The Institute

of Human Origins and Hyde Family Foundations provided publication funding support. **Competing interests:** The authors declare that they have no competing interests. **Data and materials availability:** All data are available in the main text, cited references, or the Supplementary Materials. Lake core sedimentation, magnetic susceptibility, lake level, and charcoal data can be found at the NOAA NCDC at https://ncdc. noaa.gov/paleo/study/24631, https://ncdc.noaa.gov/paleo/study/19424, and https://doi. org/10.1016/j.palaeo.2009.04.014. Pollen data are archived at Neotoma/African Pollen Database at https://neotomadb.org dataset #47600. Full code for the data downsampling and PCoA is archived at https://doi.org/10.17605/OSF.IO/7H94N; code for the KDE and supplementary analyses is at https://github.com/DaudiW/MalawiR.git. There were no human or animal subjects in this study. Submitted 2 December 2020 Accepted 17 March 2021 Published 5 May 2021 10.1126/sciadv.abf9776

Submitted 2 December 2020

Accepted 17 March 2021

Published 5 May 2021

10.1126/sciadv.abf9776

Citation: J.C. Thompson, D.K. Wright, S.J. Ivory, J.-H. Choi, S. Nightingale, A. Mackay, F. Schilt, E. Otárola-Castillo, J. Mercader, S. L. Forman, T. Pietsch, A. S. Cohen, J. R. Arrowsmith, M. Welling, J. Davis, B. Schiery, P. Kaliba, O. Malijani, M.W. Blome, C. A. O'Driscoll, S.M. Mentzer, C. Miller, S. Heo, J. Choi, J. Tembo, F. Mapemba, D. Simengwa, E. Gomani Chindebvu, Early human impacts and ecosystem reorganization in southern-central Africa. Sci. Adv. 7, eabf9776 (2021).

Supplementary Materials for paper D: Thompson et al. 2021

Early Human Impacts and Ecosystem Reorganization in Southern-Central Africa

Jessica C. Thompson*, David K. Wright*, Sarah J. Ivory*, Jeong-Heon Choi, Sheila Nightingale, Alex Mackay, Flora Schilt, Erik Otárola-Castillo, Julio Mercader, Steven L. Forman, Timothy Pietsch, Andrew S. Cohen, J. Ramón Arrowsmith, Menno Welling, Jacob Davis, Benjamin Schiery, Potiphar Kaliba, Oris Malijani, Margaret W. Blome, Corey A. O'Driscoll, Susan M. Mentzer, Christopher Miller, Seoyoung Heo, Jungyu Choi, Joseph Tembo, Fredrick Mapemba, Davie Simengwa, Elizabeth Gomani Chindebvu

*Corresponding author. Email: jessica.thompson@yale.edu (J.C.T); david.wright@iakh.uio.no (D.K.W.); sji15@psu.edu (S.J.I.)

Published 5 May 2021, Sci. Adv. 7, eabf9776 (2021)

DOI: 10.1126/sciadv.abf9776

Contents:

Other Supplementary Material for this manuscript includes the following:

(available at advances.sciencemag.org/cgi/content/full/7/19/eabf9776/DC1)

Tables S1 to S3, S5, and S7 (excel files not included in this PhD thesis)

SUPPLEMENTARY MATERIALS AND METHODS

Optical dating at the Luminescence Dating Laboratory Korea Basic Science Institute

Sampling and sample preparation. The majority of the OSL samples presented in this study were analyzed at the Korea Basic Science Institute (Table S1). In a subdued darkroom, pure quartz grains were extracted using routine sample preparation procedures. First, the size fraction of 180-

250 μm was separated by wet sieving. This fraction was then treated with 10% hydrochloric acid (HCl) and 10% hydrogen peroxide (H_2O_2) to remove carbonate and organic matter. After the density separation using sodium polytungstate solution (~ 2.60 $g \cdot cm^{-3}$), pure quartz grains were finally recovered through 40% hydrofluoric acid (HF) etching for 40 min., followed by a cleaning with concentrated HCl for 1 hr.

The quartz grains thus obtained were checked for the absence of feldspar contamination by IR stimulation on the natural and beta-irradiated (20 Gy) aliquots. After the chemical treatment mentioned above, the Infrared Stimulated Luminescence (IRSL) signal intensities in all samples were negligible compared with that of Blue Stimulated Luminescence (BSL), less than ~2%. As feldspars emit a luminescence signal when stimulated with both IR and blue light while quartz grains respond only to blue, this test implies that the feldspar grains in the samples were effectively removed.

Equivalent Dose (D_e) estimation. OSL measurements on quartz were carried out using a conventional Risø TL/OSL reader (Model TL/OSL-DA-20C/D) installed at Korea Basic Science Institute. The stimulation light source was blue-LEDs (470 nm, FWHM = 20 nm), which delivers ~ 30 $mW \cdot cm^{-2}$ to the sample position. The reader was also equipped with a $^{90}Sr/^{90}Y$ beta source delivering 0.091±0.002 $Gy \cdot s^{-1}$ to the samples. The OSL signal detection was through 7 mm Hoya U-340 optical filter. OSL signal measured during the initial 0.8 of optical stimulation (less the last 4 s as a background) was used to construct dose response growth curves and the estimation of D_e values.

Prior to D_e estimation of the samples, we performed prerequisite performance tests ("dose recovery tests") of the Single Aliquot Regenerative (SAR) dose protocol (74), which is now a widely applied robust experimental procedure for D_e estimation (75). For OSL measurements, aliquots consisting of hundreds of sand-sized quartz grains (3 mm aliquots) were used.

The dose recovery test was designed to see the ability of the SAR protocol to recover the known laboratory doses. In this study, this test was carried out using a selected set of samples from Chaminade II (CHA-II) (lab code LM12-10) and Chaminade III (CHA-III) trenches (lab codes LM13-01, LM13-02, LM13-03, LM13-04, LM13-05, LM13-06). In these experiments, the natural quartz grains were artificially bleached with blue-LEDs for 1000 s at room temperature and then stored for 10000 s to allow for the photo-transferred electrons in the shallow traps to thermally decay. After repeating the optical bleaching (for 1000 s at room temperature), known amount of beta dose (90 Gy) was administered to the samples LM12-10, which is regarded as a surrogate for

natural doses (given doses). Then, the SAR protocol was applied to measure the dose using various preheat temperatures (220°C – 295°C for 10 s in 15°C steps) with a fixed cut-heat of 220°C for 0 s. As shown in Fig. S11a, the given doses were well recovered, with the measured/given dose ratios being well within ±10% of unity. For samples from CHA-III, dose recovery results using a fixed preheat (260°C for 10 s) and cut-heat (220°C for 0 s) condition also showed the measured/given dose ratios within 10% of unity, which implies that those samples are suitable for the SAR protocol for dating (Fig. S11b).

All quartz D_e values were obtained by applying a Central Age Model (76) to D_e values that were independent of preheat temperatures (i.e. from preheat plateaus) as exemplified in Fig. S12. For the final D_e estimation, only aliquots showing recycling ratios within ±10% of unity and recuperations <10% of natural OSL signals were used for the statistical analysis. Aliquots whose D_e values were $>2D_0$ were also rejected for dating (75).

Dosimetry. Radionuclide concentrations of the samples were measured using a low-level high-resolution gamma spectrometer at the Korea Basic Science Institute. Conversion of the radionuclide concentrations to dose rates (D_r) used the model presented by Olley et al. (77). The final dose rates were derived based on assumed water content of 5±2 % and the attenuation factors given by Zimmerman (78) were applied. The contribution of cosmic ray to dose rate was calculated using the method presented in Prescott and Hutton (79).

Optical dating at the Luminescence Dating Research Laboratory (LDRL), University of Illinois at Chicago

Sample preparation. Sample preparations and measurements at Chaminade I (CHA-I), Mwanganda's Village (MGD) and Kafula Ridge West (KRW1) were performed at the Luminescence Dating Research Laboratory (LDRL) at the University of Illinois at Chicago (Table S2). The samples were prepared under subdued illumination from indirect light emitted from a sodium vapor bulb. The 150-250 μm quartz fraction was separated by sieving sediments, with magnetic minerals separated by agitation within an aqueous solution with multiple magnetic bars. The quartz fraction was then isolated by two density separations at 2.60 and 2.70 g/cm^3 using the heavy liquid Na-polytungstate. A 40-min immersion in HF was applied to remove the outer 10μm of grains and non-quartz minerals (80). The purity of the quartz extract was evaluated by petrographic inspection. Samples that showed >1% non-quartz minerals were retreated with HF and checked petrographically. Three representative quartz aliquots for each sample were exposed

to infrared light to detect for feldspathic components and yielded emissions < 300 counts per second, reflecting background counts and thus is a spectrally pure signal from quartz.

Application of Single Aliquot Regeneration protocols. SAR protocols (58) were used to estimate the D_e of the quartz fraction. Each aliquot covered about 1.5 to 2.0 mm circular area, which translates to about 200-500 quartz grains adhered to approximately 1-cm-diameter aluminum disc. Before the application of SAR protocols (Table S9), a series of tests was performed to evaluate the effect of preheating at 200°C, 220°C, 240°C, and 260°C on the regenerative signal as a dose recovery test (74). The first preheat temperature of 240°C yielded a consistent recovered dose well within 1-σ errors (< 5%) of the known dose. The second (or "cut" heat) was also 240°C and the final heating was at 280°C for 40 s to eliminate carryover of signal. Tests for dose recycling were also performed for each aliquot within the regenerative dose sequence and the results showed the last dose coincided well with the initial dose (at one-sigma errors).

For each sample, 30 aliquots of quartz were analyzed. SAR analyses were conducted by an Automated Risø TL/OSL–DA–15 system (81) with blue light excitation (90% power at 470±20 nm). Blue light excitation (470 ± 20 nm) is from an array of 30 light-emitting diodes that delivers ~15 mW/cm^2 to the sample position at 90% power. A Thorn EMI 9235 QA photomultiplier tube coupled with three 3-mm thick Hoya U-340 detection filters, transmitting between 290 and 370 nm, measured photon emissions. Laboratory irradiations used a calibrated ^{90}Sr/^{90}Y beta source coupled with the Risø Reader. All SAR emissions were integrated over the first 0.8 s of stimulation out of 40 s and background based on emissions for the last 30 to 40 s interval.

Luminescence characteristics. Typical OSL shine-down curves for 150-250 μm quartz grains from the assayed samples in this study are shown in Fig. S13. The curve shapes show that OSL signal was probably dominated by a fast component, with the OSL emission decreasing by 90 to 95% during the first four seconds of stimulation. The regenerative growth curves are modeled by using the exponential plus linear form. For many aliquots the regenerative growth curves (Fig. S13) show that (1) the recuperation was close to zero; (2) the recycling ratio was consistent with unity at 1-σ; (3) the OSL signal was not saturated at the level of the natural signal. Recuperation was lower than 2% for all samples, which indicates insignificant charge transfer during the measurements. These favorable luminescence characteristics for a majority of aliquots indicate that credible De values for these sediments can be determined using the SAR protocol.

Determination of D_e by the single aliquot protocols was accomplished by measuring 30 aliquots/sample (Table S2). A small (26 out of 480) number of aliquots were omitted in the final

D_e and age determination. Aliquots were removed from analysis for the following reasons: (1) if the recycling ratio was not between 0.90 and 1.10, (2) the "zero" L_x/T_x ratio was > 5% of the natural L_x/T_x ratio and/or (3) the natural L_x/T_x ratio was within 20% of the saturated level. Most aliquots were removed because of unacceptable recycling ratios and D_e values at or close to saturation with errors of >10%. Error analysis for D_e calculations assumed measurement error of 1% based on 2000 independent Monte Carlo simulations.

Equivalent Dose (D_e) values. Calculation of D_e by the single aliquot protocols was accomplished for 24 to 30 aliquots. Equivalent dose distributions were usually log normal and the scatter in the data was quantified with overdispersion values (Table S2; Fig. S14). An overdispersion percentage of a D_e distribution is an estimate of the relative standard deviation from a central D_e value in context of a statistical estimate of errors (58, 76). A lower overdispersion percentage indicates high internal consistency in D_e values within 2-σ errors. Overdispersion values >20% (at 2-σ limits) may indicate mixing of grains of various ages or partial solar resetting of grains, particularly for a D_e distribution that is negatively skewed (58, 76). Seven of the samples (UIC2858, UIC2855, UIC2853, UIC3095, UIC3096, UIC3119, UIC3092 and UIC3134) had overdispersion values >20% (at 2-σ), which may indicate the mixing of grains of different ages. However, some studies have concluded that overdispersion values between 20 and 32% may reflect a signal D_e population, particularly if the D_e distribution is symmetrical, with the dispersion related to variability associated with micro-dosimetry and/or sedimentary processes (e.g., 82). Seven samples from MGD had D_e distributions for quartz grains with overdispersion values of >31% (Table S2) and with highly negatively skewed distributions, thus the minimum age model provided the most appropriate estimate of D_e (58, 76). D_e values are presented in context of a radial plot that shows the associated precision, relative standard error and the 2-σ limits (Fig. S14).

Multiple Aliquot Regeneration (MAR) equivalent dose determinations. MAR dose protocols, similar to those used in Londoño et al. (83) were employed on two samples (UIC3091 and UIC3098), to test the accuracy of the SAR-based ages. The MAR analyses are predicated on different assumptions than SAR with resetting of naturals under UV light for two days prior to regenerative dosing. In turn, each aliquot is used for a single measurement, rather than a series with SAR, which necessitates just one sensitivity correction. The MAR equivalent doses overlap with the corresponding SAR values (Table S2), which yield greater confidence in the rendered equivalent doses.

Environmental dose rate (D_r). The environmental D_r is critical measurement for calculating a luminescence age, which is an estimate of the exposure of quartz grains to ionizing radiation from

the decay of the U and Th series, ^{40}K, and cosmic sources during the burial period. The U, Th and K concentrations were determined by inductively coupled plasma mass spectrometry (ICP-MS) by Activation Laboratory LTD, Ontario, Canada. The beta and gamma doses were adjusted according to grain diameter to compensate for mass attenuation for the D_r (84). Beta and gamma attenuation coefficients for 150 to 250 μm were 0.876 and 0.999, respectively. The U, Th and K2O content were determined from bulk sediment to calculate the D_r. A cosmic ray component, taking into account location, elevation and depth of strata sampled was between 0.17 and 0.20 mGy/yr and is included in the estimated D_r (79). There is uncertainty in assessing the moisture content of a sample during burial. We estimated moisture contents from present values, particle size characteristics and in reference to the water table. It is unknown, with the absence of gamma spectrometry, if there is disequilibrium in the U and Th decay series. A number of samples have relatively high thorium values, 10 to 25 ppm, with thorium to uranium ratios that exceed 6, which suggests a granitic source (85), though diagenetic processes cannot be dismissed for these elevated ratios.

Optical dating at the Griffith University Centre for Coastal Management.

OSL sample preparation. Samples from the Airport Site (APS) were prepared and analyzed at the Griffith University Centre for Coastal Management (Table S3). Sample preparation was designed to isolate pure extracts of 180-212 μm light safe quartz grains following standard procedures (e.g., 86). Acid treatments were applied to remove contaminant carbonates, feldspars, organics, heavy minerals and acid soluble fluorides. The outer ~10 μm alpha-irradiated rind of each grain was removed by double etching in 48% HF acid.

OSL analytical methods. A burial dose was determined from measurement of the OSL signals emitted by single grains of quartz. The etched quartz grains were loaded on to custom-made aluminum discs drilled with a 10 x 10 array of chambers, each of 300 μm depth and 300 μm diameter (81). The OSL measurements were made on a Risø TL/OSL DA-20 reader using a green (532 nm) laser for optical stimulation, and the ultraviolet emissions were detected by an Electron Tubes Ltd. 9235QA photomultiplier tube fitted with 7.5 mm of Hoya U-340 filter. Laboratory irradiations were conducted using a calibrated $^{90}Sr/^{90}Y$ beta source mounted on the reader. D_e were determined using a modified SAR protocol (87). A dose-response curve was constructed for each grain. OSL signals were measured for 1 s at 125°C (laser at 90% power), using a preheat temperature of 240°C (held for 10 s) for the 'natural' and regenerative doses, and a pre-heat of 160°C (held for 10 s) for the test doses (5 Gy). The OSL signal was determined from the initial 0.1 s of data, using the final 0.2 s to estimate the background count rate. Five hundred grains were

analyzed for samples 12_1, 12_3, 12_4, and 12_6 with 1000 grains analyzed for samples 12_2 and 12_5. Each disc was exposed to infrared (IR) radiation for 40 s at 125°C prior to measurement of the OSL signal to bleach any IR-sensitive signal. Dose recovery tests were also undertaken to confirm that this treatment did not diminish the OSL signal from quartz. Grains were rejected if they did not produce a measurable OSL signal in response to the 1 Gy test dose, had OSL decay curves that did not reach background after 1 s of laser stimulation, produced natural OSL signals that did not intercept the regenerated dose-response curves, or had unacceptable sensitivity changes throughout the measurement cycle, i.e. they were rejected if either of the second or third test dose signals varied in sensitivity from the first test dose (associated with the natural dose) by more than 20%. Recovery ratios varied between 1.6% and 5.6%, with most grains being rejected for failing to produce a measurable signal. Of the grains that did produce a measurable signal, most grains were rejected for displaying unacceptable test dose sensitivity change. Burial doses were calculated using the finite mixture model of Roberts et al., (88), with the number of components selected by observing the effect of changing the number of components on the Bayes Information Criterion, which was at a minimum where the ideal number of parameters in a model was found.

Lithogenic radionuclide activity concentrations of material extracted from sampling tubes were determined using Neutron Activation Analysis (Becquerel Laboratories Inc. Mississauga, Ontario, Canada). Dose rates were calculated assuming secular equilibrium, using the conversion factors of Stokes et al. (89) with β-attenuation factors taken from Mejdahl (90). Cosmic dose rates were calculated from Prescott and Hutton (79).

Equivalent dose (D_e) determination and age calculation. The age calculated from the highest proportion dose component as determined by MAR (91) are in bold font in Table S3. Fig. S14 shows radial plots of the dose components. The measured D_e (in Gy) for a grain can be read by tracing a line from the y-axis origin through the point until the line intersects the radial axis (log scale) on the right-hand side. The corresponding standard error for this estimate can be read by extending a line vertically to intersect the x-axis. The x-axis has two scales: one plots the relative standard error of the D_e estimate (in %) and the other ('precision') plots the reciprocal standard error. Therefore, values with the highest precisions and the smallest relative errors plot closest to the radial axis on the right of the diagram, and the least precise estimates plot furthest to the left. Values within the light grey shaded band are within 2-σ of the highest proportion dose component calculated using the Finite Mixture Model (88), with the grey line positioned within the center of the next highest proportion dose component.

The samples were determined to be generally poor candidates for single grain OSL dating, with poor recovery ratios and over-dispersed single grain dose distributions. Assuming the samples to comprise a dominant dose population with varying degrees of admixtures of younger or older material from higher or lower in the profile, then the most likely age for each sample is that calculated from the dose component making up the highest proportion of the sample (see Table S3). Calculating ages in this way resulted in one age inversion between samples 12_2 and 12_1 (see Fig. S14a, b), albeit that this age inversion is not apparent at 2-σ, nor if the second largest dose component from sample 12_2 is used to calculate an age. This second dose component was equivalent in size to the largest component, when considering the uncertainties on the proportional estimates (~3%). Considering the otherwise consistent age development with depth, we consider it possible that the correct age for sample 12_2 may be found by calculating the age using this alternative dose component, that is, 27.3 ± 2.0 Gy, resulting in an age calculated for 12_2 of 11.1 ± 1.0 ka.

SUPPLEMENTARY TEXT

Background geomorphic and depositional context of the Karonga region.

Systematic archaeological and geologic reconnaissance of the Karonga region necessitated detailed mapping of surficial deposits. A schematic overview of Dinosaur and Chiwondo beds was initially made by Ring and Betzler (17) in the Mwenirondo region south of Karonga (Fig. S16).

Dinosaur Beds are comprised of iron-rich sandstones dating to the Jurassic and Cretaceous periods. Chiwondo Beds are comprised of multiple aggraded fluvial and lacustrine phases that overlie the Dinosaur Beds in an angular unconformity. Initial deposition of the Chiwondo Beds was from braided streams during the upper Miocene (17). Bioclastic beaches, lagoons, ponds and "minor beach complexes" form over the basal Chiwondo indicating a phase of lake transgression (17). Meandering streams and deltaic deposits form the lake regression phase, on top of which diatomaceous limestone is discontinuously formed indicating a final lake high stand during the lower Pliocene (17).

Chitimwe Beds are alluvial fan deposits that unconformably overlie Chiwondo Beds (Fig. S17a). Their thickness varies from <10 m in the eastern sections to 10s of m thick to the west, where exposed. The schematic profile provided here is a general overview of the sedimentary structures, which indicate formation processes. Subangular to subrounded coarse sands in massive depositional units constitute the majority of the alluvial fan sediment package, but are variably

intercalated with cross-bedded sands, indicative of braided or anastomosing stream beds (19) (Fig. S17a,b).

Stone lines comprised of rounded to subrounded quartzite cobbles as well as Fe- Mn nodules are found discontinuously across the Karonga region (Fig. S17c). Basal sedimentary materials observed in the eastern portions of the project area (e.g., Mwanganda's Village, Bruce) are comprised of bioturbated sandy clay loam lagoon sediments (55). Stratified above these are clay-rich silt loams formed within overbank bar-like settings, which include Bk and Btk (pedogenic carbonate-rich) soil horizons. Based on OSL ages (Tables S1, S2, S3) and geomorphic interpretations, Chitimwe Beds formed between 92 and 15 ka as pulses of enhanced erosion and increased sediment flux due to fire-modified hillslopes across most of northern Malawi east of the Rift Valley escarpment and uplands west of Lake Malawi. Distinguishing features of the Chitimwe Beds are the well-developed laterite soils (Oxisols) that overprint the sediments. To date, buried laterite soils have not been identified.

Close to extant drainageways (e.g., the Rukuru River), eroded terraces dating to the middle to late Holocene have been documented, and are associated with phases of river aggradation followed by downcutting. Soils imprinted on the Holocene terraces are typically Entisols and have been previously identified by Clark and Haynes (92) as the Karonga Formation (Fig. S17d).

Context and timing of $CaCO_3$ nodule formation, Fe-Mn nodule formation, and lateritization in excavations in the Karonga area.

Carbonates

Carbonate-rich horizons in the Karonga area can be divided into four main groups: (1) Plio-Pleistocene Chiwondo deposits, (2) palustrine-pedogenic carbonates in clay deposits, (3) nodular calcretes (Bkm and B(t)k horizons), also known as (petro)calcic horizons, and (4) $CaCO_3$ features in near-surface horizons. Groups 2-4 are all subcomponents of the Late Pleistocene Chitimwe fan system. Age control of carbonate formation was made on the basis of radiocarbon ages, calibrated in Oxcal v.4.2.4 (93) using SHCal20 atmospheric curve (62) within the 95.4% cal BP range (Table S4).

(1) The Chiwondo beds are of Plio-Pleistocene age and have been described as whitish or greyish sandstones, marls and clays of mainly lacustrine origin (94, 95). Micromorphological samples from outcrops of the Chiwondo Formation at Malema (10.03°S, 33.94°E) and in profiles

nearby the excavation of Sadala South, confirm that these sediments are rich in shells and small (fish) bones, surrounded by a secondary calcite cement which under cathodoluminescence microscopy appears as large (max. 0.5 mm) equant calcite crystals with numerous growth phases.

The mainly lacustrine Chiwondo Beds are overlain with an angular unconformity by alluvial fan and fluviatile deposits of the Chitimwe Beds, consisting of sands and gravels which are oftentimes red in color, but not necessarily (94). The Chitimwe Beds form the context of the archaeological layers excavated by MEMSAP and contain numerous lithic artifacts. Profiles that capture the contact between Chiwondo and red or reddish-brown channel fill of the Chitimwe were documented in test pits nearby the Sadala South excavation (SS-TP4, SS-TP5, and SS-TP13). Chiwondo Bed sediments at SS-TP4 and SS-TP5 consisted of yellowish-white well-sorted silt rich in shells and fish bones, whereas at SS-TP13 it consisted of white, cemented very coarse angular sand to very fine gravel-sized quartz. Both facies show a violent effervescent reaction with HCl, indicating a high $CaCO_3$ content. The boundary with the overlying deposits is smooth, very abrupt, and characterized by many bioturbation features of termites and roots, originating from and filled with reddish-brown sediment of the Chitimwe. No carbonate accumulation was observed in the horizons directly overlying the Chiwondo, supporting the interpretation that biogenic and physicochemical precipitation are the main mechanisms in the formation of pedogenic carbonate horizons (discussed below), rather than the transportation of carbonates from the Chiwondo Beds within the phreatic system (96-98) or by eolian processes (99-101).

(2) Lagoonal clay and palustrine-pedogenic carbonates (paleosols). In low-elevation areas in distal parts of the fan system, carbonate horizons are found in laminated silty to very fine sandy clays and organic-rich wetland deposits. These palustrine-pedogenic carbonates formed in transitional horizons reflective of periodic inundation and consist of sandy to very fine gravelly deposits mixed with lagoonal clay deposits. Thorough mixing was brought about by bioturbation and soil cracking, and post-depositionally transformed the separate deposits into one unit (paleosol) of sandy to very fine gravelly loam. In earlier studies, these carbonate-rich lagoonal clay horizons have been assigned to the Chiwondo Beds (92, 102-104), possibly because they have a similar color as the fossil-bearing Chiwondo Beds, and because a vertical contact between the two facies (Chiwondo and lagoonal clay) had not been documented (104) and has still not been found. However, OSL dates from excavations at Mwanganda´s Village (MGD-I and MGD-III) indicate a Late Pleistocene age of the lagoonal deposits rather than Plio-Pleistocene, and radiocarbon dates on palustrine carbonates provided a terminus ante quem for the wetland soil between 40 ka cal BP and 28 ka cal BP (Table S4). At Mwanganda´s village (MGD-I, MGD-II, MGD-III) and in

excavations at Bruce (BRU-III, and BRU-GT2), lagoonal and palustrine deposits underlie fluvial and alluvial fan Chitimwe Bed deposits.

The carbonates in Group 2 result from early exposure and pedogenesis in lacustrine and wetland deposits (105, 106). Thin section analysis shows that physicochemical $CaCO_3$ precipitation, linked to evapotranspiration of surface- and groundwater, alternated with biogenic $CaCO_3$ precipitation, which typically occurs under vadose conditions, indicating changes in a near-surface groundwater level (105). Features indicative of per decensum illuvial leaching of calcium carbonate (107), such as finely laminated pendant coatings or link-cappings (108) were not observed in the palustrine carbonates. The importance of microbial activity catalyzing carbonate precipitation at these sites is stressed by abundant decaying plant remains and common calcified vegetal remains at MGD-II and BRU-GT2 (108-110). The palustrine soil components of these carbonate horizons show that they did not precipitate under permanently saturated conditions (111), but rather under (seasonally) changing wetland conditions (97). This suggests that the time gap between host sediment deposition and carbonate formation was not very large and that the depositional environment at these locations was relatively stable for several millennia before terrestrial sedimentation (fluvial, alluvial fan) become more dominant.

(3) Nodular calcretes (Bkm) and B(t)k horizons (paleosols). This group consists of buried calcic soil horizons, which formed within the vadose zone of well-aerated sandy to gravelly (Chitimwe) deposits under the influence of seasonally fluctuating groundwater perched on poorly permeable (clay) deposits (96, 111, 112). The transition between palustrine-pedogenic carbonates (group 2) and nodular calcretes is fluent and their formation mechanisms very similar. Extensive pedogenic carbonate formation is documented at MGD-III, BRU-III, and NGA-I. Nearby these sites, carbonate nodules can also be found cropping out at the surface, indicating that these soils are horizontally extensive. At MGD-III, MGD-II and BRU-III, argillic B(t)k horizons directly overlie laminated clay deposits with palustrine-pedogenic carbonates (group 2). Secondary carbonate formation has been significant in these horizons, with carbonates not only precipitating in void spaces, but also replacing clay, feldspar and quartz minerals (113, 114). Alpha-type (physicochemical) carbonate features dominate, though beta-type (biogenic) features can also be found (115). Physicochemical processes appear to have dominated and overprinted biogenic $CaCO_3$ features during the course of a complex formation history involving physicochemical precipitation from dissolved $CaCO_3$ in groundwater (capillary rise), biogenic precipitation, processes related to meteoric water input from rain and rivers, and vegetation (109, 110). Besides climatic conditions allowing for a high evapotranspiration potential, the position in the landscape

and the close association with lagoonal and palustrine clay mud deposits played decisive roles in the formation of nodular carbonate horizons. OSL dates give a relatively young age to the top of the mixed lagoonal/terrestrial deposits (paleosol) at Mwanganda´s Village: ca. 26 ka at MGD-I and ca. 24 ka at MGD-III. A radiocarbon dated pedogenic nodule from the nodular calcrete at MGD-III gave an ante quem date of 12,734-12,626 cal BP and palustrine and pedogenic carbonates from a Btk carbonate horizon at BRU-III fall between 29,612 and 19,747 cal BP (Table S4), signaling the presence of a stable soil surface which existed for many millennia. Also other pedogenic carbonates formed in sedimentary hosts of older age: the nodules at BRU-III formed in reddish brown Chitimwe Bed sediments dated to 41±5 ka (OSL sample LM13-19) and carbonate horizons at NGA-I formed in sediment dating to ca. 48 ka. Carbonate nodules from this soil were radiocarbon dated (providing a terminus ante quem of carbonate formation) to 23,486-19,455 cal BP (Table S4). While the major phases of pedogenic carbonate soil formation at NGA-I and BRU-III roughly overlap, a date from the calcrete at MGD-III (ca. 12,680 cal BP) suggests that in this area, carbonate formation continued until more recent times, possibly due to its low position in the landscape.

Based on our observations, carbonate horizons never overlie units of the red (laterized) alluvial fan sediments, which would also be very unlikely based on the soil properties of these soils. Carbonate horizons occur in mixed transitional sediments of lagoonal clay and coarse sandy terrestrial deposits (MGD-III, BRU-III) and in alluvial fan deposits (NGA-I). They are overlain and truncated by thick red alluvial sand and gravel deposits (NGA-I) or by stream deposits (MGD-III, BRU-III).

Initial phases of $CaCO_3$ precipitation appear to have taken place in a lagoonal wetland setting, gradually aggrading and transitioning into a terrestrial (fluvial/alluvial fan) environment. Changing soil conditions are reflected by extensive recrystallization in some horizons, evidence of dissolution around the periphery of nodules located near unit boundaries to more acidic channel fill (MGD-III), and the formation of many well-developed limpid clay coatings in carbonate horizons, deeply penetrating through cracks in carbonate nodules (BRU-III).

(4) More recent $CaCO_3$ features in higher parts of the vadose zone. The uppermost unit of MGD-I (Unit 7) provides an example of $CaCO_3$ features in a relatively well-drained near-surface soil horizon. In this modern soil, $CaCO_3$ precipitation is much more limited than carbonate paleosol horizons located deeper in the same profile or in lower parts of MGD. A variety of carbonate features can be observed, with a stronger representation of biogenic carbonate features compared to the lower carbonate horizons, in which physicochemical fabrics were more dominant

(115). Biogenic carbonate precipitation is mostly associated with bioturbation features of soil fauna and roots and includes common needle fiber calcite (NFC), a form of biomineralization related to fungi forming under vadose conditions (116-118). Therefore, precipitation was primarily promoted by organic activities involving fungi and microbial activity, with NFC as an early stage in the precipitation of the carbonates, and only secondarily by physicochemical precipitation related to groundwater aquifers (113). Pedogenic carbonate from this horizon was dated to 1179-989 cal BP (Table S4). Redox features commonly overprint $CaCO_3$ features, reflecting recurrent changes in soil moisture likely related to the climatic regime of dry and rainy seasons in Malawi.

Many $CaCO_3$ nodules in the upper units and transitional mixed unit of MGD-I derive from reworked lagoonal and palustrine deposits, occurring together with other reworked fragments of the paleosol. One of these nodules was dated to 40,403-39,502 cal BP, pre-dating the surrounding sediment, which was dated to 26±1 ka with OSL, by more than 13,000 years. Most near-surface alluvial fan sediments in Karonga are lateritic (see below) and contain very few $CaCO_3$ features, which only occur in association with roots and faunal bioturbation features.

Alluvial fan deposits, Fe-Mn nodules and lateritization

Several archaeological sites are located in the artifact-rich alluvial fan deposits composed of red (oxidized) sands and gravels, known as the Chitimwe Beds. The alluvial fan sands and gravels have been strongly modified by tropical soil formation, leading to the formation of iron-manganese (Fe-Mn) nodule horizons and deeply weathered soils. In many profiles, advanced soil weathering has led to lateritization. Besides chemical weathering, termite activity is an important component of lateritization, and has transformed the fine fraction (materials smaller than ca. 0.01 mm) of many laterites into a fine-granular microstructure, reaching down until the groundwater fluctuation zone.

The three processes of alluvial fan sedimentation (1), precipitation of Fe-Mn nodules (2) and pedogenic laterite formation (3) offer insight in the formation of artifact contexts and the timing and environmental circumstances of human occupation in the Karonga area. For the sake of clarity, they are discussed separately. However, considerable overlap exists between the different processes.

(1) Alluvial fan deposits form the main sedimentary context of artifacts in the Karonga area. The alluvial fans are characterized by abundant stream cut-and-fill. Alluvial fan sedimentation was originally thought to have activated during the Middle to Late Pleistocene by an interplay between tectonism, leading to localized uplift in the area, and climatic changes (94, 119, 120). This created an inviting landscape for humans who may have focused their activities especially in

palustrine environments (19). This general scenario may still be true, but no alluvial fan deposits have been directly dated to beyond ~92 ka. Furthermore, human-induced ecological changes that transformed the relationship between precipitation and tree cover likely contributed to the mobilization of sediments across the Late Pleistocene landscape.

(2) Fe-Mn nodules are often part of laterites but are also found in non-lateritic soil profiles. They can form as hydromorphic groundwater features (121) or in the vadose zone. In Karonga, the groundwater fluctuation zone is usually characterized by distinct redox masses (mottles), whereas Fe-Mn nodules form primarily in the lower part of the vadose zone in relation to intensive soil wetting following seasonal rains (122, 123). Profiles with coarse deposits contain irregular Fe-Mn nodules with many sand inclusions, while profiles with fine textures contain smaller nodules with concentric bands (Supplementary Online Material by Schilt in (124)). The formation of concentric nodules is linked to vertic soil properties of loamy sediments, in which repeated shrinking and swelling can lead to centrifugal cortification (125). The concentric bands form in response to seasonal changes in soil moisture when soil permeability is restricted (125- 127). Several profiles in Karonga (APS, CHA-II) do not have concentric nodules, but larger, irregular nodules (Supplementary Online Material in Wright et al. (19) by Schilt et al.). With time, pedogenic Fe-Mn nodules gently travel downward due to bioturbation by termites and continuous dissolution and evacuation of materials (saprolite collapse), which can also lead to leveling and lowering of surfaces (114, 128). The residual Fe-Mn nodules accumulate at a point of resistance, for example closely packed grain-supported gravels, or where pedo- and bioturbation stops. This is generally in the lowermost regions of the laterite and at or near the upper limit of the groundwater fluctuation zone. At CHA-I and CHA-II, Fe-Mn nodules show zones containing inclusions of different grain sizes reflecting different phases of formation, as well as signs of damage and dissolution, indicating an old age (125).

Winnowed surfaces of Fe-Mn nodules and horizons with redeposited Fe-Mn nodules are also observed in the Karonga area. Where found inside a profile as part of gravels, the occurrence of redeposited, detrital nodules indicates that soils with Fe-Mn nodules were present in the area at time of their (re)deposition.

(3) Lateritization. Here, we use the terms laterite, lateritization and laterite formation to describe the general process of severe weathering in the vadose zone. Lateritization leads to the depletion of silica and relative accumulation of kaolinite and iron oxides, resulting in thick, homogeneous reddened horizons (129). Lateritic soils are usually underlain by old, buried soil

horizons reflecting multiple phases of accretion and soil formation and by clay-rich gleyed sediments, forming a light-colored, reduced groundwater and mottled zone (110, 130).

The timing of Fe-Mn nodules, laterites and artifacts of the Chitimwe Beds.

It is typical to find concentrations of Fe-Mn nodules just below, or in the lower regions of laterites (e.g., CHA-II). However, lateritization also occurs without accompanying Fe-Mn horizons (e.g., CHA-III, CHA-TP7). The other way around, in situ Fe-Mn nodules can be found in profiles with less advanced lateritization (e.g., CHA-I, SS-TP9), or actively forming in non-lateritic profiles in which other soil processes, such as vertic activity, dominate (CHA-TP9).

In Karonga, artifacts in excavations in the Chitimwe Beds are found in large quantities among and directly above Fe-Mn nodule concentrations, and are less frequent below any lowermost Fe-Mn nodule concentration in a profile. In cases where artifacts directly overlie Fe-Mn concentrations, the possibility of a winnowed surface composed of exposed Fe-Mn nodules needs to be considered. Redeposited Fe-Mn nodules in a gravel unit dating to ca. 40 ka in CHA-I (UIC3470, (124)) indicate that soils with Fe-Mn nodules were already forming in the area by that time.

The exact timing of lateritization is difficult to determine. However, a few things are known about the environment in which laterites form. Laterite formation occurs where seasons are marked and soils are exposed to the changing weather conditions, leading to alternating soil conditions in the upper horizons. Forest cover protects the soil climate from heat and precipitation, and therefore laterites will more likely form in more exposed soils in unforested grassland environments. In 1807, Buchanan (cited in 122) reported on laterites found in grassland areas, which were in many cases created and maintained by human action, involving grazing of cattle but especially fires for clearance and cultivation, or to aid in hunting. Although wildfires might have a similar effect, it is thought that especially the intensity and duration of human-induced fires may have led to the widespread formation of laterites. Advanced lateritization is very difficult to reverse, which is why these soils can also be found in (re)forested areas (122).

Characterization of lithic artifact assemblages

The presence of foraging populations around Karonga, northern Malawi, is documented in the archaeological record by the regular and persistent production, use, and discard of stone tools. Characterized through extensive survey and excavations, the stone tool assemblages of the Karonga region are attributable to the MSA, and record the landscape-scale technological activities of forager groups. As the most durable evidence of human behavior, stone tools reflect foragers'

adaptive responses to environmental and social conditions, and their interaction with variable topographies and resources.

The MSA is a technologically defined entity with pan-African distribution that is common in the period from roughly 315 – 40 ka (24, 131, 132). The MSA is associated with the proliferation of *Homo sapiens* and complex behavior such as long-distance transportation or trade of material, expanded foraging regimes, regionalization of technologies, symbolism, and an increase in activity-specific tools that required extended chains of planning and technological activity (133). Elements typical of the MSA have been documented as early as 500 ka (134, 135), and persist until the very late Pleistocene and into the Holocene in places (136, 137). As a technological designation, the MSA was initially defined according to the production of pointed forms and the regular use of prepared core technology (138, 139), in which successive stages of stone reduction were required to produce flakes of an intended shape and size. Such core preparation is taken to be indicative of an increasing ability to plan and execute complex chains of activity, and is generally associated with increasingly task-driven stone reduction.

MSA stone tool assemblages were first identified in the alluvial fan deposits of the Chitimwe Beds of northern Malawi by J.D. Clark and colleagues in the 1960s (92, 140); since 2009, archaeological research has been undertaken by the Malawi Earlier- Middle Stone Age Project (MEMSAP) (19, 53-55). Across the study area, hundreds of thousands of MSA artifacts can be found eroding from the Chitimwe Beds, and subsurface investigation has uncovered many dense, in situ archaeological deposits. These assemblages have been studied with the intent of understanding the techno-cultural repertoires of MSA foraging groups, landscape-use patterns (including raw material acquisition and transport) across the region, and the depositional integrity of the individual sites. Details of the artifact assemblages are found in Table S5.

Quartz and quartzite are the most commonly used stone types in all assemblages from northern Malawi, and derive from abundant and locally-available river cobble beds (53). Chert and other fine-grained, siliceous materials are very occasionally recovered in the stone tool assemblages; their relative scarcity as stone tools reflects their low frequencies in the cobble beds. During excavation at sites APS-I, BRU-I, SS-I, and NGAI, exposed cobble beds were sampled to assess the types and frequency of materials that would have been available to MSA foragers. The results indicate that raw material use closely mirrors raw material availability from nearby cobble beds, which are influenced by the underlying geology of distinct catchment areas. A north-south gradient of quartzite and quartz use thus exists across the study region: assemblages from the sites further north (Chaminade study area) are generally dominated by quartzite, but in as one moves

south, into the Sadala region, quartz becomes the dominant material. At the southern extremes of the study region, at NGA-I, WW-I, and VIN-I, quartz artifacts almost exclusively represent the assemblages. An outlier in this trend is CHA-III which includes >70% quartz in most of the MSA contexts. A secondary aspect of raw material choice in the Karonga assemblages is clast size: in catchments where quartzite and quartz are relatively equally represented in the cobble beds, quartzite clasts are larger on average, and larger cobbles appear to have been preferentially selected over small clasts. This has a contributing effect to the predominance of quartzite as a preferred material in these areas.

The northern Malawi MSA stone tool assemblages comprise a variety of approaches to stone tool production, as witnessed in both the cores and the flake products removed from them. In most Karonga MSA assemblages, radially flaked cores - in which a series of flakes are initiated from an outer perimeter delimiting two opposed surfaces, directed inward to the center of the flaking surface - are the most common (Fig. S4c-e, i-k).

The majority of radial cores in the Karonga assemblages are only partially reduced, with cobble cortex remaining on one or both flaking surfaces. The next most common core type is the casual core, which has five or fewer flake removals (Fig. S4a). These removals may exhibit a variety of orientations, and thus the casual core designation is in reference to the degree of exploitation of the core, rather than an approach to producing flakes. Nevertheless, casual core reduction signals a short use-life and a relative expediency of flaking, with minimal investment in preparation or maintenance. Single platform cores feature a single row of adjacent removals from the same flaking platform, oriented normal to the platform's plane. Multiplatform cores have removals initiated from two or more platform surfaces, with flakes often removed perpendicular to one another (Fig. S4l). The final type of core most commonly found in the Karonga assemblages is a Levallois core (Fig. S4b, f). Like radially flaked cores, Levallois cores feature two opposed flaking surfaces, although with this method of reduction, flakes are removed from both surfaces as a means of preparing the core for the removal of a flake or flakes of some predetermined size or shape. In general, cores from the Karonga MSA assemblages are not greatly reduced—most retain some degree of cobble cortex coverage, and even the most heavily flaked cores rarely show more than 12 flake removals. This implies that cores were not extensively transported or maintained, but had relatively short use-lives. It is likely that the abundance of cobbles from easily accessible cobble beds made it unnecessary to conserve or transport raw materials clasts.

Flakes recovered from the Karonga assemblages show varied preparation and reduction techniques, and typically have a length:width ratio around 1.0, indicating that the elongation of

flakes (and thus, elongated cutting edges) was not a priority for MSA toolmakers in this region. Elongated flakes, or blades, are rare in all assemblages, appearing at less than 2% frequency. Similarly rare are pointed forms, such as might indicate an investment in hunting armatures as seen elsewhere in the African MSA. Also missing from the Karonga assemblages is the regular use of retouching to modify the margins of flake blanks. Retouching shapes edges and surfaces to produce tools, presumably toward some intended final form, or rejuvenates cutting edges to extend the use-life of a tool. Its near-absence in northern Malawi may indicate a flexibility with regard to how stone tools were produced and used across a resource-abundant landscape (18).

The depositional integrity of the recovered stone tool assemblages is affirmed by the degree of post-depositional modification of individual lithic artifacts. Stone tools may become damaged or their edges rounded through fluvial movement or long-term exposure on a land surface; therefore, assessing the degree of weathering, rounding, or edge damage to stone tools can indicate the degree to which artifacts have been displaced since their original discard and deposition. A further indicator of site integrity is the presence of groups of artifacts that belong to discrete episodes of tool production. Conjoining artifacts are fragments of a single artifact that broke incidentally either during the original flaking process, as it was being used, or following deposition. Refitting artifacts (flakes, or flakes and cores) represent successive removals from a single tool stone clast. In addition to showing the stages of reduction, the presence of refitting and conjoining artifacts indicates that the artifacts were likely flaked and deposited in the location where they were ultimately buried, and that post-depositional translocation is minimal. Thus, refitting artifacts evidence a time-restricted event of hominin technological activity. The majority of the dated assemblages from northern Malawi show a high frequency of artifacts in a fresh or unweathered condition, as detailed in Table S5, and many feature refitting and conjoining sets of artifacts, including long sequences that show successive flake removals in a reduction sequence (Fig. S4d, h).

Construction of the age-depth profile and paleoenvironmental analysis of Lake Malawi

Age model and macrocharcoal analysis

Details of regarding the lake level reconstruction and its paleoclimatic context can be found in Ivory et al. (21). Sediment samples were taken at 16-cm intervals, resulting in a total sample set of 1945 and a temporal resolution of 570 yr. Samples were split into two aliquots; the first was weighed then disaggregated using deionized water and freezethaw treatment (often requiring

multiple cycles), and finally washed through 63-μm mesh stainless steel sieves to recover all material sand-sized and greater. The second aliquot was weighed wet, oven-dried at 60°C for at least 48 hours, and re-weighed to determine water content. This calculated water content was then used to determine the dry weight of the sieved aliquot.

Sediment samples for microcharcoal analysis were taken at ~50cm intervals (for MAL05-2A) and 16-cm intervals for MAL05-1B/1C. Samples were split into two aliquots; the first was weighed and then disaggregated using deionized water and freeze– thaw treatment when required, and finally washed through 63-μm mesh stainless steel sieves to recover all microcharcoal fragments. A second aliquot was weighed wet, ovendried at 60 °C for at least 48 h, and reweighed to determine water content. This calculated water content was then used to determine the dry weight of the sieved aliquot. Charcoal samples were counted at 60X using an Olympus SZX12 stereomicroscope. Flux rates were determined by normalizing dry sample volumes by sedimentation rates for that portion of the record.

Wet-sieved residues were counted for total number of ostracodes per sample (normalized to abundance/gram dry weight), taphonomic condition (% broken, whole carapace, adult, carbonate coated, oxidation/reduction stained), and each valve was identified to the species level where possible, using an Olympus SZH binocular microscope. Additionally, the wet-sieved residues were counted for absolute abundance of other common fossil remains in this same size range (chaoborid fragments, macrocharcoal, fish (including bones, teeth, and scales), algae (*Pediastrum* and *Botryococcus*), *Polypodiaceae sori*, and the relative abundance of mollusk fragments, and both monomineralic and lithic grains in the sand fraction (specifically quartz, mica, pyrite, siderite, vivianite, aragonite needles, and ooids).

The lake level reconstruction itself is based on a principal components analysis (PCA) on the indicators. These included: the relative abundance of the key ostracode taxa *Cypridopsines, Limnocythere, Candonopsis, Ilyocypris*, and *Sclerocypris*, their taphonomic condition (broken, whole carapace, adult, carbonate coated), the LOG-concentrations of chaoborid fragments, macrocharcoal, fish (including bones, teeth, and scales), algae (*Pediastrum* and *Botryococcus*), *Polypodiaceae sori*, and the relative abundance mollusk fragments, and authigenic and terrigenous mineral grains in the sand fraction (quartz, mica, pyrite, siderite, and ooids). PCA of 23 variables was performed using the "vegan" package and the program R(21). The age model was created using a monotonic polynomial spline (Fig. S8) and shows consistently older ages as a function of increasing depth (Table S10).

Palynology

The pollen record from core MAL05-1B/1C is based on 402 total samples spanning 10.5-170mblf within the composite section. In depth detail about the pollen record can be found in Ivory et al. (25). The samples were processed using standard protocols following the method of Faegri and Iverson (141) and were sieved at 10 μm. A total pollen count of 300-500 grains was achieved for all samples with the exception of six samples which range from 17-149 grains/sample which occur during the extremely arid episode at ~100 ka. Average temporal resolution is 1400 yr for the whole record, however, within the last 250 ka, the resolution is higher (620 yr). The fossil pollen record is comprised of 227 total pollen taxa which were identified using atlases of pollen morphology (142, 143) and the African Pollen Database.

To produce the pollen diagram presented in Fig. S6, percentages for each taxon were calculated against the sum of all pollen and spores minus the undeterminable grains, aquatic taxa, and bryophytes. Fig. S6 was drawn using TILIA 2.0 (144), and the zonation, which highlights the transition between forest and semi-arid vegetation, was calculated using constrained cluster analysis (145). Brachystegia and Uapaca represent miombo woodland, as these are the most characteristic, high-dispersing pollen taxa in this biome.

Species richness was also presented in Ivory et al. (25). This metric was calculated based on the pollen counts using Margalef's Index (Dmg), which is highly correlated with species richness in populations (146). The formula is: $Dmg=(S-1)/lnN$ where S is the number of pollen taxa in a sample and N is the number of individual pollen grains counted. High values suggest high species richness.

Phytoliths

Sediment samples from stratigraphic columns were processed from the CHAI (124) and CHA-II(19) sites for phytolith analysis to attempt a vegetation landscape reconstruction. Extraction protocols were followed that were successfully employed on neighboring Middle Stone Age sites (66) and modern topsoils (65) from the Mozambican side of the lake. The procedure included sieving, drying, deflocculating, acid/base treatment, and sequential density separation by manipulating the specific gravity of sodium polytungstate. Aliquot mounting was with 'Entellan New', which allowed for microscopic inspection (40×) and 3D rotation before drying. The average count per slide was 380 phytoliths. In samples with grass representation higher than 10% within the grand total, the minimum short cell count was 200 phytoliths.

Phytolith analysis in northern Malawi was grounded on an inferential baseline from local present-day soils and plants representing the phytolith assemblages of Zambezian woodlands (30, 65, 147). Supporting phytolith literature was used for adjacent ecosystems, with which a number of plant species are shared, such as the Guineo- Congolian region (64), and the Somalia-Masai zone (148). The total number of phytoliths published pertinent to this work is 13,738 (19, 124), with a range of 28-59 discrete morphotypes that could be classified typologically according to the international code of phytolith nomenclature (63). Table S8 includes a complete list of phytoliths identified from CHA-I, with a summary published in Wright et al. (19).

Summary of results

Visualization of all data from the full ~636 kyr record show that after 85 ka a fire-tolerant vegetation community developed on the shores of Lake Malawi. In addition to a reduction to <20% *Podocarpus* after 85 ka, fire-tolerant trees such as Olea rose by >50% above their pre-85 ka abundances with an average overall representation in the paleoecological record of 6.6%, compared to 4.1% for prior highstands (25) (Fig. S7). Pollen from the lake cores shows a dominance of fire-intolerant trees like *Podocarpus* (often >50%) during earlier lake highstands. Samples that post-date 85 ka cluster together with the exception of samples ~78-79 ka (Fig. S7). These three samples are characterized by a much higher proportion of *Podocarpus* than in other samples dating with the last 85 kyr.

The increase in wildfire disturbance and fire-tolerant vegetation was accompanied by a sharp decline in species richness. Wet periods dominated by trees from 636-115 ka typically showed species richness values between 3.0 and 6.0. However, after 85 ka, species richness indices averaged 1.65 with the dominance of fire-tolerant forests. Miombo woodland today is notable for its paucity of species in contrast to similar biomes throughout the world (149). This ecosystem distribution is strongly influenced by fire, often with closed canopies dominating in the absence of fire and transitioning to more open woodlands and grasslands under an annual burning regime (150). The post-85 ka decline in species richness, with subsequent maintenance of miombo woodland, grassland and fire-tolerant tree species, indicates a shift into an ecological system mediated by fire resistance (151).

Fire as a component of ecosystem status is further supported by the charcoal record from the central basin Lake Malawi MAL05-1B/1C core, which shows two periods of high influx between ~124 – 164 ka and 74 – 90 ka, followed by a sustained baseline increase relative to the 636-kyr average documented in the lake core (Figs. 2B, S5). This evidence for increased fire activity

contains peaks that are exceptional within the context of the last 636 kyr, as shown by calculating the z-scores for charcoal influx over the last 636 kyr (Fig. S9). The northern MAL05-2A core, which receives input from the alluvial fans containing the archaeological sites, shows a steady influx of charcoal after the last chronological anchor point at the Youngest Toba Tuff (~74 ka). Converting the charcoal influxes for this core into z-scores shows that almost all samples prior to 30 ka have negative z-scores, and the pattern reverses to positive a-scores after this time. This implies an increase in macrocharcoal influx in the northern basin specifically after ~30 ka. Although the longer central basin macrocharcoal record shows an even influx of charcoal after the large peaks diminish, evidence for increased erosion from a landscape experiencing more burning is present in the magnetic susceptibility data (33, 34). These show a strongly positive and significant relationship between magnetic susceptibility and charcoal over the last 85 kyr (0.2542, $p = 0.0002$), and a strongly negative relationship between them between 85 – 636 ka (-0.2509, $p < 0.0001$) (Table S7).

We created correlation matrices in the "corrplot" package in R, in order to compare how relationships between variables changed during periods of analogous lake stands before and after the time when the OSL record shows the most abundant evidence for human occupation. Although human occupation of the northern Lake Malawi basin is traced to at least ~92 ka, most of the OSL dates cluster between 60 and 21 ka (Fig. 2). The Late Pleistocene interval of the Lake Malawi Drill Core MAL1B/1C also does not have any pollen samples between ca. 74 ka and 57 ka. We therefore focused on a comparison of the relationships between different vegetation types as inferred from the pollen, charcoal abundances, and lake levels before and after ~60 ka to best understand potential effects of forager settlement in shaping the ecology of the region.

Correlation matrices generated from normalized lake level and fossil pollen data demonstrate significant ecological reorganization after 60 ka even when lake levels are held constant (Fig. S10). Normalized variables were transformed to a scale between 0 and 1 in order to equally weight their importance in the correlation matrix. The modeled variables included normalized lake levels, charcoal influx, pollen species richness and pollen abundances of selected taxa (Poaceae (grasses), *Podocarpus* (fire-intolerant trees), *Olea* (fire-tolerant trees) and miombo (woodland)). Based on these data, there is no significant difference in variable correlation before 60 ka regardless of lake level (Fig. S10). However, following 60 ka, there is a significant reorganization of structured ecological relationships between the independent variables. We interpret this disentanglement of variables as a function of anthropogenic influences, which restructured the ecology of the Lake Malawi basin. A finer-scale analysis of these impacts within

the last 60 ka is not possible, as there are only 15 pollen data points after 60 ka. However, the 315 data points before 85 ka provide an ample record of what vegetation conditions were like prior to intensive evidence of human occupation, and during periods when lake level (as a proxy for precipitation) was analogous to the modern level (PCA values between -0.130-σ and -0.198-σ) (25).

To further evaluate the changing environmental conditions before 85 ka, between ~85 – 60 ka, and after 60 ka, we created bivariate plots of species richness and lake levels, supported by box and whisker charts of charcoal, species richness, and key pollen indicators. A bivariate plot of non-normalized, non-parameterized lake conditions shows that lake level and species richness variables after 85 ka cluster together and away from the majority of data points that represent the period before 85 ka (Fig. S11). Overall, lake level over the last 85 kyr has been high relative to the average over the last ~636 ka. However, species richness in the last 85 ka has been low. Box and whisker plots of the inferred dependent variables when lake level is held constant between -0.130-σ and - 0.198-σ illustrate some reorganization of ecological patterns for the two general time periods. During the initial period of human settlement of the Karonga region following a period of extreme aridity (85 – 60 ka), there is a significant increase in charcoal production, which we potentially attribute to an initial phase of primary forest clearance. An increase on the prevalence of *Olea* and decrease in *Podocarpus* after 85 ka reflect a stronger tendency toward fire tolerant vegetation during periods of higher rainfall relative to the long record. A wider range of grass pollen abundances (Poaceae) during initial human settlement accord with fire disturbance, but the post-85 ka pollen abundances of miombo and Poaceae are within the 1-σ of variance of pre-85 ka high lake conditions.

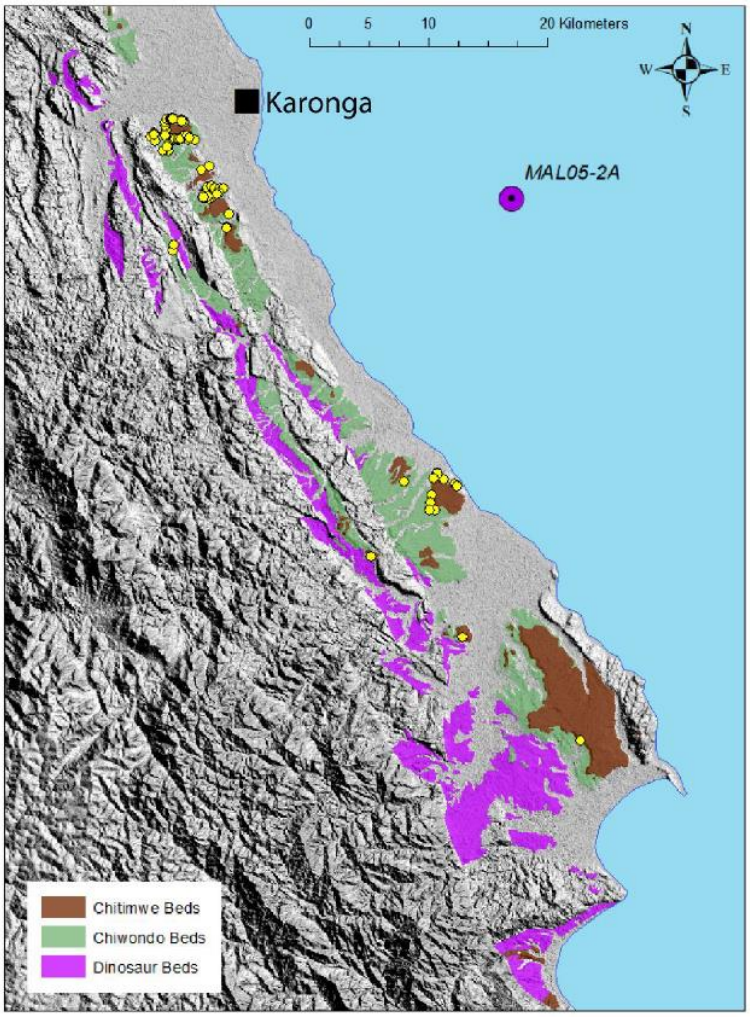

Fig S1. Mapped bedrock and surficial deposits in the northwest corner of Lake Malawi (refer to Fig. 1 for an overview of the project location). Yellow circles are the locations of archaeological or geologic excavations. MAL05-2A is the northernmost lake core sample of the Lake Malawi Scientific Drilling Project (152). Base imagery: ASTER.

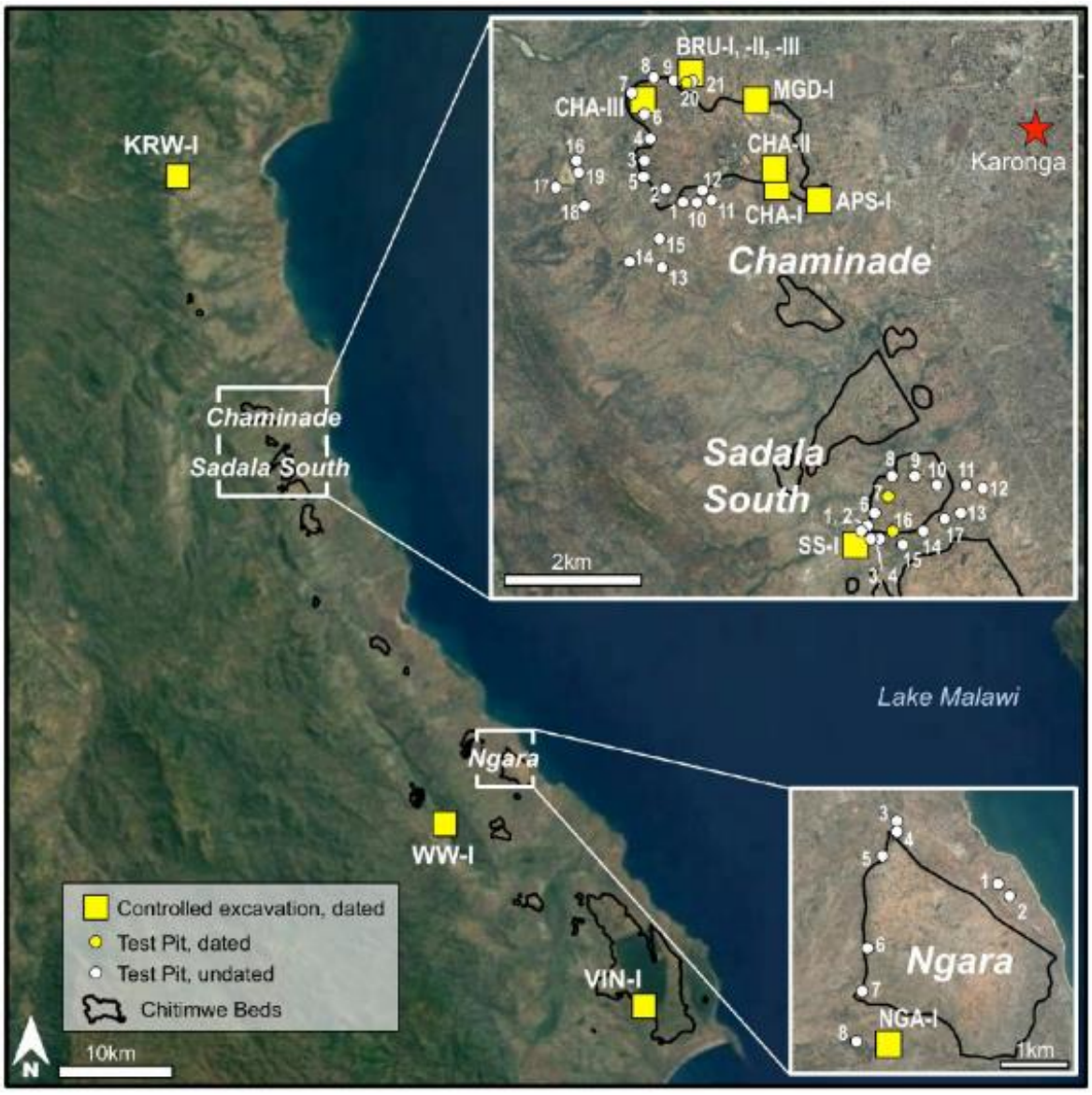

Fig. S2. Locations of geologic and archaeological test pits in the Karonga region of northern Malawi. Refer to Fig. 1 for project area location overview. Base imagery: Google Earth.

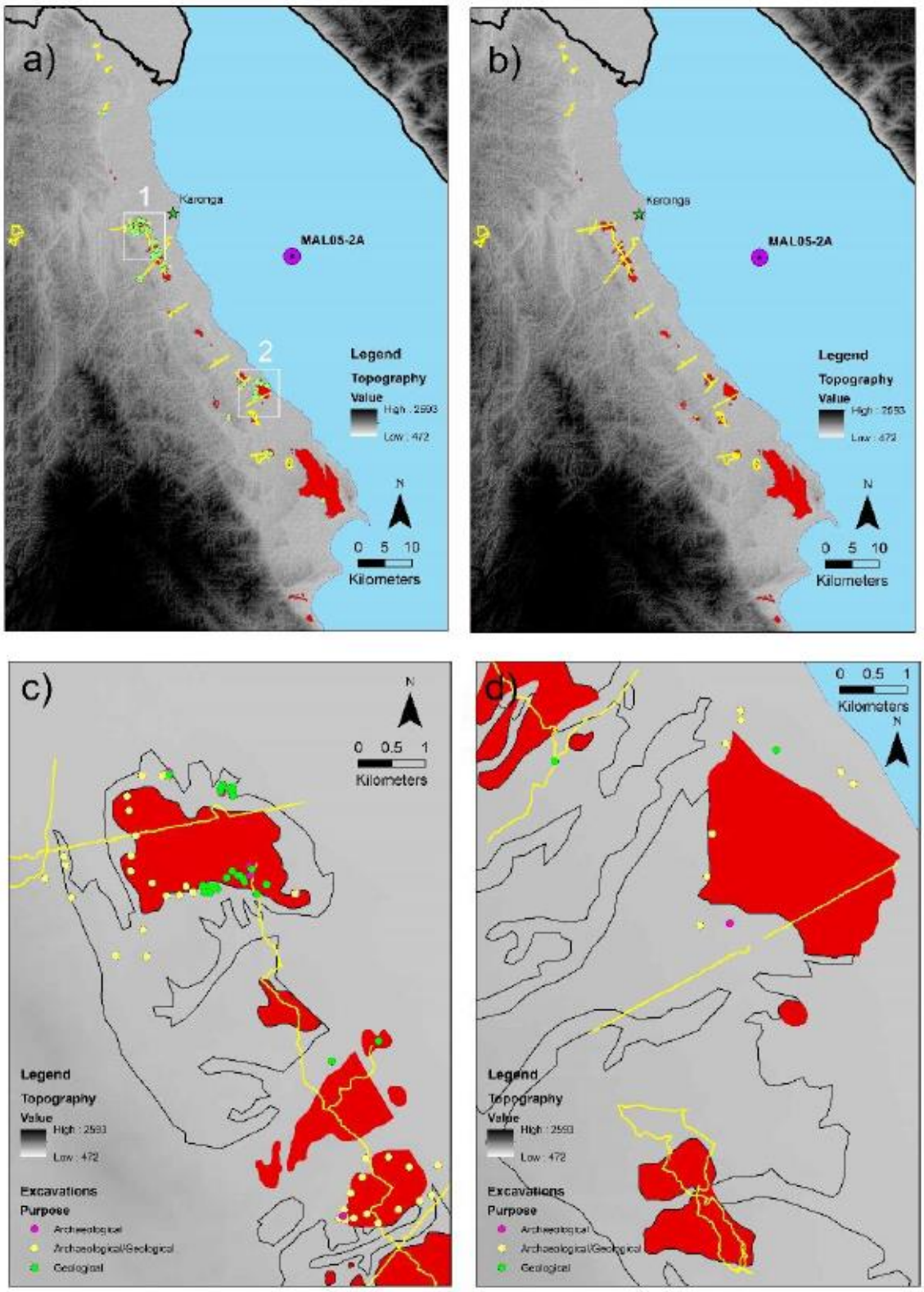

Fig. S3. Total areas surveyed (yellow lines) with (a) and without (b) excavations indicated as green dots. Red is Chitimwe Beds and the grey outline is the Chiwondo beds showing close-ups (boxed areas of 1 and 2) of the Karonga and Sadala South (c) and Ngara (d) excavation locations.

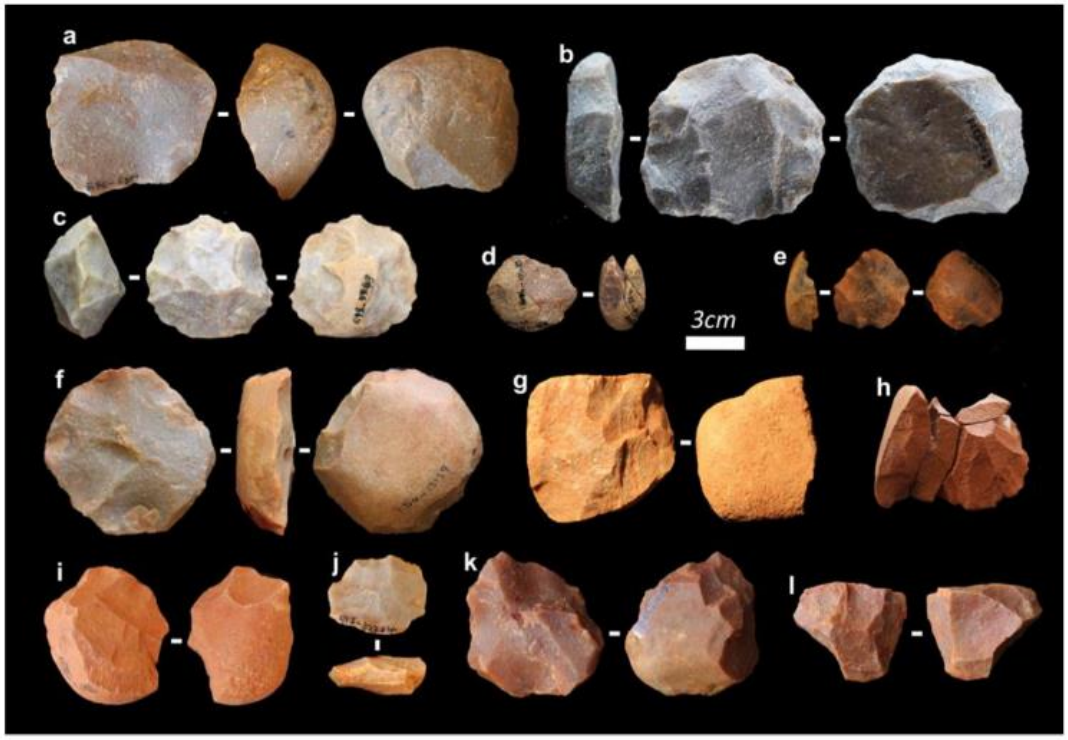

Fig. S4. Selected artifacts from northern Malawi MSA assemblages (all quartzite); (a) casual core, CHA-I; (b) Levallois core, CHA-I; (c) radial core, CHA-I; (d) radial core with refitting flakes, CHA-I; (e) radial core, CHA-II; (f) Levallois core, CHA-II; (g) radial-platform core, CHA-II; (h) prismatic/polyhedral core with refitting flakes, SS TP 16; (i) radial core, CHA TP 7; (j) radial core, CH TP 7A; (k) radial core, SS-I; (l) multiplatform core, SS-I.

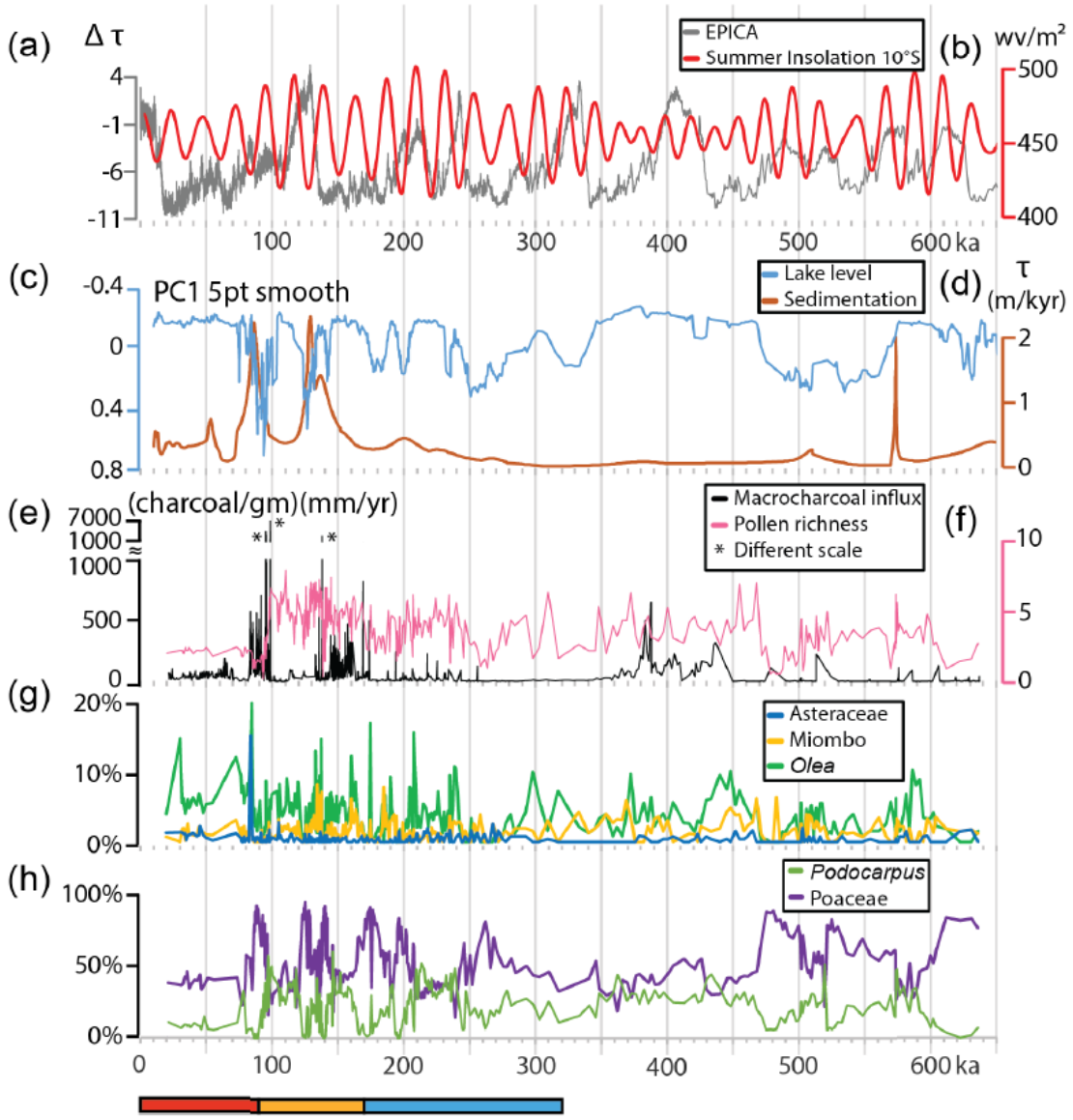

Fig. S5. Lake level (21), pollen (25), and macrocharcoal influx data from the MAL05-1B/1C core, plotted under EPICA global temperature variation from the EPICA Dome C bag deuterium data (153), summer insolation at 15°S from the Orbital Variations and Insolation Database (154), and sedimentation rate calculated using the age model in Ivory et al. (21). The thick red line on the x-axis is the age range within which all dated human occupation in the region falls. The orange line represents the period by when complex use of fire to transform raw materials has been documented elsewhere in Africa (12), and the blue line shows the oldest known date by which anatomically modern humans and MSA technology are known (24).

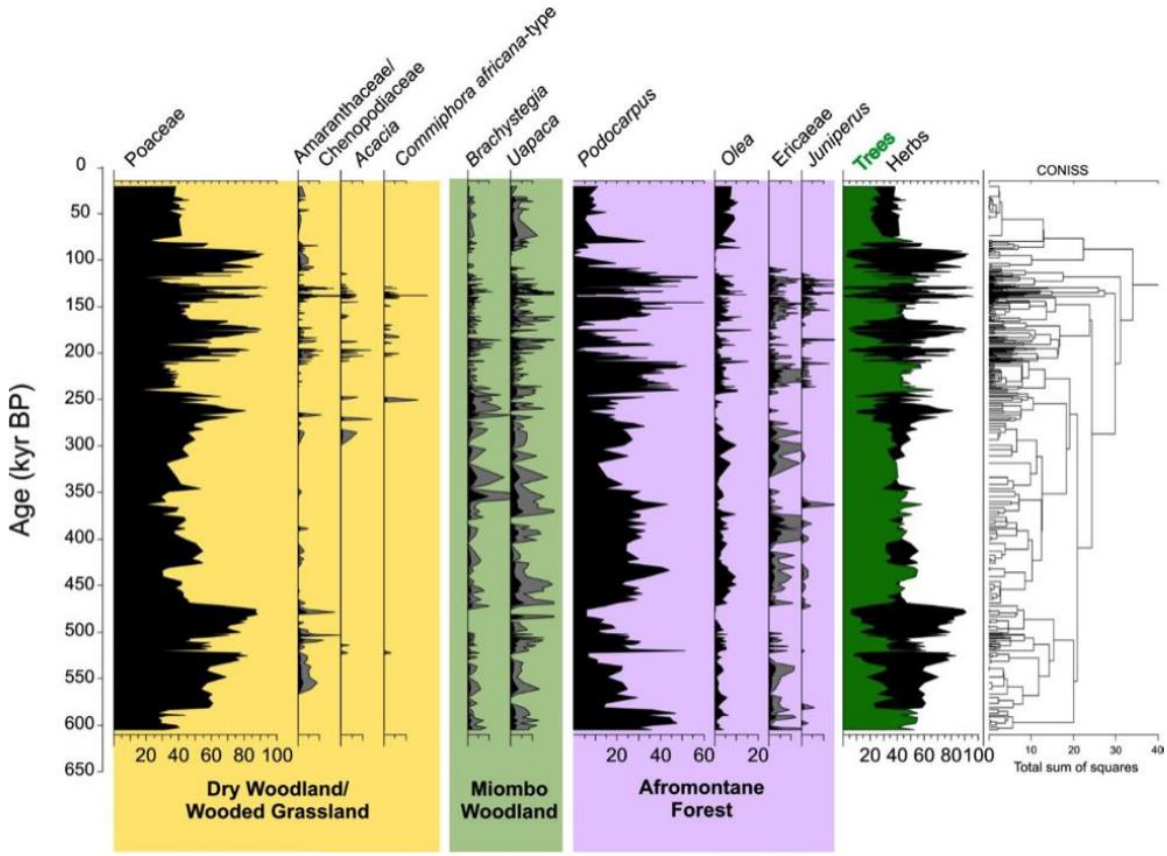

Fig. S6. Pollen diagram for MAL05-1B/1C. Only dominant pollen taxa are pictured, and these are color-coded based on vegetation type. Gray shading represents 5x exaggeration. CONISS cluster analysis as well as a bar representing the assignment of zones to forest (green) or semi-arid (yellow) phases is pictured to the right of the diagram.

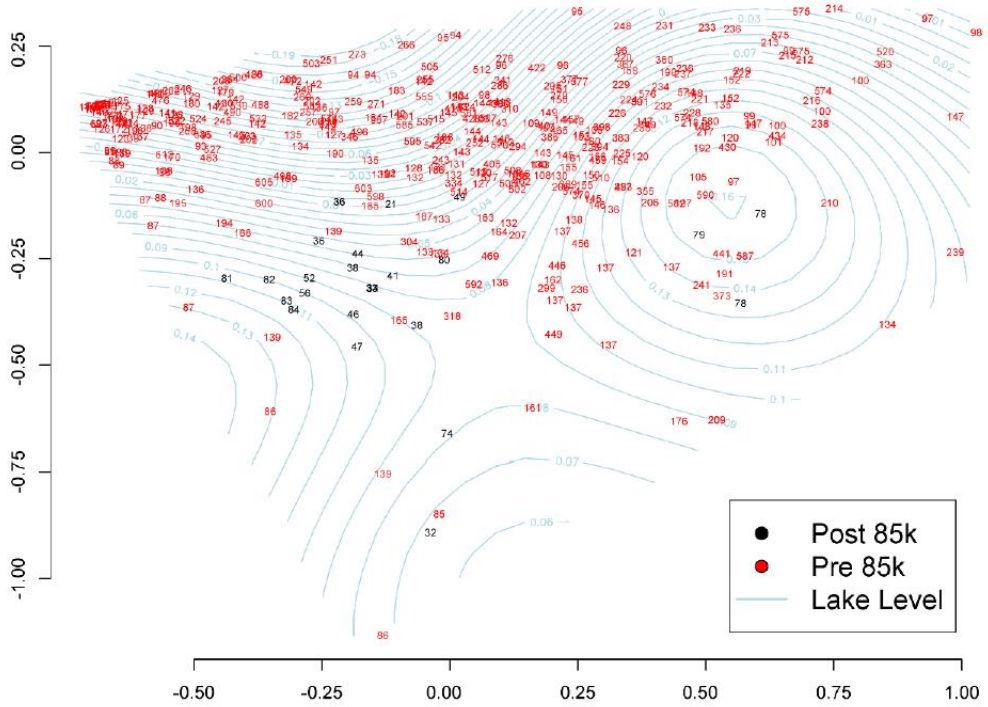

Fig. S7. PCoA data from Fig. 3 with data points coded as their ages, rounded to the nearest thousand years.

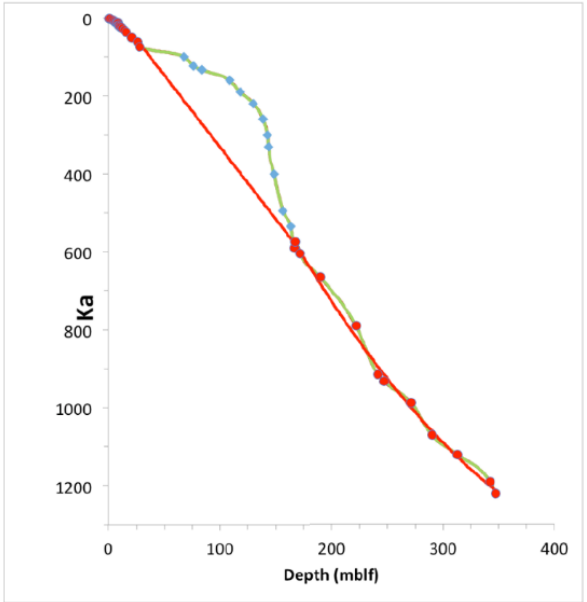

Fig. S8. Age-depth model for core MAL05-1B/1C for this study (green line with blue points) based on Ivory et al. (21) with chronological control in Table S10 using a monotonic polynomial spline fit. For comparison, the age model which does not include the paleomagnetic stratigraphy from Lyons, et al. (27) is shown in red.

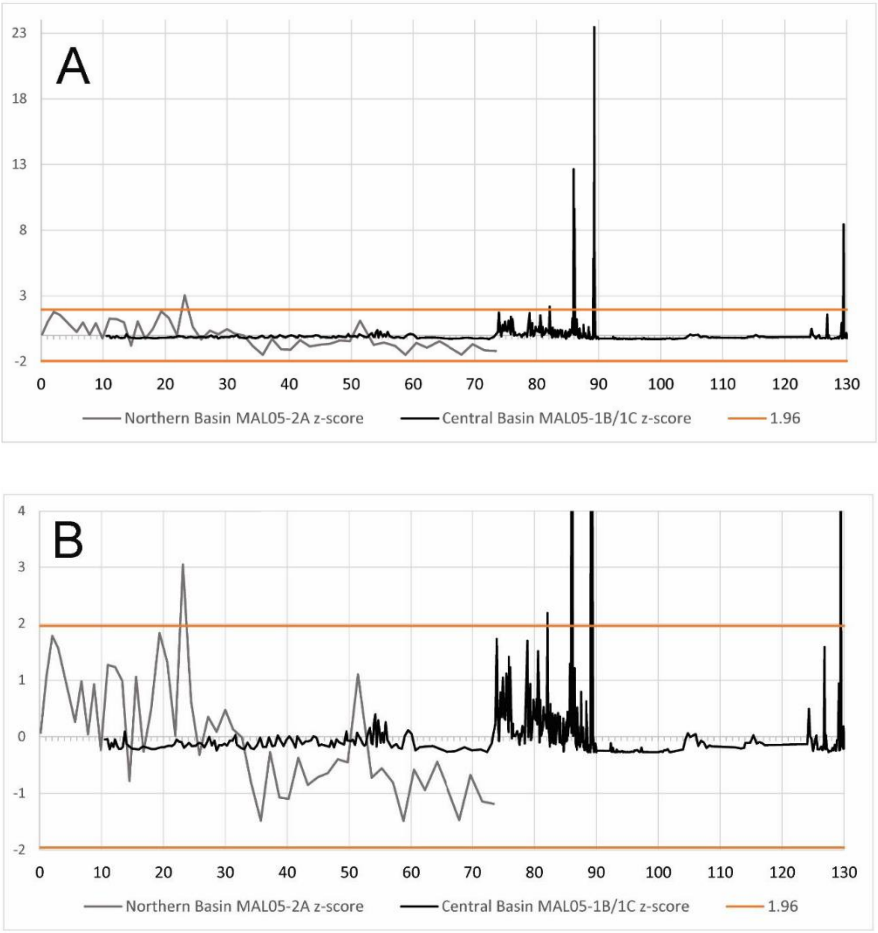

Fig. S9. z-scores for the central basin macrocharcoal record over the last 130 kyr, based on charcoal influx over the last 636 kyr (the time period over which there are pollen data, in black) and z-scores for the northern basin macrocharcoal record, based on charcoal influx over the last 73 kyr (the time period over which there are age-constrained macrocharcoal data, in grey). A shows the entire span of the z-scores that includes major peaks, and B modifies the x-axis to show a more limited span, but allows better visualization of the details. Orange bars represent the 95% distribution of z-scores.

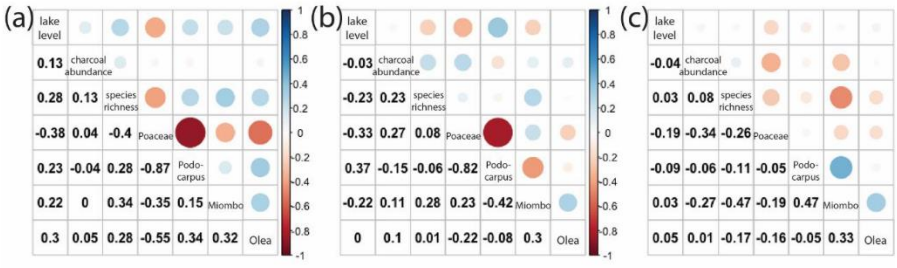

Fig. S10. Multivariate correlation matrix of a 636-kyr record from Lake Malawi core MAL05- 1B/1C of charcoal, lake level, species richness and fossil pollen abundances of Poaceae, *Podocarpus*, *Olea* and miombo taxa (25) (a) before 85 ka, (b) before 85 ka within -0.130 and -0.198-σ normalized lake level and (c) after 60 ka. Shades of blue from light to dark indicate relative positive correlations between variables on a scale of 0 to +1, whilst shades of red from light to

dark indicate negative (inverse) correlations between variables on a scale of 0 to -1. Asteraceae is not shown, as it peaks in only a single sample (Fig. S7G).

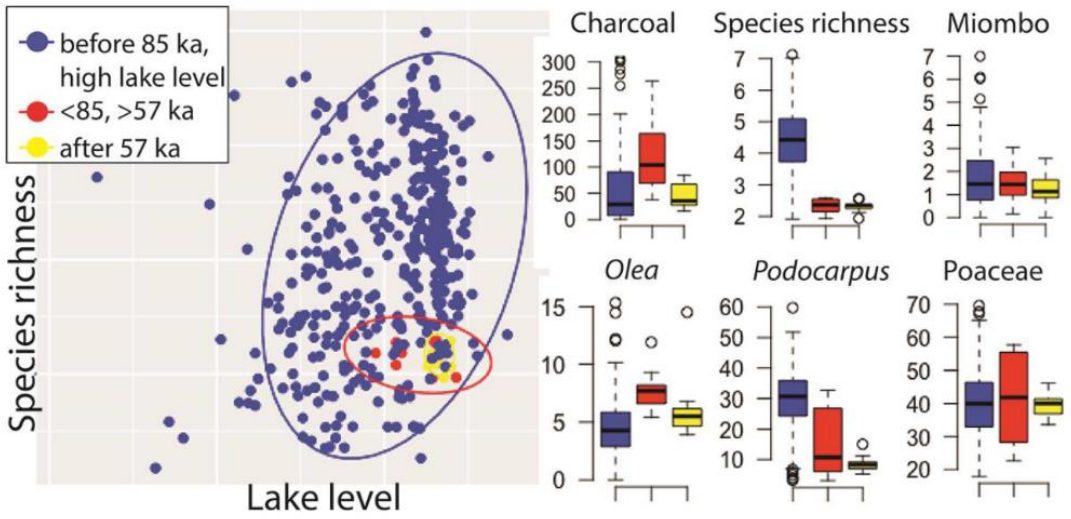

Fig. S11. (left) Bivariate ggplot2 with ellipses encapsulating 95% of the variance of species richness vs. PCA-reconstructed lake level of the 636-kyr record from Lake Malawi core MAL05-1B/1C (25) (right) box and whisker charts plotting quartiles of data at times when lake level was analogous to modern levels (-0.130-σ and -0.198-σ around the mean PCA eigenvalue between 21.4 – 56.2 ka; refer to main text for explanation). Units in (b) are the same as in Fig. 2.

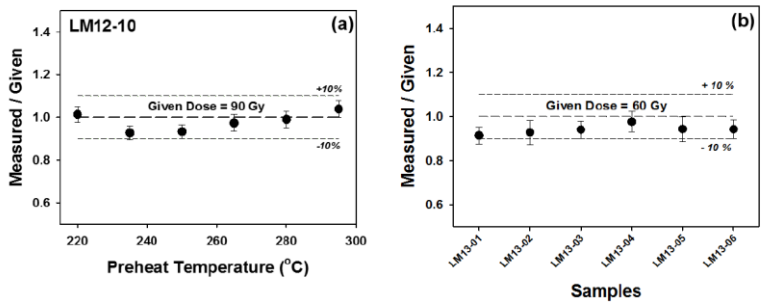

Fig. S12. Dose recovery test using samples from CHA-II and CHA-III trenches. (a) Measured/given dose ratios of the sample LM12-10 are within ±10% of unity for all the preheat temperatures. (b) The given doses of the samples from CHA-III are well recovered using the SAR protocol with a fixed preheat of 260°C for 10 s and a cut-heat to 220°C.

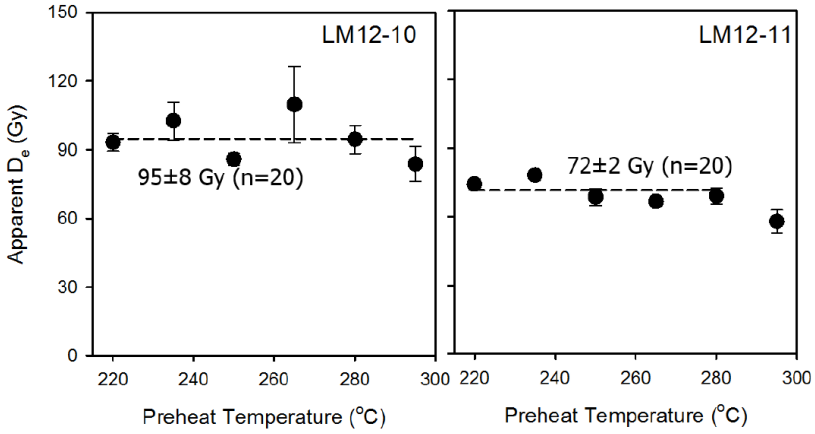

Fig. S13. Preheat plateau tests to derive quartz D_e values.

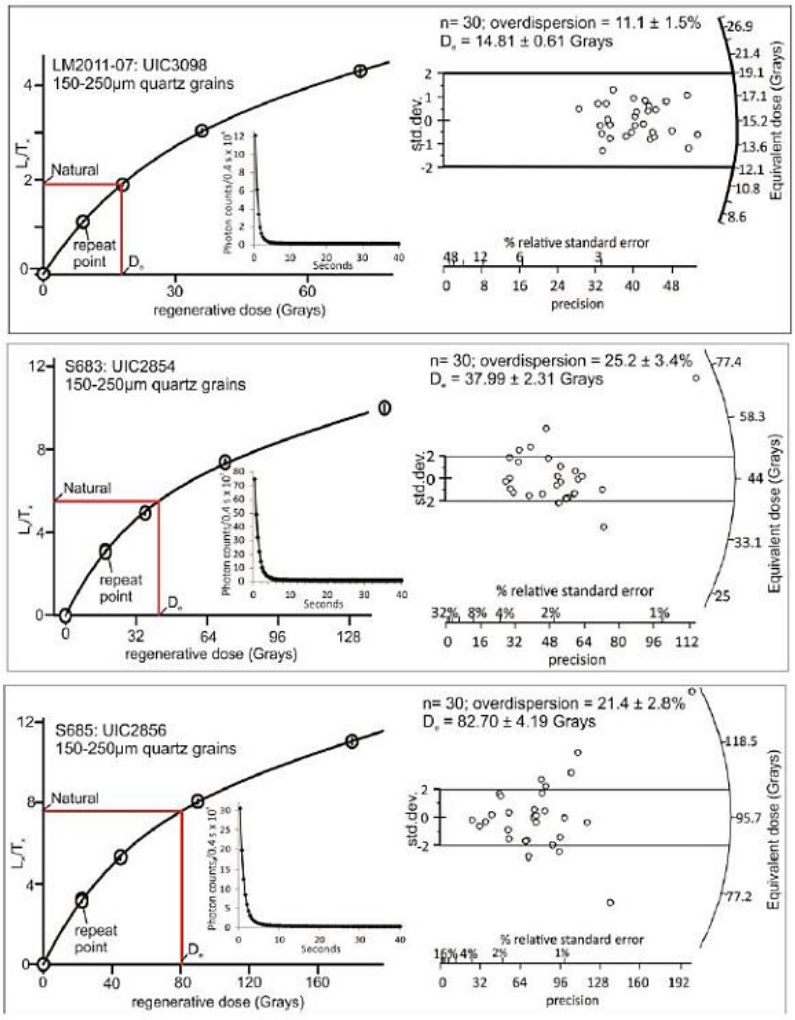

Fig. S14. Representative regenerative dose growth curves, with inset representative natural shine down curve, and radial plots of equivalent dose values on small aliquots (2-mm plate of 150-250 µm quartz fraction grains).

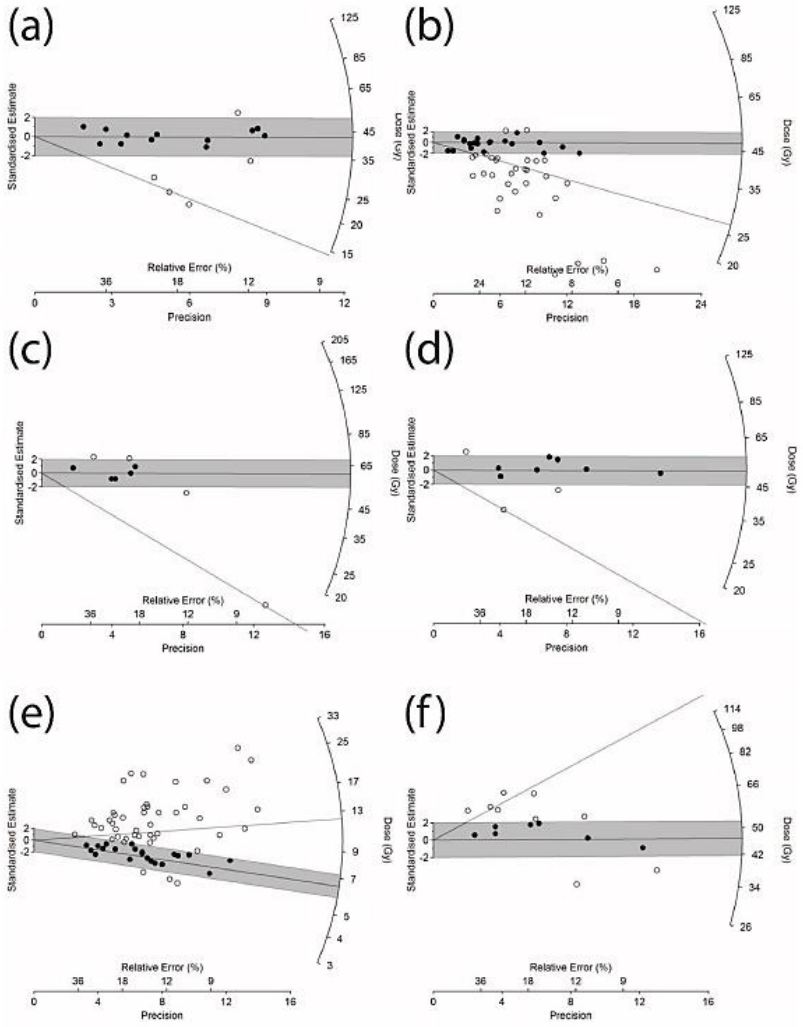

Fig. S15. Radial plots of sample (a) 12_1, (b) 12_2, (c) 12_3, (d) 12_4, (e) 12_5, (f) 12_6.

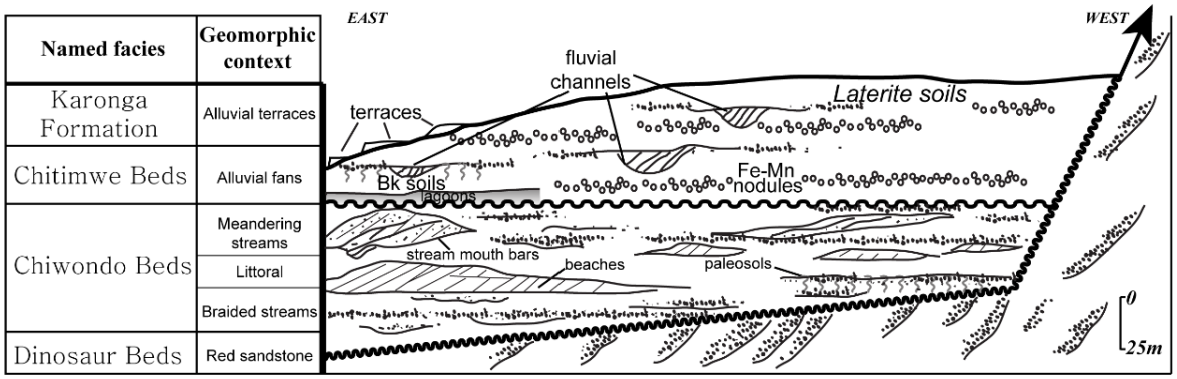

Fig S16. Stratigraphic and sedimentary scheme for Karonga area. Modified and updated from Fig. 5 of Ring and Betzler (17).

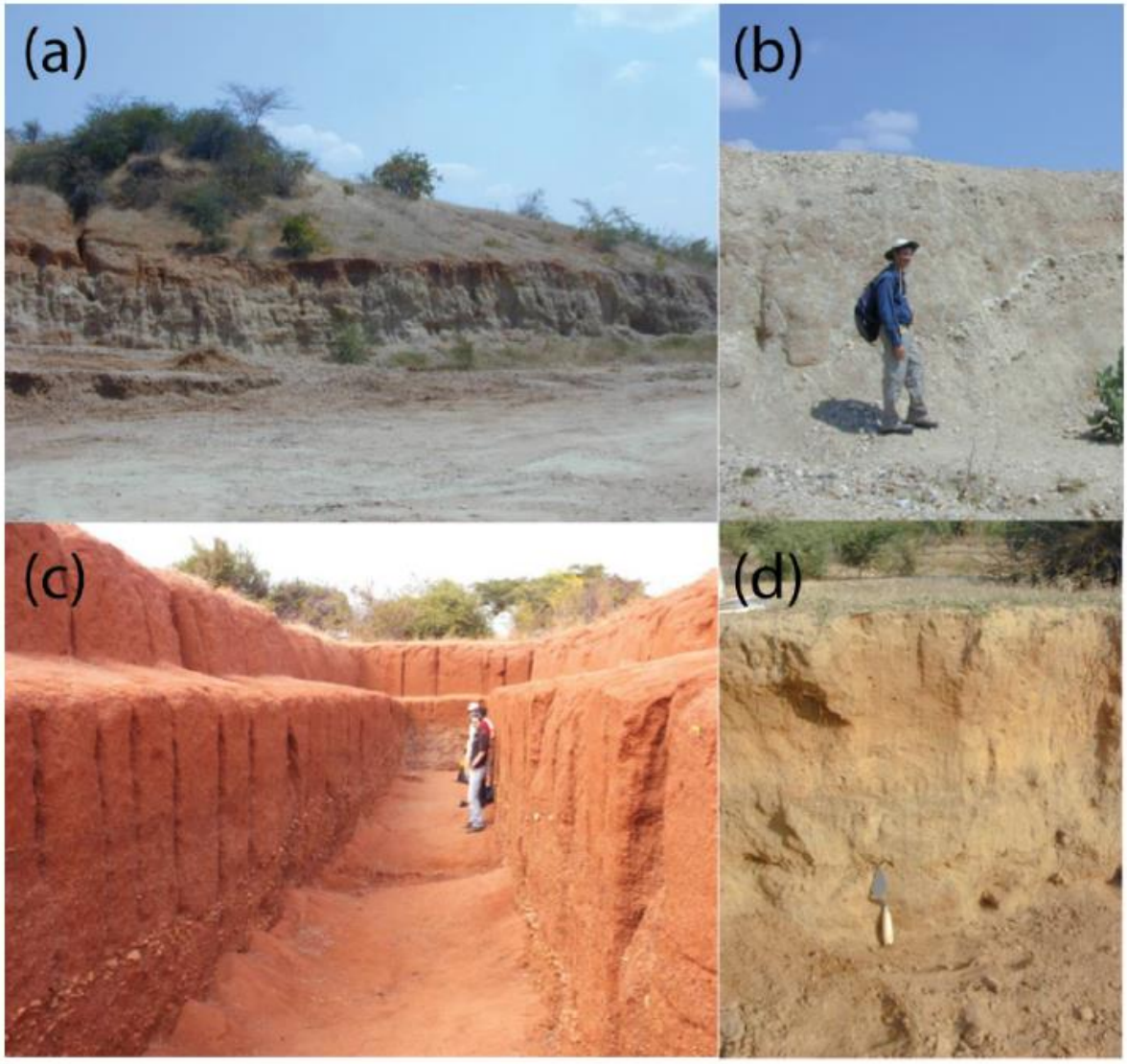

Fig. S17. (a) Exposure of eroded Chitimwe Beds in the western portion of the project area (S 9.955°, E 33.8659°). Laterite soils formed in the upper portion of the unit and overlie massive, sandy exposures intercalated with gravel lenses. Subaerial redoximorphic weathering of sediments can be observed in the foreground. (b) Deformed gravel lenses located in the western portion of the project area (S 9.955°, E 33.8659°). Lateritic soils can be observed in the background. (c) Lateritic alluvial fan deposits at CHA-II (19). Deformation of gravel lenses and stone lines are interpreted as a result of extensive subsidence due to groundwater pumping. (d) Terrace of the Karonga Formation exposed near Mwanganda's Village (55). Photo Credit: David Wright, University of Oslo.

REFER TO THE TAB TITLED "S1" IN THE ATTACHED EXCEL FILE (not included in this PhD thesis)

Table S1. Equivalent doses, dose rates and the OSL ages of the samples (*Multiple Grain Single Aliquots, 180-212 μm*); Korea Basic Science Institute. "Max MSA" and "Min MSA" are provided when diagnostic MSA artifacts at this location must date at least to this age (min) or at most to this age (max); MSA refers to a date from within a layer containing diagnostic MSA artifacts; Few artifacts references an artifact-bearing horizon lacking diagnostic MSA elements. "Fig. 2 #" references the date used in Fig. 2 of the main text.

REFER TO THE TAB TITLED "S2" IN THE ATTACHED EXCEL FILE (not included in this PhD thesis)

Table S2. Equivalent doses, dose rates and the OSL ages of the samples; University of Illinois at Chicago Luminescence Dating Research Laboratory. "Max MSA" and "Min MSA" are provided when diagnostic MSA artifacts at this location must date at least to this age (min) or at most to this age (max); MSA refers to a date from within a layer containing diagnostic MSA artifacts; Few artifacts references an artifact-bearing horizon lacking diagnostic MSA elements. "Fig. 2 #" references the date used in Fig. 2 of the main text.

REFER TO THE TAB TITLED "S3" IN THE ATTACHED EXCEL FILE (not included in this PhD thesis)

Table S3. Equivalent doses, dose rates and the OSL ages of the samples (*Single Grain Single Aliquots, 180-212 μm*); Griffith University. "Max MSA" and "Min MSA" are provided when diagnostic MSA artifacts at this location must date at least to this age (min) or at most to this age (max); MSA refers to a date from within a layer containing diagnostic MSA artifacts; Few artifacts references an artifact-bearing horizon lacking diagnostic MSA elements. "Fig. 2 #" references the date used in Fig. 2 of the main text.

Sample	*UGAMS sample #*	*Depth (cm)*	*Material*	*δ ^{13}C, (‰)*	*^{14}C yr BP*	*cal. yr BP**	*site*	*context*
MEM-9999 A	35986	230	bulk carbonate	-10.6	26620±70	31080-30774	MGD-I	palustrine
MEM-6877 B	35987	193	bulk carbonate	-10.1	27130±70	31235-31070	MGD-I	palustrine
MEM-6877 D	35988	193	bulk carbonate	-10.6	25670±60	30077-29886	MGD-I	palustrine
MEM-5038	35989	113	bulk carbonate	-10.8	34790±170	40403-39502	MGD-I	mixed horizon
MEM-5035	35990	81	bulk carbonate	-9.7	1220±20	1179-989	MGD-I	pedogenic
MEM-5055 A	35991	84	bulk carbonate	-7.6	10710±30	12734-12626	MGD-III	nodular calcrete
MEM-6885 B	35992	98	bulk carbonate	-7.6	23920±60	28204-27777	BRUGT2	palustrine
MEM-6886	35993	128	bulk carbonate	-8.0	27150±70	31244-31075	BRUGT2	palustrine
MEM-6887 B	35994	82	bulk carbonate	-8.4	28840±80	33687-32946	BRUGT2	palustrine
MEM-6887 B(r)	35994r	82	bulk carbonate	-9.4	29000±80	33794-33164	BRUGT2	palustrine
MEM-7271 A	35995	92	bulk carbonate	-9.3	21970±80	26376-25951	BRU-III	Btk
MEM-7272 C	35996	116	bulk carbonate	-9.7	16420±60	19929-19565	BRU-III	Btk-palustrine
MEM-7273 A	35997	134	bulk carbonate	-10.0	25400±60	29925-29300	BRU-III	Btk
MEM-7276 B	35998	125	bulk carbonate	-8.8	23740±60	27919-27705	BRU-III	Btk-palustrine
MEM-10655 B	35999	312	bulk carbonate	-6.8	18210±40	22264-22011	NGA-I	Bk
MEM-10639 B	36000	215	bulk carbonate	-5.7	16160±40	19580-19330	NGA-I	Bk
MEM-10645 B	36001	213	bulk carbonate	-5.2	17280±40	20934-20619	NGA-I	Bk
MEM-10654	36002	114	bulk carbonate	-3.7	19490±40	23748-23225	NGA-I	Bk

Table S4. Radiocarbon ages from carbonates in the Karonga region. Methods for collection, analysis, and formation context are provided in Materials and Methods SOM S2. All ages were calibrated for atmospheric production of 14C to 2-σ using the southern hemisphere application of the INTCAL20 calibration curve (62).

REFER TO THE TAB TITLED "S5" IN THE ATTACHED EXCEL FILE (not included in this PhD thesis)

Table S5. Descriptions of recovered stone tool assemblages. Divisions in dated horizons are shown in stratigraphic order. All coordinates are in UTM Zone 36L (S), WGS84; P = Preliminary observations; work ongoing.

Map Geology|	Geology	Group	Distance (km)
Alluvium/ Dambo	Alluvium/Dambo	Superficial Deposits	27.22
Cd	Dinosaur Beds	Alluvial and Lacustrine Sedimentary Rocks	5.42
Dambo	Lakeshore/River Alluvium	Superficial Deposits	0.26
Kc	Coal Measures and Basal Beds (Undifferentiated)	Karroo System	0.61
Kn	North Rukuru Sandstone and Shale Beds	Karroo System	10.41
Plc	Chitimwe Beds	Alluvial and Lacustrine Sedimentary Rocks	25.96
Pld	Chiwondo Beds	Alluvial and Lacustrine Sedimentary Rocks	30.95
Ts	Sungwa Beds	Alluvial and Lacustrine Sedimentary Rocks	0.84
Xh	Amphibolite	Ubendian Belt: Granitic Rocks and Metabasites	0.64
Xh'	Amphibolite Gneiss with Amphibolite Dykes	Ubendian Belt: Gneisses	2.98
Xq	Quartzite	Ubendian Belt: Gneisses	1.13
Xs""	Biotite Gneiss with Amphibolite Dykes	Ubendian Belt: Gneisses	13.44
Xs"" / Xs""sl	Biotite Gneiss (Some with Sillimanite)	Granulites, Gneisses, and Schists	12.24
Xsm	Coarse Mica Gneisses and Tectonic Schists	Post-Mafingi Cataclasis	1.81

Table S6. Total distances surveyed across mapped geological types. "Map Geology" refers to the designation on the Malawi Government maps.

REFER TO THE TAB TITLED "S7" IN THE ATTACHED EXCEL FILE (not included in this PhD thesis)

Table S7. Magnetic susceptibility data of the MAL05-1B/1C central basin core from Lyons et al. (34), downsampled using the spline function in R to fit the number of samples available in the macrocharcoal data, shown alongside the macrocharcoal influx and lake level calculations.

Taxa		Sample																
		700	701	702	703	704	705	706	707	708	709	710	711	712	713	714	716	N
Panicoids	Bilobate – long, concave	0	0	0	0	0	0	0	0	1	0	0	0	0	0	1	0	2
	Bilobate – long, flat	1	0	0	0	0	0	0	0	0	0	0	0	0	0	0	0	1
	Bilobate – long, notched	4	0	0	0	0	0	0	0	0	0	0	0	0	0	0	0	4
	Bilobate – short, concave	24	11	0	5	0	0	0	0	0	1	1	1	1	0	1	2	47
	Bilobate – short, convex	4	2	0	0	1	0	4	0	0	0	0	0	0	1	0	2	14
	Bilobate – short, flat	1	0	0	0	0	0	0	0	0	1	0	0	0	1	0	3	6
	Cross	0	0	0	0	0	0	0	0	0	2	0	0	0	0	0	0	2
	Polylobate	1	0	0	1	0	0	0	0	1	0	0	0	0	0	0	2	5
Pooids	Rondel	143	64	20	12	0	2	5	4	5	13	12	10	7	3	0	3	303
	Tower	56	37	8	6	0	3	7	2	4	6	8	7	4	0	1	2	151
	Tower – beveled	2	1	0	0	0	0	0	0	0	0	0	0	0	0	0	0	3
	Tower – horned	13	3	0	0	0	0	0	0	0	1	0	1	1	0	0	0	19
Chloridoids	Saddle - short	40	44	19	7	2	2	4	4	3	5	7	8	4	1	0	2	152
Bambusoids	Saddle – long	1	2	0	0	0	0	0	0	1	2	2	1	1	0	2	0	12
Grass, Undetermined	Bulliform	24	8	0	14	3	23	8	12	5	4	1	4	2	7	5	3	123
	Scutiform	11	0	0	9	2	8	7	11	8	2	2	1	0	4	1	0	66
Other	Globular – echinate	0	0	0	0	0	0	0	0	0	0	0	0	0	0	0	1	1
	Globular – psilate	62	27	48	17	0	2	1	0	1	0	1	0	0	0	3	0	162
Dicot, Woody	Blocky	71	126	108	53	161	53	49	91	69	89	91	69	109	120	133	103	1495
	Clavate	18	3	0	8	1	12	1	0	3	1	0	0	1	0	2	0	50
	Cylindrical	17	2	0	2	0	0	11	6	9	4	2	8	3	4	1	10	79
	Globular – granulate	337	176	165	113	48	124	135	124	159	145	122	135	156	134	138	138	2349
	Tabular – cavate	0	156	88	106	31	99	55	87	77	87	70	97	67	59	46	13	1138
	Tabular – crenate	3	2	3	3	0	0	0	1	1	1	2	1	2	0	1	4	24
	Tabular – dendriform	8	1	0	1	0	0	0	0	1	2	1	4	5	0	0	0	23
	Tabular – elongate	95	16	8	4	19	5	12	11	7	13	9	11	17	4	7	20	258
	Tabular – scrobiculate	135	156	96	100	57	41	33	53	42	48	55	79	72	64	66	61	1158
	Vessel	2	0	0	0	0	0	0	0	0	0	0	0	0	0	0	0	2
Sample Total		243	665	104	407	76	46	45	64	369	390	261	335	432	68	73	81	

Table S8. Phytolith counts for CHA-I. Detailed stratigraphic relationships of phytolith taxa are in Nightingale et al. (124). Phytolith counts for CHA-II were previously published in the Supplementary Material in Wright et al. (19).

Step	Treatment
1	Natural dose or give beta dose
2	Preheat 240°C for 10 s
3	Stimulate with blue light (470 nm) for 40 s at 125°C
4	Give beta test dose (6.6 Gray)
5	Preheat 240 °C for 10s
6	Stimulate with blue light (470 nm) for 40s at 125°C
7	Stimulate with blue light for 40 s at 280 °C
8	Return to step 1

Table S9. Single Aliquot Regeneration protocols at UIC LDRL

Depth (mblf)	Age (ka)	±1-σ	Feature	Reference
0.555	0.816	0.067	cal. ^{14}C	(*26*)
1.7	1.772	0.05	cal. ^{14}C	(*26*)
3.705	4.273	0.095	cal. ^{14}C	(*26*)
5.46	7.141	0.09	cal. ^{14}C	(*26*)
6.705	11.009	0.138	cal. ^{14}C	(*26*)
7.5075	12.528	0.079	cal. ^{14}C	(*26*)
7.9	13.329	0.145	cal. ^{14}C	(*26*)
8.5075	14.565	0.313	cal. ^{14}C	(*26*)
9.4565	18.451	0.222	cal. ^{14}C	(*26*)
9.5565	18.799	0.18	cal. ^{14}C	(*26*)
10.5455	21.528	0.47	cal. ^{14}C	(*26*)
11.5235	23.973	0.267	cal. ^{14}C	(*26*)
12.4575	26.59	0.427	cal. ^{14}C	(*26*)
14.0895	30.89	0.214	cal. ^{14}C	(*26*)
15.806	36.139	0.423	cal. ^{14}C	(*26*)
21.053	50.457	3.243	cal. ^{14}C	(*26*)
26.3	61		4a	(*21*)
28.09	73.5		Toba in 1C	(*21*)
68	100		5a	(*21*)
76	123		5b	(*21*)
83.7	133		6a	(*21*)
108.5	160		6b	(*21*)
118.3	190		7a	(*21*)
130	220		7b	(*21*)
138.5	260		8a	(*21*)
142.5	300		9a	(*21*)
143.5	330		9b	(*21*)
148.5	400		11a	(*21*)
156.5	495		13a	(*21*)
163.5	535		14a	(*21*)
167	590		Ar/Ar	(*27*)
167.5	575	20	15a	(*27*)
172	605		15b	(*27*)
190	665		17a	(*27*)
222	790		B/M	(*27*)
241.63	915	6	Ar/Ar	(*27*)
247	932		Santa Rosa	(*27*)
271.5	987		Upper Jaramillo	(*27*)
290	1070		Lower Jaramillo	(*27*)
313	1120		Panaruu	(*27*)
342	1190		Cobb Mtn Top	(*27*)
347	1220		Cobb Mtn Bottom	(*27*)

Table S10. Chronological constraints used for constructing the age-depth relationship for core MAL05- 1B/1C. 14C ages from Scholz et al. (26). Gray highlighted ages are based on the palaeomagnetic excursions and reversal stratigraphy that are discussed in depth in Ivory et al. (21) and Lyons et al. (27).

REFERENCES

1. N. L. Boivin, M. A. Zeder, D. Q. Fuller, A. Crowther, G. Larson, J. M. Erlandson, T. Denham, M. D. Petraglia, Ecological consequences of human niche construction: Examining long-term anthropogenic shaping of global species distributions. Proc. Natl. Acad. Sci. U.S.A. 113, 6388–6396 (2016).

2. F. Scherjon, C. Bakels, K. MacDonald, W. Roebroeks, Burning the land: An ethnographic study of off-site fire use by current and historically documented foragers and implications for the interpretation of past fire practices in the landscape. Curr. Anthropol. 56, 299–326 (2015).

3. S. White, Grass páramo as hunter-gatherer landscape. Holocene 23, 898–915 (2013).

4. R. Bliege Bird, C. McGuire, D. W. Bird, M. H. Price, D. Zeanah, D. G. Nimmo, Fire mosaics and habitat choice in nomadic foragers. Proc. Natl. Acad. Sci. U.S.A. 117, 12904–12914 (2020).

5. E. M. L. Scerri, M. G. Thomas, A. Manica, P. Gunz, J. T. Stock, C. Stringer, M. Grove, H. S. Groucutt, A. Timmermann, G. P. Rightmire, F. d'Errico, C. A. Tryon, N. A. Drake, A. S. Brooks, R. W. Dennell, R. Durbin, B. M. Henn, J. Lee-Thorp, P. deMenocal, M. D. Petraglia, J. C. Thompson, A. Scally, L. Chikhi, Did our species evolve in subdivided populations across Africa, and why does it matter? Trends Ecol. Evol. 33, 582–594 (2018).

6. P. Roberts, B. A. Stewart, Defining the 'generalist specialist' niche for Pleistocene *Homo sapiens*. Nat. Hum. Behav. 2, 542–550 (2018).

7. R. Biggs, W. Boonstra, G. Peterson, M. Schlüter, The domestication of fire as a social-ecological regime shift. PAGES—Past Global Chang. Mag. 24, 22–23 (2016).

8. J. A. J. Gowlett, The discovery of fire by humans: A long and convoluted process. Philos. Trans. R. Soc. Lond. B Biol. Sci. 371, 20150164 (2016).

9. M. I. Bird, J. A. Cali, A million-year record of fire in sub-Saharan Africa. Nature 394, 767–769 (1998).

10. C. W. Marean, Implications of late Quaternary mammalian fauna from Lukenya Hill (south-central Kenya) for paleoenvironmental change and faunal extinctions. Quatern. Res. 37, 239–255 (1992).

11. J. C. Thompson, D. K. Wright, S. J. Ivory, The emergence and intensification of early huntergatherer niche construction. Evol. Anthropol. 30, 17–27 (2021).

12. K. S. Brown, C. W. Marean, A. I. R. Herries, Z. Jacobs, C. Tribolo, D. Braun, D. L. Roberts, M. C. Meyer, J. Bernatchez, Fire as an engineering tool of early modern humans. Science 325, 859–862 (2009).

13. R. Bliege Bird, D. W. Bird, L. E. Fernandez, N. Taylor, W. Taylor, D. Nimmo, Aboriginal burning promotes fine-scale pyrodiversity and native predators in Australia's Western Desert. Biol. Conserv. 219, 110–118 (2018).

14. P. W. Wiessner, Embers of society: Firelight talk among the Ju/'hoansi Bushmen. Proc. Natl. Acad. Sci. 111, 14027–14035 (2014).

15. A. Glikson, Fire and human evolution: The deep-time blueprints of the Anthropocene. Anthropocene 3, 89–92 (2013).

16. N. Pinter, S. Fiedel, J. E. Keeley, Fire and vegetation shifts in the Americas at the vanguard of Paleoindian migration. Quat. Sci. Rev. 30, 269–272 (2011).

17. U. Ring, C. Betzler, Geology of the Malawi Rift: Kinematic and tectonosedimentary background to the Chiwondo Beds, northern Malawi. J. Hum. Evol. 28, 7–21 (1995).

18. J. C. Thompson, A. Mackay, S. Nightingale, D. Wright, J.H. Choi, M. Welling, H. Blackmore, E. Gomani Chindebvu, Ecological risk, demography and technological complexity in the Late Pleistocene of northern Malawi: Implications for geographical patterning in the Middle Stone Age. J. Quat. Sci. 33, 261–284 (2018).

19. D. K. Wright, J. C. Thompson, F. Schilt, A. S. Cohen, J.H. Choi, J. Mercader, S. Nightingale, C. E. Miller, S. M. Mentzer, D. Walde, M. Welling, E. Gomani Chindebvu, Approaches to Middle Stone Age landscape archaeology in tropical Africa. J. Archaeol. Sci. 77, 77: 64–77 (2017).

20. E. Mortimer, D. A. Paton, C. A. Scholz, M. R. Strecker, P. Blisniuk, Orthogonal to oblique rifting: Effect of rift basin orientation in the evolution of the North basin, Malawi Rift, East Africa. Basin Res. 19, 393–407 (2007).

21. S. J. Ivory, M. W. Blome, J. W. King, M. M. McGlue, J. E. Cole, A. S. Cohen, Environmental change explains cichlid adaptive radiation at Lake Malawi over the past 1.2 million years. Proc. Natl. Acad. Sci. U.S.A. 113, 11895–11900 (2016).

22. D. Delvaux, Peri-Tethys Memoir: PeriTethyan Rift/Wrench Basins and Passive Margins, P. A. Ziegler, W. Cavazza, A. H. F. Robertson, S. Crasquin-Soleau, Eds. (Memoirs of the National Museum of Natural History, Paris 2001), pp. 545–567.

23. J. Mercader, J. C. Gosse, T. Bennett, A. J. Hidy, D. H. Rood, Cosmogenic nuclide age constraints on Middle Stone Age lithics from Niassa, Mozambique. Quat. Sci. Rev. 47, 116–130 (2012).

24. D. Richter, R. Grün, R. Joannes-Boyau, T. E. Steele, F. Amani, M. Rué, P. Fernandes, J.P. Raynal, D. Geraads, A. Ben-Ncer, J.J. Hublin, S. P. McPherron, The age of the hominin fossils from Jebel Irhoud, Morocco, and the origins of the Middle Stone Age. Nature 546, 293–296 (2017).

25. S. J. Ivory, A.-M. Lézine, A. Vincens, A. Cohen, Waxing and waning of forests: Late Quaternary biogeography of southeast Africa. Glob. Chang. Biol. 24, 2939–2951 (2018).

26. C. A. Scholz, T. C. Johnson, A. S. Cohen, J. W. King, J. A. Peck, J. T. Overpeck, M. R. Talbot, E. T. Brown, L. Kalindekafe, P. Y. O. Amoako, R. P. Lyons, T. M. Shanahan, I. S. Castaneda, C. W. Heil, S. L.

Forman, L. R. McHargue, K. R. Beuning, J. Gomez, J. Pierson, East African megadroughts between 135 and 75 thousand years ago and bearing on early-modern human origins. Proc. Natl. Acad. Sci. U.S.A. 104, 16416–16421 (2007).

27. R. P. Lyons, C. A. Scholz, A. S. Cohen, J. W. King, E. T. Brown, S. J. Ivory, T. C. Johnson, A. L. Deino, P. N. Reinthal, M. M. McGlue, M. W. Blome, Continuous 1.3-million-year record of East African hydroclimate, and implications for patterns of evolution and biodiversity. Proc. Natl. Acad. Sci. U.S.A. 112, 15568–15573 (2015).

28. S. J. Ivory, R. Early, D. F. Sax, J. Russell, Niche expansion and temperature sensitivity of tropical African montane forests. Glob. Ecol. Biogeogr. 25, 693–703 (2016).

29. D. M. J. S. Bowman, J. Balch, P. Artaxo, W. J. Bond, M. A. Cochrane, C. M. D'Antonio, R. Defries, F. H. Johnston, J. E. Keeley, M. A. Krawchuk, C. A. Kull, M. Mack, M. A. Moritz, S. Pyne, C. I. Roos, A. C. Scott, N. S. Sodhi, T. W. Swetnam, R. Whittaker, The human dimension of fire regimes on Earth. J. Biogeogr. 38, 2223–2236 (2011).

30. J. Mercader, F. Astudillo, M. Barkworth, T. Bennett, C. Esselmont, R. Kinyanjui, D. L. Grossman, S. Simpson, D. Walde, Poaceae phytoliths from the Niassa Rift, Mozambique. J. Archaeol. Sci. 37, 1953–1967 (2010).

31. N. van Breemen, P. Buurman, Soil Formation, N. van Breemen, P. Buurman, Eds. (Springer Netherlands, Dordrecht, 1998), pp. 291–312.

32. B. P. Finney, T. C. Johnson, Sedimentation in Lake Malawi (East Africa) during the past 10,000 years: A continuous paleoclimatic record from the southern tropics. Palaeogeogr. Palaeoclimatol. Palaeoecol. 85, 351–366 (1991).

33. C. Whitlock, C. Larsen, Charcoal as a fire proxy, in Tracking Environmental Change Using Lake Sediments: Terrestrial, Algal, and Siliceous Indicators, J. P. Smol, H. J. B. Birks, W. M. Last, R. S. Bradley, K. Alverson, Eds. (Springer Netherlands, 2001), pp. 75–97.

34. R. P. Lyons, C. A. Scholz, M. R. Buoniconti, M. R. Martin, Late Quaternary stratigraphic analysis of the Lake Malawi Rift, East Africa: An integration of drill-core and seismic-reflection data. Palaeogeogr. Palaeoclimatol. Palaeoecol. 303, 20–37 (2011).

35. C. L. Yost, L. J. Jackson, J. R. Stone, A. S. Cohen, Subdecadal phytolith and charcoal records from Lake Malawi, East Africa imply minimal effects on human evolution from the ~74 ka Toba supereruption. J. Hum. Evol. 116, 75–94 (2018).

36. S. van der Kaars, G. H. Miller, C. S. M. Turney, E. J. Cook, D. Nürnberg, J. Schönfeld, A. P. Kershaw, S. J. Lehman, Humans rather than climate the primary cause of Pleistocene megafaunal extinction in Australia. Nat. Commun. 8, 14142 (2017).

37. G. R. Summerhayes, M. Leavesley, A. Fairbairn, H. Mandui, J. Field, A. Ford, R. Fullagar, Human adaptation and plant use in highland New Guinea 49,000 to 44,000 years ago. Science 330, 78–81 (2010).

38. C. O. Hunt, D. D. Gilbertson, G. Rushworth, A 50,000-year record of late Pleistocene tropical vegetation and human impact in lowland Borneo. Quat. Sci. Rev. 37, 61–80 (2012).

39. Y. Le Page, D. Oom, J. M. N. Silva, P. Jönsson, J. M. C. Pereira, Seasonality of vegetation fires as modified by human action: Observing the deviation from eco-climatic fire regimes. Glob. Ecol. Biogeogr. 19, 575–588 (2010).

40. L. Wadley, L. Backwell, F. d'Errico, C. Sievers, Cooked starchy rhizomes in Africa 170 thousand years ago. Science 367, 87–91 (2020).

41. T. Kraaij, F. Engelbrecht, J. Franklin, R. M. Cowling, A fiery past: A comparison of glacial and contemporary fire regimes on the Palaeo-Agulhas Plain, Cape Floristic Region. Quat. Sci. Rev. 235, 106059 (2020).

42. J. A. Moody, R. A. Shakesby, P. R. Robichaud, S. H. Cannon, D. A. Martin, Current research issues related to post-wildfire runoff and erosion processes. Earth Sci. Rev. 122, 10–37 (2013).

43. R. A. DiBiase, M. P. Lamb, Vegetation and wildfire controls on sediment yield in bedrock landscapes. Geophys. Res. Lett. 40, 1093–1097 (2013).

44. S. J. Ivory, M. M. McGlue, G. S. Ellis, A.M. Lézine, A. S. Cohen, A. Vincens, Vegetation controls on weathering intensity during the last deglacial transition in Southeast Africa. PLOS ONE 9, e112855 (2014).

45. E. Istanbulluoglu, R. L. Bras, Vegetation-modulated landscape evolution: Effects of vegetation on landscape processes, drainage density, and topography. J. Geophys. Res. Earth 110, F02012 (2005).

46. C. A. Orem, J. D. Pelletier, The predominance of post-wildfire erosion in the long-term denudation of the Valles Caldera, New Mexico. J. Geophys. Res. Earth 121, 843–864 (2016).

47. I. P. J. Smit, H. H. T. Prins, Predicting the effects of woody encroachment on mammal communities, grazing biomass and fire frequency in African savannas. PLOS ONE 10, e0137857 (2015).

48. Y. Garcin, A. Vincens, D. Williamson, G. Buchet, J. Guiot, Abrupt resumption of the African Monsoon at the Younger Dryas—Holocene climatic transition. Quat. Sci. Rev. 26, 690–704 (2007).

49. S. J. Ivory, A.-M. Lézine, A. Vincens, A. S. Cohen, Effect of aridity and rainfall seasonality on vegetation in the southern tropics of East Africa during the Pleistocene/Holocene transition. Quatern. Res. 77, 77–86 (2012).

50. G. H. DeBusk, A 37,500-year pollen record from Lake Malawi and implications for the biogeography of afromontane forests. J. Biogeogr. 25, 479–500 (1998).

51. E. C. Ellis, Anthropogenic transformation of the terrestrial biosphere. Philos. Trans. R. Soc. A Math. Phys. Eng. Sci. 369, 1010–1035 (2011).

52. A. M. Bauer, E. C. Ellis, The anthropocene divide: Obscuring understanding of social-environmental change. Curr. Anthropol. 59, 209–227 (2018).

53. J. C. Thompson, A. Mackay, V. de Moor, E. Gomani Chindebvu, Catchment survey in the Karonga District: A landscape-scale analysis of Provisioning and core reduction strategies during the Middle Stone Age of northern Malawi. African Archaeol. Rev. 31, 447–478 (2014).

54. J. C. Thompson, A. Mackay, D. K. Wright, M. Welling, A. Greaves, E. Gomani Chindebvu, D. Simengwa, Renewed investigations into the Middle Stone Age of northern Malawi. Quatern. Int. 270, 129–139 (2012).

55. D. K. Wright, J. Thompson, A. Mackay, M. Welling, S. L. Forman, G. Price, J.X. Zhao, A. S. Cohen, O. Malijani, E. Gomani Chindebvu, Renewed geoarchaeological investigations of Mwanganda's Village (Elephant Butchery Site), Karonga, Malawi. Geoarchaeology 29, 98–120 (2014).

56. P. J. Schoeneberger, D. A. Wysocki, E. C. Benham; Soil Survey Staff, Field Book for Describing and Sampling Soils, Version 3.0 (Natural Resources Conservation Service, National Soil Survey Center, 2012).

57. A. S. Murray, A. G. Wintle, The single aliquot regenerative dose protocol: Potential for improvements in reliability. Radiat. Meas. 37, 377–381 (2003).

58. R. F. Galbraith, R. G. Roberts, Statistical aspects of equivalent dose and error calculation and display in OSL dating: An overview and some recommendations. Quat. Geochronol. 11, 1–27 (2012).

59. C. Clarkson, An index of invasiveness for the measurement of unifacial and bifacial retouch: A theoretical, experimental and archaeological verification. J. Archaeol. Sci. 29, 65–75 (2002).

60. G. Stoops, Guidelines for Analysis and Description of Soil and Regolith Thin Sections (Soil Science Society of America, Inc., 2003).

61. M. A. Courty, P. Goldberg, R. Macphail, Soils and Micromorphology in Archaeology (Cambridge Manuals in Archaeology, Cambridge Univ. Press, 1989).

62. A. G. Hogg, T. J. Heaton, Q. Hua, J. G. Palmer, C. S. M. Turney, J. Southon, A. Bayliss, P. G. Blackwell, G. Boswijk, C. B. Ramsey, C. Pearson, F. Petchey, P. Reimer, R. Reimer, L. Wacker, SHCal20 southern hemisphere calibration, 0–55,000 years Cal BP. Radiocarbon, 759–778 (2020).

63. M. Madella, A. Alexandré, T. Ball, International code for phytolith nomenclature 1.0. Ann. Bot. 96, 253–260 (2005).

64. F. Runge, The opal phytolith inventory of soils in central Africa—Quantities, shapes, classification, and spectra. Rev. Palaeobotany Palynol. 107, 23–53 (1999).

65. J. Mercader, T. Bennett, C. Esselmont, S. Simpson, D. Walde, Soil phytoliths from miombo woodlands in Mozambique. Quatern. Res. 75, 138–150 (2011).

66. J. Mercader, T. Bennett, C. Esselmont, S. Simpson, D. Walde, Phytoliths from Middle Stone Age habitats in the Mozambican Rift (105-29 ka). J. Hum. Evol. 64, 328–336 (2013).

67. P. Vermeesch, On the visualisation of detrital age distributions. Chem. Geol. 312-313, 190–194 (2012).

68. C. Kappler, K. Kaiser, M. Küster, A. Nicolay, A. Fülling, O. Bens, T. Raab, Late Pleistocene and Holocene terrestrial geomorphodynamics and soil formation in northeastern Germany: A review of geochronological data. Phys. Geogr. 40, 405–432 (2019).

69. G. Geenens, C. Wang, Local-likelihood transformation Kernel Density Estimation for positive random variables. J. Comput. Graph. Stat. 27, 822–835 (2018).

70. S. J. Sheather, M. C. Jones, A reliable data-based bandwidth selection method for Kernel Density Estimation. J. R. Stat. Soc. B. Methodol. 53, 683–690 (1991).

71. E. Otárola-Castillo, M. G. Torquato, H. C. Hawkins, E. James, J. A. Harris, C. W. Marean, S. P. McPherron, J. C. Thompson, Differentiating between cutting actions on bone using 3D geometric morphometrics and Bayesian analyses with implications to human evolution. J. Archaeol. Sci. 89, 56–67 (2018).

72. R Core Team, R: A Language and Environment for Statistical Computing (R Foundation for Statistical Computing, 2020).

73. R. J. Hijmans, S. E. Cameron, J. L. Parra, P. G. Jones, A. Jarvis, Very high resolution interpolated climate surfaces for global land areas. Int. J. Climatol. 25, 1965–1978 (2005).

74. A. S. Murray, A. G. Wintle, Luminescence dating of quartz using an improved single-aliquot regenerative-dose protocol. Radiat. Meas. 32, 57–73 (2000).

75. A. G. Wintle, A. S. Murray, A review of quartz optically stimulated luminescence characteristics and their relevance in single-aliquot regeneration dating protocols. Radiat. Meas. 41, 369–391 (2006).

76. R. F. Galbraith, R. G. Roberts, G. M. Laslett, H. Yoshida, J. M. Olley, Optical dating of single and multiple grains of quartz from Jinmium Rock Shelter, Northern Australia: Part I, Experimental design and statistical models. Archaeometry 41, 339–364 (1999).

77. J. M. Olley, A. Murray, R. G. Roberts, The effects of disequilibria in the uranium and thorium decay chains on burial dose rates in fluvial sediments. Quat. Sci. Rev. 15, 751–760 (1996).

78. D. W. Zimmerman, Thermoluminescent dating using fine grains from pottery. Archaeometry 13, 29–52 (1971).

79. J. R. Prescott, J. T. Hutton, Cosmic ray contributions to dose rates for luminescence and ESR dating: Large depths and long-term time variations. Radiat. Meas. 23, 497–500 (1994).

80. V. Mejdahl, H. H. Christiansen, Procedures used for luminescence dating of sediments. Quat. Sci. Rev. 13, 403–406 (1994).

81. L. Bøtter-Jensen, E. Bulur, G. A. T. Duller, A. S. Murray, Advances in luminescence instrument systems. Radiat. Meas. 32, 523–528 (2000).

82. L. J. Arnold, R. G. Roberts, Stochastic modelling of multi-grain equivalent dose (De) distributions: Implications for OSL dating of sediment mixtures. Quat. Geochronol. 4, 204–230 (2009).

83. A. C. Londoño, S. L. Forman, T. Eichler, J. Pierson, Episodic eolian deposition in the past ca. 50,000years in the Alto Ilo dune field, southern Peru. Palaeogeogr. Palaeoclimatol. Palaeoecol. 346- 347, 12–24 (2012).

84. J. Fain, S. Soumana, M. Montret, D. Miallier, T. Pilleyre, S. Sanzelle, Luminescence and ESR dating beta-dose attenuation for various grain shapes calculated by a Monte-Carlo method. Quat. Sci. Rev. 18, 231–234 (1999).

85. W. R. Van Schumus, Natural radioactivity in crust and mantle, in Global Earth Physics: A Handbook of Physical Constants, T. J. Ahrens, Ed. (American Geophysical Union, 1995), pp. 283– 291.

86. M. J. Aitken, An Introduction to Optical Dating: The Dating of Quaternary Sediments by the Use of Photon-Stimulated Luminescence (Oxford Univ. Press, 1998).

87. J. M. Olley, T. Pietsch, R. G. Roberts, Optical dating of Holocene sediments from a variety of geomorphic settings using single grains of quartz. Geomorphology 60, 337–358 (2004).

88. R. G. Roberts, R. F. Galbraith, H. Yoshida, G. M. Laslett, J. M. Olley, Distinguishing dose populations in sediment mixtures: A test of single-grain optical dating procedures using mixtures of laboratory-dosed quartz. Radiat. Meas. 32, 459–465 (2000).

89. S. Stokes, S. Ingram, M.J. Aitken, F. Sirocko, R. Anderson, D. Leuschner, Alternative chronologies for Late Quaternary (Last Interglacial–Holocene) deep sea sediments via optical dating of silt-sized quartz. Quat. Sci. Rev. 22, 925–941 (2003).

90. V. Mejdahl, Thermolumiscence dating: Beta-dose attenuation in quartz grains. Archaeometry 21, 61–72 (1997).

91. M. Jain, L. Bøtter-Jensen, A. Singhvi, Dose evaluation using multiple-aliquot quartz OSL: Test of methods and a new protocol for improved accuracy and precision. Radiat. Meas. 37, 67–80 (2003).

92. J. D. Clark, C. V. Haynes Jr, An elephant butchery site at Mwanganda's Village, Karonga, Malawi, and its relevance for Palaeolithic archaeology. World Archaeol. 1, 390–411 (1970).

93. C. B. Ramsey, M. Scott, J. van der Plicht, Calibration for archaeological and environmental terrestrial samples in the time range 26–50 ka cal BP. Radiocarbon 55, 2021–2027 (2013).

94. C. Betzler, U. Ring, Sedimentology of the Malawi Rift: Facies and stratigraphy of the Chiwondo Beds, northern Malawi. J. Hum. Evol. 28, 23–35 (1995).

95. F. Dixey, The Tertiary and post-Tertiary lacustrine sediments of the Nyasan Rift-Valley. Quat. J. Geol. Soc. Lond. 83, 432–442 (1927).

96. A. M. Alonso-Zarza, V. P. Wright, Calcretes, in Carbonates in Continental Settings: Facies, Environments and Processes, Developments in Sedimentology, A. M. Alonso-Zarza, L. H. Tanner, Eds. (Elsevier, 2010), vol. 61, pp. 225–267.

97. G. M. Ashley, D. M. Deocampo, J. Kahmann-Robinson, S. G. Driese, Groundwater-fed wetland sediments and paleosols: It's all about water table, in New Frontiers In Paleopedology And Terrestrial Paleoclimatology, S. G. Driese, L. C. Nordt, Eds. (SEPM Society for Sedimentary Geology, 2013), vol. 104, pp. 47–61.

98. K. Zamanian, K. Pustovoytov, Y. Kuzyakov, Pedogenic carbonates: Forms and formation processes. Earth Sci. Rev. 157, 1–17 (2016).

99. M. N. Machette, Calcic Soils of the Southwestern United States, in Soils and Quaternary Geology of the Southwestern United States: Geological Society of America Special Paper, D. L. Weide, M. L. Faber, Eds. (Geological Society of America, 1985), vol. 203, pp. 1–21.

100. Z. Naiman, J. Quade, P. J. Patchett, Isotopic evidence for eolian recycling of pedogenic carbonate and variations in carbonate dust sources throughout the southwest United States. Geochim. Cosmochim. Acta 64, 3099–3109 (2000).

101. J. Quade, A. R. Chivas, M. T. McCulloch, Strontium and carbon isotope tracers and the origins of soil carbonate in South Australia and Victoria. Palaeogeogr. Palaeoclimatol. Palaeoecol. 113, 103– 117 (1995).

102. C. V. Haynes, Interim report on the Quaternary geology of northern Malawi and southern Tanzania. Quaternaria 13, 307–318 (1970).

103. Z. M. Kaufulu, Sedimentary environments at the Mwanganda site, Malawi. Geoarchaeology 5, 15– 27 (1990).

104. E. A. Stephens, Geological account of the northwest coast of Lake Malawi between Karonga and Lion Point, Malawi. Am. Anthrop. 68, 50–58 (1966).

105. A. M. Alonso-Zarza, V. P. Wright, Palustrine carbonates, in Carbonates in Continental Settings: Facies, Environments and Processes, Developments in Sedimentology A. M. Alonso-Zarza, L. H. Tanner, Eds. (Elsevier, 2010), vol. 61, pp. 103–131.

106. P. Freytet, E. P. Verrecchia, Lacustrine and palustrine carbonate petrography: An overview. J. Paleolimnol. 27, 221–237 (2002).

107. A. S. Goudie, Calcrete, in Chemical Sediments and Geomorphology, A. S. Goudie, K. Pye, Eds. (Academic Press, 1983), pp. 93–131.

108. E. P. Verrecchia, Litho-diagenetic implications of the calcium oxalate-carbonate biogeochemical cycle in semiarid Calcretes, Nazareth, Israel. Geomicrobiol. J. 8, 87–99 (1990).

109. R. Amit, Biogenic calcic horizon development under extremely arid conditions, Nizzana Sand Dunes, Israel. Adv. GeoEcol. 28, 65–88 (1995).

110. R. J. Schaetzl, S. Anderson, Soil Genesis and Geomorphology (Cambridge Univ. Press, 2005). 111. J. L. Slate, G. A. Smith, Y. Wang, T. E. Cerling, Carbonate-paleosol genesis in the Plio-Pleistocene St. David Formation, southeastern Arizona. J. Sediment. Res. 66, 85–94 (1996).

112. V. P. Wright, Calcrete, in Geochemical Sediments and Landscapes, D. J. Nash, S. J. McLaren, Eds. (Blackwell Publishing, 2007), pp. 10–45.

113. P. Alonso, C. Dorronsoro, J. A. Egido, Carbonatation in palaeosols formed on terraces of the Tormes river basin (Salamanca, Spain). Geoderma 118, 261–276 (2004).

114. G. Taylor, R. A. Eggleton, Regolith Geology and Geomorphology (John Wiley & Sons, Chicester, 2001).

115. V. P. Wright, Soil Micromorphology: A Basic and Applied Science, L. A. Douglas, Ed. (Elsevier, 1990), pp. 401–407.

116. G. Cailleau, E. P. Verrecchia, O. Braissant, L. Emmanuel, The biogenic origin of needle fibre calcite. Sedimentology 56, 1858–1875 (2009).

117. E. P. Verrecchia, K. E. Verrecchia, Needle-fiber calcite; A critical review and a proposed classification. J. Sediment. Res. 64, 650–664 (1994).

118. M. Wieder, D. H. Yaalon, Micromorphological fabrics and developmental stages of carbonate nodular forms related to soil characteristics. Geoderma 28, 203–220 (1982).

119. R. Crossley, Controls of sedimentation in the Malawi rift valley, Central Africa. Sediment. Geol. 40, 33–50 (1984).

120. J. R. Stone, K. S. Westover, A. S. Cohen, Late Pleistocene paleohydrography and diatom paleoecology of the central basin of Lake Malawi, Africa. Palaeogeogr. Palaeoclimatol. Palaeoecol. 303, 51–70 (2011).

121. M. J. Vepraskas, L. P. Wilding, L. R. Drees, Aquic conditions for Soil Taxonomy: Concepts, soil morphology and micromorphology, in Developments in Soil Science, A. J. Ringrose-Voase, G. S. Humphreys, Eds. (Elsevier, 1993), vol. 22, pp. 117–131.

122. M. J. McFarlane, Laterite and Landscape (Academic Press, 1976).

123. M. J. McFarlane, Mechanisms for lateritisation and the formation of erosion surfaces in parts of east and southern Africa. Bulletin de la Société Géographique de Liège 27, 149–155 (1991).

124. S. Nightingale, F. Schilt, J. C. Thompson, D. K. Wright, S. Forman, J. Mercader, P. Moss, S. Clarke, M. Itambu, E. Gomani Chindebvu, M. Welling, Late Middle Stone age behavior and environments at chaminade I (Karonga, Malawi). J. Paleolithic Archaeol. 2, 258–297 (2019).

125. J. E. Delvigne, Atlas of Micromorphology of Mineral Alteration and Weathering (Mineralogical Association of Canada, 1998).

126. I. Kovda, A. R. Mermut, Vertic features, in Interpretation of Micromorphological Features of Soils and Regoliths, G. Stoops, V. Marcelino, F. Mees, Eds. (Elsevier, 2010), pp. 109–127.

127. C. A. Stiles, C. I. Mora, S. G. Driese, Pedogenic iron-manganese nodules in Vertisols: A new proxy for paleoprecipitation? Geology 29, 943–946 (2001).

128. M. J. McFarlane, D. J. Bowden, Mobilization of aluminium in the wathering profiles of the African surface in Malawi. Earth Surf. Process. Landf. 17, 789–805 (1992).

129. E. Fritsch, C. R. Montes-Lauar, R. Boulet, A. J. Melfi, E. Balan, P. Magat, Lateritic and redoximorphic features in a faulted landscape near Manaus, Brazil. Eur. J. Soil Sci. 53, 203–217 (2002).

130. Y. Tardy, Petrology of Laterites and Tropical Soils (A. A. Balkema Publishers, 1997).

131. S. H. Ambrose, Chronology of the Later Stone Age and food production in East Africa. J. Archaeol. Sci. 25, 377–392 (1998).

132. K. Douze, A. Delagnes, The pattern of emergence of a Middle Stone Age tradition at Gademotta and Kulkuletti (Ethiopia) through convergent tool and point technologies. J. Hum. Evol. 91, 93–121 (2016).

133. S. McBrearty, A. S. Brooks, The revolution that wasn't: A new interpretation of the origin of modern human behavior. J. Hum. Evol. 39, 453–563 (2000).

134. C. R. Johnson, S. McBrearty, 500,000 year old blades from the Kapthurin Formation, Kenya. J. Hum. Evol. 58, 193–200 (2010).

135. J. Wilkins, M. Chazan, Blade production ~500 thousand years ago at Kathu Pan 1, South Africa: Support for a multiple origins hypothesis for early Middle Pleistocene blade technologies. J. Archaeol. Sci. 39, 1883–1900 (2012).

136. E. M. Scerri, J. Blinkhorn, K. Niang, M. D. Bateman, H. S. Groucutt, Persistence of Middle Stone Age technology to the Pleistocene/Holocene transition supports a complex hominin evolutionary scenario in West Africa. J. Archaeol. Sci. Rep. 11, 639–646 (2017).

137. C. Tribolo, A. Asrat, J.J. Bahain, C. Chapon, E. Douville, C. Fragnol, M. Hernandez, E. Hovers, A. Leplongeon, L. Martin, D. Pleurdeau, O. Pearson, S. Puaud, Z. Assefa, Across the gap: Geochronological and sedimentological analyses from the Late Pleistocene-Holocene sequence of Goda Buticha, Southeastern Ethiopia. PLOS ONE 12, e0169418 (2017).

138. A. J. H. Goodwin, An introduction to the Middle Stone Age in South Africa. S. Afr. J. Sci. 25, 410–418 (1928).

139. A. J. H. Goodwin, C. Van Riet Lowe, The Stone Age cultures of South Africa. Ann. S. Afr. Mus. 27, 1–289 (1929).

140. J. D. Clark, C. V. Haynes, J. E. Mawby, A. Gautier, Preliminary investigations in Malawi. Quaternaria, 305–354 (1970).

141. K. Faegri, J. Iversen, P. E. Kaland, K. Krzywinski, Textbook of Pollen Analysis (Blackburn Press, ed. 4th, 1989).

142. J. Maley, Contributions a l'etude du Bassin tchadien Atlas de pollens du Tchad. Bull. Jard. Bot. Nat. Belg. 40, 29–48 (1970).

143. R. Bonnefille, G. Riollet, Pollens de Savanes d'Afrique Orientale (Éditions du Centre national de la recherche scientifique, Paris, 1980).

144. E. C. Grimm, Tilia and Tiliagraph (Illinois State Museum, 1991).

145. E. C. Grimm, CONISS: A FORTRAN 77 program for stratigraphically constrained cluster analysis by the method of incremental sum of squares. Comput. Geosci. 13, 13–35 (1987).

146. R. Margalef, Information theory in ecology. Int. J. Gen. Syst. 3, 36–71 (1958).

147. J. Mercader, T. Bennett, C. Esselmont, S. Simpson, D. Walde, Phytoliths in woody plants from the miombo woodlands of Mozambique. Ann. Bot. 104, 91–113 (2009).

148. R. M. Albert, M. K. Bamford, D. Cabanes, Taphonomy of phytoliths and macroplants in different soils from Olduvai Gorge (Tanzania) and the application to Plio-Pleistocene palaeoanthropological samples. Quatern. Int. 148, 78–94 (2006).

149. B. M. Campbell, The Miombo in transition: Woodlands and welfare in Africa (Bogor, Indonesia, Center for International Forestry Research, 1996).

150. C. M. Ryan, M. Williams, How does fire intensity and frequency affect miombo woodland tree populations and biomass? Ecol. Appl. 21, 48–60 (2011).

151. W. A. Hoffmann, E. L. Geiger, S. G. Gotsch, D. R. Rossatto, L. C. R. Silva, O. L. Lau, M. Haridasan, A. C. Franco, Ecological thresholds at the savanna-forest boundary: How plant traits, resources and fire govern the distribution of tropical biomes. Ecol. Lett. 15, 759–768 (2012).

152. C. A. Scholz, A.S. Cohen, T.C. Johnson, J. King, M.R. Talbot, E.T. Brown, Scientific drilling in the Great Rift Valley: The 2005 Lake Malawi Scientific Drilling Project—An overview of the past 145,000 years of climate variability in Southern Hemisphere East Africa. Palaeogeogr. Palaeoclimatol. Palaeoecol. 303, 3–19 (2011).

153. J. Jouzel, V. Masson-Delmotte, O. Cattani, G. Dreyfus, S. Falourd, G. Hoffmann, B. Minster, J. Nouet, J M Barnola, J. Chappellaz, H. Fischer, J C Gallet, S. Johnsen, M. Leuenberger, L. Loulergue, D. Luethi, H. Oerter, F. Parrenin, G. Raisbeck, D. Raynaud, A. Schilt, J. Schwander, E. Selmo, R. Souchez, R. Spahni, B. Stauffer, J. P. Steffensen, B. Stenni, T. F. Stocker, J. L. Tison, M. Werner, E. W. Wolff, Orbital and millennial Antarctic climate variability over the past 800,000 years. Science 317, 793–796 (2007).

154. A. Berger, M.-F. Loutre, Insolation values for the climate of the last 10 million years. Quat. Sci. Rev. 10, 297–317 (1991).

E - Hunter-Gatherer Environments at the Late Pleistocene Sites of Mwanganda´s Village and Bruce, Northern Malawi

Flora C. Schilt [a, b], Christopher M. Miller [a, c], David K. Wright [d, e], Susan M. Mentzer [a, f], Julio Mercader [g, h, i], Patrick Moss [j], Jeong-Heon Choi [k], Gunnar Siljedal [g], Siobhán Clarke [g], Aloyce Mwambwiga [g, l], Kelly Thomas [g], Alvise Barbieri [b], Potiphar Kaliba [m], Elizabeth Gomani Chindebvu [n], Jessica C. Thompson [o, p]

Quaternary Science Reviews 292: 107638. Open access under
https://www.sciencedirect.com/science/article/pii/S0277379122002694
Below follows an earlier manuscript, under review at the time of thesis submission.

[a] Institute for Archaeological Sciences and Senckenberg Centre for Human Evolution and Paleoenvironment, University of Tübingen, Tübingen, Germany. [b] Interdisciplinary Center for Archaeology and Evolution of Human Behaviour, University of Algarve, FCHS, Campus Gambelas, J27, Faro, Portugal. [c] SFF Centre for Early Sapiens Behaviour (SapienCE), University of Bergen, Bergen, Norway. [d] Department of Archaeology, Conservation and History, University of Oslo, Oslo, Norway. [e] State Key Laboratory of Loess and Quaternary Geology, Institute of Earth Environment, Chinese Academy of Sciences, Xian, China. [f] School of Anthropology, University of Arizona, Tucson, AZ. [g] Department of Anthropology & Archaeology, University of Calgary, 2500 University Drive NW, Calgary, Alberta, T2N 1N4, Canada. [h] Department of Archaeology, Max Planck Institute for the Science of Human History, Jena, 07745, Germany. [i] Institut Català de Paleoecologia Humana i Evolució Social (IPHES), Zona Educacional, 4 – Campus Sescelades URV (Edifici W3), Tarragona, 43007, Spain. [j] School of Earth and Environmental Sciences, The University of Queensland, Queensland, Brisbane 4072, Australia. [k] Research Center for Geochronology and Isotope Analysis, Korea Basic Science Institute, Ochang, Republic of Korea. [l] National Natural History Museum, PO Box 2160, Arusha, Tanzania. [m] Malawi Department of Museums and Monuments, Lilongwe, Malawi. [n] Ministry of Civic Education and National Unity, Lilongwe, Malawi. [o] Department of Anthropology, Yale University, New Haven, CT, USA. [p] Institute of Human Origins, P.O. Box 874101, Tempe, AZ 85287, USA.

keywords: Karonga, geoarchaeology, paleoecology, micromorphology, pedogenic carbonates, Middle Stone Age, stable carbon and oxygen isotopes, phytoliths, pollen

1. ABSTRACT

Mwanganda's Village (MGD) and Bruce (BRU) are two open-air site complexes in northern Malawi with deposits dating to between 15 and 58 thousand years ago (ka) and containing Middle Stone Age (MSA) assemblages distinctive for the region. The sites have been known since 1966 and 1965, respectively, but lacked chronometric and site formation data necessary for their

interpretation. The area hosts a rich stone artifact record, eroding from and found within alluvial fan deposits exhibiting poor preservation of organic materials. Although this generally limits opportunities for site-based environmental reconstructions, MGD and BRU are located at the distal margins of the alluvial fan, where lacustrine lagoonal deposits were overprinted by a calcrete paleosol. This has created locally improved organic preservation and allowed us to obtain ecological data from pollen, phytoliths, and pedogenic carbonates, producing a regional to site-scale environmental context for periods of site use and abandonment. Here, we integrate the ecological data into a detailed site formation history, based on field observations and micromorphology, supplemented by cathodoluminescence microscopy and μ-XRF. By comparing local, on-site environmental proxies with more regional indicators we can better evaluate how MSA hunter-gatherers made decisions about the use of resources across the landscape. Our data indicate that while tree cover similar to modern miombo woodland and evergreen gallery forest prevailed at most times, MSA hunter-gatherers chose more locally open environments for activities that resulted in a lithic artifact record at multiple locations between 51-15 ka.

2. INTRODUCTION

Lithic artifact assemblages assigned to the MSA are found in Africa from ~315 to 20 thousand years ago [ka] and are associated with an increase in technological complexity among hunter-gatherers, as well as developments in abstract thinking and symbolism (Richter et al. 2017; Brooks et al. 2018; Scerri et al. 2018). At present, most of the MSA archaeological record comes from northern Africa, the northern part of the East African Rift Valley, and southern Africa (Mackay et al. 2014; Wadley 2015; Scerri 2017; Tryon 2019). Malawi is situated in the important connecting region between the latter two regions (Mercader, Asmerom, et al. 2009; Bicho et al. 2016; Thompson et al. 2018).

The physical environment played a significant role in shaping human adaptation in eastern-central Africa, both regionally and locally (Basell 2008; Kandel et al. 2016; Patalano et al. 2021). The choice of hunter-gatherers to use certain places was influenced by local conditions of resource availability (Kandel et al. 2016). However, most environmental records derive from large, basin-wide datasets, which cannot be linked directly to archaeological sites and human occupation (Cohen et al. 2007; Scholz et al. 2007; Scholz et al. 2011; Lyons et al. 2015; Ivory et al. 2018; Thompson, Wright, Ivory, et al. 2021). In northern Malawi, paleoenvironmental research has focused on the study of sediment cores from Lake Malawi, dating back to 1.3 million years ago

(Scholz et al. 2006; Cohen et al. 2007; Scholz et al. 2011; Beuning et al. 2011; Lyons et al. 2015). These studies show that lakeshores transgressed and regressed hundreds of meters in elevation through time, and that there were extreme arid periods of near desiccation of the lake (Lyons et al. 2015). After 85 ka, lake levels remained relatively high, which has been attributed to more stable, wetter conditions caused by a shift in the position of the Intertropical Convergence Zone related to changes in orbital eccentricity and precession (Ivory et al. 2016). This may be a major reason why the region developed an abundant MSA record after this time (Thompson, Wright, Ivory, et al. 2021), but it does not explain how MSA people selected their activity areas across that landscape.

Previous studies showed that MSA sites in northern Malawi became more abundant after 75 ka within the context of the expansion of miombo woodland and mosaic savanna (Thompson, Wright, and Ivory 2021). Complicating interpretations, though, is the fact that most archaeological sites are found in alluvial fan deposits with thick lateritic soils (also known as Oxisols or Ferralsols), inhibiting the preservation of organic materials. These soils formed during periods of stability, overprinting the sedimentary layers created by the alluvial fan (Wright et al. 2017). Subsequent bioturbation and chemical weathering in laterites have homogenized deposits, erasing fine structural features, including former land surfaces (Wright et al. 2017). This confounds a clear understanding of local scale environments where MSA people concentrated their activities, and how these relate to different kinds of artifact production.

Mwanganda´s Village (MGD) and Bruce (BRU) are two MSA sites located at the margins of the alluvial fan system to the west of Lake Malawi (fig. 1). Overviews of artifact (in the case of MGD), fossil assemblages, and macro-scale geoarchaeological observations were previously reported from both sites (Clark et al. 1970; Clark and Haynes 1970; Clark et al. 1973; Kaufulu 1990; Wright et al. 2014). However, these studies lack essential data on timing and context of the artifacts.

With our work, we have taken advantage of the location of these neighboring sites on the distal part of the fan (fig. 1) to access alluvial fan sediments as well as lake-lagoon deposits and paleosols. Combining geoarchaeological, paleoenvironmental, and chronological data, this paper aims to (1) investigate past environments, (2) achieve detailed reconstructions of site formation, and (3) place late MSA occurrences in a regional- to site-scale environmental context to address aspects of MSA forager behaviors.

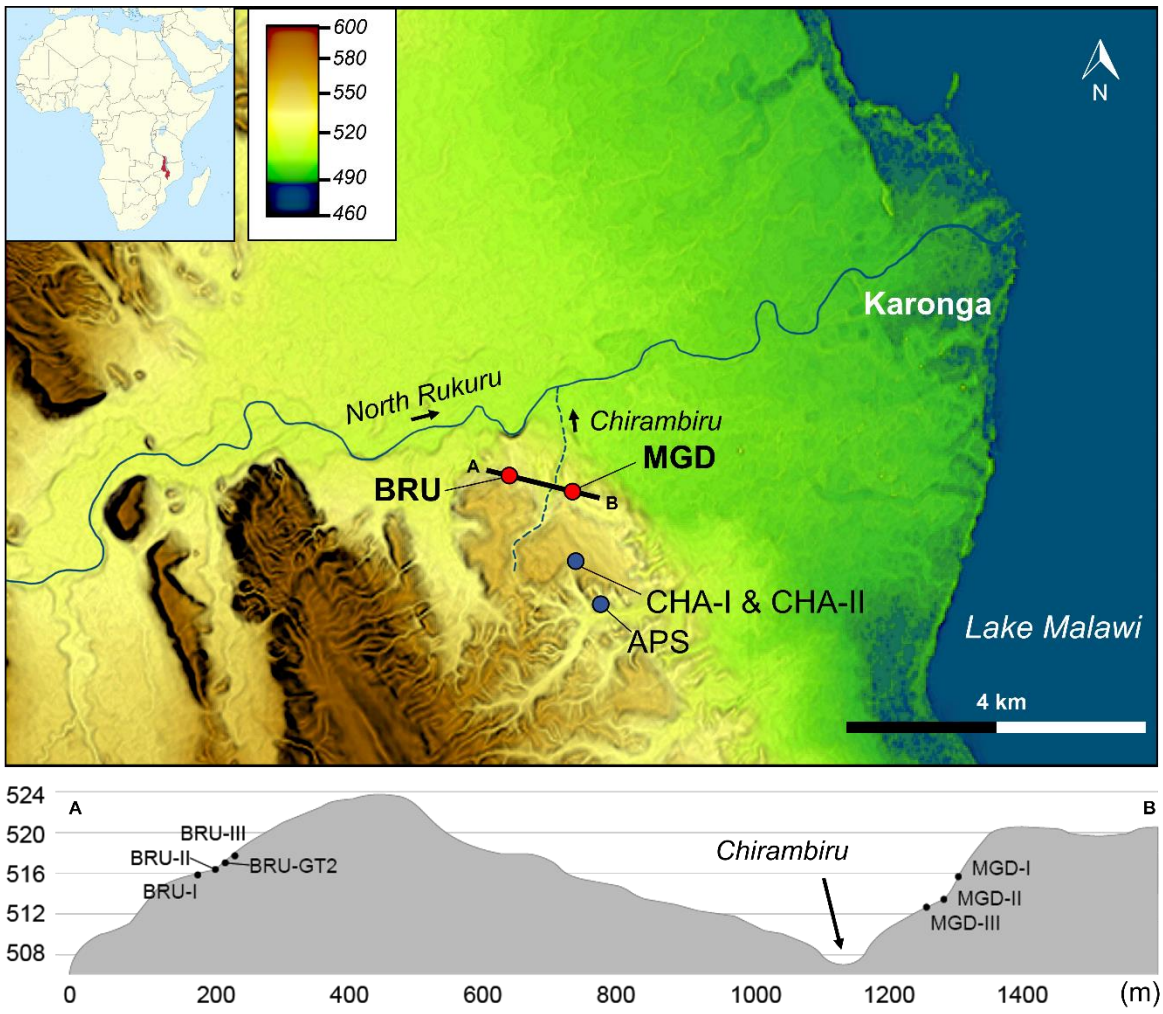

Fig. 1. Map of the area west of Karonga town indicating the site locations of Bruce (BRU) and Mwanganda´s Village (MGD) on the hill slopes facing the catchment area of the North Rukuru River, which drains into Lake Malawi to the east (map produced with AW3D30 data). Lake lagoons are visible as blue areas along the shore. The blue dots indicate other published localities: Airport Site (APS), Chaminade-I (CHA-I), and Chaminade-II (CHA-II). Below the map the modern topography is shown on a transect line between BRU and MGD (A, B) with the incision of the Chirambiru seasonal stream indicated in between the site areas.

Geologic setting

The sites are located in the southern branch of the East African Rift System, which runs NNW-SSE and forms Lake Malawi (also known as Lake Nyasa or Lago Niassa), a large extensional graben lake. The down-faulted rift valley is bounded to the east and west by mountain ranges (Ring et al. 1992; Ring and Betzler 1995). The underlying Malawi Basement consists mainly of gneisses and granulites of Precambrian to lower Paleozoic age. These metamorphic rocks are covered with Permian to the lower Jurassic volcanic and sedimentary formations of the Karoo system. Locally, the upper contact of the metamorphic Basement Complex and Karoo sediments are overlain by Early Cretaceous Dinosaur Beds consisting of friable sandstones, sandy marls, and clays (Betzler

and Ring 1995). The Chiwondo Beds unconformably overlie the Dinosaur Beds and have been temporally attributed to the Late Pliocene and Early Pleistocene based on biostratigraphy (Dixey 1927; Stephens 1963; Clark et al. 1966; Bromage et al. 1995), although they may extend into the early Middle Pleistocene (Kullmer 2008). Chiwondo Beds mainly consist of sandstones and siltstones of lacustrine origin, which have been deeply incised (Stephens 1963) and are unconformably overlain by the Chitimwe Beds. The latter consist of eroded remnants of an extensive alluvial fan system, which drained into the lake (S-Fig. 1).

The Chitimwe Beds have long been recognized as hosting an abundance of MSA and LSA lithic artifacts (Dixey 1930; Clark 1966; Thompson et al. 2012; Wright et al. 2017; Nightingale et al. 2019). The alluvial fans originate from periodic erosion of the upland catchment of the western rift shoulder where colluvium and weathering bedrock produce new sediments, which aggrade in lowland areas (Blair and McPherson 1994). The movement and transport of catchment sediment depends on water input, gravity, vegetation, and mass wasting, and is especially promoted by flood conditions, which are common in Malawi between November and March due to monsoon-driven rainfall. Thompson *et al.* (2021) have further suggested that anthropogenic use of fire starting ~90 ka cleared tree cover to such an extent that it accelerated alluvial fan formation. Secondary processes modifying the sands and gravels of the Chitimwe Formation include surficial reworking by water and winnowing, as well as intensive weathering and laterite formation (Blair and McPherson 1994; Wright et al. 2017). In the Karonga area, lateritic soil formation is widespread and likely induced by increased exposure of the soil to extremes in temperature and humidity after clearance of the forest cover (McFarlane 1976). Agriculture and construction activities have increased erosion of alluvial fan deposits in many places, exposing numerous lithic artifacts.

Archaeological context

MEMSAP has taken a landscape approach to build a sequence of regional MSA behaviors and environments that would not be possible at a single locality. This has included survey (Thompson et al. 2014), geological and archaeological test pitting (Thompson et al. 2018; Thompson, Wright, Ivory, et al. 2021), and more detailed archaeological excavations such as at MGD and BRU (fig. 1) (Thompson *et al.*, 2012, in press; Wright *et al.*, 2014, 2017; Nightingale *et al.*, 2019).

Unlike most of areas investigated with detailed excavations, where Chitimwe Beds exhibit thick lateritic deposits (Wright et al. 2017), MGD and BRU are situated at the fringe of the alluvial fan. These localities are situated on north-facing slopes overlooking the floodplain of the North Rukuru River, which drains into Lake Malawi ~7 km to the east (fig. 1). Archaeological excavations

in all trenches exposed MSA artifacts, but only two of them, MGD Area I and BRU Area II (fig. 2), yielded assemblages demonstrably in primary context. Likely in situ lithic artifacts were also uncovered from two additional tests pits at BRU (BRU-TP20 and BRU-TP21). The analysis of all these lithic materials is currently underway.

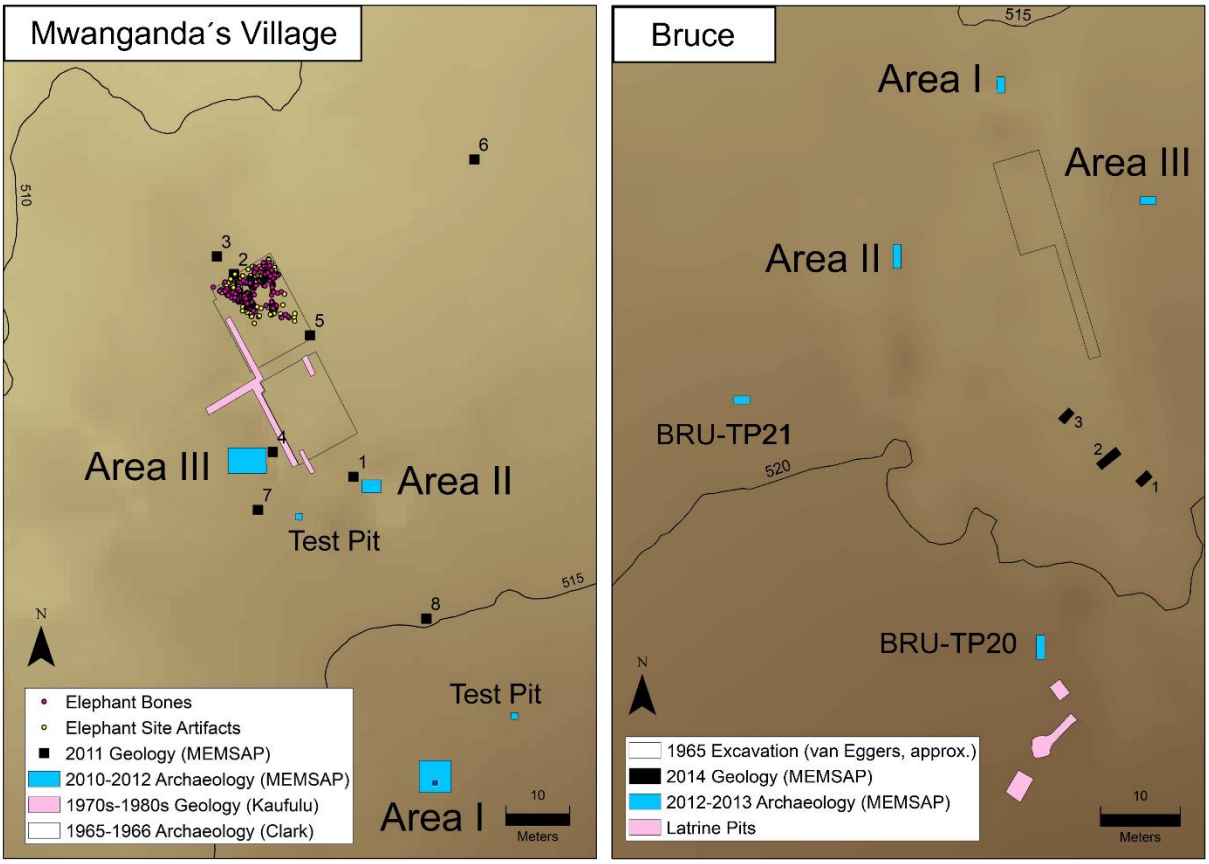

Fig. 2 Overview maps showing excavation areas of Clark and colleagues, Kaufulu, and MEMSAP at Mwanganda's Village (left) and Bruce (right). Darker browns are higher elevations, contour elevations in m. The original designations for the two test pits at BRU were CHA-TP20 and CHA-TP21, as they were part of a larger survey program starting in the general area of Chaminade Secondary School (near CHA-I and CHA-II, fig. 1). Here and in the text, they will be referred to as BRU-TP20 and BRU-TP21 for clarity.

Mwanganda's Village (MGD)

In 1966, Clark led excavations at MGD, which had skeletal remains of an elephant, too fragmentary to assign to genus, with artifacts scattered around the bones. He inferred that MGD was an ancient elephant butchery site associated with Sangoan tools, a type of artifact thought to occur in the earlier part of the MSA (Clark and Haynes 1970). Later, Kaufulu (1990) reinvestigated the site with large geological trenches to further understand the relationship between the Chitimwe and Chiwondo Beds that were reported as occurring in contact at the location by Clark and Haynes

(1970). This "Elephant Butchery Site" at MGD has since been cited as an early MSA or Sangoan industry site with evidence for the in situ disarticulation of an elephant (e.g., Piperno and Tagliacozzo, 2001; Surovell and Waguespack, 2008; Yravedra *et al.*, 2012). From 2009-2013, the Malawi Earlier-Middle Stone Age (MEMSAP) team mapped the area, collected samples, and conducted new excavations at MGD (MGD-I to III, fig. 2). They conducted excavations adjacent to and upslope of the original elephant discovery and dated the newly exposed sediments with Optically Stimulated Luminescence (OSL). They also examined the elephant remains for evidence of butchery, determined the age of elephant enamel fragments with Uranium-Thorium, and corrected maps from Kaufulu (1990), which show inaccurate positions of some of the geological trenches (Thompson et al. 2013; Wright et al. 2014). Based on these analyses, MEMSAP team members concluded that the fossils and artifacts were likely brought together through post-depositional processes (Wright et al. 2017).

Wright *et al.* (2014) distinguished a total of four fluvial cut terraces across MGD dating to the Holocene, that significantly post-date MSA occupation. This Holocene terrace formation may be partially responsible for mixing of sediments near the present-day surface but has not affected more deeply buried Pleistocene sediments. Excavation area MGD-I (5 x 5 m) was positioned on a terrace uphill from Clark´s trenches to obtain a longer sequence (fig. 1, 2). MGD-II (4 x 5 m) and MGD-III (4 x 5 m) were placed on a lower terrace next to Clark´s excavations, with the purpose of re-examining the context of the "Elephant Butchery Site" (fig. 2, 6). A test pit located 13 m to the north and 10 m to the east of MGD-I showed a gravelly coarse sand deposit buried 1.7 m below the ground surface, which exhibited artifacts and is bracketed by OSL ages between 43±4 ka and 22±2 ka (Wright et al. 2014). At MGD-I, unweathered "classic" MSA lithic artifacts were found just above sediments dating to 26±1 ka. Above this, terminal MSA lithics with multiple refits were recovered from sediments dating to between 26±1 ka and 15±1 ka (Thompson, Wright, Ivory, et al. 2021). The terminal MSA assemblage displays both MSA and LSA approaches to artifact reduction on the same objects, e.g., a centripetal reduction strategy on small (2-4 cm) quartz pebbles rather than larger quartzite cobbles, resulting in pyramidal cores with neither final preferential detachments nor evidence for microlith production. This sequence supports an interpretation of the site as a place where people with varying MSA technological approaches returned multiple times, potentially over the course of ~10,000 years (fig. 3).

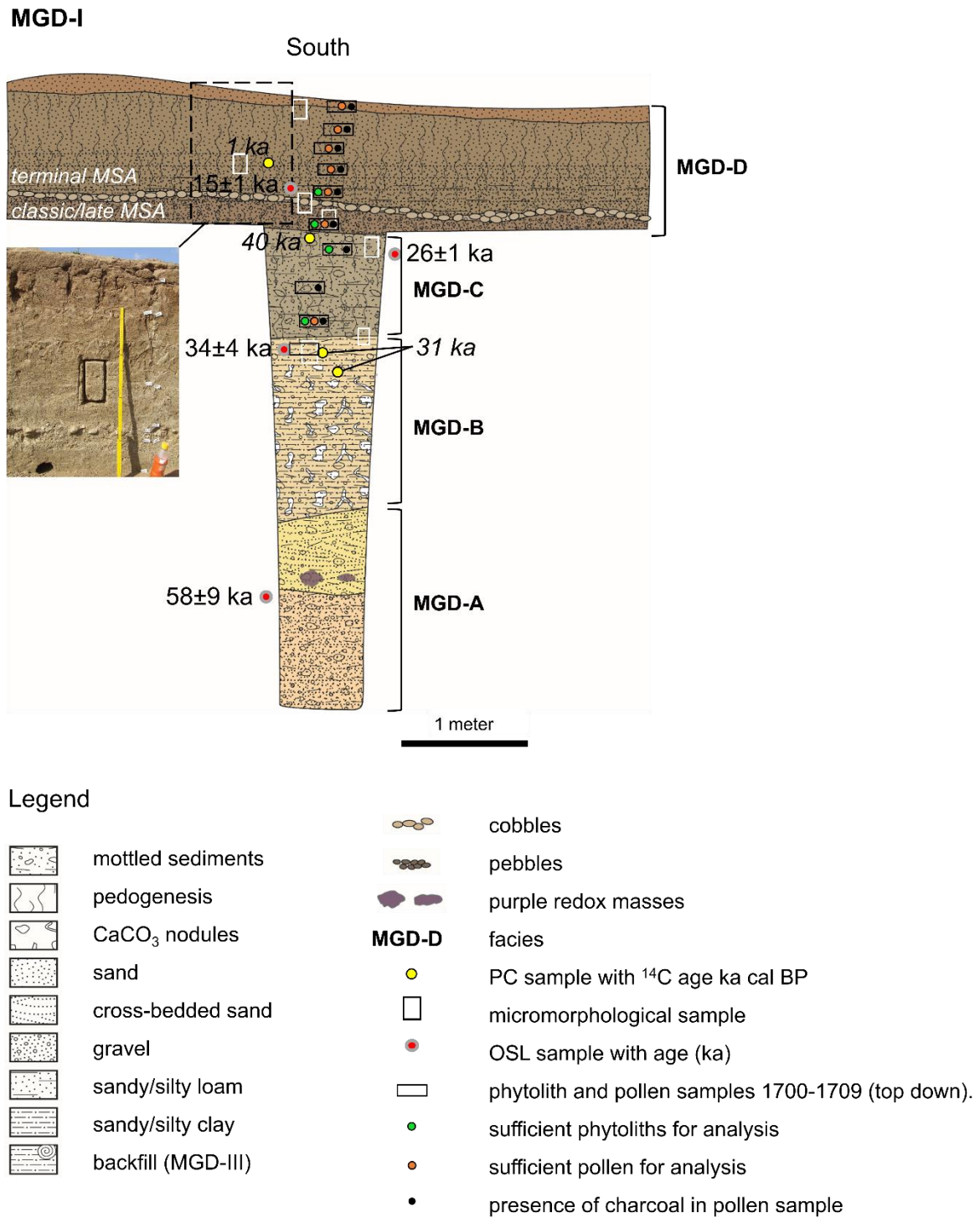

Fig. 3. Profile drawing of MGD-I with depositional facies indicated with brackets to the right, which are described in detail in the results section. OSL dates are in roman typeface and radiocarbon dates on pedogenic carbonates are in italics. Classic/late MSA lithic artifacts were recovered from below the cobble layer within facies *MGD-D*, and terminal MSA was found above the cobble horizon. The inset photo shows facies *MGD-D* with a partly carved out micromorphology sample, and an empty termite fungus chamber in the lower left. The modern soil rubifies towards the top.

Bruce (BRU)

In 1965, one of Clark´s doctoral students, van Eggers, supervised excavations at a site called Chaminade 1A, about 1 km northwest of MGD on the NNW facing slope of an adjacent distal lobe of the alluvial fan (fig. 1). Although this was not described as a Sangoan site, there is a core-axe illustrated by Clark et al. (1970), alongside "classic" MSA artifacts such as Levallois points. Clark et al. (1970, 1973) also report pigments, which are absent at MGD, suggesting variation in activities carried out between the two sites. Through systematic test-pitting, local knowledge, and analysis of archive documents, MEMSAP identified a locality named BRU, later determined to be equivalent to Chaminade 1A. The high density of lithic artifacts and the presence of worked ochre on the surface also match the description in Clark, Haynes and Mawby (1973). Although we are confident it is the same locality, unlike at MGD we could not identify the exact location of the original van Eggers excavation relative to our new MEMSAP excavations. We therefore continue to use the MEMSAP designation BRU for the site.

Three archaeological excavation areas of 1 x 2 m (BRU-I to III), two archaeological test pits (BRU-TP20 and BRU-TP21), and three geo-trenches (BRU-GT1 to 3) were placed on the hillslope (fig. 2). Beside the archaeological excavations and test pits, one of the geo-trenches, BRU-GT2, is included in this paper, as it exposed thick lagoonal deposits not well-represented in the archaeological excavations. Numerous lithic artifacts occur on the ground surface at BRU due to water erosion, which is especially active at this location due to agricultural activity and house construction. Although lithic assemblages were not stratified in a single pit but were exposed in several small excavations, the area shows repeated human occupation over many thousands of years. At BRU-II, unweathered artifacts occur in deposits dating between 34±3 and 33±3 ka, while at BRU-TP20 numerous concentrations of artifacts with some refits date between 51±4 and 31±2 ka (Thompson, Wright, Ivory, et al. 2021). Bedrock was not reached in any of the excavations.

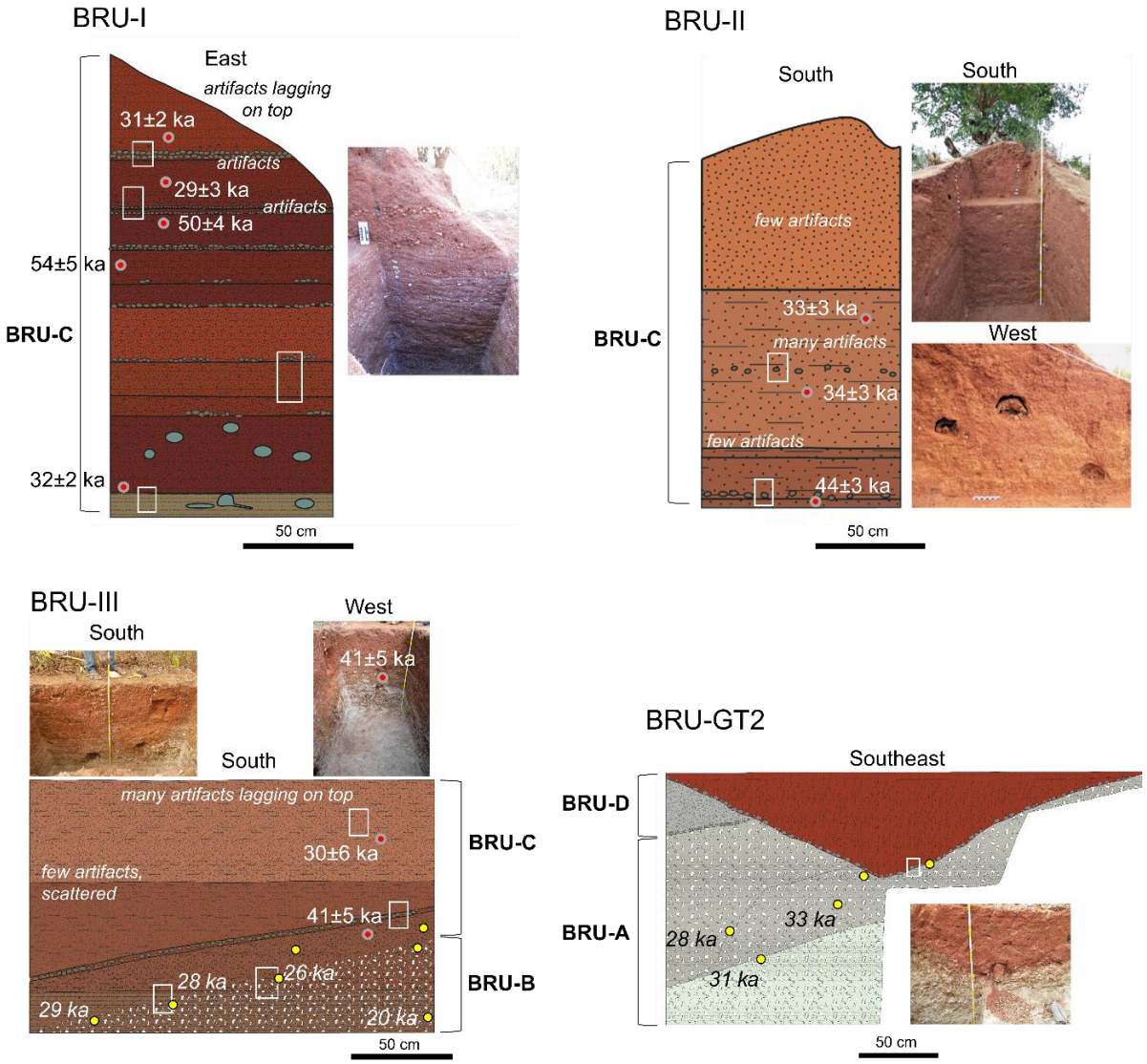

Fig. 4. Profile drawings of three excavation areas (BRU-I, BRU-II, BRU-III) and a geo-trench (BRU-GT2) at BRU with facies (detailed in the results section) indicated, as well as OSL ages (roman) and radiocarbon dates (italic) from selected pedogenic carbonate samples. For the legend, see fig. 3. One of the facies (*BRU-B*, found at BRU-III) is defined by calcrete soil formation. Different from the similar paleosol horizon of facies *MGD-C*, there are no signs that *BRU-B* was truncated and the soil horizon with pedogenic carbonates formed after burial by *BRU-C*. Consequently, sediments of *BRU-C* are older than the paleosol (^{14}C dates on pedogenic carbonate) they cover.

3. METHODS

The primary methods of analysis involved micromorphological study of block sediment samples and carbonate nodules, pollen and phytoliths analysis, and stable isotopes from pedogenic carbonates. In this paper we also report two new OSL ages from BRU-TP21. Methods are summarized in this section; additional information is provided in supplementary material (S1).

3.1 Field descriptions

All exposed sections were described following the "USDA Field Book for Describing and Sampling Soils" (Schoeneberger et al. 2012). Visual observations were aided by a hand lens, and included for each sedimentary unit descriptions of texture, color, structure, weathering features, inclusions, carbonate content, consistency, clay films, disturbances, and unit boundaries. Colors on dry sediment were described using the Munsell soil-color charts (M Color and X-rite 2009). A feel-test was regularly performed when textures were loamy or clayey (Thien 1979).

3.2 Micromorphology, cathodoluminescence, and microscopic X-ray fluorescence

Micromorphology was used to reconstruct site formation processes and served as a basis for other analyses and sub-sample collection. 47 block samples and 15 carbonate nodule samples were collected from exposed profiles at BRU and MGD, producing 95 thin sections.

In addition to the analysis with stereoscopic and petrographic microscopes, we used a cathodoluminescence (CL) microscope on a selection of thin sections. Observations were recorded with photomicrographs (S5). Microscopic X-ray fluorescence (μ-XRF) was used to determine relative abundances of major and trace elements (Mentzer and Quade 2013), and was performed on a selection of samples.

3.3 Paleoecology

Pollen and phytolith samples were collected in the field as bulk sediment samples from exposed profiles. The profiles were first cleaned from top to bottom with a hard brush to remove loose sediments and sampled from bottom to top with a trowel and dustpan. The trowel and dustpan were cleaned in soapy water and rinsed in plain water between sampling episodes.

Palynology

Pollen analysis was attempted only at MGD (fig. 3). Ten sediment samples were processed for pollen and micro-charcoal (particles <125 μm) following the methods described in Moss (2013). Seven of the samples contained pollen (1700-1705, and 1708) with concentrations between 200 to 700 grains per cm^3. Nine of the samples contained charcoal (1700-1708).

Phytolith analysis

The nomenclature for phytolith classification used in this paper follows Madella *et al.*, (2005). Supporting keys from pertinent regions include: Runge, 1999; Fahmy, 2008; Albert, Bamford and

Cabanes, 2009; Barboni and Bremond, 2009; Neumann *et al.*, 2009, 2017; Eichhorn, Neumann and Garnier, 2010; Novello *et al.*, 2012; Albert, Bamford and Esteban, 2015; Collura and Neumann, 2017, as well as past phytolith work on referentials and archaeological localities from both the Malawi side of the lake (Wright et al. 2017; Nightingale et al. 2019; Thompson, Wright, Ivory, et al. 2021) and the Mozambican shore (Mercader, Bennett, et al. 2009; Mercader et al. 2010; Mercader et al. 2011).

Stable isotope analysis ($\delta^{13}C_{PC}$ and $\delta^{18}O_{PC}$)

Stable isotopes from pedogenic carbonates ($\delta^{13}C_{PC}$, $\delta^{18}O_{PC}$) were measured to reconstruct aspects of vegetation and climate during soil formation (Cerling 1984). The analyses were performed on 27 sub-samples from 18 pedogenic carbonate nodules. The samples were calibrated against the NBS 18 standard: $\delta^{13}C$ = -5.014‰ and $\delta^{18}O$ = -23.2‰. All $\delta^{13}C_{PC}$ and $\delta^{18}O_{PC}$ measurements are expressed in permille (‰) in relation to the VPDB standard.

3.4 OSL dating

OSL ages on quartz grains from two samples (LM13-10, LM13-11) collected at BRU-TP21 were determined by protocols similar to Wright *et al.* (2017), using small aliquots (~3 mm mask size), consisting of several hundreds of quartz grains (180–212 μm diameter). OSL measurements were carried out using a Risø TL/OSL reader (Model TL/OSL-DA-20C/D) at Korea Basic Science Institute. Burial equivalent doses were calculated using Single Aliquot Regenerative dose (SAR) procedure. Dose rate estimations were determined by low-level high-resolution gamma spectrometer. The resulting ages are included in table 2, more details are reported in the supplementary material (Table S-T6, S-Fig. 2a and b).

4. RESULTS

4.1 Lithostratigraphy of MGD and BRU— key field and micromorphological observations

We have grouped sedimentary and pedogenic units described at MGD and BRU into facies (Walther 1894; Middleton 1973). For a complete overview of the units see the supplementary material (tables S-T12 and S-T13). A schematic overview of profiles of the archaeological excavations and their facies is given in fig. 5. The facies are further summarized and contextualized with the ecological data, chronology, and archaeology in table 1 for MGD, and table 2 for BRU.

More detailed field and micromorphological descriptions, CL-microscopy, and μ-XRF results can be found in the supplementary material (S4, S5, and S6, respectively).

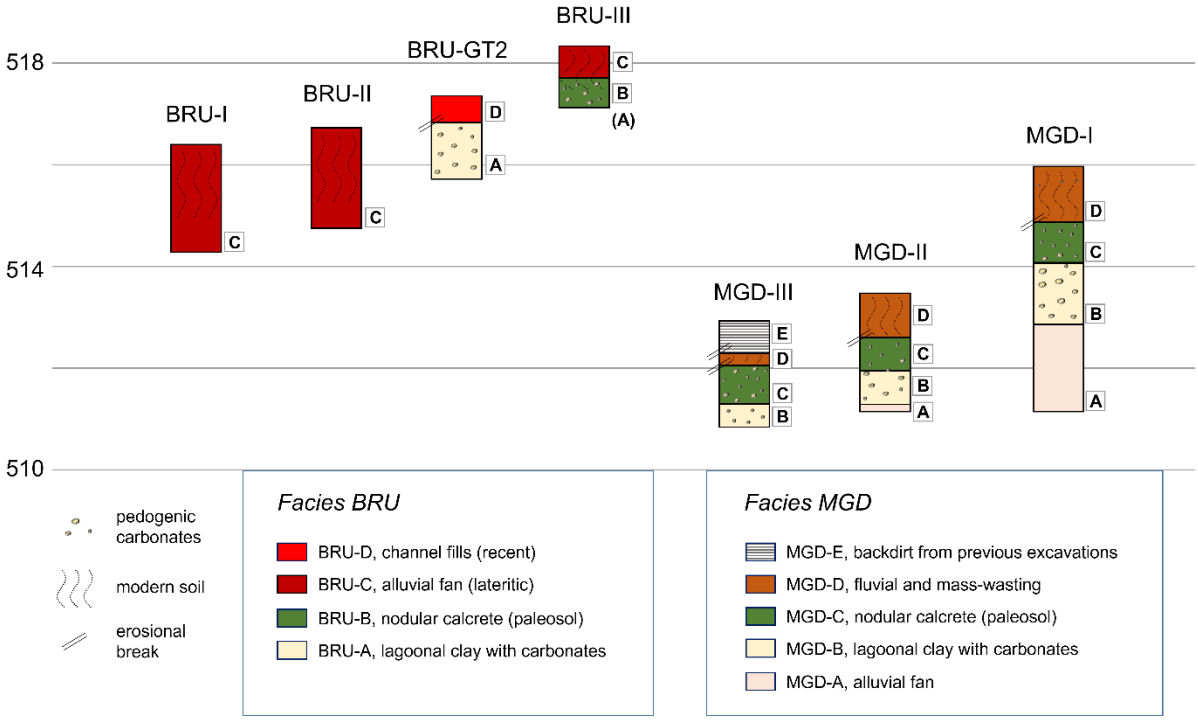

Fig. 5. Overview of four trenches at BRU (left) and three at MGD (right) along a NW-SE transect, indicating the different facies within each profile. At BRU-III, facies *BRU-A* was only observed at the bottom of the pit and is therefore indicated between brackets. Facies *BRU-A* is equivalent to *MGD-B*, and carbonate paleosols developed in *BRU-B* and *MGD-C* but extend with palustrine-pedogenic carbonates into the underlying facies *BRU-A* and *MGD-B*.

Mwanganda's Village

The stratigraphy at MGD shows some variability between the site areas related to their position on different parts of the slope.

The lowermost facies, *MGD-A*, consists of angular coarse sands and fine gravel with 1-2 % coarse rounded pebbles. Clear horizontal depositional planes and cross-bedding are preserved. The facies is grayish white to yellowish in color with faint, dm-scale yellow and purple redox masses.

Facies *MGD-B* was formed under non-turbid, subaqueous conditions and included the deposition of silty clay as suspended load with intercalated laminations of fine sand. The clay is rich in mica, giving it a greenish color (fig. 7a). Carbonate nodules are common in this facies and vary in size from 1 mm to ~15 cm. Inclusions of organic remains inside the nodules and the occurrence of both alpha-type microfabrics (formed by physical and chemical processes) and beta-type

microfabrics (formed by biogenic processes) within the nodules are indicative of palustrine-pedogenic formation (Wright 1990a; Alonso-Zarza and Wright 2010a). Because the finely laminated deposit is well-structured, bioturbation features appear very distinct (fig. 7a). They mainly consist of chambers (1-2 cm in diameter), interconnected by a network of channels. Towards the top, an increase in bioturbation by soil fauna, desiccation cracks and root disturbances is observed.

MGD-C is a welded buried paleosol, corresponding to the paleosol described by Clark and Haynes (1970), the top 10 cm of which was the context of the elephant bones and lithic artifacts. *MGD-C* formed in a lagoonal environment and was subsequently overprinted by soil formation and the admixture of coarse alluvial sediment through cracks and bioturbation, which gave *MGD-C* a loamy texture (fig. 7b, c, f, g). After this, a calcrete formed in the mixed sediments. *MGD-C* appeared massive in the field but in thin section, many mixing agents were distinguished, including shrink-swell within the soil, the formation and infilling of desiccation cracks, root action, bioturbation by soil fauna, and pedogenic carbonate formation. Their compounding effects obliterated pre-existing potential sedimentary structures (fig. 7c, h, i, k). However, rare 1-3-cm sized angular and pillar-shaped peds of laminated clay (similar to facies *MGD-B*) were found in their original depositional orientation, revealing the sedimentary origin of the soil parent material (fig. 7g). CL-microscopy of the pedogenic carbonate nodules has shown that both types of sediment have been replaced by carbonate, indicating that mixing of the lagoonal clay with alluvial deposits occurred well before the paleosol became a mature calcrete. Generally, the formation of nodular calcretes constitute the final stage of soil development in this type of environment (Blokhuis et al. 1990). Clay coatings and reworked fragments of clay coatings are rare, but few intact and fragmented, laminated, limpid yellow clay coatings were observed near and inside carbonate nodules, some of which are partially dissolved and substituted by microsparitic carbonate.

MGD-D consists of fluvial and alluvial fan-related deposits, which overly *MGD-C* with an abrupt (0.5 to <2cm) to clear (<5cm) boundary (Schoeneberger et al. 2012). The sediments are coarse, ranging from fine- to very coarse sand and sandy loam, to very coarse gravels and cobbles. Sand- to fine gravel-sized materials are subangular to subrounded, while coarse gravels (pebbles) and cobbles are generally subrounded to rounded. At the site area located uphill, MGD-I, bedded fine gravels and a cobble layer were deposited directly on top of facies *MGD-C*, which have been overprinted by different episodes of soil formation involving the formation a subangular blocky microstructure and thick, typic pale yellow dusty clay coatings with irregular laminations and

deformations (fig. 7j). This type of clay coating forms as a result of repeated cycles of wetting and drying with vertic activity (shrink-swell) and can form at shallow depths (Kühn et al. 2010). The overlying deposits are richer in clay (sandy loam), due to the inclusion of inherited materials from facies *MGD-B* and *MGD-C*, in particular weathered and rolled fragments of laminated clay peds, and reworked carbonate nodules. In situ (orthic) carbonate features are rare or weakly developed compared to the two facies below and consist of biogenic, beta-type features such as micritic hypocoatings, needle fiber calcite, and small micritic nodules, typical for the vadose zone (Wright 1990a; Alonso-Zarza and Wright 2010a). Clay coatings are common and become more abundant towards the top where they exhibit pendant and crescent shapes typical for clay illuviation in a part of the soil where top-down soil processes are dominating. They are very distinct from the clay coatings in the fluvial deposits below, and indicative of improved drainage.

At MGD-II and MGD-III, facies *MGD-D* is defined by a paleochannel incision (fig. 6), which is infilled with reddish sediment of bedded sandy clay loam, dispersed cobbles, and gravels, which are strongly bioturbated (fig. 7k). Shrink-and-swell activity is evidenced by grano- and poro-striated b-fabrics. Clay coatings and in situ carbonate features are rare. The red color of the sediment shows similarity to lateritic soils in the alluvial fans. The carbonate nodules present in some of the coarser channel fill sediments were likely redeposited from eroding parts of the paleosol of *MGD-B* or *MGD-C*. Needle fiber calcite has formed adjacent to some carbonate nodules, possibly in relation to dissolution and disintegration of the nodule edges. Common small (1-3 mm) Fe-Mn disorthic and orthic nodules can be found, indicative of weak lateritic soil formation (Marcelino et al. 2010). A thin, dark brown organic topsoil composed of pebbles in clay loam represents the historic ground surface and directly overlies *MGD-C* in the northern part of MGD-III and caps the channel fill of *MGD-D* where it is present (fig. 6).

MGD-E is comprised of the overburden (~50 cm) from Clark's old excavations covering the historic surface on the eastern part of MGD-III.

Facies	Area	OSL (ka)	$^{14}C_{PC}$ (cal, yrs ka)	Description	Pollen	Charcoal	Phytoliths	$\delta^{13}C_{Pc}$ (‰)	Interpretation	Archaeology
MGD-E	II I	-	-	Laminated silty clay, $CaCO_3$ nodules with inclusions of yellow clay coatings	N/A	N/A	N/A	N/A	Overburden from previous excavations	Reworked
			« Clear to abrupt boundary »						*« (Historic) ground surface »*	
MGD-D **PP 1700-1704**	I	15±1*	1	Coarse textures ranging from very coarse sands to very coarse gravels, cobbles, & sandy loam	Dominated by grasses, with reeds, evergreens	Abundant in the top. Declining downward.	Morphologies closest to referentials of gallery forest & woodland.	-9.7	Riverbed & mass-wasting deposits containing reworked soil & sediment.	Sharp-edged classic/late MSA & terminal MSA with conjoins
	II III	11±1-1.9±0.1* 8.2±0.1*	-						Stream channel fill & mass-wasting deposits containing reworked soil & sediment	Rolled lithics
			«Abrupt boundary»						*«Erosional contact»*	
MGD-C **PP 1705-1708**	I II III	26±1-16±1	13	Coarse to very coarse sandy loam, abundant secondary carbonates	Generally higher proportion of aquatic taxa	Present in all samples	Morphologies most common in trees & bushes	-7.6	Wooded seasonal wetland. Paleosol in mixed fluvial & lagoonal deposit with pedogenic carbonates indicating gradual increase of dry surface conditions	Locally, rolled. Bones & lithic artifacts in the top 10 cm of this facies at Clark´s Elephant Butchery Site
MGD-B **PP 1709**	I II III	34±4 (top)	31-30, 40	Laminated silty clay with secondary carbonates	Not preserved	Not preserved	Not preserved	-10.8 to -10.1	Lake-lagoon	None
MGD-A	I II	58±9	-	Pale colored bedded angular medium to coarse sands & fine gravel	N/A	N/A	N/A	N/A	Stream deposits in the distal part of the alluvial fan, Chitimwe Formation	None

Table 1. Facies at MGD from top to bottom with OSL ages of the deposits at each site area ("Area"), radiocarbon dates on pedogenic carbonates (PC), brief descriptions of sediments, ecological data, interpretation, and archaeology. *The shallow *MGD-D* channel fill deposits at MGD-II and MGD-III date to the Holocene, while the deeper artifact bearing deposits at MGD-I are Late Pleistocene and preserve a segment of sediments lacking at the other site areas.

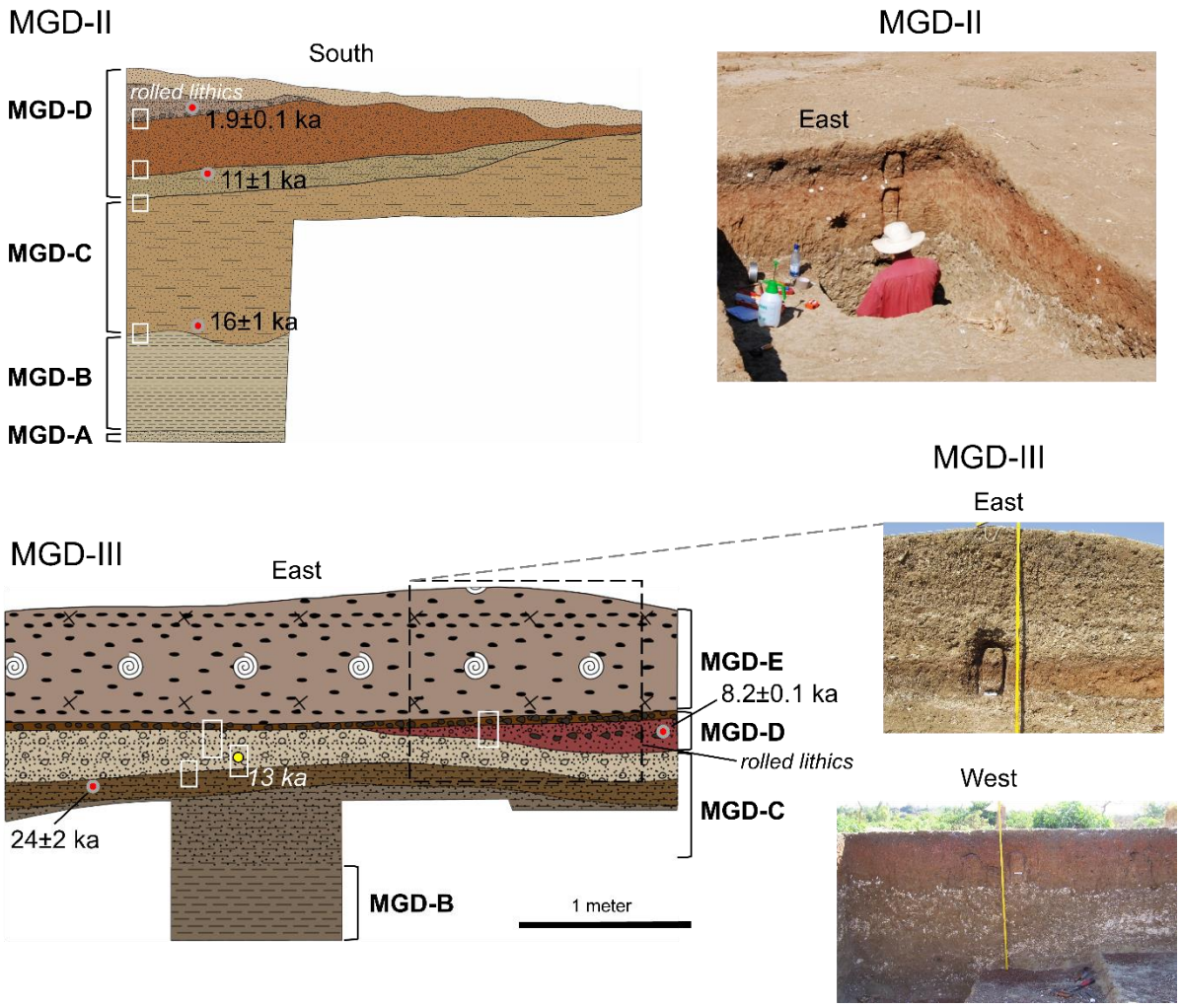

Fig. 6. South profile of MGD-II (top) and East profile of MGD-III. The photo at the top right shows the East and South profiles of MGD-II during sample collection. The middle photo shows part of the East profile of MGD-III with shallow channel fill deposits (orange red) and thick overburden from the historic excavations, whitish gray from carbonates and clay deriving from *MGD-B* and *MGD-C*. The lowermost photograph from the opposite side of the excavation, the West profile, shows a stratigraphic sequence without overburden, topped by a thin stony organic horizon of winnowed cobbles and pebbles, underlain by coarse sand and gravel (red), filling the channel incision into facies *MGD-B* and *MGD-C*. See fig. 3 for legend.

Bruce

The site areas at Bruce contained four facies with 24 sedimentary units (table S-T13). An overview of the facies is given in Table 2. Figure 4 shows profiles of the three excavation areas and geo-trench BRU-GT2.

Facies	Area	OSL (ka)	$^{14}C_{PC}$ (cal, yrs ka)	$\delta^{13}C_{PC}$ (‰)	Description	Interpretation	Archaeology
BRU-D	GT2	-	-	N/A	Coarse sand to medium gravel	Recent channel fill	-
		« Clear erosional break between BRU-D & BRU-A (observed at BRU-GT2) »					
BRU-C	I	54±5-29±3	-	N/A	Beds of imbricated medium sands to medium gravels. Sandy clay & loamy sand in the lowest units. Mineral weathering, in situ silt & clay formation. Redox depletions & concentration in lower units	Chitimwe Formation. Distal part of the alluvial fan, defined by gullying & stream bed deposition.	Many MSA lithic artifacts, ochre fragments
	II	-					
	III	-					
	TP20	51±4-31±2					
	TP21	39±2-20±1					
BRU-B	III	>41±5	29-20	-10.9 to -8.8	Silty clay with 10-15% coarse sand to fine gravel	Nodular calcrete in sediment mixed by soil cracking & bioturbation	Few lithic artifacts
BRU-A	GT2 III	-	33-28	-9.2 to -7.6	Silty clay with few very fine sand inclusions, decomposing organic matter, large $CaCO_3$ nodules	Lagoon, overprinted by wetland soil with palustrine carbonate nodules	-

Table 2. Facies at BRU from top to bottom with OSL ages of the deposits at each site area ("Area"), radiocarbon dates on pedogenic carbonates (PC), brief descriptions of sediments, interpretation, and archaeology. The sediments at Bruce did not yield enough phytoliths for analysis and pollen analysis was not attempted. The complete radiocarbon and OSL dates including the new ages for BRU-TP21 can be found in the supplementary material (S-T4 and S-T6) and Thompson *et al.* (2021).

Facies *BRU-A* consists of white, fine carbonate silt and lagoonal deposits of laminated silty clay similar to facies *MGD-B*. It contains abundant large fragments of partly decomposed organic matter.

Facies *BRU-B* was exposed at BRU-III and is represented by a welded calcrete paleosol similar to *MGD-C*, with coarse sand introduced by bioturbation and soil cracking. Many siliceous minerals, including both the lagoonal clay and sand grains, have been (partly) dissolved and gradually replaced by carbonate (fig. 8a-h). Petrography and CL-microscopy reveal the primary source material reflected in the shapes of pseudomorphic pore spaces after dissolved minerals, calcite replacement of dissolved siliceous grains, and sparitic neoformation around the edges of sand grains affected by dissolution (fig. 8g, h). This process is better visible in *BRU-B* than in *MGD-C*, which may be attributed to a less advanced maturity reached by the calcrete at BRU than at MGD, although both fall in the same calcrete category (stage 3), following Machette (1985).

BRU-C comprises artifact-bearing, lateritic sands and gravels, which formed mainly by gullying, stream deposition, debris flow, and winnowing. Sand and very fine gravel-sized grains are subangular to subrounded, while fine to medium gravel is generally subrounded to well-rounded.

The deposits vary from site area to site area and include breaks in sedimentation likely associated with numerous erosional events. However, OSL dates the excavated deposits to 29±3 to 54±5 and soil formation and mineral weathering confirm the temporal constraint of depositional processes at BRU. Lateritic soil formation with extensive mineral weathering impacted the sediments considerably at all site areas. A multi-step formation sequence could be observed, beginning with the formation of authigenic (silty) clay (fig. 8j, k), followed by its vertical translocation, and ending with the formation of limpid, finely laminated clay coatings (fig. 8l, m, n, o). Indications for erosional processes within the soil were observed at BRU-I (S-Fig. 15). As opposed to *MGD-D*, *BRU-C* deposits do not contain inherited soil materials, suggesting that the calcrete (*BRU-B*) was not truncated at the Bruce site location.

BRU-D consists of relatively recent channel fill with clast-supported, very coarse sand to fine gravel.

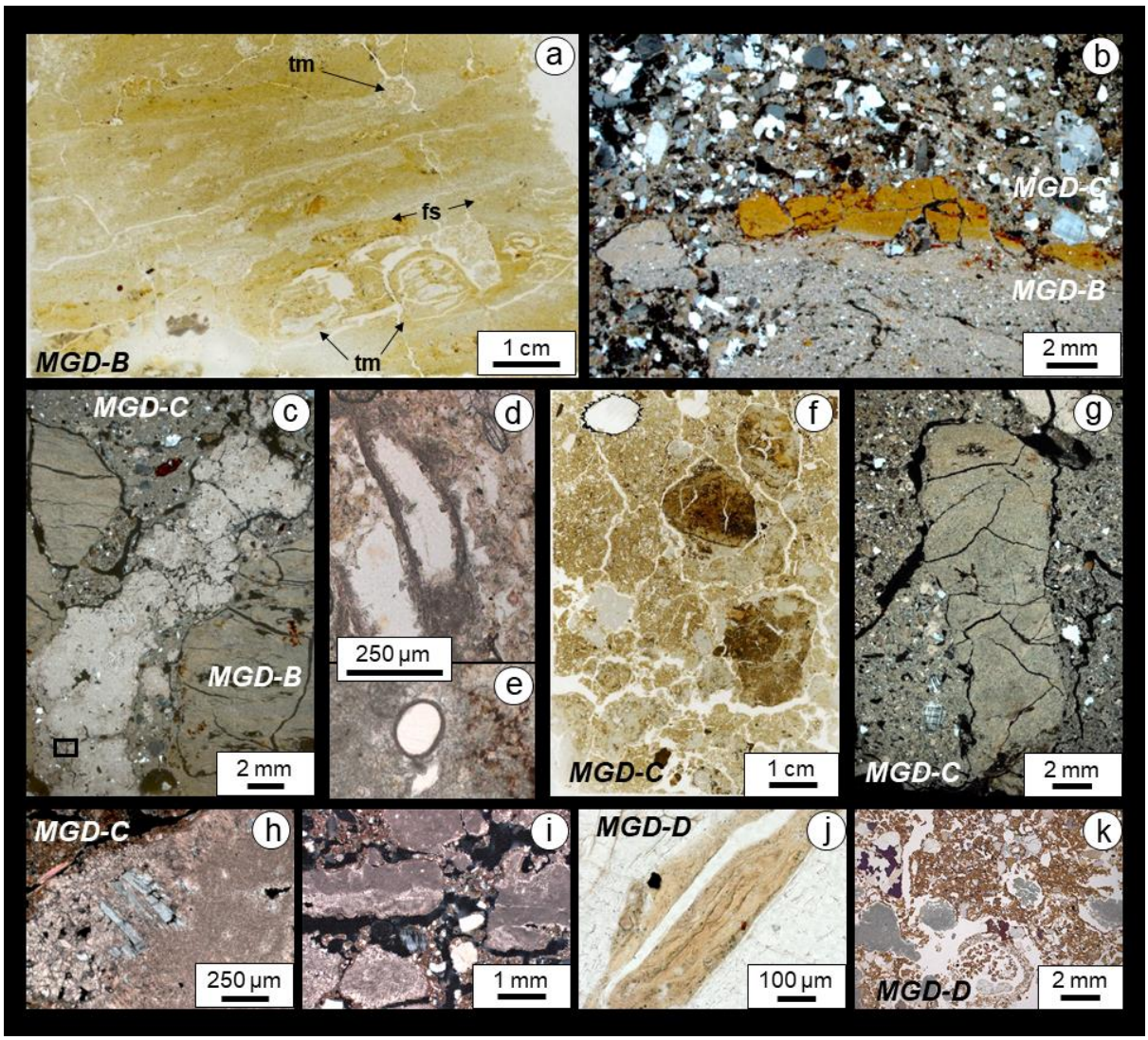

Fig. 7. Micromorphology of MGD. a) Thin section of silty clay with interbedded laminations of fine sand (fs) and termite features (tm). b) Boundary between intact clay in *MGD-B* and bioturbated *MGD-C*, showing contrasting grain sizes of *MGD-B* (silt, clay) and *MGD-C* (coarse sand, clay) and a fragmented orange slaking crust at the contact (XPL). c) Sandy loam infilling envelops a pedogenic carbonate nodule in a crack within facies *MGD-B* (XPL). d) and e) show calcified organic remains including a root fragment in a biogenic carbonate nodule shown in (c) (small black frame). f) Thin section from a part of *MGD-C* with organic remains and carbonate nodules. g) Pillar-shaped remnant of laminated silty clay in sandy matrix (XPL). h) Brecciated feldspar with dissolution voids and microsparite (~5-15 µm) (XPL). i) Flat blocky merging carbonate nodules with internal microlayers of different calcite crystal sizes. j) Deformed pale yellow dusty clay coatings. k) Vertical channel (upper left) leading to a circular termite feature in between carbonate nodules (gray) affected by dissolution.

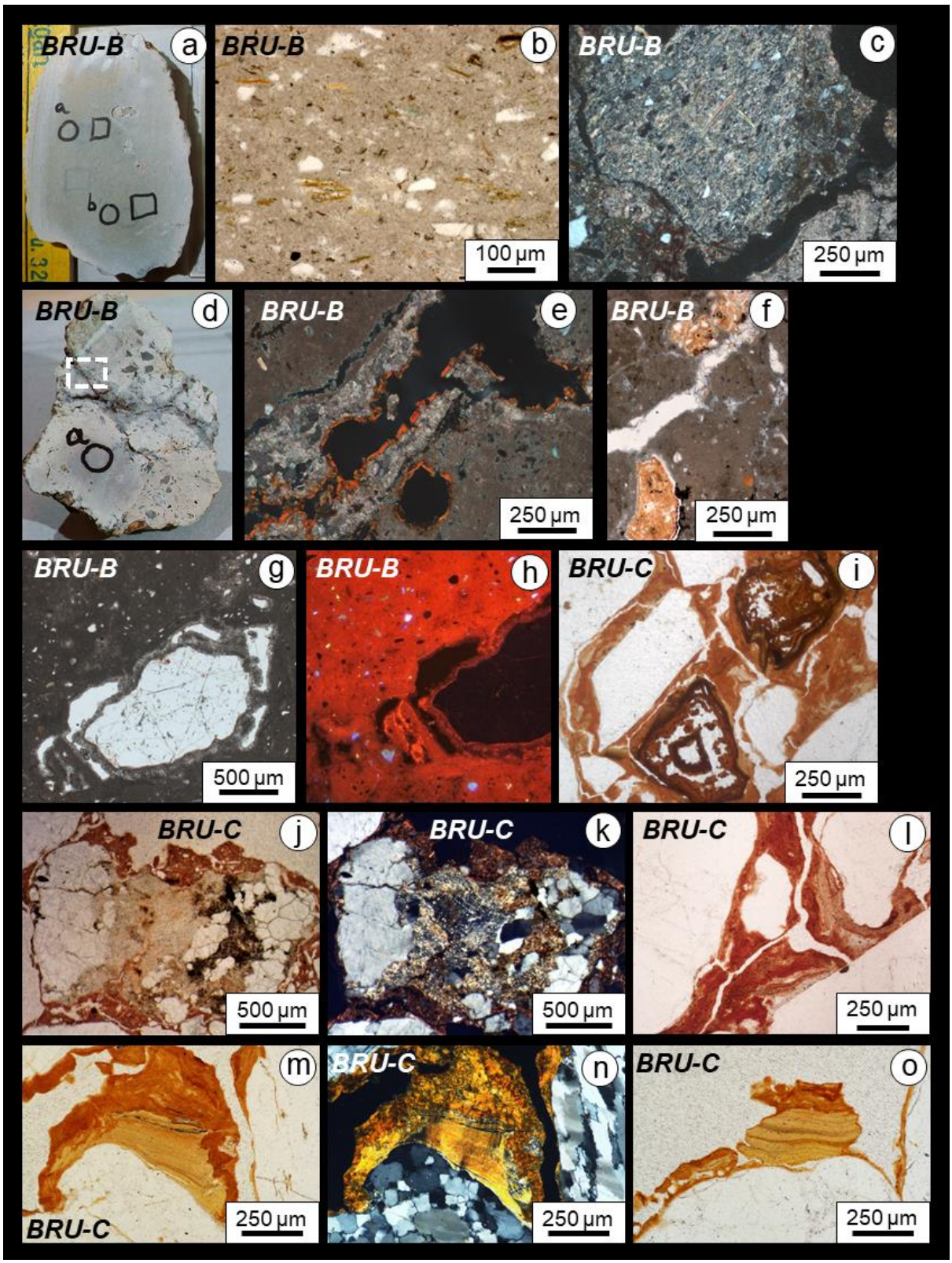

Fig. 8. Micromorphology of BRU. a) Carbonate nodule after laminated silty clay (*BRU-A*) of fine micrite. b) laminated mica inside a carbonate nodule. c) Tilted ped of laminated clay showing partial dissolution and calcite replacement. d) Carbonate nodule from the top of *BRU-B* with zones with sand inclusions and cracks with sparite infillings and clay coatings. e) Crack (black) with a sparite (light) coating starting to infill the crack, overlain by an orange limpid clay coating (rectangle in [d], XPL). f) Two inclusions of clay domains in a micritic nodule with an accommodating plane

(fissure) partially infilled with sparite. g) Sand grain inside a carbonate nodule with multiple dissolution phases represented by void spaces and carbonate. Equivalent to the one displayed in (h). h) Episodes of dissolution around a siliceous sand grain have been partially filled with sparitic (bright red) and micritic (darker red) calcite. Some silt in the surrounding micrite appears blue (quartz) or yellow (feldspar). Black specks may indicate pore spaces pseudomorphic after dissolved silt grains (CL). i) Ferruginous open boxworks of alteromorphs (Delvigne and Stoops 1990). j-k) In situ clay (yellowish, probably sericite) formation inside a heavily weathered feldspar pebble (k in XPL). l) Different phases of clay illuviation represented by coarse yellow to orange clay coatings. m-n) A yellow laminated clay coating has been truncated on the side and overprinted by dark orange coarser clay illuviation (n in XPL). o) Remnant clay coating on a sand grain, indicative of erosional processes within the soil.

4.3 Paleoecology

Pollen

Facies MGD-D contained pollen from the six consecutive samples (samples 1700-1705), and the lowermost (1708) sample from the MGD-C yielded enough pollen for analysis as well (fig. 9). Overall, the pollen record was dominated by herbs, particularly grass (30 to 40% of the pollen sum), of which aquatic taxa, particularly sedge, was the next most important group, and arboreal taxa (montane forest, evergreen forest, and woodland) making up between 10 to 15% of the pollen sum. Pteridophytes were also present in samples 1702 to 1705 and 1708. In terms of general trends with changes in pollen taxa there is a clear transition from samples 1705 to 1703 and 1702 to 1700, with a decline in woodland taxa (particularly Blighia sp. and Asteraceae) and an increase in Brassicaceae and Eucalyptus sp. Charcoal values are generally around 200,000 particles per cm^3, except for samples 1709 (no charcoal present), 1707 (<100.000 particles per cm^3), 1701 (<50,000 particles per cm^3) and 1700 (~400,000 particles per cm^3).

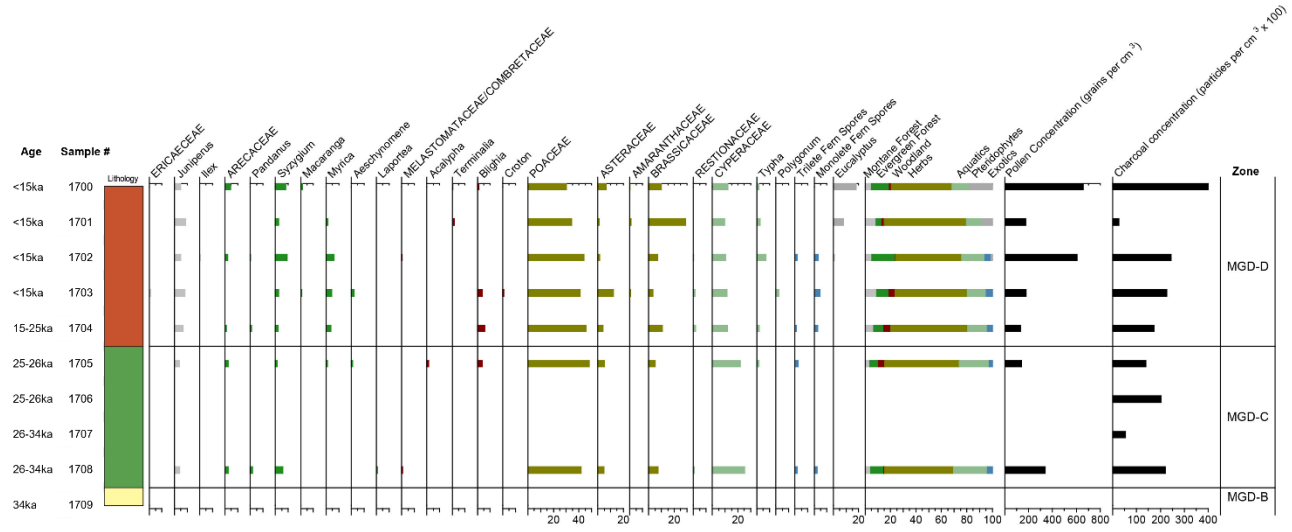

Fig. 9. Pollen diagram with ages and facies indicated on the left and right. Graph created by the Tilia pollen diagram software (Grimm 2004). Asterisks indicate samples with both pollen and phytolith results available.

Phytoliths

The total number of phytoliths tallied for the current study is 1077 from 12 archaeological samples, seven of them coming from MGD-I (tally of 908) and five from BRU-TP20 (SI, table ST-7). Their respective phytolith records vary, with very poor counts (n = 0 - 31) for BRU-TP20 and for samples 1703, 1707, and 1709 from MGD-I (fig.3), which were thus excluded from further analysis and paleoenvironmental interpretation. For the productive samples from MGD-I, phytolith weathering/dissolution affects a very minor part of the assemblage: <2%. Morphotype diversity is somewhat limited, totaling 33 discrete shapes. Mean morphotype frequency is ~6 (range = 1-556). Five morphotypes are very common, representing more than 85% of the total variability, and in numbers above the mean (n= 31-556). These morphotypes are, in order of dominance: 1) globular granulate (~53% from the total), 2) blocky (~14%), 3) cylindroid psilate (~10%), 4) tabular elongate (~6%), and 5) bilobate short cells (~6%), with the remainder of the assemblage representing 11% from the total phytolith count (S-Fig.4).

Archaeological phytolith assemblages from MGD-I follow a non-normal distribution. A Principal Components Analysis (PCA) transformed 12 variables (phytolith classes) into loading values upon standardization. Raw counts used for PCA are in the supplementary material (table S-T8). The first and second components account for 61.32% of the variance. This PCA includes samples from MGD (fig. 3), along with three comparative datasets representing the phytolith spectra from known modern local and regional environments, which represent various ecofacies within Zambezian woodlands (Mercader et al. 2011). The archaeological data processed for the PCA come from MGD-I (this paper), along with contemporaneous MSA sites in Mozambique

(Mercader et al. 2013) and Tanzania (Mercader et al. 2021), for comparison. The PCA shows two clusters, which together represent a continuum of wooded and forested paleoenvironments (fig. 10). Quadrant no. 2 clusters the Mozambican MSA sites with woodlands. Quadrant no. 4 groups all samples from MGD-I between a Zambezian gallery forest of Guineo-Congolian affinity and the mesic woodland reconstructed from the Nasera Industry site of Mumba, in Tanzania (Mercader et al. 2021). For contrast, we also included a hydromorphic grassland nested within a Miombo woodland, locally known as a "Dambo," noticing that all archaeological and reference samples plot far from this outlier.

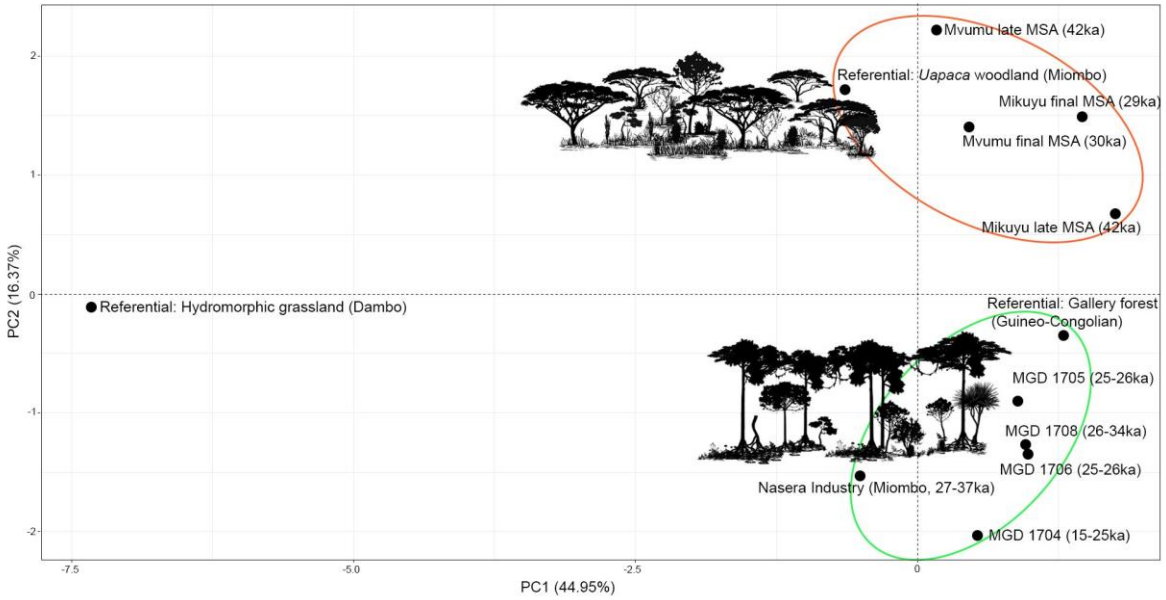

Fig. 10. Principal Component Analysis of MGD-I phytoliths along with penecontemporaneous regional sites.

Stable isotopes

The results of the carbon and oxygen stable isotope analysis of pedogenic carbonate nodules ($\delta^{13}C_{PC}$ and $\delta^{18}O_{PC}$) from MGD and BRU are represented in figure 11. $\delta^{13}C_{PC}$ (pedogenic carbonate) PDB values are between -10.9‰ (min) and -7.6‰ (max) (range of 3.2‰), with a mean value of -9.3‰. The standard deviation for the values from all carbonate horizons is 1.05. $\delta^{18}O_{PC}$ values of the carbonate nodules range from min -9.1‰ to max -6.3‰ PDB, range of 2.8‰, average -8.2‰, SD 0.5. The scatterplot further gives an overview of the stable isotopes, the facies they belong to, and the inferred wood cover associated with decreasing $\delta^{13}C_{PC}$ values. The complete results are provided in the supplementary material (S-T1, S-T3).

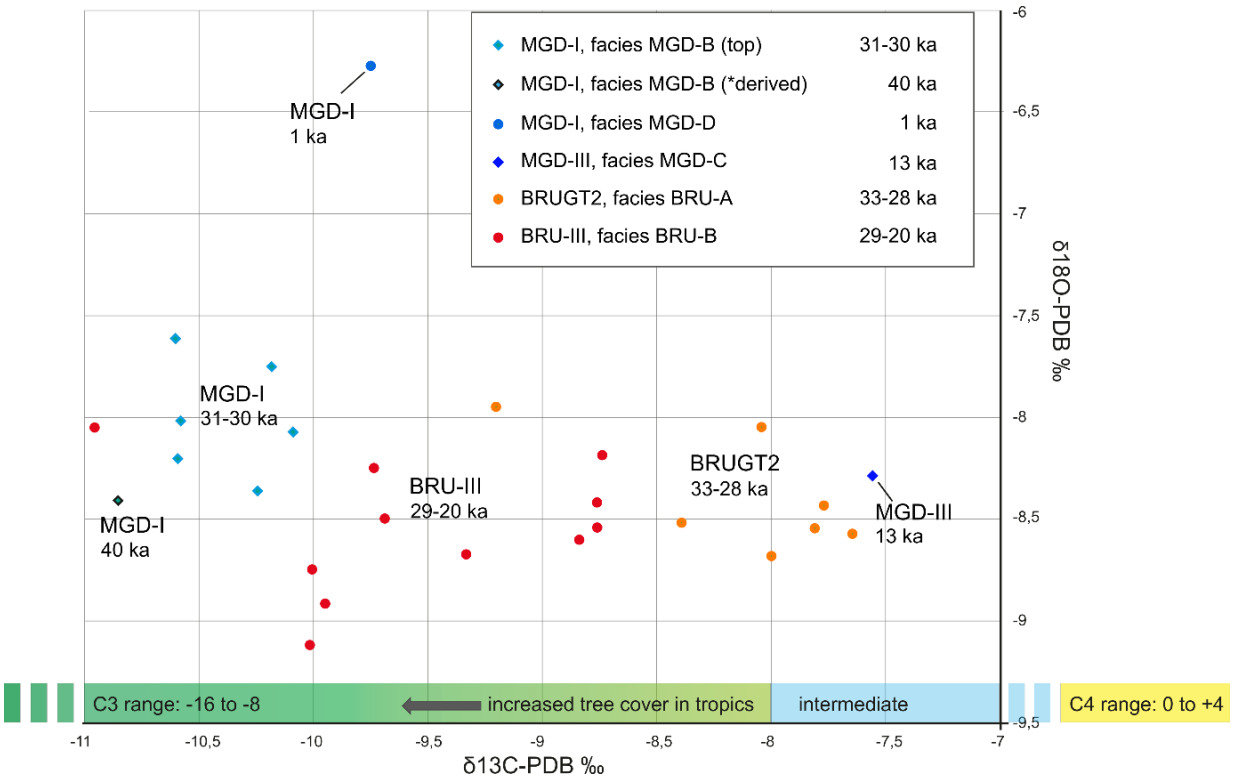

Fig. 11. Scatterplot of the $\delta^{13}C_{PC}$ and $\delta^{18}O_{PC}$ values (both presented relative to PDB) from carbonate nodules organized according to facies with the ranges of radiocarbon dates (cal BP) indicating the time of their formation, *ante quem*. The bar at the bottom on the x-axis shows the ranges of C_3 and C_4 vegetation, with more negative $\delta^{13}C_{PC}$ values associated with denser tree cover. The original isotopic compositions in organic matter, prior to carbonate formation, are between −20‰ and −35‰ for plants following the C_3 photosynthetic pathway, and between −9‰ and −17‰ or plants following the C_4 photosyntehtic pathway (Cerling and Quade 1993). Due to fractionation, pedogenic carbonates forming below C_3 vegetation have values between -16‰ and -8‰, and C_4 vegetation, shown in yellow, has values between 0‰ and +4‰. The values for C_4 vegetation lie to the right from the shown ranges on the x-axis of the scatterplot (-7‰ to -11‰ δ13C-PDB), and the distance has been truncated.

5. DISCUSSION

5.1 Complications of OSL dating

Out-of-order OSL ages (fig. 4) are attributed to potential partial resetting of OSL signals in quartz during fan formation, soil formation processes and/or uncalculated errors in time-averaged water content in the different parts of the profile. Soils are dynamic environments as minerals undergoing secular equilibrium are mobile, which moves sources of ionizing radiation into new aspects of the profile over the time of formation. In addition, water attenuates the absorption of radiation in the crystal matrix of sedimentary minerals, but the relative content of water mass over the duration of burial can be variable, particularly in open environments, and therefore is a common source of

uncertainty in OSL dating (Diaz et al. 2016). Other bioturbation effects such as termite and root disturbance can affect grain distributions over the course of millennia (Kristensen et al. 2015).

5. 2 Soils: Laterites and welded calcrete paleosols.

Site formation processes of open-air sites in the humid tropics are often complex due to the high biological activity and marked periodic changes in humidity and temperature in these environments (Friesem et al. 2016; Wright et al. 2017; Morley and Goldberg 2017). Such complexities can confound clear interpretations of past human behavior and the environments in which they occurred. The deposits at MGD and BRU have been subject to various post-depositional alterations, including pedogenic and biogenic mixing, the formation of authigenic clay and silt, precipitation of carbonates and iron-manganese, and the formation of redoximorphic features resulting from fluctuations in the groundwater table. Both lateritic soils and carbonate paleosol horizons are the result of prolonged formation histories.

Lateritic soils

Lateritic soils have formed in many parts of the Chitimwe alluvial fan deposits of the Karonga area, especially where the removal of protecting tree cover has encouraged their development (Thompson, Wright, Ivory, et al. 2021). The laterites represent a late phase of soil formation, overprinting earlier pedogenetic phases which typically involved clay illuviation, as seen for example at Chaminade-II (Wright et al. 2017). At BRU, the laterites of facies *BRU-C* exhibit a wider variety of features related to mineral weathering than at the excavations at Chaminade (Wright et al. 2017; Nightingale et al. 2019), possibly due to different sedimentary sources including alkali granite, sandstone, and gneiss. Much of the clay and silt appears to have formed in situ by chemical and physical mineral weathering. Bt horizons in the alluvial fan deposits (facies *BRU-C*) contain various types of clay coatings, frequently overprinting one another, as well as localized zones with evidence of fracturing and removal of clay coatings by erosional processes within the soil (fig. 8l-o).

Based on these observations, we hypothesize that *BRU-C* resulted from the cyclic alternation of alluvial deposition, episodes of landform stability during which Bt horizons formed, and erosional events. The Bt horizons may reflect multiple hiatuses in deposition, as indicated by the age range for the aggradation of ten coarse channel beds at BRU-I during Marine Isotope Stage (MIS) 3 that broadly spans from 54 to 29 ka (fig. 4).

Calcrete paleosols

Carbonate nodules are the most prominent feature of the paleosols at BRU and MGD (*MGD-C, BRU-B*), and also formed in the underlying deposits which exhibit less pedogenic development (*MGD-B*, *BRU-A*). Overprinting by carbonate formation has been intensive in these paleosols and deposits, obliterating earlier soil and sedimentary features. Micromorphological and field observations of partly oxidized organic matter and desiccation cracks in facies *MGD-B* and *BRU-A* show that soil formation started when the lake-lagoon began to dry up (Pons and Zonneveld 1965). This process occurred periodically, probably during the dry season, while the wet season introduced alluvial fan deposits. Bioturbation thoroughly mixed these coarse stream deposits with the upper part of the underlying lagoonal clay, creating a welded soil composed of two different types of sediment (Ruhe and Olson 1980). As the lagoon retreated, stream deposits buried the paleosol, and clay illuviation (fig. 8e) and carbonate precipitation (fig. 7c-f, i) ensued. The overprinting of clay coatings by carbonates demonstrates that these soil processes alternated, probably following seasonal rhythms. Ultimately, carbonate formation became the most dominant process, enhanced by soil plugging due to the increase and expansion of the carbonate nodules.

Micromorphology and CL-petrography show that carbonate formation occurred in three main ways. (i) The first is especially common in horizons with less pronounced carbonate precipitation (*MGD-D*) and consists of small (<2 mm) nodules or hypocoatings of micrite. In horizons with more intense carbonate formation, (ii) displacement and disruption of the original sediment fabric (fig. 7c, 7f-g), and (iii) mineral replacement are more prevalent. The latter is best observed in the calcrete paleosols (*MGD-C*, *BRU-B*) and occurred under extreme alkalinity (pH >9), when the opposite trend in solubility of silica and carbonates as a function of pH led to dissolution of siliceous minerals and intense carbonate precipitation (Durand, Monger and Canti, 2010). Within *MGD-C* and *BRU-B*, we observed that carbonates substituted a range of siliceous soil components, including clay domains (e.g., lagoonal clay, fig. 8c, f), clay coatings, feldspar and quartz grains (Alonso, Dorronsoro and Egido, 2004; Wright, 2007; Alonso-Zarza and Wright, 2010a; Durand, Monger and Canti, 2010). The process of silicate dissolution and subsequent substitution by calcite is further expressed as fragmentation (fig. 8j-k) and brecciation (fig. 7h) of mineral grains, ghost (or pseudomorphic) features (fig. 8g), and partly dissolved siliceous grains floating in a carbonate matrix from which they are separated by empty pore spaces (fig. 8g, h) (Alonso et al. 2004).

Depending on the primary material, carbonate replacement resulted in two main types of carbonate nodules;

Nodules formed by replacement of laminated clay, which exhibit fine laminations of silt (fig. 8b). These nodules are present in all carbonate horizons, but especially in the facies with less pedogenic development (*MGD-B* and *BRU-A*).

Nodules formed in the bioturbated portions of the paleosols with abundant coarse sand (*MGD-C* and *BRU-B*), which show zones with different crystal sizes (from 1-5 μm to >15 μm) and contain various mineral inclusions, such as sand, fragments of clay coatings, or clay domains. We hypothesize that the frequency and size of these inclusions within the nodules does not only reflect the source material but may also depend on the maturity of the calcrete, as we expect that increased maturity (continued dissolution and carbonate replacement) will reduce the number and size of inclusions.

In the literature, nodules comparable to the two types we observed at MGD and BRU are classified into two separate categories: palustrine-pedogenic and calcrete nodules, respectively (Wright 1990a; Freytet and Verrecchia 2002). Applying this classification to the nodule types observed at MGD and BRU, however, could be misleading because the mechanism that formed these pedofeatures is the same, as also supported by carbon and oxygen stable isotope analysis (figs. 11, 12). Therefore, both nodule types should be considered as pedogenic carbonates.

The conditions promoting intense carbonate formation at MGD and BRU may have been created by several factors, including the location of the soils within the landscape, the presence of a perched water table, and other climatic conditions such as temperature and precipitation variability. The contribution of carbonate dust was likely not a decisive factor, as carbonate horizons only formed at certain locations. Namely, the low to middle position in the landscape of the paleosol horizons allowed for soil carbonate in solution, leached from higher parts of the landscape, to be moved into the paleosols and continuously refreshed (Zamanian et al. 2016). In the older, fossiliferous Chiwondo Beds, pedogenic carbonates (Lüdecke et al. 2016) and groundwater carbonate (own observations, S-Fig. 23) are common, but geologic sources for carbonate such as limestone are locally absent, excluding a considerable inherited geogenic input of calcite in the paleosols. This leads us to hypothesize that the supply of calcite and the associated stable isotope values from the nodules indeed reflect the local environment at MGD and BRU. A second formation factor is the poor permeability of the lagoonal clays, which would have caused water to stagnate during heavy (seasonal) rain, forming a perched water table and forcing water to move at shallow depths. This groundwater aquifer may have played an essential role in transporting carbonate-saturated waters into the subsoils, facilitating carbonate precipitation in the capillary zone. Soil-plugging by carbonate formation would have retarded water filtration once the first

carbonates had formed. Despite the important role of the aquifer, these carbonate horizons do not classify as groundwater carbonates because they did not form under continuously saturated conditions (Slate et al. 1996; Alonso-Zarza and Wright 2010b). Lastly, we believe that a more pronounced seasonality could have led to enhanced evapotranspiration and carbonate precipitation in the soil after the rainy season, possibly coinciding with increased plant growth.

As outlined above, the long formation history of the paleosol horizons is evidenced by a range of pedofeatures, which in part pre-date carbonate formation. Radiocarbon dates on the nodules provide an age for the later end of soil formation and the associated episode of ground surface stability. They most likely also date a late (final) phase of calcium carbonate formation within the nodules, providing an *ante quem* age for their formation. Although the amount of time required for the formation of calcretes similar to the paleosols of MGD and BRU varies significantly, a minimum of 10 ka has been suggested for calcretes developed in areas where the geogenic contribution of carbonate is low (Wright 1990b). This timeframe agrees with our OSL and radiocarbon dating, which show that the carbonate nodules of MGD and BRU are up to 10 ka younger than the sediment in which they formed (see for example MGD-III and BRU-III, figs. 4 and 6).

5.2 Paleoecology

The general lack of pollen in facies *MGD-B* and *MGD-C* (samples 1706, 1707 and 1709, fig. 9) may reflect environments that are not conducive to preservation, possibly linked to oxidation, which generally significantly impacts pollen preservation (Moss 2013). Palynology results indicate that the study region was covered with woodland or savanna vegetation, with high values of grass and consistent presence of arboreal taxa (fig. 9). Throughout *MGD-D* we observed a decrease in woodland and aquatic taxa, which may reflect a transition from moist (early formation of paleosol *MGD-C*) to drier conditions (stream and mass-wasting deposits *MGD-D*). The top three samples from *MGD-D* (1700-1702, fig. 9) may reflect the influence of Iron Age or historical agricultural activity, with a clear decline in pteridophytes and increase in Brassicaceae (particularly sample 1701). In addition, the presence of exotic species of the genus *Eucalyptus* in the top of the profile down to ca. 30 cm of depth (1700-1702, fig. 3 and 9) does not necessarily signal the continuous presence of this vegetational component but rather pollen grains migrating through the soil profile by bioturbation.

The micro-charcoal records suggest frequent fires on the landscape (fig. 9). The sharp increase in micro-charcoals in the topmost sample (1700) from *MGD-D* potentially reflects changes in fire regimes, associated with the presence of the fire tolerant *Eucalyptus*.

Recent phytolith work in East African has confirmed that for the most part soil phytoliths represent catchment areas smaller than 5 hectares (Blinnikov 1994; Fredlund and Tieszen 1994; Blinnikov et al. 2002). Therefore, unlike the pollen and micro-charcoals, phytolith data can be used to reconstruct local or semi-local environments. The richest phytolith morphotypes from MGD are similar to dominant phytoliths in the modern regional soil and botanical record (S-Fig. 4) (Mercader et al. 2019; Mercader et al. 2020; Mercader et al. 2021), with closest comparison in paleoenvironments of the woodland ecozone. PCA analysis (fig. 10) shows that between ~34 ka and 15 ka, when late and final MSA groups inhabited MGD, this area or its surroundings consisted of mesic environments similar to the modern evergreen gallery forest, forming along rivers and wetlands, and Miombo woodland, widespread in southern central Africa and characterized by the presence of trees of the *Brachystegia* and *Julbernardia* species. This conclusion contrasts somewhat with the reconstruction based on the pollen data, which besides the presence of trees emphasizes a dominance of grasses (Poaceae) and sedges (Cyperaceae). Such discrepancy, however, can be explained by the different scales of the two archaeobotanical methods, with the pollen deriving from a wider, regional catchment.

Stable isotopes from pedogenic carbonate nodules provide even more local, on-site environmental signatures. All $\delta^{13}C_{PC}$ values consistently fall within the range of the C3 photosynthetic pathway (fig. 11), generally associated with closed woodland environments (Cerling 2009). $\delta^{13}C_{PC}$ values cluster per carbonate soil horizon (fig. 11), but variation can be noted between different horizons. The carbonate horizons of BRU-GT2 (~33-28 ka cal BP) and MGD-I (~31-30 ka cal BP) overlap in age and formed when MSA hunter-gatherers were present at BRU. Our $\delta^{13}C_{PC}$ data suggest a more open vegetation regime at BRU at this time than at MGD, where tree-cover has generally been denser (fig. 11). This open woodland at BRU was followed by an increase in tree cover, with the younger carbonate nodules from BRU-III (~29-20 ka cal BP) indicative of more C3-dominant vegetation (fig. 11).

Broader environmental context

Regional-scale reconstructions of vegetation and paleoenvironments at the end of MIS3 and during MIS2 are available from cores from Lake Malawi (core 1C, central basin) (Debusk 1998; Beuning et al. 2011; Stone et al. 2011) and the nearby maar-lake of Masoko (Garcin et al. 2006;

Vincens et al. 2007). Currently, the lake is at its highest level in history. Diatom records from Lake Malawi suggest deep but fluctuating lake levels between 70-55 ka (Stone et al. 2011). Stone et al. (2011) further reconstructed a significant drop in lake level between 47-30 ka, in agreement with pollen records indicative of an extremely dry phase between 37.5 and 35.9 ka BP (Debusk 1998). Our reconstructions of MGD and BRU indicate that the lake-lagoon formed after ~58 ka, and before ~41 ka. The approach of a lagoon to these sites, which are today located ~6 km inland (fig. 1), may have been caused by a change in base-level and geometry of the shore deposits, leading to a relative rise in lake level flooding the area. After ~41 ka, a shift to drier climate with longer dry seasons may have played a role in the recession of the lake margins and the formation of a wetland with palustrine-pedogenic carbonates.

Between 33 and 23 ka, a dry climate characterized by longer dry seasons and open savanna vegetation is indicated by pollen spectra from Lake Masoko, located 70 km north from MGD and BRU. This phase was followed by a period with increasing rainfall and shorter dry seasons with less pronounced seasonality between 23 and 19 ka (Vincens et al. 2007; Gasse et al. 2008). The pronounced dry season detected from the pollen record of Lake Masoko may have been a key factor in calcrete formation at MGD and BRU, which was most active between 33 and 20 ka (fig. 11). The seasonal aridity may also have driven people to MGD and BRU, where streams or places with permanent water, such as the modern springs, may have formed attractive areas, and provided lithic raw materials from pebble and cobble deposits.

5.3 Environments, late MSA occurrences, and forager behaviors

Six chronological stages of landscape development leading to the formation of MGD and BRU could be identified. Here we outline these environments in chronological order, based on our geoarchaeological and paleoecological analyses, to contextualize the archaeological occurrences associated with them.

(1) Alluvial fan (~58 ka, MGD-A and by at least ~54 ka at BRU-C)

Non-lateritic alluvial fan deposits at MGD (facies *MGD-A*) underlie lagoonal clays (facies *MGD-B*). Their age (58±9 ka) overlaps with the earliest ages of alluvial fan sedimentation at BRU (fig. 4), demonstrating that both sites consisted of a terrestrial, alluvial fan landscape before they were flooded by a lake-lagoon. This timing is in line with previous studies, which reconstructed that early Chitimwe alluvial fan deposition was active by 92 ka (Thompson, Wright, Ivory, et al. 2021). Our field observations indicate that no significant landform stability occurred during the formation of the early alluvial fan deposits at MGD (facies *MGD-A)*, which exhibit minimal pedogenic

development. This supports further interpretations by Thompson et al. (2021), who demonstrated an increase in human occupation and anthropogenic burning after 70 ka, which enhanced alluvial fan activity and contributed to burial of MSA artifacts such as those recovered in the test pits at BRU.

(2) Lagoon (after ~58 ka and before 41 ka, BRU-A and MGD-B)

MGD and part of BRU became flooded by a non-turbid body of water, such as a lake-lagoon, in which clays intercalated with fine laminations of silt and fine sand. Episodes of alluvial fan aggradation continued at some locations of BRU (BRU-I and BRU-II), signaling a different physical environment from MGD, which was entirely covered by the lagoon. The lagoonal wetlands formed after ~58 ka and well before ~41 ka, based on OSL ages obtained from alluvial fan sediments underlying (*MGD-A*, fig. 3*)* and overlying (*BRU-C* at BRU-III, fig. 4) lagoonal clay deposits.

(3) Seasonal wetland (BRU-A, MGD-B) and late MSA lithic assemblages at BRU (BRU-C) (~34-28 ka)

This stage includes episodes of landform stability as well as continued aggradation of alluvial fan deposits (*BRU-C*) at the margins of the lake-lagoon, which was retreating and developing into a seasonal wetland (*BRU-A and MGD-B*). Periods of stability are reflected by soil horizons, such as Bt horizons in the alluvial fan deposits (*BRU-C*) and early carbonate nodules forming in the lagoonal deposits (*MGD-B*, *BRU-A*). At MGD, a dense stand of forest cover is indicated by $\delta^{13}C_{PC}$ compositions from carbonate nodules dating to ~40 ka cal and ~31-30 ka cal BP, while the isotopic signal from contemporaneous carbonate formation at BRU (BRUGT2, dating to between ~33-28 ka) indicates a more open vegetation, reflecting a patchier landscape (fig. 11). Pollen assemblages from MGD-I, dating to this time (1708), contain higher amounts of aquatic species and sedges in comparison with the younger samples, but also show presence of evergreens indicative of a forested wetland environment (fig. 9). The timing of carbonate formation and the corresponding reconstructed vegetation overlap with the age brackets of late MSA occupations on the exposed surfaces of the alluvial fan at BRU (facies *BRU-C*). At BRU-II, two archaeological occurrences were uncovered within these alluvial fan deposits. Few dispersed lithic artifacts were unearthed from sediments dating to between 44±3 ka and 34±3 ka. Additionally, a richer in situ assemblage of sharp-edged late MSA artifacts was found in and on a pebble layer dating to between 34±3 ka and 33±3 ka (fig. 4), which may represent an ancient, winnowed ground surface. The fact

that these occupations bordered facies *BRU-A* and *MGD-B* suggests that foragers at the time used open environments of the alluvial fans adjacent to a seasonal wetland.

(4a) Calcrete paleosol (BRU-B, MGD-C) (~29-20, up to 13 ka cal BP)

Carbonate precipitation ultimately led to the formation of a stage 3 nodular calcrete paleosol (*sensu* Machette, 1985; Wright, 1990; Durand, Monger and Canti, 2010), dating to between 29 and 20 ka cal BP at BRU (*BRU-B*), with stable carbon isotope compositions indicative of increased tree cover. The calcrete of paleosol *MGD-C* was under-sampled for radiocarbon dating and stable isotope analysis. However, a sample from MGD-III indicates that at this site area carbonate formation continued until ~13 ka cal BP, with stable carbon isotope compositions reflective of reduced tree cover (fig. 11). This more open tree cover may be reflective of the environment created by the processes described in the next stage (4b), which is roughly contemporaneous to 4a.

(4b) Erosion, late MSA stone tools at MGD, meandering stream (MGD-D), and terminal MSA lithic assemblages at MGD (26-15 ka cal BP)

While calcrete formation (stage 4a, facies *MGD-C*) continued in the downhill site areas of MGD, a meandering stream truncated the paleosol at MGD-I, after ~26 ka but before ~15 ka (*MGD-D*, fig. 3).

Late MSA lithics were introduced by the meandering stream and deposited with fluvial sands at the base of facies *MGD-D* (fig. 3). A similar process probably led to the co-occurrence of MSA stone tools and elephant bones in the top 10 cm of the calcrete reported by Clark and Haynes (1970), which likely corresponds to our truncated *MGD-C* paleosol. This hypothesis is supported by the high abrasion of the lithics and elephant bones, which also do not show evidence of forager cutmarks but of crocodile gnawing (Wright et al. 2014).

The fluvial sands with reworked late MSA stone tools were buried below a cobble streambed, within the same time bracket of ~26-15 ka. In situ terminal MSA lithic artifacts with several refits were found embedded in the deposits just above the cobbles and may relate to the approximate level of the ground surface above a Bt horizon (fig. 7j) detected below the cobbles, which formed during a relatively short period of landform stability. With the start of facies *MGD-D,* directly above the truncation, pollen spectra indicate a decline in sedges and aquatic species, and a continuous presence of grasses and evergreens (fig. 9). Phytolith spectra indicate continuous dense tree cover near MGD, comparable to modern evergreen gallery forest and Miombo (fig. 10).

Overlying the fluvial cobbles and lowermost sands of *MGD-D* are sediments with abundant redeposited soil materials and lagoonal clay deriving from the paleosol of facies *MGD-C*. This reworking of soil materials and fragments of lagoonal clay is indicative of extensive erosion in the area, which may have occurred during mass-wasting events (*MGD-D*) (fig. 3). Notably, a period of more intensive rainfall is discernible in the lakes Malawi and Masoko between 23 and 11.8 ka cal BP (Vincens et al. 2007; Gasse et al. 2008; Lyons et al. 2015). This more torrential climate may have contributed to erosion, particularly in combination with anthropogenic burning of vegetation cover (Thompson, Wright, et al. 2021).

(5) Early Holocene: channels and flash floods, formation of a winnowed surface (~12 ka – 2 ka)

Around 12 ka, truncation by a large channel incised the top of the paleosol at MGD-II and MGD-III. More recent infillings (dated to 1865±120 BP at MGD-II and 8000±100 BP at MGD-III) of gravel contain redeposited carbonate nodules, indicating further episodes of high-energy erosion in the area, probably by flash floods. The Early Holocene sequences at MGD-II and MGD-III are topped by a brown winnowed lag deposit consisting of mixed coarse sediment rich in organic matter from vegetation and human activity, forming the modern ground surface.

6. CONCLUSIONS

The unique settings of the open-air sites of MDG and BRU at the fringes of the alluvial fan provided the opportunity to reconstruct paleosols and depositional environments absent from sites located on central parts of the fan in the Karonga area. By placing MSA occurrences in their environmental and landscape context, we were able to capture previously unknown aspects of the environmental and behavioral spectrum of late MSA foragers.

Though the Karonga area had an increase in occupations after 70 ka (Thompson, Wright, Ivory, et al. 2021), at MGD and BRU we could not gather any evidence of forager occupation until 51 ka. Sediment analysis has shown that, after initial alluvial fan deposition, a lake-lagoon flooded the site areas after 58 ka. This re-configuration of the lake margins has not been reported by previous palaeogeographical and paleoenvironmental reconstruction from Lake Malawi, which were mainly based on drilling and geophysical programs from the lake itself (Scholz et al. 2006; Cohen et al. 2007; Scholz et al. 2011; Beuning et al. 2011; Lyons et al. 2015).

MSA hunter-gatherers first visited BRU between 51 and 31 ka when a mosaic of seasonal wetlands was created by the retreating lake-lagoon, which became bordered by alluvial fan deposits.

Our paleoenvironmental data show that these MSA people were producing artifacts in forested riparian zones embedded within more open landscapes. The sites of MGD attracted MSA human activity only after the formation of a meandering, seasonal stream, which locally opened the landscape after 26 ka. These findings are in line with previous interpretations emerging from our earlier works in the Karonga area, which demonstrated that MSA foragers favored mosaic/riparian landscapes (Thompson et al. 2012; Wright et al. 2014; Wright et al. 2017; Thompson et al. 2018; Nightingale et al. 2019).

Data presented in this paper enable us to further expand these reconstructions. The in situ terminal MSA occupation at MGD, dating after 26 ka, is one of the latest intact MSA assemblages known from Africa (Barton et al. 2013; Barton et al. 2016; Bader et al. 2018). Therefore, the dataset presented in this paper enables us to demonstrate that the MSA exploitation of forested riparian environments perpetuated into the latest Pleistocene. Our findings revealed that MSA hunter-gatherers might have chosen MGD and BRU not only due to the presence of riparian environments but also because these localities were positioned at the confluence of river and wetland areas, which serve as important corridors for the dispersal of biota (Wantzen et al. 2008). Therefore, MGD and BRU likely offered a wider range of resources to MSA people crucial for their foraging and tool production.

In conclusion, our work demonstrated that a holistic approach integrating geoarchaeological analyses with different ecological proxies can be very effective in achieving multi-scale landscape, environmental, and behavioral reconstructions, even in a dynamic tropical landscape with limited organic preservation. Though extremely complex, future research might target similar depositional environments to benefit from the variety of paleoenvironmental data that can be obtained, as well as the likely presence of MSA hunter-gatherer occupations.

Funding Information: Funding was provided by the Deutsche Forschungsgemeinschaft (MI 1748/3-1, MI 1748/1-1, and ME 4406/1-1). Fieldwork and analysis were funded by National Geographic-Waitt Foundation grant W115-10, the University of Queensland Archaeological Field School, and the Australian Research Council Discovery Project DP110101305.

Acknowledgements

We are grateful to Oris Malijani, Joseph Tembo, Frederick Mapemba, Harrison Simfukwe, , Chrissy Chiumia, and Malani Chinula at the Malawi Department of Museums and Monuments, Menno Welling,), thanks to Davie Simengwa, Liton Adhikari, Gervasio Ngumbira, Rachel Warren, Kingsley Pamanda and a

local crew including Henry Kalinga, Moses Nyondo, Kondwani Mwafulirwa, Daudi Mwangomba, Gladys Salanga, Violet Chirambo, Frank Kumwenda, Welani Ng'ambi, Petros Mwanganda, Nelson Sichali, Bodwin Kasimba, and many others. Also, thanks to students from the University of Queensland and MEMSAP colleagues Sheila Nightingale, Jacob Davis, Andrew Zipkin, Marina Bravo Foster, Scott Robinson, and Victor de Moor. Thanks are owed to Kathy Schick and Nick Toth at the Stone Age Institute for permission to examine the materials from the Cha-1A excavation and for archive photographs, to Andy Cohen at the University of Arizona for access to maps drawn by C.V. Haynes, and to Winston Mwagomba at the Cultural and Museum Centre, Karonga for his excellent memory of passing through the 1966 Cha-1A excavations as a child. We would further like to thank Panagiotis Kritikakis, Peter Kuehn, Heinrich Taubald, Christoph Wissing, Hervé Bocherens, Christoph Berthold, Carla Hadden, Nicholas Conard, Jian Zhao and Nicole Leonard, Michael Toffolo, Arne Meier, Diogo Spinola, Vera Aldeias, and Nuno Bicho. In memory of George Stoops.

REFERENCES

Albert RM, Bamford MK, Cabanes D. 2009. Palaeoecological significance of palms at Olduvai Gorge, Tanzania, based on phytolith remains. Quat Int. 193(1–2):41–48. https://doi.org/10.1016/J.QUAINT.2007.06.008

Albert RM, Bamford MK, Esteban I. 2015. Reconstruction of ancient palm vegetation landscapes using a phytolith approach. Quat Int. 369:51–66. https://doi.org/10.1016/J.QUAINT.2014.06.067

Alonso-Zarza AM, Wright VP. 2010a. Chapter 5 Calcretes. Dev Sedimentol. 61(C):225–267. https://doi.org/10.1016/S0070-4571(09)06105-6

Alonso-Zarza AM, Wright VP. 2010b. Chapter 2 Palustrine Carbonates. Dev Sedimentol. 61(C):103–131. https://doi.org/10.1016/S0070-4571(09)06102-0

Alonso P, Dorronsoro C, Egido JA. 2004. Carbonatation in palaeosols formed on terraces of the Tormes river basin (Salamanca, Spain). Geoderma. 118(3–4):261–276. https://doi.org/10.1016/S0016-7061(03)00211-8

Bader GD, Tribolo C, Conard NJ. 2018. A return to Umbeli Belli: New insights of recent excavations and implications for the final MSA of eastern South Africa. https://doi.org/10.1016/j.jasrep.2018.08.043

Barboni D, Bremond L. 2009. Phytoliths of East African grasses: An assessment of their environmental and taxonomic significance based on floristic data. Rev Palaeobot Palynol. 158(1–2):29–41. https://doi.org/10.1016/J.REVPALBO.2009.07.002

Barton RNE, Bouzouggar A, Collcutt SN, Carrión Marco Y, Clark-Balzan L, Debenham NC, Morales J. 2016. Reconsidering the MSA to LSA transition at Taforalt Cave (Morocco) in the light of new multi-proxy dating evidence. Quat Int. 413:36–49. https://doi.org/10.1016/J.QUAINT.2015.11.085

Barton RNE, Bouzouggar A, Hogue JT, Lee S, Collcutt SN, Ditchfield P. 2013. Origins of the Iberomaurusian in NW Africa: New AMS radiocarbon dating of the Middle and Later Stone Age deposits at Taforalt Cave, Morocco. J Hum Evol. 65(3):266–281. https://doi.org/10.1016/J.JHEVOL.2013.06.003

Basell LS. 2008. Middle Stone Age (MSA) site distributions in eastern Africa and their relationship to Quaternary environmental change, refugia and the evolution of Homo sapiens. Quat Sci Rev. 27(27–28):2484–2498. https://doi.org/10.1016/J.QUASCIREV.2008.09.010

Betzler C, Ring U. 1995. Sedimentology of the Malawi Rift: Facies and stratigraphy of the Chiwondo Beds, northern Malawi. J Hum Evol. 28(1):23–35. https://doi.org/10.1006/jhev.1995.1004

Beuning KRM, Zimmerman KA, Ivory SJ, Cohen AS. 2011. Vegetation response to glacial-interglacial climate variability near Lake Malawi in the southern African tropics. Palaeogeogr Palaeoclimatol Palaeoecol 303(1–4):81–92. https://doi.org/10.1016/j.palaeo.2010.01.025

Bicho N, Haws J, Raja M, Madime O, Gonçalves C, Cascalheira J, Benedetti M, Pereira T, Aldeias V. 2016. Middle and Late Stone Age of the Niassa region, northern Mozambique. Preliminary results. Quat Int. 404:87–99. https://doi.org/10.1016/j.quaint.2015.09.059

Blair TC, McPherson JG. 1994. Alluvial fans processes and forms. https://doi.org/10.1007/978-1-4020-5719-9J4

Blinnikov M. 1994. Phytolith analysis and the holocene dynamics of alpine vegetation. In: Onipchenko V, Blinnikov M, editors. Experimental Investigation of Alpine Plant Communities in the Northwestern Caucasus. vol. 115. Zuerich; p. 23–40.

Blinnikov M, Busacca A, Whitlock C. 2002. Reconstruction of the late Pleistocene grassland of the Columbia basin, Washington, USA, based on phytolith records in loess. Palaeogeogr Palaeoclimatol Palaeoecol. 177(1–2):77–101. https://doi.org/10.1016/S0031-0182(01)00353-4

Blokhuis WA, Kooistra MJ, Wilding LP. 1990. Micromorphology of cracking clayey soils (vertisols). In: Douglas LA, editor. Soil Micromorphol a basic Appl Sci. Elsevier; p. 123–148.

Bromage TG, Schrenk F, Juwayeyi YM. 1995. Paleobiogeography of the Malawi Rift: Age and vertebrate paleontology of the Chiwondo Beds, northern Malawi. J Hum Evol. 28(1):37–57. https://doi.org/10.1006/jhev.1995.1005

Brooks AS, Yellen JE, Potts R, Behrensmeyer AK, Deino AL, Leslie DE. 2018. Long-distance stone transport and pigment use in the earliest Middle Stone Age. Science (80-). 360(6384):90–94.

Cerling TE. 1984. The stable isotopic composition of modern soil carbonate and its relationship to climate. Earth Planet Sci Lett. 71(2):229–240. https://doi.org/10.1016/0012-821X(84)90089-X

Cerling TE. 2009. Stable Carbon Isotopes in Palaeosol Carbonates. Palaeoweathering, Palaeosurfaces Relat Cont Depos 43–60. https://doi.org/10.1002/9781444304190.CH2

Cerling TE, Quade J. 1993. Stable carbon and oxygen isotopes in soil carbonates. In: Swart PK, Lomann KC, Mckenzie J, Savin S, editors. Clim Chang Cont Isot Rec Vol 78. Geophysica: American Geophysical Union; p. 217–231. https://doi.org/10.1029/gm078p0217

Clark JD. 1966. Initial Investigation of the Archeology of Karonga District, Malawi. Am Anthropol. 68(2):67–87. https://doi.org/10.1525/aa.1966.68.2.02a00990

Clark JD, Haynes C V., Mawby JE, Gautier A. 1970. Preliminary investigations in Malawi. Quaternaria. 13:305–354.

Clark JD, Haynes CV. 1970. An elephant butchery site at Mwanganda's Village, Karonga, Malawi, and its relevance for Palaeolithic archaeology. World Archaeol. 1(3):390–411. https://doi.org/10.1080/00438243.1970.9979455

Clark JD, Haynes CV, Mawby JE. 1973. Palaeo-anthropological investigations in the Lake Malawi Rift (1965-66): an interim report. In: Hugot HJ, editor. Pap Proc 6th Pan-African Congr Prehistory Quat Stud. Dakar; p. 513–530.

Clark JD, Stephens EA, Coryndon SC. 1966. Pleistocene Fossiliferous Lake Beds of the Malawi (Nyasa) Rift: A Preliminary Report. Source Am Anthropol New Ser Recent Stud Paleoanthropology 68(2):46–87. https://doi.org/10.1525/aa.1966.68.2.02a00960

Cohen AS, Stone JR, Beuning KRM, Park LE, Reinthal PN, Dettman D, Scholz CA, Johnson TC, King JW, Talbot MR, et al. 2007. Ecological consequences of early Late Pleistocene megadroughts in tropical Africa. Proc Natl Acad Sci 104(42):16422–7. https://doi.org/10.1073/pnas.0703873104

Collura LV, Neumann K. 2017. Wood and bark phytoliths of West African woody plants. Quat Int. 434:142–159. https://doi.org/10.1016/J.QUAINT.2015.12.070

Debusk GH. 1998. A 37, 500-Year Pollen Record from Lake Malawi and Implications for the Biogeography of Afromontane Forests. J Biogeogr. 25(3):479–500.

Delvigne J, Stoops G. 1990. Morphology of Mineral Weathering and Neoformation. I. Weathering of most Common Silicates. Dev Soil Sci. 19:471–481.

Diaz N, King GE, Valla PG, Herman F, Verrecchia EP. 2016. Pedogenic carbonate nodules as soil time archives: Challenges and investigations related to OSL dating. Quat Geochronol. 36(September):120–133. https://doi.org/10.1016/j.quageo.2016.08.008

Dixey F. 1927. The Geology of Nyasaland. Q J Geol Soc. 83(3):432–47.

Dixey F. 1930. Stone implements from the Chitimwe beds, North Nyasa. Annual Report of the Geological Survey Department, Nyasaland.

Durand N, Monger CH, Canti MG. 2010. Calcium Carbonate Features. Elsevier B.V. https://doi.org/10.1016/B978-0-444-53156-8.00009-X

Eichhorn B, Neumann K, Garnier A. 2010. Seed phytoliths in West African Commelinaceae and their potential for palaeoecological studies. Palaeogeogr Palaeoclimatol Palaeoecol. 298(3–4):300–310. https://doi.org/10.1016/J.PALAEO.2010.10.004

Fahmy AG. 2008. Diversity of lobate phytoliths in grass leaves from the Sahel region, West Tropical Africa: Tribe Paniceae. Plant Syst Evol 270(1):1–23. https://doi.org/10.1007/S00606-007-0597-Z

Fredlund GG, Tieszen LT. 1994. Modern Phytolith Assemblages from the North American Great Plains. J Biogeogr. 21(3):321. https://doi.org/10.2307/2845533

Freytet P, Verrecchia EP. 2002. Lacustrine and palustrine carbonate petrography: An overview. J Paleolimnol. 27(2):221–237. https://doi.org/10.1023/A:1014263722766

Friesem DE, Lavi N, Madella M, Ajithprasad P, French C. 2016. Site Formation Processes and Hunter-Gatherers Use of Space in a Tropical Environment: A Geo-Ethnoarchaeological Approach from South India. PLoS One 11(10):164185. https://doi.org/10.1371/journal.pone.0164185

Garcin Y, Williamson D, Taieb M, Vincens A, Mathé PE, Majule A. 2006. Centennial to millennial changes in maar-lake deposition during the last 45,000 years in tropical Southern Africa (Lake Masoko, Tanzania). Palaeogeogr Palaeoclimatol Palaeoecol. 239(3–4):334–354. https://doi.org/10.1016/j.palaeo.2006.02.002

Gasse F, Chalié F, Vincens A, Williams MAJ, Williamson D. 2008. Climatic patterns in equatorial and southern Africa from 30,000 to 10,000 years ago reconstructed from terrestrial and near-shore proxy data. Quat Sci Rev. 27(25–26):2316–2340. https://doi.org/10.1016/j.quascirev.2008.08.027

Grimm EC. 2004. TGViewVersion2.0.2.

Ivory SJ, Blome MW, King JW, McGlue MM, Cole JE, Cohen AS. 2016. Environmental change explains cichlid adaptive radiation at Lake Malawi over the past 1.2 million years. Proc Natl Acad Sci U S A. 113(42):11895–11900. https://doi.org/10.1073/pnas.1611028113

Ivory SJ, Lezine A-M, Vincens A, Cohen A. 2018. Waxing and waning of forests: Late Quaternary biogeography of southeast Africa. Glob Chang Biol. 24(7):2939–2951.

Kandel Andrew W, Bolus Michael, Bretzke K, Bruch Angela A, Haidle Miriam N, Hertler Christine, Märker Michael, Kandel A W, Bolus M, Bretzke : K, et al. 2016. Increasing Behavioral Flexibility? An Integrative Macro-Scale Approach to Understanding the Middle Stone Age of Southern Africa. J Archaeol Method Theory. 23:623–668. https://doi.org/10.1007/s10816-015-9254-y

Kaufulu ZM. 1990. Sedimentary Environments at the Mwanganda Site, Malawi. Geoarchaeology - An Int J. 5(1):15–27.

Kristensen JA, Thomsen KJ, Murray AS, Buylaert JP, Jain M, Breuning-Madsen H. 2015. Quantification of termite bioturbation in a savannah ecosystem: Application of OSL dating. Quat Geochronol. 30:334–341. https://doi.org/10.1016/J.QUAGEO.2015.02.026

Kühn P, Aguilar JA, Miedema R. 2010. Textural Pedofeatures and Related Horizons. In: Interpret Micromorphol Featur Soils Regoliths. https://doi.org/10.1016/B978-0-444-53156-8.00011-8

Kullmer O. 2008. The fossil suidae from the Plio-Pleistocene Chiwondo beds of northern Malawi, Africa. J Vertebr Paleontol. 28(1):208–216.

Lüdecke T, Schrenk F, Thiemeyer H, Kullmer O, Bromage TG, Sandrock O, Fiebig J, Mulch A. 2016. Persistent C3 vegetation accompanied Plio-Pleistocene hominin evolution in the Malawi Rift (Chiwondo Beds, Malawi). J Hum Evol 90:163–175. https://doi.org/10.1016/j.jhevol.2015.10.014

Lyons RP, Scholz CA, Buoniconti MR, Martin MR. 2011. Late Quaternary stratigraphic analysis of the Lake Malawi Rift, East Africa: An integration of drill-core and seismic-reflection data. Palaeogeogr Palaeoclimatol Palaeoecol 303(1–4):20–37. https://doi.org/10.1016/j.palaeo.2009.04.014

Lyons RP, Scholz CA, Cohen AS, King JW, Brown ET, Ivory SJ, Johnson TC, Deino AL, Reinthal PN, McGlue MM, Blome MW. 2015. Continuous 1.3-million-year record of East African hydroclimate, and implications for patterns of evolution and biodiversity. Proc Natl Acad Sci 112(51):201512864. https://doi.org/10.1073/pnas.1512864112

M Color, X-rite. 2009. Munsell soil-color charts with genuine Munsell color chips. Grand Rapids, Michigan, USA.

Machette MN. 1985. Calcic soils of the southwestern United States:1–22. https://doi.org/10.1130/SPE203-p1

Mackay A, Stewart BA, Chase BM. 2014. Coalescence and fragmentation in the Late Pleistocene archaeology of southernmost Africa. J Hum Evol. 72:26–51.

Madella M, Alexandre A, Ball T. 2005. International Code for Phytolith Nomenclature 1.0. Ann Bot 96(2):253–260. https://doi.org/10.1093/AOB/MCI172

Marcelino V, Stoops G, Schaefer CEGR. 2010. Oxic and Related Materials. In: Interpret Micromorphol Featur Soils Regoliths; p. 305–327.

McFarlane MJ. 1976. Laterite and Landscape: Academic Press, London.

Mentzer SM, Quade J. 2013. Compositional and Isotopic Analytical Methods in Archaeological Micromorphology. Geoarchaeology. 28(1):87–97. https://doi.org/10.1002/gea.21425

Mercader J, Akuku P, Boivin N, Bugumba R, Bushozi P. 2020. Hominin Ecology of the Early Oldowan 2 Ma. https://doi.org/10.21203/RS.3.RS-49789/V1

Mercader J, Asmerom Y, Bennett T, Raja M, Skinner A. 2009. Initial excavation and dating of Ngalue Cave: A Middle Stone Age site along the Niassa Rift , Mozambique. J Hum Evol. 57:63–74. https://doi.org/10.1016/j.jhevol.2009.03.005

Mercader J, Astudillo F, Barkworth M, Bennett T, Esselmont C, Kinyanjui R, Grossman DL, Simpson S, Walde D. 2010. Poaceae phytoliths from the Niassa Rift, Mozambique. J Archaeol Sci. 37(8):1953–1967. https://doi.org/10.1016/J.JAS.2010.03.001

Mercader J, Bennett T, Esselmont C, Simpson S, Walde D. 2009. Phytoliths in woody plants from the Miombo woodlands of Mozambique. Ann Bot 104(1):91–113. https://doi.org/10.1093/AOB/MCP097

Mercader J, Bennett T, Esselmont C, Simpson S, Walde D. 2011. Soil phytoliths from miombo woodlands in Mozambique. Quat Res 75(1):138–150. https://doi.org/10.1016/J.YQRES.2010.09.008

Mercader J, Bennett T, Esselmont C, Simpson S, Walde D. 2013. Phytoliths from Middle Stone Age habitats in the Mozambican Rift (105–29 ka). J Hum Evol. 64(5):328–336. https://doi.org/10.1016/J.JHEVOL.2012.10.013

Mercader J, Clarke S, Bundala M, Favreau J, Inwood J, Itambu M, Larter F, Lee P, Lewiski-McQuaid G, Mollel N, et al. 2019. Soil and plant phytoliths from the Acacia-Commiphora mosaics at Oldupai Gorge (Tanzania). PeerJ 7(12):e8211. https://doi.org/10.7717/PEERJ.8211

Mercader J, Clarke S, Itambu M, Mohamed A, Mwitondi M, Siljedal G, Soto M, Bushozi P. 2021. Phytolith Palaeoenvironments at Mumba Rock Shelter. Front Ecol Evol. 0:423. https://doi.org/10.3389/FEVO.2021.699609

Middleton G V. 1973. Johannes Walther's Law of the Correlation of Facies. Geol Soc Am Bull. 84:979–988.

Morley MW, Goldberg P. 2017. Geoarchaeological research in the humid tropics: A global perspective. J Archaeol Sci. 77:1–9. https://doi.org/10.1016/J.JAS.2016.11.002

Moss PT. 2013. 14.26 Palynology and Its Application to Geomorphology. Treatise Geomorphol. 14:315–325. https://doi.org/10.1016/B978-0-12-374739-6.00395-X

Neumann K, Fahmy A, Lespez L, Ballouche A, Huysecom E. 2009. The Early Holocene palaeoenvironment of Ounjougou (Mali): Phytoliths in a multiproxy context. Palaeogeogr Palaeoclimatol Palaeoecol. 276(1–4):87–106. https://doi.org/10.1016/J.PALAEO.2009.03.001

Neumann K, Fahmy AG, Müller-Scheeßel N, Schmidt M. 2017. Taxonomic, ecological and palaeoecological significance of leaf phytoliths in West African grasses. Quat Int. 434:15–32. https://doi.org/10.1016/J.QUAINT.2015.11.039

Nightingale S, Schilt F, Thompson JC, Wright DK, Forman S, Mercader J, Moss P, Clarke S, Itambu M, Gomani Chindebvu E, Welling M. 2019. Late Middle Stone Age Behavior and Environments at Chaminade I (Karonga, Malawi). https://doi.org/10.1007/s41982-019-00035-3

Novello A, Barboni D, Berti-Equille L, Mazur JC, Poilecot P, Vignaud P. 2012. Phytolith signal of aquatic plants and soils in Chad, Central Africa. Rev Palaeobot Palynol. 178:43–58. https://doi.org/10.1016/J.REVPALBO.2012.03.010

Olley JM, Murray A, Roberts RG. 1996. The effects of disequilibria in the uranium and thorium decay chains on burial dose rates in fluvial sediments. Quat Sci Rev. 15(7):751–760. https://doi.org/10.1016/0277-3791(96)00026-1

Patalano R, Hamilton R, Finestone E, Amano N, Heddell-Stevens P, Itambu M, Petraglia M, Roberts P. 2021. Microhabitat Variability in Human Evolution. Front Earth Sci 9:1208. https://doi.org/10.3389/FEART.2021.787669

Piperno M, Tagliacozzo A. 2001. The Elephant Butchery Area at the Middle Pleistocene site of Notarchirico (Venosa , Basilicata , Italy). World Elephants - Int Congr Rome.:230–236.

Pons LJ, Zonneveld IS. 1965. Soil ripening and soil classification: initial soil formation of alluvial deposits with a classification of the resulting soils. Wageningen: Veenman.

Richter D, Gruen R, Johannes-Boyau R, Steele TE, Amani F, Rue M. 2017. The age of the hominin fossils from Jebel Irhoud, Morocco, and the origins of the Middle Stone Age. Nature. 546(7657):293–296.

Ring U, Betzler C. 1995. Geology of the Malawi Rift: Kinematic and tectonosedimentary background to the Chiwondo Beds, northern Malawi. J Hum Evol. 28(1):7–21. https://doi.org/10.1006/jhev.1995.1003

Ring U, Betzler C, Delvaux D. 1992. Normal vs. strike-slip faulting during rift development in East Africa: The Malawi rift. Geology. 20(11):1015–1018. https://doi.org/10.1130/0091-7613(1992)020<1015:NVSSFD>2.3.CO;2

Roberts RG, Galbraith RF, Yoshida H, Laslett GM, Olley JM. 2000. Distinguishing dose populations in sediment mixtures: a test of single-grain optical dating procedures using mixtures of laboratory-dosed quartz. Radiat Meas. 32(5–6):459–465. https://doi.org/10.1016/S1350-4487(00)00104-9

Ruhe R V., Olson CG. 1980. Soil welding. Soil Sci 130(3):132–139. https://doi.org/10.1097/00010694-198009000-00004

Runge F. 1999. The opal phytolith inventory of soils in central Africa —quantities, shapes, classification, and spectra. Rev Palaeobot Palynol. 107(1–2):23–53. https://doi.org/10.1016/S0034-6667(99)00018-4

Scerri EM, Thomas MG, Manica A, Gunz P, Stock JT, Stringer C. 2018. Did our species evolve in subdivided populations across Africa, and why does it matter? Trends Ecol Evol. 33(8):582–584.

Scerri EML. 2017. The North African Middle Stone Age and its place in recent human evolution. Evol Anthropol Issues, News, Rev. 26(3):119–135.

Schoeneberger PJ, Wysocki DA, Benham EC, Staff SS. 2012. Field Book for Describing and Sampling Soils. Version 3. Lincoln, NE: National Resources Conservation Service, National Soil Survey Center. https://doi.org/10.1111/j.1600-0587.2009.05973.x

Scholz C a., Cohen AS, Johnson TC, King JW, Moran K. 2006. The 2005 Lake Malawi Scientific Drilling Project. Sci Drill.(2, March 2006):2005–2007. https://doi.org/10.2204/iodp.sd.2.04.2006

Scholz CA, Cohen AS, Johnson TC, King J, Talbot MR, Brown ET. 2011. Scientific drilling in the Great Rift Valley: The 2005 Lake Malawi Scientific Drilling Project - An overview of the past 145,000years of climate variability in Southern Hemisphere East Africa. Palaeogeogr Palaeoclimatol Palaeoecol 303(1–4):3–19. https://doi.org/10.1016/j.palaeo.2010.10.030

Scholz CA, Johnson TC, Cohen AS, King JW, Peck JA, Overpeck JT, Talbot MR, Brown ET, Kalindekafe L, Amoako PYO, et al. 2007. East African megadroughts between 135 and 75 thousand years ago and bearing on early-modern human origins. Proc Natl Acad Sci 104(42):16416–16421. https://doi.org/10.1073/pnas.0703874104

Slate JL, Smith GA, Wang Y, Cerling TE. 1996. Carbonate-paleosol Genesis in the Plio-Pleistocene St. David Formation, Southeastern Arizona. J Sediment Res. 66(1):85–94.

Stephens EA. 1963. Geological Account of the Northwest Coast of Lake Malawi Between Karonga and Lion Point, Malawi. Am Anthropol. 68(2):50–58. https://doi.org/10.1525/aa.1966.68.2.02a00970

Stone JR, Westover KS, Cohen AS. 2011. Late Pleistocene paleohydrography and diatom paleoecology of the central basin of Lake Malawi, Africa. Palaeogeogr Palaeoclimatol Palaeoecol 303(1–4):51–70. https://doi.org/10.1016/j.palaeo.2010.01.012

Surovell TA, Waguespack NM. 2008. How many elephant kills are 14?. Clovis mammoth and mastodon kills in context. Quat Int. 191(1):82–97. https://doi.org/10.1016/j.quaint.2007.12.001

Thien SJ. 1979. A flow diagram for teaching texture by feel analysis. J Agron Educ. 8:54–55.

Thompson JC, Mackay A, de Moor V, Gomani Chindebvu E. 2014. Catchment Survey in the Karonga District: a Landscape-Scale Analysis of Provisioning and Core Reduction Strategies During the Middle

Stone Age of Northern Malawi. African Archaeol Rev. 31(3):447–478. https://doi.org/10.1007/s10437-014-9167-2

Thompson JC, Mackay A, Nightingale S, Wright D, Choi JH, Welling M, Blackmore H, Gomani Chindebvu E. 2018. Ecological risk, demography and technological complexity in the Late Pleistocene of northern Malawi: implications for geographical patterning in the Middle Stone Age. J Quat Sci. 33(3):261–284. https://doi.org/10.1002/jqs.3002

Thompson JC, Mackay A, Wright DK, Welling M, Greaves A, Gomani Chindebvu E, Simengwa D. 2012. Renewed investigations into the Middle Stone Age of northern Malawi. Quat Int 270:129–139. https://doi.org/10.1016/j.quaint.2011.12.014

Thompson JC, Welling M, Gomani Chindebvu E. 2013. Using GIS to Integrate Old and New Archaeological Data from Stone Age Deposits in Karonga, Malawi. Int J Herit Digit Era. 2(4):611–630. https://doi.org/10.1260/2047-4970.2.4.611

Thompson JC, Wright D. K., Nightingale S, Kaliba PM. 2022. Pleistocene archaeology of northern Malawi. In: Beyin A, Wright David K., Wilkins J, Bouzouggar A, Olszewski D, editors. Handb Pleistocene Archaeol Africa Hominin Behav Geogr Chronol (in Press).

Thompson JC, Wright DK, Ivory SJ. 2021. The emergence and intensification of early hunter-gatherer niche construction. Evol Anthropol 30:17–27. https://doi.org/DOI: 10.1002/evan.21877

Thompson JC, Wright DK, Ivory SJ, Choi J-H, Nightingale S, Mackay A, Schilt F, Otarola-Castillo E, Mercader J, Forman S, et al. 2021. Early human impacts and ecosystem reorganization in southern-central Africa. Sci Adv 7(9776):1–13. https://advances.sciencemag.org/content/7/19/eabf9776

Tryon CA. 2019. The Middle/Later Stone Age transition and cultural dynamics of late Pleistocene East Africa. Evol Anthropol. 28(5):267–282. https://doi.org/10.1002/evan.21802

Vincens A, Garcin Y, Buchet G. 2007. Influence of rainfall seasonality on African lowland vegetation during the Late Quaternary: Pollen evidence from Lake Masoko, Tanzania. J Biogeogr 34(7):1274–1288. https://doi.org/10.1111/j.1365-2699.2007.01698.x

Wadley L. 2015. Those marvellous millennia: the Middle Stone Age of Southern Africa. Archaeol Res Africa. 50(2):155–226.

Walther J. 1894. Einleitung in die Geologie als historische Wissenschaft, Bd. 3. G. Fischer, editor. Jena.

Wantzen KM, Yule CM, Tockner K, Junk WJ. 2008. Riparian Wetlands of Tropical Streams. Trop Stream Ecol.:199–217. https://doi.org/10.1016/B978-012088449-0.50009-1

Wright DK, Thompson J, Mackay A, Welling M, Forman SL, Price G, Zhao J xin, Cohen AS, Malijani O, Gomani Chindebvu E. 2014. Renewed Geoarchaeological Investigations of Mwanganda's Village (Elephant Butchery Site), Karonga, Malawi. Geoarchaeology. 29(2):98–120. https://doi.org/10.1002/gea.21469

Wright DK, Thompson JC, Schilt F, Cohen AS, Choi JH, Mercader J, Nightingale S, Miller CE, Mentzer SM, Walde D, et al. 2017. Approaches to Middle Stone Age landscape archaeology in tropical Africa. J Archaeol Sci 77:64–77. https://doi.org/10.1016/j.jas.2016.01.014

Wright VP. 1990a. A Micromorphological Classification of Fossil and Recent Calcic and Petrocalcic Microstructures. Dev Soil Sci. 19(C):401–407. https://doi.org/10.1016/S0166-2481(08)70354-4

Wright VP. 1990b. Estimating rates of calcrete formation and sediment accretion in ancient alluvial deposits. Geol Mag. 127(3):273–276. https://doi.org/10.1017/S0016756800014539

Wright VP. 2007. Calcrete. In: Nash DJ, McLaren SJ, editors. Geochemical Sediments and Landscapes. Blackwell Publishing Ltd; p. 10–45.

Yravedra J, Rubio-Jara S, Panera J, Uribelarrea D, Pérez-González A. 2012. Elephants and subsistence. Evidence of the human exploitation of extremely large mammal bones from the Middle Palaeolithic site of PRERESA (Madrid, Spain). J Archaeol Sci 39(4):1063–1071. https://doi.org/10.1016/j.jas.2011.12.004

Zamanian K, Pustovoytov K, Kuzyakov Y. 2016. Pedogenic carbonates: Forms and formation processes. Earth-Science Rev 157:1–17. https://doi.org/10.1016/j.earscirev.2016.03.003

Supplementary materials for paper E: Schilt et al. (in review)

S1. METHODS AND NOTES

Micromorphology

Depending on the consistency of the sample, blocks were either partly carved out and stabilized with plaster-of-Paris before removal (following Goldberg and Macphail 2003), or completely carved out from the profile, wrapped in toilet paper, and fixed with packaging tape. At the laboratory of the Institute for Archaeological Sciences, University of Tübingen, Germany, the samples were dried in the oven for several days at 50 °C and impregnated with resin under vacuum. The resin mixture consisted of 7 volume units of unpromoted polyester resin (Viscovoss N 55S), 3 volume units of styrene (styrene for synthesis) and 5-6 ml/l hardener (methylethylketone peroxide, MEKP). After hardening, the blocks were sliced with a rock saw into slabs.

Some of the samples were processed into 6x9 cm-sized thin sections of ~30 μm thick at the Laboratory of Soil Science and Geoecology of the University of Tübingen, Germany, and the remaining samples were made into small (4.5x2.6 cm) and medium-sized (5x7.5 cm) thin sections at Spectrum Petrographics in Vancouver, WA, USA.

The thin sections were scanned with a flat-bed scanner to observe macroscopic characteristics and studied with transmitted light stereomicroscopes with built-in polarizing filters (6,5–160x magnification) and a petrographic microscope (25–500x magnification), using plane polarized light (PPL), crossed polarized light (XPL), incident light, and oblique incident light. Micromorphological analysis followed Stoops et al. (2003), and Delvigne (1998), Bullock et al (1985), and Courty et al. (1989).

Cathodoluminescence (CL) microscopy

The size and morphology of calcite crystals shed light on the type of carbonate (for instance groundwater vs. pedogenic), potential areas with recent recrystallization or dissolution, and the type of sediment it replaced or formed in (Machel, 2000; Götze, 2002). CL microscopy is a useful technique to visualize and study the formation of calcite crystals and the transformation of siliceous minerals within carbonate nodules (Delvigne and Stoops, 1990; Delvigne, 1998; Islam *et al.*, 2002; Alonso, Dorronsoro and Egido, 2004; N. Durand, Monger and Canti, 2010). Mineral growth phases of calcite crystals become better visible in CL and zones of calcium carbonate

nodules that are enriched in certain trace elements or areas with different calcite crystal type and size appear more pronounced than under normal light (Machel, 2000).

Cathodoluminescence microscopy was performed on a selection of thin sections using a system with a cold cathode electron source attached to an optical microscope with a low vacuum chamber in the Applied Mineralogy Working Group at the University of Tübingen.

Microscopic X-ray fluorescence

The thin sections, or their corresponding resin-indurated chips, were scanned under full vacuum using a Bruker M4 Tornado equipped with a rhodium x-ray source and dual detectors. All scans were conducted with no filters, with a beam voltage of 50 kV and current of 600 μA. Elemental distribution maps were generated from scans across a grid with a spot spacing that varied from 15 microns for detailed images, to 30, 55 and 75 microns for overview images. Dwell time that varied from 1 to 50 ms, depending on the elements desired and their relative abundance. Mapped elements were selected for each sample based on the presence of peaks in the fluorescence spectra. Deconvolution prior to final image production was applied based on the selected elements.

Carbonate nodule samples

During three field seasons (2012, 2013, 2014), a total of 18 carbonate nodules of 4-15 cm was collected from pedogenic carbonate horizons at MGD and BRU. All carbonate samples were collected from a likely depth of >30 cm beneath the associated ground surface prior to Holocene erosion, thus minimalizing chances of diffusional mixing with atmospheric CO_2 during their formation (Cerling *et al.*, 1989). The nodules were documented prior to collection and their orientation was marked with a small dot on the top of each nodule. The location of the nodules was registered with a Nikon Nivo 3" total station.

Before the collection of sub-samples for stable isotopes analysis and radiocarbon dating, the carbonate nodules were carefully studied in thin section to determine their formation processes. While pedogenic carbonates form in connection to a stable ground surface, groundwater carbonates form independently from a ground surface, making it problematic to place any data obtained from them in a stratigraphical and chronological framework. Therefore, relations between environmental conditions, timing of carbonate formation, and potential human occupations above ground can only be inferred from pedogenic carbonates.

The following laboratory protocol was designed for maximum control on sub-sample location to avoid zones with late recrystallization, abundant mineral inclusions, or great variability

in calcite crystal sizes. The nodules were sliced in half, so that one half could be impregnated and processed into a small petrographic thin section (4.5 x 2.6 cm), while the other half could be used for other analyses. The thin sections were analyzed using standard stereoscopic and petrographic microscopes, as well as cathodoluminescence microscopy. The non-impregnated halves of the nodules were used for stable isotopic and radiocarbon analyses. Subsamples for these analyses were drilled with a precision drill from selected areas of c. 3 mm in diameter, chosen based on petrographic analysis of the corresponding opposite nodule-half. In this way, zones rich in sparite, often linked to recrystallization or late infilling of cracks (Alonso, Dorronsoro and Egido, 2004; Candy *et al.*, 2012; Zamanian, 2017), could be avoided, as well as parts that were particularly heterogeneous regarding calcite crystal size, internal fabric, or mineral inclusions.

In order to detect potential differences within nodules related to the timing or type of formation, multiple subsamples were analyzed from nodules exhibiting different zones. For example, some carbonate nodules contained a dark brown inner core, and others contained zones with different carbonate crystal sizes, which may result from recrystallization or carbonate replacement. However, with respect to stable isotopes the different sub-samples had similar outcomes.

Not enough nodules were collected to make clear inferences about trends within nodule horizons through time and/or depth.

Stable isotope analysis

Background

Stable carbon isotope signatures in soil organic matter are determined by the different photosynthetic sugar-fixation mechanisms used by plants. The three main mechanisms are the Calvin-Benson or C3 pathway, which uses a three-carbon sugar molecule, the Hatch-Slack or C4 pathway, which uses a four-carbon sugar molecule, and Crassulacean Acid Metabolism (CAM), and result in different $\delta^{13}C$ values based on discrimination against the heavier ^{13}C isotope vs. ^{12}C. Because of CO_2 diffusion in the soil (accounting for c. +4.4‰) and equilibrium fractionation during carbonate precipitation (+11‰), $\delta^{13}C$ in pedogenic carbonate ($\delta^{13}C_{PC}$) is enriched by about 14‰ at 25 °C compared to plants (but for example at 0°C by about 17‰) (Cerling *et al.*, 1989). Therefore, during soil formation at 25 °C, a C3 canopy cover results in $\delta^{13}C_{PC}$ values between -8‰ to -16‰, while a C4 vegetation cover produces values between 0‰ and +4‰. In tropical environments, C3 plants are common in warm areas with abundant water and have $\delta^{13}C$ values ranging between -22‰ to -30‰. Most trees, herbs and shrubs in the tropics follow the C3

photosynthetic pathway, while grasses follow the C4 pathway, with $\delta^{13}C$ values ranging between 10‰ and 14‰ (Kowler, 2007).

Oxygen stable isotopic compositions in pedogenic carbonate ($\delta^{18}O_{PC}$) derive from $\delta^{18}O$ of regional meteoric water ($\delta^{18}O_{MW}$), which is related to temperature, precipitation regimes, and evaporation (Kowler, 2007; Golubtsov *et al.*, 2014). A full review of the occurrence of stable isotopes in carbonates and their relationship to hydrology, temperature and edaphic conditions can be found in Quade and Cerling (2007).

Approach

A total of 15 carbonate nodules followed the protocol described above (under "carbonate nodule samples") and were studied in thin section before the drilling of sub-samples. Some excavation pits had however been backfilled by the time of carbonate sampling. Therefore, three samples were selected from mapped sediment samples collected during the 2012 excavations at MGD-I and MGD-III. These small (c. 0.5-1 cm) carbonate nodules were taken from loose sediment samples that had been collected alongside micromorphology block samples. The corresponding micromorphological samples contained many carbonate nodules, providing ample information on carbonate nodules in the same horizons. However, the three selected subsamples were too small to be sliced in half for the production of a corresponding control thin section.

The $\delta^{13}C_{PC}$ and $\delta^{18}O_{PC}$ analyses were conducted at the Biogeology Laboratory, University of Tübingen, equipped with a Stable isotope mass spectrometer (Elementar Isoprime 100) with multi-flow module for carbonate analysis. The ratio of the ^{12}C and ^{13}C stable isotopes, $\delta^{13}C$, is expressed in parts per mille (‰) relative to the standard VPDB (±0.1). The ration ^{18}O:^{16}O ($\delta^{18}O$) from pedogenic carbonates is expressed in per mille relative to VPDB (±0.2), while measurements from water samples are reported in VSMOW2 (±0.2).

In addition to pedogenic carbonate samples, three water samples were collected in 2012 and 2013 for reference from two springs at MGD and BRU and from a borehole nearby MGD. The samples were analyzed for $\delta^{18}O$ and $\delta^{2}H$ (deuterium, or δD) and $\delta^{18}O$ and $\delta^{2}H$ measurements were reported in VSMOW2 (±0.2). Stable isotope analysis on water samples ($\delta^{18}O$ and $\delta^{2}H$) was performed in the laboratory for isotope geochemistry at the Department of Geoscience, University of Tübingen.

Note on stable oxygen isotopes

Modern $\delta^{18}O$ rainwater values for the area of MGD and BRU (-9.564 S, 33.530 E, elevation 520 m) are estimated to fluctuate between -30.5 ‰ (PDB) during the driest part of the year (June), and -32.7 ‰ during the rainy season (December), the latter reflecting the amount effect of intense rainfall leading to lower $\delta^{18}O$ values (Bowen, 2017). Modern groundwater samples that we collected from shallow springs at MGD and BRU during the dry season measured -31.7‰ and -32.2‰, and a groundwater sample from a borehole gave a value of -34.8‰. Pedogenic carbonates are expected to have mainly precipitated after the rainy season in concurrence with increased plant-growth. Most $\delta^{18}O_{PC}$ values from MGD and BRU lie between -8 and -9‰ (PDB) and are ~20‰ more enriched compared to modern meteoric values. Besides isotopic compositions of groundwater, enrichment of ^{18}O in pedogenic carbonates has to be taken into account, occurring with isotopic fractionation during carbonate precipitation, which is determined by soil temperature (Zanchetta *et al.*, 2000). Unfortunately, the isotopic compositions of the meteoric and soil water at the time of carbonate formation are unknown, as well as paleotemperatures, and we have no modern pedogenic carbonates for comparison. Therefore, we cannot determine to what extent $\delta^{18}O_{PC}$ values reflect the composition of meteoric water and to what extent they have been altered by fractionation during carbonate precipitation, affected by temperature.

It is known that evaporation and/or low temperatures can lead to ^{18}O enrichment, which is important to consider in the context of interpreting the paleoclimatic significance of the carbonate isotope record. For example, lake waters of Lake Malawi are generally more enriched as compared to inland precipitation as a result of fractionation by evaporation from the lake's surface, and the paleosols at MGD and BRU may have been bordering closely to lagoonal wetlands at the edges of the lake during soil formation (Barker *et al.*, 2007). However, while local drizzle or fog may transport evaporated lake surface water to land, monsoonal rain transports water from more distant water sources, namely the western Indian Ocean and the tropical Atlantic (Barker *et al.*, 2007). Another process to be taken into consideration are evaporative processes in the soil. These may also lead to the enrichment of $\delta^{18}O$ in the remaining water before carbonate precipitation. This is reported to occur primarily in arid to semi-arid environments, contradicting the proximity of a wetland environment, but not the notion of more pronounced seasonality between the wet season and dry season (Quade and Cerling, 1995; Zanchetta *et al.*, 2000). Especially the enriched value of the youngest (and smallest) carbonate nodule (1 ka) collected from the upper soil at MGD-I, may be a response to enrichment of water near the evaporation front.

Phytolith analysis

Analysis took place in a cleanroom laboratory at the University of Calgary (Earth Sciences Building 833/811). Samples (3g) were mixed with 0.1% sodium hexametaphosphate $(NaPO_3)_6$ and sonicated (5 minutes), then subjected to orbital shaking overnight (200 rpm). After clay dispersal, 3N hydrochloric and nitric acids (HCl) (HNO_3) plus hydrogen peroxide (H_2O_2). Sodium polytungstate ($3Na_2WO_4 \cdot 9WO_3 \cdot H_2O$) (Poly-Gee) at specific gravity 2.4 separated out phytoliths. Rinsing and centrifugation was done at 3000 rpm for 5 minutes. Aliquots (0.001 g) were mounted on a microscope slide with either Entellan New or water (cover: 20x40 mm=inspected area). System microscopy was done at 40x (Olympus BX41, Motic BA410E). A minimum of 200 phytoliths was counted where possible, or until sample extinction.

We checked for normality through Shapiro-Wilk normality tests. To compare archaeological distributions with analogous baselines, we grouped all phytolith morphotypes per class. Phytolith distributions were standardized by a Z-score, making archaeological and ecological samples comparable. Principal Component Analysis (PCA) determined variance across stratigraphic units, sites, and habitats. All quantitative analyses were conducted using the software RStudio (RStudio; (Wickham *et al.*, 2020). We restrict our comparative analysis to large plant and soil datasets and to regional archaeological localities where prior phytolith analysis was conducted using the same classification scheme and was inclusive of raw data amenable to reanalysis by PCA. We excluded baselines that are restricted to a few samples, or report information whose data structure or ecological relatedness cannot be directly compared to the phytolith spectrum reported here. Calibration is from the xeric Somalia – Masai woodland mosaics (29 plant species, 35 soils - Mercader *et al.*, 2019, cf. Albert et al., 2015) and local Zambezian woodlands (116 plant species, 25 soils - Mercader, Bennett, et al., 2009; Mercader et al., 2010, 2011).

Optically Stimulated Luminescence Dating (OSL)

OSL measurements on quartz were carried out using a conventional Risø TL/OSL reader (Model TL/OSL-DA-20C/D) installed at Korea Basic Science Institute. The stimulation light source was blue-LEDs (470 nm, FWHM = 20 nm), which delivers ~80 $mW \cdot cm^{-2}$ to the sample position. The reader was also equipped with a $^{90}Sr/^{90}Y$ beta source delivering 0.082±0.002 $Gy \cdot s^{-1}$ to the samples. The OSL signal detection was through 7 mm Hoya U-340 optical filter. OSL signal measured during the initial 0.32 of optical stimulation, less the signals integrated immediately following 0.8 s as a background (Early Background Subtraction), was used to construct dose response growth curves and the estimation of D_e values.

OSL signals were measured using small aliquots (~3 mm mask size), consisting of several hundreds of quartz grains (180–212 μm in size).

All quartz D_e values were obtained by applying a Central Age Model to D_e values that were independent of preheat temperatures (i.e. from preheat plateaus). For the final D_e estimation, only aliquots showing recycling ratios within ±10% of unity and recuperations <10% of natural OSL signals were used for the statistical analysis.

Radionuclide concentrations of the samples were measured using a low-level high-resolution gamma spectrometer at the Korea Basic Science Institute. Conversion of the radionuclide concentrations to dose rates (Dr) used the model presented by (Liritzis, Stamoulis and Ioannides, 2013). The final dose rates were derived based on present water contents (8.4% and 6.9% for samples LM13-10 and LM13-11, respectively) and the attenuation factors given by Zimmerman were applied. The contribution of cosmic ray to dose rate was calculated using the method presented in (Prescott and Hutton, 1994).

S2. GEOLOGICAL MAP

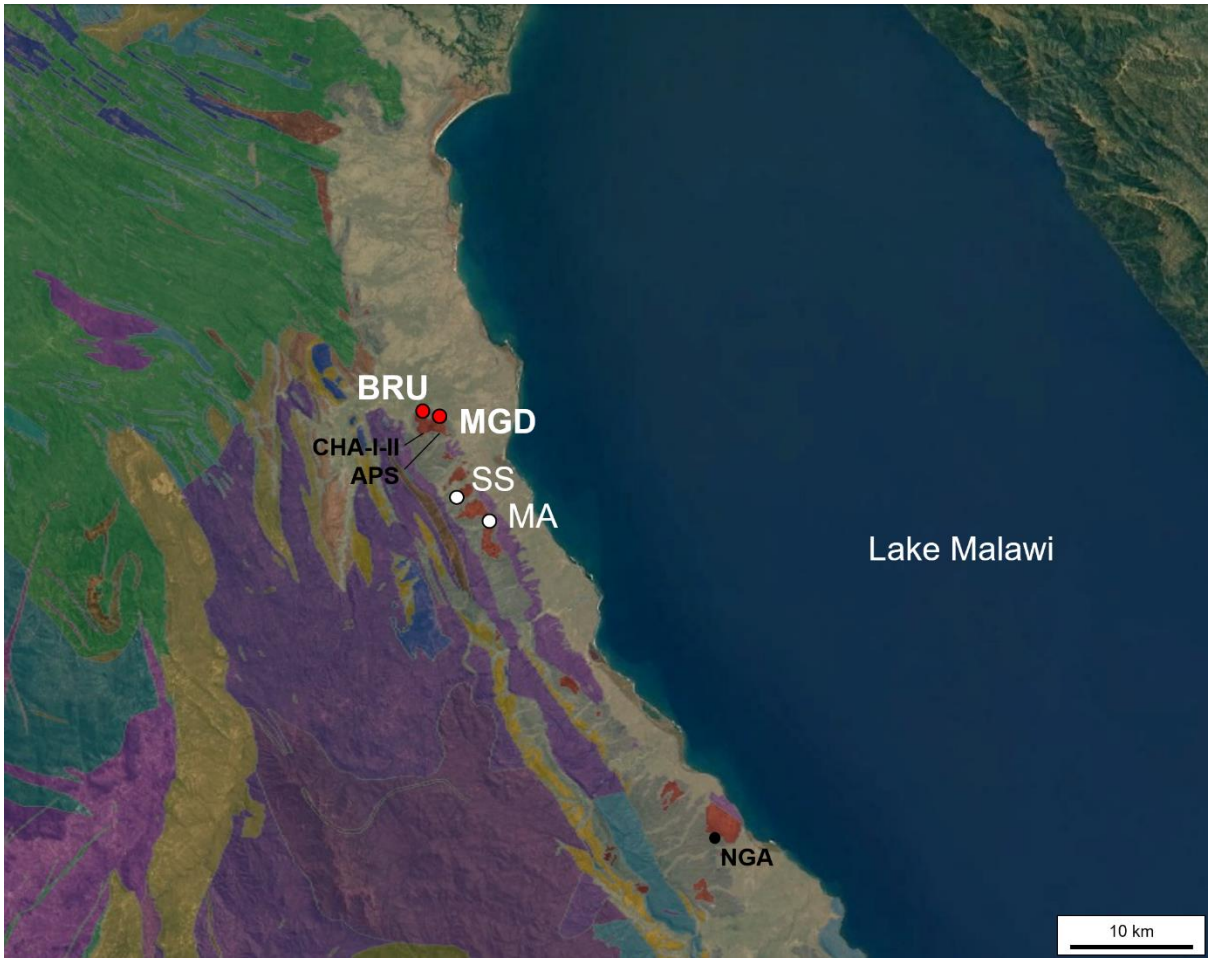

S-Fig. 1. Overview map with the geology of northern Malawi. Mwanganda´s Village (MGD) and Bruce (BRU) are located on the northernmost remnant of the Chitimwe Formation. Reference carbonate samples of the Chiwondo Formation were collected at Sadala South (SS) and Malema (MA). Color key: Red: Chitimwe Beds; Light gray: recent alluvium; Dark gray: Chiwondo Beds; Yellow: Dinosaur Beds; Blue: Sungwa Beds; Purple: basement rocks of the Ubendian Belt, including biotite gneiss with amphibolite dykes; Green: biotite gneiss, granulites, and schists of the Ubendian Belt.

S3. TABLES

Table S-T1. Stable carbon and oxygen isotope results of pedogenic carbonate nodules

Site and sample	δ^{13}C-PDB ±0.1	δ^{18}O-PDB ±0.2	δ^{18}O-SMOW ±0.2	%carbonate ±10%	Depth (cm)	Facies
MGD-I						
9999 A	-10.6	-7.6	23.0	54.4	230	MGD-B
9999 B	-10.2	-8.4	22.2	72.9	230	MGD-B
6877 A	-10.6	-8.0	22.6	27.5	193	MGD-B
6877 B	-10.1	-8.1	22.5	62.7	193	MGD-B
6877 C	-10.2	-7.8	22.9	23.8	193	MGD-B
6877 D	-10.6	-8.2	22.4	69.2	193	MGD-B
5038	-10.8	-8.4	22.2	86.4	113	MGD-B
5035	-9.7	-6.3	24.4	53.1	81	MGD-D
MGD-III						
5055 A	-7.6	-8.3	22.3	98.5	84	MGD-C
BRU-III						
7271 A	-9.3	-8.7	21.9	91.0	92	BRU-B
7272 A	-9.7	-8.5	22.1	72.8	116	BRU-B
7272 B	-10.0	-8.8	21.8	77.5	116	BRU-B
7272 C	-9.7	-8.3	22.3	78.0	116	BRU-B
7273 A	-10.0	-9.1	21.5	92.6	134	BRU-B
7273 B	-9.9	-8.9	21.7	97.6	134	BRU-B
7274	-8.8	-8.5	22.0	81.6	80	BRU-B
7275	-8.8	-8.6	22.0	77.6	83	BRU-B
7276 A	-8.7	-8.2	22.4	75.5	125	BRU-B
7276 B	-8.8	-8.4	22.2	90.4	125	BRU-B
7277	-10.9	-8.1	22.6	83.9	70	BRU-B
BRUGT2						
6885 A	-7.8	-8.4	22.2	103.1	98	BRU-A
6885 B	-7.6	-8.6	22.0	98.4	98	BRU-A
6886	-8.0	-8.1	22.6	84.2	128	BRU-A
6887 A	-9.2	-8.0	22.7	76.2	82	BRU-A
6887 B	-8.4	-8.5	22.1	91.1	82	BRU-A

6888	-8.0	-8.7	21.9	84.0	65	BRU-A
6889	-7.8	-8.6	22.0	89.9	60	BRU-A

Calibrated against NBS 18: $\delta^{13}C$ = -5.014‰ and $\delta^{18}O$ = -23.2‰.

Table S-T2. Results stable oxygen ($\delta^{18}O$) and hydrogen ($\delta^{2}H$) isotopes of modern water samples

Sample location	Lab #	$\delta^{18}O$	$\delta^{2}H$	comments	Year
near MGD (Mwakasungura)	4012	-5,0 ±0,2	-30 ±1	borehole water (pump)	2012
Bruce site area	7258	-1,8 ±0,2	-16 ±1	surficial spring water	2013
MGD Village	7256	-2,3 ± 0,5	-19 ± 2	surficial spring/watering hole	2013

Table S-T3. Summarized stable isotope results from pedogenic carbonate nodules from the different facies within profiles of MGD and BRU and reference samples from modern water

The table further states the number of nodules from which subsamples were collected (#Nn), as well as the number of (sub)samples (#Ns), range of values (‰), mean (μ), standard deviation (σ), and the mean of the calibrated radiocarbon age ranges. *A possibly reworked or derived (anorthic) nodule is marked with an asterisk. $\delta^{13}C$ and $\delta^{18}O$ ranges are given in PDB, and $\delta^{18}O$ values of modern water samples in VSMOW [2]). PDB and SMOW2 values of $\delta^{18}O$ (PC and water) have been converted to enable comparison of the different data. However, fractionation of stable oxygen isotopes during carbonate precipitation has not been accounted for, as temperatures and isotopic compositions of meteoric water during carbonate formation are unknown.

Site	Facies	#Nn	#Ns	$\delta^{13}C$ range PDB ‰	μ	σ	$\delta^{18}O$ range PDB ‰	μ	σ	$\delta^{18}O$ VSMOW2 ‰	$\delta^{2}H$ VSMOW2 ‰	ka cal BP
MGD-I	MGD-B	3	6	-10.6, -10.1	-10.4	0.2	-8.4, -7.6	-8.0	0.3	22.2, 23	-	31-30
MGD-I	MGD-B	1	1	-10.8	-	-	-8.4	-	-	22.2	-	40*
MGD-I	MGD-D	1	1	-9.7	-	-	-6.3	-	-	24.4	-	1
MGD-III	MGD-C	1	1	-7.6	-	-	-8.3	-	-	22.3	-	13
BRU-III	BRU-B	7	11	-10.9, -8.8	-9.5	0.7	-9.1, -8.1	-8.6	0.3	21.5, 22.6	-	29-20
BRU-GT2	BRU-A	5	7	-9.2, -7.6	-8.1	0.5	-8.7, -8.0	-8.4	0.3	21.9, 22.7	-	33-28
MGD spring	water	-	-	-	-	-	-32.2	-	-	-2.3±0.5	-19±2	-

MGD borehole	water	-	-	-	-	-	-34.8	-	-	-5.0±0.2	-30±1	-	
BRU spring	water	-	-	-	-	-	-31.7	-	-	-1.8±0.2	-16±1	-	

Table S-T4. Radiocarbon dates of pedogenic carbonate nodules, originally published in Thompson, Wright and Ivory et al (2021)

Radiocarbon analysis

Radiocarbon dating of pedogenic carbonate nodules provides ages for the latest stages of carbonate formation in the nodules, giving an *ante quem* age of soil formation. Fourteen splits of subsamples used for stable isotope analysis were radiocarbon dated at the Center for Applied Isotope Studies, University of Georgia, USA. The results are presented were published in Thompson et al. 2021 (Thompson, Wright and Ivory, 2021) and are here provided in table ST3. The carbonate samples were reacted with 100% phosphoric acid in evacuated reaction vessels to produce CO^2. CO^2 samples were cryogenically purified from the other reaction products and catalytically converted to graphite using the method of Vogel et al. (Vogel *et al.*, 1984). Graphite $^{14}C/^{13}C$ ratios were measured using a 0.5 MeV accelerator mass spectrometer. The sample ratios were compared to the ratio measured from the Oxalic Acid I standard (NBS SRM 4990). Carrara marble (IAEA C1) was used as the background, and travertine (IAEA C2) was used as a secondary standard. The dates have been corrected for isotope fractionation based on IRMS-measured $\delta^{13}C$ values and calibrated in Oxcal v.4.2.4 (Ramsey, Scott and van der Plicht, 2013) using SHCal20 atmospheric curve (Hogg *et al.*, 2020), within the 95.4% cal BP range.

Site and sample	Facies	Depth (cm)	^{14}C yr BP	Cal yr BP [1,2]	Mean cal yr BP
MGD-I					
9999 A	MGD-B	230	26 620±70	31 080-30 774	30 927
6877 B	MGD-B	193	27 130±70	31 235-31 070	31 153
6877 D	MGD-B	193	25 670±60	30 077-29 886	29 982
5038*	MGD-C	113	34 790±170	40 403-39 502	39 953
5035	MGD-D	81	1 220±20	1 179-989	1 084
MGD-III					
5055 A	MGD-C	84	10 710±30	12 734-12 626	12 680
BRU-III					
7271 A	BRU-B	92	21 970±80	26 376-25 951	26 164
7272 C	BRU-B	116	16 420±60	19 929-19 565	19 747
7273 A	BRU-B	134	25 400±60	29 925-29 300	29 613
7276 B	BRU-B	125	23 740±60	27 919-27 705	27 812
BRUGT2					
6885 B	BRU-A	98	23 920±60	28 204-27 777	27 991
6886	BRU-A	128	27 150±70	31 244-31 075	31 160
6887 B	BRU-A	82	28 840±80	33 687-32 946	33 317
6887 B(R)	BRU-A	82	29 000±80	33 794-33 164	33 479

[1] Radiocarbon ages calibrated in Oxcal v.4.4 (Ramsey, Scott and van der Plicht, 2013) using SHCal20 atmospheric curve (Hogg *et al.*, 2020)
[2] 95.4% cal BP range
*reworked nodule.

Table S-T5. Optically Stimulated Luminescence ages published in Thompson et al. (2018) and Thompson, Wright and Ivory et al. (2021)

Site	Sample	Depth (cm)	OSL age	Facies
MGD-I	3166Q	3.86	58,000 ± 9000	MGD-A
MGD-I	4003.2Q	2.02	34,000 ± 4000	MGD-B
MGD-I	LM12-01	1.85	26,000 ± 1000	MGD-C
MGD-I	4002.2Q	0.86	15,000 ± 1000	MGD-D
MGD-II	LM2011-10	1.56	15,955 ± 1285 14,245 ± 820	MGD-C
MGD-II	LM2011-09	0.65	11,380 ± 1165	MGD-D
MGD-II	LM2011-08	0.3	1865 ± 120	MGD-D
MGD-III	UIC2858	1.13	23,613 ± 1900	MGD-C
MGD-III	LM12-15 (KBSI)	0.69	8200 ± 100	MGD-D
BRU-I	LM13-16	2.07	32,000 ± 2000	BRU-C
BRU-I	LM12-03	1.09	54,000 ± 5000	BRU-C
BRU-I	LM12-04	1.01	50,000 ± 4000	BRU-C
BRU-I	LM12-05	0.76	29,000 ± 3000	BRU-C
BRU-I	LM12-06	0.55	31,000 ± 2000	BRU-C
BRU-II	LM13-21	1.88	44,000 ± 3000	BRU-C
BRU-II	LM13-22	1.61	34,000 ± 3000	BRU-C
BRU-II	LM13-23	1.17	33,000 ± 3000	BRU-C
BRU-III	LM13-19 (KBSI)	1.16	41,000 ± 5000	BRU-B/C
BRU-III	LM13-20 (KBSI)	0.66	30,000 ± 6000	BRU-C

Table S-T6. New OSL ages (Jeong-Heon Choi)

Equivalent dose, dose rate and quartz OSL ages of the samples

Sample	Depth[I] (cm)	Water Content[$] (wt. %)	^{238}U (Bq·kg^{-1})	^{226}Ra (Bq·kg^{-1})	^{232}Th (Bq·kg^{-1})	^{40}K (Bq·kg^{-1})	Dry beta[a] (Gy·ka^{-1})	Dry gamma[a] (Gy·ka^{-1})	Cosmic ray[b] (Gy·ka^{-1})	Total dose rate (Gy·ka^{-1})	D_e (Gy)	O.D (%)	*n*	Age[c]
LM13-10	250	8	14.9±4.3	15.3±0.5	38.4±1.2	435±11	1.32±0.05	0.85±0.02	0.13±0.01	2.30±0.06	91±5	17	12	39±2
LM13-11	85	7	16.9±4.5	15.9±0.4	41.2±1.2	374±9	1.22±0.05	0.85±0.02	0.18±0.02	2.25±0.05	45±2	19	16	20±1

[I] Depths of the samples are the vertical distance from the modern ground surface.
[$] Present water contents.
[a] Data from high-resolution low level gamma spectrometer were converted to infinite matrix dose rates using conversion factors given in Olley et al. (1996).
[b] Cosmic ray dose rates were calculated using the equations provided by Prescott and Hutton (1994).
[c] Central age ± 1σ error

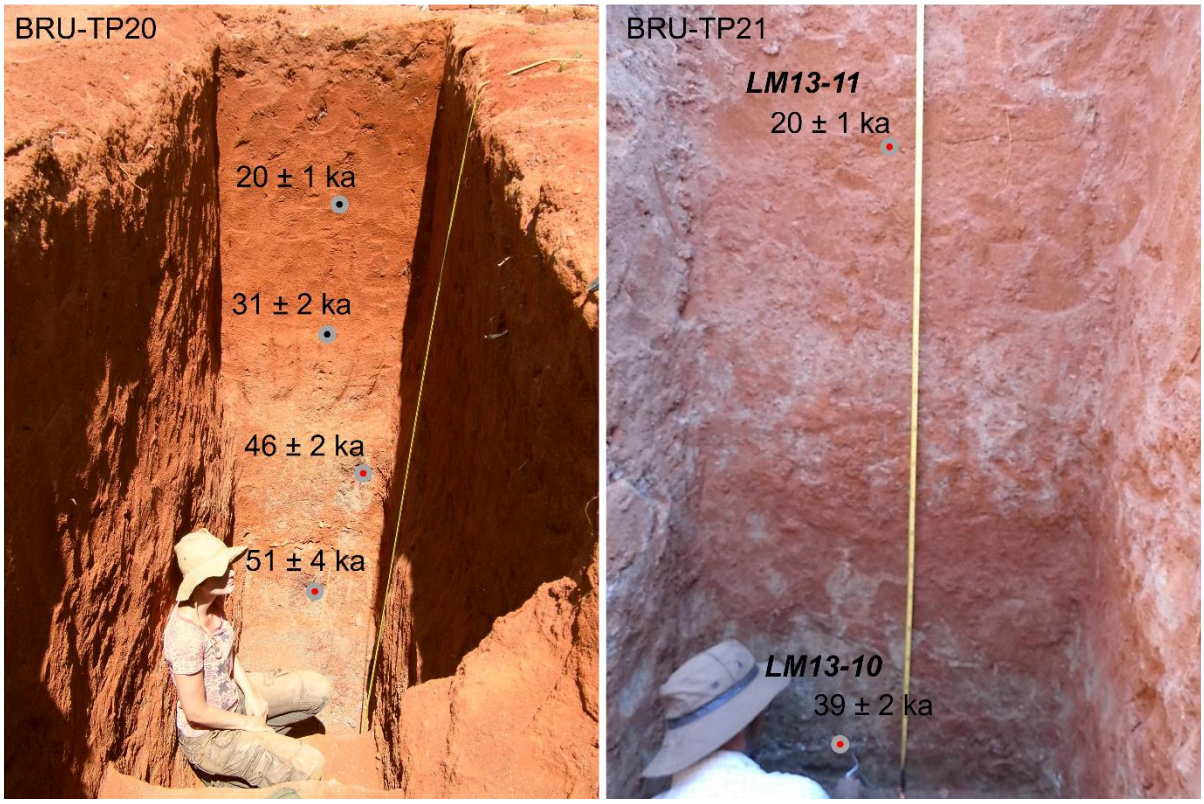

S-Fig. 2a. Sample locations with OSL ages of BRU-TP20 and BRU-TP21. Redox in the lower regions of the test pit BRU-TP21, seen as red color, had formed after excavation due to exposure. Scaping with a trowel has partly removed the red outer surface and exposed gray sediment.

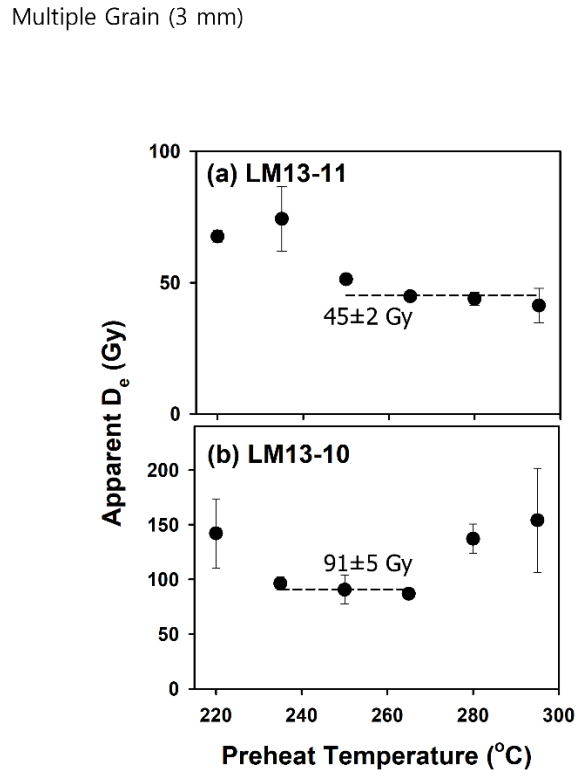

S-Fig. 2b. Preheat plateau tests and equivalent dose (De) of LM13-10 and LM13-11

Table S-T7. Phytolith tally for MGD-I and BRU-TP-20.

Sample	MGD-I 1703	MGD-I 1704	MGD-I 1705	MGD-I 1706	MGD-I 1707	MGD-I 1708	MGD-I 1709	BruTP-20 8149	BruTP-21 8147	BruTP-20 8145	BruTP-20 8143	BruTP-20 8141
Depth (cm)	60	85	100	115	150	165	180	170	195	245	255	275
Bilobate, long notched			1									
Bilobate, short concave					3		1					
Bilobate, short convex	1	4	1	1	1							
Bilobate, short flat		4	1	1								
Bilobate, short notched		1	4	2	1	1						
Bilobates undif.	5	8	5	1	4	8						
Rondel	1	1	5	4	1							
Rondel tower			2			1						
Saddle			1		1							
Bulliform	1	5			2							
Scutiform		3	4		3	1	1					
Blocky	3	27	34	15	28	26	4			1	19	
Blocky cavate						1						
Blocky echinate		1										
Clavate			3	1	2	2						
Fusiform					3							
Cylindroid psilate	6	30	19	9	19	17			1			
Cylindroid scrobiculate	1	2		1	2							
Cylindroid oblong						2						
Cylindroid laminate			1									
Cylindroid cavate			1									
Cylindroid granulate				1								
Cylindroid echinate					1							
Sclereid		1	1		1	1						
Globular granulate	10	160	175	76	15	116	4	1			9	
Globular psilate		8	7	4		1						
Globulose	1	1										
Tabular velloate		1				2						
Tabular ridged		1										
Tabular echinate		1	1			1						
Tabular elongate	1	37	12	5	4	10					3	
Tabular scrobiculate		6	1			4						
Tabular sinuate		3	3	2	2	6						
Total	**30**	305	282	123	93	200	10	1	1	1	31	0

Table S-T8. Raw counts and categories used for PCA.

Sample	*Lobates*	*Poaceae und.*	*Blockies*	*Clavate & Sclereid*	*Cylindroids*	*Epidermal*	*Globulars*	*Tabular woody*	*Tabular und.*	*Rondels*	*Saddles*	*Prism*	*Hair*	*Papillae*
MGD-1704	17	8	28	1	32	0	169	9	40	1	0	0	0	0
MGD-1705	12	4	34	4	21	0	182	2	15	7	1	0	0	0
MGD-1706	5	0	15	1	11	0	80	0	7	4	0	0	0	0
MGD-1708	9	1	27	3	19	0	117	5	16	1	0	0	0	0
Nasera industry	35	20	10	1	22	6	166	17	27	17	11	0	0	0
Acacia referential	695	311	1409	146	880	3	915	4485	417	750	633	2	0	1
Miombo referential	2118	540	853	17	535	154	2613	434	213	272	569	0	51	43
Guineo-Congolian gallery forest	19	2	59	0	7	48	122	2	1	0	0	0	0	0
Hydromorphic grassland	159	48	30	0	117	4	58	63	13	27	1	0	5	11
Uapaca woodland	5	24	98	1	45	0	165	24	2	3	1	0	3	0
Mikuyu FINAL	2	16	37	24	0	0	220	8	0	0	25	0	0	3
Mvumu FINAL	5	21	34	0	0	0	149	4	0	8	58	0	2	0
Mikuyu LATE	4	14	39	4	10	0	336	3	0	0	0	0	0	0
Mvumu LATE	2	48	82	0	3	0	167	26	0	2	18	0	0	0

Table S-T9. Standardized z-values for PCA.

Sample	*Lobates*	*Poaceae und.*	*Blockies*	*Clavate & Sclereid*	*Cylindroids*	*Epidermal*	*Globulars*	*Tabular woody*	*Tabular und.*	*Rondels*	*Saddles*	*Hair*	*Papillae*
MGD-1704	-0.133	-0.553	-0.501	-0.336	0.251	-0.352	0.114	-0.257	2.330	-0.584	-0.550	-0.507	-0.363
MGD-1705	-0.247	-0.794	-0.271	0.112	-0.090	-0.352	0.297	-0.649	0.383	0.141	-0.493	-0.507	-0.363
MGD-1706	-0.406	-1.035	-0.999	-0.336	-0.401	-0.352	-1.140	-0.762	-0.240	-0.221	-0.550	-0.507	-0.363
MGD-1708	-0.315	-0.975	-0.540	-0.037	-0.152	-0.352	-0.619	-0.481	0.461	-0.584	-0.550	-0.507	-0.363
Nasera industry	0.277	0.171	-1.191	-0.336	-0.059	0.085	0.072	0.192	1.318	1.349	0.081	-0.507	-0.363
Acacia referential	-0.087	-0.914	0.686	-0.485	-0.525	3.142	-0.548	-0.649	-0.708	-0.705	-0.550	-0.507	-0.363
Miombo referential	3.100	1.859	-0.425	-0.485	2.887	-0.061	-1.449	2.771	0.227	2.557	-0.493	2.537	3.059
Guineo-Congolian gallery forest	-0.406	0.412	2.180	-0.336	0.654	-0.352	0.058	0.584	-0.630	-0.342	-0.493	1.319	-0.363
Hydromorphic grassland	-0.474	-0.070	-0.156	3.096	-0.742	-0.352	0.832	-0.313	-0.785	-0.705	0.885	-0.507	0.570
Uapaca woodland	-0.406	0.231	-0.271	-0.485	-0.742	-0.352	-0.168	-0.537	-0.785	0.262	2.781	0.710	-0.363
Mikuyu FINAL	-0.429	-0.191	-0.080	0.112	-0.432	-0.352	2.466	-0.593	-0.785	-0.705	-0.550	-0.507	-0.363
Mvumu FINAL	-0.474	1.859	1.568	-0.485	-0.649	-0.352	0.086	0.696	-0.785	-0.463	0.483	-0.507	-0.363

Table S-T10. Principal components.

Samples	*PC1*	*PC2*	*PC3*	*PC4*	*PC5*	*PC6*	*PC7*	*PC8*	*PC9*	*PC10*	*PC11*	*PC12*
Lobates	-0.395	-0.112	-0.016	-0.011	-0.188	-0.175	-0.058	-0.030	0.213	0.279	0.402	0.075
Poaceae und.	-0.281	0.395	-0.059	-0.025	0.244	-0.306	0.388	-0.287	0.114	-0.157	-0.459	-0.264
Blockies	0.015	0.491	0.451	-0.266	0.170	0.160	0.228	0.257	-0.212	0.486	0.085	0.153
Clavate & Sclereid	0.113	0.178	-0.474	-0.252	-0.580	0.223	0.340	0.150	-0.312	-0.098	-0.006	-0.103
Cylindroids	-0.388	-0.107	0.047	-0.230	0.003	0.125	-0.159	0.229	0.030	0.112	0.090	-0.782
Epidermal	0.033	-0.082	0.567	0.203	-0.535	-0.449	0.175	0.242	-0.029	-0.174	-0.096	-0.086
Globulars	0.217	0.215	-0.254	-0.460	0.057	-0.647	-0.371	0.242	0.047	-0.005	0.051	0.055
Tabular woody	-0.391	0.141	0.019	-0.148	0.067	-0.061	0.258	-0.101	-0.024	-0.471	0.571	0.229
Tabular und.	-0.063	-0.546	-0.150	-0.137	0.328	-0.108	0.490	0.502	0.047	0.038	-0.134	0.152
Rondels	-0.362	-0.119	-0.149	0.219	0.034	-0.271	-0.124	-0.117	-0.767	0.242	-0.098	0.100
Saddles	0.048	0.350	-0.330	0.678	0.081	-0.100	0.105	0.377	0.167	0.151	0.235	-0.124
Hair	-0.356	0.193	0.054	0.068	0.037	0.255	-0.390	0.487	-0.052	-0.420	-0.296	0.232
Papillae	-0.369	0.043	-0.155	-0.080	-0.359	0.035	0.000	-0.057	0.417	0.356	-0.322	0.337

Table S-T11. Normality test values.

Samples	*MGD-I 1704*	*MGD-I 1705*	*MGD-I 1706*	*MGD-I 1708*	*Mumba C3*	*Guineo-Congolian*
Shapiro-Wilk W	0.538	0.460	0.468	0.510	0.533	0.614
p(normal)	0.000	0.000	0.000	0.000	0.000	0.000
Samples	Hydromorphic grassland	Uapaca	Mikuyu Final	Mikuyu Late	Mvumu Final	Mvumu Late
Shapiro-Wilk W	0.793	0.625	0.458	0.372	0.570	0.612
p(normal)	0.004	0.000	0.000	0.000	0.000	0.000

RStudio: Integrated Development Environment for R. RStudio, PBC, Boston, MA URL http://www.rstudio.com/.

Hadley Wickham, Romain François, Lionel Henry and Kirill Müller (2020). dplyr: A Grammar of Data Manipulation. R package version 1.0.2. https://CRAN.R-project.org/package=dplyr

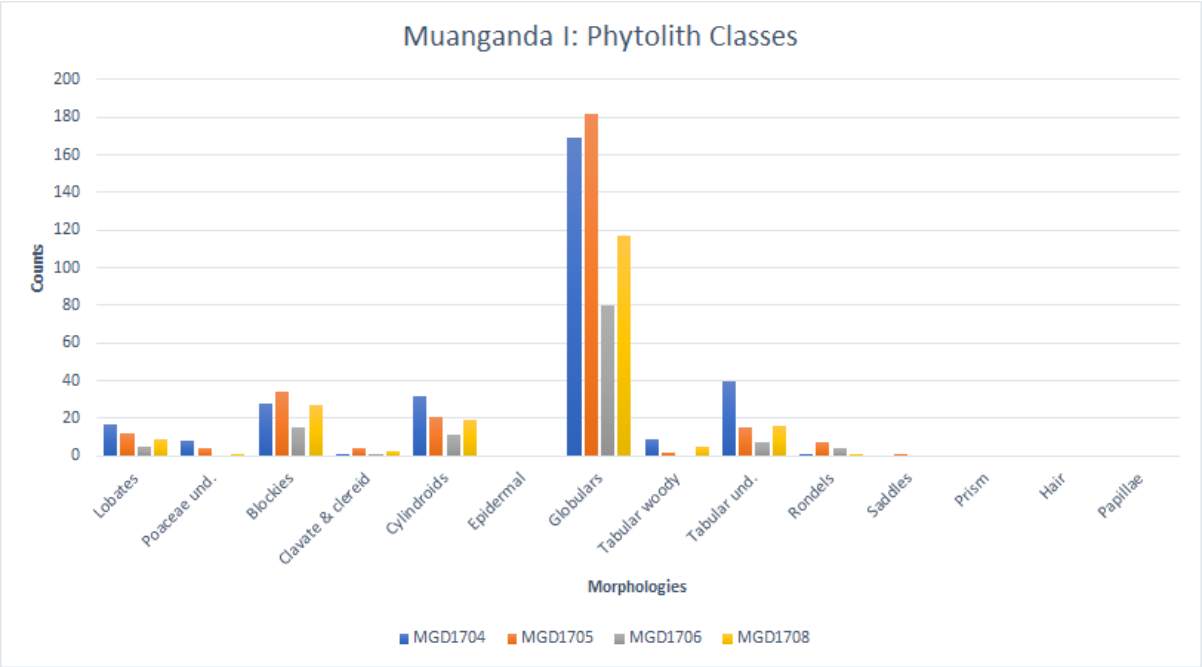

S-Fig. 3. Representation of phytolith classes in samples from Mwanganda-I.

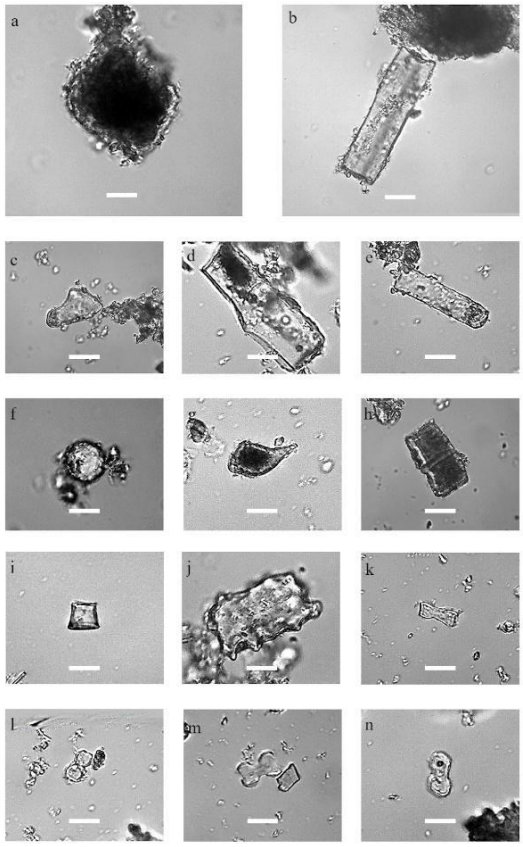

S-Fig. 4. Selected phytolith morphotypes from MGD-I: a. Blocky, sample 1708; b. Cylindroid psilate, 1704; c. Sclereid, 1707; d. Tabular velloate, 1708; e. Tabular elongate, 1705; f. Globular granulate, 1705; g. Fusiform, 1706; h. Bulliform, 1704; i. Tower, 1705; j. Blocky echinate, 1704; k. Bilobate, short notched, 1705; l. Bilobate, short flat, 1704; m. Bilobate short concave, 1707; n. Bilobate short convex, 1706. Length of scale is 25µm.

S-Fig. 5. Modern-day backwaters of Lake Malawi/Lake Niassa may represent a similar environment to the early wetland environments of stage 3. Photo taken on the eastern, Mozambican, side of the lake.

Summary tables of sedimentary units described in the field and micromorphological descriptions: abbreviations.

The following tables summarize field observations, micromorphology, and interpretation with facies designation. The top units, with the highest unit numbers, are listed first and the lowermost last.

Abbreviations used: cc = clay coatings, nod = nodules, TM = termite, w/ = with. Texture codes are adopted from the Field Book for Describing and Sampling Soils and provided below (Schoeneberger *et al.*, 2012).

Coarse Sand	cos	Loam	l
Sand	s	Silt Loam	sil
medium sand	ms		
Fine Sand	fs	Silt	si
Very Fine Sand	vfs	Sandy Clay Loam	scl
Loamy Coarse Sand	lcos	Clay Loam	cl
Loamy Sand	ls	Silty Clay Loam	sicl
Loamy Fine Sand	lfs	Sandy Clay	sc
Loamy Very Fine Sand	lvfs	Silty Clay	sic
Coarse Sandy Loam	cosl	Clay	c
Sandy Loam	sl		
Fine Sandy Loam	fsl		
Very Fine Sandy Loam	vfsl		

Table S-T12: Sedimentary units at MGD

	field (macro)						micromorphology				interpretation	
	u	*cm a.s.*	*texture*	*bedding*	*color*	*inclusions*	*microstructure*	*c/f150µm*	*fine*	*pedofeatures*	*interpretation*	*facies*
↑	**MGD-I**											
	8	453-465	f.to v. c. s	no	5YR 5/6	-	-	-	more f. organic matter	fissured dusty cc; redox masses (>90%); very few Fe-Mn nodules; TM circles	plow zone	MGD-D
	7	385/388-453	f. to v. c. scl to f.to v. c. s	weak horizontal bedding	2.5Y 6/3 (bottom, 5YR 5/6 (top)	-	weak (sub)angular blocky (lowermost), channel	close spaced porphyric	dusty yellow, sometimes dotted clay	Fragments of cc; in situ cc; microlaminated, limpid yellow; orange, dustier/organic towards top; few-common $CaCO_3$ (beta); redeposited laminated clay nod, TM circles	mass waste and/or overbank deposits w/ several Btm horizons and a Btkm horizon	MGD-D
↑	**6**	383-385/388	c. rounded gr - cb	no-horizontally oriented, imbricated	n/a	-	aggregate, tendency to angular blocky	close spaced porphyric	yellow clay	yellow dusty cc; fragments of cc; deformations of cc	stream bed w/ mature soil (Bt)	MGD-D
	5	373-383	v. c. s to v. f. gr	weak cross bedding	10YR 6/3	weak redox masses and clay intraclasts	angular blocky ped	close spaced porphyric	yellow dusty speckled and limpid clay	pressure faces, microlaminated cc, fragments of cc kink-band fabric, few $CaCO_3$ nod, diffuse redox	fluvial coarse sandy sediment, intact terrestrial w/ bedding preserved but prolonged soil formation as indicated by cc (Bt)	MGD-D
	erosional contact											
	4	293-373	c. to v.c. scl	massive	Gley1 6/10 Y	common redox masses, lenticular sandy intraclasts,	channel and crumb	single-spaced porphyric to single-	light greenish speckled dusty clay	redox, moderate $CaCO_3$: NFC, hypocoatings, orthic/disorthic nod	mixed deposit. Soil cracking and bioturbation has mixed coarse sand w/ laminated clay deposits. Soil formation further characterized by	MGD-C

						$CaCO_3$ nod (variable)		spaced enaulic		common fragments of cc, thin yellow limpid cc, 1-3 cm fragments of laminated clay, TM chambers	orange and yellow cc, beta-type $CaCO_3$. Termite activity is indicated by fossil (empty) chambers for fungus cultivation.	
	3	170-293	sc, sic	few intercalations of fine sand	2.5Y 8/3	blackish-purple redox masses, few Fe-Mn nod (<0.5cm) 5-10% $CaCO_3$ nod (5-15 cm)	massive, angular blocky to prismatic peds	fine monic	light greenish, weakly speckled laminated sic	redox, termite chambers, many $CaCO_3$ nod; $CaCO_3$ hypocoatings in laminated clay; slaking crusts	intact lagoonal clay, moderate soil formation ($CaCO_3$), redox, termites, beta-type $CaCO_3$ features	MGD-B
↑	**2**	82-170	ms-cos	cross and horizontal bedding	2.5Y 8/3	purple redox masses (10-30cm)	n/a				fluvial deposits, no soil formation	MGD-A
	1	0-82	ms to f. gr (angular)	clear bedding planes	10YR 8/3	few redox masses, very few $CaCO_3$ nod (<1cm)	n/a				fluvial deposits, no soil formation	MGD-A
	MGD-II											
	7	219-238	-	-	-	-	-	-	-	-	topsoil Ap	MGD-D
	6	176-219	v. c gr, s		7.5Y R 6/6	$CaCO_3$ nod	intergrain microaggregate bioturbation	close to single-spaced porphyric and enaulic	yellowish brown black speckled clay	mixed $CaCO_3$ nod, dissolution; NFC; TM yellow rings	coarse infilling of gravel and Bk material	MGD-D
↑	**5**	161-176	sl, v. f. grl	horizontal stratification	5YR 6/8		channel	close to single spaced porphyric	densely stipple speckled greenish orange clay	roots in lowermost; faunal bioturbation in higher; brown humic and weak irregular Fe-Mn impregnations	Chitimwe alluvium	MGD-D
	4	136-161	sl	massive	5YR 6/6		channel	close to single-	densely stipple speckled	bioturbation features (narrow channels); greenish remnants of	mixed overbank deposit w/ redeposited lagoonal clay. Acidic (no $CaCO_3$), organic,	MGD-D

								spaced porphyric	greenish orange-brown clay	laminated clay; abundant fine OM	clay-rich but no cc (weak grano-striations)	
	erosional contact												
↑	**3**	75-136	c.-v.c. scl	massive, granular	Gley1 6/10 Y	common redox masses, lenticular sandy intraclasts, $CaCO_3$ nod (variable)	well-developed (subangular) ped structure, channel	single to double spaced porphyric/enaulic	light greenish speckled dusty clay	many $CaCO_3$ nod (2-3 cm); large fragments of vegetal material (2-3 cm); bioturbation	mixed - palustrine organic rich carbonate mud, wetland environment, transitional	MGD-C
	2	10-75	sc, sic	few sandy intercalations	2.5Y 8/3	$CaCO_3$ nods	massive, blocky/prismatic ped	fine monic	light greenish, weakly speckled laminated silty clay	many small $CaCO_3$ nod (0,5 cm); common large (~3-8 cm), calcification OM, sand, clay; NFC; bioturbation; cracks; organic remains/dark redox	lagoonal-palustrine (fluctuating/transitional) drying up phase of lagoonal	MGD-B
	1	0-10	m.-c. s	cross and horizontal bedding	10YR 8/3	-	n/a	n/a	n/a	n/a	lagoonal deposits, no soil formation	MGD-A
	MGD III												
↑	**7**	142-187	sic	laminated overburden	10YR 6.5/4	2-5% f. – m. subrounded to rounded pebbles, 20-30% mm to cm-scale $CaCO_3$ nod	n/a	n/a	n/a	red clay adhering to pebbles (rolling); thin (0.5 cm) layer of f. - m. sand, $CaCO_3$ nodules w/ yellow clay, yellow aggregates (phosphatic); clay from lagoonal	mixed historical excavation overburden w/ some horizontal stratification, $CaCO_3$ dissolution, modern bioturbation into Unit 6	MGD-E
	6	137-142	f. – v. c. gr, cl	surfaces/winnowing	7.5Y R 5/4	30-40% poorly sorted fine to very coarse subangular to rounded pebbles;			brown stipple speckled humic	few NFC; few (redeposited) $CaCO_3$ nod; common pale yellow aggregates (phosphatic); TM circle; many black opaque sand-sized;	historic surface	MGD-D

						reworked $CaCO_3$ nod				common yellow TM rings and single yellow fibers		
	5	122-137	scl, f. gr, v. c. s	horizontal stratification	5YR 6/6	few cb	complex: weakly developed subangular ped and channel	single spaced and close porphyric	speckled brownish yellow clay, cloudy limpidity	few yellow TM rings; TM circles; birefringent circular flakes (poss. Gastropod operculi);	channel fill	MGD-D
	erosional contact											
↑	**4**	109-122	cl, sicl	weak planar zones (changing CaO_3 intensity)	10YR 6/3	30-40% $CaCO_3$ nod (0.5-2 cm)	channel, nodule	close to single spaced porphyric	speckled greenish brown, locally w/ very few calcite crystals	many $CaCO_3$ nod (0.02-1.5 cm), horizontal subangular blocky; rare NFC; common Fe-Mn specks, fine OM; TM yellow rings; TM circles; very few yellow cc/papules; few redox (top)	mixed lagoonal/fluvial, intense soil formation (calcrete), termite activity.	MGD-C
	3	95-109	c. – v. c. sl	massive	2.5Y 6/3		channel, subangular blocky	single spaced porphyric	light greenish clay w/ common opaque specks	common CaCO3 nod, TM yellow rings	mix-transitional lagoonal and fluvial, soil formation, termite activity	MGD-C
	2	45-95	scl	massive	10YR 6/4	10-20% of 2-5 cm $CaCO_3$ nod	-	-	-	-	mixed-transitional	MGD-C
	1	0-45	sicl	massive	2.5Y 7/3.5	1-2% 2-4 cm yellowish brown redox masses	-	-	-	many TM	lagoonal	MGD-B

Table S-T13: Sedimentary units at BRU

	field (macro)						micromorphology				interpretation	
	u	*cm a.s.*	*texture*	*bedding*	*color*	*inclusions*	*microstructure*	*c/f150µm*	*fine*	*pedofeatures*	*interpretation*	*facies*
	BRU-I											
	10	160 – 210	m. gr, ls, f.-m. s (fining up)	imbricated, alternating beds	2.5YR 4/6	well-rounded f. gr (5-10%)	locally subangular blocky, channel, close porphyric	close porphyric	dark red silty (angular) clay	orange dusty cc; abundant angular si to fs; few fine-cos black particles;		BRU-C
↑	9	140 – 160	cos-f. gr (fining up)	imbricated, subplanar, and wavy cm-scale beds	2.5YR 3.5/6	well-rounded medium pebbles (10-30%)	locally weak ped structure	close porphyric	red silty clay, many microaggregates	large bioturbation features; roots; OM; common orange-red dusty cc (few compound 100-300 µm); few yellow cc; very few (yellow) fragments of cc; mineral weathering; pale clay patches (root channels)		BRU-C
	8	120 – 140	f. gr, f. – m. gr (fining up)	imbricated, subplanar, slightly wavy	2.5YR 3.5/6	-	poorly developed subangular blocky, close to single spaced porphyric	close to single spaced porphyric	dark-red silty (angular) clay	many orange-red, few yellow cc; many fragmented cc; common pressure cc; microlaminated brown dusty cc; few fragmented cc; silty non-oriented clay; bioturbation; roots; mineral weathering; common si to fs-sized black opaque particles	Bt	BRU-C
	7	105 – 120	f. –m. gr (fining up)	imbricated, subplanar slightly wavy cm-scale beds	2.5YR 3.5/6	-	-	-	-	-		BRU-C
	6	95 – 105	f. – m. gr (fining up)	imbricated, subplanar slightly	2.5YR 3.5/6	-	-	-	-	-		BRU-C

	field (macro)						micromorphology				interpretation	
	u	*cm a.s.*	*texture*	*bedding*	*color*	*inclusions*	*microstructure*	*c/f150µm*	*fine*	*pedofeatures*	*interpretation*	*facies*
				wavy cm-scale beds								
↑	5	70 – 95	f – m. gr (fining up)	imbricated, subplanar slightly wavy cm-scale beds	2.5YR 4/8	-	-	-	-	-		BRU-C
	4	55–70	f. gr, cos, m. s	subplanar, slightly wavy cm-scale beds	2.5YR 4/7	-	chitonic	chitonic	very little, limited to bio-features and authigenic pale yellow (angular) sic	many multi-phased yellow (under) and orange (over) cc; chambers w/ constructed walls, filled w/ pale yellow clay-rich cos; mineral weathering/disintegration; cappings of silty clay; infillings of silty clay		BRU-C
↑	3	45–55	f. – m. gr (fining up)	imbricated, wavy cm-scale beds	2.5YR 4/7	gr is subrounded	close porphyric	close porphyric	finely speckled orange-brown clay, many inclusions of si (angular)	irregular cc w/ few si incl; many pressure cc; few small limpid cc; mineral weathering: feldspar-authigenic clay formation (light yellow), disintegrating gravel (feldspatic); sic aggregates; few black fs-sized particles; localized microaggregates (TM)		BRU-C
	2	10–45	cos, f. gr	cm-scale planar beds	2.5YR 3/6	clay intraclasts (~10 cm)	close-spaced chitonic	close-spaced chitonic		many yellow and orange cc, moderate deform, compound; desiccation cracks, mineral weathering: alteromorphs, disintegrating polycrystalline quartz; little localized non-oriented clay; localized black specks (lowermost 2 cm); localized fs		BRU-C
	1	0–10	m. s – f. gr	planar	2.5Y5/3	clay intraclast	close-spaced porphyri	close-spaced porphy	speckled yellow to dark red c,	diffuse 1-2 cm redox masses; OM (root), excrements and greenish biotite-rich clay in infilled chamber		BRU-C

	field (macro)						micromorphology				interpretation	
	u	*cm a.s.*	*texture*	*bedding*	*color*	*inclusions*	*microstructure*	*c/f150µm*	*fine*	*pedofeatures*	*interpretation*	*facies*
						s (~10 cm)	c to v. fine enaulic	ric to v. fine enaulic	slightly aggregate, common angular si	(intraclast); common dusty cc w/ common inclusions of si, typic-hydromorphic, compound, bright yellow, red, orange; rare fragmented cc; some non-oriented clay; biochannel wall plastered w/ dark-red silty cc		
	BRU-II											
↑	5	110-200	f. gr	-	2.5YR 5/8	-	-	-	-	-		BRU-C
	4	30–110	ls, cos-f. gr	-	2.5YR 5/6	wavy pebble stringer; MnO concentrations and masses above pebbles stringer	weak subangular blocky	close spaced porphyric, close to single spaced enaulic	red silty clay	very bioturbated; many orange and yellow dusty laminated cc w/ few si inclusions; common thick cc; common deformation of cc; common fragments of cc; 1 cm-sized bioturbation features w/ reinforced walls; microaggregates, fecal/mastication pellets; roots	multiple phases of Bt formation, TM	BRU-C
	3	25-30	ls, cos, f. gr	-	2.5YR 4/6	rounded to subrounded m. gr (15-25%)	weak subangular blocky microstructure	close porphyric	see unit 2	few bioturbation features; few roots; microaggregates; similar to Unit 2		BRU-C
↑	2	5-25	ls, cos, f. gr	-	2.5YR 4/6	rounded m. gr (<1%)	locally weak subangular blocky microstructure	close porphyric	very little red silty clay, common patches of green speckled sic from chemically induced	many thick orange multi-phased cc, alternating w/ greenish/grey silty clay; dusty brown cc in top; mineral weathering; greenish silty isotropic clay cappings and pendants; banded green silty coatings; few bioturbation features		BRU-C

	field (macro)						micromorphology				interpretation	
	u	*cm a.s.*	*texture*	*bedding*	*color*	*inclusions*	*microstructure*	*c/f150µm*	*fine*	*pedofeatures*	*interpretation*	*facies*
									disintegration			
	1	0-5	ls, cos, f. gr	-	2.5YR 4/6	m. gr (5-10%)	-	-	-	-		BRU-C
	BRU-III											
↑	5	75–125	ls, cos, f. gr	-	2.5YR 5/6	rounded to subrounded m. gr (2-5%)	moderate channel, localized weak irregular ped	close spaced porphyric	orange dusty clay, and light greenish speckled silty clay	common-many thick orange dusty cc w/ inclusions of si; very rare clay pap; mineral weathering		BRU-C
	4	63-75 (W), 28-75 (E)	ls, cos, f. gr		2.5YR 4/6	very weak redox depletions	channel/ bioturbated	close spaced porphyric	orange or light brown speckled (80%), very pale yellowish clay (20%)	much authigenic clay formation; diverse mineralogy; mineral weathering; few to common thin orange dusty cc; bioturbation features TM; common black opaque particles of f. to m. sand		BRU-C
	3	60–63 (W), 25-28 (E)	m. – c. gr	imbricated pebble lens	2.5YR 4/4	pebbles are well rounded	-	-	-	bioturbated; mineral weathering: Fe infilling cracks, fragmentation		BRU-C
	2	20–60 (W), 20–25 (E)	ls, f. gr	-	5Y6/3, 2.5YR 4/4	rounded to subrounded m. gr; clayey intraclasts; $CaCO_3$ nod	channel	single-spaced and close porphyric	yellowish irregularly dotted and speckled sic	common thin dusty cc; few thick yellow and red cc; rare fragments of cc; roots; bioturbation features; black opaque sand-sized particles		BRU-B
↑	1	0–20	sic	-	7.5YR 4/4	rounded to subround	channel	open porphyric	v. pale yellow to orange	abundant channels; bioturbation; physical/chemical weathering of sand and replacement by $CaCO_3$; intact	transitional: soil (Bk) in lagoonal clay	BRU-B

	field (macro)						micromorphology				interpretation	
	u	*cm a.s.*	*texture*	*bedding*	*color*	*inclusions*	*microstructure*	*c/f150µm*	*fine*	*pedofeatures*	*interpretation*	*facies*
						ed cos, f. gr (10-15%); common MnO masses; $CaCO_3$ nod			black speckled silty clay	laminated silty clay pillars/ped and (partly) carbonatized (micritic); heterogeneous $CaCO_3$ nodules w/ sparite; common and thick orange cc		
	BRUGT2											
↑	4	159-163	cos	planar	2.5YR 4/8	-	-	-	-	-	topsoil, colluvium	BRU-D
	3	155-159, 90-159	cos – f. gr	some horiz stratification	2.5YR 4/8	c.to v.c. rounded pebbles at lower 2-3 cm	close fine enaulic	close fine enaulic, chitonic, coarse monic	orange or yellowish silty clay	very thin cc; link capping cc; concentrated black opaque Mn in lowermost/transition to Unit 1	red channel fill	BRU-D
	2	120-155	v. f. – m. gr	planar, basal bed of v. c. pebbles	10Y 7/1	distinct irregular RMF masses	-	-	-	-	channel fill in NE part	BRU-D
	erosional contact											
↑	1	0-120, 0-90 (deepest trunc)	si, sic	-	5GY 8/1, 10Y 7/1, 10Y 7/1	decomposing OM; cos infilling from above via bioturbation; large $CaCO_3$ nod	massive, subangular prismatic ped (cracks)	fine monic, channel	sic w/ few vfs	carbonatization of lagoonal clay; $CaCO_3$ hypocoatings (top); common orange cc (top), dustier and dotted towards very top; few root remains		BRU-A

S4. MICROMORPHOLOGY AND FIELD DESCRIPTIONS

Mwanganda´s Village (MGD)

22 sedimentary units were described at MGD (S4, table S-T5) and were grouped into five facies: MGD-A to MGD-E, with MGD-E being the topmost facies represented by back dirt form previous excavations.

Facies *MGD-A* (S-Fig. 6) is represented by the deepest deposits exposed at the site at MGD-I geotrench, which was ~465 cm deep (fig. 4). The sediments consist of unconsolidated grayish white and yellowish medium- to coarse sands and fine gravel with 1-2% coarse rounded pebbles (S-Fig. 6d) with clear horizontal planes and cross-bedding (S-Fig. 6c, e). The lowermost unit (0-82 cm) shows faint dm-scale redox masses (S-Fig. 6c) and 10-30 cm diameter purple redox masses were observed between ~82-170 cm (S-Fig. 6a, b).

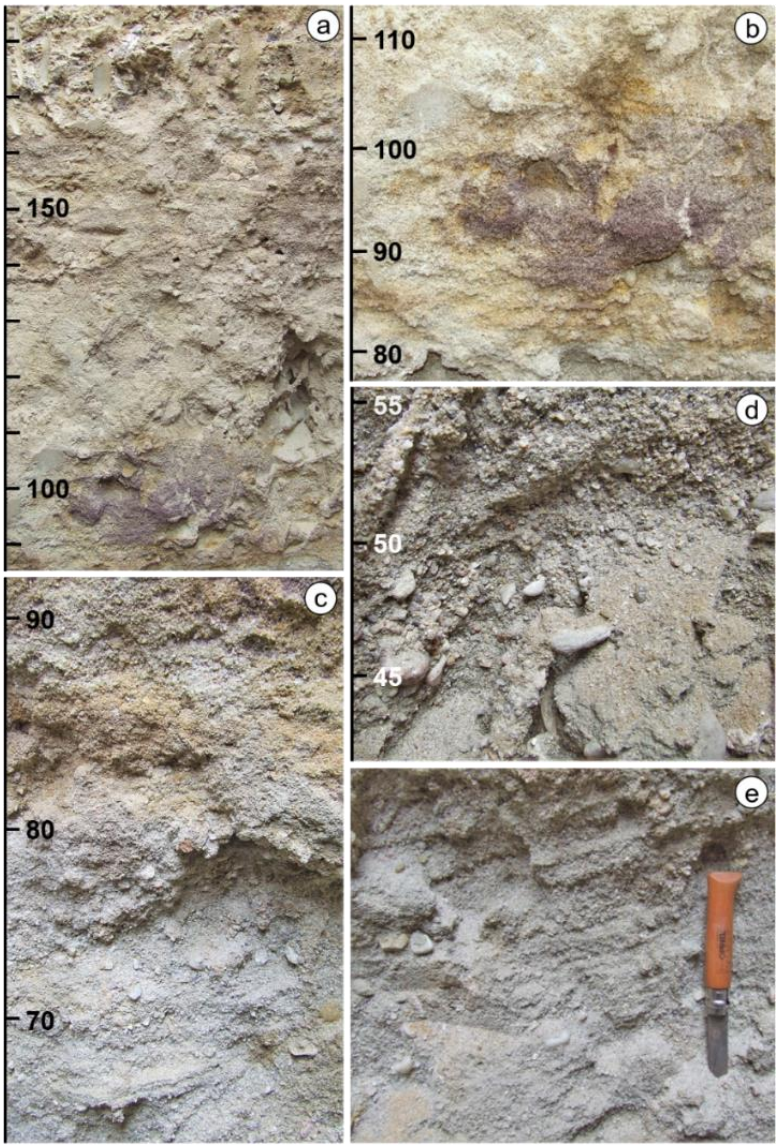

S-Fig. 6. Field photographs of facies *MGD-A* (no micromorphological blocks were taken from this facies). a) Yellowish medium to coarse sand with distinct purple redox. b) Yellow to purple redox. c) Unconsolidated angular medium sand to fine gravel with rounded medium pebbles and yellow redox masses. d) Inclusions of medium pebbles. The unconsolidated sediment is collapsing, and termites have constructed galleries post-excavation. (e) Clear bedding planes (size of the wooden handle is ~8 cm).

MGD-B (S-Fig. 7) consists of laminated silty clay with intercalated fine sand inclusions (S-Fig. 7a, b). The clay is greenish in color and contains abundant well-sorted horizontally oriented mica. Streaks of reddish redox follow the course of better-aerated features such as intercalations of very fine to fine sand and bioturbation features in which pore spaces have allowed for oxygen to enter the deposits (S-Fig. 7b). Bioturbation features appear very distinct in the fine deposits and include networks of channels interconnecting chambers (1-2 cm) and collections of well-sorted fine sand in smaller, 0.5-cm diameter chambers, presumably made by termites (S-Fig. 7a, c).

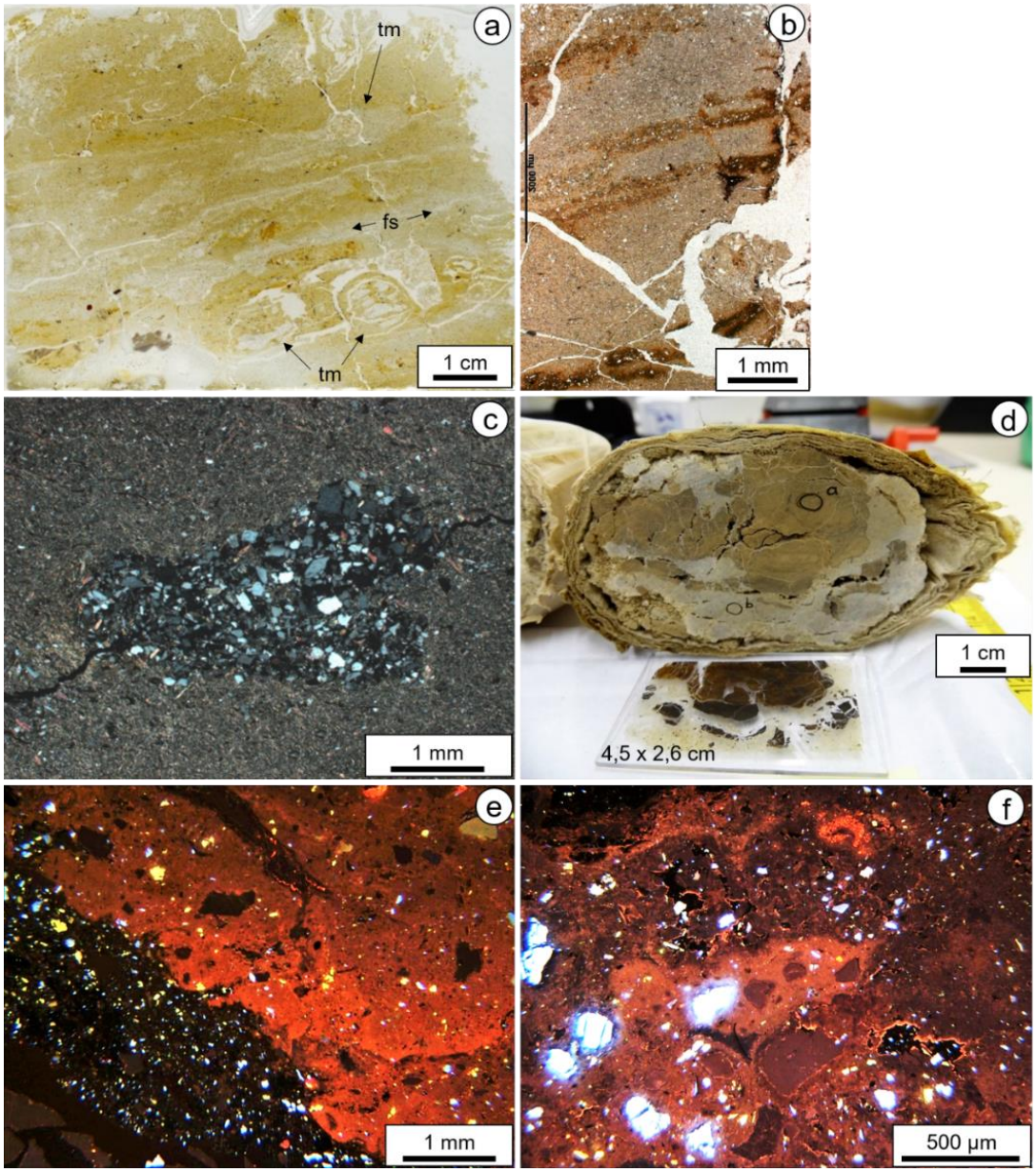

S-Fig. 7. Facies *MGD-B*. a) Thin section of silty clay with interbedded laminations of fine sand (fs) and termite features (tm). b) Intact laminated clay is disrupted by desiccation cracks and termite channels. Rust-colored redox along intercalations of fine sand. c) Chamber filled with fine sand in a matrix of silty clay with channels connecting to the chamber from the left and right (XPL). d) Sliced carbonate nodule and corresponding thin section with iron-rich inner core. Two areas have been marked (a, b) for the collection of sub-samples for isotopic analysis and radiocarbon dating with a precision drill. e) Silty clay (lower left) on the external side of a carbonate nodule (red) with sand inclusions of feldspar and quartz appearing yellow, blue, or dark (black) when weathered (CL). f) Sand-sized inclusions of quartz (appearing blue) and feldspar (mostly yellow/green, but also blue) inside a carbonate nodule (red). Sand grains affected by weathering appear dark.

The top of facies MGD-B (S-Fig. 8) is marked by an increase in mixing by bioturbation and desiccation cracks (S-Fig. 8g). Open spaces created by bioturbation and cracks are infilled with coarse sandy sediment, secondary carbonates, and roots. The top of facies *MGD-B* is in some

places topped by orange-brown slaking crusts of oxidized (iron-rich) clay (S-Fig. 8h and 8i). Carbonate nodules are common, especially in desiccation cracks and root voids (S-Fig. 8a, b, g). The nodules are irregular and vary in size from 1mm in small pore spaces inside the laminated clay to several centimeters in soil cracks or where they have replaced clay peds exposed to weathering. Alpha-type microfabrics with relatively large sparitic (>15μm) and microsparitic (~5-15 μm) calcite crystal sizes, ascribed to physical and chemical processes, are much more common than beta-type carbonate features associated with biogenic processes, following the end-member assemblages of calcrete microtextures as outlined by V. P. Wright (Wright, 1990; Alonso-Zarza and Wright, 2010). In some parts of the facies, nodules have inner cores of dark orange brown material, which do not consist of calcite. μ-XRF elemental mapping has shown that these inner cores are rich in iron, manganese, titanium, and phosphorus relative to the surrounding sediment (S-Fig. 24). Remains of organic matter are common inside carbonate nodules, and appear as stacked fragments of roots in desiccation cracks (S-Fig. 8b, c, e, f). Biogenic (beta-type) carbonate features such as needle fiber calcite are present but are not common, and are indicative of non-saturated soil conditions (Wright, 1990).

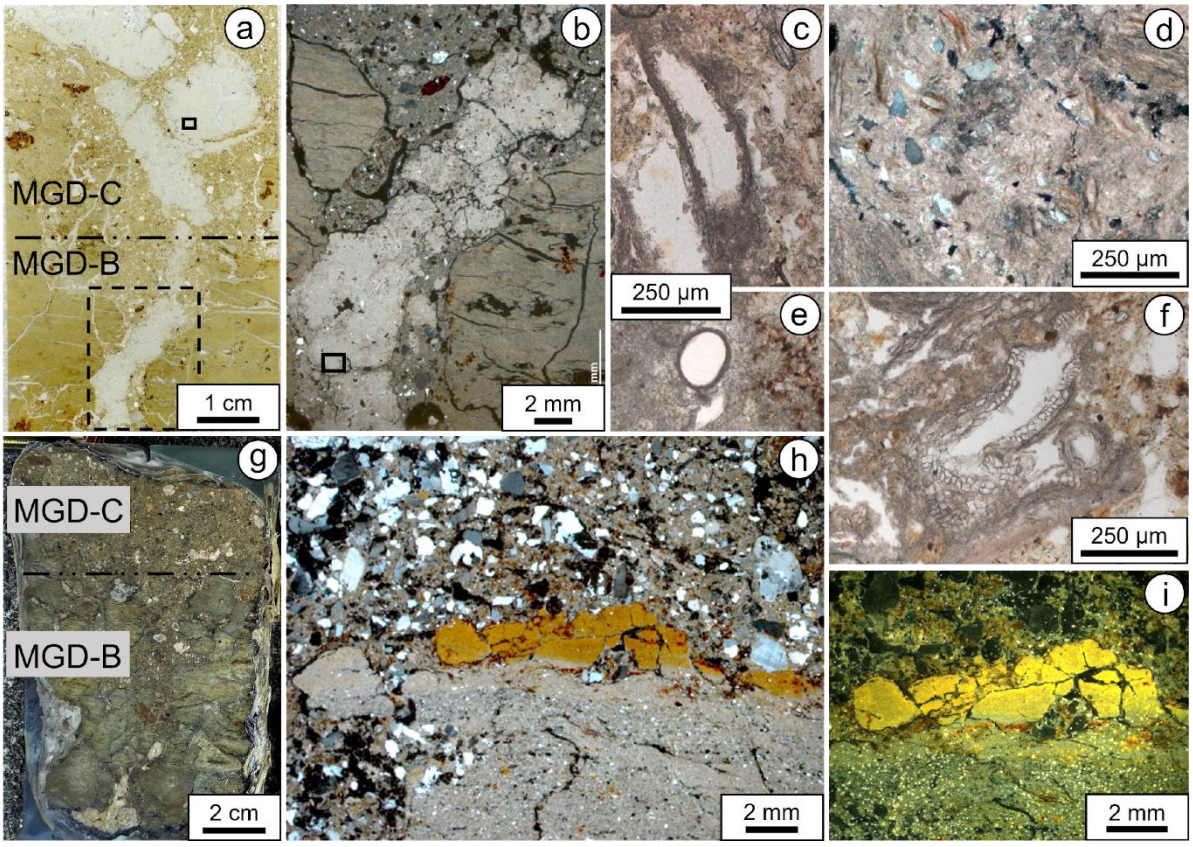

S-Fig. 8. Contact between facies *MGD-B* and *MGD-C*. a) Thin section from area MGD-II, showing the transition from intact laminated clay (lower half) to bioturbated sandy loam (upper half). A desiccation crack is filled with sand and biogenic carbonate (b). b) Sandy loam infilling envelopes pedogenic carbonate in a crack within facies *MGD-B*

(XPL). c) calcified root fragment in a biogenic carbonate nodule. d) silt-sized biotite and quartz in a nodule in facies *MGD-C* (indicated in [a] which formed by replacement of silty clay [XPL]). e) and f) show calcified organic remains, including roots. g) Boundary between *MGD-B* and *MGD-C* in a slice from an impregnated sample from MGD-I, showing deep cracks in the greenish laminated clays filled with slightly reddish sands from above and secondary carbonate formation (white). h) Boundary between intact clay in *MGD-B* and bioturbated *MGD-C*, showing contrasting grain sizes of *MGD-B* (silt, clay) and *MGD-C* (coarse sand, clay) and a fragmented orange slaking crust at the contact (XPL). i) The same weathered crust as in (h) in oblique incident light. Overlying deposits contain ferruginous nodules deriving from similar crust fragments.

Facies *MGD-C* is marked by an increase in soil formation and identified as the buried paleosol described by Clark and Haynes (1970), the top 10 cm of which was the context from which the elephant bones and lithic artifacts derived. *MGD-C* has a loamy texture with varying amounts of coarse to very coarse sand in greenish clay organized in subangular blocky ped structures (S-Fig. 9d, 10b) and crumb or channel microstructures (S-Fig. 9a). The facies appeared massive in the field but in thin section, many mixing agents were distinguished, including shrink-swell within the soil (pedoturbation), the formation and infilling of desiccation cracks, root action, bioturbation by soil fauna, and pedogenic carbonate formation, their compounding effects obliterating any pre-existing potential sedimentary structures. However, rare 1-3 cm sized intact laminated clay peds, very similar to facies *MGD-B*, were found in their original depositional position (S-Fig. 9a, b, h), offering a glimpse of the original deposit. According to Blokhuis, Kooistra and Wilding (1990), the formation of a nodular calcrete, as seen here, constitutes the final stage of the soil. S-Fig. 9 illustrates typical features observed at MGD-I and MGD-II, and S-Fig. 10 shows examples from areas with more advanced or more intense calcrete formation at MGD-III. Carbonate formation has strongly impacted and altered the mixed sediment at all site areas, but samples show differences related to the maturity of the carbonates sampled and the original deposit. For example, samples from MGD-II are rich in decomposed plant remains, which have been partially replaced by secondary carbonate and become incorporated in carbonate nodules (S-Fig. 9d, e), while samples from the top of the facies at MGD-III lack apparent vegetal remains and capture more intense carbonate formation with concentrated, coalescing, carbonate nodules (S-Fig. 10). Clay coatings and reworked fragments of clay coatings (in older literature known as clay papules) are rare, but few intact and fragmented laminated limpid yellow clay coatings were observed near and inside carbonate nodules, some of which are partially dissolved and substituted by microsparitic carbonate (S-Fig. 9c, 10d).

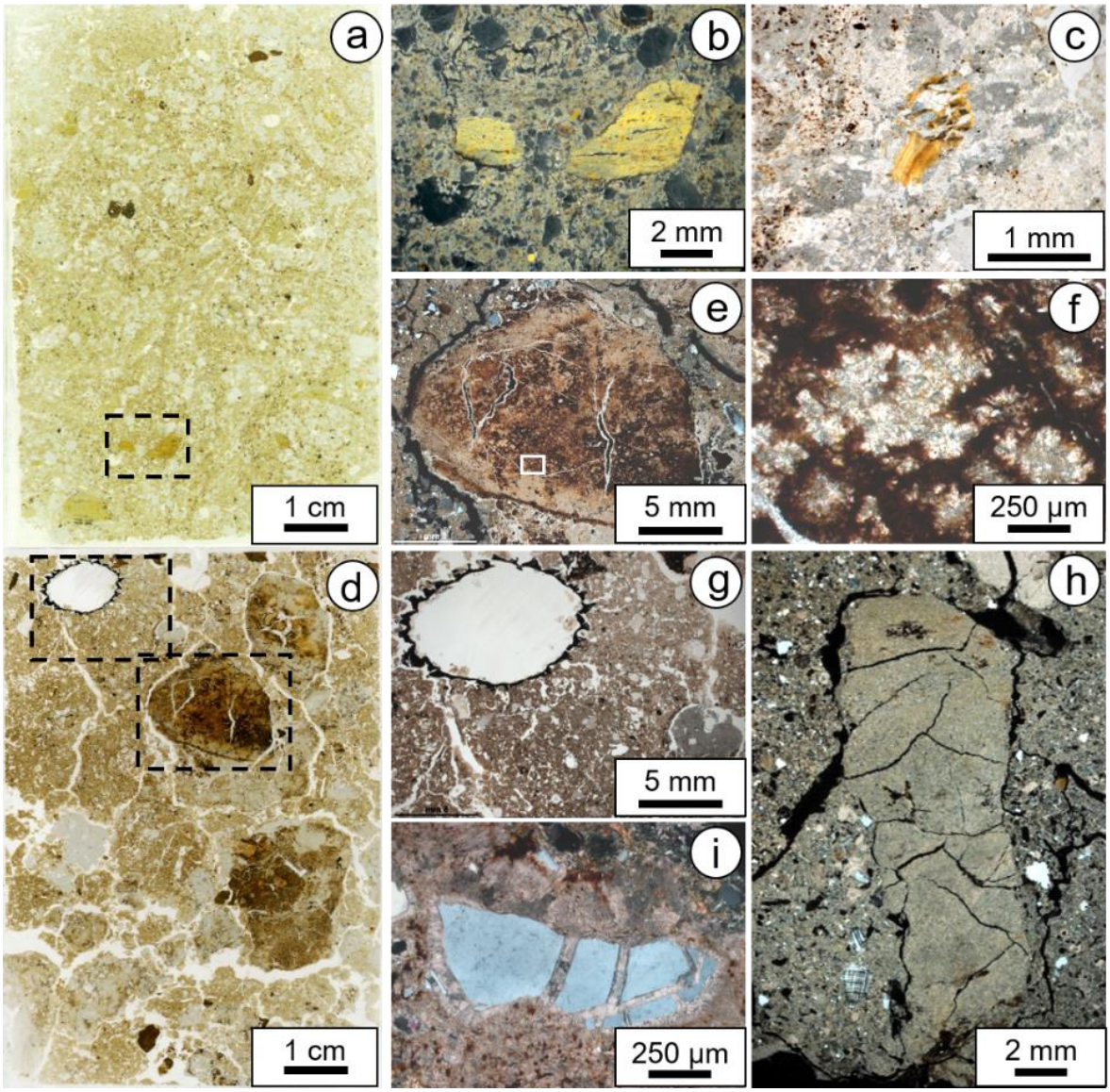

S-Fig. 9. *MGD-C* at MGD-I and MGD-II. a) Thin section showing greenish, clay-rich bioturbated sediment with few small remnants of laminated clay. b) Remnant fragments of laminated clay (corresponding to the dashed rectangle in [a]) (XPL with added oblique incident light). c) Fragments of a laminated yellow limpid clay coating inside a sparitic carbonate nodule. d) Thin section from a part of *MGD-C* with organic remains and carbonate nodules. e) $CaCO_3$ nodule (~2 cm, lower rectangle in [d]) containing druses (aggregates of calcium oxalate crystals), often found in plant tissue (XPL). f) Drusic calcite crystals in a carbonate nodule of organic origin (e). g) Intact organic remains (top left in [d]). h) Pillar-shaped remnant of laminated silty clay in sandy matrix (XPL). i) Feldspar sand grain fragmented along cleavage planes and partially replaced by sparite (XPL).

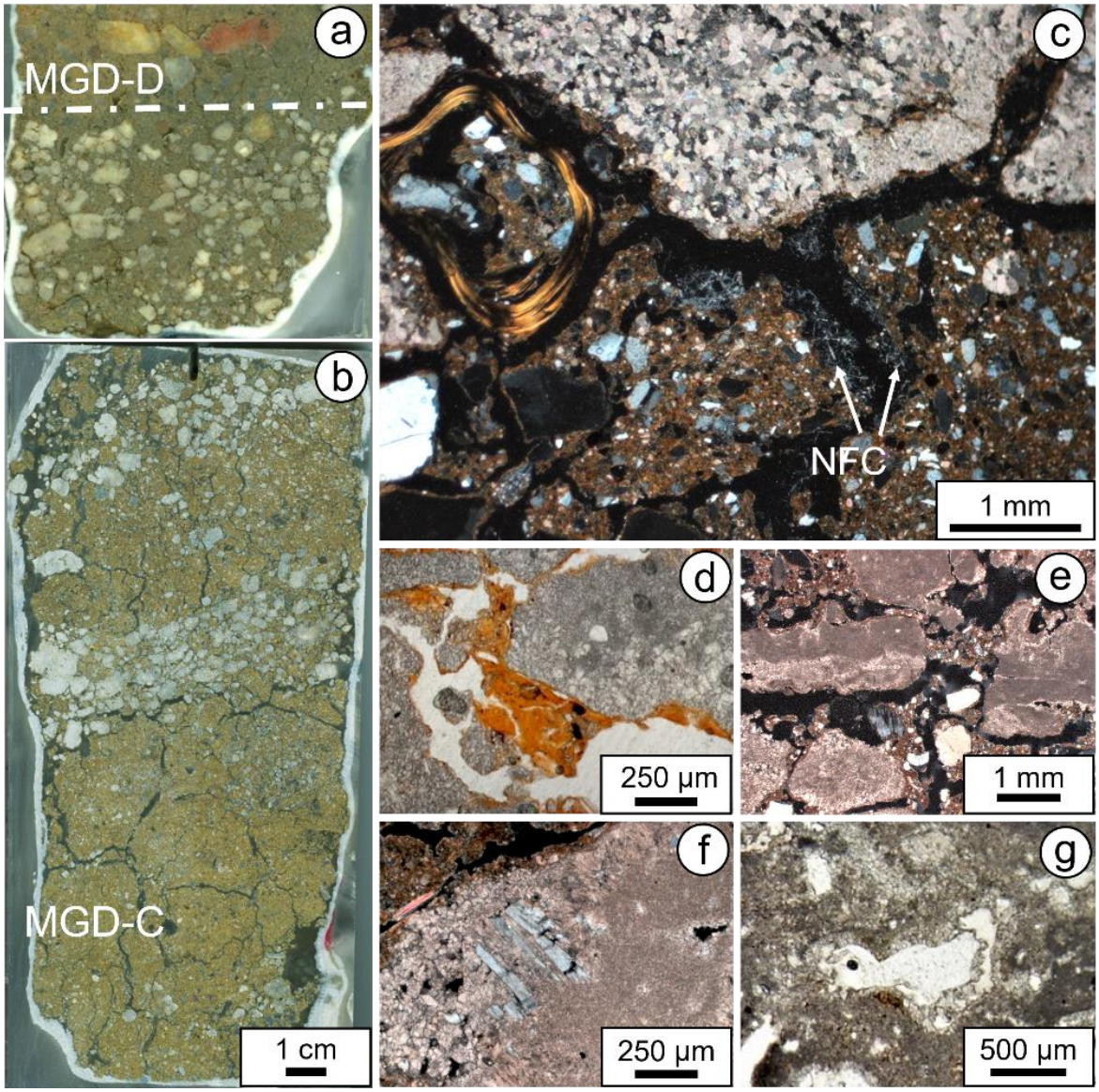

S-Fig. 10. Samples from the top of *MGD-C* at MGD-III contain densely concentrated carbonate nodules. a) Sediment in the top of *MGD-C* at this location is slightly reddish compared to below due to bioturbation and mixing with overlying deposits. b) Greenish sandy loam with a network of biochannels and horizons with concentrated carbonate nodules (the top of the sample-slice overlaps with the bottom of the slice shown in (a)). c) A sparitic recrystallized carbonate nodule in the top of *MGD-C* and needle fiber calcite (NFC) in nearby pore spaces. In the upper left is an insect ring feature of grass fibers (XPL). d) Yellow clay coatings between carbonate nodules. e) Flat blocky merging carbonate nodules with internal microlayers of different calcite crystal sizes. f) Brecciated feldspar with dissolution voids and microsparite (XPL). g) Sand inclusion in a carbonate nodule with surrounding pore space remaining after dissolution.

MGD-D consists of different fluvial and alluvial fan-related deposits and overlies *MGD-C* with an abrupt (0.5 to <2 cm) to clear (<5 cm) lower boundary (Schoeneberger *et al.*, 2012). The sediments are coarse, ranging from fine to very coarse sand and sandy loam, to very coarse gravels and cobbles. Sand- to fine gravel-sized materials are subangular to subrounded, while coarse

gravels (pebbles) and cobbles are more often subrounded to rounded. The two downslope site areas (MGD-II and MGD-III) show a similar stratigraphy of reddish sandy loam to fine gravels and reworked channel fill. MGD-I, located uphill to the south (fig. 2 in main article), is markedly different as it includes fluvial deposits dating to after 26 ka until ~15 ka, which are lacking at the other site areas and contain late and terminal MSA artifact assemblages (fig. 4 in main article). We therefore present *MGD-D* separately for MGD-I, followed by a description of the facies as observed at the other two site areas.

The sedimentary sequence of *MGD-D* at MGD-I is ~92 cm thick. From bottom to top it consists of ~10 cm of close-spaced very coarse sand to very fine gravel exhibiting weak cross-bedding above an abrupt and wavy lower boundary. This is capped by a ~5 cm-thick bed of imbricated coarse, rounded spherical gravels and cobbles (S-Fig. 11). Overlying the cobble layer is a unit of ~70 cm of fine to very coarse sandy loam, grading to fine to very coarse sand in the top of the profile. The deposit contains inherited *MGD-B/MGD-C* soil materials including yellow weathered and rounded fragments of laminated clay peds (S-Fig. 11d), and some carbonate nodules, as suggested by their occurrence near reworked ped fragments of laminated clay (S-Fig. 11d). Several large (~10 cm wide) chambers were observed underneath the cobble layer in the field, likely the remains of abandoned termite fungus gardens (fig. 4 in main article, photo inset). Until ~10 cm above the cobble layer, *in situ* soil formation in the yellowish green fluvial deposits is expressed by an angular to subangular blocky microstructure, the result of shrink-and-swell processes (S-Fig. 11l, m) (Nettleton and Sleeman, 1985; Blokhuis, Kooistra and Wilding, 1990; Kovda and Mermut, 2010). Bioturbation is relatively restricted and consists of narrow channels and distinct bioturbated zones, locally disturbing the subangular blocky microstructure (S-Fig. 11i). Abundant typic pale yellow dusty clay coatings are found on ped faces, channel walls, and along the walls of fissures, displaying irregular laminations and common deformations resulting from shrink-swell (S-Fig. 11k, l, m). Reworked fragments of clay coatings can be found inside soil peds as well (S-Fig. 11h). Common *in situ* fragmentation of sand and gravel as well as cracks in cobbles and pebbles are indicative of soil weathering and shrink- swell processes. *In situ* vertic activity is further demonstrated by the fracturing of clay coatings along the walls of fissures inside a disintegrating pebble due to continued widening of the fissure (S-Fig. 11k), proving that fracturing of cobbles and pebbles is indeed related to soil processes rather than pre-depositional physical damage.

Above the cobble layer (and especially in the first 10 cm above), bioturbation increases and a channel microstructure dominates in the rest of the profile. Orthic micritic and sparitic carbonate nodules occur localized in the middle of the unit in association with bioturbation features.

Carbonate features in general are rare and mainly consist of beta-type features, which are primarily biogenic and therefore typical for the vadose zone, and include micritic hypocoatings, needle fiber calcite, and small micritic nodules (Wright, 1990; Alonso-Zarza and Wright, 2010). Overprinting of carbonate features by clay coatings is common (S-Fig. 11g). Clay coatings become more abundant towards the top where they often show pendant and crescent shapes typical for top-down processes in this uninterruptedly well-drained part of the profile. Besides dusty yellow, orange, and brown clay coatings, very pale yellow isotropic (amorphous) clay coatings are found as well (S-Fig. 11b). Reddening from redox increases towards the top, including few orthic small iron-manganese nodules (S-Fig. 11a, f). In the bioactive zone of the modern soil, finely comminuted organic material, circular termite features (S-Fig. 12) and channels increase in abundance.

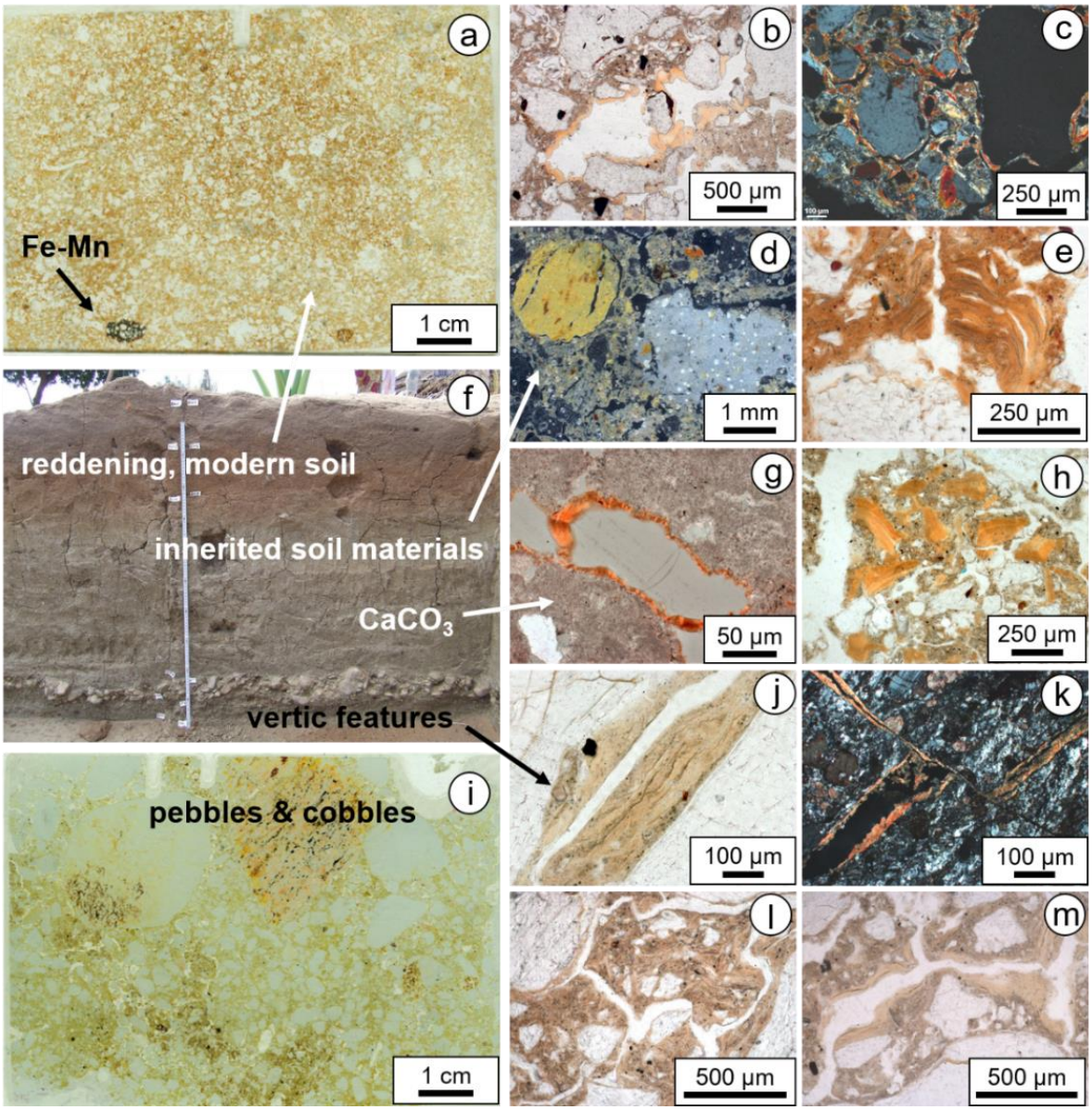

S-Fig. 11. Facies *MGD-D* at MGD-I. a) Thin section from near the top, showing the rubified part of the soil with few orthic iron-manganese nodules. b) Yellow isotropic clay coating of amorphous silica. c) Dark red and yellow clay coatings inside a redox mass (mottle) (XPL). d) Rounded fragment of ferruginised laminated clay (upper left) and carbonate nodule, both reworked and likely inherited from *MGD-B* or *MGD-C*. e) Laminated orange dusty clay coating with desiccation fissure. f) Upper profile containing a modern soil in the top, a horizon in the middle with localized carbonate features, and an older soil horizon with vertic properties at the level of the cobble layer and below. g) Orange clay coating inside a carbonate nodule, possibly inherited. h) Fragmented yellow clay coatings. i) Thin section with pebbles from the streambed (cobble layer) and light greenish coarse sand below with distinct bioturbation features (darker). j) Deformed pale yellow dusty clay coatings. k) A clay coating formed inside a crack in a pebble before further fragmentation of the pebble. l) Soil peds separated by accommodating planes and m) Planes or channels in a subangular ped structure with dusty yellow pressure clay coatings.

At MGD-II and MGD-III, the lower contact of facies *MGD-D* is bounded by a paleochannel incision which is infilled with reddish sediment of bedded sandy clay loam, dispersed cobbles, and gravels. This in turn is topped by a ~5 cm thick continuous layer of pebbles in organic-rich clay loam, representing the historic ground surface (fig. 5 in main article). Bioturbation is intense in all sediments and some characteristic features are likely related to termite or possibly ant activity. Near-vertical channels (S-Fig. 12a) connect chambers with circular features of well-sorted fine sand and chambers with pore wall linings of yellow fiber (S-Fig. 12b, d, f, g). The yellow fiber may be of vegetal origin, such as straw suggested by Stoops (2003), but in some cases appears altered, possibly by mastication. Few circular features of strongly birefringent material (~100-200 μm) are similar to but smaller than the snail operculi described by Canti in (Durand, Monger and Canti, 2010; Canti, 2017) (S-Fig. 12c). The channels and reinforced chambers are mainly restricted to facies *MGD-D* but a few channels enter into the top of *MGD-C* reaching chambers constructed between the uppermost carbonate nodules (S-Fig. 12f).

Shrink-and-swell activity is evidenced by grano- and poro-striated b-fabrics. Clay coatings are rare. Gravel infillings at MGD-II contain disorthic carbonate nodules affected by dissolution around their edges. As the likely acidic sediment of *MGD-D*, deriving from lateritic soils in the alluvial fan, is not conducive to carbonate formation, these nodules were likely redeposited from eroding parts of the paleosol of *MGD-C*. Needle fiber calcite has formed adjacent to some carbonate nodules, possibly in relation to dissolution and disintegration of the nodule edges. Common small (1-3mm) Fe-Mn orthic and disorthic nodules can be found, indicative of *in situ* red (lateritic) soil formation (Marcelino, Stoops and Schaefer, 2010), as well as weathered quartz grains with micro-cracks, infilled with iron oxides (also called runiquartz) (S-Fig. 12e), which may have been either inherited or formed in place.

The organic topsoil and historic ground surface, composed of pebbles in clay loam, directly overlies *MGD-C* in the northern part of MGD-III, and caps the channel fill where *MGD-C* has been truncated by the paleochannel. It is brown with a speckled micromass with abundant finely comminuted organic matter and many metallic black opaque grains. Phosphatic aggregates commonly occur on or near yellow ring features. The yellow fibers present in these features appear to derive from near the surface and to have been transported in fragments downwards through channels by insects (probably termites), to be used for the fortification of circular chambers (S-Fig. 12g).

MGD-E is comprised of the overburden (~50 cm) from Clark's old excavations covering the historic surface on the eastern part of MGD-III.

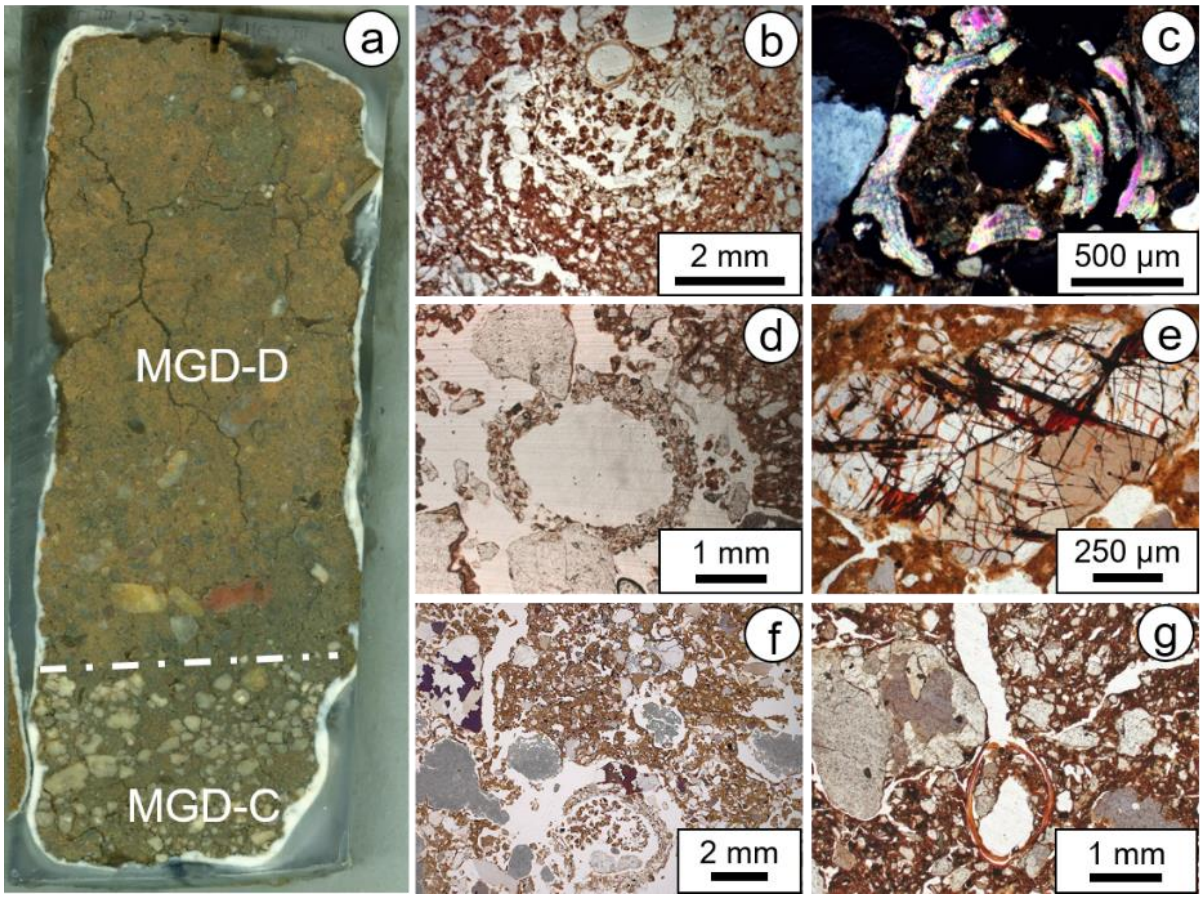

S-Fig. 12. Facies *MGD-D* at site areas MGD-II and MGD-III. a) Slice of a micromorphological sample showing red channel fill with a network of biochannels in *MGD-D*, overlying the top of the nodular calcrete (*MGD-C*) at MGD-III. b) Pore lining of yellow fibers in the top, appearing in association with a larger (termite) bioturbation feature. c) Bioturbation feature with strongly birefringent material, possibly snail operculi (XPL). d) Ring (termite) feature of sorted fine sand. e) Weathered quartz grain with fractures filled with iron oxides (also called runiquartz). f) Vertical channel (upper left) leading to a circular termite feature in between carbonate nodules (gray) affected by dissolution. g) Yellow fibers lining a chamber connected by a biochannel.

Bruce

The different site areas at Bruce contained 24 sedimentary units (table S-T13) which are grouped into four facies.

BRU-A was observed at BRU-GT2 and BRU-III, both located about halfway up the hillslope (fig. 3 in main article). At BRU-III, facies *BRU-A* is hard and cemented by calcite so that the excavation halted here, leaving the white facies exposed at the bottom (fig. 6 in main article). At BRU-GT2, the facies is soft and contains abundant large fragments of decomposing organic matter (S-Fig. 13a) and carbonate nodules of homogeneous fine micritic carbonate (S-Fig. 13b). The sediment consists of white, fine carbonate silt and finely laminated silty clay with rare very fine sand inclusions and carbonate nodules. Laminations of silt in the fine micritic carbonate nodules show an identical structure to that of the laminated silty clay (S-Fig. 13c, d). *BRU-A* is very similar to facies *MGD-B* but finer, lacking intercalations of fine sand. CL-microscopy reveals pillar-shaped zones of more intense carbonate formation in which mineral inclusions (silt) are scarcer than in the surrounding carbonate, however, the same primary material, silty clay, is revealed by the occurrence of abundant ghost features of silt-sized pseudomorphs after mica (elongate), feldspar, quartz and other minerals replaced by the carbonate (S-Fig. 13d, e).

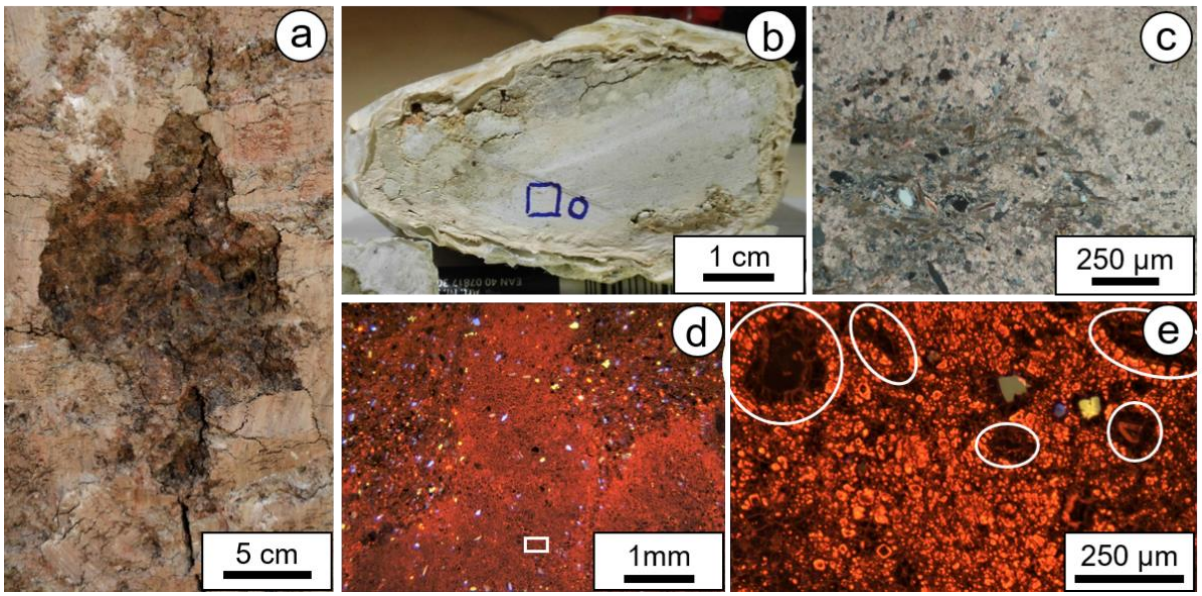

S-Fig. 13. Facies *BRU-A* (at BRU-GT2). a) A fresh break reveals organic remains in carbonate silt. b) Half section of a pedogenic carbonate nodule of micrite. The tops of pillars are visible in the upper part, where carbonate formation becomes less intensive (grayish). c) Silty clay inside a carbonate nodule recognizable by its color (darker than the surrounding carbonate) and the occurrence of mica and quartz silt (XPL). d) Pillar-shaped areas (fingers) of more intense carbonate formation inside a carbonate nodule contain less silt. e) Siliceous silt grains (green, yellow, blue)

showing signs of dissolution and ghost features (circled) inside a pillar-shaped zone with intense carbonate formation (rectangle on fig d).

BRU-B is marked by soil formation. Carbonate nodules were observed outcropping in fallow fields and paths nearby Bruce but the in situ nodular carbonate horizon, a stage 3 calcrete, was only found in profile at BRU-III. The horizon directly overlies the cemented *BRU-A* facies. *BRU-B* is inclined towards the SW, running parallel to a lens of imbricated pebbles located ~20 cm above in *BRU-C* deposits. Laminated clay, similar to *BRU-A*, is organized in dispersed subangular blocky peds, surrounded by very bioturbated coarse sandy to fine gravelly sediment, presumably deriving from the overlying facies (*BRU-C*) (fig. 6 in main article). Thick intact as well as fragmented and reworked orange clay coatings are observed in areas with intense carbonate formation, indicating repeated extreme changes in soil conditions and pH (S-Fig. 14b). Blocky ped-shaped micritic carbonate nodules (S-Fig. 14i, j, k), apparent replacements of *BRU-A*-type sediment occur alongside nodules with common coarse sand to fine gravel inclusions and mixed micritic and sparitic zones, which formed in *BRU-C*-type sediment, due to mixing of the two facies prior to calcrete formation (S-Fig. 14a, c, e, f, g). Besides sand grains, clay domains (S-Fig. 14d) and clay coatings (S-Fig. 14h) also appear as inclusions in carbonate nodules. Open pore spaces or ghost features appear as pseudomorphs that remained after sand, clay domains, as well as fragments of clay coatings, have been gradually dissolved and left open or replaced by calcite (S-Fig. 14c, e, f, g, h). CL microscopy demonstrates the gradual dissolution of all types of siliceous constituents (laminated clay, mica, feldspar, quartz, clay coatings etc.), which is especially well visible inside carbonate nodules (S-Fig. 14e, k). After each phase of dissolution, the residual empty pore space, often along the sides of an affected sand grain, has been filled with newly forming calcite, usually as sparite, creating circles of radiating sparite around dissolving grains and sparitic infillings in a micritic groundmass. The sparite appears to have been replaced by micrite during subsequent phases of recrystallization.

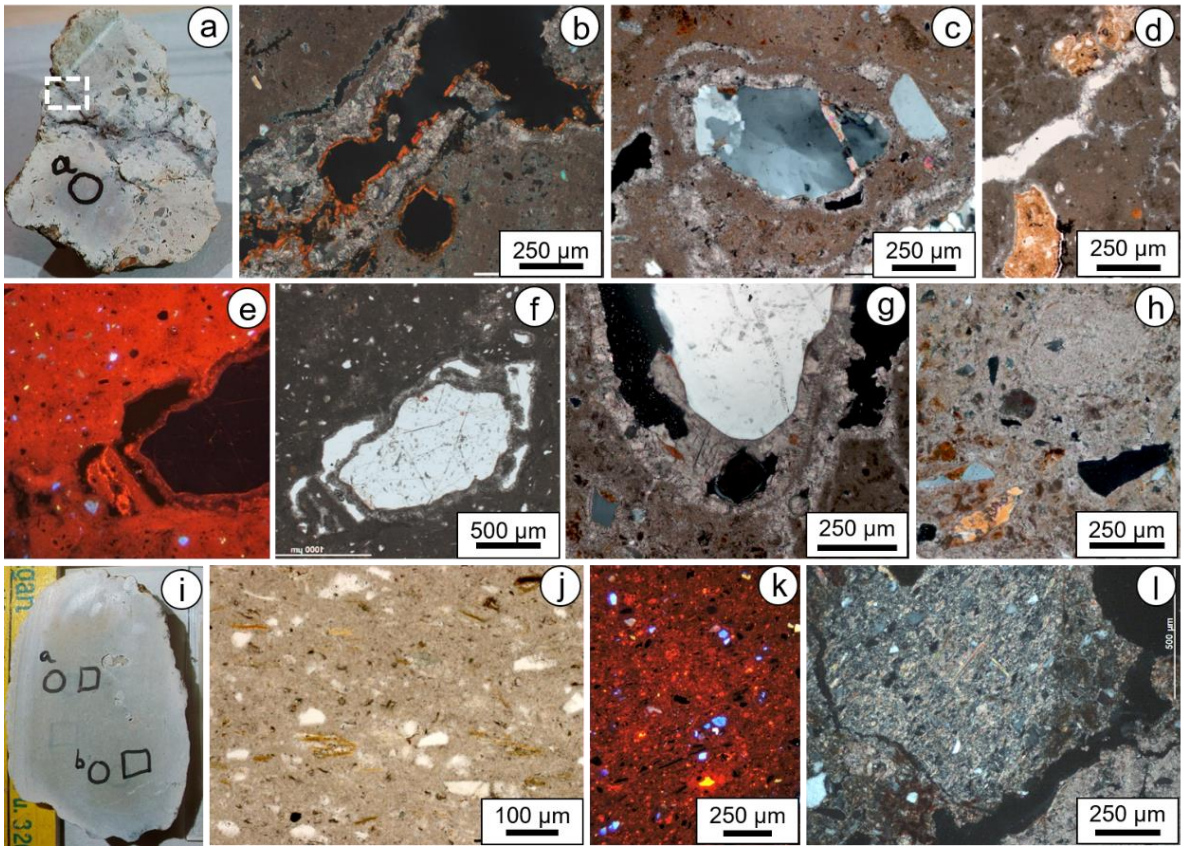

S-Fig. 14. Facies *BRU-B* (excavation area BRU-III). a) Carbonate nodule from the top of *BRU-B* with zones (top and right) with sand inclusions and cracks with sparite and clay coatings. b) Crack (black) with a sparite (light) coating starting to infill the crack, overlain by an orange limpid clay coating (rectangle in fig. a, XPL). c) Phases of dissolution of the sand grain and replacement by sparite (light) in a micritic (dark) nodule. d) Two inclusions of clay domains in a micritic nodule with an accommodating plane (fissure) partially infilled with sparite (top). e) Episodes of dissolution around a siliceous sand grain have been partially filled with sparitic (bright red) and micritic (darker red) calcite. Some silt in the surrounding micrite appears blue (quartz) or yellow (feldspar), but black specks may indicate dissolved silt grains (CL). f) Complete sand grain equivalent to the one displayed in (e) in plane polarized light. g) Sparite forming a crown in pore space (black) created around the dissolving edges of a sand grain. h) Micritic ghost feature after a sand grain and clay coating included in a carbonate nodule. i) Carbonate nodule after laminated silty clay (*BRU-A*) of fine micrite with one chamber and channel leading to it. j) laminated silt-sized mica inside a carbonate nodule. k) Carbonate nodule after laminated silty clay (*BRU-A*). l) Tilted ped of laminated clay showing partial dissolution and calcite replacement.

BRU-C comprises artifact-bearing sands and gravels, formed by processes typical for the distal part of alluvial fans, most notably gullying and stream deposition, as well as debris flow and winnowing (Blair and McPherson, 1994). Grains of sand and very fine gravel-size are subangular to subrounded, while fine to medium gravel is generally subrounded to well-rounded. The deposits vary from site area to site area and include breaks in sedimentation likely associated with numerous erosional events. However, OSL dates the excavated deposits to 29±3 to 54±5 and soil formation and mineral weathering confirm the temporal constraint of depositional processes at BRU. Out-

of-order OSL ages are attributed to potential non-solar resetting of sediments during fan formation, soil formation processes and/or uncalculated errors in water content in the different parts of the profile. Soils are dynamic environments as minerals undergoing secular equilibrium are mobile, which moves sources of ionizing radiation into new aspects of the profile over the time of formation. In addition, water attenuates the absorption of radiation in the crystal matrix of sedimentary minerals, but the relative content of water mass over the duration of burial can be variable, particularly in open environments, and therefore is a common source of imprecision in OSL dating. Soil formation impacted the sediments considerably and to a similar extent at all site areas. As opposed to *MGD-D*, *BRU-C* deposits do not contain inherited (redeposited) soil materials from *BRU-B*, suggesting that the calcrete (*BRU-B*) was not truncated at the Bruce site location.

The lowermost excavation area of Bruce, BRU-I, was placed near gully deposits exposed towards the foot of the hill (fig. 3 and 6 in main article). The ~210 cm of *BRU-C* alluvial fan deposits at BRU-I consist of eight planar beds of imbricated subrounded, subprismoidal to spherical fine to medium gravel, each fining upwards. The beds are 5-30° inclined to the west. Near the bottom of the profile, rounded chambers (10 cm) are filled with sandy clay and organic matter. At BRU-II and BRU-III, the facies consists of loamy sands with few diffuse lenses of pebbles. BRU-II is located in a small sedimentary remnant forming a mound, protected from erosion by a small tree, and part of the mound is occupied by fungi-growing termites. Excavations exposed a 200 cm deep profile. It contains two wavy pebble lenses spaced ~40 cm apart, which are slightly inclined to the southeast, following the slope of the hill. The upper 90 cm of the profile consist of a bioactive zone (biomantle) with termite chambers (~10 cm in diameter) for fungus cultivation and roots (fig. 6), but bioturbation in the lower part of the profile is limited to a few roots from the tree which grows on top of the mound. At BRU-III, *BRU-C* deposits overlie the *BRU-B* soil horizon and are similar to BRU-II. The deposits contain a lens of imbricated pebbles, which shows a dip to the northwest, parallel to the top of the calcrete paleosol (*BRU-B)* underneath.

Soil formation in facies *BRU-C* shows similar aspects in the different site areas. The well-drained deposits are mostly reddened due to oxidation and only show diffuse 1-2 cm sized redox masses in the lower ~20 cm, especially at wetter locations near the foot of the slope (BRU-I and BRU-II, TP21). Weak subangular blocky microstructures with close-spaced porphyric and close-spaced chitonic c/f related distributions are most common, with channel microstructures where bioturbation is more pronounced. At BRU-I, the facies contains a series of Bt horizons with different prevailing types of clay coatings as well as overprinted clay coatings. In all site areas, a

multi-step formation sequence of clay and silty clay coatings could be reconstructed, ending with the formation of limpid, finely laminated clay coatings. Products of all steps are present, indicating that this is an ongoing process in the lateritic soils at BRU. During the initial stage, mineral chemical and physical weathering of sand and gravels of different rock types including alkali granite, sandstone, and gneiss leads to the formation of pale-colored authigenic clay and green speckled silty clay (S-Fig. 15e, f) through sericitization and kaolinization (S-Fig. 15a-c). The removal of silica (Si) and magnesium (Mg) is also evidenced by common boxworks of iron oxides highlighting the fracture pattern in grains affected by dissolution (Delvigne and Stoops, 1990) (S-Fig. 15d). Translocation of coarser, silty weathering products has created silt, silty clay cappings, and coarse clay coatings with common silt inclusions (S-Fig. 15e-h). Clay coatings overprinting these features show that during later translocation, clay coatings have become finer and the originally pale authigenic clay has become more oxidized, reflected in bright yellow and orange colors. Thick, layered clay coatings show that fine clay coatings have commonly overprinted coarser clay coatings and silt accumulations (S-Fig. 15f, g, h). Locally, a fabric with open pore spaces, truncated (S-Fig. 15j) and reworked clay coatings and broken silt cappings (S-Fig. 15k, l, m, n, o, p) may have been formed by erosional processes within the soil and possibly by termites selecting silty clay for the construction and reinforcement of chambers (S-Fig. 15i). Clear indications for significant amounts of non-authigenic, non-translocated, sedimentary clay and silt could not be found, suggesting that clay and silt mostly post-date deposition.

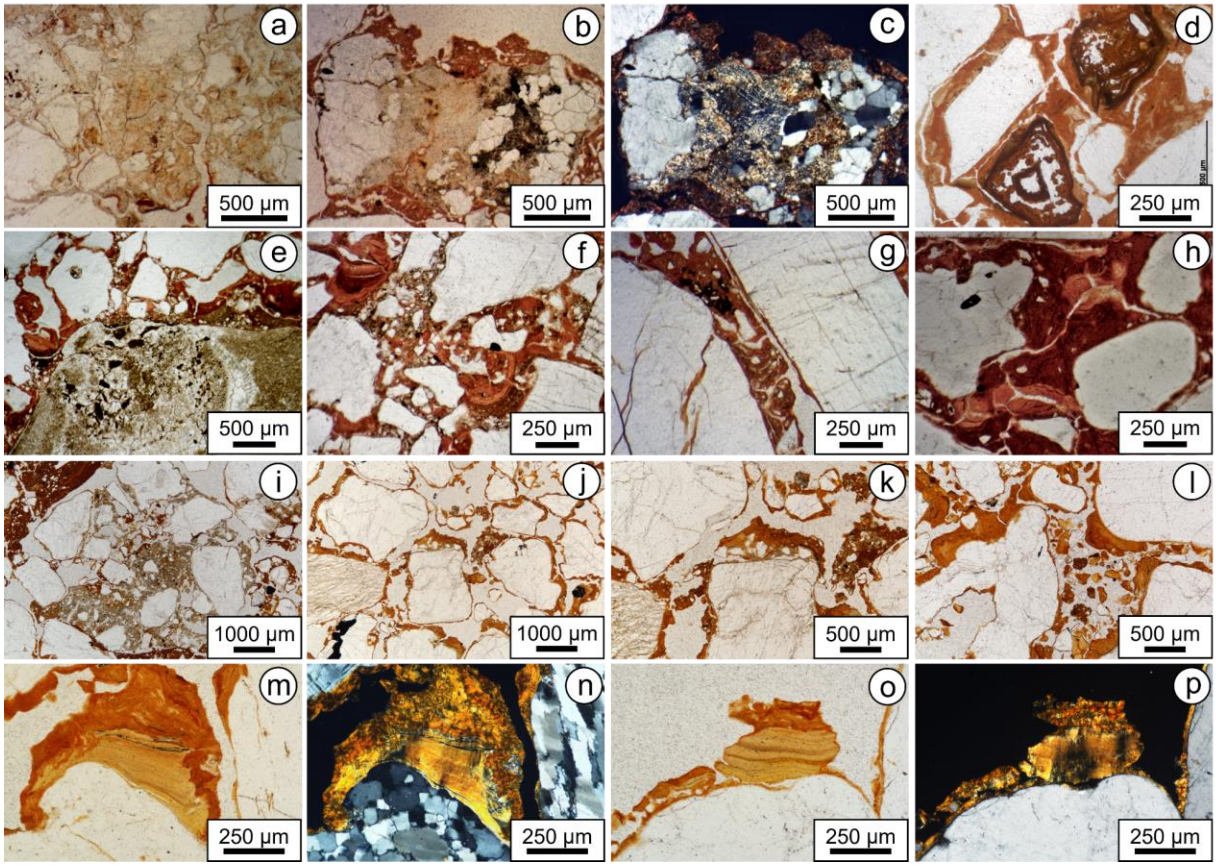

S-Fig. 15. *BRU-C.* a) Mineral weathering producing pale yellow clay and disintegration of arkosic sandstone. b-c) In situ clay (yellowish, probably sericite) formation inside a heavily weathered feldspar pebble (c in XPL). d) Ferruginous open boxworks of alteromorphs (Delvigne and Stoops, 1990). e) Silt cappings on a pebble of green schist. f) Green silty clay alternating with coarse orange clay coatings. g) Greenish silty clay accumulated in between pebbles, forming crescent-shaped moderately oriented silty clay coatings. h) Fine yellow clay overprints silty dark orange clay coatings. i) The dark orange walls of a fossil termite chamber are composed of silty clay. The chamber is infilled with sand and pale clay. j) Truncated laminated yellow clay coating. k) Truncated silty clay coating and reworked fragments in open pore spaces. l) Reworked fragments of clay coatings. m-n) A yellow laminated clay coating has been truncated on the side and overprinted by dark orange coarser clay illuviation (n in XPL). o-p) Remnant clay coating on a sand grain, indicative of erosional processes within the soil.

BRU-D is a relatively recent channel fill at test pit BRU-GT2 consisting of open-spaced very coarse sand to fine gravel.

S5. CATHODOLUMINESCENCE MICROSCOPY.

Cathodoluminescence is a form of luminescence (the transformation of different kinds of energy into visible light) that is caused by the interaction of an electron beam with a solid. This type of luminescence is mainly activated by defects and enables the visualization of the real structure of minerals. A given mineral can accept different activators, and produce a different CL color for each. Feldspar, for example, can accept Eu^{3+}, giving it a blue color, Mn^{2+}, leading to greenish

yellow, or Fe^{3+}, producing red. The defects are related to lattice defects or to the structural incorporation of certain trace elements. As a result, different phases, as well as zoning and internal structures can be revealed using CL microscopy (Götze, 2012). The CL set-up consisted of a cold cathode electron source attached to an optical microscope with a low vacuum chamber to study carbonate nodules. CL microscopy is well-suited for this, as it helps visualize different regions of minerals with a complicated history, including growth zonation, dissolution surfaces, and healed cracks. Calcite appears red, quartz appears blue, and feldspars are predominantly green (Mn^{2+}), but may also accept blue (Eu^{3+}). The technique is somewhat destructive as it causes scorching of thin sections where the electron beam has bombarded the sample.

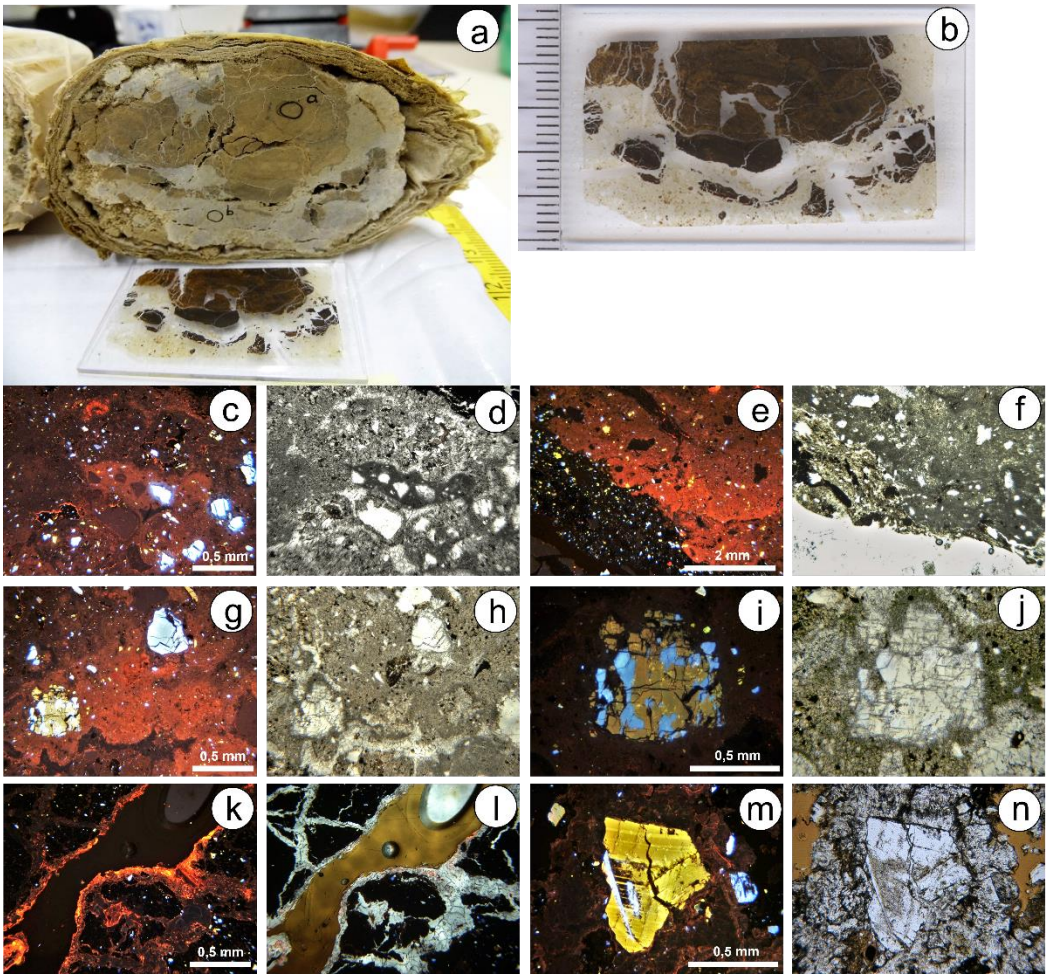

S-Fig 16. MGD-I facies MGD-B (6877b and 9999). (a) Slice of nodule 6877b with sub-sample locations (a, b) for stable isotope analysis and radiocarbon dating indicated. Location (a) had a much lower carbonate content (23.8%, isotope sample 6877 C) than location (b) (69.2%, isotope sample 6877 D), see table S-T1. Corresponding thin section below. (b) Scan of thin section 6877 A. (c-d) Ghost features of sand (pseudomorphs of carbonate after dissolved sand grains, appearing darker red than the surrounding carbonate) alongside blue-appearing sand and silt of quartz. (e-f) Silty clay (lower left) sticking to the side of a carbonate nodule, containing similar silt and fine sand inclusions. The approximate equivalent location is shown in f in PPL. (g-h) Illustrating the dissolution and disintegration of feldspar

and quartz sand. (i-j) The same feldspar sand grain as shown in (g-h) at higher magnification, illustrating disintegration leading to silt formation and dissolution followed by carbonate replacement within the nodule. (k-l) Dark iron-rich material (possibly of organic origin) in the core of some nodules from MGD-I is poor in carbonate, appearing dark with CL, while the sparite that precipitated along and inside cracks shows bright red. (m-n) weathering feldspar.

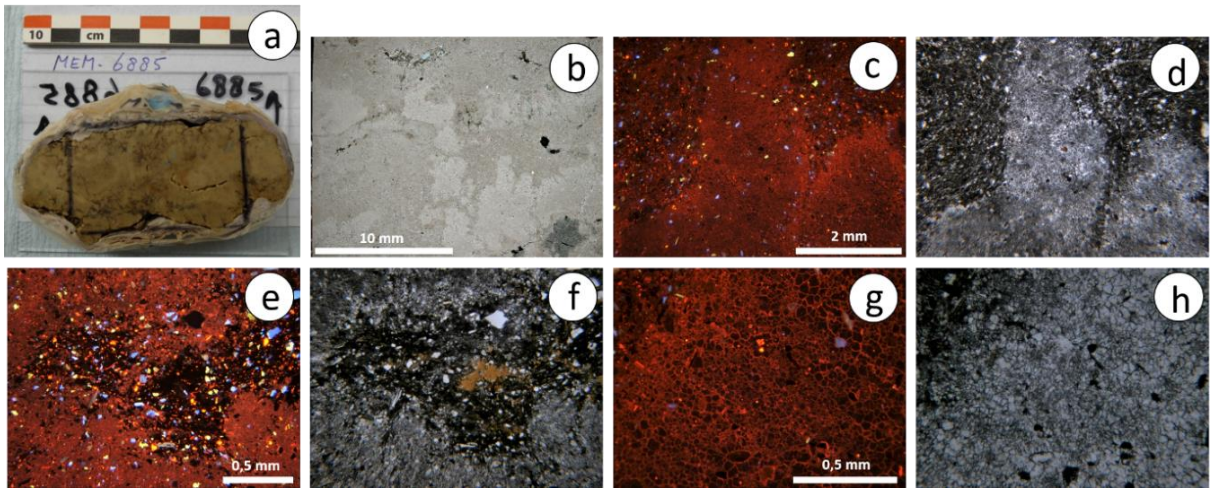

S-Fig 17. Bruce Geotrench 2, facies BRU-A (6885). (a) Sliced carbonate nodule (sample 6885) with outline of thin section marked. (b) This carbonate nodule after lagoonal clay is very fine micritic and contains pillar-shaped fingers of increased carbonate replacement. (c-d) At higher magnification, differences in silt-content can be observed within and outside of the "fingers", especially in CL, with more intense carbonate formation and dissolution of siliceous minerals inside the fingers. (e-f) A patch of remaining silty clay surrounded by carbonate, showing preserved dark material (clay) and silt (blue and green/yellow). (g-h) Ghost features of dissolved sand and silt are marked by rings of fresh calcite.

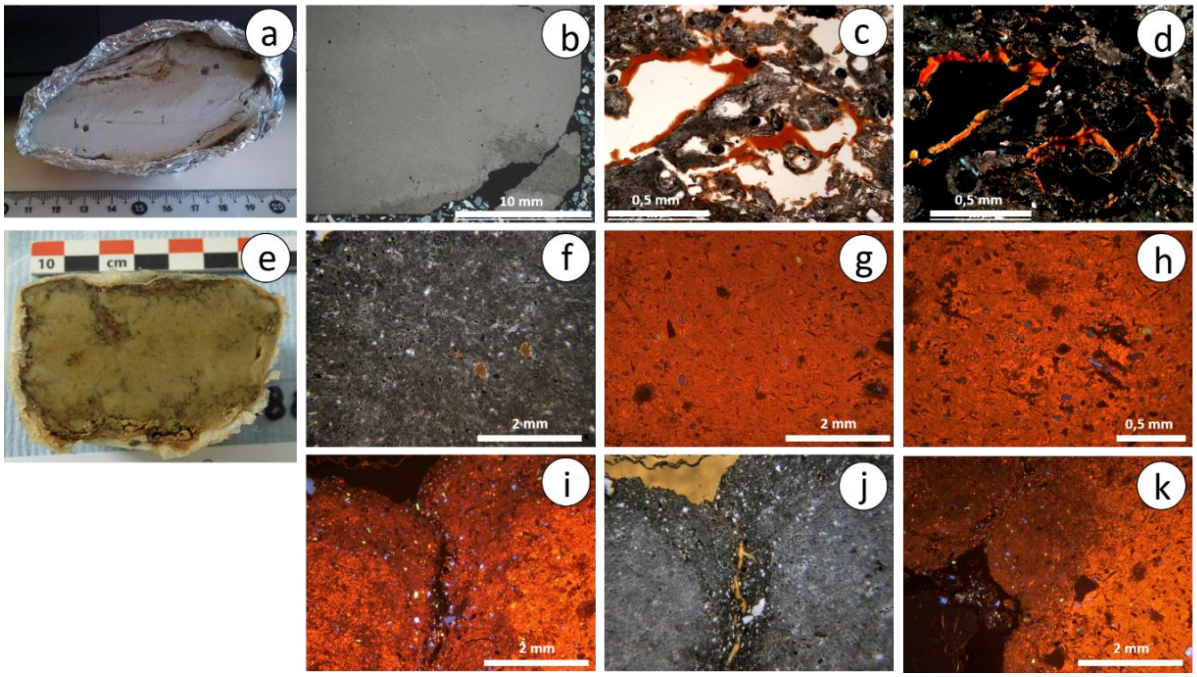

S-Fig 18. (a) Bruce Geotrench 2, facies BRU-A: sample 6887 is an example of homogeneous micritic carbonate, with very little indications left for the origin: lagoonal clay. (b) a band of fine silty clay at the edge of the nodule has been less affected by carbonate replacement (XPL). (c-d) Root remains. Orange clay coatings have entered from the

overlying channel deposit (BRU-D). (e) Carbonate nodule sample 6888 as prepared for thin section production. (f-h) In CL, common elongate pseudomorphic "ghost" features after mica can be recognized, besides more equant silt grains. Although carbonate formation can disturb the original laminated fabric, a near-horizontal orientation of mica silt is still prevalent. (i-k) Deformation of the original laminated structure by carbonate formation. Darker zones have been less affected by carbonate replacement, preserving more clay and silt.

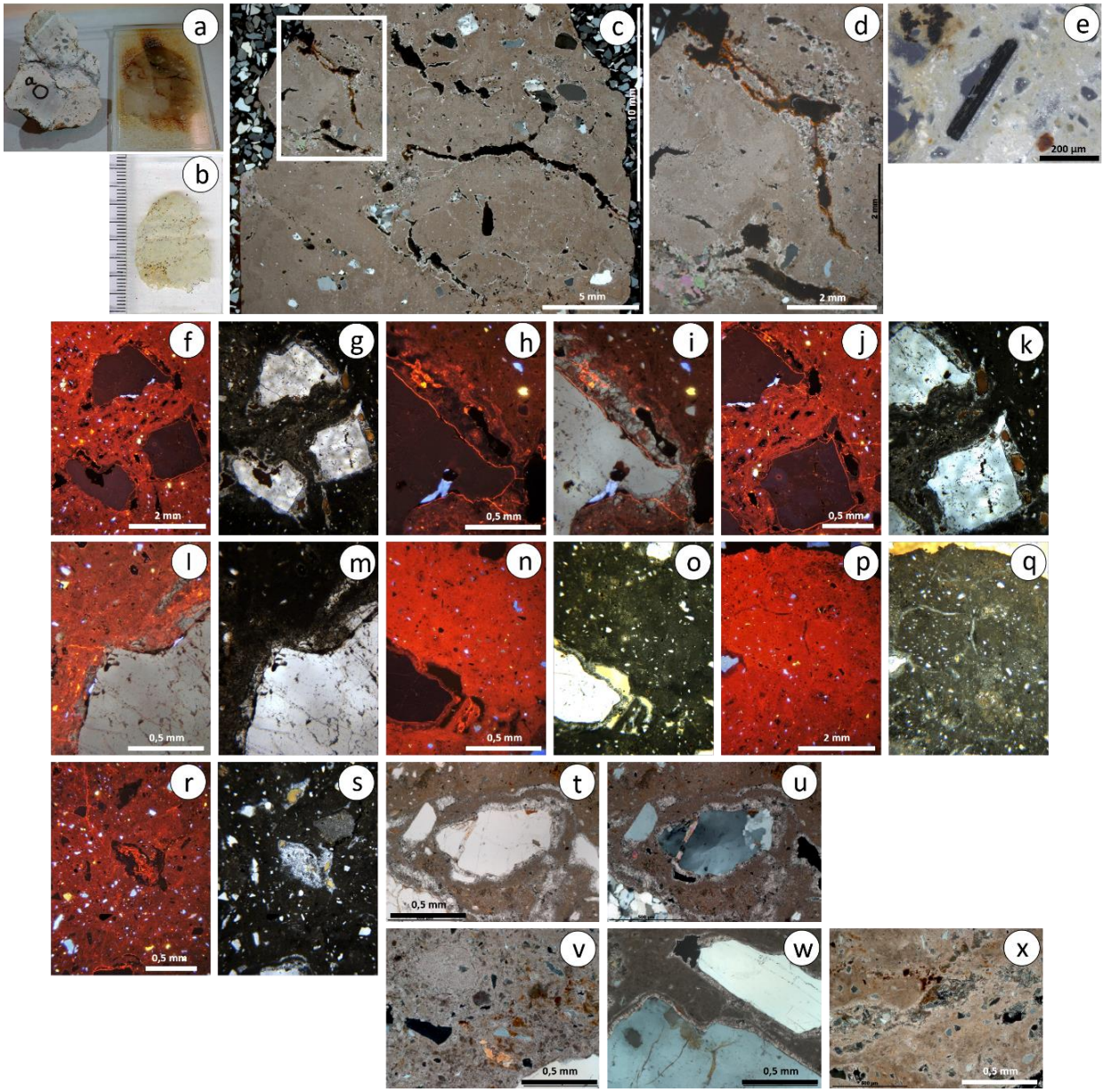

S-Fig. 19. BRU-III facies BRU-B. (a) Sliced nodule (7271) and corresponding thin section, burnt during CL microscopy. (b) Scan of the thin section before CL showing different zones separated by cracks. (c) Photomicrograph at low magnification, showing common sand inclusions and cracks (XPL). (d) A crack in the upper left (indicated in (c)) of the nodule contains well-developed orange clay coatings. Zones of sparite along cracks and at the outer edge of the nodule (XPL). (e) Inclusions of a heavy mineral high in titanium (ilmenite) are common (OIL). (f-o) Sand grains (quartz) are fragmenting, dissolving and being replaced by calcite. (i) and (l) are taken with CL and some plane polarized light to show the (quartz) inclusions as well as the calcite. (p-q) A clay-rich zone replaced by micrite. (r-s) Sand grains replaced by calcite (top) appear as grey ghost features or pseudomorphs. (t-u) Phases of feldspar dissolution are also

recognizable in PPL and XPL. (v) Fragment of a limpid yellow clay coating included in a carbonate nodule (7272) (XPL). (w) Sand grains in nodule 7272. Mineral dissolution phases (feldspar) followed by (micro-)sparite replacement form rims around the grains and have left an open pore space (top), which would usually get infilled with sparite. (x) Laminated silty clay preserved in nodule 7272 (XPL).

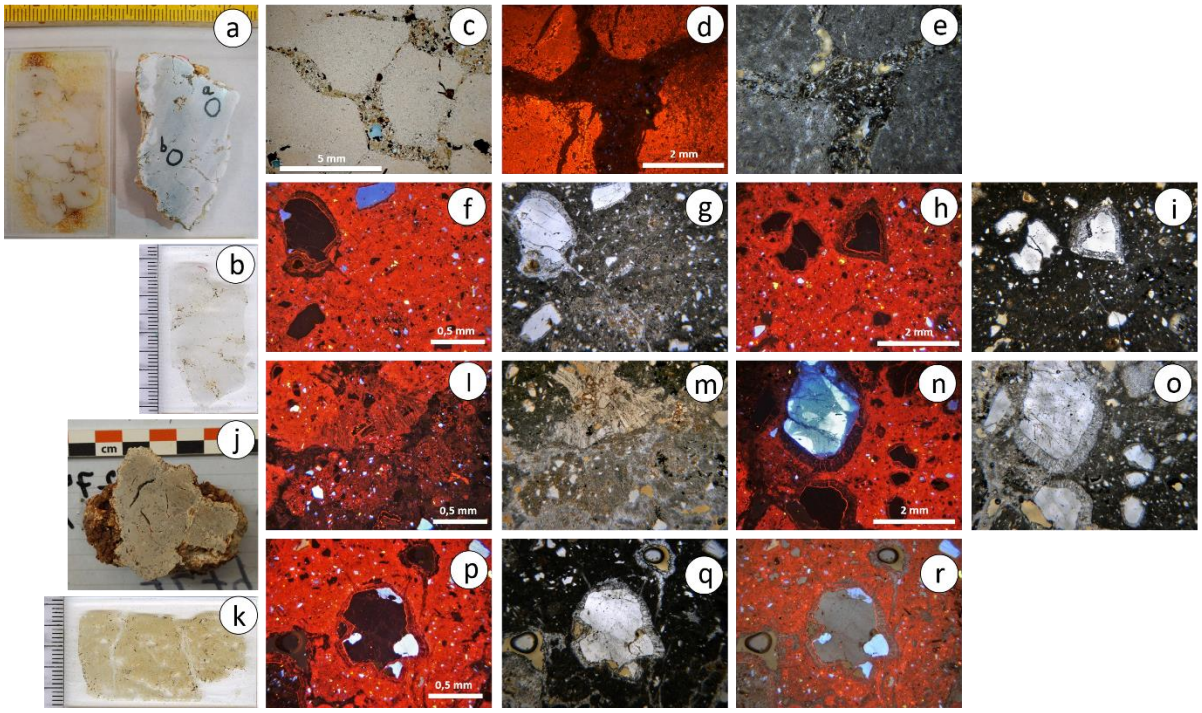

S-Fig 20. BRU-III facies BRU-B (a) Slice of nodule 7273 with sub-sample locations for stable isotope analysis and radiocarbon dating indicated. Corresponding thin section to the left, partly scorched as a result of CL microscopy. (b) Scan of thin section of nodule 7273. (c) Nodule 7273 consists of merging micritic carbonate nodules separated by cracks infilled with sandy clay (XPL). (d-e) CL highlights the micritic calcite at a junction of coalescing nodules forming a crack filled with clay. (f-i) Inclusions of sand and clay domains in nodule 7274. (j) Sliced carbonate 7274, a slightly iron stained nodule with common inclusions of sand and clay. (k) Scan of thin section of nodule 7274. (l-m) A recrystallized fringe (upper left) of elongate sparite crystals at the edge of the nodule. Adjacent (below) is a patch of dark fine micrite replacing silty clay (7274). (n-r) Gradual dissolution and fragmentation of sand grains appearing blue in CL, likely quartz. Rims of sparite around the sand grains appear as red strings in CL. Some plane polarized light was added to the CL in (o) (two bubbles trapped in pore spaces during thin section production).

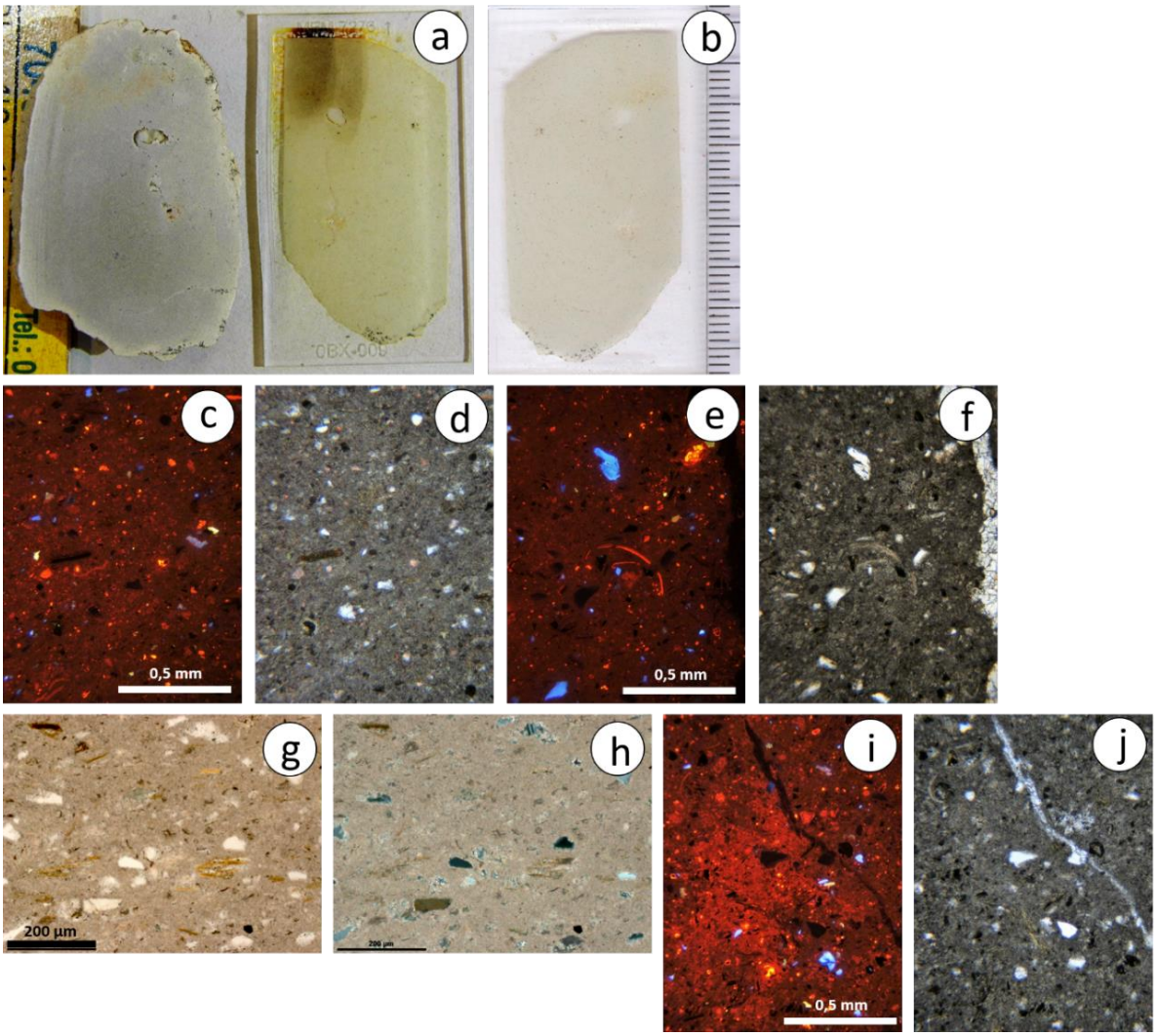

S-Fig 21. BRU-III facies BRU-B. (a) Cut-face of nodule 7276 with thin section after CL. This nodule is formed by the replacement of laminated silty clay. The fine micrite is only disrupted by a chamber and a channel leading to and from the chamber. The carbonate is very hard, and this burrowed feature, as well as the horizontally oriented silt (mica), are evidence of the laminated silty clay origin of the nodule. (b) Scan of the thin section. (c-d) Micrite and fine silt with flat-lying mica. (e-f) Possible shell fragments included in the nodule. (g-h) Horizontally oriented silt in micrite (PPL and XPL). (i-j) Slight enrichment in carbonate near the bioturbation feature.

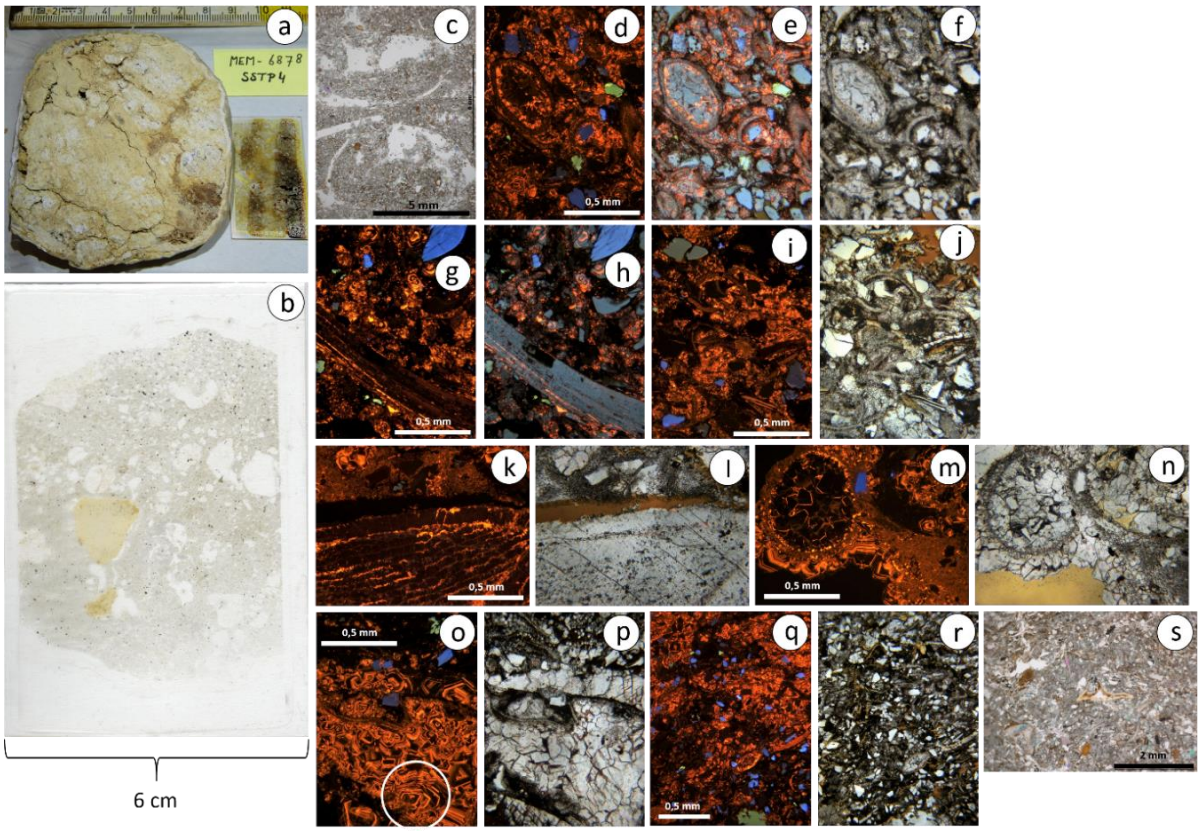

S-Fig 22. Chiwondo deposits containing shells and (fish)bones, many of which dissolved and visible as void-pseudomorphs. Very large hexagonal calcite crystals with multiple growth phases are indicative of formation under saturated conditions, as in a groundwater carbonate, forming a carbonate cement. (a) Slice of a Chiwondo sample from a test pit near Sadala (6878) with the scorched thin section. (b) Large thin section of a sample collected at Malema with phosphatized fragments of organic origin (6 x 9 cm) (c) Void pseudomorphs of stacked mollusk shells. (d-f) Shells and coarse sand in calcite cement. (g-h) A larger shell fragment. (i-j) Shells and silt. (k-l) Weathered feldspar. (m-n) Sparite infilling round shapes, possibly mollusks pseudomorphs. (o-p) Very large crystal growths of calcite. (q-r) Stacked shells (appearing dark), blue (quartz) silt, and feldspar with dissolution around the edges (green, bottom). (s) Possible fish bone (PPL).

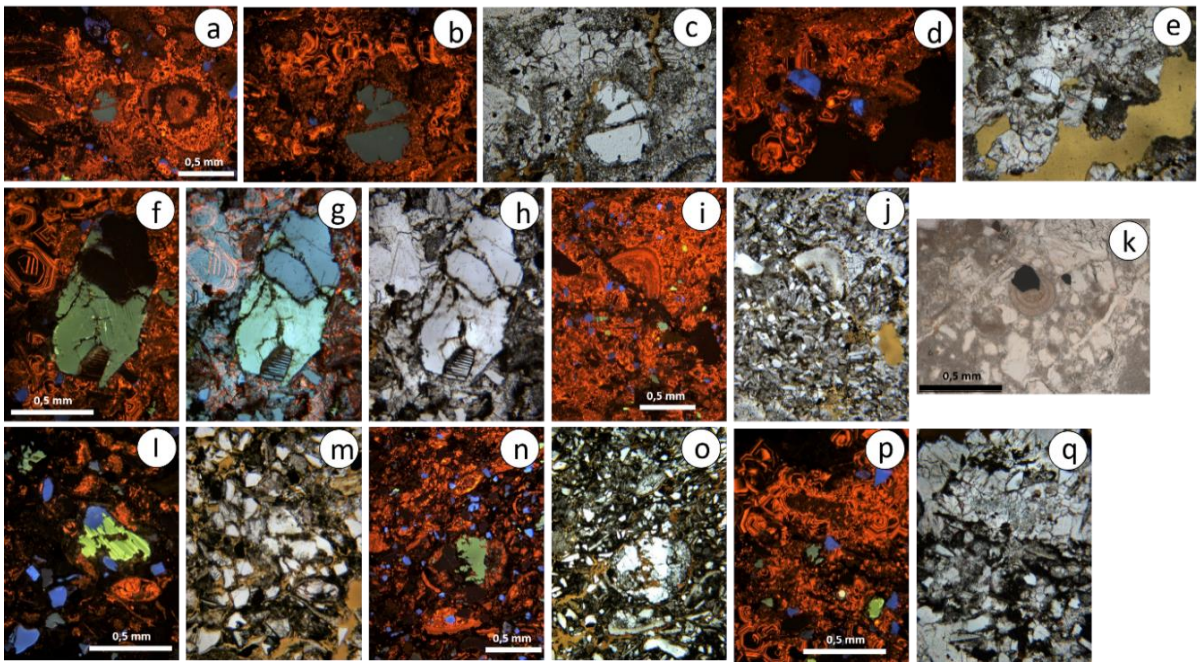

S-Fig 23. Examples of calcite cement in the fossiliferous and shell-rich Chiwondo Beds, as well as feldspar and quartz dissolution and disintegration of coarse sand into smaller silt grains.

S6. MICRO-XRF RESULTS.

Microscopic X-ray fluorescence (μ-XRF or micro-XRF) is used to measure the relative abundances of major and trace elements over exceptionally small areas. Fluorescence spectra reflecting semi-quantitative elemental compositions can be generated at single points, in a line scan, or series of points along a transect. Spectra from a series of points spaced on a grid can be processed into compositional maps (Mentzer and Quade, 2013).

Micro-xrf observations per site

Below a selection of carbonate and micromorphological samples containing carbonates are shown for each site with corresponding elemental mappings in figures.

Notes: Cl reflects pore space (resin) only, and Zr is also contained in resin. Most results were obtained with 10 ms (milliseconds) dwell time per pixel. No micro-xrf elemental mapping was performed on carbonate samples 7274, 7275, and 7277 (Bruce III) and 6888 and 6889 from BRU-GT2.

Mwanganda´s Village Area I

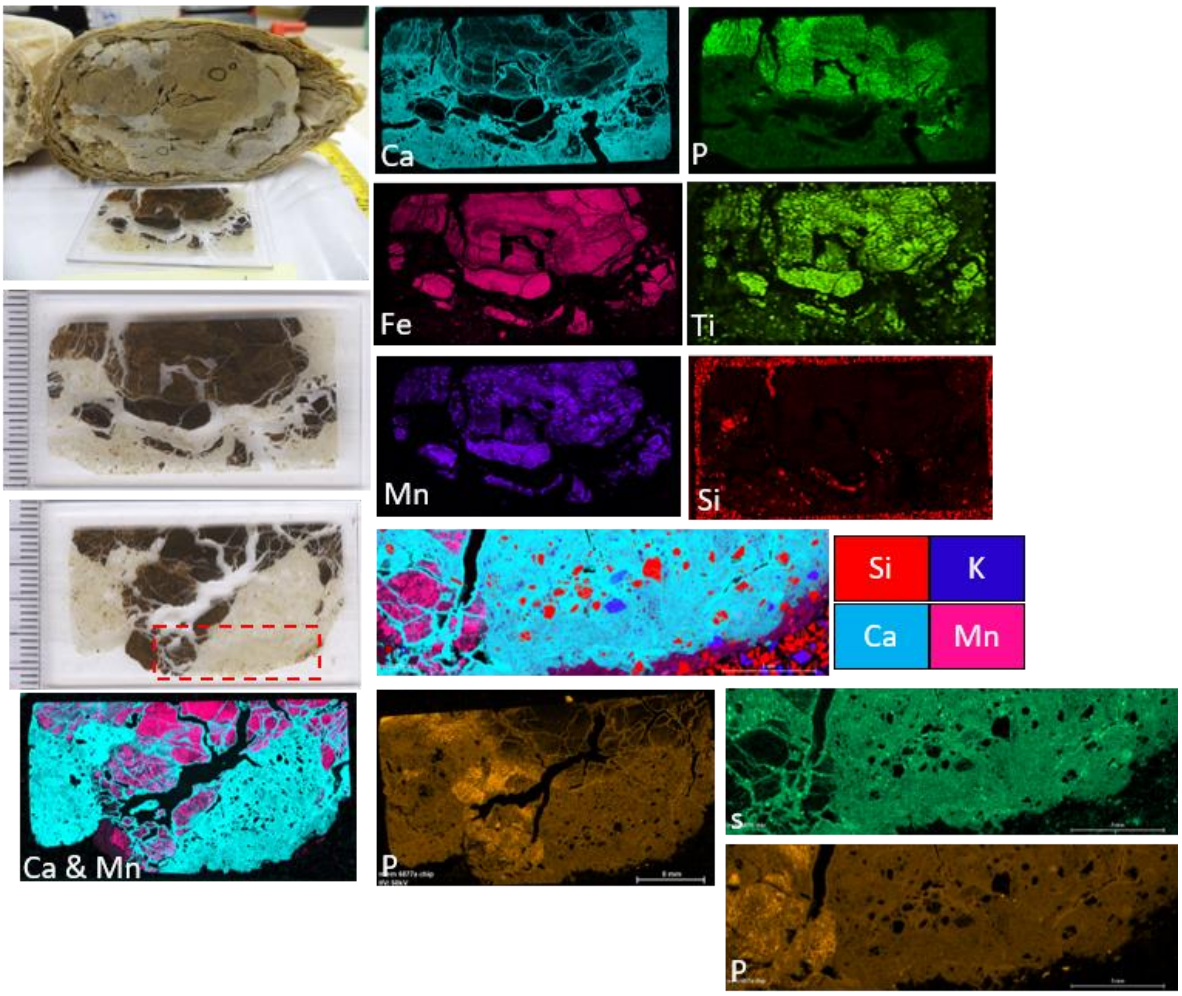

S-Fig. 24. MEM-6877 B and A are two small thin sections from the same $CaCO_3$ nodule collected at MGD I. The dark (organic) zones are poor in Ca and contain no mineral inclusions, which is most clearly visible in the mapping of Si, which only appears in the carbonate part of the sample, reflecting sand inclusions in the micritic carbonate. The dark zones are especially rich in Fe, but also in Mn. P is only enriched in certain parts and may be related to decomposition. This partial P enrichment can be seen in both thin sections. In the calcium carbonate part of the nodule, besides Ca, S is also present. The details were taken directly from an impregnated block sample and the approximate location is indicated on the thin section scan (red frame, dashed line).

The elemental maps show that the dark brown zone in MEM-6877 is enriched in Fe, and for the most part also in Mn, and Ti. A similar core zone occurs in MEM-9999, but here it is much lighter in color. The elemental maps of MEM-9999 indicate a much subtler enrichment in Fe, Mn, and Ti, and a strong enrichment in P. P enrichment is also pronounced in MEM-6877, especially in the outer parts of the core material, where Mn and Ti become patchy.

In the dark brown zone, Ca only occurs in crack fillings.

Other elements such as Al, Ca, K, Mg, Na, S, Si did not appear in the dark material of the core zone.

The white calcareous part of the nodules shows strong Ca, S, moderate Mg, P, Sr (mapped for 6877a), Al, and little Na. Dispersed distinct specks of Ti and Zr show a similar dotted pattern but do not overlap, as Zr mostly reflects resin, appearing in pore spaces.

Inclusions are revealed by points of high Si, Al, K, and Zr.

Mwanganda´s Village Area II

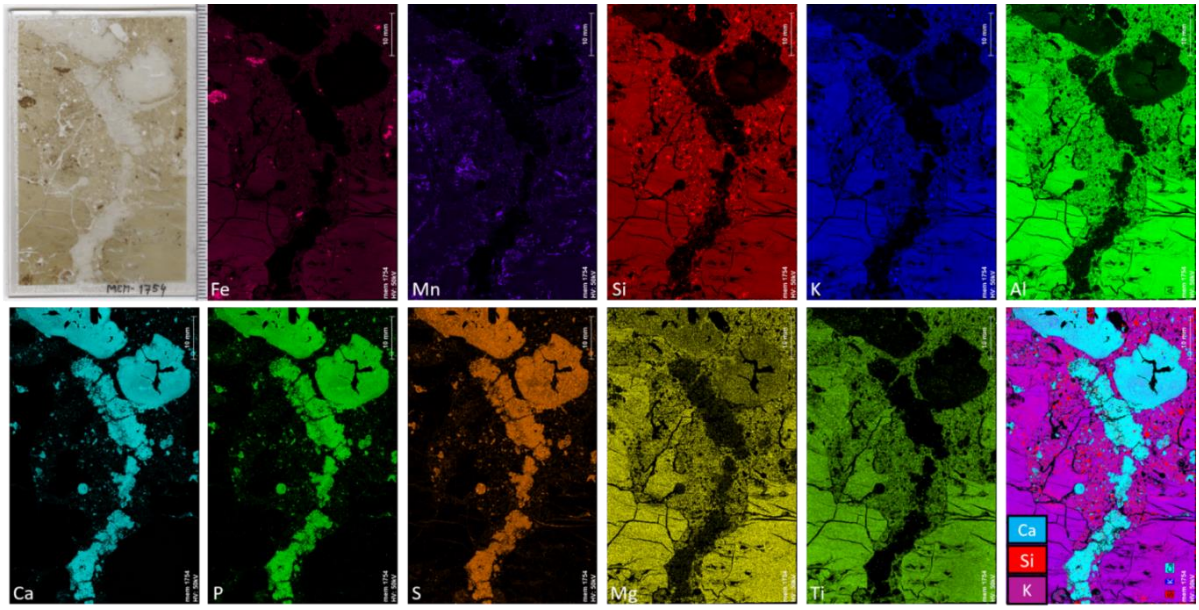

S-Fig. 25. Micro-xrf mapping of sample MEM-1754 from MGD II of the boundary between facies MGD-B to MGD-C shows the distribution of the elements Fe, Mn, Si, K, Al, Ca, P, S, Mg, and Ti. Distinct redox features are highlighted by concentrations of Fe and Mn. The deposit is composed of (1) laminated silty clay with abundant mica (muscovite, biotite, illite) and chlorite. The clay is especially enriched in Al, as well as Si, K, Mg, Fe, Ti, Mn. In (2) bioturbated sediment with sand mixed in from above the elements typical for clay are less bright but Si appears bright where sand grains occur. (3) Large $CaCO_3$ nodules are found in the top of the sample and infilling a vertical desiccation crack which has also been occupied by roots. The carbonates are enriched in Ca, P, and S and the mapping of these three elements shows almost perfect overlap. Mg, however, is present in the large nodules in the top of the thin section, but is nearly absent in the root channel/desiccation crack. This distribution may be because Mg is an important element in the lagoonal clay. It probably remains where $CaCO_3$ nodules have formed by replacing clay-rich sediment. More clearly are dots of Ti lighting up in the nodules in the top, which is also a dominant element in the clay.

Bruce Area III

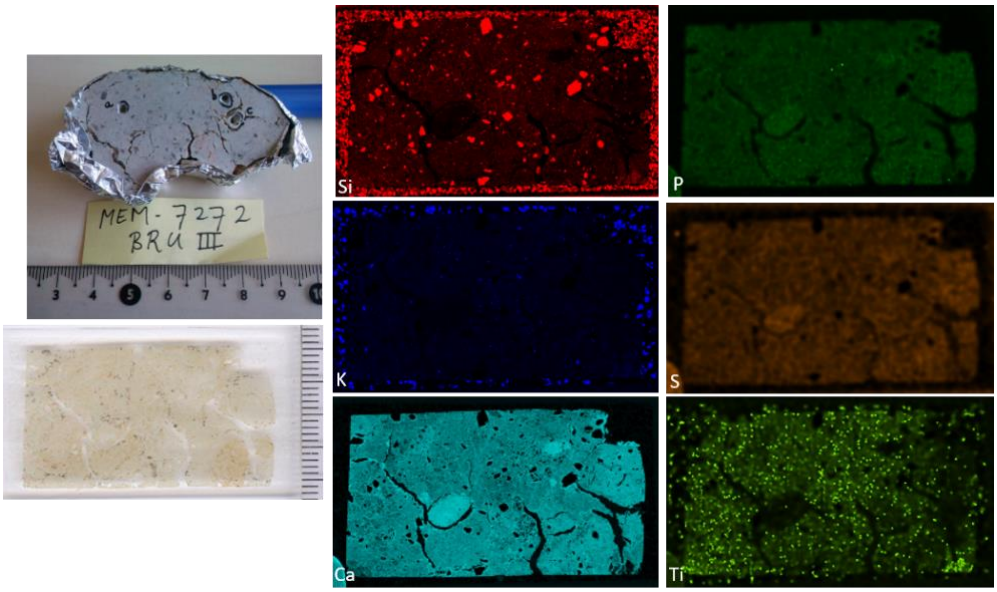

S-Fig. 26. Sample 7272 from BRU-III.

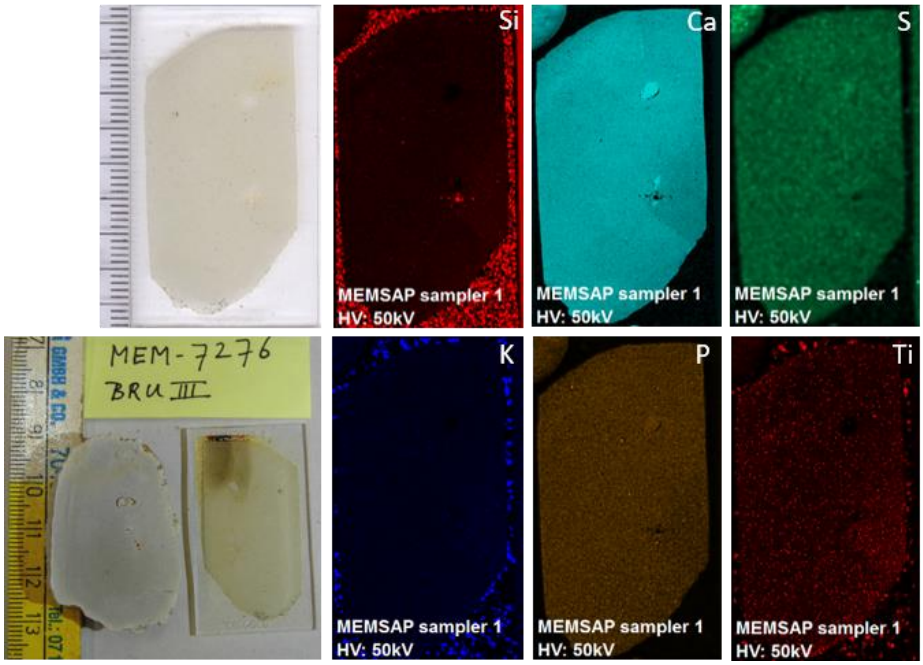

S-Fig. 27. MEM-7272 and MEM-7276 are both from Unit 1 (facies BRU-B) of Bruce III. MEM-7272 has many sand-sized inclusions (see Si), common cracks, dendritic staining of Mn (not displayed here), and a dense micritic "core" zone (Ca, lower left) which is enriched in Ca, P, and S and contains no mineral inclusions. MEM-7276 however is a very homogeneous and fine micritic nodule with fine silt inclusions only (Ti). It contains one bioturbation feature: a now carbonized chamber with channels leading to it up- and downwards, which must have formed at a time when the hard nodule was a soft carbonate mud in lagoonal clay sediment. Some inclusions are contained in the channel in the lower part, best visualized by Si mapping (red). K and Si are low outside the bioturbation feature. These elements

are dominant in the lagoonal clay, which formed the original sediment of nodule 7276. After carbonatization, Ca, P, S replace the clay and only the silt (Ti, K) and Mg (even staining, not displayed here but compare figure above, MEM-1754) remains.

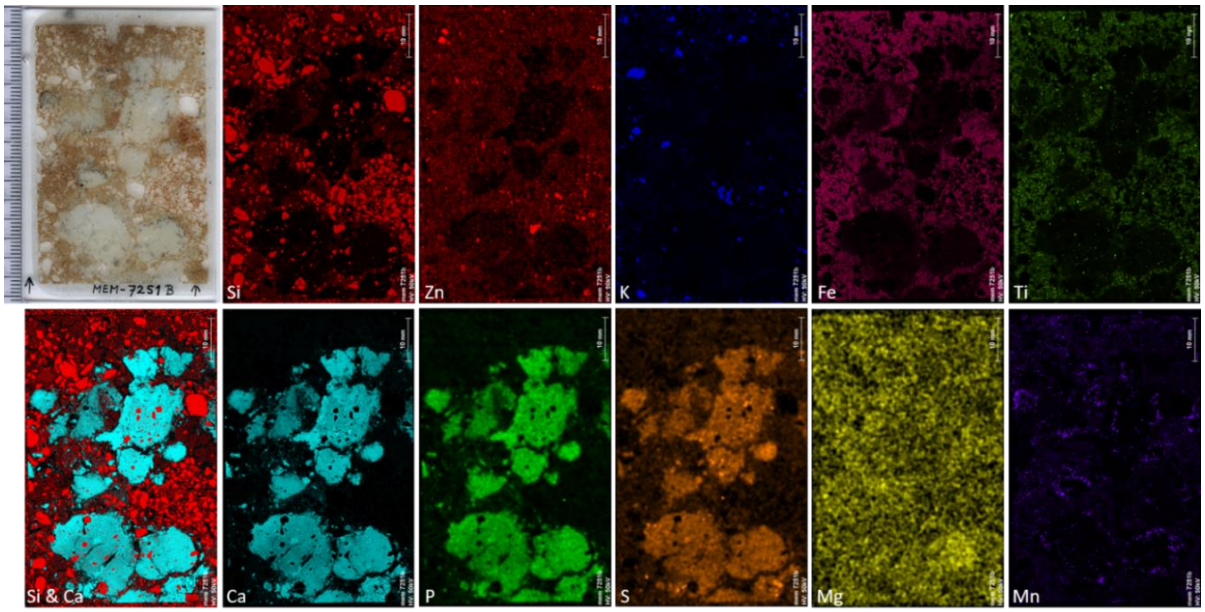

S-Fig. 28. Elemental mappings of thin section MEM-7251 B, collected at Bruce area III (Units 1-2, facies BRU-B). Silica appears in quartz (very red), feldspars (less red, or zoned), and clay (very faint). Note the fractured quartz sand grains. Zinc shows some overlap with siliceous (bright red) grains, probably indicating the presence of minerals such as rutile and ilmenite, and is also present in the clay, but in lower concentrations and evenly dispersed. K indicates primarily potassium feldspars such as microcline and orthoclase, minerals that are less abundant in the sand fraction compared to quartz or quartzite. Fe shows that the fine groundmass of the sediment has been iron-stained and zones rich in clay therefore also appear most pronounced in the Fe map. The distribution of Ti corresponds with the abundant small and few fine sand-sized black opaque particles with a metallic luster in oblique incident light, likely ilmenite. This shows that, although Mn is oftentimes assumed to be present in black opaque particles in thin section, this is not necessarily the case. Si and Ca mapped together illustrates the distribution of quartz sand in the matrix and as inclusions inside $CaCO_3$ nodules, but also shows where patches of silty clay (dark red, e. g. just above the middle on the right side) are present. Ca, with lesser amounts of P and S are the main constituents of the carbonate nodules. Mg is present in the clay, but also appears enriched in one particular silty nodule in the lower right. Mn mapping nicely shows the black dendritic staining on $CaCO_3$ nodules in this sample.

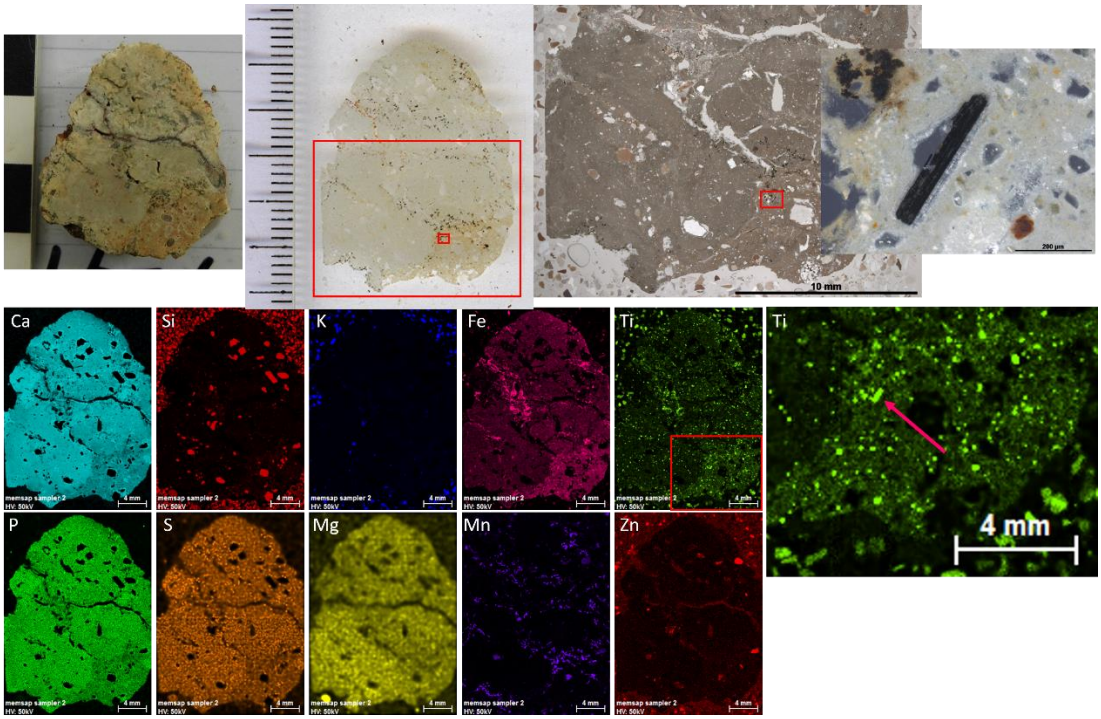

S-Fig 29. Carbonate nodule 7271 was collected from Bruce Area III, Unit 2 (facies BRU-B). Although a larger black opaque particle looked very similar to charcoal, the elemental mapping shows that it is rich in Ti, making it most likely a heavy mineral such as ilmenite. Mapping of the other elements shows a similar pattern to that of other heterogeneous nodules with sand inclusions. The lower left part of the nodule contains few sand inclusions and slightly more Ca, P, S, and Mg than the rest of the nodule. Fe staining is stronger in impure zones in the lower right and upper left. Here, higher amounts of Ti partly correspond with Fe. However, Fe is thought to be secondary (staining) and Ti integral part of the original sediment, since lagoonal (silty) clay is richest in Ti, relative to mixed sandy sediments and $CaCO_3$ nodules (the other two main components).

Bruce Geotrench 2 (BRUGT2)

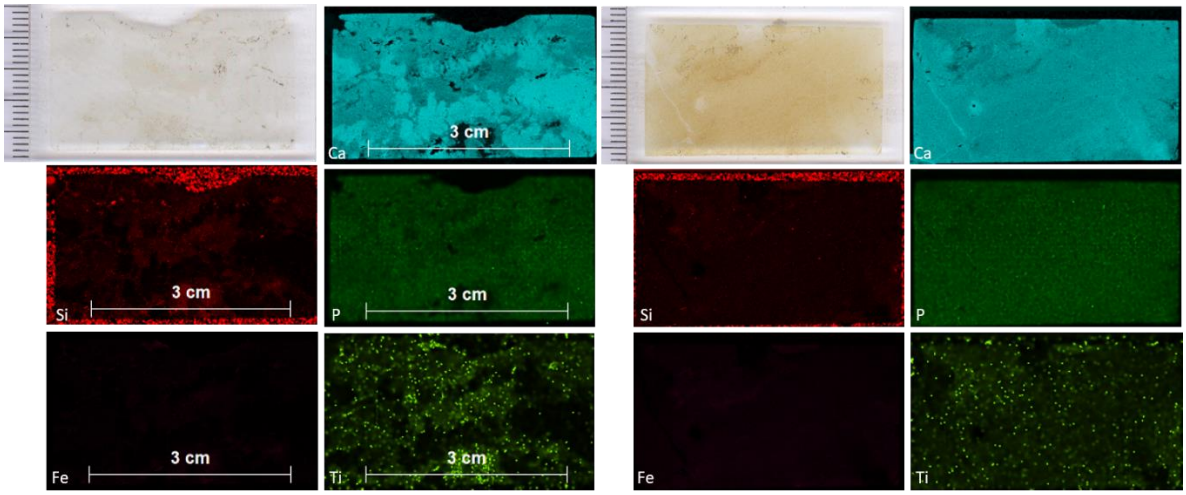

S-Fig. 30. A few elements are mapped for two $CaCO_3$ nodules from BRUGT2: 6885 (left) and 6886 (right). Finger-shaped dense micritic zones in 6885 (left) contain more Ca and P (and slightly more S, not shown here). Si and Ti (representing clay and silt minerals) are nearly absent from the more intensely carbonized "finger" zones. 6886 (on

the right) is more homogeneous. Iron staining is slight and possibly better illustrated in the mapping of phosphorus which is slightly enriched in comparison to other samples. A fresh cut from the calcareous sediment at BRUGT2 would always reveal organic vegetal remains, which soon after exposure disappeared, making the profile appear entirely white/calcareous again.

Titanium comparison

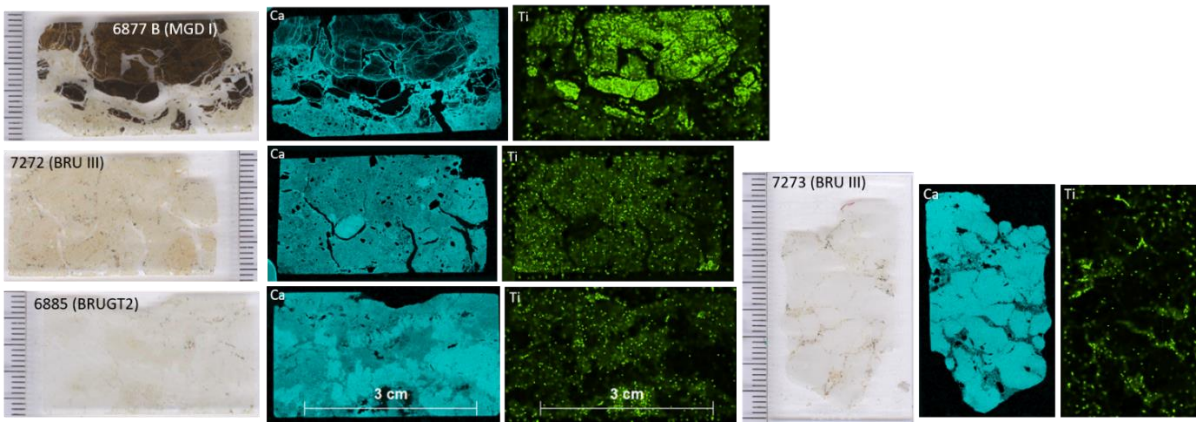

S-Fig 31. Titanium, together with Fe, Mn and P (but P partially, see first figure) is contained in the dark non-calcareous material in carbonate nodules from MGD-I where it appears as a mottled staining. A comparison of the elemental mapping of Ca and Ti in samples from Buce III and BRUGT2, shows that Ti is only present outside of zones of dense micritic carbonate formation.

KEY OBSERVATIONS X-RAY FLUORESCENCE

The elemental distribution maps provided information that aided in distinguishing the three main components of carbonate nodules: (1) intact silty clay, (2) sandy (mixed with clay) sediment, and (3) the calcium carbonates. The maps also provided possible elemental indices to identify different pathways of carbonate formation: (1) replacement of intact silty clay with calcite taking the place created by dissolving quartz and feldspar minerals, (2) replacement of sandy mixed material containing quartz, and (3) void filling with minor or complete replacement of organic matter.

- Intact silty (laminated) clay contains Al, K, Si, Mg, Ti, as well as little Fe (even staining) and Mn (localized). Thin section analysis shows that the clay contains abundant mica, biotite and illite/muscovite, contributing to the Mg content.
- Sandy sediment contains: Si, Al, K, Ti, Mg, as well as very little or locally concentrated Fe, Mn, and elements related to carbonate features.
- $CaCO_3$ nodules contain Ca, as well as P and S
- In $CaCO_3$ nodules, a variation is observed in the presence of Mg, Al, Ti, K, Si, Mn.

- Mn is related to staining that occurred after $CaCO_3$ precipitation.
- Fe is also secondary, but staining is often more diffuse, covering a zone or entire nodule.
- Relatively high amounts of Mg, Al, and Ti in carbonate nodules may be indicative of carbonate replacement of less mixed and less disturbed intact clay, due to high amounts of these elements that are only present in intact lagoonal (silty) clay. As soon as this clay is disrupted and mixed, these elements become less dominant through admixture of minerals or organic material and through the effects of increased porosity.
- Concentrations of Si in nodules reflect mainly quartz sand and indicate that the nodule is formed in mixed (often bioturbated) sediment containing more siliceous (sand) grains together with clay.
- In some carbonate infillings or nodules, Mg is scarce compared to nodules in the same sample. Observations on MEM-1754 suggest that where $CaCO_3$ precipitated in a pre-existing void space, only replacing some vegetal (root) remains but no sediment, Mg is less abundant.
- This shows how carbonatation follows different paths in the same sediment and can help identify whether replacement took place and if so, which was the primary sediment.

The elemental mapping aided in the identification of certain black opaque particles. The identification of ilmenite was based on black opaque silt particles which have a metallic luster under oblique incident light. Larger grains (very fine sand) can show tabular crystals or platy masses, not to be confused with charcoal. The mapping of Ti generally showed a homogeneous distribution of bright distinct Ti specks, apart from strongly carbonized zones which are likely non-replacive, e. g. formed in voids. They appear for example in 7272 (BRU III), 7273 (BRU III), and 6885 (BRUGT2). Other heavy minerals mined from sands in Malawi include magnetite, zirconite, rutile, and monazite. Black sand composed of ilmenite is deposited on the shore of lake Malawi. The dark possibly organic material included in MGD-I is also high in Ti. Here it does not appear as distinct dots but more diffuse.

REFERENCES

Alonso-Zarza, A. M. and Wright, V. P. (2010) 'Chapter 5 Calcretes', *Developments in Sedimentology*, 61(C), pp. 225–267. doi: 10.1016/S0070-4571(09)06105-6.

Alonso, P., Dorronsoro, C. and Egido, J. A. (2004) 'Carbonatation in palaeosols formed on terraces of the Tormes river basin (Salamanca, Spain)', *Geoderma*, 118(3–4), pp. 261–276. doi: 10.1016/S0016-7061(03)00211-8.

Barker, P. A. *et al.* (2007) 'Century-to-millennial scale climatic variability in Lake Malawi revealed by isotope records', *Earth and Planetary Science Letters*, 261(1–2), pp. 93–103. doi: 10.1016/j.epsl.2007.06.010.

Blair, T. C. and McPherson, J. G. (1994) *Alluvial fans processes and forms*, *Geomorphology of Desert Environments*. doi: 10.1007/978-1-4020-5719-9J4.

Blokhuis, W. A., Kooistra, M. J. and Wilding, L. P. (1990) 'Micromorphology of cracking clayey soils (vertisols)', in Douglas, L. A. (ed.) *Soil micromorphology: a basic and applied science*. Elsevier, pp. 123–148.

Bowen, G. J. (2017) 'The Online Isotopes in Precipitation Calculator, version 3.1'. Available at: http://www.waterisotopes.org.

Bullock, P. *et al.* (1985) *Handbook for Soil Thin Section Description*. Albrighton: Waine Research Publications.

Candy, I. *et al.* (2012) 'Oxygen and carbon isotopic composition of Quaternary meteoric carbonates from western and southern Europe: Their role in palaoenvironmental reconstruction', *Palaeogeography, Palaeoclimatology, Palaeoecology*, 326–328, pp. 1–11. doi: 10.1016/j.palaeo.2011.12.017.

Canti, M. G. (2017) 'Mollusc Shell', in Nicosia, C. and Stoops, G. (eds) *Archaeological Soil and Sediment Micromorphology*. Wiley and Sons Ltd, pp. 43–46.

Cerling, T. E. *et al.* (1989) 'Carbon isotopes in soils and palaeosols as ecology and palaeoecology indicators', *Nature*, 341(6238), pp. 138–139. doi: 10.1038/341138a0.

Courty, M.-A., Goldberg, P. and Macphail, R. I. (1989) *Soils and Micromorphology in Archaeology*. Cambridge: Cambridge University Press.

Delvigne, J. (1998) *Atlas of Micromorphology of Mineral Alteration and Weathering*, *The canadian Mineralogist*. Available at: http://petrology.oxfordjournals.org/content/41/3/475.2.short.

Delvigne, J. and Stoops, G. (1990) 'Morphology of Mineral Weathering and Neoformation. I. Weathering of most Common Silicates', *Developments in Soil Science*, 19, pp. 471–481.

Durand, N., Monger, H. C. and Canti, M. G. (2010) 'Calcium Carbonate Features', in Stoops, G., Marcelino, V., and Mees, F. (eds) *Interpretation of Micromorphological Features of Soils and Regoliths*. 1st edn. Elsevier, pp. 149–195.

Golubtsov, V. A. *et al.* (2014) 'Stable Carbon and Oxygen Isotopes in Pedogenic Carbonate Coatings of Chernozems in the Southern Cis Baikalia as Indicators', 47(10), pp. 1015–1026. doi: 10.1134/S1064229314100032.

Götze, J. (2002) 'Potential of cathodoluminescence (cl) microscopy and spectroscopy for the analysis of minerals and materials', *Analytical and Bioanalytical Chemistry*, 374(4), pp. 703–708. doi: 10.1007/s00216-002-1461-1.

Götze, J. (2012) 'Application of cathodoluminescence microscopy and spectroscopy in geosciences', *Microscopy and Microanalysis*, 18(6), pp. 1270–1284. doi: 10.1017/S1431927612001122.

Hogg, A. G. *et al.* (2020) 'SHCal20 Southern hemisphere calibration, 0–55,000 years CAL BP', *Radiocarbon*, 00(5), pp. 1–20. doi: 10.1017/RDC.2020.59.

Islam, M. R. *et al.* (2002) 'Mineralogical changes during intense chemical weathering of sedimentary rocks in Bangladesh', *Journal of Asian Earth Sciences*, 20(8), pp. 889–901. doi: 10.1016/S1367-9120(01)00078-5.

Kovda, I. and Mermut, A. R. (2010) 'Vertic Features', in Stoops, G., Marcelino, V., and Mees, F. (eds) *Interpretation of Micromorphological Features of Soils and Regoliths*. 1st edn. Elsevier, pp. 109–127.

Kowler, A. (2007) 'The Stable Carbon and Oxygen Isotopic Composition of Pedogenic Carbonate and its Relationship to Climate and Ecology in Southeastern Arizona', p. 57. Available at: http://www.geo.arizona.edu/Antevs/Theses/KowlerAL_07.pdf.

Liritzis, I., Stamoulis, K. and Ioannides (2013) 'A re-evaluation of radiation dose-rate conversion factors', *Mediterranean Archaeology and Archaeometry*, 13(3), pp. 1–15. Available at: http://www.nndc.bnl.gov (Accessed: 14 March 2022).

Machel, H. G. (2000) 'Application of Cathodoluminescence to Carbonate Diagenesis', in Pagel, M. et al. (eds) *Cathodoluminescence in Geosciences*. Springer Verlag Berlin Heidelberg, pp. 271–303.

Marcelino, V., Stoops, G. and Schaefer, C. E. G. R. (2010) 'Oxic and Related Materials', in *Interpretation of Micromorphological Features of Soils and Regoliths*, pp. 305–327.

Mentzer, S. M. and Quade, J. (2013) 'Compositional and Isotopic Analytical Methods in Archaeological Micromorphology', *Geoarchaeology*, 28(1), pp. 87–97. doi: 10.1002/gea.21425.

Mercader, J. *et al.* (2009) 'Phytoliths in woody plants from the Miombo woodlands of Mozambique', *Annals of Botany*, 104(1), pp. 91–113. doi: 10.1093/AOB/MCP097.

Mercader, J. *et al.* (2010) 'Poaceae phytoliths from the Niassa Rift, Mozambique', *Journal of Archaeological Science*, 37(8), pp. 1953–1967. doi: 10.1016/J.JAS.2010.03.001.

Mercader, J. *et al.* (2011) 'Soil phytoliths from miombo woodlands in Mozambique', *Quaternary Research*, 75(1), pp. 138–150. doi: 10.1016/J.YQRES.2010.09.008.

Mercader, J. *et al.* (2019) 'Soil and plant phytoliths from the Acacia-Commiphora mosaics at Oldupai Gorge (Tanzania)', *PeerJ*, 2019(12), p. e8211. doi: 10.7717/peerj.8211.

Nettleton, W. D. and Sleeman, J. R. (1985) 'Micromorphology of vertisols', in Douglas, L. A. and Thompson, M. L. (eds) *Soil micromorphology and soil classification: proceedings of a symposium*. Madison: S. S: S: A., pp. 165–196.

Pagel, M. *et al.* (2000) *(Eds .) Cathodoluminescence in Geosciences*. Springer.

Prescott, J. R. and Hutton, J. T. (1994) 'Cosmic ray contributions to dose rates for luminescence and ESR dating: Large depths and long-term time variations', *Radiation Measurements*, 23(2–3), pp. 497–500. doi: 10.1016/1350-4487(94)90086-8.

Quade, J. *et al.* (2007) 'Soils at the hyperarid margin: The isotopic composition of soil carbonate from the Atacama Desert, Northern Chile', *Geochimica et Cosmochimica Acta*, 71(15), pp. 3772–3795. doi: 10.1016/j.gca.2007.02.016.

Quade, J. and Cerling, T. E. (1995) 'Expansion of C4 grasses in the Late Miocene of Northern Pakistan: evidence from stable isotopes in paleosols', *Palaeogeography, Palaeoclimatology, Palaeoecology*, 115(1–4), pp. 91–116. doi: 10.1016/0031-0182(94)00108-K.

Ramsey, C. B., Scott, E. M. and van der Plicht, J. (2013) 'Calibration for Archaeological and Environmental Terrestrial Samples in the Time Range 26–50 ka cal BP', *Radiocarbon*, 55(4), pp. 2021–2027. doi: 10.2458/azu_js_rc.55.16935.

Schoeneberger, P. J. *et al.* (2012) *Field Book for Describing and Sampling Soils*. Version 3. Lincoln, NE: National Resources Conservation Service, National Soil Survey Center. doi: 10.1111/j.1600-0587.2009.05973.x.

Stoops, G. (2003) *Guidelines for Analysis and Description of soil regolith thin sections - Chpt.04 - p.33-56.pdf*. Edited by M. J. Vepraskas. Madison, Wisconsin, USA: Soil Science Society of America, Inc.

Thompson, J. C. *et al.* (2018) 'Ecological risk, demography and technological complexity in the Late Pleistocene of northern Malawi: implications for geographical patterning in the Middle Stone Age', *Journal of Quaternary Science*, 33(3), pp. 261–284. doi: 10.1002/jqs.3002.

Thompson, J. C. *et al.* (2021) 'Early human impacts and ecosystem reorganization in southern-central Africa', *Science Advances*, 7(9776), pp. 1–13. Available at: https://advances.sciencemag.org/content/7/19/eabf9776.

Thompson, J. C., Wright, D. K. and Ivory, S. J. (2021) 'The emergence and intensification of early hunter-gatherer niche construction', *Evolutionary Anthropology*, 30, pp. 17–27. doi: DOI: 10.1002/evan.21877.

Vogel, J. S. *et al.* (1984) 'Performance of catalytically condensed carbon for use in accelerator mass spectrometry.', *Nuclear Instruments & Methods*, 223(B5), pp. 289–293.

Wickham, H. *et al.* (2020) 'dplyr: A Grammar of Data Manipulation. R Package Version 1.0.2.' Available at: https://cran.r-project.org/package=dplyr.

Wright, V. P. (1990) 'A Micromorphological Classification of Fossil and Recent Calcic and Petrocalcic Microstructures', *Developments in Soil Science*, 19(C), pp. 401–407. doi: 10.1016/S0166-2481(08)70354-4.

Zamanian, K. (2017) *Recrystallization of pedogenic and biogenic carbonates in soil : Kazem Zamanian*. Goettingen.

Zanchetta, G. *et al.* (2000) 'Stable isotopes of pedogenic carbonates from the somma-vesuvius area, southern Italy,over the past 18 kyr: palaeoclimatic implications', *Journal of Quaternary Science*, 15(8), pp. 813–824. doi: 10.1002/1099-1417(200012)15:8<813::AID-JQS566>3.0.CO;2-Z.